INORGANIC MATERIALS FOR ENERGY AND ENVIRONMENTAL CATALYSIS

EDITED BY: Qingyi Zeng, Lai Lyu, Chong-Chen Wang, Zhu Xiong,
Suqing Wu and Shuaifei Zhao

PUBLISHED IN: Frontiers in Chemistry

frontiers Research Topics

ISSN 1664-8714
ISBN 978-2-88976-837-0
DOI 10.3389/978-2-88976-837-0

About Frontiers

Frontiers is more than just an open-access publisher of scholarly articles: it is a pioneering approach to the world of academia, radically improving the way scholarly research is managed. The grand vision of Frontiers is a world where all people have an equal opportunity to seek, share and generate knowledge. Frontiers provides immediate and permanent online open access to all its publications, but this alone is not enough to realize our grand goals.

Frontiers Journal Series

The Frontiers Journal Series is a multi-tier and interdisciplinary set of open-access, online journals, promising a paradigm shift from the current review, selection and dissemination processes in academic publishing. All Frontiers journals are driven by researchers for researchers; therefore, they constitute a service to the scholarly community. At the same time, the Frontiers Journal Series operates on a revolutionary invention, the tiered publishing system, initially addressing specific communities of scholars, and gradually climbing up to broader public understanding, thus serving the interests of the lay society, too.

Dedication to Quality

Each Frontiers article is a landmark of the highest quality, thanks to genuinely collaborative interactions between authors and review editors, who include some of the world's best academicians. Research must be certified by peers before entering a stream of knowledge that may eventually reach the public - and shape society; therefore, Frontiers only applies the most rigorous and unbiased reviews.

Frontiers revolutionizes research publishing by freely delivering the most outstanding research, evaluated with no bias from both the academic and social point of view. By applying the most advanced information technologies, Frontiers is catapulting scholarly publishing into a new generation.

What are Frontiers Research Topics?

Frontiers Research Topics are very popular trademarks of the Frontiers Journals Series: they are collections of at least ten articles, all centered on a particular subject. With their unique mix of varied contributions from Original Research to Review Articles, Frontiers Research Topics unify the most influential researchers, the latest key findings and historical advances in a hot research area! Find out more on how to host your own Frontiers Research Topic or contribute to one as an author by contacting the Frontiers Editorial Office: frontiersin.org/about/contact

INORGANIC MATERIALS FOR ENERGY AND ENVIRONMENTAL CATALYSIS

Topic Editors:
Qingyi Zeng, University of South China, China
Lai Lyu, Guangzhou University, China
Chong-Chen Wang, Beijing University of Civil Engineering and Architecture, China
Zhu Xiong, Guangzhou University, China
Suqing Wu, Wenzhou University, China
Shuaifei Zhao, Deakin University, Australia

Citation: Zeng, Q., Lyu, L., Wang, C-C., Xiong, Z., Wu, S., Zhao, S., eds. (2022).
Inorganic Materials for Energy and Environmental Catalysis.
Lausanne: Frontiers Media SA. doi: 10.3389/978-2-88976-837-0

Table of Contents

frontiers | Frontiers in Chemistry

TYPE Editorial
PUBLISHED 22 July 2022
DOI 10.3389/fchem.2022.977501

Check for updates

OPEN ACCESS

EDITED AND REVIEWED BY
Sukhendu Mandal,
Indian Institute of Science Education and Research, Thiruvananthapuram, India

*CORRESPONDENCE
Shuaifei Zhao,
s.zhao@deakin.edu.au
Qingyi Zeng,
qingyizeng@usc.edu.cn
Chong-Chen Wang,
wangchongchen@bucea.edu.cn

SPECIALTY SECTION
This article was submitted to Inorganic Chemistry,
a section of the journal
Frontiers in Chemistry

RECEIVED 24 June 2022
ACCEPTED 05 July 2022
PUBLISHED 22 July 2022

CITATION
Zhao S, Zeng Q and Wang C-C (2022), Editorial: Inorganic materials for energy and environmental applications.
Front. Chem. 10:977501.
doi: 10.3389/fchem.2022.977501

Editorial: Inorganic materials for energy and environmental applications

Shuaifei Zhao[1]*, Qingyi Zeng[2]* and Chong-Chen Wang[3]*

[1]Institute for Frontier Materials, Deakin University, Geelong, VIC, Australia, [2]School of Resources and Environment and Safety Engineering, University of South China, Hengyang, Hunan, China, [3]Beijing Key Laboratory of Functional Materials for Building Structure and Environment Remediation, Beijing University of Civil Engineering and Architecture, Beijing, China

KEYWORDS

heterogeneous catalysis, adsorption, energy conversion, pollutant removal, catalyst

Editorial on the ResearchTopic
Inorganic materials for energy andenvironmental applications

Inorganic materials have played significant roles in both energy conversion and environmental decontamination, relevant to chemical and environmental engineering. These inorganic materials are diverse, such as metals, metal oxides, nonmetallic oxides, sulphides, nitrides, phosphides and haloids. Inorganic materials often have high thermal stabilities, unique physicochemical properties and diverse nanostructures, making them highly desirable in various heterogeneous adsorption and catalytic applications (Goodman et al., 2020). As a result, they have been widely used as heterogeneous catalysts and/or adsorbents for CO_2 conversion, fuel production, pollutant degradation or adsorption (He et al., 2020; Yang et al., 2021). Figure 1 summarizes the typical applications of inorganic materials in the energy and environmental fields, including as catalysts (Kuang et al., 2020), electrodes (Li et al., 2020), adsorbents (Zito and Shipley, 2015) and membranes (Song et al., 2016) for energy conversion via oxidation/reduction, or environmental decontamination *via* adsorption, rejection, oxidation or reduction (Zeng et al., 2020; Xu et al., 2021).

Numerous metals and metal oxides have been employed as electro- or photo-catalysts for energy conversion and pollutant degradation. Qi et al. developed a porous Ti_4O_7 electrocatalytic membrane by employing Ti powder as the reducing agent to thermally reduce TiO_2 in vacuum. The prepared electrocatalytic membrane showed a high oxygen evolution potential (~2.7 V/SHE). Wang et al. develop a new iron cathode electro-Fenton process coupled with a pH-regulation divided electrolysis cell for p-nitrophenol degradation. In the electrochemical Fenton system, an iron plate was used as the cathode to inhibit the release of iron ions and promote the reduction of Fe^{3+} to Fe^{2+}. Therefore, excellent electrocatalytic degradation performance towards organic pollutants was achieved. Wang and Wang synthesized a NiO modified $BiVO_4$ nanocomposite by a hydrothermal and calcination method. The as-prepared nanocomposite showed enhanced photoelectrochemical performance due to the unique NiO lamellar structure that provided a large number of active sites.

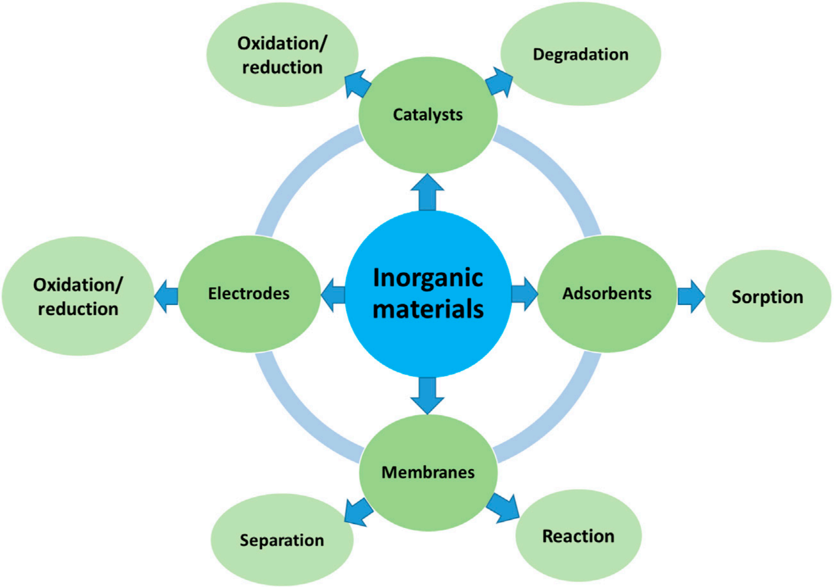

FIGURE 1
Typical applications of inorganic materials in the energy and environmental fields.

Wang et al. used a sol-gel self-combustion method to prepare carboxylate-rich carbon-modified Fe_3O_4 magnetic catalysts for heterogeneous Fenton degradation of organic pollutants. The prepared Fe_3O_4-based catalysts displayed improved heterogeneous Fenton degradation performance due to the enhanced pollutant adsorption. Zhu et al. synthesized a CdS/microcrystalline cellulose nanocomposite photocatalyst using an ultrasonic-assisted method. The prepared nanocomposite photocatalyst displayed enhanced pollutant degradation performance under visible light due to the heterojunction formation that efficiently separates the photogenerated electrons and holes of the photocatalyst. Wang et al. prepared a Co_3O_4/Ti cathode by electrodeposition for electrocatalytic reduction of nitrate, in which the NO_3^- was reduced to N_2 and NH_4^+ by the catalysis of Co_3O_4/Ti, and then NH_4^+ was selectively oxidized into N_2 assisted by chloride ions and using IrO_2-RuO_2/Ti as the anode. Qiu et al. prepared Pt-modified TiO_2 nanotubes as catalysts for photocatalytic degradation of Rhodamine B (RhB) under UV light. It was reported that the superoxide radical anions ($O_2^-\cdot$), photogenerated hole (h^+) and hydroxyl radical ($OH\cdot$) were the main active species contributing for RhB degradation.

In addition, metal and metal oxide based or modified materials have also been used for other catalytic applications. Bai et al. reported the Fischer–Tropsch synthesis performance of Co-based catalysts supported on graphitized ordered mesoporous carbon. The high catalytic performance resulted from the highly crystallized graphitic structure of the mesoporous carbon and the uniform dispersion of CoO on the support. Dai et al. used ion-exchange, *in situ* modification and complexation-excessive impregnation modification methods to modify SAPO-11 molecular sieves with Ni. The Ni-modified SAPO-11 molecular sieves were supported by NiWS catalysts for hydroisomerization of n-Hexadecane. The complexation-excessive impregnation modification method led to the best hydroisomerization performance. Huang et al. studied the effect of Ga_2O_3 on the hydrodesulfurization performance of 4,6-dimethyldibenzothiophene catalyzed by the stepwise impregnation method. Ga_2O_3 promoted Ni and Mo species to disperse uniformly and doping of more Ni atoms into the MoS_2 crystals, increasing the average stacking number and the length of MoS_2. As a result, enhanced hydrodesulfurization performance was achieved due to the formation of more NiMoS active phases in the system.

Adsorption is a simple but effective way for environmental decontamination (Zhang et al., 2018; Samadi et al., 2021). Various inorganic materials have been used for contaminant removal by adsorption. Zhang et al. prepared a series of nanostructured Fe-Cu binary oxides for arsenic removal. The crystallinity and structure of the Fe-Cu binary oxides had a significant impact on the arsenic adsorption performance. The oxides with lower crystallinity showed higher surface hydroxyl density and better adsorption performance. Li et al. reviewed the preparation, classification and applications of templated materials, particularly adsorbents in wastewater treatment. The templating method can endow materials with high specific area and unique porous structures, thereby enhancing the material sorption performance towards aqueous pollutants. Wei et al. reviewed the composite adsorbents for fluoride removal, including the adsorbent types (i.e., metal oxides/hydroxides, biopolymers, carbon-based, and others), preparation and sorption performance. The adsorption mechanisms for fluoride removal involving electrostatic attraction, ion exchange, complexation, and hydrogen bonding were also discussed.

Recently, with the promotion of the circular economy, waste based materials have attracted growing interest for various applications, such as fertilizers (Ye et al., 2019), carbon capture (Ji et al., 2018), membrane separation (Ni et al., 2022). Yu et al. prepared new biochar from excess sludge, followed by acetic acid modification. The modified sludge-derived biochar displayed improved porosity and enriched–COOH functional groups, thereby enhancing its adsorption performance to uranium. However, the catalytic performance of the sorbent was not discussed. Zeng et al. fabricated porous glass-ceramics based on coal fly ash without using pore forming agents by direct overfiring, in which borax was used to destroy the structure of quartz and amorphous vitreous body in coal fly ash and thus reduce the sintering temperature by the B-O bond. Chen et al. fabricated a non-sintered ceramsite from pyrite tailings for phosphorus removal. Both Plackett-Burman Design (PBD) and Box-Behnken Design (BBD) based response surface methodology were used to optimize the fabrication parameters.

Cellulase plays a key role in the production of fuel ethanol by enzymatic hydrolysis of lignocellulose, and immobilization of cellulase on the nanocarriers is an effective way to improve the hydrolysis efficiency. Wang et al. reviewed the significant roles of surfactants in oriented immobilization of cellulase on nanocarriers as well as a surfactant reversed micelle system.

In summary, this Research Topic discussed various inorganic materials as catalysts or adsorbents with unique nanostructures and functionalities for energy conversion and environmental decontamination. In the future, inorganic materials will continue to play a vital role in addressing global energy and environmental challenges, such as climate change, energy shortages and environmental pollution. Engineering new high performance heterogeneous catalysts and understanding the limiting factors and their mechanisms in the catalytic reaction are two key research directions that should be paid more attention to.

Author contributions

SZ, QZ and C-CW contributed to the writing of this editorial.

Conflict of interest

The authors declare that the research was conducted in the absence of any commercial or financial relationships that could be construed as a potential conflict of interest.

Publisher's note

References

Goodman, E. D., Zhou, C., and Cargnello, M. (2020). Design of organic/inorganic hybrid catalysts for energy and environmental applications. *ACS Cent. Sci.* 6 (11), 1916–1937. doi:10.1021/acscentsci.0c01046

He, Z., Mahmud, S., Yang, Y., Zhu, L., Zhao, Y., Zeng, Q., et al. (2020). Polyvinylidene fluoride membrane functionalized with zero valent iron for highly efficient degradation of organic contaminants. *Sep. Purif. Technol.* 250, 117266. doi:10.1016/j.seppur.2020.117266

Ji, L., Yu, H., Yu, B., Jiang, K., Grigore, M., Wang, X., et al. (2018). Integrated absorption–mineralisation for energy-efficient CO_2 sequestration: Reaction mechanism and feasibility of using fly ash as a feedstock. *Chem. Eng. J.* 352, 151–162. doi:10.1016/j.cej.2018.07.014

Kuang, H., He, Z., Li, M., Huang, R., Zhang, Y., Xu, X., et al. (2020). Enhancing co-catalysis of MoS_2 for persulfate activation in Fe^{3+}-based advanced oxidation processes via defect engineering. *Chem. Eng. J.* 417, 127987. doi:10.1016/j.cej.2020.127987

Li, C., Feng, G., Pan, Z., Song, C., Fan, X., Tao, P., et al. (2020). High-performance electrocatalytic microfiltration CuO/Carbon membrane by facile dynamic electrodeposition for small-sized organic pollutants removal. *J. Membr. Sci.* 601, 117913. doi:10.1016/j.memsci.2020.117913

Ni, T., You, Y., Xie, Z., Kong, L., Newman, B., Henderson, L., et al. (2022). Waste-derived carbon fiber membrane with hierarchical structures for enhanced oil-in-water emulsion separation: Performance and mechanisms. *J. Membr. Sci.* 653, 120543. doi:10.1016/j.memsci.2022.120543

Samadi, A., Xie, M., Li, J., Shon, H., Zheng, C., Zhao, S., et al. (2021). Polyaniline-based adsorbents for aqueous pollutants removal: A review. *Chem. Eng. J.* 418, 129425. doi:10.1016/j.cej.2021.129425

Song, H., Zhao, S., Chen, J., and Qi, H. (2016). Hydrothermally stable Zr-doped organosilica membranes for H_2/CO_2 separation. *Microporous Mesoporous Mater.* 224, 277–284. doi:10.1016/j.micromeso.2016.01.001

Xu, X., Zhang, Y., Zhou, S., Huang, R., Huang, S., Kuang, H., et al. (2021). Activation of persulfate by MnOOH: Degradation of organic compounds by nonradical mechanism. *Chemosphere* 272, 129629. doi:10.1016/j.chemosphere.2021.129629

Yang, Y., Xiong, Z., Wang, Z., Liu, Y., He, Z., Cao, A., et al. (2021). Super-adsorptive and photo-regenerable carbon nanotube based membrane for highly efficient water purification. *J. Membr. Sci.* 621, 119000. doi:10.1016/j.memsci.2020.119000

Ye, W., Liu, H., Jiang, M., Lin, J., Ye, K., Fang, S., et al. (2019). Sustainable management of landfill leachate concentrate through recovering humic substance as liquid fertilizer by loose nanofiltration. *Water Res.* 157, 555–563. doi:10.1016/j.watres.2019.02.060

Zeng, Q., Chang, S., Beyhaqi, A., Wang, M., and Hu, C. (2020). Efficient electricity production coupled with water treatment via a highly adaptable, successive water-energy synergistic system. *Nano Energy* 67, 104237. doi:10.1016/j.nanoen.2019.104237

Zhang, X., Fang, X., Li, J., Pan, S., Sun, X., Shen, J., et al. (2018). Developing new adsorptive membrane by modification of support layer with iron oxide microspheres for arsenic removal. *J. Colloid Interface Sci.* 514, 760–768. doi:10.1016/j.jcis.2018.01.002

Zito, P., and Shipley, H. J. (2015). Inorganic nano-adsorbents for the removal of heavy metals and arsenic: A review. *RSC Adv.* 5 (38), 29885–29907. doi:10.1039/c5ra02714d

ORIGINAL RESEARCH
published: 20 January 2022
doi: 10.3389/fchem.2021.840446

Efficient Sorption of Arsenic on Nanostructured Fe-Cu Binary Oxides: Influence of Structure and Crystallinity

Gaosheng Zhang*, Zhijing Wu, Qianying Qiu and Yuqi Wang*

Key Laboratory for Water Quality and Conservation of the Pearl River Delta, School of Environmental Science and Engineering, Ministry of Education, Guangzhou University, Guangzhou, China

To study the structure-performance relationship, a series of nanostructured Fe-Cu binary oxides (FCBOs) were prepared by varying synthesis conditions. The obtained binary oxides were well characterized using X-ray diffraction (XRD), transmission electron microscope (TEM), Brunner-Emmet-Teller (BET), magnetic and Zeta potential measurement techniques. Both As(V) and As(III) sorption on the FCBOs were evaluated by batch tests. Results show that the surface structure and crystallinity of FCBOs are greatly dependent on preparation conditions. The crystallinity of FCBOs gradually increases as the synthesis pH value increasing from 9.0 to 13.0, from amorphous phase to well-crystalline one. Simultaneously, the morphology change of FCBOs from irregular agglomerate to relatively uniform polyhedron has been observed. The sorption of arsenic is greatly influenced by the crystallinity and structure of FCBOs, decreasing with increasing degree of crystallinity. The amorphous FCBO has higher surface hydroxyl density than well-crystalline one, which might be the reason of higher sorption performance. As(V) is sorbed by the FCBOs via formation of inner-sphere surface complexes and As(III) is sorbed through formation of both inner- and outer-sphere surface complexes. This investigation provides new insights into structure-performance relationship of the FCBO system, which are beneficial to develop new and efficient sorbents.

Keywords: Fe-Cu binary oxide, arsenic, sorption, structure-performance relationship, crystallinity

Edited by:
Qingyi Zeng,
University of South China, China

Reviewed by:
Jingyang Luo,
Hohai University, China
Xia Ligang,
Shanghai University of Electric Power, China

****Correspondence:***
Gaosheng Zhang
gszhang@gzhu.edu.cn
Yuqi Wang
yqwang@gzhu.edu.cn

Specialty section:
This article was submitted to Inorganic Chemistry, a section of the journal Frontiers in Chemistry

Received: *21 December 2021*
Accepted: *31 December 2021*
Published: *20 January 2022*

Citation:
Zhang G, Wu Z, Qiu Q and Wang Y (2022) Efficient Sorption of Arsenic on Nanostructured Fe-Cu Binary Oxides: Influence of Structure and Crystallinity. Front. Chem. 9:840446. doi: 10.3389/fchem.2021.840446

INTRODUCTION

Arsenic contamination has emerged as one of global environmental issues in the last decades due to its high toxicity (Smedley and Kinniburgh, 2002). In natural waters, arsenic exists mainly in two inorganic forms as arsenate [As(V)] and arsenite [As(III)]. In view of the serious adverse effects of arsenic, a number of treatment techniques such as coagulation/precipitation, ion exchange, adsorption, membrane filtration and biological treatment, have been exploited for arsenic removal from drinking water and wastewater. Among them, adsorption is commonly and extensively used, due to its simplicity in operation, high efficiency and cost-effectiveness (Mohan and Pittman, 2007; Hu et al., 2015). Various adsorbents have been developed and used for arsenic removal (Mohan and Pittman, 2007). Recently, metal (hydr)oxides such as Fe (hydr)oxides (Sowers et al., 2017; Usman et al., 2020), feroxyhyte (Usman et al., 2021), Al oxides (Han et al., 2013; Mertens et al., 2016), TiO_2 (Guan et al., 2012; Yan et al., 2015), ZrO_2 (Hristovski et al., 2008; Cui et al., 2012; Shehzad et al., 2019), CeO_2 (Srivastava, 2010; Li et al., 2012), CuO

(Martinson and Reddy, 2009; Yu et al., 2012; Reddy et al., 2013) etc., have attracted considerable attention because they exhibit strong sorption properties towards arsenic.

More recently, composite sorbents containing two or more metal oxides have been emphasized for their enhanced sorption performance and synergistic effect. For example, an Fe-Mn binary oxide prepared by Zhang and coworkers demonstrates a greater enhancement in both As(V) and As(III) removal (Zhang et al., 2014); amorphous Fe-Ti bimetal oxides synthesized by Rao and coworkers have higher performance in both As(V) and As(III) removal than pure component oxides (Rao et al., 2015); a Ce-Mn binary oxide synthesized by Chen and coworkers exhibits higher arsenic removal efficiency than parent oxides (Chen et al., 2018); an Fe-Ni-Mn trimetal oxide reported by Nasir and coworkers is found to be efficient for As(III) removal (Nasir et al., 2018); an Fe-Cu-Mn trimetal oxide fabricated by Zhang and coworkers displays high sorption capacity for both As(V) and As(III) (Zhang et al., 2020).

Many literatures demonstrated that the sorption ability of metal oxides was strongly affected by their structure and crystallinity. Therefore, it is very necessary to study systemically the structure-performance relationship of synthesized metal oxides. Some researchers have investigated this relationship of single metal oxide system (Jegadeesan et al., 2010; Dou et al., 2016). However, very few researches have been done about binary metal oxide systems (Dou et al., 2018). In our previous study, a novel amorphous Fe (III)-Cu (II) binary oxide prepared with a Cu/Fe molar ratio of 1:2 was found to have high sorption ability towards arsenic (Zhang G et al., 2013). Moreover, it was superior to its parent components (ferrihydrite and cupric oxide) and crystalline $CuFe_2O_4$ (Tu et al., 2012; Wei et al., 2019). This Fe(III)-Cu(II) binary oxide system is very interesting because it can exist as a pure compound of $CuFe_2O_4$ or a mixture of ferrihydrite and cupric (hydr)oxide, depending on preparation conditions (Tu et al., 2012; Zhang G et al., 2013), which is very different from other binary systems (Zhang et al., 2014; Rao et al., 2015). Therefore, to investigate the structure-performance relationship of Fe(III)-Cu(II) binary oxide system is very vital, which will facilitate further understanding the arsenic sorption behaviors on binary oxide system and developing new composite adsorbents. To our best knowledge, until now, no information about the structure-performance relationship of Fe (III)-Cu (II) binary oxide is available in literatures.

Therefore, the main objectives of this study are 1) to synthesize a series of Fe-Cu binary oxides with different structure and crystallinity degree by varying the synthesis solution pH; 2) to characterize the morphology and crystallinity of as-synthesized binary oxides using a variety of techniques; 3) to evaluate the arsenic adsorption behavior and performance of binary oxides by batch tests; and finally 4) to investigate the structure-performance relationship of Fe-Cu binary oxide system.

MATERIALS AND METHODS

Materials

Analytical grade chemicals including $FeCl_3.6H_2O$, $CuSO_4.5H_2O$ and NaOH were purchased from Sinopharm Chemical Reagent Beijing Co., Ltd. (Beijing, China). They were directly used and no further purification was done. As (V) and As (III) stock solutions were prepared with deionized water using $Na_2HAsO_4.7H_2O$ and $NaAsO_2$, respectively. Arsenic working solutions were freshly prepared by diluting stock solutions with deionized water. Glass vessels were used as reactors. Before use, reactors were firstly cleaned using 1% HNO_3 solution and then washed several times with deionized water.

Preparation of Fe-Cu Binary Oxides (FCBOs)

A series of FCBOs with a Fe/Cu molar ratio of 2:1 were prepared at different pHs, according to a slightly modified method described by Zhang G et al. (2013). Specifically, about 10.8 g ferric chloride hexahydrate ($FeCl_3.6H_2O$) and 5.0 g copper (II) sulfate pentahydrate ($CuSO_4.5H_2O$) were dissolved in 400 ml deionized water. Under vigorous mechanical-stirring, NaOH solution (3 M) was added dropwise to raise the pH of mixture to a predetermined value (9.0 or 11.0 or 12.0 or 13.0). The formed suspensions were continuously stirred for 0.5 h, aged at 100°C for 6 h using a hot water bath. After cooling, the prepared suspensions were washed several times with distilled water. Afterwards, they were treated by filtration and dried at 55°C for about 24 h. The dried FCBOs were crushed into fine powders (0.5–50 μm) and stored in a desiccator. According to the synthesis pH value, these FCBOs are denoted as FC1, FC2, FC3, and FC4, respectively.

Characterization of FCBOs

X-ray diffraction analyses were performed on a Rigaku D/Max-3A diffractometer using Ni-filtered copper Kα one radiation (XRD, Rigaku, Japan). The morphology of FCBOs was analyzed using a transmission electron microscope (TEM, Hitachi H-800, Japan). Specific saturation magnetization (M_s) and magnetization remanence (M_r) measure of particles' magnetism, was determined using vibrating sample magnetometer at room temperature (VSM, Model 7,307 Lakeshore, United States). Specific surface area was determined by nitrogen adsorption (BET-method) using a surface area analyzer (Nova 2000e; Quantachrome Instruments, United States). A zeta potential analyzer (Zatasizer 2000; Malvern, UK) was used to analyze zeta potential of the FCBOs.

The density of surface hydroxyl sites was determined by a surface titration method (Dou et al., 2016). Fe-Cu binary oxide (0.3000 g) was added into 50 ml of 0.05 mol/L NaOH solution. Its accurate molar concentration was titrated using a 0.0500 mol/L Na_2CO_3 solution-calibrated HCl solution (0.0502 mol/L). After 4 h shaking at 130 rpm with the temperature maintained at 25°C, the mixture solution was passed through a 0.45 μm membrane. The filtrate was titrated using the HCl solution and residual NaOH in it was neutralized until pH up to 7.0, then the amount of surface hydroxyl can be calculated based on the amount of NaOH consumed.

Batch Sorption Experiments

A series of batch experiments were performed to investigate the sorption of arsenic on FCBOs. A certain amount of FCBO was put

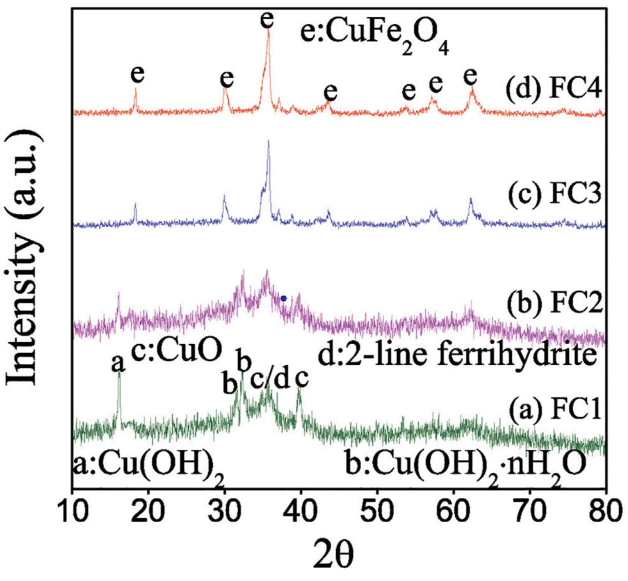

FIGURE 1 | X-ray diffraction patterns of the Fe-Cu binary oxides: (a) FC1, (b) FC2, (c) FC3 and (d) FC4. (a: $Cu(OH)_2$, b: $Cu(OH)_2 \cdot nH_2O$, c: CuO, d: 2-line ferrihydrite and e: $CuFe_2O_4$).

into 100 ml glass vessels containing 50 ml arsenic solution of different concentrations. The vessels were then oscillated on a shaker at 170 rpm for 24 h. After reaction, all samples collected were filtrated using 0.45 μm membrane and then were analyzed for arsenic. More detailed description of sorption experiments can be seen in the Supplementary Material.

Analytical Methods

Prior to arsenic analysis, the aqueous samples were diluted to a concentration below 100 μg/L, acidified with concentrated HNO_3, and stored in acid-washed glass vessels. Arsenic concentration was determined using an inductively coupled plasma mass spectrometry machine (ICP-MS, ELAN DRC II, Perkin Elmer Co. United States).

RESULTS AND DISCUSSION

Properties of the FCBOs

X-ray diffraction patterns of the as-prepared FCBOs are presented in **Figure 1**. For FC1, five broad peaks at approximately 16.2, 31.7, 32.3, 35.8 and 39.8° are observed. The characteristic peak at 16.2° belongs to the copper hydroxide ($Cu(OH)_2$) (JCPDS 80-0656); the peaks at 31.7 and 32.3° are attributed to the hydrated copper hydroxide ($Cu(OH)_2 \cdot nH_2O$) (JCPDS: 42-0638); the peak at 35.8° might be ascribed to both copper oxide (CuO) (JCPDS: 45-0937) and 2-line ferrihydrite formation (Hofmann et al., 2004); the peak at 39.8° might belong to the CuO (JCPDS: 45-0937). Obviously, the FC1 exists mainly as an amorphous mixture of 2-line ferrihydrite and copper (hydr)oxides. The X-ray diffraction pattern of FC2 is closely similar to that of FC1. However, the intensity of peaks belonging to copper hydrated hydroxide, hydroxide and oxide decreases with an increase in synthesis pH value. When the synthesis pH reaches 12.0 (FC3), these peaks disappear almost completely, and new diffraction peaks appear at 18.3, 30.0, 35.8, 43.6, 53.7, 57.8 and 62.4°, respectively. These characteristic peaks are attributed to the well-crystalline copper ferrite ($CuFe_2O_4$) (JCPDS: 34-0425). With a further increase in synthesis pH value from 12.0 to 13.0 (FC4), the intensity of these peaks increases, indicating a greater crystallinity.

Transmission electron micrographs (TEMs) of the FCBOs are shown in **Figure 2**. It can be seen that the FCBO particles produced at pH 9.0 (FC1, **Figure 2A**) are agglomerates of smaller nanoparticles. The morphology of FC2 (**Figure 2B**) is very similar to that of FC1. When the synthesis pH increases from 11.0 to 12.0, the major of amorphous particles (FC3, **Figure 2C**) becomes crystallized grains with visible grain boundaries and polyhedron shapes. For FC4 (**Figure 2D**), much more uniform grains are observed, suggesting well-crystalline $CuFe_2O_4$ particles are dominant under this condition. These results agree with those of XRD analysis.

The magnetic hysteresis curves of FCBOs are depicted in **Figure 3**. The hysteresis loops of FC3 and FC4 show a normal *S*-shape type, while those of FC1 and FC2 exhibit a nonhysteresis straight line, indicating that they are paramagnetic or superparamagnetic. The parameters of magnetic properties are summarized in **Table 1**. It can be seen that the saturation magnetization (M_s) increases with increasing synthesis pH value. For FC1 and FC2, they demonstrate very weak magnetism and the value of saturation magnetization is less than 0.4 emu/g. As the synthesis pH increases from 11.0 to 12.0, the saturation magnetization of FC3 rises sharply to 19.5 emu/g, which is far higher than that of FC2 and is very close to the $CuFe_2O_4$ nanoparticle (20.6 emu/g) synthesized via citrate-nitrate combustion method (Anandan et al., 2017). The magnetism of FC4 is the strongest and the saturation magnetization is as high as 26.9 emu/g. These results indicate that the magnetic properties of the FCBOs are closely related to their crystallinity.

The results of BET surface area measurements of the FCBOs are listed in **Table 1**. It can be clearly seen that the BET surface area of FCBOs decreases gradually with an increase in synthesis pH value. The BET surface area of FC1 is 268 m^2/g. However, the surface area of FC4 is only 90 m^2/g. It seems that the BET surface area of FCBOs is inversely proportional to its crystallinity.

Sorption Envelope

The influence of solution pH on arsenic sorption was investigated and the results are shown in **Figure 4**. For all FCBOs, the sorption of As (V) depends evidently on solution pH value. The greatest sorption occurs under acidic conditions and decreases with increasing solution pH, which is a typical characteristic for anions sorption by metal oxides and oxyhydroxides (Ren et al., 2011; Jordan et al., 2014). Over the tested pH range (3.0–11.0), As(V) mainly exists as negatively charged $H_2AsO_4^-$ and $HAsO_4^{2-}$ in water (pKa of dissociation is 2.20, 6.97 and 11.53, respectively). Under weak acidic conditions, the surface of the FCBO is positively charged because of protonation and $H_2AsO_4^-$ is dominant species in aqueous solution, which is beneficial for electrostatic attraction between the surface of FCBO and the

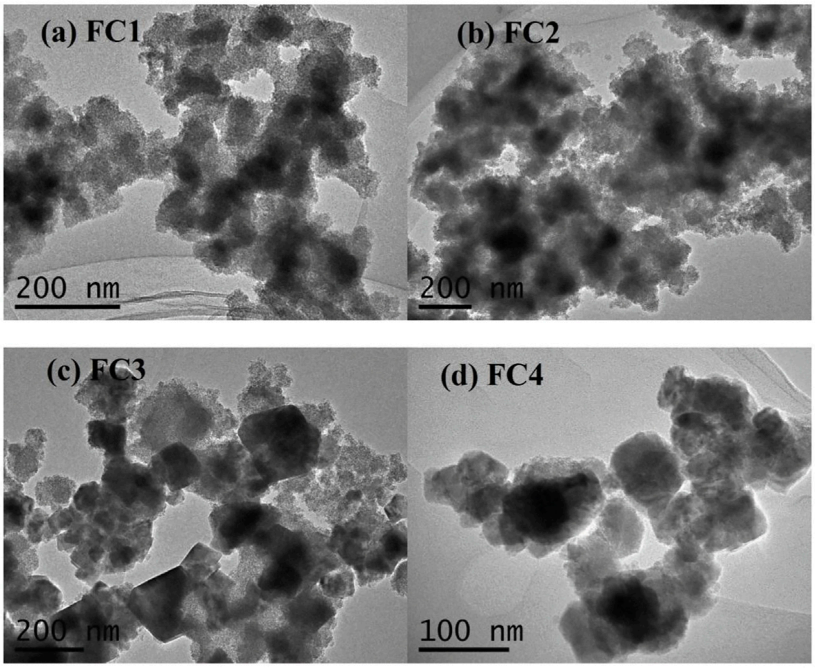

FIGURE 2 | TEM images of the Fe-Cu binary oxides: **(A)** FC1, **(B)** FC2, **(C)** FC3 and **(D)** FC4.

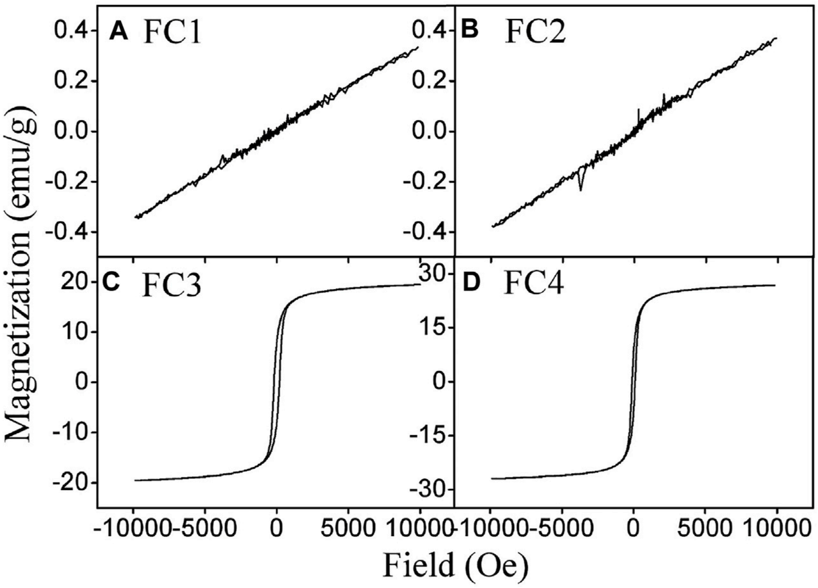

FIGURE 3 | Magnetization loops of the prepared Fe-Cu binary oxides: **(A)** FC1, **(B)** FC2, **(C)** FC3 and **(D)** FC4.

aqueous $H_2AsO_4^-$. With an increase in solution pH, the surface of FCBO becomes less positively charged and even negatively charged. At the same time, $HAsO_4^{2-}$ (a more negatively charged As (V) species) becomes to be dominant. Therefore, the attraction between the surface of FCBO and As (V) species weakens and as a consequence, As (V) sorption decreases.

Compared to As (V), the influence of solution pH on As (III) sorption is markedly different. Its sorption enhances gradually as solution pH increases and a maximum sorption occurs at about pH 9.1. Afterwards, further increase in pH decreases the sorption of As (III). Similar phenomena have been reported for the As (III) sorption by other binary metal oxides (Ren et al.,

TABLE 1 | Saturation magnetization and BET specific surface area of the as-prepared Fe-Cu binary oxide samples.

Samples	Synthesis pH	Saturation magnetization (emu g^{-1})	Specific surface area (m^2 g^{-1})
FC1	9.0	0.34	268
FC2	11.0	0.37	202
FC3	12.0	19.52	130
FC4	13.0	26.88	90

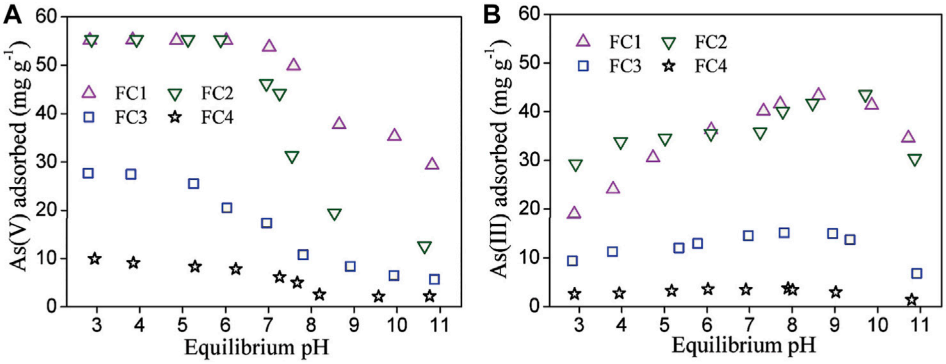

FIGURE 4 | Effect of solution pH on **(A)** As (V) and **(B)** As (III) sorption by Fe-Cu binary oxides. Initial arsenic concentration = 11.0 mg/L, adsorbent dose = 200 mg/L and T = 25 ± 1°C.

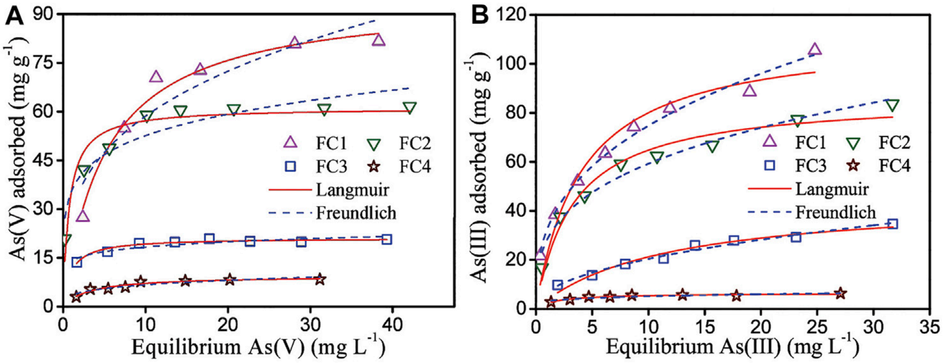

FIGURE 5 | Adsorption isotherm of **(A)** As (V) and **(B)** As (III) by Fe-Cu binary oxides. Initial arsenic concentration = 2–60 mg/L, adsorbent dose = 200 mg/L, pH = 7.0 ± 0.1 and T = 25 ± 1°C.

2011). Generally, a maximal sorption of weak acid anions onto metal oxides occurs at pH values close to pk_{a1} of the acid. The pk_{a1} of H_3AsO_3 is 9.2. The reduction in As (III) sorption at pH above 9.1 may be ascribed to the Coulombic repulsion between the negative surface of FCBOs (pH_{pzc} = 7.3-9.0) and negatively charged As (III), whereas the predominant form of As (III) species is $H_2AsO_3^-$.

Sorption Isotherm

The sorption isotherms of arsenic on the FCBOs are depicted in **Figure 5**. Obviously, the sorption of arsenic by the FCBO is closely related with its crystallinity. The FC1 has the strongest uptake ability for both As(V) and As(III) and the maximum sorption capacities are 83.3 and 112.2 mg/g at pH 7.0 (Langmuir model), respectively. The arsenic uptake ability of FCBOs decreases in the following order: FC1>FC2>FC3>FC4. Furtherly, the maximum sorption capacities of FC1 and FC2 are far larger than those of FC3 and FC4. The sorption performance of metal oxides depends generally on their surface area. However, the decrease in arsenic uptake by the FCBOs is not completely proportional to the reduction of specific surface area. This can be explained as follows. The specific surface area of the FCBOs is determined by N_2 molecule, which is smaller than the arsenic molecule. Partial surfaces of the FCBOs are inaccessible to arsenic molecule. Additionally, the As(V) and As(III) maximal sorption capacities

TABLE 2 | Langmuir and Freundlich isotherm parameters for As (V) and As (III) adsorption on Fe-Cu binary oxides at pH 7.0 ± 0.1.

Adsorbent	As species	Langmuir model			Freundlich model		
		q_{max} (mg/g)	K_L (L/mg)	R^2	K_F ($mg^{1-1/n}L^{1/n}g^{-1}$)	1/n	R^2
FC1	As(V)	83.3	0.19	0.977	58.9	0.31	0.844
FC2	As(V)	61.3	1.40	0.900	35.5	0.17	0.884
FC3	As(V)	21.1	1.03	0.935	14.0	0.12	0.806
FC4	As(V)	9.5	0.31	0.935	3.5	0.28	0.842
FC1	As(III)	112.2	0.25	0.936	32.6	0.36	0.988
FC2	As(III)	86.5	0.30	0.961	28.4	0.32	0.974
FC3	As(III)	45.3	0.09	0.959	6.9	0.47	0.980
FC4	As(III)	6.4	0.55	0.920	3.1	0.22	0.819

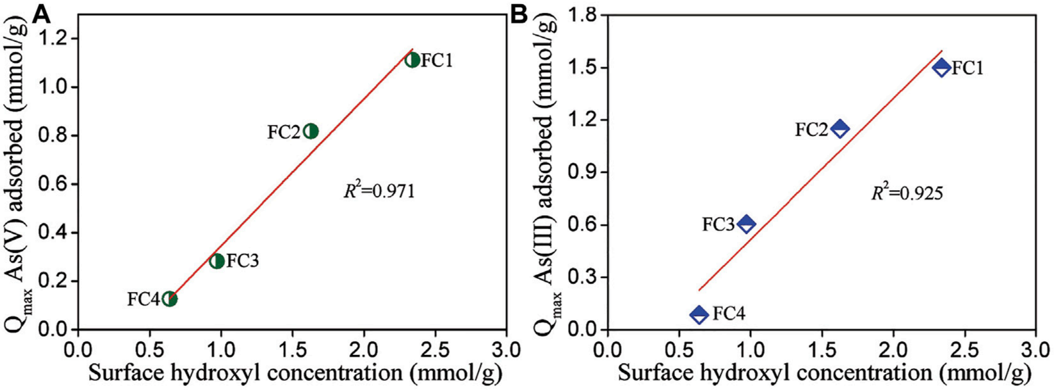

FIGURE 6 | Relationship between surface hydroxyl concentration and **(A)** As (V) and **(B)** As (III) adsorption capacities of Fe-Cu binary oxides.

of Fe-Cu binary oxide synthesized at pH 7.5 are 82.7 and 122.3 mg/g, respectively (Zhang G et al., 2013). Obviously, the arsenic sorption ability of FC1 is to very close to that of Fe-Cu binary oxide prepared under neutral condition.

Both Langmuir and Freundlich models (seen in the Supplementary Material) were employed to fit the isotherm data. The fitting results and obtained parameters are shown in **Figure 5** and **Table 2**, respectively.

For As (V), the Langmuir model is more favorable for fitting the data, giving higher correlation coefficients (R^2). However, the Freundlich model is more suitable to describe the adsorption of As(III) on Fe-Cu binary oxides except for FC4, according to the correlation coefficients. The As (V) adsorption is likely a monolayer adsorption because the Langmuir model supposes that the adsorption process is a monolayer adsorption. While As (III) adsorption is a multilayer adsorption since the Freundlich model presumes that adsorption occurs on the heterogeneous surface and follows multilayer adsorption.

Relationship Between Surface Hydroxyl Concentration and Arsenic Adsorption Capacity

The surface of metal oxides in water is easily hydroxylated, due to the dissociation of chemisorbed water molecules, and the formed surface hydroxyl groups are responsible for anions adsorption from water by the exchange with hydroxide ions (Tamura et al., 1999). To reveal the relationship between surface hydroxyl concentration and arsenic adsorption capacity of FCBOs, the amounts of surface hydroxyl groups were determined by titration method and the results are demonstrated in **Figure 6**. It can be seen that FC1 has the largest amount of surface hydroxyl groups per unit weight (2.34 mmol/g), followed by FC2 (1.63 mmol/g), FC3 (0.97 mmol/g), and FC4 (0.64 mmol/g). Evidently, surface hydroxyl concentration of FCBO is negatively correlated with its crystallinity. However, arsenic sorption capacity of FCBO is well positively correlated with its surface hydroxyl concentration. The data was fitted using a linear equation and the coefficient of determination (R^2) of linear regression for As (V) and As(III) is 0.971 and 0.925, respectively. It should be noted that the intercept is negative, indicating that not all surface hydroxyl groups are efficient for arsenic, especially for FCBO with high crystallinity. This could be explained as follows. The space structure of arsenic species ($H_2AsO_4^-$, $HAsO_4^{2-}$ or H_3AsO_3) is remarkably larger than that of hydrogen ions, which was used to determine the amounts of surface hydroxyl groups. Therefore, partial hydroxyl groups on the surfaces could not be available for the arsenic molecules. To some extent, the arsenic sorption capacity of FCBO could be evaluated by the amounts of surface hydroxyl groups.

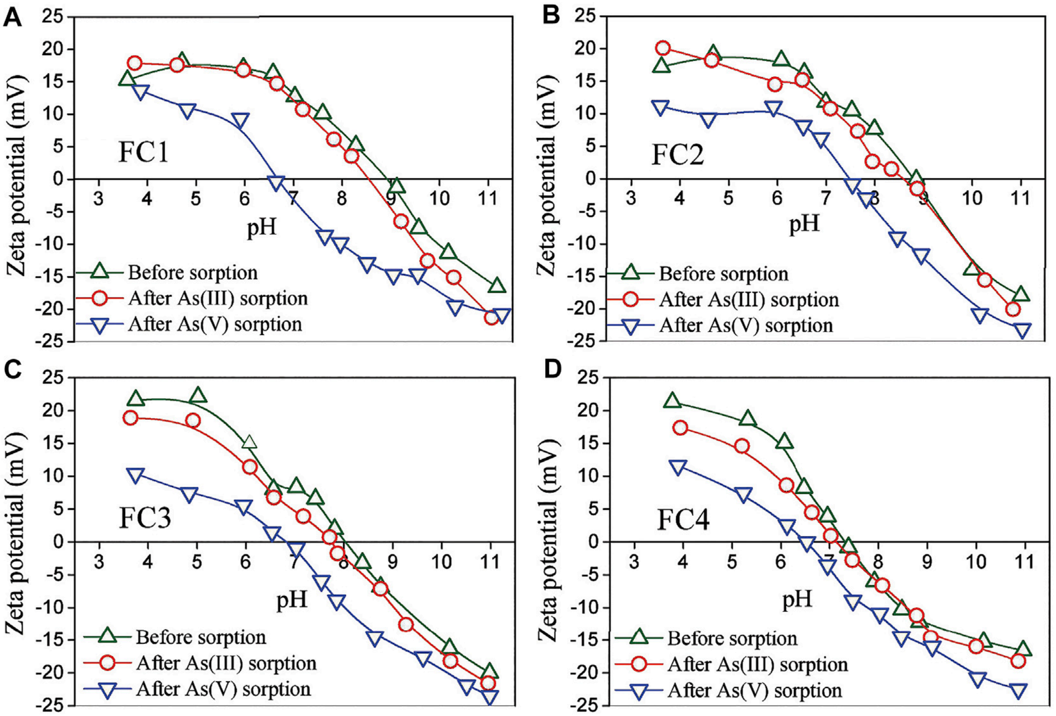

FIGURE 7 | Zeta potential of Fe-Cu binary oxides before and after arsenic adsorption. Initial arsenic concentration = 10 mg/L, adsorbent dose = 200 mg/L, ionic strength = 0.01 M $NaNO_3$, equilibrium time = 72 h.

Zeta Potential and FTIR Analysis Before and After Arsenic Adsorption

The zeta potentials of synthesized Fe-Cu binary oxides before and after reaction with arsenic were measured. As presented in **Figure 7**, the pH_{pzc} (pH at point of zero charge) of the virgin FC1, FC2, FC3 and FC4 were about 9.0, 8.8, 8.1 and 7.3, respectively. Evidently, the pH_{pzc} of the FCBOs decreases with increasing in crystallinity. This could be explained as follows. The pH_{pzc} values of CuO and $Cu(OH)_2$ are commonly over 9.2 (Martinson and Reddy, 2009; Kosmulski, 2009; Yu et al., 2012), and the pH_{pzc} of amorphous ferrihydrite is mostly in the range of 7.6–8.7 (Kosmulski, 2009; Antelo et al., 2010). As a mixture of these compounds, the amorphous FC1 and FC2 show relatively higher pH_{pzc} values. However, the crystalline $CuFe_2O_4$ illustrates a lower pH_{pzc} value, which is consistent with previously reported values (Zhang T et al., 2013; Tu et al., 2014; Sun et al., 2015). For the FC1, a remarkable decrease in pH_{pzc} value has been observed after reaction with As(V) and the pH_{pzc} of As(V)-adsorbed FC1 is about 6.7. Apparently, As (V) is specifically adsorbed by the FC1, since the specific sorption of anions leads to a shift of the pH_{pzc} of adsorbent to a lower pH value (Hsia et al., 1999; Ren et al., 2011). However, a slight decrease in pH_{pzc} of FC1 has been found after reaction with As(III). Commonly, the adsorption of uncharged As(III) species can not result a significant shift in pH_{pzc} of adsorbents (Ren et al., 2011). The slight decrease in pH_{pzc} might be explained as follows. A small part of As (III) adsorbed on the FC1 was oxidized to As(V) by the dissolved oxygen because the experiments were conducted in an open system and the present CuO content might catalyze this reaction. For the FC2, FC3 and FC4, similar phenomena have been observed.

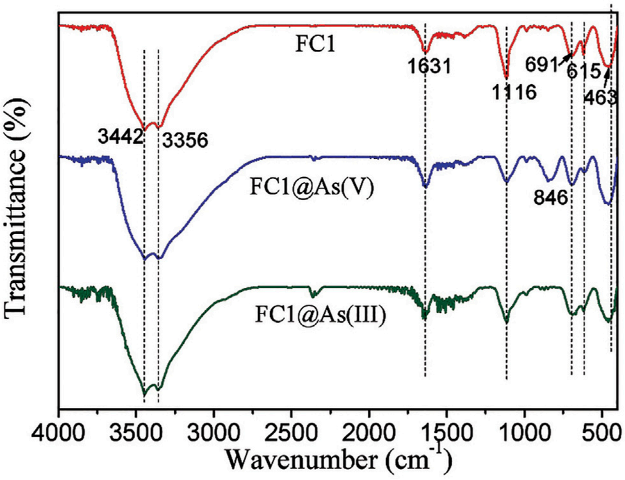

FIGURE 8 | FTIR spectra of Fe-Cu binary oxides before and after arsenic adsorption. Initial arsenic concentration = 10 mg/L, adsorbent dose = 200 mg/L, pH = 7.0 ± 0.1.

FTIR spectra of the FC1 before and after arsenic adsorption are depicted in **Figure 8**. For the pristine FC1, the peaks at 3,442 and 3,356 cm^{-1} may belong to the vibration of O-H stretching and the peak at 1,631 cm^{-1} may be ascribed to the deformation vibration of water molecules, implying that the surface of FC1 sorbed water molecules through physical adsorption; the peak at 1,116 cm^{-1} may be assigned to the vibration of SO_4^{2-} (Lefevre, 2004); the three peaks at 691, 615 and 463 cm^{-1} may be ascribed to the overlap of the HO- deformation vibration of ferrihydrite and Cu–O stretching (Kliche and Popovic, 1990). After As (V) adsorption, the intensity of peak at 1,116 cm^{-1} weakens and a new peak appears at 846 cm^{-1}, which may be due to the vibration (As-OH) of As-O-M groups (Goldberg and Johnston, 2001). This result suggests that the As (V) is mainly sorbed through the formation of inner-sphere surface complexes. While no significant change has been observed after As (III) adsorption. Similar phenomena were also observed for arsenic adsorption by other metal oxides (Ren et al., 2011).

Based on the analyses of zeta potentials and FTIR sepctra, it could be reasonably concluded that the As (V) is specifically sorbed by the FCBOs via formation of inner-sphere surface complexes, while As (III) is sorbed through formation of both inner- and outer-sphere surface complexes.

CONCLUSION

A series of Fe-Cu binary oxides were prepared under different solution pH values. The crystallinity and saturation magnetization of prepared Fe-Cu binary oxide increased with an increase in synthetic pH value. Simultaneously, the morphology of FCBO changed gradually from irregular agglomerate to relatively uniform polyhedron. The adsorption of arsenic on FCBOs is remarkably affected by the surface structure and crystallinity, decreasing as the degree of crystallinity increases. Surface hydroxyl density of FCBOs is an important parameter to evaluate its arsenic adsorption ability. Nevertheless, the adsorption ability may be overestimated if only this parameter is used. As (V) is sorbed by the FCBOs via formation of inner-sphere surface complexes and As (III) is sorbed through formation of both inner- and outer-sphere surface complexes. This investigation provides new insights into structure-performance relationship of FCBOs system, which are beneficial to develop new and efficient sorbents. However, the characterization of FCBOs is still not insufficient in this study and more powerful techniques such as X-Ray Absorption Fine Structure (XAFS) are needed to reveal further the structure-performance relationship of FCBOs system in future study.

DATA AVAILABILITY STATEMENT

The original contributions presented in the study are included in the article/**Supplementary Material** further inquiries can be directed to the corresponding authors.

AUTHOR CONTRIBUTIONS

GZ: Conceptualization, Writing—Original draft preparation. ZW: Investigation, Formal analysis. QQ: Investigation. YW: Conceptualization, Writing—Reviewing and Editing.

ACKNOWLEDGMENTS

The authors acknowledge financial support by Guangzhou Science and Technology Project (202102010385) and Rural Revitalization Strategy Project from the Department of Science and Technology of Guangdong Province(620096-3).

SUPPLEMENTARY MATERIAL

The Supplementary Material for this article can be found online at: https://www.frontiersin.org/articles/10.3389/fchem.2021.840446/full#supplementary-material

REFERENCES

Anandan, S., Selvamani, T., Prasad, G. G., M. Asiri, A. A., and J. Wu, J. (2017). Magnetic and Catalytic Properties of Inverse Spinel $CuFe_2O_4$ Nanoparticles. *J. Magnetism Magn. Mater.* 432, 437–443. doi:10.1016/j.jmmm.2017.02.026

Antelo, J., Fiol, S., Pérez, C., Mariño, S., Arce, F., Gondar, D., et al. (2010). Analysis of Phosphate Adsorption onto Ferrihydrite Using the CD-MUSIC Model. *J. Colloid Interf. Sci.* 347 (1), 112–119. doi:10.1016/j.jcis.2010.03.020

Chen, J., Wang, J., Zhang, G., Wu, Q., and Wang, D. (2018). Facile Fabrication of Nanostructured Cerium-Manganese Binary Oxide for Enhanced Arsenite Removal from Water. *Chem. Eng. J.* 334, 1518–1526. doi:10.1016/j.cej.2017.11.062

Cui, H., Li, Q., Gao, S., and Shang, J. K. (2012). Strong Adsorption of Arsenic Species by Amorphous Zirconium Oxide Nanoparticles. *J. Ind. Eng. Chem.* 18 (4), 1418–1427. doi:10.1016/j.jiec.2012.01.045

Dou, X., Li, Y., Mohan, D., Pittman, C. U., and Hu, M. (2016). A Property-Performance Correlation and Mass Transfer Study of As(v) Adsorption on Three Mesoporous Aluminas. *RSC Adv.* 6 (84), 80630–80639. doi:10.1039/c6ra14408j

Dou, X., Wang, G.-C., Zhu, M., Liu, F., Li, W., Mohan, D., et al. (2018). Identification of Fe and Zr Oxide Phases in an Iron-Zirconium Binary Oxide and Arsenate Complexes Adsorbed onto Their Surfaces. *J. Hazard. Mater.* 353, 340–347. doi:10.1016/j.jhazmat.2018.04.004

Goldberg, S., and Johnston, C. T. (2001). Mechanisms of Arsenic Adsorption on Amorphous Oxides Evaluated Using Macroscopic Measurements, Vibrational Spectroscopy, and Surface Complexation Modeling. *J. Colloid Interf. Sci.* 234, 204–216. doi:10.1006/jcis.2000.7295

Guan, X., Du, J., Meng, X., Sun, Y., Sun, B., and Hu, Q. (2012). Application of Titanium Dioxide in Arsenic Removal from Water: A Review. *J. Hazard. Mater.* 215-216, 1–16. doi:10.1016/j.jhazmat.2012.02.069

Han, C., Li, H., Pu, H., Yu, H., Deng, L., Huang, S., et al. (2013). Synthesis and Characterization of Mesoporous Alumina and Their Performances for Removing Arsenic(V). *Chem. Eng. J.* 217, 1–9. doi:10.1016/j.cej.2012.11.087

Hofmann, A., Pelletier, M., Michot, L., Stradner, A., Schurtenberger, P., and Kretzschmar, R. (2004). Characterization of the Pores in Hydrous Ferric Oxide Aggregates Formed by Freezing and Thawing. *J. Colloid Interf. Sci.* 271, 163–173. doi:10.1016/j.jcis.2003.11.053

Hristovski, K. D., Westerhoff, P. K., Crittenden, J. C., and Olson, L. W. (2008). Arsenate Removal by Nanostructured ZrO_2 Spheres. *Environ. Sci. Technol.* 42 (10), 3786–3790. doi:10.1021/es702952p

Hsia, T.-H., Lo, S.-L., Lin, C.-F., and Lee, D.-Y. (1994). Characterization of Arsenate Adsorption on Hydrous Iron Oxide Using Chemical and Physical Methods. *Colloids Surf. A: Physicochem. Eng. Aspects* 85, 1–7. doi:10.1016/0927-7757(94)02752-8

Hu, X., Ding, Z., Zimmerman, A. R., Wang, S., and Gao, B. (2015). Batch and Column Sorption of Arsenic onto Iron-Impregnated Biochar Synthesized through Hydrolysis. *Water Res.* 68, 206–216. doi:10.1016/j.watres.2014.10.009

Jegadeesan, G., Al-Abed, S. R., Sundaram, V., Choi, H., Scheckel, K. G., and Dionysiou, D. D. (2010). Arsenic Sorption on TiO_2 Nanoparticles: Size and Crystallinity Effects. *Water Res.* 44 (3), 965–973. doi:10.1016/j.watres.2009.10.047

Jordan, N., Ritter, A., Scheinost, A. C., Weiss, S., Schild, D., and Hübner, R. (2014). Selenium(IV) Uptake by Maghemite (γ-Fe2O3). *Environ. Sci. Technol.* 48 (3), 1665–1674. doi:10.1021/es4045852

Kliche, G., and Popovic, Z. V. (1990). Far-infrared Spectroscopic Investigations on CuO. *Phys. Rev. B* 42, 10060–10066. doi:10.1103/physrevb.42.10060

Kosmulski, M. (2009). Compilation of PZC and IEP of Sparingly Soluble Metal Oxides and Hydroxides from Literature. *Adv. Colloid Interf. Sci* 152 (1), 14–25. doi:10.1016/j.cis.2009.08.003

Lefèvre, G. (2004). *In Situ* fourier-transform Infrared Spectroscopy Studies of Inorganic Ions Adsorption on Metal Oxides and Hydroxides. *Adv. Colloid Interf. Sci.* 107, 109–123. doi:10.1016/j.cis.2003.11.002

Li, R., Li, Q., Gao, S., and Shang, J. K. (2012). Exceptional Arsenic Adsorption Performance of Hydrous Cerium Oxide Nanoparticles: Part A. Adsorption Capacity and Mechanism. *Chem. Eng. J.* 185-186, 127–135. doi:10.1016/j.cej.2012.01.061

Martinson, C. A., and Reddy, K. J. (2009). Adsorption of Arsenic(III) and Arsenic(V) by Cupric Oxide Nanoparticles. *J. Colloid Interf. Sci.* 336 (2), 406–411. doi:10.1016/j.jcis.2009.04.075

Mertens, J., Rose, J., Wehrli, B., and Furrer, G. (2016). Arsenate Uptake by Al Nanoclusters and Other Al-Based Sorbents during Water Treatment. *Water Res.* 88, 844–851. doi:10.1016/j.watres.2015.11.018

Mohan, D., and Pittman, C. U. (2007). Arsenic Removal from Water/wastewater Using Adsorbents--A Critical Review. *J. Hazard. Mater.* 142 (1), 1–53. doi:10.1016/j.jhazmat.2007.01.006

Nasir, A. M., Goh, P. S., and Ismail, A. F. (2018). Novel Synergistic Hydrous Iron-Nickel-Manganese (HINM) Trimetal Oxide for Hazardous Arsenite Removal. *Chemosphere* 200, 504–512. doi:10.1016/j.chemosphere.2018.02.126

Rao, P., Sun, Z., Zhang, W., Yao, W., Wang, L., and Ding, G. (2015). Preparation and Application of Amorphous Fe-Ti Bimetal Oxides for Arsenic Removal. *RSC Adv.* 5 (109), 89545–89551. doi:10.1039/c5ra12039j

Reddy, K. J., McDonald, K. J., and King, H. (2013). A Novel Arsenic Removal Process for Water Using Cupric Oxide Nanoparticles. *J. Colloid Interf. Sci.* 397, 96–102. doi:10.1016/j.jcis.2013.01.041

Ren, Z., Zhang, G., and Paul Chen, J. (2011). Adsorptive Removal of Arsenic from Water by an Iron-Zirconium Binary Oxide Adsorbent. *J. Colloid Interf. Sci.* 358 (1), 230–237. doi:10.1016/j.jcis.2011.01.013

Shehzad, K., Ahmad, M., Xie, C., Zhan, D., Wang, W., Li, Z., et al. (2019). Mesoporous Zirconia Nanostructures (MZN) for Adsorption of As(III) and As(V) from Aqueous Solutions. *J. Hazard. Mater.* 373, 75–84. doi:10.1016/j.jhazmat.2019.01.021

Smedley, P. L., and Kinniburgh, D. G. (2002). A Review of the Source, Behaviour and Distribution of Arsenic in Natural Waters. *Appl. Geochem.* 17 (5), 517–568. doi:10.1016/s0883-2927(02)00018-5

Sowers, T. D., Harrington, J. M., Polizzotto, M. L., and Duckworth, O. W. (2017). Sorption of Arsenic to Biogenic Iron (Oxyhydr)oxides Produced in Circumneutral Environments. *Geochim. Cosmochim. Acta* 198, 194–207. doi:10.1016/j.gca.2016.10.049

Srivastava, R. (2010). Eco-friendly and Morphologically-Controlled Synthesis of Porous CeO_2 Microstructure and its Application in Water Purification. *J. Colloid Interf. Sci.* 348 (2), 600–607. doi:10.1016/j.jcis.2010.04.076

Sun, W., Pan, W., Wang, F., and Xu, N. (2015). Removal of Se(IV) and Se(VI) by MFe_2O_4 Nanoparticles from Aqueous Solution. *Chem. Eng. J.* 273, 353–362. doi:10.1016/j.cej.2015.03.061

Tamura, H., Tanaka, A., Mita, K.-Y., and Furuichi, R. (1999). Surface Hydroxyl Site Densities on Metal Oxides as a Measure for the Ion-Exchange Capacity. *J. Colloid Interf. Sci.* 209 (1), 225–231. doi:10.1006/jcis.1998.5877

Tu, Y.-J., You, C.-F., Chang, C.-K., Wang, S.-L., and Chan, T.-S. (2012). Arsenate Adsorption from Water Using a Novel Fabricated Copper Ferrite. *Chem. Eng. J.* 198-199, 440–448. doi:10.1016/j.cej.2012.06.006

Tu, Y.-J., You, C.-F., Chang, C.-K., Chan, T.-S., and Li, S.-H. (2014). XANES Evidence of Molybdenum Adsorption onto Novel Fabricated Nano-Magnetic $CuFe_2O_4$. *Chem. Eng. J.* 244, 343–349. doi:10.1016/j.cej.2014.01.084

Usman, M., Zarebanadkouki, M., Waseem, M., Katsoyiannis, I. A., and Ernst, M. (2020). Mathematical Modeling of Arsenic(V) Adsorption onto Iron Oxyhydroxides in an Adsorption-Submerged Membrane Hybrid System. *J. Hazard. Mater.* 400, 123221. doi:10.1016/j.jhazmat.2020.123221

Usman, M., Belkasmi, A. I., Kastoyiannis, I. A., and Ernst, M. (2021). Pre-deposited Dynamic Membrane Adsorber Formed of Microscale Conventional Iron Oxide-based Adsorbents to Remove Arsenic from Water: Application Study and Mathematical Modeling. *J. Chem. Technol. Biotechnol.* 96, 1504–1514. doi:10.1002/jctb.6728

Wei, Y., Liu, H., Liu, C., Luo, S., Liu, Y., Yu, X., et al. (2019). Fast and Efficient Removal of As(III) from Water by $CuFe_2O_4$ with Peroxymonosulfate: Effects of Oxidation and Adsorption. *Water Res.* 150, 182–190. doi:10.1016/j.watres.2018.11.069

Yan, L., Huang, Y., Cui, J., and Jing, C. (2015). Simultaneous As(III) and Cd Removal from Copper Smelting Wastewater Using Granular TiO_2 Columns. *Water Res.* 68, 572–579. doi:10.1016/j.watres.2014.10.042

Yu, X.-Y., Xu, R.-X., Gao, C., Luo, T., Jia, Y., Liu, J.-H., et al. (2012). Novel 3D Hierarchical Cotton-candy-like CuO: Surfactant-free Solvothermal Synthesis and Application in As(III) Removal. *ACS Appl. Mater. Inter.* 4 (4), 1954–1962. doi:10.1021/am201663d

Zhang, G., Liu, F., Liu, H., Qu, J., and Liu, R. (2014). Respective Role of Fe and Mn Oxide Contents for Arsenic Sorption in Iron and Manganese Binary Oxide: An X-ray Absorption Spectroscopy Investigation. *Environ. Sci. Technol.* 48 (17), 10316–10322. doi:10.1021/es501527c

Zhang, G., Liu, Y., Wang, J., and Li, H. (2020). Efficient Arsenic(III) Removal from Aqueous Solution by a Novel Nanostructured Iron-Copper-Manganese Trimetal Oxide. *J. Mol. Liquids* 309, 112993. doi:10.1016/j.molliq.2020.112993

Zhang G, G., Ren, Z., Zhang, X., and Chen, J. (2013). Nanostructured Iron(III)-Copper(II) Binary Oxide: A Novel Adsorbent for Enhanced Arsenic Removal from Aqueous Solutions. *Water Res.* 47 (12), 4022–4031. doi:10.1016/j.watres.2012.11.059

Zhang T, T., Zhu, H., and Croué, J.-P. (2013). Production of Sulfate Radical from Peroxymonosulfate Induced by a Magnetically Separable $CuFe_2O_4$ Spinel in Water: Efficiency, Stability, and Mechanism. *Environ. Sci. Technol.* 47 (6), 2784–2791. doi:10.1021/es304721g

Conflict of Interest: The authors declare that the research was conducted in the absence of any commercial or financial relationships that could be construed as a potential conflict of interest.

frontiers in Chemistry

ORIGINAL RESEARCH
published: 28 January 2022
doi: 10.3389/fchem.2021.837761

An Eco-friendly Iron Cathode Electro-Fenton System Coupled With a pH-Regulation Electrolysis Cell for p-nitrophenol Degradation

Xiaohui Wang[1,2]*, *Jingang Zhao*[1,2], *Chunyan Song*[1,2], *Xian Shi*[1,2] and *Haipeng Du*[1,2]

[1]*Technical Test Center of Sinopec Shengli OilField, Dongying, China,* [2]*Shengli Oilfield Testing and Evaluation Research Co., Ltd., SINOPEC, Dongying, China*

The high consumption of salt reagents and strict pH control are still bottlenecks for the full-scale application of the Fenton reaction. In this work, a novel eco-friendly iron cathode electrochemical Fenton (ICEF) system coupled with a pH-regulation divided electrolysis cell was developed. In a pH-regulation divided electrolysis system, the desired pH for an effective Fenton reaction and for a neutral treated media could be obtained by H_2O splitting into H^+ and OH^- at the anode and cathode, respectively. In an ICEF system, an iron plate was used as the cathode to inhibit the release of iron ions and promote the reduction of Fe^{3+} to Fe^{2+}. It was found that when a potential of 1.2 V/SCE was applied on the iron cathode, 98% of p-nitrophenol was removed in the combined system after 30 min with continuously adding 200 mg/L of H_2O_2. Meanwhile, a COD and TOC removal efficiency of 79 and 60% was obtained, respectively. In this case, the conductivity just slightly increased from 4.35 to 4.37 mS/cm, minimizing the increase of water salinity, as compared with the conventional Fenton process. Generally, this combined system was eco-friendly, energy-efficient, and has the potential of being a promising technology for the removal of bio-refractory organic pollutants from wastewaters.

Keywords: pH-regulation, electrolysis, iron cathode, electro-fenton, salt

Edited by:
Suqing Wu,
Wenzhou University, China

Reviewed by:
Fuzhen Liu,
Hubei University, China
Weilu Yang,
Jinan University, China
Shuaijun Wang,
Jiangsu University, China

***Correspondence:**
Xiaohui Wang
wangxiaohui153.slyt@sinopec.com

Specialty section:
This article was submitted to Inorganic Chemistry, a section of the journal Frontiers in Chemistry

Received: *17 December 2021*
Accepted: *20 December 2021*
Published: *28 January 2022*

Citation:
Wang X, Zhao J, Song C, Shi X and Du H (2022) An Eco-friendly Iron Cathode Electro-Fenton System Coupled With a pH-Regulation Electrolysis Cell for p-nitrophenol Degradation. Front. Chem. 9:837761. doi: 10.3389/fchem.2021.837761

INTRODUCTION

Over the past few decades, advanced oxidation processes (AOPs) have attracted increasing interests for wastewater treatment since the highly oxidative hydroxyl radical ($^{\bullet}OH$, $E^0 = 2.80$ V/SHE) was generated *in situ* and found to be capable of degrading any refractory organic molecules present in the aqueous solution until total mineralization at the kinetic constant values as high as 10^8~10^{10} $M^{-1}s^{-1}$ (Andreozzi et al., 1999; Oturan and Aaron, 2014; Gao et al., 2018). Among various AOPs, the conventional Fenton reaction process has been most widely applied for the treatment of wastewater streams because it exhibits the advantages of fast reaction rates, mild operating conditions, and simplicity to control (Bello et al., 2019). The Fenton reaction mainly proceeds via two steps (Neyens and Baeyens, 2003; Moreira et al., 2017; Gao et al., 2020). The first stage is characterized by the rapid formation of •OH from the homogeneous reaction between Fe^{2+} and H_2O_2 (**Eq. 1**), most of the pollutant degradation is achieved in this stage. The second stage is characterized by a slow reaction between Fe^{3+} and H_2O_2 for the regeneration of Fe^{2+} (**Eq. 2**), maintaining the continuous Fenton reaction (Babuponnusami and Muthukumar, 2014; Bello et al., 2019).

$$Fe^{2+} + H_2O_2 \rightarrow Fe^{3+} + OH^- + {}^{\bullet}OH \quad k_1 = 63 - 76\left(L\,mol^{-1}s^{-1}\right) \tag{1}$$

$$Fe^{3+} + H_2O_2 \rightarrow Fe^{2+} + {}^{\bullet}HO_2 + H^+ \quad k_2 = 0.001 - 0.01\left(L\,mol^{-1}s^{-1}\right) \tag{2}$$

However, the Fenton process has some drawbacks, which greatly hamper its industrial application (Babuponnusami and Muthukumar, 2014; Gao et al., 2020). The addition of concentrated acid reagent is indispensable to adjust the solution pH to ~3.0, that is the optimum condition for the Fenton reaction. However, working in such acidic pH requires the addition of a large amount of acid. In addition, massive alkaline reagents were also consumed for the subsequent neutralization of the treated solution. In addition, the employment of iron salt inevitably increases water salinity (Li et al., 2013). The increased salt content probably makes this wastewater unacceptable for natural environments or poses significant pressure on the subsequent reverse osmosis unit (Wang et al., 2014; Fang et al., 2018). Besides, most of the Fenton reagents are added at once while over-dosage of either H_2O_2 or iron ions would lead to side reactions (**Eq. 3** and **Eq. 4**). As a result, Fe^{3+} is massively accumulated from the oxidation of Fe^{2+} in the Fenton reaction system since Fe^{2+} regeneration from Fe^{3+} is very slow (Qiang et al., 2003). Thus, the reduction of Fe^{3+} to Fe^{2+} greatly limits the treatment performance of the Fenton reaction for pollutants degradation.

$$Fe^{2+} + {}^{\bullet}OH \rightarrow Fe^{3+} + OH^- \quad k3 = 3.2 \times 10^8 \left(L\,mol^{-1}s^{-1}\right) \tag{3}$$

$${}^{\bullet}OH + H_2O_2 \rightarrow {}^{\bullet}HO_2 + H_2O \quad k_4 = 3.3 \times 10^7 \left(L\,mol^{-1}s^{-1}\right) \tag{4}$$

Over the recent decades, there has been growing interest in the research community to address the above limitations of the conventional Fenton process. The development of a heterogeneous Fenton system has been demonstrated to be a feasible strategy to avoid salt reagents addition, where iron oxides and other metal oxides such as goethite (α-FeOOH), magnetite (Fe_3O_4), hematite (α-Fe_2O_3), and maghemite (γ-Fe_2O_3) have been commonly utilized as heterogeneous catalysts (Davarnejad and Azizi, 2016; He et al., 2016; Hassani et al., 2018; Görmez et al., 2019; Cai et al., 2021; Chen et al., 2021). Unlike the homogenous Fenton system, in a heterogeneous Fenton system, iron sources are immobilized within/on the catalyst structure, and the Fenton reaction occurs when the H_2O_2 molecule is in contact with the iron sites of the carrier, so that it is not necessary to continuously add the iron salts and pH limitation is reduced to some extent (Ganiyu et al., 2018; Cai et al., 2021; Hu et al., 2021). In spite of this, the most heterogeneous Fenton catalysts still operate optimally at pH 3–5 and its catalytic performance is reduced in near-neutral water bodies because the catalyst turnover frequency is reduced by up to 100-fold under neutral conditions (Cai et al., 2021; Chen et al., 2021).

Electro-Fenton is an emerging technology with well-known outstanding oxidation power, where the electron is utilized as the reagent to facilitate the regeneration of Fe^{2+} at the cathode (**Eq. 5**). Thus, this process exhibits higher performance in comparison with the conventional Fenton system because of the high utilization efficiency of Fe^{2+} (Oturan et al., 2000; Yuan et al., 2006; Brillas et al., 2009). Consequently, much more •OH can be produced at a much smaller amount of iron salt addition. In fact, the addition of iron salts can be completely avoided with using a metal iron plate as the sacrificial anode material, where the electrochemically released Fe^{2+} can serve as the Fenton catalyst. In spite of this, the produced ferric sludge amount cannot be controlled effectively. Besides, concentrated acid and basic reagents are still required to regulate the solution pH. In fact, in the typical electrolysis system, OH^- and H^+ are produced at the cathode and anode, respectively, which can be separated well in the divided electrolysis cell. Inspired by this characteristic, the divided electrolysis cell can be used as the pH-regulation unit before and after the Fenton system to automatically acidify and neutralize the wastewaters without the requirement of chemicals. Besides, in the acid solution, the acidic dissolution of the metal iron plate can release the iron ions into the solution. Under the cathodic polarization of metal iron, the released iron ion amount can be well regulated. At the same time, Fe^{3+} can be also reduced to Fe^{2+} at the iron cathode. These collectively eliminate the limitations of the conventional Fenton process and promote its treatment efficiency for pollutants.

$$Fe^{3+} + e^- \rightarrow Fe^{2+} \tag{5}$$

In this study, a novel electro-Fenton process coupled with a pH-regulation divided electrolysis cell was developed for p-nitrophenol (PNP) degradation. In the pH-regulation divided electrolysis cell with a PTFE membrane as the separated material, the desired pH for an effective Fenton reaction and for a neutral treated media could be obtained by H_2O splitting into H^+ and OH^- at the anode and cathode, respectively. In the electro-Fenton process with external addition of H_2O_2, metal iron and a DSA electrode were applied as the cathode and anode, respectively, where the cathodic polarization of the metal iron electrode could effectively reduce the release of iron ions with diminishing ferric sludge generation.

EXPERIMENTAL SECTION

Materials

An iron plate (Fe, >99%) of 50 × 50 mm was purchased from Tengfeng Metallic Material Co. Ltd. (Hebei, China). p-nitrophenol (PNP, $C_6H_5NO_3$, 99%) was supplied from Shanghai Yien Chemical Technology Co. Ltd. 1,10-phenanthroline ($C_{12}H_8N_2 \cdot H_2O$, 99%), glacial acetic acid ($C_2H_4O_2$, 99%), sodium acetate (CH_3COONa, 99%), ferrous sulfate ($FeSO_4.7H_2O$, 99%), hydroxylamine hydrochloride ($HONH_3Cl$, 98.5%), sodium sulfate (Na_2SO_4, 99%), hydrogen peroxide (H_2O_2, 30%), titanium oxalate, potassium ($K_2TiO(C_2O_4)_2$, 98%), ferrous ammonium sulfate hexahydrate ($Fe(NH_4)_2 \cdot (SO_4)_2 \cdot 6H_2O$, 99%), potassium permanganate ($KMnO_4$, 99%), sulfuric acid (H_2SO_4, 98%), and sodium

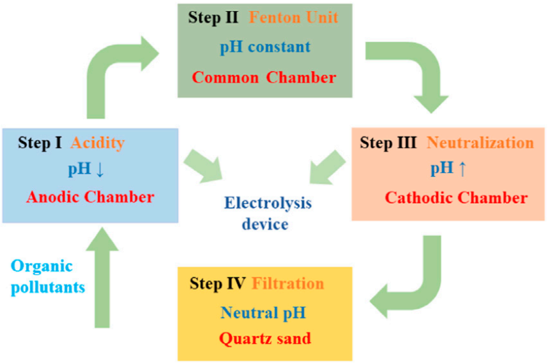

FIGURE 1 | Scheme of the iron cathode electrochemical Fenton (ICEF) system (steps 2 and 4) coupled with the pH-regulation divided electrolysis system (steps 1 and 3).

hydroxide (NaOH, 98%) were provided by Sinopharm Chemical Reagent Co. Ltd., China. All chemicals were analytical grade and were used without further purification. Ultrapure water (18.2 MΩ cm) was used to prepare reaction solutions for all the experiments.

Experimental Procedures

As shown in **Figure 1**, the combined electrochemical treatment process mainly consisted of four steps. Prior to step 1, a 100 mg/L PNP solution with pH 7.0 was performed in the beaker, 3 g/L of Na_2SO_4 was used as the electrolyte solution. In step 1, pH adjustment was carried out in the divided electrolysis cell, which used a plexiglass rectangular tank with the cathode and anode chambers isolated by a PTFE microfiltration membrane. The anode consisted of a 50 × 80 mm boron-doped diamond (BDD) electrode while the cathode consisted of titanium mesh of the same dimensions with the distance of 25 mm; the PTFE membrane was between the anode and cathode. The galvanostatic electrolysis reactions were performed by a DC power supply (voltage 0–30.0 V, electric current 0–5.0 A). In step 1, the PNP solution concurrently entered into the cathode and anode chambers, pH was reduced to near 3.0 in the anodic chamber within 1 min. In step 2, the solution with the reduced pH was added into the iron cathode electrochemical Fenton (ICEF) system for PNP degradation with a chamber volume of 500 ml using a three-electrode potentiostat (Model CHI1130C, Chenhua instrument Co. Ltd. Shanghai, China) coupled with a saturated calomel reference electrode (SCE), where the cathodic potential was precisely controlled by the potentiostat and SCE. The working electrode was a 50 × 50 mm iron plate, and the counter electrode was a 50 × 50 mm DSA ($Ti\text{-}RuO_2\text{-}IrO_2$) mesh; 200 mg/L of H_2O_2 was continuously added by a pump within 15 min. In step 3, after the treatment of PNP solution in the ICEF system, the solution was transferred into the cathode chamber of the divided electrolysis cell to increase the pH. In addition, the pH of the cathode effluent was further regulated to neutral (~9.0) by NaOH solution. In step 4, the neutral solution was passed through a filter device to remove iron ions, which was carried out in a container filled with quartz sand (80–120 mm). The removal ratio of p-nitrophenol, COD, or TOC (η, %) was calculated via **Eq. 8**.

$$\eta = \frac{C_0 - C_t}{C_0} \times 100\% \tag{6}$$

Analytical Determinations

The concentrations of PNP were determined by high performance liquid chromatography (HPLC-1100, Agilent) with an Eclipse XDB-C18 column (4.6 mm × 150 mm, 5 μm), (Nakatsuji et al., 2015). The mobile phase was methanol/water (50/50), the flow rate was 1.0 ml/min, and the UV detector was set at 314 nm. The chemical oxygen demand (COD) was detected using a COD analyzer (ASH 6B-80, China) [37]. A total organic carbon analyzer (multi N/C® 2,100, Analytik Jena AG) was applied to monitor total organic carbon (TOC). (Kavitha and Palanivelu, 2004). The concentration of H_2O_2 was measured by the potassium titanium (IV) oxalate method at 400 nm with a UV-Vis spectrophotometer (UV 6000 PC Yuanxi instrument Co. Ltd. Shanghai, China) (Wang and Chu, 2011). Fe^{2+} and Fe (tot) were determined at 510 nm using a modified phenanthroline method with an Fe^{2+} detection limit of 0.5 μM, and Fe^{3+} concentration was estimated as the difference between Fe (tot) and Fe^{2+} (Xin et al., 2018). Solution pH and conductivity were measured by a water quality analyzer. The reaction was quenched in the collected samples by immediately adding 1.0 mol/L of NaOH since Fenton oxidation cannot occur at pH > 10.0. For COD measurements, the samples were pretreated with NaOH to remove any residual H_2O_2. All experiments were performed twice at least, with relative errors less than 3%.

RESULTS AND DISCUSSION

pH-Regulation in a Divided Electrolysis Cell

For the Fenton reaction, it is recommended to acidify the solution pH to ~3.0 for •OH production and then neutralize the solution for the precipitation of Fe^{3+} (Chen et al., 2021). In this study, we developed a divided electrolysis cell using a hydrophilic PTFE microfilter membrane as the separated material. In this system, H_2O splitting reactions at the anode and cathode could produce H^+ and OH^- (**Eq. 7** and **Eq. 8**), respectively, which could be used to regulate the solution pH required for the Fenton reaction. Thus, the substrate solution pH could reduce to nearly 3.0 when it flowed through the anode chamber in step 1 (**Figure 1**). After the Fenton reaction, the solution pH was raised to promote the formation of $Fe(OH)_3$ in step 3. The above pH adjustment objective could be achieved by regulating the applied current density and flow velocity. Here, a neutral solution containing 100 mg/L of PNP and 3 g/L of Na_2SO_4 electrolyte was pumped into the electrolysis device at a flow rate of 20 ml/min by a peristaltic pump, where the residence time was 1 min. The current density applied is the key parameter for the electrochemical pH regulation because it fundamentally affects the yield of H^+ in the anode compartment and OH^- in the cathode compartment, respectively. As shown in **Figure 2A**, the pH of the anode effluent continuously decreased with the increase of current density; as the current density increased from 0.5 to 6 mA/cm^2, the

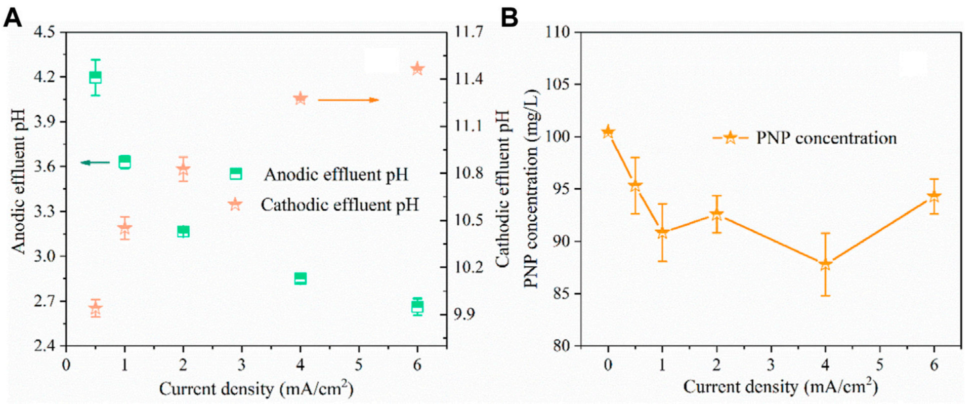

FIGURE 2 | The influence of current density on effluent pH **(A)** and PNP concentration **(B)**. (PNP concentration = 100 mg/L, Na_2SO_4 = 3 g/L, pH_0 = 7.0, anode compartment flow velocity = 20 ml/min, cathode compartment flow velocity = 20 ml/min).

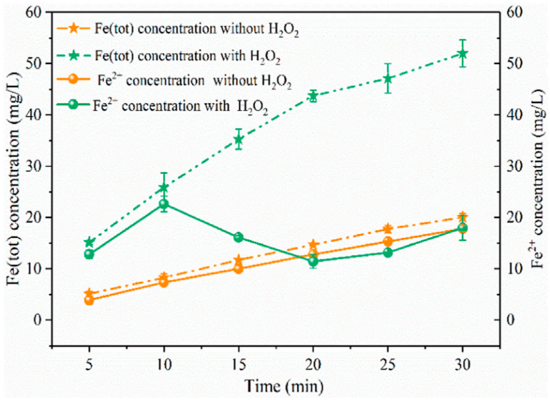

FIGURE 3 | Concentration variations of iron ions under different conditions. (PNP = 100 mg/L, Na_2SO_4 = 3 g/L, pH_0 = 3.0).

pH of anodic effluent decreased from 4.2 to 2.7, while the cathodic effluent pH increased from 9.9 to 11.5. This was consistent with what we expected, because as the current increased, effective water-splitting resulted in more H^+ produced at the anode and more OH^- produced at the cathode. In particular, when the applied current density was 2 mA/cm^2, an acidic effluent with pH of 3–3.2 was automatically attained at the steady state (Neyens and Baeyens, 2003). It has been demonstrated that the Fenton process is inhibited at extremely acidic environments due to the formation of $(Fe(H_2O))^{2+}$ and Fe(III)-hydroxyl complexes, $Fe(OH)^{2+}$. Thus, to achieve the most favorable Fenton reaction condition, an applied current density of 2 mA/cm^2 was adopted in this study.

$$2H_2O + 2e^- \rightarrow 2OH^- + H_2\uparrow \quad (7)$$

$$2H_2O - 4e^- \rightarrow 4H^+ + O_2\uparrow \quad (8)$$

The results in **Figure 2B** show that the PNP degradation efficiency increased as the current density increased initially from 0 to 1 mA/cm^2, but it became nearly constant when the current density was elevated above 1 mA/cm^2. Specifically, as the current density increased from 0.5 to 1 mA/cm^2, the PNP removal efficiency increased from 5 to 10%. Nevertheless, further increasing the current density to 6 mA/cm^2 did not increase the further removal of PNP. In this case, the BDD anode had little effect on the degradation of pollutants in this system because of a too short residence time.

Iron Plate Immersed in Water Without Electricity

As shown in **Figure 3**, when the solution pH reduced to nearly 3.0, the iron plate immersed in water without power could produce 20 mg/L of Fe (tot) within 30 min, of which 89% was Fe(II). In this process, the iron plate would be dissolved by H^+ to generate Fe^{2+} under acidic conditions through **Eq. 9**, and the oxidation of Fe^{2+} to Fe^{3+} by O_2 was slow and the solution pH increased slightly from 3.0 to 3.2. The average production rate of Fe (tot) (approximately 0.33 mg/min) and Fe^{2+} (approximately 0.3 mg/min) was stable and closed within 30 min, indicating the stable release of Fe^{2+} by the iron plate under the acid solution. Under the same conditions, Fe (tot) significantly increased to 52 mg/L after 200 mg/L of H_2O_2 was continuously added into the solution within 15 min. The average production rate of Fe (tot) was stable within 20 min (approximately 1.1 mg/min), which was three times higher than that without the addition of H_2O_2. But these two reactions exhibited a similar average production rate of Fe (tot), approximately 0.41 mg/min, within the reaction period of 20–30 min, which may be ascribed to the fact that most of the H_2O_2 was consumed within 20 min. As for Fe^{2+} concentration, it continuously increased within 10 min with the production rate of approximately 1.13 mg/min and decreased from 23 to 11 mg/L between 10 and 20 min, which was explained by the consumption of Fe^{2+} during the Fenton reaction process (**Eq. 1**). And after 20 min, the concentration continuously increased, finally reaching 18 mg/L at 30 min, accounting for 35% of the Fe (tot). Within 20–30 min, the Fe (tot) concentration increased by 8 mg/L, close to the value of Fe^{2+} increase (7 mg/L), this can also be explained by the fact that little H_2O_2 remained after 20 min and the increase of Fe (tot) concentration was mostly due

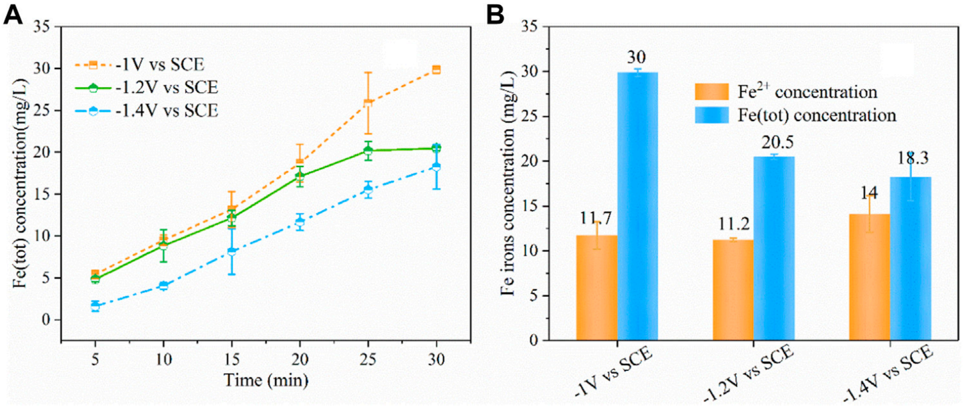

FIGURE 4 | Concentration variations of Fe (tot) under different cathodic potentials **(A)**, concentration of Fe irons at 30 min under different cathodic potentials **(B)**. (PNP = 100 mg/L, Na_2SO_4 = 3 g/L, pH_0 = 3.0).

to the Fe^{2+} released (**Eq. 9**). The above results revealed that the presence of H_2O_2 could facilitate the release of iron ions from Fe^0 in the acid solution. In this case, a large amount of iron sludge was produced and side reactions (**Eq. 3**) might consume produced •OH, leading to inferior degradation of pollutants.

$$Fe + 2H^+ \rightarrow Fe^{2+} + H_2 \tag{9}$$

Effect of Different Potential Applied to Iron Plate Cathode in ICEF System

To further reduce the release of iron ions from the iron cathode and improve the regeneration of Fe^{2+} from Fe^{3+}, we developed a novel iron cathode electro-Fenton system, applying a potential on the iron cathode. **Figure 4A** shows that concentration variations of Fe (tot) under different cathodic potentials, it was found that as the applied cathodic potential increased, the produced Fe (tot) decreased continuously. At the cathodic potential of −1.0 and −1.2 V/SCE, the produced Fe (tot) concentration was 30 and 21 mg/L within 30 min, which reduced by 42 and 61%, respectively, compared with no electricity input. Further increasing the cathodic potential from −1.2 to −1.4 V/SCE resulted in the slight decrease of Fe (tot) concentration to 18 mg/L. The production rate of Fe (tot) (0.43 mg/min) at the cathodic potential of −1.2 V/SCE was significantly higher than −1.4 V/SCE (0.29 mg/min) within the initial 20 min, while the value was apparently decreased to 0.17 mg/min within 20–30 min, and the rate slightly increased to 0.33 mg/min during the same time at −1.4V/SCE. **Figure 4B** shows the Fe^{2+} and Fe (tot) concentrations produced at 30 min under different cathodic potentials. It was found that the ratio of Fe^{2+} to Fe (tot) concentration enhanced significantly from 0.39 to 0.77 with the decrease of cathodic potential from −1.0 to −1.4V/SCE. This can be explained by the fact that the regeneration from Fe^{3+} to Fe^{2+} increased with the decrease of cathodic potential.

The results of PNP concentration versus time are shown in **Figure 5A**. It was found that only 75% of PNP was degraded within 30 min under the conditions of the iron plate immersed in water with 200 mg/L of H_2O_2 without electricity (WE Fenton process). And PNP removal efficiency was enhanced to 87, 91, and 90% at cathodic potentials of −1.0, −1.2, and −1.4 V/SCE, respectively (Kavitha and Palanivelu, 2004). However, it is noted that the removal efficiency was inferior initially then reached similar levels as the others after 20 min at −1.4 V/SCE. In addition, COD removal efficiency was basically the same in the case of −1 and −1.2 V/SCE, whereas the treatment at −1.4V/SCE exhibited an inferior degradation rate. As shown in **Figure 5B**, the COD removal efficiency was 67% without electricity, and increased to 76 and 75% at the cathodic potentials of −1.0 and −1.2 V/SCE, respectively, with residual COD concentration below 50 mg/L. However, when the cathodic potential was decreased to −1.4 V/SCE, the COD concentration reduced from 154 to 73 mg/L within 30 min, which can be ascribed to the inferior production of Fe (tot) for the Fenton reaction. According to the above results, −1.2 V/SCE was chosen as the optimal cathodic potential, and the released Fe (tot) concentration decreased by approximately 61% with the COD concentration further decreasing from 52 to 40 mg/L as compared with the WE Fenton process. The degradation of the 100 mg/L PNP solution was carried out in the traditional Fenton system with initially adding 20 mg/L of Fe^{2+} and 200 mg/L of H_2O_2 at pH_0 3.0. It was found that PNP was destructed quickly within 5 min and exhibited faster decay of PNP and COD than the present combined process within 20 min. However, its final COD removal efficiency was outperformed by the present combined process at 30 min and was slightly surpassed by the latter (Babuponnusami and Muthukumar, 2014).

The variation of H_2O_2 concentration is shown in **Figure 5C**. It was observed that when applying potential at the iron cathode, the H_2O_2 concentration increased initially within 15 min and then decreased afterwards in the late reaction stage. As compared with the WE Fenton reaction system, the H_2O_2 concentration was higher, which was probably due to the smaller release of iron ions from the iron

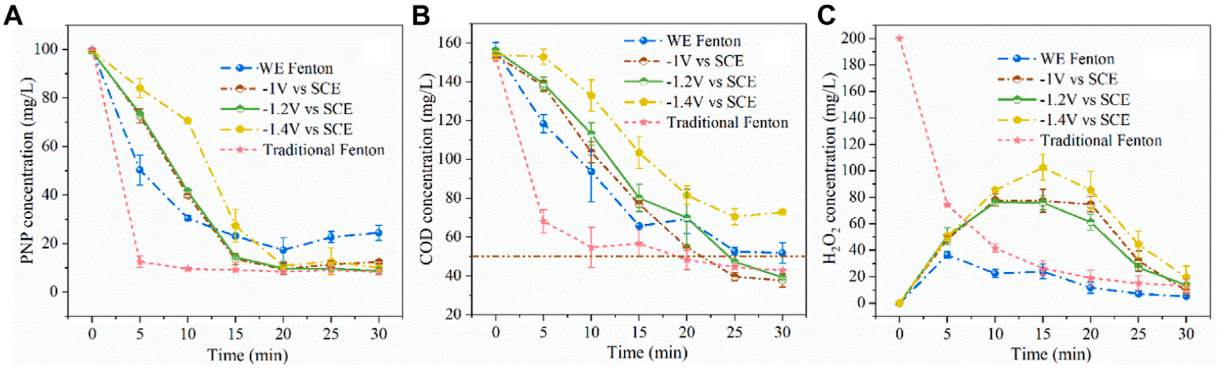

FIGURE 5 | Concentration variations of PNP **(A)**, COD **(B)**, and H_2O_2 **(C)** during the degradation under different conditions (PNP = 100 mg/L, Na_2SO_4 = 3 g/L, pH_0 = 3.0).

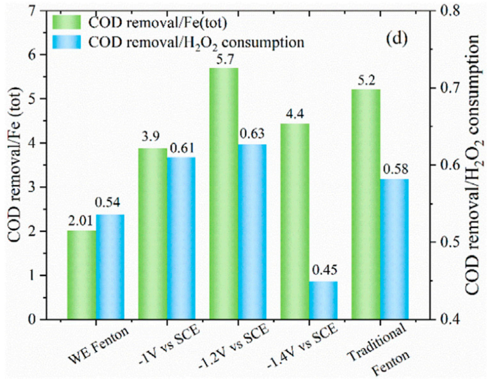

FIGURE 6 | The ratio of COD removal to Fe (tot) concentration and H_2O_2 consumption under different conditions (PNP = 100 mg/L, Na_2SO_4 = 3 g/L).

cathode. As the applied cathodic potential decreased from −1.0 to −1.4 V/SCE, the remaining concentration of H_2O_2 was slightly higher over the whole reaction period, which was also associated with the production of iron ions. In the traditional Fenton system, the concentration of H_2O_2 significantly decreased from 200 to 126 mg/L within 5 min, which corresponded to the quick reaction between Fe^{2+} and H_2O_2, and the remaining H_2O_2 concentration at 30 min was 13 mg/L. From **Figure 6**, it could be clearly observed that as the cathodic potential decreased from −1.0 to −1.2 V/SCE, the ratio of COD removal to produced Fe (tot) and H_2O_2 consumption was increased from 3.9 to 5.7 and 0.61 to 0.63, while the value significantly decreased to 4.4 and 0.45 at a higher cathode potential of 1.4 V/SCE. These results demonstrated that -1.2 V/SCE was the optimal cathodic potential with suitable Fe (tot) production for the electro-Fenton reaction, which exhibited slightly higher COD removal/Fe (tot) and COD removal/H_2O_2 consumption for the traditional Fenton reaction system. In the WE Fenton process, the much lower value, i.e., 2 for COD removal/Fe (tot) and 0.54 for COD removal/H_2O_2 consumption, was obtained, respectively.

The Divided Electrolysis Cell and ICEF Combined System

According to the aforementioned experimental results, the optimal current density for solution pH regulation and cathodic potential for the ICEF reaction have been obtained. The results of PNP and COD concentration time are shown in **Figure 7A**. It was found that the PNP concentration of the anodic effluent slightly decreased from 100 to 91 mg/L while the COD removal efficiency was only 5%, owing to the oxidation at the BDD anode. During the combined process, the removal efficiency of PNP and COD attained 93 and 72% within 30 min, and the PNP pollutant was further destructed after filtration because of the coagulation of iron ions with the concentration decreased from 6 to 2 mg/L. **Figure 7B** shows the TOC removal efficiency of traditional Fenton and ICFE systems, the removal efficiency was 42% within 5 min by traditional Fenton but maintained relatively stable in the remaining time, finally the value reached 48%. This can be explained by the rapid consumption rate of Fenton reagents. However, the TOC removal efficiency achieved 60% in the combined system, which was much higher than traditional Fenton (Kavitha and Palanivelu, 2004). The high removal efficiency of PNP (98%), COD (79%), and TOC (60%) revealed more efficient degradation of pollutants in the combined system than the traditional Fenton system.

For traditional Fenton, pH was adjusted to the desired values with H_2SO_4 and NaOH solution while ferrous sulfate was used as the iron ions source (Gao et al., 2020). As shown in **Figure 8**, the conductivity was increased from 4.35 to 4.68 mS/cm after acidification during traditional Fenton, and the value continuously enhanced to 4.95 after the Fenton reaction, while the pH slightly decreased from 3.07 to 2.73, which can be explained by the large quantity of organic acids production. The pH of the effluent was neutralized to approximately 9.0 with the conductivity reduced to 4.76 mS/cm, which might be caused by acid-base

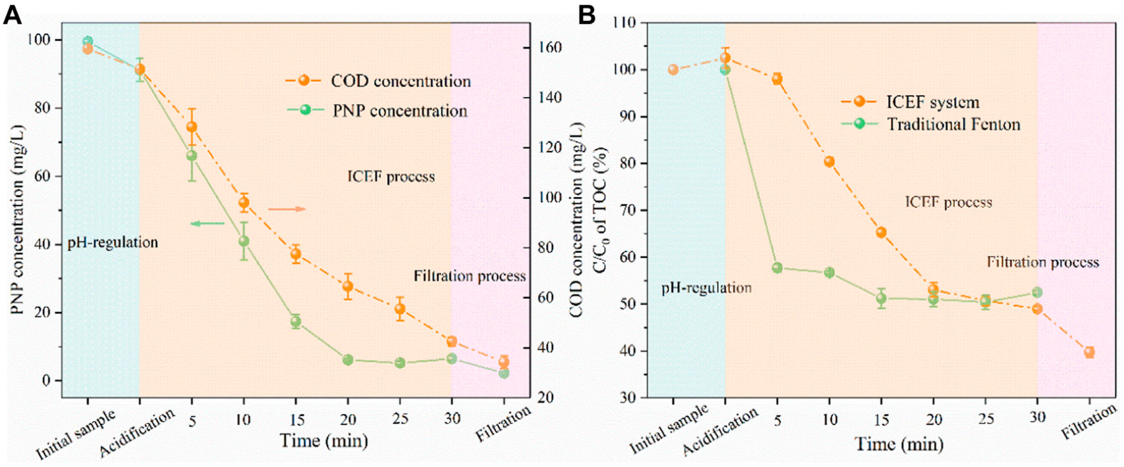

FIGURE 7 | Concentration variations of PNP and COD **(A)** and TOC concentration reduction **(B)** during the EIC-EF system degradation (PNP = 100 mg/L, Na_2SO_4 = 3 g/L, pH_0 = 7.0).

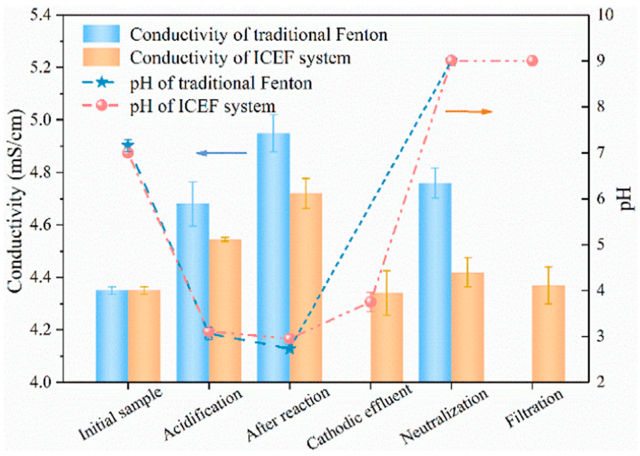

FIGURE 8 | Concentration variations of conductivity and pH under different conditions. (PNP = 100 mg/L, Na_2SO_4 = 3 g/L).

neutralization. As for the present combined process, the conductivity of the anodic effluent increased to 4.55 mS/cm with the pH decreasing from 7.0 to 3.1, the cathodic effluent pH only slightly increased from 2.95 to 3.75 at the same current density (2 mA/cm^2), owing to the buffering effect of organic acids on pH. During the neutralization process, pH was further adjusted to neutral (~9.0) by the NaOH solution (Chen et al., 2021), driving the complete precipitation of $Fe(OH)_3$. In this case, the conductivity further decreased to 4.37 mS/cm. Generally, the salinity of traditional Fenton increased by 9% compared with the initial solution while the present combined process remained basically unchanged after the reaction, avoiding the obvious increase of water salinity caused by the addition of a large amount of chemical reagents in traditional Fenton.

Mechanism Discussion

A set of experiments was performed to verify the main mechanism of pollutant degradation. As shown in **Figures 9A,B**, the PNP removal efficiency was only 9% without front-end pH adjustment, owing to basically no Fe^{2+} production under the neutral solution, indicating that the pH-regulation process is indispensable for the ICEF system. In addition, only 7% of PNP was oxidized by H_2O_2 in solution. In the above two reaction system, COD concentration slightly increased after the reaction, which was possibly subject to formation of some intermediates which interfered with the COD concentration. The direct oxidation of PNP by the DSA anode was also examined without H_2O_2 at pH_0 = 3.0, the removal efficiency of PNP and COD concentration were 38 and 13%, respectively. Thus, the direct PNP degradation at the anode was ruled out, indicating that PNP in solution was mainly oxidized by •OH produced by the Fenton reaction.

To further investigate the effect of cathode potential on iron ion concentration, we conducted the following experiments. As shown in **Figure 10A**, at the cathode potential of −1.2V/SCE without adding H_2O_2, the produced Fe (tot) concentration was 4 mg/L, which reduced by 80% compared with no electricity as shown in **Figure 3** (20 mg/L). And in the case of adding 200 mg/L of H_2O_2 and applying the cathode potential of -1.2 V/SCE, the Fe (tot) concentration increased to 17 mg/L. There are two reasons for this phenomenon, one is that the iron plate would react with H_2O_2 in the presence of H^+ through **Eq. 10** (Pan et al., 2019); the other is that the presence of H_2O_2 promoted the conversion of Fe^{2+} to Fe^{3+} and the generated Fe^{3+} may further react with the iron plate to produce Fe^{2+} through **Eq. 11**. As shown in **Figure 10B**, 30 mg/L of Fe^{3+} was also added into the solution at the cathodic potential of -1.2 V/SCE without H_2O_2, the Fe (tot) concentration slightly increased to 35 mg/L within 30 min and Fe^{3+} concentration reduced to 26 mg/L. The results demonstrated that the reaction between Fe^{3+} and Fe^0 contributed marginally to

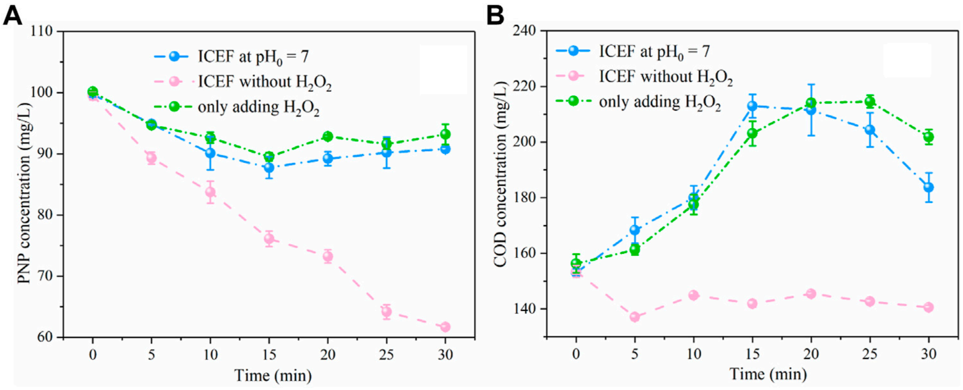

FIGURE 9 | Concentration variations of PNP **(A)** and COD **(B)** under different conditions (PNP = 100 mg/L, Na_2SO_4 = 3 g/L).

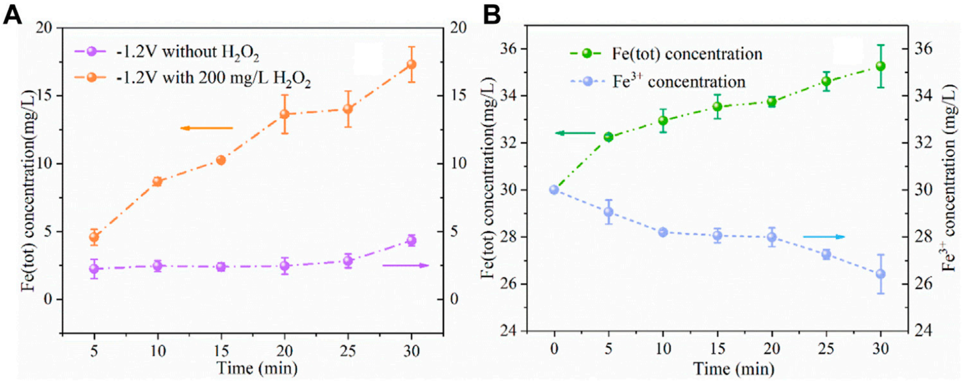

FIGURE 10 | Concentration variations of Fe (tot) and Fe^{2+} **(A)** and Fe (tot) and Fe^{3+} **(B)** under different conditions (PNP = 100 mg/L, Na_2SO_4 = 3 g/L, pH_0 = 3.0).

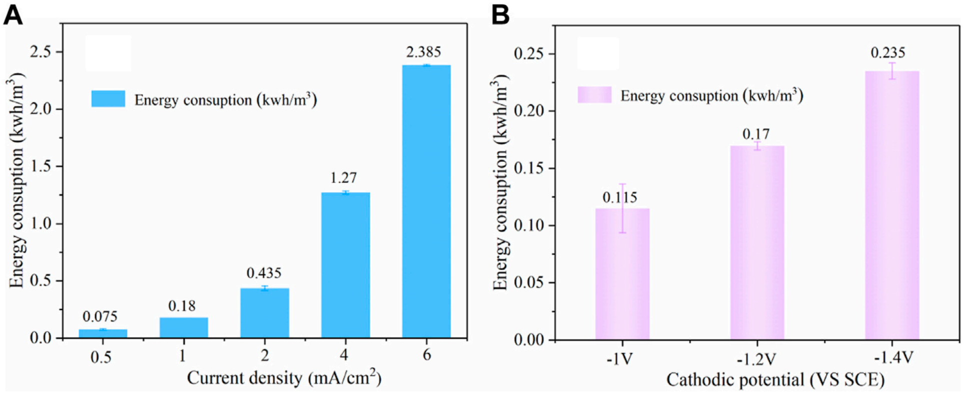

FIGURE 11 | Effect of different current densities **(A)** and cathodic potential **(B)** on energy consumption (PNP = 100 mg/L, Na_2SO_4 = 3 g/L, pH_0 = 7.0).

the release of iron ions during the ICEF process, while the direct oxidation of Fe^0 by H_2O_2 probably dominated the release of iron ions from the iron plate. As a result, in the WE Fenton system, H_2O_2 was not only consumed for the Fenton reaction but also for the release of Fe^{2+} by the reaction with the iron plate. Thus, a part of H_2O_2 cannot be utilized for •OH production via the Fenton reaction, leading to the inferior degradation efficiency of PNP.

$$Fe + H_2O_2 + 2H^+ \rightarrow Fe^{2+} + 2H_2O \tag{10}$$

$$Fe^{3+} + Fe \rightarrow Fe^{2+} \tag{11}$$

Environmental Implication

In the present combined system, the cost for electricity played an important role in the overall operating cost of the process. Apparently, the overall energy consumption is the sum of the pH adjustment unit and Fenton reaction process, the power consumption of per ton of wastewater was calculated based on **Eq. 12** (Wang and Chu, 2011).

$$E = \frac{UIT}{V} \times 10^{-3} \tag{12}$$

where E is the energy consumption, U is the voltage measured during the reaction (V), I is the applied current (A), t is the electrolysis time (h), and V is the volume of reaction solution (m^3).

As shown in **Figure 11A**, during the pH-regulation process, current density had a significant impact on energy consumption, the value increased from 0.075 to 2.385 kWh/m^3 as the current density increased from 0.5 to 6 mA/cm^2. In the present combined system, a pH of 3.0–3.2 was automatically attained by electrolysis with the energy consumption of 0.435 kWh/m^3. **Figure 11B** shows that the energy consumption was increased from 0.115 to 0.235 kWh/m^3 with the cathodic potential decreasing from −1.0 to −1.4 V/SCE. We can infer that the pH-regulation took up most energy consumption (72%) in our system, and the whole system power consumption of per ton of wastewater was 0.605 kWh/m^3, which translates into a cost of $\$0.04/m^3$ based on the average US industrial electricity rate ($0.0653/kWh). Iron sheet is very cheap and highly reusable ($1.4), which can counteract the cost. The cost of H_2O_2 was $0.16 with 0.6 L of consumption per ton of water, while the unit price of H_2O_2 was $0.27/L. Furthermore, *in situ* electrochemical synthesis of highly concentrated H_2O_2 (Yamanaka et al., 2003; Chen et al., 2017) could be used as a replacement for externally supplied H_2O_2 in the future, eliminating the chemical cost.

The specific energy consumption was calculated in terms of the removal of 1 kg of COD from PNP wastewater by the Fenton process (kWh/kg COD) using **Eq. 13**, where U, I, and t are the average voltage (V), applied current (A), and electrolysis time (s), respectively (Kurt et al., 2007; Zhao et al., 2016).

$$SEC = \frac{U \times I \times T}{(COD_0 \times V_0 - COD_t \times V_t) \times 3.6} \tag{13}$$

After pH adjustment and the 30-min ICEF process, the PNP mineralization shows an SEC value of 4.92 kWh/kg COD, the results in this study demonstrated that the ICEF system was environmentally friendly, efficient, and inexpensive in comparison. It was proven that the operation of the system greatly enhanced the treatment of PNP wastewater. Compared to traditional Fenton and other electro-Fenton systems, the ICEF system has its own merits. Firstly, the pH-regulation divided electrolysis cell with the PTFE membrane as the separating material was simple and convenient compared to others, an acidic pH of 3.0–3.2 was automatically attained at a steady state within 1 min, which is suitable for most Fenton-like reactions (Babuponnusami and Muthukumar, 2014). In contrast, ~60 min was required in the divided electrolysis cell using an ion exchange membrane as the separating material (Liu et al., 2007). Secondly, the cathode potential applied on the iron plate can decrease amounts of iron irons released under acid solution and precisely control the Fe (tot) production, avoiding the addition of iron salt and increase of water salinity. All these advantages together suggest that the ICEF system has potential for cost-effective and efficient degradation of recalcitrant organic pollutants. Future work should also focus on improving the efficiency of cathode reduction of ferric iron and improving the efficiency of H_2O_2 utilization.

CONCLUSION

In this study, a novel eco-friendly iron cathode electrochemical Fenton (ICEF) system coupled with a pH-regulation divided electrolysis cell was developed for PNP degradation. In such a system, 100 mg/L of PNP was not only effectively degraded within 30 min (97%), but also efficiently mineralized with a COD and TOC removal efficiency of 79 and 60%, respectively. The optimal cathode potential exhibited strong inhibition on Fe (tot) production with the concentration of Fe (tot) significantly decreasing from 52 to 21 mg/L, minimizing the ferric sludge generation. And the conductivity increased slightly from 4.35 to 4.37 mS/cm, indicating that the present combined process negligibly affected the salt content of the wastewater. Notably, the system was inexpensive with an energy consumption of only 4.92 kWh/kg COD. In general, this study demonstrated that the present combined system is an effective and environmentally friendly technology for wastewater treatment.

DATA AVAILABILITY STATEMENT

The original contributions presented in the study are included in the article/Supplementary Material, further inquiries can be directed to the corresponding author.

AUTHOR CONTRIBUTIONS

XW: Conceptualization, Investigation, Writing, and Original Draft preparation. JZ: Investigation and Formal analysis. CS: Formal analysis and Investigation. XS: Validation, Formal analysis, Investigation, and Supervision. PD: Software and Methodology.

REFERENCES

Andreozzi, R., Caprio, V., Insola, A., and Marotta, R. (1999). Advanced Oxidation Processes (AOP) for Water Purification and Recovery. *Catal. Today.* 53, 51–59. doi:10.1016/s0920-5861(99)00102-9

Babuponnusami, A., and Muthukumar, K. (2014). A Review on Fenton and Improvements to the Fenton Process for Wastewater Treatment. *J. Environ. Chem. Eng.* 2, 557–572. doi:10.1016/j.jece.2013.10.011

Bello, M. M., Abdul Raman, A. A., and Asghar, A. (2019). A Review on Approaches for Addressing the Limitations of Fenton Oxidation for Recalcitrant Wastewater Treatment. *Process Saf. Environ. Prot.* 126, 119–140. doi:10.1016/j.psep.2019.03.028

Brillas, E., Sirés, I., and Oturan, M. A. (2009). Electro-Fenton Process and Related Electrochemical Technologies Based on Fenton's Reaction Chemistry. *Chem. Rev.* 109, 6570–6631. doi:10.1021/cr900136g

Cai, Q. Q., Lee, B. C. Y., Ong, S. L., and Hu, J. Y. (2021). Fluidized-bed Fenton Technologies for Recalcitrant Industrial Wastewater Treatment-Recent Advances, Challenges and Perspective. *Water Res.* 190, 116692. doi:10.1016/j.watres.2020.116692

Chen, L., Alshawabkeh, A. N., Hojabri, S., Sun, M., Xu, G., and Li, J. (2021). A Robust Flow-Through Platform for Organic Contaminant Removal. *Cel Rep. Phys. Sci.* 2, 100296. doi:10.1016/j.xcrp.2020.100296

Chen, Z., Chen, S., Siahrostami, S., Chakthranont, P., Hahn, C., Nordlund, D., et al. (2017). Development of a Reactor with Carbon Catalysts for Modular-Scale, Low-Cost Electrochemical Generation of H_2O_2. *React. Chem. Eng.* 2, 239–245. doi:10.1039/c6re00195e

Davarnejad, R., and Azizi, J. (2016). Alcoholic Wastewater Treatment Using Electro-Fenton Technique Modified by Fe_2O_3 Nanoparticles. *J. Environ. Chem. Eng.* 4, 2342–2349. doi:10.1016/j.jece.2016.04.009

Fang, F., Yang, M.-M., Wang, H., Yan, P., Chen, Y.-P., and Guo, J.-S. (2018). Effect of High Salinity in Wastewater on Surface Properties of Anammox Granular Sludge. *Chemosphere.* 210, 366–375. doi:10.1016/j.chemosphere.2018.07.038

Ganiyu, S. O., Zhou, M., and Martínez-Huitle, C. A. (2018). Heterogeneous Electro-Fenton and Photoelectro-Fenton Processes: a Critical Review of Fundamental Principles and Application for Water/Wastewater Treatment. *Appl. Catal. B: Environ.* 235, 103–129. doi:10.1016/j.apcatb.2018.04.044

Gao, J., Jiang, B., Ni, C., Qi, Y., and Bi, X. (2020). Enhanced Reduction of Nitrate by Noble Metal-Free Electrocatalysis on P Doped Three-Dimensional Co3O4 Cathode: Mechanism Exploration from Both Experimental and DFT Studies. *Chem. Eng. J.* 382, 123034. doi:10.1016/j.cej.2019.123034

Gao, Y., Zhu, Y., Lyu, L., Zeng, Q., Xing, X., and Hu, C. (2018). Electronic Structure Modulation of Graphitic Carbon Nitride by Oxygen Doping for Enhanced Catalytic Degradation of Organic Pollutants Through Peroxymonosulfate Activation. *Environ. Sci. Technol.* 52, 14371–14380. doi:10.1021/acs.est.8b05246

Görmez, F., Görmez, Ö., Gözmen, B., and Kalderis, D. (2019). Degradation of Chloramphenicol and Metronidazole by Electro-Fenton Process Using Graphene Oxide-Fe_3O_4 as Heterogeneous Catalyst. *J. Environ. Chem. Eng.* 7, 102990. doi:10.1016/j.jece.2019.102990

Hassani, A., Karaca, M., Karaca, S., Khataee, A., Açışlı, Ö., and Yılmaz, B. (2018). Preparation of Magnetite Nanoparticles by High-Energy Planetary ball Mill and its Application for Ciprofloxacin Degradation through Heterogeneous Fenton Process. *J. Environ. Manage.* 211, 53–62. doi:10.1016/j.jenvman.2018.01.014

He, J., Yang, X., Men, B., and Wang, D. (2016). Interfacial Mechanisms of Heterogeneous Fenton Reactions Catalyzed by Iron-Based Materials: A Review. *J. Environ. Sci.* 39, 97–109. doi:10.1016/j.jes.2015.12.003

Hu, J., Wang, S., Yu, J., Nie, W., Sun, J., and Wang, S. (2021). Duet Fe_3C and FeNx Sites for H_2O_2 Generation and Activation Toward Enhanced Electro-Fenton Performance in Wastewater Treatment. *Environ. Sci. Technol.* 55, 1260–1269. doi:10.1021/acs.est.0c06825

Kavitha, V., and Palanivelu, K. (2004). The Role of Ferrous Ion in Fenton and Photo-Fenton Processes for the Degradation of Phenol. *Chemosphere.* 55, 1235–1243. doi:10.1016/j.chemosphere.2003.12.022

Kurt, U., Apaydin, O., and Gonullu, M. T. (2007). Reduction of COD in Wastewater from an Organized Tannery Industrial Region by Electro-Fenton Process. *J. Hazard. Mater.* 143, 33–40. doi:10.1016/j.jhazmat.2006.08.065

Li, Q., Wang, M., Feng, J., Zhang, W., Wang, Y., Gu, Y., et al. (2013). Treatment of High-Salinity Chemical Wastewater by Indigenous Bacteria - Bioaugmented Contact Oxidation. *Bioresour. Technology.* 144, 380–386. doi:10.1016/j.biortech.2013.07.004

Liu, H., Wang, C., Xiangzhong, X., Xuan, X., Jiang, C., and Cui, H. n. (2007). A Novel Electro-Fenton Process for Water Treatment: Reaction-Controlled pH Adjustment and Performance Assessment. *Environ. Sci. Technol* 41, 2937–2942. doi:10.1021/es0622195

Moreira, F. C., Boaventura, R. A. R., Brillas, E., and Vilar, V. J. P. (2017). Electrochemical Advanced Oxidation Processes: a Review on Their Application to Synthetic and Real Wastewaters. *Appl. Catal. B: Environ.* 202, 217–261. doi:10.1016/j.apcatb.2016.08.037

Nakatsuji, Y., Salehi, Z., and Kawase, Y. (2015). Mechanisms for Removal of P-Nitrophenol from Aqueous Solution Using Zero-Valent Iron. *J. Environ. Manage.* 152, 183–191. doi:10.1016/j.jenvman.2015.01.012

Neyens, E., and Baeyens, J. (2003). A Review of Classic Fenton's Peroxidation as an Advanced Oxidation Technique. *J. Hazard. Mater.* 98, 33–50. doi:10.1016/s0304-3894(02)00282-0

Oturan, M. A., and Aaron, J.-J. (2014). Advanced Oxidation Processes in Water/Wastewater Treatment: Principles and Applications. A Review. *Crit. Rev. Environ. Sci. Technology.* 44, 2577–2641. doi:10.1080/10643389.2013.829765

Oturan, M. A., Peiroten, J., Chartrin, P., and Acher, A. J. (2000). Complete Destruction of P-Nitrophenol in Aqueous Medium by Electro-Fenton Method. *Environ. Sci. Technol.* 34, 3474–3479. doi:10.1021/es990901b

Pan, Y., Zhou, M., Cai, J., Tian, Y., and Zhang, Y. (2019). Mechanism Study of Nitrilotriacetic Acid-Modified Premagnetized Fe0/H_2O_2 for Removing Sulfamethazine. *Chem. Eng. J.* 374, 1180–1190. doi:10.1016/j.cej.2019.06.005

Qiang, Z., Chang, J.-H., and Huang, C.-P. (2003). Electrochemical Regeneration of Fe2+ in Fenton Oxidation Processes. *Water Res.* 37, 1308–1319. doi:10.1016/s0043-1354(02)00461-x

Wang, X. G., Lin, B., Tang, Y. B., and Chen, H. F. (2014). Effects of High Salinity on the Removal of Pollutants in Wastewater by Aerobic Granular Sludge. *Amr.* 955-959, 339–342. doi:10.4028/www.scientific.net/amr.955-959.339

Wang, Y. R., and Chu, W. (2011). Degradation of 2,4,5-Trichlorophenoxyacetic Acid by a Novel Electro-Fe(II)/Oxone Process Using Iron Sheet as the Sacrificial Anode. *Water Res.* 45, 3883–3889. doi:10.1016/j.watres.2011.04.034

Xin, S., Nin, C., Gong, Y., Ma, J., Bi, X., and Jiang, B. (2018). A Full-Wave Rectified Alternating Current Wireless Electrocoagulation Strategy for the Oxidative Remediation of As(III) in Simulated Anoxic Groundwater. *Chem. Eng. J.* 351, 1047–1055. doi:10.1016/j.cej.2018.06.178

Yamanaka, I., Onizawa, T., Takenaka, S., and Otsuka, K. (2003). Direct and Continuous Production of Hydrogen Peroxide with 93 % Selectivity Using a Fuel-Cell System. *Angew. Chem. Int. Ed. Engl.* 42, 3653–3655. doi:10.1002/anie.200351343

Yuan, S., Tian, M., Cui, Y., Lin, L., and Lu, X. (2006). Treatment of Nitrophenols by Cathode Reduction and Electro-Fenton Methods. *J. Hazard. Mater.* 137, 573–580. doi:10.1016/j.jhazmat.2006.02.069

Zhao, H., Qian, L., Guan, X., Wu, D., and Zhao, G. (2016). Continuous Bulk FeCuC Aerogel with Ultradispersed Metal Nanoparticles: An Efficient 3D Heterogeneous Electro-Fenton Cathode over a Wide Range of pH 3-9. *Environ. Sci. Technol.* 50, 5225–5233. doi:10.1021/acs.est.6b00265

Conflict of Interest: Authors XW, JZ, CS, XS and HD were employed by company Shengli Oilfield Testing and Evaluation Research Co., Ltd., SINOPEC.

frontiers in Chemistry

ORIGINAL RESEARCH
published: 10 February 2022
doi: 10.3389/fchem.2022.849505

Highly Dispersed CoO Embedded on Graphitized Ordered Mesoporous Carbon as an Effective Catalyst for Selective Fischer–Tropsch Synthesis of C_{5+} Hydrocarbons

Jirong Bai[1†], Mingyao Song[2†], Jiazheng Pang[1], Lingling Wang[1], Jianping Zhang[1], Xiankai Jiang[1], Zhijiang Ni[3], Zhilei Wang[4] and Quanfa Zhou[1*]*

[1]Research Center of Secondary Resources and Environment, School of Chemical Engineering and Materials, Changzhou Institute of Technology, Changzhou, China, [2]Department of Wood Science, The University of British Columbia, Vancouver, BC, Canada, [3]School of Mechanical Engineering and Urban Rail Transit, Changzhou University, Changzhou, China, [4]Department of Environmental Science and Engineering, Fudan University, Shanghai, China

Edited by:
Qingyi Zeng,
University of South China, China

Reviewed by:
Min Wang,
Jinan University, China
Linsen Li,
Hebei University, China

***Correspondence:**
Zhilei Wang
16210740046@fudan.edu.cn
Quanfa Zhou
zqf@czu.cn

†These authors have contributed equally to this work

Specialty section:
This article was submitted to Inorganic Chemistry, a section of the journal Frontiers in Chemistry

Received: *06 January 2022*
Accepted: *17 January 2022*
Published: *10 February 2022*

Citation:
Bai J, Song M, Pang J, Wang L, Zhang J, Jiang X, Ni Z, Wang Z and Zhou Q (2022) Highly Dispersed CoO Embedded on Graphitized Ordered Mesoporous Carbon as an Effective Catalyst for Selective Fischer–Tropsch Synthesis of C_{5+} Hydrocarbons. Front. Chem. 10:849505. doi: 10.3389/fchem.2022.849505

Herein, we report the high Fischer–Tropsch synthesis performance of the Co-based catalysts supported on graphitized ordered mesoporous carbon (GMC-900) by using a facile strategy. Compared with CMK-3 and active carbon (AC), the obtained GMC-900 by using pollution-free soybean oil as a carbon source exhibited enhanced catalytic performance after loading Co species due to its highly crystallized graphitic structure and uniform dispersion of CoO. As a result, Co/GMC-900 was an effective catalyst with the maximum C_{5+} selectivity of 52.6%, which much outperformed Co/CMK-3 and Co/AC. This research provides an approach to produce advanced Co-based catalysts with satisfactory performance for efficient Fischer–Tropsch synthesis.

Keywords: Fischer–Tropsch synthesis, clean soybean oil, cobalt catalyst, order mesoporous carbon, active carbon

INTRODUCTION

With the rapid development of human society and economy, it becomes more and more difficult for crude oils to meet people's demands (Guo et al., 2016; Hao et al., 2016; Zhang et al., 2017). Furthermore, the serious problems of air pollution and greenhouse effect caused by the consumption of fossil fuels have impelled the search for more clean alternatives (Qin et al., 2016). Fischer–Tropsch synthesis (FTS) is an alternative route that can transform synthesis gases resulting from gasification of biomass, natural gases, and coals into clean liquid fuels or chemicals without containing nitrogen, sulfur, or aromatics (Liu et al., 2018; Lyu et al., 2018). Traditionally, Ru-based catalysts exhibit high low-temperature selectivity and activity for long-chain hydrocarbons (Guo et al., 2019). However, the large-scale commercial application in industry is severely hampered by some major problems, especially the scarcity in nature and expensive prices (Liu et al., 2018; Guo et al., 2019). In comparison, Co-based catalysts, one of the most optimal choices for FTS due to their low costs, are highly active and selective toward long-chain hydrocarbons, and possess water deactivation stability and low water–gas shift activity during the reaction (Johnson and Bell, 2016; Cheng et al., 2018).

The support of Co-based catalysts greatly influences the catalytic performance during the reaction (Fu and Li, 2015; Qin et al., 2016). Conventionally, various oxide materials such as SiO_2, Al_2O_3, and

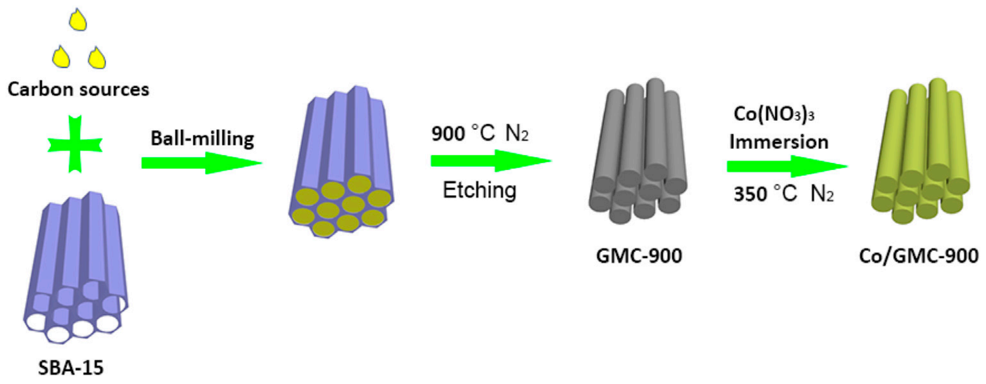

FIGURE 1 | Schematic scheme for synthesis of Co/GMC-900.

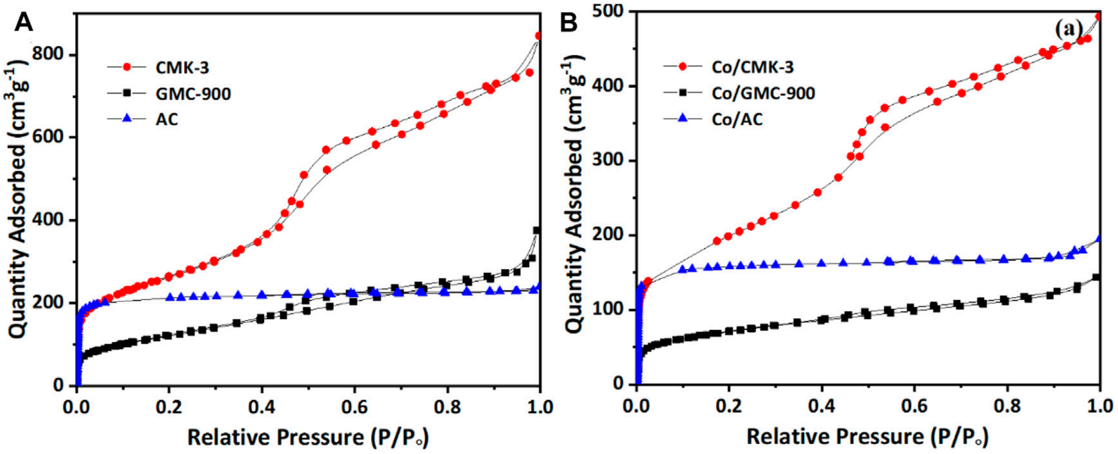

FIGURE 2 | The N_2 adsorption–desorption isotherms of CMK-3, GMC-900, and AC **(A)**, and Co/CMK-3, Co/GMC-900, and Co/AC **(B)**.

TiO_2 are used to support Co-based catalysts. SiO_2 and Al_2O_3 are preferentially used owing to their large surface areas, abrasion resistance, and excellent mechanical properties (Bustamante et al., 2020; Wolf et al., 2020; Xu et al., 2020). However, the relatively strong interaction between cobalt oxide and the support leads to the generation of irreducible substances, such as $CoAl_2O_4$ or Co_2SiO_4 (Bustamante et al., 2020; Li et al., 2020). As a result, the number of surface active sites on the support decreases, which limits the activity for long-chain hydrocarbons (Wang et al., 2020). Therefore, exploring suitable Co-based catalysts with the low formation of hardly reducible materials is highly desirable.

Carbon materials are also considered as some of the most desirable supports in FTS owing to their unique specific structure and chemistry, such as surface inertness, controllable crystallized graphitic structure, high conductivity, and acid or alkali resistance (Lyu et al., 2019; Dlamini et al., 2020). Reuel and Bartholomew (1984) found that the catalytic performance in CO hydrogenations dropped considerably with the increase of cobalt dispersion degree as follows: $Co/TiO_2 > Co/SiO_2 > Co/Al_2O_3 > Co/C > Co/MgO$. Tavasoli et al. (2008) reported that Co/CNT catalysts prepared from the impregnation method exhibited much larger activity than Co/Al_2O_3 on hydrocarbon yield, which can be ascribed to the weak interaction between Co species and CNT. In addition, mesoporous carbon (MC) using mesoporous silica as a precursor has also received much attention on FTS owing to its ordered pore structure and large surface area (Wu et al., 2019). Zhao et al. (2020) prepared Co/MC-1300 (where MC was prepared from pyrolysis of furfuryl alcohol and SBA-16 as the hard template), which showed improved cobalt reducibility and C_{5+} selectivity up to 74%.

The structure of carbon supports, particularly the porous structure, greatly influences the FTS performance (Xiong et al., 2011). Nonetheless, the impact of different carbon sources as the support on the structure and catalysis in FTS is rarely reported. Herein, we report the high Fisher-Tropsch synthesis performance of the Co catalysts supported on graphitized ordered mesoporous carbon (GMC-900) by using pollution-free soybean oil as a carbon source. We also chose the porous CMK-3 prepared and commercial AC from other carbon sources as the supports and controls to evaluate the catalytic performance of GMC-900 in FTS.

TABLE 1 | Physicochemical properties of carbon supports and catalysts.

Sample	Surface area (m^2 g^{-1})	Pore size (nm)	Pore volume (cm^3 g^{-1})
GMC-900	442	5.24	0.58
CMK-3	939	5.57	1.31
AC	657	2.25	0.37
Co/GMC-900	306	3.51	0.26
Co/CMK-3	709	4.30	0.76
Co/AC	492	2.44	0.30

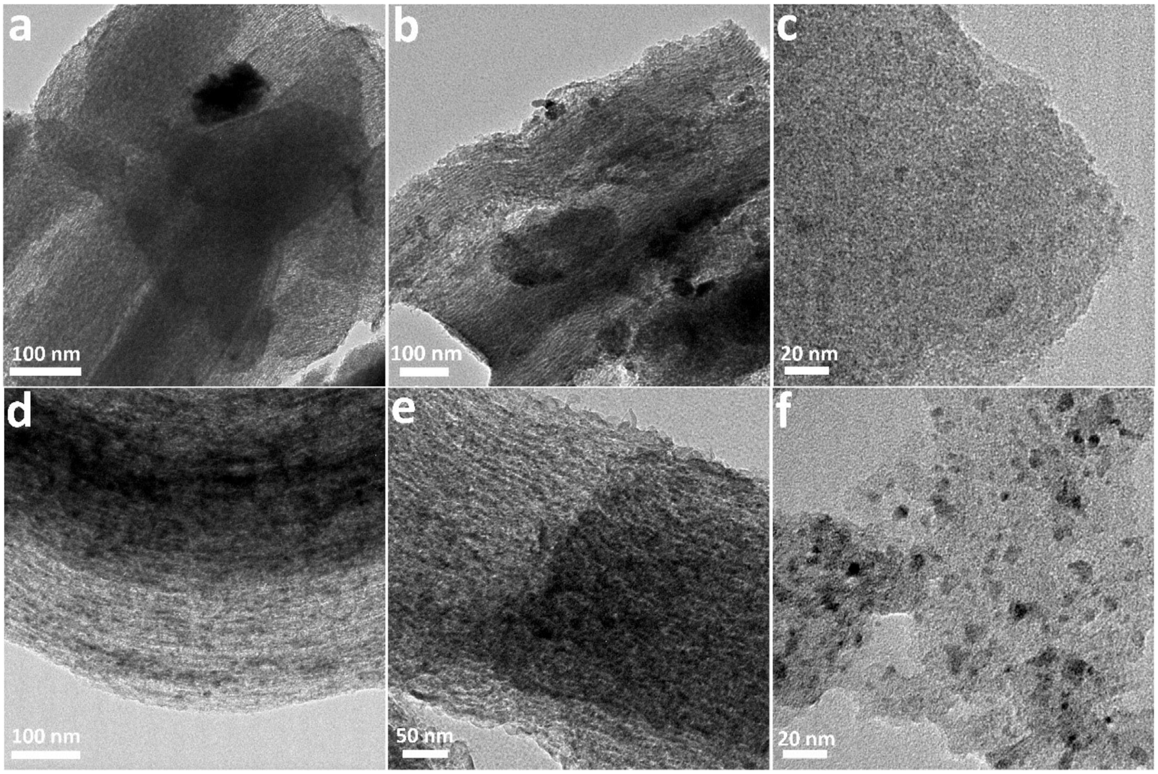

FIGURE 3 | TEM images of CMK-3 **(A)**, GMC-900 **(B)**, AC **(C)**, and the corresponding Co-based catalysts **(D–F)**.

EXPERIMENTAL

Chemicals

Poly-(ethylene glycol)-block-poly-(propylene glycol)-poly-(ethylene glycol) (P123, average Mn ~5,800) was supplied from Sigma-Aldrich. Ethyl silicate (TEOS, $SiO_2 \geq 28\%$) was purchased from Shanghai Lingfeng Chemical Reagent Co., Ltd., China. Active carbon (AC) was obtained from Huajing Activated Carbon Co., Ltd., China. CMK-3 was supplied from Nanjing Xianfeng Nanomaterials Technology Co. Ltd., and soybean oil was obtained from Jiangsu Junqi Grain and Oil Co., Ltd. Ethanol, glycerol, hydrochloric acid, sodium hydroxide, cobalt nitrate, and dicyandiamide were obtained from Sinopharm Chemical Reagent Co., Ltd. (China). Nitrogen (99.5%), argon (99.999%), hydrogen argon mixed gas (V_{H2}/V_{Ar} = 5/95), and syngas ($V_{H2}/V_{CO}/V_{Ar}$ = 64:32:4) were purchased from Shanghai Pujiang Gas Co., Ltd. (China). All chemicals were used as received.

Sample Preparation

Synthesis of Mesoporous Molecular Sieve SBA-15

Typically, 6 g of the mixture of P123 and glycerol with the same mass ratio was dispersed into 115 g of hydrochloric acid aqueous solution (M_{HCl} = 1.5 M) under vigorous stirring at 37°C for 3 h. Then, 6.45 g of ethyl silicate (TEOS) was added dropwise under vigorous stirring. After 5 min, the resulting mixture was kept static for 24 h, and then the obtained mixture was treated with a drying box at 110°C for 12 h. The dried product was gathered by filtering and washing, and dried at 80°C overnight. Finally, SBA-15 was obtained *via* calcination at 550°C for 5 h to get rid of the surfactant.

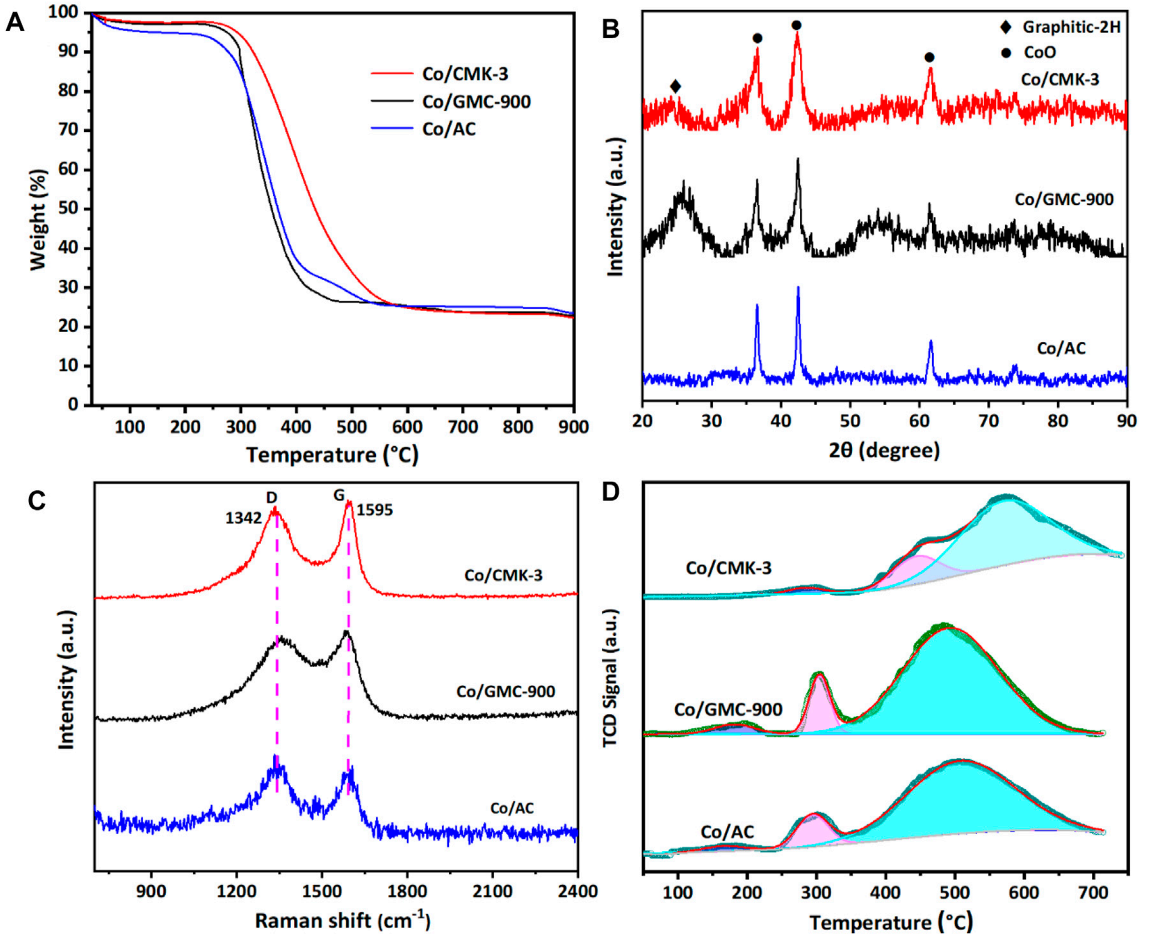

FIGURE 4 | TGA **(A)**, XRD patterns **(B)**, Raman spectra **(C)**, and H2–TPR **(D)** of Co/CMK-3, Co/GMC-900, and Co/AC.

Synthesis of GMC-900

GMC-900 was prepared by a simple solid–liquid grinding/templating route and calcination using SBA-15 as a hard template and soybean oil as a carbon source. In a typical synthesis, the mixture of SBA-15 and soybean oil with a mass ratio of 1:2 was ground together homogeneously under ball milling (400 rpm min^{-1}) for 5 h; then the mixture obtained was transferred into a quartz boat and calcined at 900°C for 5 h (heating ramp 4°C min^{-1}) in nitrogen gas. Finally, the obtained product was treated by NaOH aqueous solution etching to remove SBA-15, and then filtered and dried to collect GMC-900.

Synthesis of Co/GMC-900, Co/CMK-3, and Co/AC

In general, Co/C was prepared using the impregnation method. Briefly, 0.8 g of GMC-900 (or CMK-3 or AC) was added into a cobalt nitrate ethanol solution (0.8719 g, Co $(NO_3)_2 \cdot 6H_2O$) under stirring, and stirring was continued for 1 h. Then the cobalt nitrate ethanol solution was evaporated at 35°C in a rotary evaporator. Finally, the obtained mixture was dried at 50°C for 12 h, and then carbonized at 350°C in nitrogen gas. The products were marked as Co/GMC-900, Co/CMK-3, and Co/AC, respectively.

Characterizations

The microstructure of materials was characterized by a JEOL JEM-2010 transmission electron microscope (TEM, 200 kV). The Barrett–Joyner–Halenda (BJH) pore size distributions and Brunauer–Emmett–Teller (BET) specific surface areas were measured by N_2 ad-/desorption isotherms. X-ray diffraction (XRD) was measured on a Rigaku D/Max2rB-II device (Cu Kα radiation, λ = 1.5406 Å) at a rate of 4°min^{-1} from 20 to 90°. Thermogravimetric analysis (TGA) was carried out by a TGA 8000 analyzer by heating to 900 °C at a rate of 10°C min^{-1}. Raman spectra were observed on a Dilor Labram-1B spectrometer with a 632-nm laser. The behaviors of the samples in H_2 temperature-programmed reduction (TPR) were investigated on a home-made instrument with a thermal conductivity detector (TCD).

Catalysis Measurement

Catalytic performances were assessed using a tubular fix-bed reactor at 270°C, p = 2 MPa, and H_2/CO = 2. Briefly, the isothermal zone of the reactor was placed with a catalyst (0.3 g) blended with quartz granules (40–60 meshes, 2.4 g), and its remaining part was filled with the quartz granules. The

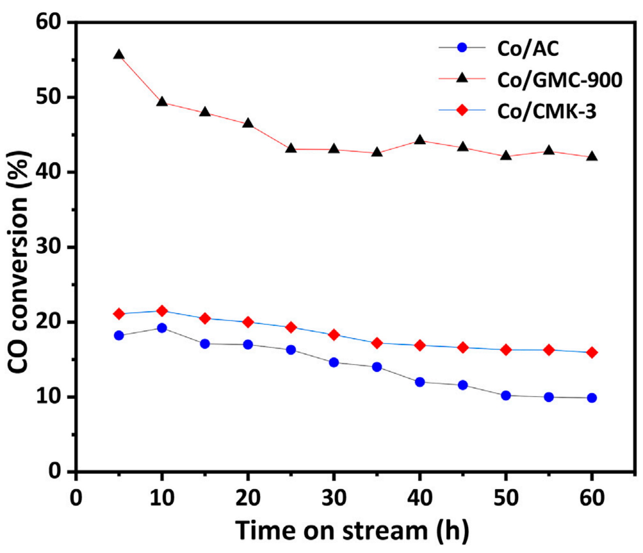

FIGURE 5 | Temporal CO conversion of the catalysts on stream.

TABLE 2 | FTS catalytic performance of Co/GMC-900, Co/CMK-3, and Co/AC catalysts.

Catalyst	CO conv. (%)	Selectivity (%)			CO_2 selectivity (%)
		CH_4	C_2–C_4	C_{5+}	
Co/GMC-900	45.2	22.4	25.1	52.6	36.4
Co/CMK-3	18.1	32.1	29.2	24.3	30.7
Co/AC	13.3	43.7	36.0	20.8	88.7

reactor was maintained at 450°C and 0.4 MPa in H_2 atmosphere (H_2/Ar = 5/95, v/v) for 16 h. After *in situ* catalyst reduction, the reactor was cooled to 120°C in H_2 atmosphere. Then the syngas H_2/CO/Ar (64:32:4) flowed at a rate of 30 ml min^{-1} (GHSV = 3.6 L h^{-1} g^{-1}) through the catalysis bed at 2 MPa and 270°C. Unreacted gases (H_2, N_2, and CO) and by-products (CH_4 and CO_2), and hydrocarbons (C_1–C_{30}) can be detected by TCD and flame ionization detector, respectively.

RESULTS AND DISCUSSION

The procedure for Co/GMC-900 preparation is demonstrated in **Figure 1**. In brief, SBA-15 was synthesized in an acidic environment with ethyl silicate as the silicate source and P123 as the soft template. Subsequently, the obtained SBA-15 was mixed with edible soybean oil through ball-milling to form a homogeneous mixture. Then GMC-900 was collected through carbonizing and etching the above mixture. Finally, Co $(NO_3)_3$ and GMC-900 were mixed by immersion and heat treatment to form Co/GMC-900.

N_2 ad-/desorption isotherms used to explore the specific area before and after cobalt loading are displayed in **Figure 2**. Both GMC-900 and CMK-3 correspond to class IV curves with a typical hysteresis loop at relative pressure P/P_0 of 0.4–1.0

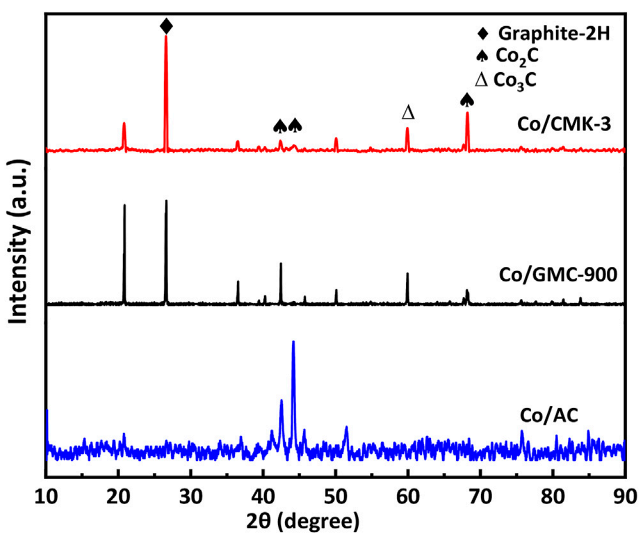

FIGURE 6 | XRD patterns of Co/CMK-3, Co/GMC-900, and Co/AC after FTS for 60 h.

(**Figure 2A**), which suggests the existence of a mesoporous structure (Zhao et al., 2020). The ad-/desorption isotherm of AC is a class I curve, which is characteristic of microporous structures (Asami et al., 2013). After cobalt impregnation, similar ad-/desorption isotherms were found for these catalysts (**Figure 2B**), suggesting the carbon supports are almost structurally constant (Fu and Li, 2015). The physicochemical properties of carbon supports and catalysts are listed in **Table 1**. The specific surface areas of CMK-3 and AC (939 and 657 m^2 g^{-1}, respectively) greatly surpass that of GMC-900. However, the average pore diameter of AC (2.25 nm) is smaller than those of CMK-3 and GMC-900. Furthermore, the pore volumes and specific surface areas of catalysts decrease after loading Co species on the carbon supports. The reason for these results is that the adsorption of cobalt oxide particles onto mesoporous walls leads to the blockage of small pores (Khodakov et al., 2002). Compared with other catalysts, the pore volume of AC decreases slightly, resulting from the entrance of micropores being more easily blocked than that of mesopores.

As shown in **Figure 3**, the TEM images further reveal the typical mesoporous and morphological structures of mesoporous carbon materials and the corresponding Co-based catalysts. **Figure 3A** exhibits the ordered mesoporous structure of CMK-3. GMC-900 is similar to CMK-3, while the mesoporous structure was damaged slightly due to the high-temperature treatment (**Figure 3B**) (Hanzawa et al., 2002). After Co species loading, the morphological structures of catalysts are very different. As for Co/CMK-3 and Co/GMC-900, CoO was uniformly dispersed in the mesopores (**Figures 3D,E**). However, the ordered meso-structure of Co/GMC-900 was partially damaged, which can be due to both high temperature and Co species loading (Fu and Li, 2015). As for Co/AC, some particles appeared due to the aggregation of CoO after Co species loading (**Figure 3F**).

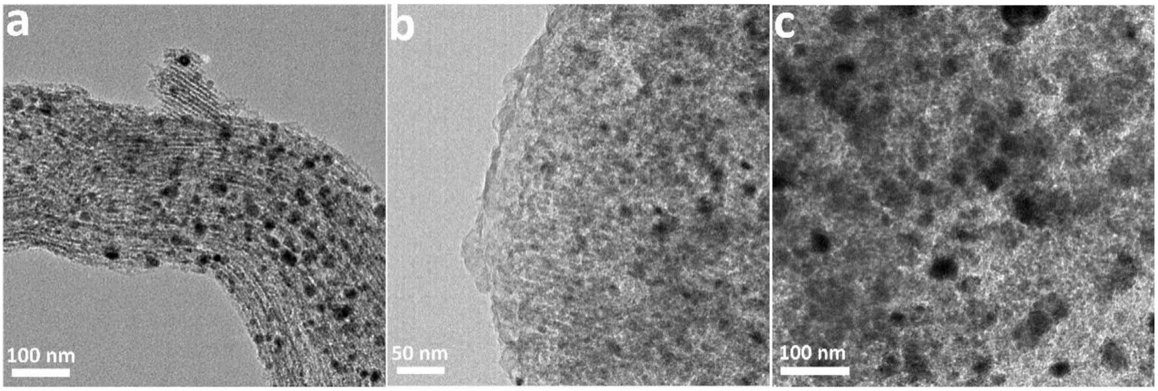

FIGURE 7 | TEM images of Co/CMK-3 **(A)**, Co/GMC-900 **(B)**, and Co/AC **(C)** after 60 h for FTS.

The thermal stability and amount of CoO in the catalysts were analyzed by TGA in air atmosphere (**Figure 4A**). All the catalysts experienced mass losses of about 76.3% during calcination. The first mass loss below 200 °C was due to the desorption of physically adsorbed water (Liu et al., 2018). The second remarkable mass loss occurs at 240–600 °C, corresponding to the combustion of graphitic carbon (Qin et al., 2016; Sun et al., 2012). The structural characteristics of Co/CMK-3, Co/GMC-900, and Co/AC were determined by XRD patterns (**Figure 4B**). The peaks at around 36.4, 42.3, 61.6, 73.9, and 77.8° are indexed to the (111), (200), (220), (311), and (222) reflection for the CoO phase (JCPDS no. 43-1004) (Loewert et al., 2020; Xu et al., 2020). The broad peak at around 26.6° can be attributed to the graphitic carbon (JCPDS no. 41-1487) (Qiu et al., 2014). Compared with Co/CMK-3 and Co/AC, the intensity of this strong graphitic peak for GMC-900 indicates a high degree of graphitization (Torshizi et al., 2020). In addition, the strong peaks of CoO in Co/AC suggest that the particle size of CoO is larger than those of Co/CMK-3 and Co/GMC-900, which is in accordance with the TEM image (**Figure 3F**). Calculation shows that the average particle sizes of CoO in Co/CMK-3, Co/GMC-900, and Co/AC are 6.9, 11.6, and 19.2 nm, respectively.

To further check the carbon structures of the obtained materials, we conducted Raman spectra to recognize the changes of carbon species and the defects in the graphite layer. All catalysts display a D band at around 1342 cm^{-1} and a G band at around 1595 cm^{-1} (**Figure 4C**). The D band corresponds to a defect in the lattice of carbon atoms, while the G band reflects the change of sp^2 hybridized carbon atoms in the graphite layer (Trépanier et al., 2009; Vosoughi et al., 2016; Zeng et al., 2021). Generally, the ratio of relative integrated intensity (I_D/I_G) between these two bands implies the degree of graphitization and the disorder degree of functionalized groups and defects, which was calculated to be 1.98, 1.55, and 2.65 for Co/CMK-3, Co/GMC-900, and Co/AC, respectively. These results indicate that GMC-900 has a high degree of graphitization than Co/CMK-3 and Co/AC, which are in accordance with the above XRD results.

The reducibility of catalysts can be evaluated by H_2-TPR measurements (**Figure 4D**). Obviously, all the catalysts display three partially overlapped peaks. The first and second peaks reflect the reduction of Co_3O_4 to CoO, and the reduction of CoO to Co, respectively, and the third reduction peak in the TPR spectra implies the gasification of carbon support (Sun et al., 2012). The third reduction peak around 574°C for Co/CMK-3 is higher than that for Co/GMC-900 and Co/AC, which indicates that it is more irreducible. The absence of the reduction peak above 600°C suggests no formation of hardly reducible substances on the catalyst surface because of the much lower interaction of carbon support with Co species than with traditional oxides (TiO_2, Al_2O_3, or SiO_2) (Bai et al., 2012; Cheng et al., 2018).

Catalytic behaviors of all the catalysts were explored by FTS performed at p = 2 MPa, T = 270°C, H_2/CO = 2, and GHSV = 3.6 L h^{-1} g^{-1}. Before reaction, the catalysts were reduced *in situ* in H_2 flow at 450°C for 16 h. **Figure 5** exhibits the temporal CO conversion on stream within a time period of 60 h. Among the catalysts, the Co/GMC-900 exhibits relatively higher CO conversion, and even after 60 h, it still has the CO conversion above 40%. As for the Co/CMK-3, the CO conversion is relatively lower than that of Co/GMC-900, while the catalytic activity is more stable (CO conversion decreasing from 21 to 15%). These results can be explained by its ordered pore structure, large specific surface area and pore volume, and open pore structure, benefiting the adsorption and diffusion of syngas in the catalysts (Ahn et al., 2016). By contrast, the Co/AC exhibits lower CO conversion, which can be ascribed to the poor dispersion of CoO (**Figure 3C**).

Table 2 lists the results of catalysts in FTS, including the catalytic behaviors and production distribution. These data were the mean values over 60 h. Clearly, Co/GMC-900 has a maximum CO conversion rate of 45.2%, resulting from the more reducible of Co/GMC-900 than that of Co/CMK-3 and Co/AC so that it can offer more active sites for FTS. In addition, the highly crystallized graphitic structure of GMC-900 can accelerate the electron transport between CoO and CO, thus facilitating the activation of CO (Reuel and Bartholomew, 1984; Fan et al., 2009). In comparison, despite the high dispersion of CoO on CMK-3, large specific surface area, and the orderly mesoporous structure, Co/CMK-3 only achieved the CO conversion of

18.1%, which can be attributed to the less crystallized graphitic structure of CMK-3. In addition, compared with Co/CMK-3 and Co/AC, Co/GMC-900 was less selective toward CH_4 (22.4%) and C_2–C_4 hydrocarbons (25.1%) (**Table 2**), resulting in the increased C_{5+} selectivity of Co/GMC-900. For Co/CMK-3, the higher CH_4 selectivity can be assigned to smaller CoO particles.

Figure 6 exhibits the XRD patterns of all the catalysts after 60 h for FTS. Three strong diffraction peaks at 42.5, 45.7, and 68.3° in the XRD patterns of these catalysts are assigned to Co_2C (JCPDS 72-1369) (LÜ et al., 2012). The other diffraction peaks at 60 and 75° correspond to Co_3C (JCPDS 89-2866) (Liu et al., 2019). These results suggest the appearance of new species of catalysts during FTS, resulting from the decreased conversion of CO. Compared with unreacted catalysts, the peak at around 26.1° in the XRD patterns of used Co/CMK-3 and Co/GMC-900 is stronger, indicating the slight carbon deposition on the catalyst surface (Qin et al., 2019). The aggregation of Co species in catalysts with different sizes was shown in the TEM images (**Figure 7**). In comparison, Co/GMC-900 has a slight aggregation, resulting in the CO conversion which is decreased slowly than that of Co/CMK-3 and Co/AC. This result is in accordance with the results of **Table 2**.

CONCLUSION

In summary, we demonstrate a simple method to prepare Co-based catalysts supported on graphitized ordered mesoporous carbon (GMC-900) for FTS. Compared with other mesoporous carbon (CMK-3 and AC), the obtained GMC-900 by using pollution-free soybean oil as a carbon source exhibited enhanced catalytic performance after loading Co species due to its highly crystallized graphitic structure and uniform dispersion of CoO. FTS results indicate Co/GMC-900 has high catalytic effectiveness with the largest C_{5+} selectivity up to 52.6%, which greatly surpasses those of Co/CMK-3 and Co/AC. Therefore, our work provides important information to produce high-performance FTS catalysts through ball-milling of clean soybean oil as a carbon source.

DATA AVAILABILITY STATEMENT

The original contributions presented in the study are included in the article/Supplementary Material; further inquiries can be directed to the corresponding authors.

AUTHOR CONTRIBUTIONS

JB contributed to conceptualization, methodology, and writing—original draft. MS contributed to methodology and investigation. JP contributed to investigation. LW contributed to investigation resources. JZ contributed to resources. XJ contributed to resources and funding acquisition. ZN contributed to resources and supervision. ZW contributed to conceptualization and project administration. QZ contributed to resources and funding acquisition. All authors contributed to manuscript revision, and read and approved the submitted version.

FUNDING

This work was supported by the National Key Research and Development Program of China (2018YFC1902503-2), the National Natural Science Foundation of China (grant no. 21905031), the Natural Science Foundation of Jiangsu Province (no. BK20200176), the Fundamental Research Project from Changzhou Science and Technology (nos. CJ20210134 and CJ20200029), and Higher Educations Institutions of Jiangsu Province (grant no. 20KJB430038).

REFERENCES

Ahn, C.-I., Park, Y. M., Cho, J. M., Lee, D. H., Chung, C.-H., Cho, B. G., et al. (2016). Fischer-Trospch Synthesis on Ordered Mesoporous Cobalt-Based Catalysts with Compact Multichannel Fixed-Bed Reactor Application: A Review. *Catal. Surv. Asia* 20, 210–230. doi:10.1007/s10563-016-9219-5

Asami, K., Iwasa, A., Igarashi, N., Takemiya, S., Yamamoto, K., and Fujimoto, K. (2013). Fischer-Tropsch Synthesis over Precipitated Iron Catalysts Supported on Carbon. *Catal. Today* 215, 80–85. doi:10.1016/j.cattod.2013.04.020

Bai, S., Huang, C., Lv, J., and Li, Z. (2012). Comparison of Induction Behavior of Co/CNT and Co/SiO2 Catalysts for the Fischer-Tropsch Synthesis. *Catal. Commun.* 22, 24–27. doi:10.1016/j.catcom.2012.02.006

Bustamante, T. M., Campos, C. H., Fraga, M. A., Fierro, J. L. G., and Pecchi, G. (2020). Promotional Effect of Palladium in Co-SiO2 Core@shell Nanocatalysts for Selective Liquid Phase Hydrogenation of Chloronitroarenes. *J. Catal.* 385, 224–237. doi:10.1016/j.jcat.2020.03.006

Cheng, Q., Tian, Y., Lyu, S., Zhao, N., Ma, K., Ding, T., et al. (2018). Confined Small-Sized Cobalt Catalysts Stimulate Carbon-Chain Growth Reversely by Modifying ASF Law of Fischer-Tropsch Synthesis. *Nat. Commun.* 9, 3250. doi:10.1038/s41467-018-05755-8

Dlamini, M. W., Phaahlamohlaka, T. N., Kumi, D. O., Forbes, R., Jewell, L. L., and Coville, N. J. (2020). Post Doped Nitrogen-Decorated Hollow Carbon Spheres as a Support for Co Fischer-Tropsch Catalysts. *Catal. Today* 342, 99–110. doi:10.1016/j.cattod.2019.01.070

Fan, Z., Chen, W., Pan, X., and Bao, X. (2009). Catalytic Conversion of Syngas into C2 Oxygenates over Rh-Based Catalysts-Effect of Carbon Supports. *Catal. Today* 147, 86–93. doi:10.1016/j.cattod.2009.03.004

Fu, T., and Li, Z. (2015). Review of Recent Development in Co-based Catalysts Supported on Carbon Materials for Fischer-Tropsch Synthesis. *Chem. Eng. Sci.* 135, 3–20. doi:10.1016/j.ces.2015.03.007

Guo, K., Li, H., and Yu, Z. (2016). *In-situ* Heavy and Extra-heavy Oil Recovery: A Review. *Fuel* 185, 886–902. doi:10.1016/j.fuel.2016.08.047

Guo, S., Wang, Q., Wang, M., Ma, Z., Wang, J., Hou, B., et al. (2019). A Comprehensive Insight into the Role of Barium in Catalytic Performance of Co/Al2O3 Catalyst for Fischer-Tropsch Synthesis. *Fuel* 256, 115911. doi:10.1016/j.fuel.2019.115911

Hanzawa, Y., Hatori, H., Yoshizawa, N., and Yamada, Y. (2002). Structural Changes in Carbon Aerogels with High Temperature Treatment. *Carbon* 40, 575–581. doi:10.1016/s0008-6223(01)00150-6

Hao, X., An, H., Qi, H., and Gao, X. (2016). Evolution of the Exergy Flow Network Embodied in the Global Fossil Energy Trade: Based on Complex Network. *Appl. Energ.* 162, 1515–1522. doi:10.1016/j.apenergy.2015.04.032

Johnson, G. R., and Bell, A. T. (2016). Effects of Lewis Acidity of Metal Oxide Promoters on the Activity and Selectivity of Co-based Fischer-Tropsch Synthesis Catalysts. *J. Catal.* 338, 250–264. doi:10.1016/j.jcat.2016.03.022

Khodakov, A. Y., Griboval-Constant, A., Bechara, R., and Zholobenko, V. L. (2002). Pore Size Effects in Fischer Tropsch Synthesis over Cobalt-Supported Mesoporous Silicas. *J. Catal.* 206, 230–241. doi:10.1006/jcat.2001.3496

Li, X., Chen, Y., Nisa, M. U., and Li, Z. (2020). Combating Poison with Poison-Irreducible Co2SiO4 as a Promoter to Modify Co-based Catalysts in Fischer-Tropsch Synthesis. *Appl. Catal. B: Environ.* 267, 118377. doi:10.1016/j.apcatb.2019.118377

Liu, B., Li, W., Xu, Y., Lin, Q., Jiang, F., and Liu, X. (2019). Insight into the Intrinsic Active Site for Selective Production of Light Olefins in Cobalt-Catalyzed Fischer-Tropsch Synthesis. *ACS Catal.* 9, 7073–7089. doi:10.1021/acscatal.9b00352

Liu, C., He, Y., Wei, L., Zhang, Y., Zhao, Y., Hong, J., et al. (2018). Hydrothermal Carbon-Coated TiO2 as Support for Co-based Catalyst in Fischer-Tropsch Synthesis. *ACS Catal.* 8, 1591–1600. doi:10.1021/acscatal.7b03887

Loewert, M., Serrer, M.-A., Carambia, T., Stehle, M., Zimina, A., Kalz, K. F., et al. (2020). Bridging the gap between Industry and Synchrotron: an Operando Study at 30 Bar over 300 H during Fischer-Tropsch Synthesis. *React. Chem. Eng.* 5, 1071–1082. doi:10.1039/c9re00493a

Lü, J., Huang, C., Bai, S., Jiang, Y., and Li, Z. (2012). Thermal Decomposition and Cobalt Species Transformation of Carbon Nanotubes Supported Cobalt Catalyst for Fischer-Tropsch Synthesis. *J. Nat. Gas Chem.* 21, 37–42. doi:10.1016/S1003-9953(11)60330-7

Lyu, S., Liu, C., Wang, G., Zhang, Y., Li, J., and Wang, L. (2019). Structural Evolution of Carbon in an Fe@C Catalyst during the Fischer-Tropsch Synthesis Reaction. *Catal. Sci. Technol.* 9, 1013–1020. doi:10.1039/c8cy02420k

Lyu, S., Wang, L., Zhang, J., Liu, C., Sun, J., Peng, B., et al. (2018). Role of Active Phase in Fischer-Tropsch Synthesis: Experimental Evidence of CO Activation over Single-phase Cobalt Catalysts. *ACS Catal.* 8, 7787–7798. doi:10.1021/acscatal.8b00834

Qin, C., Hou, B., Wang, J., Wang, G., Ma, Z., Jia, L., et al. (2019). Stabilizing Optimal Crystalline Facet of Cobalt Catalysts for Fischer-Tropsch Synthesis. *ACS Appl. Mater. Inter.* 11, 33886–33893. doi:10.1021/acsami.9b10174

Qin, H., Kang, S., Wang, Y., Liu, H., Ni, Z., Huang, Y., et al. (2016). Lignin-Based Fabrication of Co@C Core-Shell Nanoparticles as Efficient Catalyst for Selective Fischer-Tropsch Synthesis of C5+ Compounds. *ACS Sustain. Chem. Eng.* 4, 1240–1247. doi:10.1021/acssuschemeng.5b01269

Qiu, T., Li, X., Liang, H., Liu, X., and Lei, Y. (2014). A Method for Estimating the Temperature Downstream of the SCR (Selective Catalytic Reduction) Catalyst in Diesel Engines. *Energy* 68, 311–317. doi:10.1016/j.energy.2014.02.101

Reuel, R., and Bartholomew, C. H. (1984). Effects of Support and Dispersion on the CO Hydrogenation Activity/selectivity Properties of Cobalt. *J. Catal.* 85, 78–88. doi:10.1016/0021-9517(84)90111-8

Sun, B., Liu, H., Munroe, P., Ahn, H., and Wang, G. (2012). Nanocomposites of CoO and a Mesoporous Carbon (CMK-3) as a High Performance Cathode Catalyst for Lithium-Oxygen Batteries. *Nano Res.* 5, 460–469. doi:10.1007/s12274-012-0231-4

Tavasoli, A., Sadagiani, K., Khorashe, F., Seifkordi, A. A., Rohani, A. A., and Nakhaeipour, A. (2008). Cobalt Supported on Carbon Nanotubes - A Promising Novel Fischer-Tropsch Synthesis Catalyst. *Fuel Process. Technol.* 89, 491–498. doi:10.1016/j.fuproc.2007.09.008

Torshizi, H. O., Nakhaei Pour, A., Mohammadi, A., and Zamani, Y. (2020). Fischer-Tropsch Synthesis Using a Cobalt Catalyst Supported on Graphitic Carbon Nitride. *New J. Chem.* 44, 6053–6062. doi:10.1039/d0nj01041c

Trépanier, M., Tavasoli, A., Dalai, A. K., and Abatzoglou, N. (2009). Fischer–Tropsch Synthesis over Carbon Nanotubes Supported Cobalt Catalysts in a Fixed Bed Reactor: Influence of Acid Treatment. *Fuel Process. Technol.* 90, 367–374. doi:10.1016/j.fuproc.2008.10.012

Vosoughi, V., Badoga, S., Dalai, A. K., and Abatzoglou, N. (2016). Effect of Pretreatment on Physicochemical Properties and Performance of Multiwalled Carbon Nanotube Supported Cobalt Catalyst for Fischer-Tropsch Synthesis. *Ind. Eng. Chem. Res.* 55, 6049–6059. doi:10.1021/acs.iecr.5b04381

Wang, Y., Wang, C., Chen, M., Hu, J., Tang, Z., Liang, D., et al. (2020). Influence of CoAl2O4 Spinel and Co-phyllosilicate Structures Derived from Co/sepiolite Catalysts on Steam Reforming of Bio-Oil for Hydrogen Production. *Fuel* 279, 118449. doi:10.1016/j.fuel.2020.118449

Wolf, M., Gibson, E. K., Olivier, E. J., Neethling, J. H., Catlow, C. R. A., Fischer, N., et al. (2020). In-depth Characterisation of Metal-Support Compounds in Spent Co/SiO2 Fischer-Tropsch Model Catalysts. *Catal. Today* 342, 71–78. doi:10.1016/j.cattod.2019.01.065

Wu, Y., Chen, X., Han, Y., Yue, D., Cao, X., Zhao, Y., et al. (2019). Highly Efficient Utilization of Nano-Fe(0) Embedded in Mesoporous Carbon for Activation of Peroxydisulfate. *Environ. Sci. Technol.* 53, 9081–9090. doi:10.1021/acs.est.9b02170

Xiong, H., Motchelaho, M. A. M., Moyo, M., Jewell, L. L., and Coville, N. J. (2011). Correlating the Preparation and Performance of Cobalt Catalysts Supported on Carbon Nanotubes and Carbon Spheres in the Fischer-Tropsch Synthesis. *J. Catal.* 278, 26–40. doi:10.1016/j.jcat.2010.11.010

Xu, R., Hou, C., Xia, G., Sun, X., Li, M., Nie, H., et al. (2020). Effects of Ag Promotion for Co/Al2O3 Catalyst in Fischer-Tropsch Synthesis. *Catal. Today* 342, 111–114. doi:10.1016/j.cattod.2019.04.004

Zeng, Q., Chang, S., Wang, M., Li, M., Deng, Q., Xiong, Z., et al. (2021). Highly-active, Metal-free, Carbon-Based ORR Cathode for Efficient Organics Removal and Electricity Generation in a PFC System. *Chin. Chem. Lett.* 32, 2212–2216. doi:10.1016/j.cclet.2020.12.062

Zhang, M., Xin, X., Xiao, Z., Wang, R., Zhang, L., and Sun, D. (2017). A Multi-Aromatic Hydrocarbon Unit Induced Hydrophobic Metal-Organic Framework for Efficient C2/C1 Hydrocarbon and Oil/water Separation. *J. Mater. Chem. A.* 5, 1168–1175. doi:10.1039/c6ta08368d

Zhao, Y., Huang, S., Wei, L., Zhang, Y., Lin, A., Liu, C., et al. (2020). Highly Dispersed CoO on Graphitic Mesoporous Carbon as an Efficient Catalyst for Fischer-Tropsch Synthesis. *Ind. Eng. Chem. Res.* 59, 3279–3286. doi:10.1021/acs.iecr.9b06041

Conflict of Interest: The authors declare that the research was conducted in the absence of any commercial or financial relationships that could be construed as a potential conflict of interest.

frontiers in Chemistry

ORIGINAL RESEARCH
published: 14 February 2022
doi: 10.3389/fchem.2021.833024

Fabrication and Characterization of the Porous Ti_4O_7 Reactive Electrochemical Membrane

Guangfeng Qi[1,2†], **Xiaohui Wang**[1,2*†], **Jingang Zhao**[1,2], **Chunyan Song**[1,2], **Yanbo Zhang**[1,2], **Feizhou Ren**[1,2] **and Nan Zhang**[1,2]

[1]Technical Test Center of Sinopec Shengli OilField, Dongying, China, [2]Testing and Evalution Research Co. Ltd. of Sinopec Shengli OilField, Dongying, China

Preparation of the Magnéli Ti_4O_7 reactive electrochemical membrane (REM) with high purity is of great significance for its application in electrochemical advanced oxidation processes (EAOPs) for wastewater treatment. In this study, the Ti_4O_7 REM with high purity was synthesized by mechanical pressing of TiO_2 powders followed by thermal reduction to Ti_4O_7 using the Ti powder as the reducing reagent, where the TiO_2 monolith and Ti powder were separated from each other with the distance of about 5 cm in the vacuum furnace. When the temperature was elevated to 1333 K, the Magnéli phase Ti_4O_7 REM with the Ti_4O_7 content of 98.5% was obtained after thermal reduction for 4 h. Noticeably, the surface and interior of the obtained REM bulk sample has a homogeneous Ti_4O_7 content. Doping carbon black (0wt%-15wt%) could increase the porosity of the Ti_4O_7 REM (38–59%). Accordingly, the internal resistance of the electrode and electrolyte and the charge-transfer impedance increased slightly with the increasing carbon black content. The optimum electroactive surface area (1.1 m^2) was obtained at a carbon black content of 5wt%, which increased by 1.3-fold in comparison with that without carbon black. The as-prepared Ti_4O_7 REMs show high oxygen evolution potential, approximately 2.7 V/SHE, indicating their appreciable electrocatalytic activity toward the production of •OH.

Keywords: Ti4O7, reactive electrochemical membrane, Ti, TiO_2, thermal reduction

1 INTRODUCTION

Ceramic porous sub-stoichiometric Ti oxides (Ti_nO_{2n-1}, $4 \le n \le 10$), known as Magnéli phases, were first synthesized and characterized in the 1950s (Zhou et al., 2018). Among these oxides, Ti_4O_7 exhibits excellent performance owing to its unique structure, e.g., excellent corrosion resistance and outstanding electrical conductivity with a value of 1000 S cm^{-1}, which is higher than the 727 S cm^{-1} of graphitized carbon (Walsh and Wills, 2010). In light of this, the Ti_4O_7 material has been widely used as a cathodic protection during the electrodeposition process, in batteries as either an electrode material or an additive to the active materials (Zhang et al., 2017). In addition, due to its stability under anodic polarization and high oxygen evolution overpotential, Ti_4O_7 has been recently utilized as the inert anode material for weekly sorbed •OH production in the field of electrochemical wastewater treatment, which shows comparable electrocatalytic activity to the boron-doped diamond (BDD) anode for pollutant degradation (Bejan et al., 2009).

Recently, depositing Ti_4O_7 films at the Ti surface has been manufactured successfully by the plasma coating approach, which is a widely spread technology for many types of applications (corrosion protection, abrasion resistance, thermal barriers, etc.) (Ganiyu et al., 2016; Oturan et al.,

Edited by:
Suqing Wu,
Wenzhou University, China

Reviewed by:
Xing Xu,
Shandong University, China
Dongting Yue,
Shanghai University, China
Hu Haiyang,
Ludwig Maximilian University of Munich, Germany

***Correspondence:**
Xiaohui Wang
wangxiaohui153.slyt@sinopec.com

†These authors have contributed equally to this work

Specialty section:
This article was submitted to Inorganic Chemistry,
a section of the journal
Frontiers in Chemistry

Received: 10 December 2021
Accepted: 20 December 2021
Published: 14 February 2022

Citation:
Qi G, Wang X, Zhao J, Song C, Zhang Y, Ren F and Zhang N (2022) Fabrication and Characterization of the Porous Ti_4O_7 Reactive Electrochemical Membrane.
Front. Chem. 9:833024.
doi: 10.3389/fchem.2021.833024

2017). This preparation process is mainly proceeded by two steps: 1) reduction of TiO_2 with coke to produce Ti_xO_{2x-1} powder and 2) plasma elaboration of Ti_xO_{2x-1} on the Ti-alloy substrate at 10,000–15,000°C accompanied by conversion of all sub-oxides of Ti to Ti_4O_7 [46]. However, the application of this Ti_4O_7 electrode is greatly limited by mass diffusion since there is a thick stagnant boundary layer (~100 μm) at the plate electrode surface (Liu and Vecitis, 2012; Zaky and Chaplin, 2013). The flow-through mode, which is defined as operating with convective flow perpendicular to the porous electrode surface, allowed for enhanced mass transport rates relative to the traditional parallel flow mode by restricting the diffusional distance of reactants to a length-scale on the order of the pore radius of the electrode (Vecitis et al., 2011; Zaky and Chaplin, 2013; Guo et al., 2016a; Guo et al., 2016b). Thus, significant attention has been recently paid to the integration of membrane filtration and electrochemical process, known as the Ti_4O_7 reactive electrochemical membrane (REM), for aqueous contaminant degradation because this operation mode promotes the reaction between the contaminant and •OH produced at the anode surface. As a result, REMs based on electrochemical advanced oxidation processes (EAOPs) are a cutting edge class of electrodes that hold great promise in revolutionizing water/wastewater treatment (Zaky and Chaplin, 2013).

As for the preparation of the Ti_4O_7 REM, TiO_2 is typically used as the main feedstock due to its abundance and relatively low cost. The mechanical pressing of Ti_4O_7 powders, followed by thermal sintering, has been widely used to fabricate the Ti_4O_7 REMs. There are many conventional approaches available to synthesize the Ti_4O_7 materials under controlled reducing conditions at relatively high temperature using different reducers such as metals (Kitada et al., 2012), carbon (Ganiyu et al., 2016), carbonaceous organic materials (Guo et al., 2019), and reducing atmosphere (H_2 and NH_3) (Li et al., 2010; Zhang et al., 2013; Lin et al., 2018). However, most of the production methods are energy and time-consuming. For example, the Ti_4O_7 REM was synthesized by reduction of commercial TiO_2 ultrafiltration membranes at 1333 K for 50 h in the H_2 atmosphere (Guo et al., 2016b). As another example, an ultrafiltration membrane layer composed of Ti_4O_7 and Ti_6O_{11} was obtained by dip-coating of a TiO_2 layer on the inner surface of a tubular Al_2O_3 membrane, followed by a reduction step under 30% H_2 in the Ar atmosphere at 1308K for 7 h (Geng and Chen, 2016). High processing temperatures over 1000°C and such long time not only inevitably leads to morphology deformation but also results in particle aggregation and dense low surface area materials, which limit its practical applications as electrode materials, where high surface area, a large number of active sites, and a porous structure are all important for the performance (Lin et al., 2018). In addition to the cases under the reducing atmosphere (H_2 and NH_3), the as-prepared Ti_4O_7 REMs did not have high purity since the residual reducing reagents and their derivatives eventually reduce the purity of the obtained Magnéli Ti_4O_7 REM. However, the gaseous reduction process usually brings about high costs and potential danger. The high preparation costs and rigorously controlled fabrication conditions (H_2 atmosphere) might limit their commercial development to some extent. Overall, the control of the stoichiometry of Magnéli phases according to the choice of precursors and thermal treatment is an interesting challenge for material science.

In the present study, thermal reduction of TiO_2 by metal Ti under the vacuum condition was developed to prepare the Ti_4O_7 REM with high purity. The influences of the preparation temperature and thermal sintering time were optimized for Ti_4O_7 REM preparation. The Ti_4O_7 REM was characterized using X-ray diffraction (XRD), scanning electron microscopy (SEM), and mercury intrusion porosimetry. The water filtration performance of these REMs was evaluated based on the pressure-normalized permeate flux. In addition, the electrochemical properties of the REMs were studied by sweep voltammetry (CV) and electrochemical impedance spectroscopy (EIS).

2 MATERIALS AND METHODS

2.1 Reagents

TiO_2 (99.99%, 25 nm particles) and Ti (99.9%, 10 nm particles) powder were purchased from Beijing Xingyuan Technology Co., Ltd. Carbon black (XC-72R) was bought from Cabot Corporation. Ethanol (EtOH) (99.99%, anhydrous), sodium sulfate (99.9%), potassium ferrocyanide (99.5%), and potassium ferricyanide (99.5%) were obtained from Sigma-Aldrich. All solutions were prepared using deionized water (18.2 MΩ cm^{-1} at 25°C).

2.2 Ti_4O_7 REM Fabrication

The Ti_4O_7 ceramic microfiltration membrane was prepared by the following route: TiO_2 powder and carbon black were first mixed together and then put into a ZrO_2 ball-milling bowl (500 ml in volume, Fritsch, Germany), where the load of carbon black was set to 7.5% of the mass of the TiO_2 powder. A planetary ball-mill (Fritsch, Pulverisette 6, Germany) was utilized to mix the membrane contents, in which the grinding balls were a mixture of Nikkato ZrO_2 balls in the diameters of 1, 2, 5, 10, and 20 mm. The volume of the balls and the material account for 1/3 of the volume of the ball mill tank, respectively. Anhydrous ethanol is used as a ball milling agent. After allowing it to dry at 60°C overnight, 10 g powders were mixed with 2–3wt% of ethanol and transferred to a disc mould and pressed under the pressure of 30 MPa by a hydraulic press (Specac, UK) to form the precursor of the REM. The membrane was first sintered in air for 4 h at 973 K for the removal of carbon black then was reduced in the presence of the Ti powder (about 4 g) in a vacuum ($<8 \times 10^{-3}$ MPa) tube furnace for the preparation of the Ti_4O_7 REM. The precursor of the Ti_4O_7 monolith and Ti powder were separated from each other, and the distance is about 5 cm. The heating/cooling rates were both 4 K min^{-1}.

2.3 Physicochemical and Electrochemical Characterization

XRD analysis was performed to obtain the phase information of the Ti_4O_7 REM. The Scherrer equation was used to calculate the

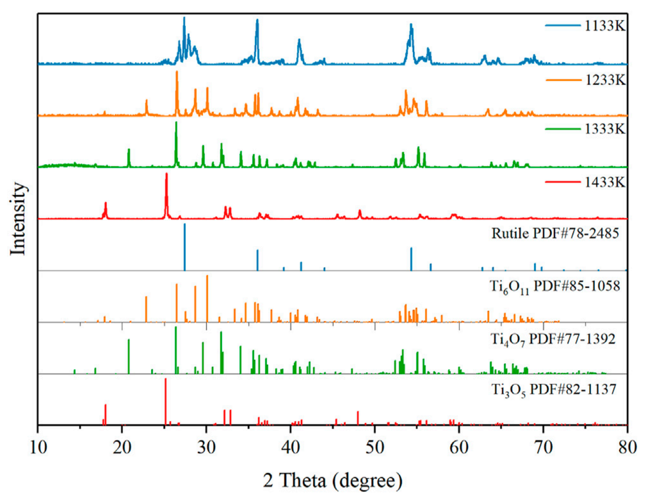

FIGURE 1 | XRD patterns of the REM sample prepared at various temperatures.

crystallite size. The Ti_4O_7 REM surface morphology was characterized by SEM. Mercury intrusion porosimetry was used to investigate the porous structures of the electrodes. The EIS and CV analyses were conducted with an electrochemical workstation (PGSTAT302N, Metrohm) and used a three-electrode setup with the Ti_4O_7 electrode as the working electrode, a platinum plate electrode (3 cm × 3 cm) as the counter electrode, and a saturated calomel electrode (SCE) as the reference electrode. EIS analysis was performed at the open circuit potential (OCP, 190 mV/SCE) over a frequency range of 10^{-2}–10^4 Hz in 100 mM Na_2SO_4 supporting electrolyte solution with the presence of 5 mM $K_4Fe(CN)_6$ and 5 mM $K_3Fe(CN)_6$ redox couple. CV measurements were recorded at a voltage step of 0.05 V in 100 mM $NaClO_4$ electrolyte. The electrochemically active surface area was calculated based on CV analysis at a scan rate from 5 to 30 mV s^{-1} in a potential range of −0.2–0.5 V.

3 RESULTS AND DISCUSSION

3.1 Ti_4O_7 REM Fabrication

The effect of thermal reduction temperature on the purity of the Ti_4O_7 REM was conducted in the range of 1133–1433 K. **Figure 1** shows the XRD patterns of the REM samples prepared at various temperatures. It was observed that the color of the REM sample turned from white to light blue after thermal reduction at the reduction temperature of 1133 K. But the obtained REM sample was mainly rutile. This indicates that this reaction temperature was sufficient for the reduction of Ti^{4+} in anatase-TiO_2 to Ti^{3+}, while it was not high enough to transform anatase-TiO_2 to the Magnéli phase. The phase transformation was observed at a sintering temperature of 1233 K, where the predominant phase was Ti_6O_{11} and Ti_5O_9 was the marginal phase. When the temperature was elevated to 1333 K, the XRD patterns show the characteristic peaks for Ti_4O_7, and almost no peaks for other Magnéli phases suggests that a high purity Magnéli phase Ti_4O_7 REM was successfully fabricated. At this temperature, the Ti_4O_7 content of the samples was 98.5%, while the Ti_3O_5 content was only 1.5%. In contrast, when the reduction temperature was further increased to 1433 K, a single phase of Ti_3O_5 is formed, indicating that this reaction temperature was too high to synthesize pure Ti_4O_7.

To further find the optimal conditions for the synthesis of Ti_4O_7, the influence of thermal reduction time on the purity of the Ti_4O_7 REM was also studied. The XRD patterns of the as-prepared REM samples prepared at 1333K for 2, 4, and 6 h are shown in **Figure 2**. It is found that the Magnéli phase Ti_4O_7 was the major component at the thermal reduction time of 2–6 h. For 2 h, the as-prepared REM sample contains 24% Ti_5O_9, 10% Ti_6O_{11}, and 66% Ti_4O_7. When the thermal reduction time reached 4 h, XRD patterns show that Ti_5O_9 and Ti_6O_{11} phases disappeared and Ti_4O_7 to be the main crystalline phase in the material with only <3% Ti_3O_5 left. Extending the reaction time to 6 h, the percentage of Ti_3O_5 phases increased slightly to 6%, and the percentage of Ti_4O_7 exhibited an insignificant change. These results mean that the thermal reduction time of 2 h is insufficient for the complete transformation of TiO_2 to Ti_4O_7. However, as for 6 h, the increase of the miscellaneous peak, especially Ti_3O_5, indicates that the sample proceeded overreduction due to the longer thermal reduction time. These results illustrate the optimum reduction time for preparing the pure Ti_4O_7 REM was 4 h.

The XRD peaks for the reduced phases are relatively sharp (fwhm = 0.117° for 2 h, 0.084° for 4 h and 0.092° for 6 h) for the peaks at 26.4°, respectively. After accounting for instrumental broadening, the estimated crystallite sizes are 67 nm for 2 h, 90 nm for 4 h, and 119 nm for 6 h according to the Sherrer's equation, while the crystallite size of the original TiO_2 is 25 nm, indicating the crystallite growth. For further investigation of the phase composition of the productions, the XRD spectrums of the REM those were not grounded into powder are showed in **Figure 3**. In addition, the XRD peaks of the REM were perfectly coincident with those grounded into powder, meaning that the component of the REM bulk was homogeneous. It is noteworthy that as for the common carbothermal reduction approach with mixing carbon powder and TiO_2, the surface and interior of the obtained bulk sample show different compositions (Tsumura et al., 2004; Toyoda et al., 2009).

3.2 Pore Properties Modification

The morphology and pore structure of the REM were characterized by SEM Hg porsimetry, respectively. The SEM images in **Figures 4A–D** show the samples prepared at 1333 K with different carbon black contents of 0wt%, 1.5wt%, 5wt%, and 10wt%. The pore size of four samples was almost similar due to the fact that the grain-growth behavior mainly depends on the sintering time and temperature (Guan et al., 2016). The SEM images of the REM exhibit a three-dimensionally assembled structure with macro porosity, and the crystallites were indeed intimately fused or even consolidated to form large single-crystal particles on the micrometer scale. During the high-temperature reduction process, the agglomerates of solid particles and particle

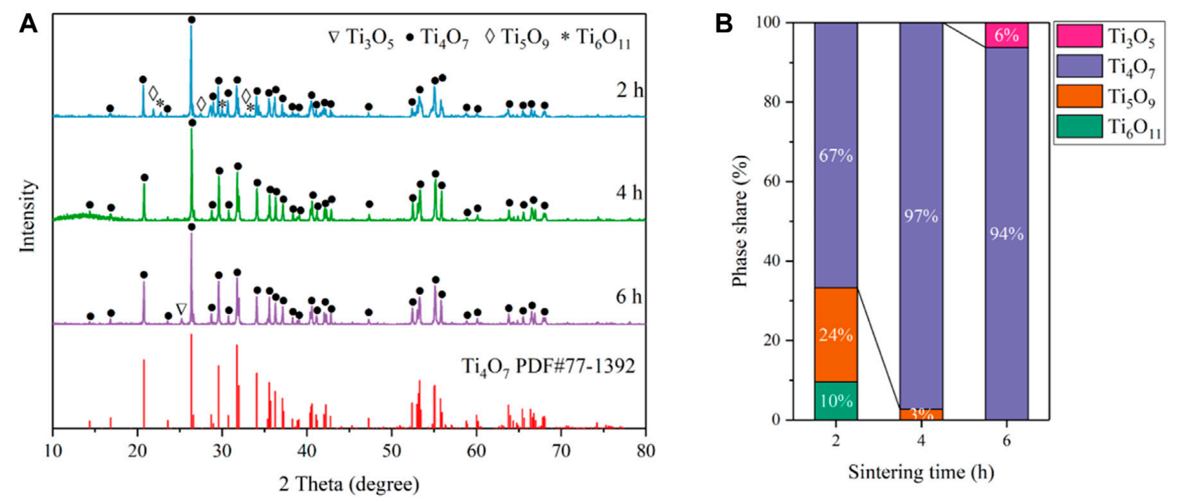

FIGURE 2 | (A) XRD patterns of the as-prepared samples obtained at 1333 K for 2, 4, and 6 h; **(B)** Phase composition percentage.

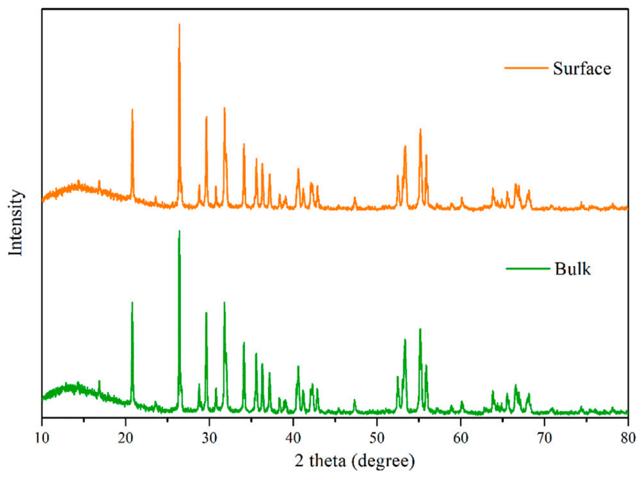

FIGURE 3 | XRD patterns of the surface and interior of the REM monolith.

bonding resulted in the formation of the porous structure inside the cavity in the presence of the porosity-producing agent. **Figure 4** shows that the pore size increased with the increasing carbon black content. The size of pores in **Figure 4D** seems to be larger than that in **Figure 4A**, which may be explained by the different carbon contents of these two samples. The detailed pore structure of these membranes was characterized by Hg porosimetry, and the results are presented in the **Figure 5**. It is demonstrated that the REM sample possessed uniform macropores of 0.4–0.5 μm (**Figure 6**). The almost same macropore diameter and volume indicate that the well-defined macroporous structure of the monolith was retained. These results are consistent with the results of SEM images. Moreover, the REM exhibits a pore size distribution with ~99% of the measured surface area associated with pores <0.5 μm, and essentially, the entire pore volume attributed to pores with 0.2–0.5 μm diameters. As shown in **Figure 5**, based on the porosimetry results, the porous surface area for the membrane without carbon black was estimated as 1.477 $m^2 g^{-1}$ with the porosity(θ) and median pore diameter of 0.382 and 0.380 μm, respectively. As the content of carbon black was elevated to 1.5wt%, the porous surface area was enhanced to 1.797 $m^2 g^{-1}$ with the increase in the porosity by 4.7%, while no difference was observed in the pore size as compared with that without the addition of carbon black. The membrane with 5wt% carbon black has a porous surface area of 2.011 $m^2 g^{-1}$, median pore diameter of 0.481 μm, and its porosity is 0.427 which is the same with the former. The porosity for the REM with 15wt% carbon black was determined as 0.594, specific surface area of 2.477 $m^2 g^{-1}$, and median pore diameter of 0.575 μm. As the volume of carbon black increased, the change of pore size is slight, and the porosity has a gap of 21% between the samples without carbon black and with 15% carbon black. Micron-sized pores dominated the REM pore volume, which facilitates water transport through the REM at low applied pressures and is expected beneficial for facilitating interfacial mass transfer during the electrochemical reaction. Porosimetry analysis results show that the average pore diameter was closed to the median pore diameter (based on pore volume data) showing symmetrically distribution pore size. The addition of high carbon black content was not recommended since it would cause the crack of the REM monolith during the flow-through operation mode.

A flow-through reactor was used to assess the permeation ability of REMs with ultra-pure water experiments which were carried out with the Ti_4O_7 REM. A digital gear pump was prepared to control the permeate flux and a pressure gage was used to record the hydraulic pressure. The evolution of the permeate flux with the carbon black content is plotted in **Figure 7**. It is found that the porosity and pore size both exerted the influence on the permeate flux. The REM without carbon black and with 1.5%wt carbon black have the same pore

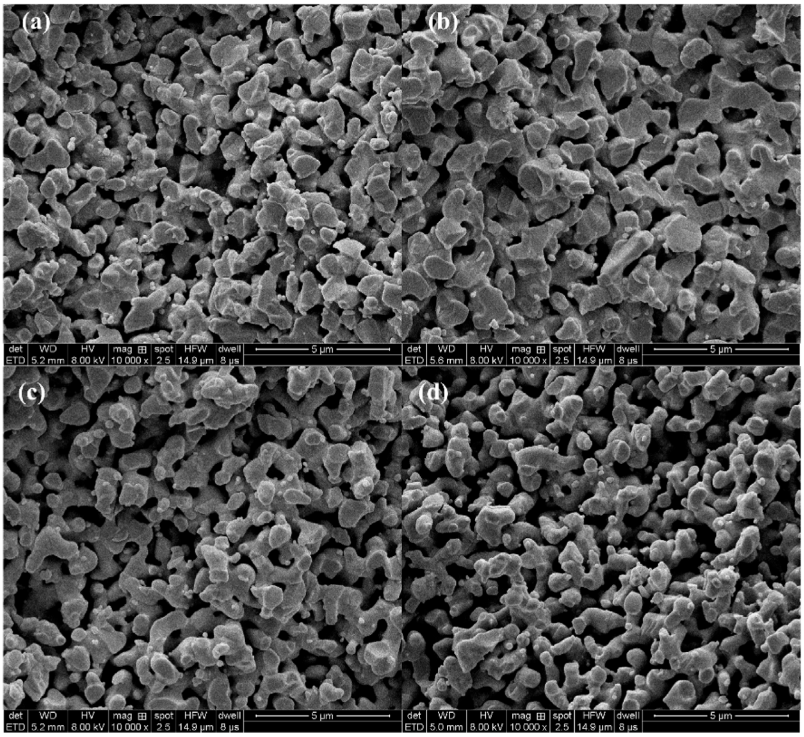

FIGURE 4 | SEM image of the samples obtained at 1333 K with different carbon black contents of 0wt% **(A)** 1.5wt%, **(B)** 5wt%, and **(C)** 10wt% **(D)**.

size of 380 nm but different porosity, e.g., 38 and 42%, respectively. The permeate flux of the latter increased 28% than the former. REMs with 1.5wt% and 5wt% carbon black have the same porosity of 0.42 and different pore size. With the bigger pore size and porosity, the increased extent of the permeate flux was much more evident. The permeate flux for the sample with the pore size of 480 nm increased by 57% than the sample with 380 nm pore size. The results of the REM membrane with 60% porosity and 580 nm pore size showed that the method improved the flux obviously with a 452% increase in the flux from 250 to 1379 L m^{-2} h^{-1} bar^{-1} than the original REM membrane. This indicates that a high content of carbon black was a crucial factor for the permeation ability of the REM membrane.

The resistance-in-series model was applied to evaluate the characteristics of the membrane flux; according to the Darcy law, the permeation flux (J) takes the following form:

$$J = \frac{\Delta P}{\eta R_m}, \quad (1)$$

where J is the permeation flux (L/m^2 h), ΔP (Pa) is the transmembrane pressure, η is the dynamic viscosity of the permeate, and R_m (m^{-1}) is the intrinsic membrane resistance. **Table 1** made a summary of pressure-normalized permeate fluxes (LMH/bar) and intrinsic membrane resistance (10^{10}/m) of the four samples. It can be seen that R_m decreased with the increases of the carbon black content. R_m of the original membrane is ~6 times higher than that of the membrane with 15 wt% content of carbon black, which suggest that a lower membrane resistance can be achieved by simply increasing the content of carbon black.

3.3 Electrochemical Characterization

The measurements of the electrochemically active surface area of each electrode were conducted within the potential region between hydrogen and oxygen evolution reaction, i.e., −0.2–0.5 V/SCE, at the sweep rates of 5–30 mV/s. As shown in **Figure 8**, the capacitive current decreases linearly with lowering sweep rates so that the apparent capacitance can be calculated from the slope of the charging current *vs* sweep rate. The double layer capacitances (C_{dl}) were determined based on the CV test according to **Eq. 2**.

$$\frac{I_a - I_c}{2} = C_{dl} v, \quad (2)$$

where I_a and I_c represent the measured plateau currents at 0.25 V/SCE, and v is the scan rate (V/s). The surface roughness factor and electroactive surface area were calculated according to the previous study with the use of the electrode geometric surface area. Assuming a double layer capacitance of 60 µF/cm^2 for a surface of oxides, the roughness factors “r” can be estimated as follows:

$$r = \frac{C_{dl}}{C_0}. \quad (3)$$

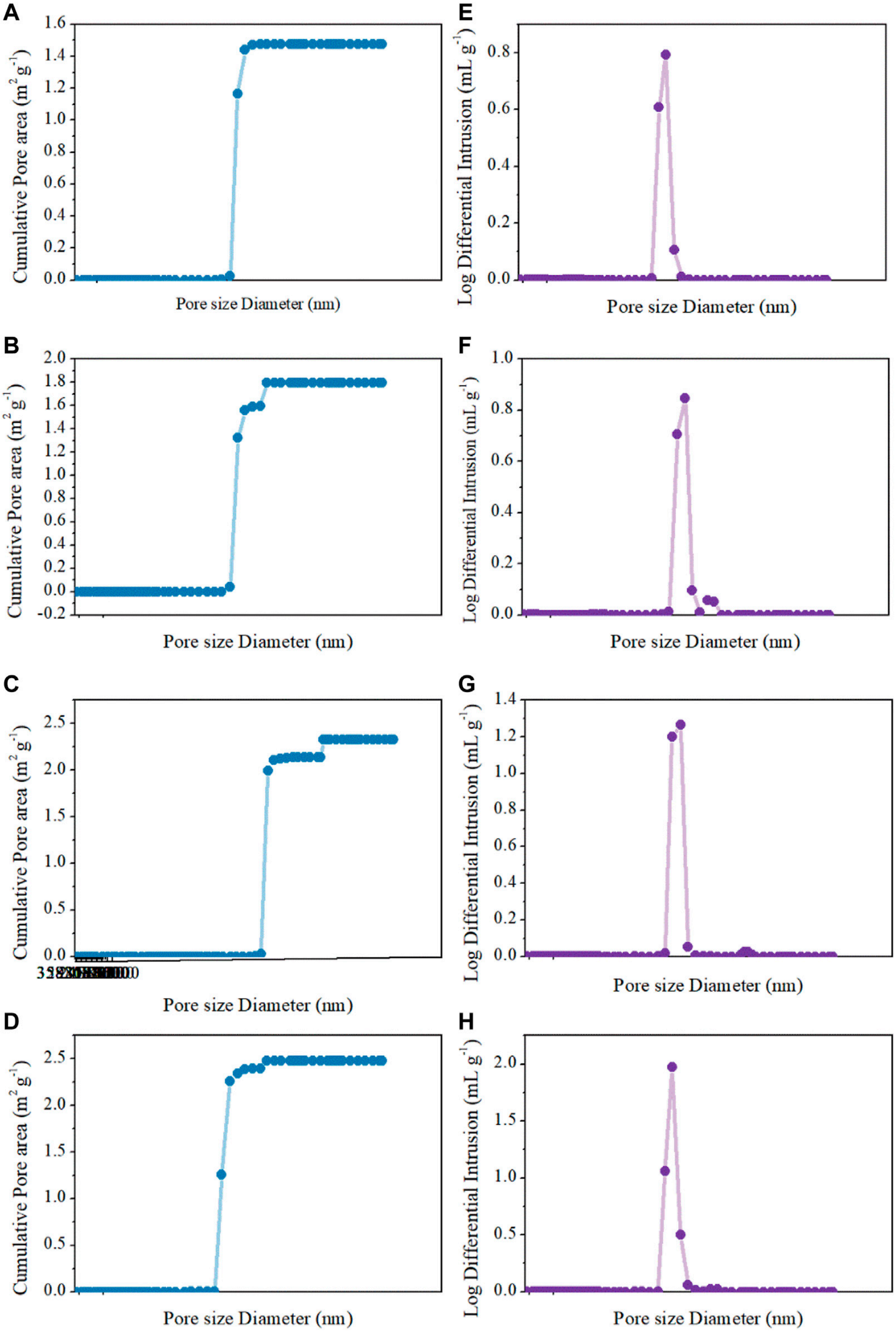

FIGURE 5 | Cumulative pore area and log differential intrusion pore volume of Hg intrusion porosimetry analysis for **(A,E)** 0wt%, **(B,F)** 1.5wt%, **(C,G)** 5wt%, and **(D,H)** 15wt%.

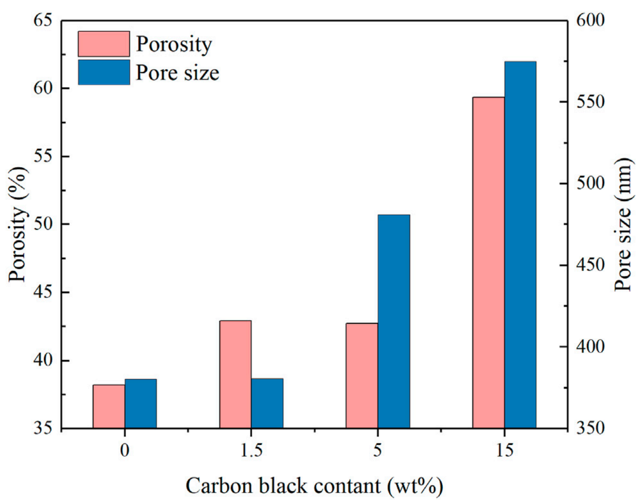

FIGURE 6 | Porosity and pore size with different carbon black contents.

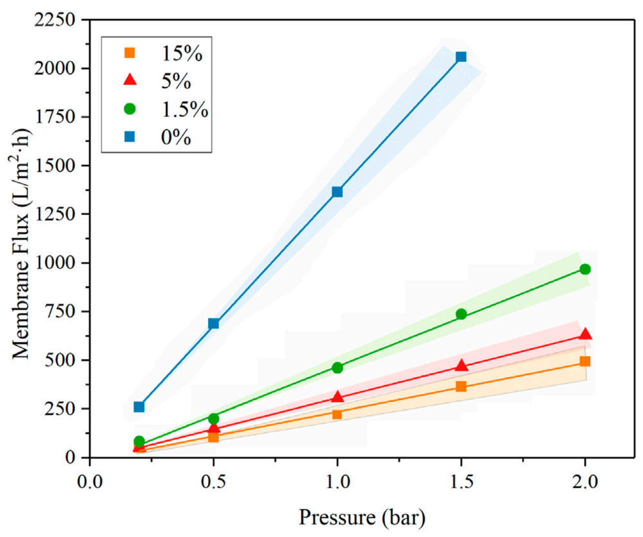

FIGURE 7 | Pressure-normalized permeate fluxes of REMs with different carbon black contents.

Comparative cyclic voltammograms of the four REM membranes with a nominal geometric surface area of 3.38 cm^2 in the potential range of −0.2–0.5 V/SCE are shown in **Figure 8**. It was calculated that the REM samples without doping carbon black and with 1.5% carbon black have the almost same average roughness (2557–2563). As for 5wt% carbon black, the calculated surface roughness was 3250 and the total electroactive surface area was 1.1 m^2, which accounted for approximately 54.6% of the porous surface area measured by Hg porosimetry and increased by 1.3-fold in comparison with that without carbon black. However, the REM membrane obtained with doping 15wt% carbon black has the lowest surface roughness at 1953. In summary, the electrochemically active area (i.e., the roughness factor) of the porous Ti_4O_7 electrode is 3 orders of magnitude higher than the apparent surface area of the REM membrane, which was favorable for the electrochemical reaction.

A stepwise increase in potential was implemented by recording the current response to obtain the water oxidation potential in the Na_2SO_4 electrolyte (**Figure 9**). For Ti_4O_7, there was a negligible response of the current when the potential was below 2.7 V/SHE. Further increasing potential resulted in an apparent enhancement of the current, indicating the potential for water oxidation was within the range of 2.5–2.7 V/SHE. This result was higher than that of the oxygen evolution potential of 2.5 V/SHE reported by Smith et al. and reached the highest reported value of 2.7 V/SHE (Miller-Folk et al., 1989; Graves et al., 1991; Kolbrecka and Przyluski, 1994; Grimm et al., 1998). Thus, we can infer that the as-prepared Ti_4O_7 REM exhibits an appreciable electrocatalytic activity toward the production of •OH.

Figure 9B shows the EIS curves of REMs at room temperature. Each of the curves consists of a straight line (at low frequency) and a depressed semicircle (at high frequency), which are related to the ion diffusion in the bulk of the electrode and the charge transfer process at the electrolyte–electrode interface, respectively. The Rs displays the internal resistance of the electrode and electrolyte, and the charge-transfer impedance (R_{ct}) is expressed vividly by the depressed semicircle in the intermediate frequency region. As shown in **Figure 9B** and **Table 1**, Rs values of Ti_4O_7 were estimated to be 17.1 ± 0.17, 17.53 ± 0.18, 18.8 ± 0.19, and 19.6 ± 0.20 Ω, respectively, indicating a minimal difference between the conductivity of these REMs. But it can be seen that as the content of carbon black increased, the value of R_s increased, which may be associated with the porosity of the REM membrane samples. The existence of a large number of voids reduced the effective cross-section of current conduction and therefore decreased the conductivity. Notably, the charge transfer resistances (R_{ct}) of these REMs were 3.57 ± 0.36, 3.68 ± 0.37, 4.14 ± 0.41, and 5.19 ± 0.52 Ω, respectively, which were three orders of magnitude smaller than that for the graphite plate electrode (You et al., 2016; Xie et al., 2020), suggesting a much higher charge transfer capacity of Ti_4O_7.

TABLE 1 | The effect of carbon black content on the property of REM samples.

Carbon black contents (wt%)	**0**	**1.5**	**5**	**10**
Pressure-normalized permeate fluxes (LMH/bar)	250 ± 10	320 ± 1	503 ± 12	1379 ± 8
Intrinsic membrane resistance (10^{10}/m)	9.25	7.3	4.83	1.59
Determinate coefficient R^2	0.9869	0.9946	0.9979	0.9997

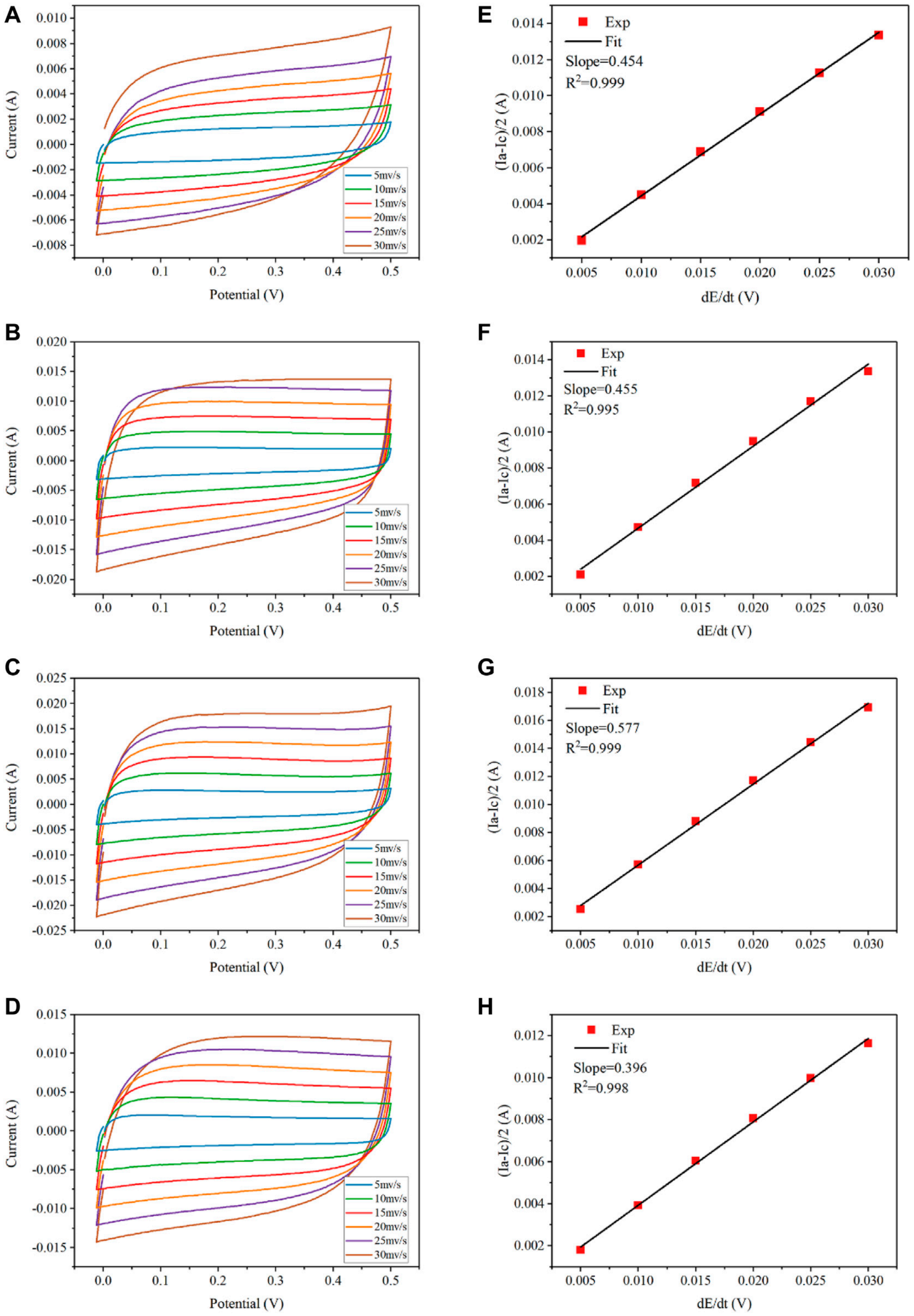

FIGURE 8 | Determination of double-layer capacitance at different scan rates (5–30 mV s^{-1}) for REMs using CV in the 100 mM Na_2SO_4 electrolyte solution. CV scans: **(A)** 0wt%, **(B)** 1.5wt%, **(C)** 5wt%, and **(D)** 15wt%. Corresponding plots of charging currents versus scan rates: **(E)** 0wt%, **(F)** 1.5wt%, **(G)** 5wt%, and **(H)** 15wt%.

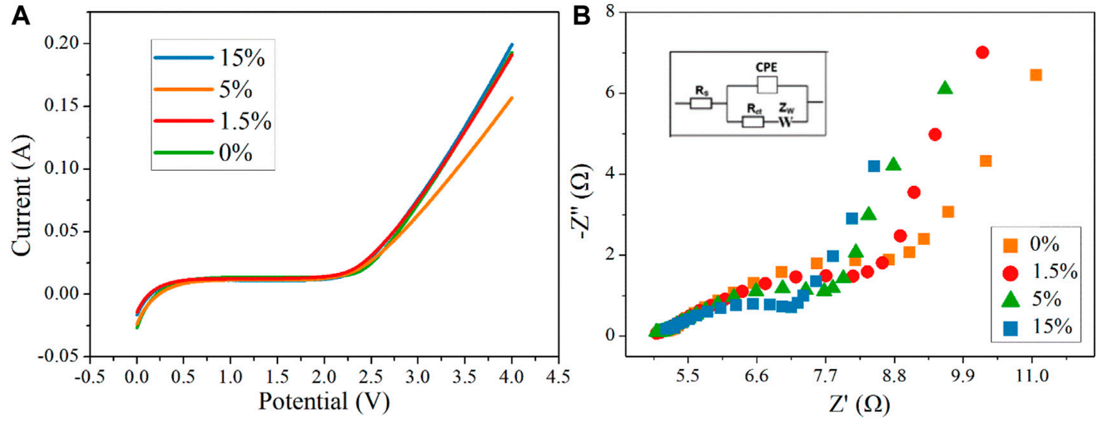

FIGURE 9 | LSV **(A)** and EIS **(B)** curves of REMs.

3.4 Thermal Reduction Mechanism

In this study, the Ti_4O_7 REM fabrication process combined the following two steps: 1) the oxygen atoms in the TiO_2 monolith reunited to oxygen and then effused into the vacuum environment at the higher reaction temperature and 2) the emanated oxygen is captured by the Ti powder. Thermodynamically, the reaction driving force enables titanium oxidation and TiO_2 reduction. For step one, the general reaction can be given as

$$2\,(n-1)Ti_nO_{2n-1\,(s)} = 2ni_{n-1}1O_{2n-3\,(s)} + O_{2\,(g)}, \qquad (4)$$

where $Ti_{n-1}O_{2n-3}$ and Ti_nO_{2n-1} are the closest compounds in the Ti–O binary phase diagram. In these reactions, only oxygen is the gas phase, and others are pure solid. Then, the Gibbs free energy could be written as

$$\Delta_r G = \Delta_r G^\theta + \frac{1}{2} RTln\frac{p_{O_2}}{p^\theta}, \qquad (5)$$

where p_{O_2} is the partial pressure of O_2, p^θ is the standard atmospheric pressure, and R is the universal gas constant. Due to the experiment being conducted in a vacuum, the practical pressure of oxygen is smaller than the total pressure of the vacuum chamber and certainly standard atmospheric pressure. This makes the value of $RT\,ln\frac{p_{O_2}}{p^\theta}$ negative, i.e., the Gibbs free energy change of the reaction at T temperature is minor as compared with the standard Gibbs free energy change, making decomposition of the metal oxide easier to occur. On the other side, the equation shows that the decomposition temperatures of the metal oxide depend on the oxygen pressure. Thus, the vacuum degree was also the critical factor for the successful fabrication of Ti_4O_7 REM samples.

When $\Delta_r G = 0$, i.e., at the equilibrium, the relationship between temperature T and ln $\frac{p_{O_2}}{p^\theta}$ was obtained:

$$\Delta_r G^\theta = -\frac{1}{2} RT\,ln\frac{p_{O_2}}{p^\theta}. \qquad (6)$$

Based on the data of the Ti–O system, the diagram of this relationship is shown in **Figure 10**, called the Ti–O system phase stable diagram.

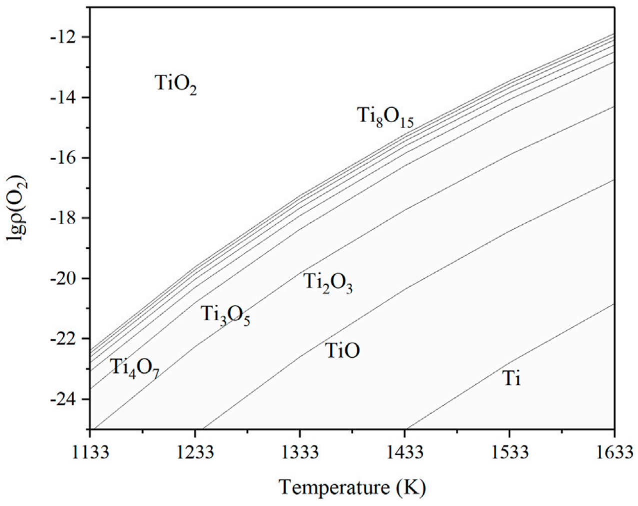

FIGURE 10 | Phase stable diagram of the Ti–O system.

TABLE 2 | Equilibrium oxygen partial pressure of reactions in the Ti–O system at a specified temperature.

Reactions	Sintering temperature T/K, when $\Delta_r G^\theta = 0$	lg $\frac{p_{O_2}}{p^\theta}$
$12TiO_2$ (s) $=2Ti_6O_{11}$ (s)$+O_2$ (g)	1233	−19.8
$8TiO_2$ (s) $=2Ti_4O_7$ (s)$+O_2$ (g)	1333	−17.9
$6TiO_2$ (s) $=2Ti_3O_5$ (s)$+O_2$ (g)	1433	−16.3

From **Figure 10**, Ti_4O_7 could be synthesized from TiO_2 if the oxygen partial pressure and temperature were accurately controlled. If the system oxygen partial pressure is higher than the equilibrium value, the metal will be oxidized, and if it is lower than the equilibrium value, then the oxide will be reduced. The lower the temperature was, the wider the range of the oxygen partial pressure for Ti_4O_7 existed.

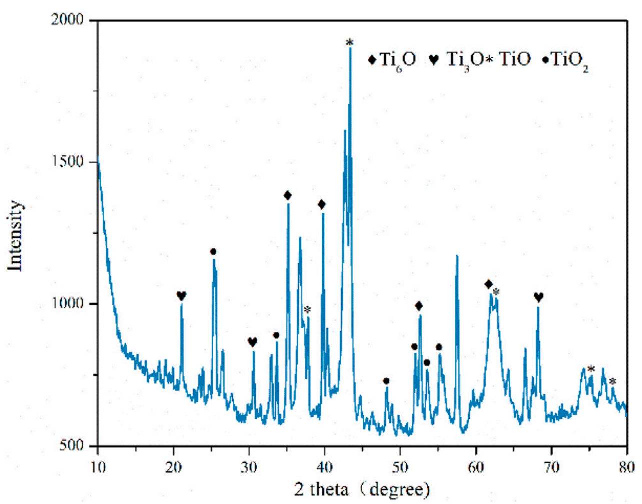

FIGURE 11 | XRD patterns of the oxidation products of the Ti reducing reagent.

When the temperature was adjacent to 1333 K and $\mathbf{lg}\frac{p_{O_2}}{p^{\theta}} < -17.9$, the domain of Ti_4O_7 was expanded.

Table 2 is the equilibrium oxygen partial pressure of reactions in the Ti-O system at the temperature of 1233, 1333, and 1433 K. As the temperature increases by every 100 K, the oxygen partial pressure can increase by several orders of magnitude. It means that raising the temperature could make the reaction occur more easily and more distinguished; thus, the possibility to fabricate a single-phase material is greatly raised. However, it should be noted that the treatment time must be reduced at a high thermal reduction temperature since it probably induced the overreduction of TiO_2 to some Ti_nO_{2n-1}, such as Ti_3O_5 (**Figure 2**).

Excess amount Ti was use to decrease the oxygen pressure and ensure more complete reduction of TiO_2 during the process. It has been shown that the growth of titanium oxide mainly in the form of rutile at and above 10^{-7} MPa and at the temperature below 1573 K. However, at lower pressures and at higher temperatures and after oxygen saturation of the a-phase, all the oxides of titanium (e.g., Ti_2O, TiO, Ti_2O_3, Ti_3O_5, and TiO_2) are formed as reaction products depending on the oxygen pressure and elapsed time of reaction. As a matter of fact, the last oxidized product is not TiO_2 but the mixture of various titanium oxide (**Figure 11**). As the temperature was 1273 K, the oxygen partial pressure $p_{O_2} = 10^{-18.6}$ MPa which is much lower than 10^{-7} MPa. The Ti powder used in our experiments is the nano-scale powder, which created a large surface area to contact with oxygen to increase the dissociation pressure of TiO_2 as much as possible kinetically.

4 CONCLUSION

In this study, the high purity Ti_4O_7 REM was successfully synthesized by mechanical pressing of TiO_2 powders followed by thermal reduction to Ti_4O_7 using the Ti powder as the reducing reagent. Carbon black was introduced to the monolithic TiO_2 precursor to control the pore size and morphology of the Ti_4O_7 REM. The pore properties modification increased the electroactive surface area by approximately 1.3-fold, which increased the reactivity of the Ti_4O_7 REM toward outer sphere electron transfer reactions. The electrodes had high porosities (38–59%), which showed high permeate fluxes of up to 1379 ± 8 LMH bar^{-1}. These results indicated that the Ti_4O_7 monolithic electrodes could find various electrochemical applications in water treatment and energy storage and conversion.

DATA AVAILABILITY STATEMENT

The original contributions presented in the study are included in the article/Supplementary Material; further inquiries can be directed to the corresponding authors.

AUTHOR CONTRIBUTIONS

GQ was responsible for conceptualization, investigation, formal analysis, and writing of the original draft. XW contributed to project administration, resources, validation, and reviewing and editing. JZ and CS carried out investigation and formal analysis. XX helped with software and methodology. YZ, FR, and NZ performed the formal analysis and investigation.

REFERENCES

Bejan, D., Malcolm, J. D., Morrison, L., and Bunce, N. J. (2009). Mechanistic Investigation of the Conductive Ceramic Ebonex as an Anode Material. *Electrochimica Acta* 54 (23), 5548–5556. doi:10.1016/j.electacta.2009.04.057

Ganiyu, S. O., Oturan, N., Raffy, S., Cretin, M., Esmilaire, R., van Hullebusch, E., et al. (2016). Sub-stoichiometric Titanium Oxide (Ti4O7) as a Suitable Ceramic Anode for Electrooxidation of Organic Pollutants: A Case Study of Kinetics, Mineralization and Toxicity Assessment of Amoxicillin. *Water Res.* 106, 171–182. doi:10.1016/j.watres.2016.09.056

Geng, P., and Chen, G. (2016). Magnéli Ti 4 O 7 Modified Ceramic Membrane for Electrically-Assisted Filtration with Antifouling Property. *J. Membr. Sci.* 498, 302–314. doi:10.1016/j.memsci.2015.07.055

Graves, J. E., Pletcher, D., Clarke, R. L., and Walsh, F. C. (1991). The Electrochemistry of Magnéli Phase Titanium Oxide Ceramic Electrodes Part I. The Deposition and Properties of Metal Coatings. *J. Appl. Electrochem.* 21 (10), 848–857. doi:10.1007/bf01042450

Grimm, J., Bessarabov, D., and Sanderson, R. (1998). Review of Electro-Assisted Methods for Water Purification. *Desalination* 115 (3), 285–294. doi:10.1016/s0011-9164(98)00047-2

Guan, K., Qin, W., Liu, Y., Yin, X., Peng, C., Lv, M., et al. (2016). Evolution of Porosity, Pore Size and Permeate Flux of Ceramic Membranes during Sintering Process. *J. Membr. Sci.* 520, 166–175. doi:10.1016/j.memsci.2016.07.023

Guo, D., Shibuya, R., Akiba, C., Saji, S., Kondo, T., and Nakamura, J. (2016). Active Sites of Nitrogen-Doped Carbon Materials for Oxygen Reduction Reaction Clarified Using Model Catalysts. *Science* 351 (6271), 361–365. doi:10.1126/science.aad0832

Guo, L., Jing, Y., and Chaplin, B. P. (2016). Development and Characterization of Ultrafiltration TiO2 Magnéli Phase Reactive Electrochemical Membranes. *Environ. Sci. Technol.* 50 (3), 1428–1436. doi:10.1021/acs.est.5b04366

Guo, Y., Li, J., Pitcheri, R., Zhu, J., Wen, P., and Qiu, Y. (2019). Electrospun Ti4O7/C Conductive Nanofibers as Interlayer for Lithium-Sulfur Batteries with Ultra Long Cycle Life and High-Rate Capability. *Chem. Eng. J.* 355, 390–398. doi:10.1016/j.cej.2018.08.143

Kitada, A., Hasegawa, G., Kobayashi, Y., Kanamori, K., Nakanishi, K., and Kageyama, H. (2012). Selective Preparation of Macroporous Monoliths of Conductive Titanium Oxides TinO2n-1 (N = 2, 3, 4, 6). *J. Am. Chem. Soc.* 134 (26), 10894–10898. doi:10.1021/ja302083n

Kolbrecka, K., and Przyluski, J. (1994). Sub-stoichiometric Titanium Oxides as Ceramic Electrodes for Oxygen Evolution—Structural Aspects of the Voltammetric Behaviour of Ti_nO_{2n-1}. *Electrochim. Acta* 39 (11), 1591–1595. doi:10.1016/0013-4686(94)85140-9

Li, X., Zhu, A. L., Qu, W., Wang, H., Hui, R., Zhang, L., et al. (2010). Magneli Phase Ti4O7 Electrode for Oxygen Reduction Reaction and its Implication for Zinc-Air Rechargeable Batteries. *Electrochimica Acta* 55 (20), 5891–5898. doi:10.1016/j.electacta.2010.05.041

Lin, H., Niu, J., Liang, S., Wang, C., Wang, Y., Jin, F., et al. (2018). Development of Macroporous Magnéli Phase Ti4O7 Ceramic Materials: As an Efficient Anode for Mineralization of Poly- and Perfluoroalkyl Substances. *Chem. Eng. J.* 354, 1058–1067. doi:10.1016/j.cej.2018.07.210

Liu, H., and Vecitis, C. D. (2012). Reactive Transport Mechanism for Organic Oxidation during Electrochemical Filtration: Mass-Transfer, Physical Adsorption, and Electron-Transfer. *J. Phys. Chem. C* 116 (1), 374–383. doi:10.1021/jp209390b

Miller-Folk, R. R., Noftle, R. E., and Pletcher, D. (1989). Electron Transfer Reactions at Ebonex Ceramic Electrodes. *J. Electroanal. Chem. Interf. Electrochem.* 274 (1), 257–261. doi:10.1016/0022-0728(89)87047-0

Oturan, N., Ganiyu, S. O., Raffy, S., and Oturan, M. A. (2017). Sub-stoichiometric Titanium Oxide as a New Anode Material for Electro-Fenton Process: Application to Electrocatalytic Destruction of Antibiotic Amoxicillin. *Appl. Catal. B: Environ.* 217, 214–223. doi:10.1016/j.apcatb.2017.05.062

Toyoda, M., Yano, T., Tryba, B., Mozia, S., Tsumura, T., and Inagaki, M. (2009). Preparation of Carbon-Coated Magneli Phases Ti_nO_{2n-1} and Their Photocatalytic Activity under Visible Light. *Appl. Catal. B: Environ.* 88 (1-2), 160–164. doi:10.1016/j.apcatb.2008.09.009

Tsumura, T., Hattori, Y., Kaneko, K., Hirose, Y., Inagaki, M., and Toyoda, M. (2004). Formation of the Ti4O7 Phase through Interaction between Coated Carbon and TiO2. *Desalination* 169 (3), 269–275. doi:10.1016/s0011-9164(04)00533-8

Vecitis, C. D., Gao, G., and Liu, H. (2011). Electrochemical Carbon Nanotube Filter for Adsorption, Desorption, and Oxidation of Aqueous Dyes and Anions. *J. Phys. Chem. C* 115 (9), 3621–3629. doi:10.1021/jp111844j

Walsh, F. C., and Wills, R. G. A. (2010). The Continuing Development of Magnéli Phase Titanium Sub-oxides and Ebonex Electrodes. *Electrochimica Acta* 55 (22), 6342–6351. doi:10.1016/j.electacta.2010.05.011

Xie, J., Ma, J., Zhang, C., Kong, X., Wang, Z., and Waite, T. D. (2020). Effect of the Presence of Carbon in Ti4O7 Electrodes on Anodic Oxidation of Contaminants. *Environ. Sci. Technol.* 54 (8), 5227–5236. doi:10.1021/acs.est.9b07398

You, S., Liu, B., Gao, Y., Wang, Y., Tang, C. Y., Huang, Y., et al. (2016). Monolithic Porous Magnéli-phase Ti4O7 for Electro-Oxidation Treatment of Industrial Wastewater. *Electrochimica Acta* 214, 326–335. doi:10.1016/j.electacta.2016.08.037

Zaky, A. M., and Chaplin, B. P. (2013). Porous Substoichiometric TiO2 Anodes as Reactive Electrochemical Membranes for Water Treatment. *Environ. Sci. Technol.* 47 (12), 6554–6563. doi:10.1021/es401287e

Zhang, L., Kim, J., Zhang, J., Nan, F., Gauquelin, N., Botton, G. A., et al. (2013). Ti4O7 Supported Ru@Pt Core-Shell Catalyst for CO-tolerance in PEM Fuel Cell Hydrogen Oxidation Reaction. *Appl. Energ.* 103, 507–513. doi:10.1016/j.apenergy.2012.10.017

Zhang, Y., Yao, S., Zhuang, R., Luan, K., Qian, X., Xiang, J., et al. (2017). Shape-controlled Synthesis of Ti4O7 Nanostructures under Solvothermal-Assisted Heat Treatment and its Application in Lithium-Sulfur Batteries. *J. Alloys Compd.* 729, 1136–1144. doi:10.1016/j.jallcom.2017.09.252

Zhou, M., Oturan, M. A., and Sires, I. (2018). *Electro-Fenton Process*. Springer.

Conflict of Interest: All authors were employed by the company Testing and Evaluation Research Co., Ltd. of Sinopec Shengli OilField.

ORIGINAL RESEARCH
published: 22 February 2022
doi: 10.3389/fchem.2022.835959

Dual Effect of Acetic Acid Efficiently Enhances Sludge-Based Biochar to Recover Uranium From Aqueous Solution

Shoufu Yu[1], *Xiaoyan Wu*[1,2,3]*, *Jian Ye*[1,2,3], *Mi Li*[1,2,3], *Qiucai Zhang*[1,4], *Xiaowen Zhang*[1,2,3], *Chunxue Lv*[1], *Wenjie Xie*[1], *Keyou Shi*[1] and *Yong Liu*[1,4]*

[1]*University of South China, Hengyang, China,* [2]*Hengyang Key Laboratory of Soil Contamination Control and Remediation, University of South China, Hengyang, China,* [3]*Key Laboratory of Radioactive Waste Treatment and Disposal, University of South China, Hengyang, China,* [4]*Decommissioning Engineering Technology Research Center of Hunan Province Uranium Tailings Reservoir, University of South China, Hengyang, China*

Edited by:
Shuaifei Zhao,
Deakin University, Australia

Reviewed by:
Jin Wang,
Guangzhou University, China
Yanbiao Liu,
Donghua University, China
Min Wang,
Jinan University, China

***Correspondence:**
Xiaoyan Wu
wuxiaoyan@usc.edu.cn
Yong Liu
1992001751@usc.edu.cn

Specialty section:
This article was submitted to Inorganic Chemistry, a section of the journal Frontiers in Chemistry

Received: *15 December 2021*
Accepted: *11 January 2022*
Published: *22 February 2022*

Citation:
Yu S, Wu X, Ye J, Li M, Zhang Q, Zhang X, Lv C, Xie W, Shi K and Liu Y (2022) Dual Effect of Acetic Acid Efficiently Enhances Sludge-Based Biochar to Recover Uranium From Aqueous Solution. Front. Chem. 10:835959. doi: 10.3389/fchem.2022.835959

Excess sludge (ES) treatment and that related to the uranium recovery from uranium-containing wastewater (UCW) are two hot topics in the field of environmental engineering. Sludge-based biochar (SBB) prepared from ES was used to recover uranium from UCW. Excellent effects were achieved when SBB was modified by acetic acid. Compared with SBB, acetic acid-modified SBB (ASBB) has shown three characteristics deserving interest: 1) high sorption efficiency, in which the sorption ratio of U(VI) was increased by as high as 35.0%; 2) fast sorption rate, as the equilibrium could be achieved within 5.0 min; 3) satisfied sorption/desorption behavior; as a matter of fact, the sorption rate of U(VI) could still be maintained at 93.0% during the test cycles. In addition, based on the test conditions and various characterization results, it emerged as a dual effect of acetic acid on the surface of SBB, i.e., to increase the porosity and add (–COOH) groups. It was revealed that U(VI) and –COO– combined in the surface aperture of ASBB *via* single-dentate coordination. Altogether, a new utilization mode for SBB is here proposed, as a means of efficient uranium sorption from UCW.

Keywords: uranium, uranium-containing wastewater, excess sludge, acetic acid, sludge-based biochar

INTRODUCTION

Uranium-containing wastewater (UCW) contains a certain concentration of nuclide ions, such as uranium ions, radium ions, and thorium ions. In addition, it also contains high concentrations of heavy metal ions, metal ions, and acid ions, such as sulfate ions and nitrate ions. This special industrial wastewater is mainly discharged by uranium mining or uranium hydrometallurgy. Generally, uranium presents in the valence form of U(IV) and U(VI). U(IV) does not dissolve in aqueous solution and usually forms precipitation, while U(VI) generally gives mobile aqueous

---

Abbreviations: ASBB, acid-modified sludge-based biochar; ASBB-U, Acetic acid-modified sludge-based biochar—uranium; BET, Brunner–Emmet–Teller; EDS, energy-dispersive x-ray spectroscopy; ES, excess sludge; FTIR, Fourier transform infrared spectroscopy; SBB, sludge-based biochar; SEM, scanning electron microscope; SSA, specific surface area; UCW, uranium-containing wastewater; WWTP, wastewater treatment plant; XPS, x-ray photoelectron spectroscopy.

complexes with CO_3^{2-} and OH^{-1} (Gerber et al., 2016; Abdi et al., 2017). Uranium ions are characterized by radioactivity and chemical toxicity, which could, in turn, cause chronic poisoning, cancer, and immunological diseases (Malenchenko et al., 1978; Baur et al., 1996; Kathren and Burklin, 2008; NaserHumood, 2013). In addition, serious damage might be caused to the surrounding organisms as well as ecosystems once UCW is discharged into the environment by accident. Consequently, it is of great significance to establish rapid and efficient processing methods for UCW treatment aimed at both reducing the hazardous effect of UCW and reusing, as added-value product, uranium recovered by UCW.

At present, the main technologies for uranium recovered from UCW or UCW treatment could be summarized as chemical precipitation, ion exchange, membrane separation, biological treatment, solvent extraction, and sorption (Khani et al., 2008; Wang et al., 2009; Abadi et al., 2011; Gerber et al., 2016; Khawassek et al., 2018; Tan et al., 2018). Among them, sorption is one of the popular technologies because of its advantages, including simple operation, wide range of application, higher removal and recovery rate, etc. (Chen et al., 2020). Generally, the uranium removal rate by sorption is mainly influenced by physical/chemical properties of adsorbents (i.e., pore structure, surface groups), uranium concentration, pH, etc. (Kataria and Garg, 2018) Biochar (Sun et al., 2013; Sun et al., 2017; Kong et al., 2020), graphene (Zhao et al., 2019), calixarene (Fang-Zhu et al., 2019), MOFs (Li et al., 2020), and mesoporous silicon (Jiang et al., 2020) were used as sorption materials. Among them, biochar has been verified as an important sorption material for uranium recovery or removal from aqueous solution (Jin et al., 2018; Li et al., 2019a), due to its simple preparation process, lower price, higher temperature resistance, radiation resistance, higher stability to almost all kinds of acidic and alkali environments, nontoxic, and environmentally friendly nature (Zhao et al., 2017; Pu et al., 2019).

Generally, excess sludge (ES) was applied for biochar preparation (Li et al., 2019b; Hu et al., 2019). ES is mainly generated by wastewater treatment plant (WWTP) with large yield (Ghosh, 2009; Ali et al., 2019). It is difficult to treat ES, and its post-processing cost is relatively high (Hossain et al., 2018). Moreover, secondary pollution might easily happen if ES is not properly treated (Sun et al., 2018). Kanterli reported that sludge-based biochar (SBB) showed high sorption capacity (112.40 mg/g) for Cr(VI) (Ismail Cem and Jale, 2009). SBB prepared from municipal sludge (11.27 mg/g) and papermaking sludge (11.78 mg/g) by hydrothermal treatment had good sorption capacity for Pb(II) removal, too (Alatalo et al., 2013). In addition, SBB and Fe_3O_4-modified SBB also showed high uranium ion sorption efficiency (more than 90.0%) (Zeng et al., 2020; Guanhai et al., 2021). What is more, the treatment of UCW by SBB cannot only effectively solve the problem from ES, but also achieve the effect of waste treatment fee and waste resource utilization. However, to make SBB more practical, its sorption capacity for uranium or other heavy metals needs to be further improved.

So far, the most effective method for improving biochar sorption capacity or removal rate of heavy metals is to increase specific surface area or functional groups on its surface. For example, the effect of nitric acid on the surface area enlargement of biochar has been reported (Ioanna et al., 2017; Mishra et al., 2017). In addition, oxygen functional groups (Anirudhan and Deepa, 2015), humus (Zong et al., 2015), amine (Zhao et al., 2015), amino amine (Deb et al., 2012), dopaminer (Wu et al., 2017), and oximer (Xiong et al., 2017) were considered as corresponding functional groups to improve heavy metal removal rate. –COOH, as a representative of oxygen functional groups, is suitable for the complexation of uranium ions (Park et al., 2019). However, there is still a lack of research on the simultaneous expansion of pores and the addition of groups to recover more uranium ions in SBB.

In order to achieve the above requirements, the removal and recovery efficiency of uranium from UCW was comprehensively studied by involving acetic acid-modified SBB (ASBB) prepared from ES and acetic acid, including 1) differences in uranium recovery efficiency from UCW when SBB or ASBB were used, 2) impacts of variety factors (reaction time, pH, dosage, initial concentration, desorption, and interfering ions) on uranium removal by ASBB, 3) kinetic and thermodynamic analysis of sorption, 4) ASBB uranium removal mechanism based on Brunauer–Emmett–Teller (BET), scanning electron microscopy (SEM), energy-dispersive x-ray spectroscopy (EDS), Fourier-transform infrared spectroscopy (FTIR), and x-ray photoelectron spectroscopy (XPS) techniques. In this paper, acetic acid was used as a modifier to modify SBB and to treat UCW. This modification method could also be used to treat other heavy metal ions in the future.

MATERIALS AND METHODS

Starting Materials

ES was obtained from a WWTP located in Hengyang, China. The reagents used in this study were of analytical grade. Chloroacetic acid ($CH_2ClCOOH$), hydrochloric acid (HCl), ferrous sulfate heptahydrate ($FeSO_4.7H_2O$) and sodium hydroxide (NaOH), potassium hydroxide (KOH), and acetic acid (CH_3COOH) were purchased from Sinopharm Group Pharmaceutical Co., Ltd. (Shanghai). Arsenio III [$(HO)_2C_{10}H_2(SO_3H)_2(N{=}NC_6H_4AsO_3H_2)_2$] and triuranium octoxide (U_3O_8) were purchased from Tianjin Kemio Chemical Reagent Co., Ltd., and China Academy of Metrology, respectively.

Uranium stock solution (1.0 g/L) was prepared by dissolving U_3O_8 in concentrated nitric acid. The specific preparation process was as follows: First, the dried 1.1792 g U_3O_8 powder was accurately weighed into a 100-ml beaker. Second, 10.0 ml of hydrochloric acid solution with a density of 1.18 g/cm³, 3.0 ml of 30 wt% hydrogen peroxide, and two drops of 1.0 mg/L of nitric acid solution were sequentially added to the beaker. Then the beaker was covered with a lid for 3 min. After time had elapsed, the solution was stirred by a glass rod for several minutes. After a violent reaction was completed, the beaker was moved a the

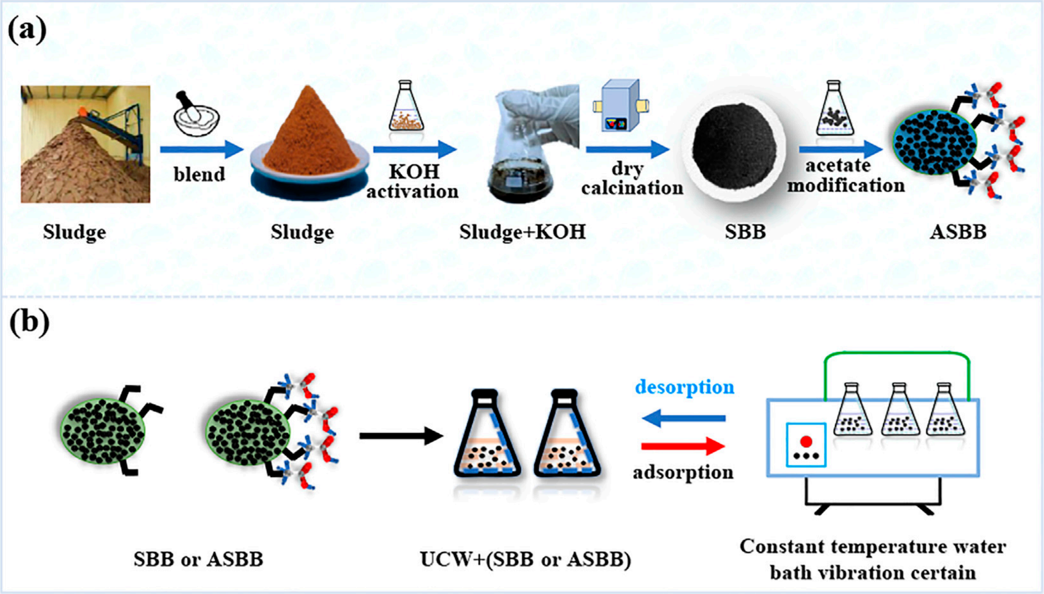

FIGURE 1 | Preparation of sludge-based biochar (SBB) and acid-modified sludge-based biochar (ASBB) and uranium recovery from uranium-containing wastewater (UCW). **(A)** Preparation of SBB and ASBB. **(B)** Uranium recovery from UCW by SBB or ASBB.

graphite heating plate for heating and dissolution. When the dissolution was completed, the solution was cooled to room temperature. Finally, the solution was transferred to a 1,000.0-ml volumetric flask, and a nitric acid solution with pH <2 was used for constant volume. More information in detail could be found in cited literature (Lu et al., 2018a). All concentrations of UCW solutions used in the experiment were diluted by 1.0 g/L uranium stock solution.

Sludge-Based Biochar and Acetic Acid-Modified SBB Preparation

The preparation process of SBB and ASBB is shown in **Figure 1A**. The dewatered ES was collected from WWTP and then dried at 105°C for 24 h. The dried ES was impregnated with KOH (3.0 mol/L) in proportion to mass and activated for 24 h. The impregnated ES was again dried at 80°C in a constant temperature drying oven. Thereafter, it was pyrolyzed to biochar in a muffle furnace at 350°C–700°C for 40–50 min under nitrogen atmosphere. Biochar was cooled down to room temperature under nitrogen atmosphere. Then it was washed to neutral by distilled water. The production rate of fresh SBB was 86.0 ± 10.0%. The biochar was immersed in CH_3COOH solution (36.0%–38.0%) for 6 h and then washed with distilled water to neutrality, thus, eventually getting ASBB.

Experimental setup

Orthogonal Experiments

Figure 1B displays the rationale of the experiments of uranium recovered from UCW with different SBB or ASBB dosages. A certain amount of SBB or ASBB was added to 100.0 ml of U(VI) solution. Temperature and stir speed were kept at 25°C and 120 r/min, respectively. The removal efficiencies of U(VI) by fresh SBB and ASBB were investigated according to orthogonal experiments. They were conducted under different mass ratios of sludge/KOH (MSK), calcination temperature (CTE), calcination time (CTI), and activation time (AT) (**Table 1**). Initial U(VI) concentration in UCW was 10.0 mg/L, pH was 3.03, and the dosage of fresh SBB or ASBB was 0.50 g/L in each investigated case.

Batch Experiment

Several values of reaction time (1.0, 2.0, 3.0, 4.0, 5.0, 10.0, 20.0, and 30.0 min), initial pH (3.0–9.0 with a minimum interval of 1.0), adsorbent dosage (0.05, 0.1, 0.1, 0.3, 0.4, and 0.5 g/L), and initial uranium ion concentration (5.0, 10.0, 20.0, 30.0, 50.0, and 100.0 mg/L) were scrutinized. U(VI) concentration in artificial UCW was kept at 10.0 mg/L except for particular cases. Dosage of SBB or ASBB was 0.30 g/L, and pH was 6.0.

The desorption of ASBB was carried out by utilizing HCl (2.0 mol/L) as a desorption agent. The interference test of the sorption of U(VI) by coexisting ions (cation) in the solution was also carried out. Except for the solution containing 10.0 mg/L of U(VI), the concentration of coexisting ions in each solution was simulated to 10.0 mg/L. The interfering ions involved were Fe^{3+}, Na^{+}, Mg^{2+}, Pb^{2+}, and Cr^{6+}. During the test, two dosages (0.3 and 0.5 g/L) of ASBB were set. HCl (0.01 mol/L) and NaOH (0.01 mol/L) were used for adjusting pH of artificial UCW.

Analysis and Characterization

U(VI) concentration was determined by Arsenazo III spectrophotometer (Ding et al., 2018). The absorbance of UCW was measured at a wavelength of 652 nm after

TABLE 1 | Effect of biochar on uranium-containing wastewater (UCW) treatment under different preparation conditions.

Influencing factors	Sludge: KOH	Calcination temperature (°C)	Calcination time (min)	Activation time (h)	Removal rate (%)		Sorption capacity (mg/g)	
	MSK	CTE	CTI	AT	SBB	ASBB	SBB	ASBB
Exp 1	3:1	400	30	3	23.6	42.8	4.72	8.56
Exp 2	2:1	400	40	6	28.1	52.2	5.62	10.44
Exp 3	1:1	400	50	12	39.3	67.3	7.86	13.46
Exp 4	1:2	400	60	24	39.9	68.9	7.98	13.78
Exp 5	1:3	400	70	48	40.8	70.8	8.16	14.16
Exp 6	3:1	450	40	12	30.6	48.6	6.12	9.72
Exp 7	2:1	450	50	24	38.7	58.3	7.74	11.66
Exp 8	1:1	450	60	48	45.2	75.1	9.04	15.02
Exp 9	1:2	450	70	3	46.3	76.2	9.26	15.24
Exp 10	1:3	450	30	6	45.1	77.5	9.02	15.5
Exp 11	3:1	500	50	48	35.1	51.2	7.02	10.24
Exp 12	2:1	500	60	3	43.1	63.1	8.62	12.62
Exp 13	1:1	500	70	6	52.2	83.1	10.44	16.62
Exp 14	1:2	500	30	12	52.5	83.6	10.5	16.72
Exp 15	1:3	500	40	24	53.2	84.1	10.64	16.82
Exp 16	3:1	550	60	6	42.8	55.8	8.56	11.16
Exp 17	2:1	550	70	12	56.2	77.2	11.24	15.44
Exp 18	1:1	550	30	24	57.8	87.1	11.56	17.42
Exp 19	1:2	550	40	48	58.6	87.2	11.72	17.44
Exp 20	1:3	550	50	3	58.9	87.4	11.78	17.48
Exp 21	3:1	600	70	24	45.1	53.1	9.02	10.62
Exp 22	2:1	600	30	48	60.7	83.9	12.14	16.78
Exp 23	1:1	600	40	3	61.2	87.9	12.24	17.58
Exp 24	1:2	600	50	6	61.6	88.1	12.32	17.62
Exp 25	1:3	600	60	12	62.3	87.9	12.46	17.58
F	87.09	9.84	4.34	1.18				
P	<0.0001	0.0106	0.0638	0.3034				

Note. The F value represents the significance of the whole fitting equation, and the larger the F implies the more significant the equation, and the better the fitting degree. p*-Value is a parameter used to determine the hypothesis test results. The smaller the* p*-value means the more significant the result. KOH, potassium hydroxide; SBB, sludge-based biochar; ASBB, acid-modified sludge-based biochar; AT, activation time; CTI, calcination time; CTE, calcination temperature; MSK, mass ratio of sludge/KOH.*

preheating the spectrophotometer for 30 min. Inductively coupled plasma-mass spectrometry (ICP-MS) was used to double check the values obtained from spectrophotometry. The difference in the results obtained with the two methods was 1.47%–1.53%, indicating that spectrophotometry was a reliable method under these operating conditions.

The uranium equilibrium specific sorption capacity q_e (mg/g) and removal rate η for each sorbent (SBB or ASBB) were calculated according to **Eqs. 1** and **2**, respectively (Liu et al., 2018):

$$q_e = \frac{v(c_0 - c_e)}{m} \tag{1}$$

$$\eta = \frac{c_0 - c_e}{c_e} \tag{2}$$

where c_0 and c_e are the initial and equilibrium concentrations of uranium in the solution, v is the solution volume, and m is the mass of adsorbent. Langmuir and Freundlich sorption isotherm models were introduced to fit the U(VI) sorption data for ASBB under equilibrium conditions (**Eqs 3**, **4**). The equations read, respectively (Christou et al., 2019):

$$q_e = \frac{q_m K_L Ce}{(1 + K_L Ce)} \tag{3}$$

$$q_e = K_F Ce^{\frac{1}{n}} \tag{4}$$

where q_m is the maximum specific sorption capacity, K_L is the Langmuir equilibrium constant (L/mg), while K_F and n are the Freundlich parameters, respectively, representing the sorption capacity and the sorption intensity.

In order to investigate in detail the U(VI) sorption process by ASBB, kinetic data were fitted by pseudo-first-order (Lagergren PFO, **Eq. 5**) and pseudo-second-order (Ho&McKay PSO, **Eq. 6**) models. The equations read, respectively (Li et al., 2018):

$$q_t = q_e\left[1 - \exp(-\kappa_1 t)\right] \tag{5}$$

$$q_t = \frac{\kappa_2 q_e^2 t}{1 + \kappa_2 q_e t} \tag{6}$$

where q_t refers to the specific sorption capacity at t time, κ_1 is the PFO sorption rate constant (min^{-1}), and κ_2 is the PSO sorption rate constant (g/mg·min^{-1}).

To compare the content of acidic functional groups on the surface of SBB, ASBB, and acetic acid-modified sludge-based biochar—uranium (ASBB-U), the contents of –OH, –COO, and –COOH were determined by the Boehm method (Kalijadis et al., 2011). Three samples of 1.0 g of each material were accurately weighed, and the samples were put into 100.0-ml conical flasks.

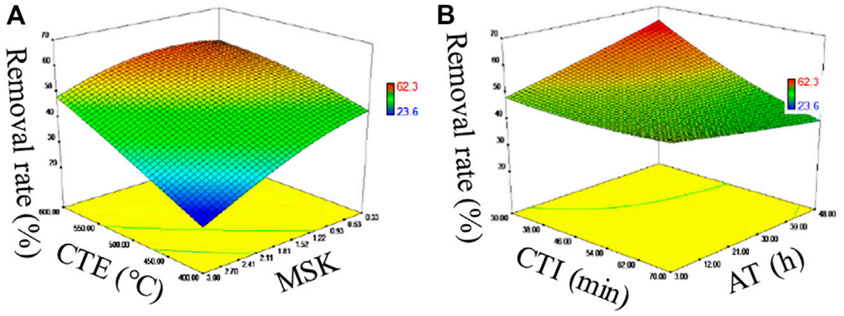

FIGURE 2 | (A) Uranium sorption from SBB and ASBB impacted by calcination temperature (CET) and sludge: KOH (MSK), **(B)** Uranium sorption from SBB and ASBB impacted by calcination time (CTI) and activation time (AT).

Then three samples of each material were added to 25.0 ml of 0.05 mol/L NaOH, Na_2CO_3, and $NaHCO_3$ standard solution, respectively. Nine samples were all stirred for a 24-h reaction and then filtered. During filtration, they were fully washed with distilled water. All the filtrates were collected independently. Methyl red was used as the end indicator of the filtrate. The unreacted alkali in the filtrate was titrated to end by a standard solution of 0.05 mol/L of HCl. The content of –OH, –COO, and –COOH was calculated by the amount of HCl.

The existing forms of uranium in UCW (10.0 mg/L) and $P_{CO2} = 10^{-3.5}$ atm under pH from 3.0 to 9.0 were simulated by Visual MINTEQ 3.1 (Schierz and Zänker, 2009; Zong et al., 2017). The specific surface area of fresh or used SBB and ASBB was determined by BET technique (TriStar II Plus 2.02, Micromeritics, USA). The morphology of fresh or used SBB and ASBB was characterized by SEM (JSM-7500F, JEOL, JPN) coupled with EDS (INCA, Oxford, USA). Functional groups on fresh or used SBB and ASBB were analyzed through FTIR (Nicolet-iS50, Thermo Fisher Scientific, USA). The composition and chemical states of ASBB after UCW sorption were examined by XPS (Escalab 250Xi, Thermo Fisher Scientific, United States) with AlKα radiation. The binding energies were calibrated by using containment carbon (C1s = 284.7 eV). The data analysis was carried out *via* Casa XPS software (Version 2.3.13).

RESULTS AND DISCUSSION

Comparison Between Sludge-Based Biochar and Acetic Acid-Modified Sludge-Based Biochar in Uranium-Containing Wastewater Sorption

The performance of U(VI) removal is presented in **Figure 2**. The removal rate of U(VI) by fresh SBB and ASBB gradually increased with the decrease in MSK and with the increase in CTE (**Figure 2A**), CTI (**Figure 2B**), and AT. The *F* values of MSK, CTE, CTI, and AT were 87.09, 9.84, 4.34, and 1.18, respectively, (refer to **Table 1**). The *p*-values were <0.0001, 0.0106, 0.0638, and 0.3034, respectively. These results indicate that the influence ranking of the explored parameters is MSK, CTE, CTI, and AT. In particular, MSK had an extremely significant effect, and CTE showed a similar tendency (Anna et al., 2018). In addition, the removal rate and sorption capacity of ASBB were higher than SBB, indicating that acetic acid modification of the biochar showed excellent effect on U(VI) removal. Altogether, the optimal preparing conditions for fresh SBB and ASBB are suggested as: MSK = 1:1, CTE = 550°C, CTI = 30 min, and AT = 24 h.

U(VI) Removal Efficiencies by Acetic Acid-Modified Sludge-Based Biochar Under Different Conditions

Reaction Time

Figure 3A depicts the removal rate of U(VI) as a function of time for SBB and ASBB. The removal rate of U(VI) by SBB and ASBB increased with time quickly, and the sorption equilibrium was practically achieved within 5.0 min. This phenomenon was mainly due to the high U(VI) concentration, and to the large number of sorption sites made available by SBB and ASBB. U(VI) could rapidly diffuse to the adsorbent particle due to the high concentration gradient, to be then adsorbed on the solid surface-active sites. However, the removal rate and sorption capacity of U(VI) were close to the peak after 5.0 min. Two main reasons could explain this observation. First, the U(VI) concentration in the solution was quite low, and the U(VI) concentration was considered as one main limiting factor for the improvement of U(VI) removal rate. Second, the surface sorption sites decreased as the reaction proceeds. The probability of U(VI) binding to sorption sites was then decreased. As shown in **Figure 3A**, the U(VI) removal rate by SBB and ASBB was 62.8% and 97.8%, respectively. Meanwhile, the specific sorption capacity of these two adsorbents was 20.9 and 32.6 mg/g, respectively. The sorption capacity of U(VI) by ASBB was 55.8% higher than that of SBB. These results showed that ASBB could adsorb

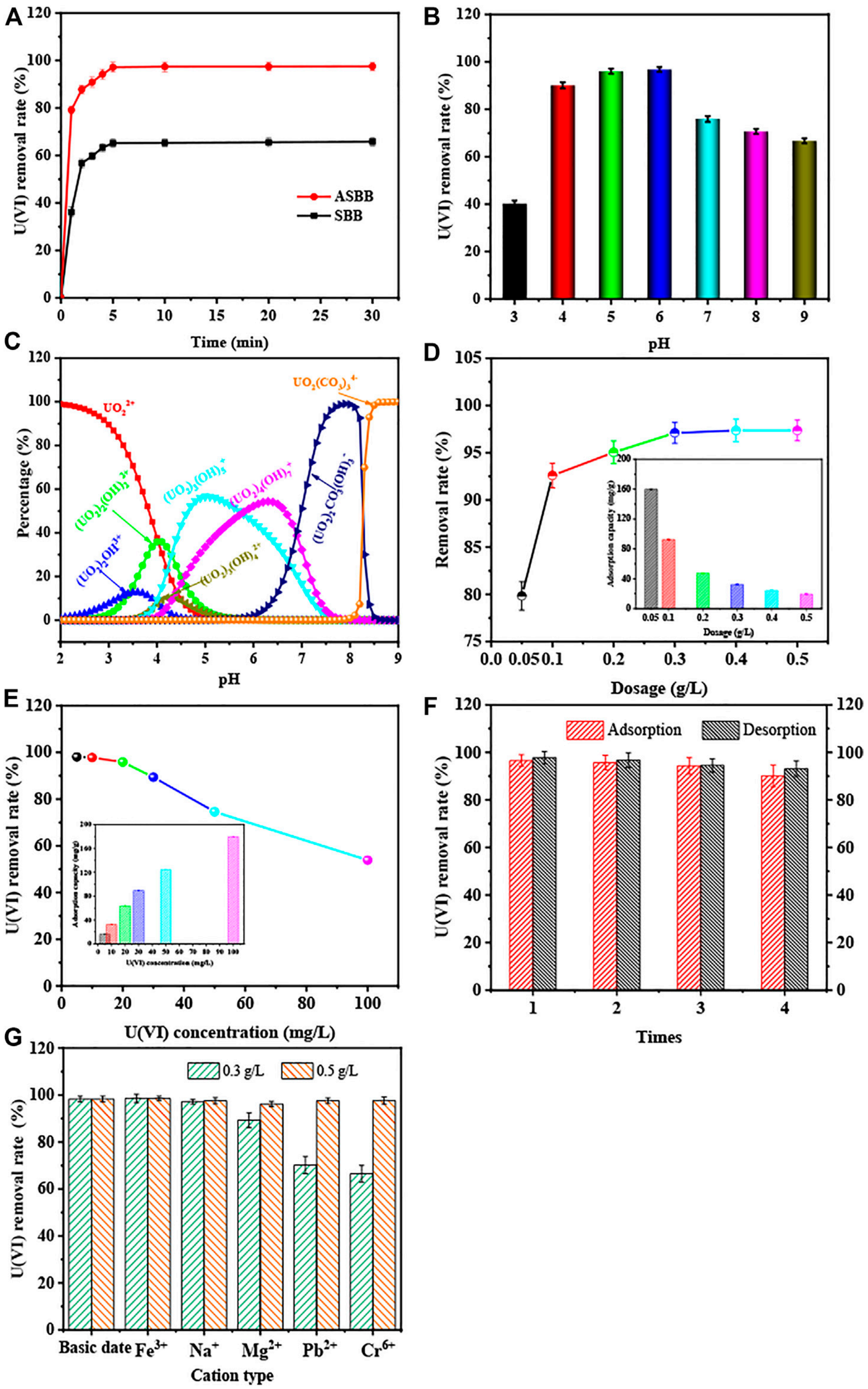

FIGURE 3 | Sorption rate of U(VI) by SBB or ASBB under different conditions. **(A)** Reaction time of SBB or ASBB for U(VI) sorption, **(B)** U(VI) sorption by ASBB under difference initial pH of USW, **(C)** simulation calculation of the existing state of uranium ions under different pH conditions, **(D)** removal rate of uranium in USW by ASBB under different dosage, **(E)** the removal rate of uranium ions by ASBB at different initial concentrations of USW, **(F)** desorption efficiency of uranium ions by ASBB, **(G)** effect of interfering ions on sorption of uranium ions by ASBB in USW.

U(VI) more rapidly and efficiently, and the sorption equilibrium could be achieved within 5.0 min.

Initial pH of Aqueous Solution

Figures 3B, C illustrate the experimental and simulation results of the influences of the initial pH value of the aqueous solution. **Figure 3B** shows that sorption of U(VI) from ASBB was greatly influenced by pH. **Figure 3C** displays that the existing uranium morphology varies under different pH conditions. The main morphologies were UO_2^{2+}, $(UO_2)_2(OH)_2^{2+}$, $(UO_2)_2OH^{3+}$, $(UO_2)_3(OH)_5^{+}$, $(UO_2)_3(OH)_4^{2+}$, $(UO_2)_4(OH)_7^{+}$, $UO_2(CO_3)_3^{4-}$, and $(UO_2)_2CO_3(OH)_3^{-}$. The U(VI) removal rate was only 42.4% when pH = 3.0, where uranium mainly exists in the form of UO_2^{2+} in UCW. Because the solution pH value was in this case too low, a lot of H^+ competed with UO_2^{2+} sorption. Meanwhile, an H^+ proton layer on the surface of ASBB could be formed, rather than UO_2^{2+}. The electrostatic repulsion of ASBB to UO_2^{2+} might increase; thus, the removal rate of uranium was relatively low (Wu et al., 2019). When the pH was between 4.0 and 6.0, the uranium in solution mainly existed in the form of $(UO_2)_2(OH)_2^{2+}$, $(UO_2)_3(OH)_5^{+}$, $(UO_2)_4(OH)_7^{+}$. The low protonation degree of these forms favored the sorption of uranium by ASBB (Zhu et al., 2018). With the increase in pH, many organic functional groups (such as –OH, –COOH, etc.) might be gradually assembled on the surface of ASBB. H^+ on these groups then decreased, so the electronegativity of these groups increased. The binding ability and reaction probability between functional groups and uranium increased due to this phenomenon. The uranium removal rate increased under this condition. When pH was 6.0, the U(VI) removal rate peak was 97.2%. When pH was between 7.0 and 9.0, the uranium was mainly in the form of $UO_2(CO_3)_3^{4-}$ and $(UO_2)_2CO_3(OH)_3^{-}$. These forms were difficult to be adsorbed by ASBB, and the removal rate of uranium was reduced. Therefore, pH = 6.0 was suggested as the optimal condition for U(VI) sorption from UCW by ASBB.

Dosage of Acetic Acid-Modified Sludge-Based Biochar

Figure 3D shows the effect of different ASBB dosages on U(VI) removal. The initial U(VI) concentration was 10.0 mg/L. The U(VI) removal rate increased from 79.8% to 97.8% when the dosage of ASBB increased from 0.05 to 0.5 g/L. With the increase in the dosing amount, the reaction sites of ASBB in UCW increased as well. The probability of U(VI) to interact with reaction sites, therefore, increased and the U(VI) removal efficiency was improved. In general, 0.30 g/L was determined as the optimal dosage used in further sections also taking into account economic reasons.

Initial U(VI) Concentration

Figure 3E illustrates the sorption capacity of ASBB and uranium removal rate under different initial U(VI) concentrations in the wastewater recovered by ASBB biochar. When the dosage of ASBB was 0.30 g/L, the UCW removal rate result is equal to 98.1% (initial concentration = 5.0 mg/L) and 97.8% (initial concentration = 10.0 mg/L). Namely, with the increase in U(VI) initial concentration, the removal rate of U(VI) by ASBB gradually decreased, while the specific sorption capacity was increased. The latter might be due to the excess U(VI) in the system, that drives the sorption process. Moreover, when the dosage of ASBB was 3.0 g/L (i.e., one order of magnitude higher), the removal efficiency for 100.0 mg/L of uranium concentration in UCW was 95.7%. These results demonstrated that ASBB was not only suitable for the uranium recovery from UCW with low uranium concentration but also for high concentration values. In addition, **Table 2** shows the results for different adsorbents. The U(VI) sorption capacity of ASBB per unit time was about 10–1,000 times that of other materials, indicating that ASBB was a rapid and efficient U(VI) adsorbent, with interesting industrial perspectives.

Desorption From Acetic Acid-Modified Sludge-Based Biochar

The desorption performance of an adsorbent is an important standard to judge whether it can be practically used. Research has shown that adsorbed U(VI) could be replaced by H^+ through ion exchange (Wen et al., 2016), and then dissolved in acidic solution (Tu et al., 2019). **Figure 3F** displays the results of uranium desorption from ASBB. It could be seen that after sorption and desorption for several cycles, the removal efficiency of uranium by ASBB remained at 90.2%, while the desorption efficiency from ASBB was 93.0%. These results showed that ASBB had good reusability potential, and the recovery of U(VI) could be achieved in practice.

Interfering Ions

Figure 3G shows the interference of coexisting ions on ASBB's sorption of U(VI). When the dosage of ASBB was 0.30 g/L, Na^+ had little effect on the removal of U(VI) by ASBB, while it would be inhibited by Mg^{2+}, Pb^{2+}, and Cr^{6+}. In particular, Cr^{6+} had the greatest impact on ASBB's sorption of U(VI). The main reason for this phenomenon might be the competitive sorption of these ions and U(VI) on the surface of ASBB. Unlike these ions, Fe^{3+} facilitated the U(VI) removal. The main reason might be that when pH = 6, Fe^{3+} could be hydrolyzed into $Fe(OH)_3$ colloids (Feng et al., 2013), and U(VI) could be combined with $Fe(OH)_3$ (Bruno et al., 1995). As a result, the efficiency of ASBB's removal of U(VI) was improved. When the dosage of ASBB was increased to 0.50 g/L, U(VI) could still be efficiently adsorbed by ASBB under the interference of various ions. Therefore, when there are interfering ions in the solution, it is recommended to increase the dosage of ASBB or add a certain amount of Fe^{3+} to improve the removal rate of U(VI).

Kinetic and Thermodynamic Analysis of Sorption

Figure 4A and **Table 3** show the results of the PFO and PSO models when they were applied to experimental data. The correlation coefficient R^2 was 0.998 (PFO) and 0.997 (PSO), indicating that both physical and chemical sorption occurred during the sorption of U(VI) by ASBB.

The results of the thermodynamic analysis are illustrated in **Figure 4B** and **Table 4**. The maximum specific sorption capacity was q_m = 178.194 mg/g (ASBB adsorbent), a value

TABLE 2 | Comparison of the maximum sorption capacities of different adsorbents toward U(VI).

Adsorbent	U(VI) (mg/L)	Dosage (g/L)	Q_{max} (mg/g)	pH	Time (h)	q_t/t[(mg/g)/h]	References
Fe_3O_4@C@ASA	4.76	0.6	46.20	4.00	24.00	1.91	Li et al. (2018)
HTC–COOH	140.0	0.5	163.00	4.50	24.00	6.79	Cai et al. (2017)
Activated carbon	200.0	2.5	45.24	6.00	5.00	9.05	Morsy and Hussein, (2011)
MAO-chitosan	480.0	1.0	117.65	6.00	5.00	23.53	Zhuang et al. (2018)
P(AO)-g-CTS/BT	100.0	2.0	49.90	8.00	1.00	49.90	Anirudhan et al. (2019)
SDACA	100.0	8.0	105.26	5.00	2.00	52.63	El-MagiedAbd et al. (2017)
PVP/CS	11.9	1.0	167.00	6.00	2.50	66.80	Christou et al. (2019)
AO-MWCNTs	10.0	1.0	67.90	5.00	1.00	67.90	Wu et al. (2018)
PAF	10.0	1.0	115.31	5.00	1.00	115.31	Saleh et al. (2017)
MWCNTs	25.0	0.1	83.40	6.25	0.67	124.45	Ebrahim et al. (2017)
P-Fe-CMK-3	20.0	0.2	150.00	4.00	0.50	300.00	Husnain et al. (2017)
ASBB	10.0	0.3	179.77	6.00	0.08	2,247.13	This work

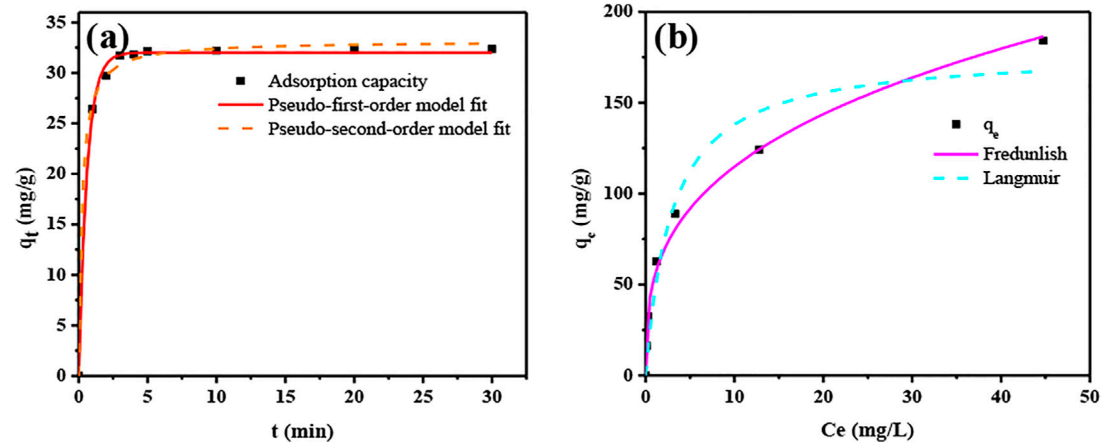

FIGURE 4 | Kinetic and thermodynamic fitted curve. **(A)** Kinetic fitted curve, **(B)** thermodynamic fitted curve.

TABLE 3 | Kinetic parameters of U(VI) sorption on ASBB.

U(VI) concentration (mg/L)	Pseudo-first-order kinetics			Pseudo-second-order kinetics		
	k_1/min^{-1}	q_e/(mg/g)	R^2	k_2/min^{-1}	q_e/(mg/g)	R^2
10.0 mg/L	1.716	31.665	0.996	0.126	33.087	0.999

consistent with the laboratory result $q_m = 179.88$ mg/g. The correlation coefficient was 0.943 (Langmuir model) and 0.989 (Freundlich model), indicating that the sorption of U(VI) by ASBB was mostly dominated by multilayer sorption.

TABLE 4 | Thermodynamic parameters of sludge-based biochar on U(VI) sorption.

Adsorbents	Langmuir			Freundlich		
	q_m/(mg/g)	K_L/(L/mg)	R^2	K_F	q_e/(mg/g)	R^2
	178.194	0.344	0.943	54.584	0.323	0.989

Characterization and Mechanism Analysis of Uranium Recovered by Acetic Acid-Modified Sludge-Based Biochar

Morphological Characteristics of Sludge-Based Biochar, Acetic Acid-Modified Sudge-Based Biochar, and Acetic Acid-Modified Sludge-Based Biochar—Uranium

The microstructure and surface elements of SBB, ASBB, and ASBB-U (i.e., used ASBB adsorbent after uranium sorption) were characterized by SEM and EDS (**Figure 5**). As shown in **Figures 5A, C, E**, the pore size of the SBB surface was quite small, while a more developed pore structure was presented on the surface of ASBB. More reaction sites could be provided by ASBB to adsorb U(VI). When the sorption was completed, the ASBB microstructure changed. The pore structure of ASBB-U obviously decreased, due to the combination of U(VI) with the functional groups on the ASBB surface, or to the direct sorption of

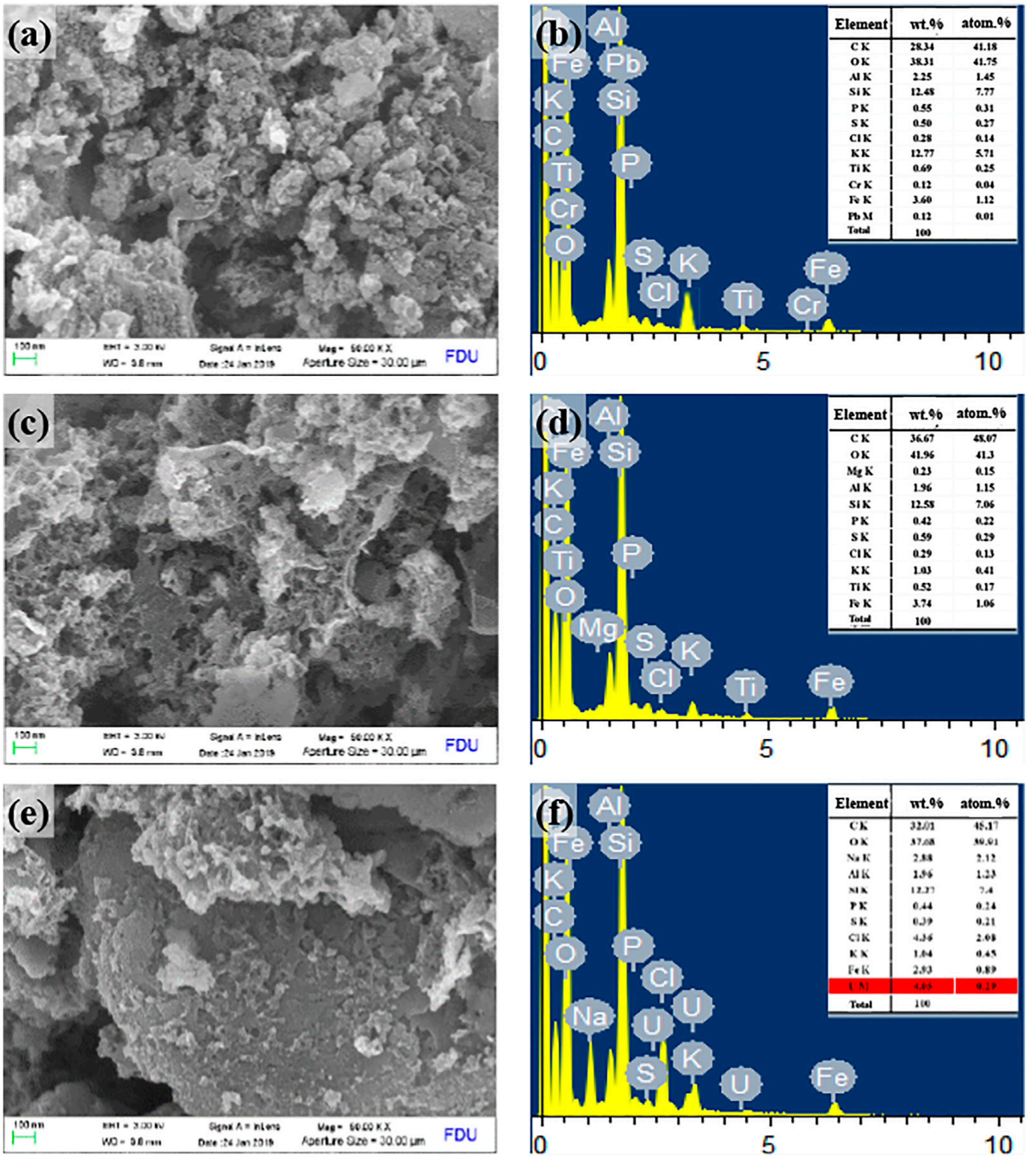

(b)

Element	wt.%	atom.%
C K	28.34	41.18
O K	38.31	41.75
Al K	2.25	1.45
Si K	12.48	7.77
P K	0.55	0.31
S K	0.50	0.27
Cl K	0.28	0.14
K K	12.77	5.71
Ti K	0.69	0.25
Cr K	0.12	0.04
Fe K	3.60	1.12
Pb M	0.12	0.01
Total	100	

(d)

Element	wt.%	atom.%
C K	36.67	48.07
O K	41.96	41.3
Mg K	0.23	0.15
Al K	1.96	1.15
Si K	12.58	7.06
P K	0.42	0.22
S K	0.59	0.29
Cl K	0.29	0.13
K K	1.03	0.41
Ti K	0.52	0.17
Fe K	3.74	1.06
Total	100	

(f)

Element	wt.%	atom.%
C K	32.01	45.17
O K	37.68	39.91
Na K	2.88	2.12
Al K	1.96	1.23
Si K	12.27	7.4
P K	0.44	0.24
S K	0.39	0.21
Cl K	4.36	2.08
K K	1.04	0.45
Fe K	2.93	0.89
U M	4.05	0.29
Total	100	

FIGURE 5 | Scanning electron microscope (SEM) and energy-dispersive x-ray spectroscopy (EDS) characterization results of SBB, ASBB, and ASBB-U, **(A)** SEM of SBB' surface, **(B)** EDS of SBB' surface, **(C)** SEM of ASBB' surface, **(D)** EDS of ASBB' surface, **(E)** SEM of ASBB-U' surface, **(F)** EDS of ASBB-U' surface.

U(VI) in the pore network of ASBB. These results were consistent with the results of BET analysis (vide infra).

According to **Figure 5B**, the main surface elements of SBB were C, O, K, and Si in general. **Figure 5D** shows that the fresh ASBB surface mainly consisted of C, O, Al, Si, P, K, and Fe. An amount of U was observed on the ASBB-U surface (**Figure 5F**). The weight percentage was about 4.05 wt%. This indicated that uranium was successfully adsorbed by ASBB.

Brunauer–Emmett–Teller Comparison of Sludge-Based Biochar, Acetic Acid-Modified Sludge-Based Biochar, and Acetic Acid-Modified Sludge-Based Biochar—Uranium

Figure 6A and **Table 5** show the BET results for SBB, ASBB, and ASBB-U. As in **Figure 6A**, the isothermal sorption–desorption curves of SBB, ASBB, and ASBB-U all belonged to the unique I/IV isothermal sorption–desorption path with the H_4 hysteresis curve (Lu et al., 2018b). It means

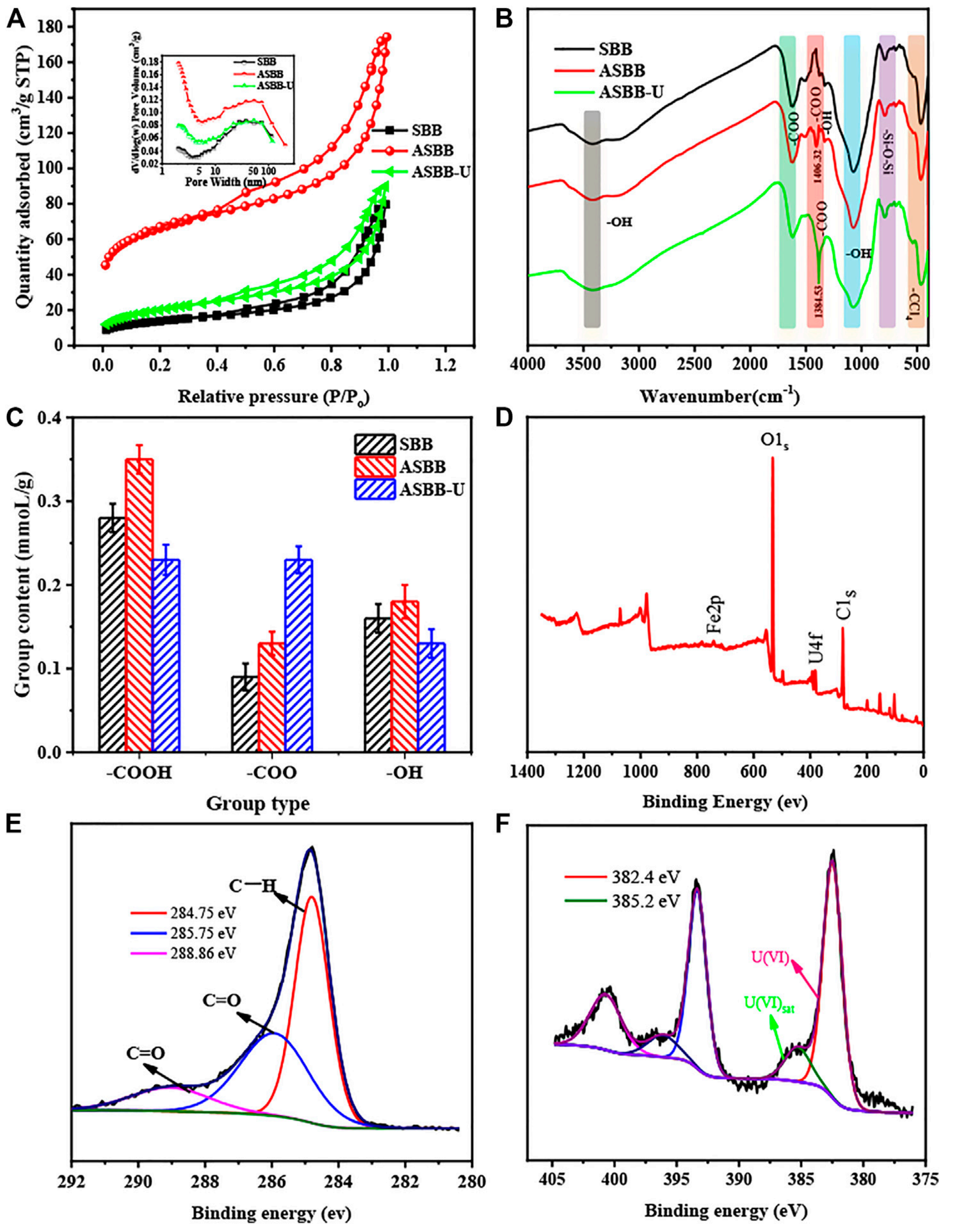

FIGURE 6 | Characteristics of SBB, ASBB, and acetic acid-modified sludge-based biochar—uranium (ASBB-U). **(A)** Brunner–Emmet–Teller (BET), **(B)** Fourier transform infrared spectroscopy (FTIR), **(C)** acidic group content, **(D)** x-ray photoelectron spectroscopy (XPS) total survey scans of ASBB-U, **(E)** XPS spectra of C1s, **(F)** XPS spectra of U4f.

TABLE 5 | Surface aperture analysis.

Sample	SSA (m^2/g)	Average pore width (nm)	Volume (cm^3/g)
SBB	49.26	10.00	0.12
ASBB	241.42	8.35	0.21
ASBB-U	72.52	7.67	0.14

Note. SSA, specific surface area; ASBB-U, acetic acid modified sludge-based biochar—uranium.

that the porosity network of these materials was structured into micropores, mesopores, and macropores. According to the pore size distribution map (**Figure 6A** inside), SBB was mainly mesoporous and macroporous (mean pore size around 50 nm), ASBB was mainly mesoporous (pores of 2 and 20–50 nm), and ASBB-U was mainly mesoporous (2 nm pores) and meso/macroporous (50 nm pores). By comparing the pore size distribution of ASBB before and after uranyl ion sorption, it was found that mesopores decreased after uranium sorption, indicating that the main reaction site was within this pore range. In addition, an inflection point near the monolayer sorption was observed in the isotherm. Multilayer sorption gradually took place with the increase in relative pressure. These phenomena were consistent with the fitting results by the sorption isotherm models above.

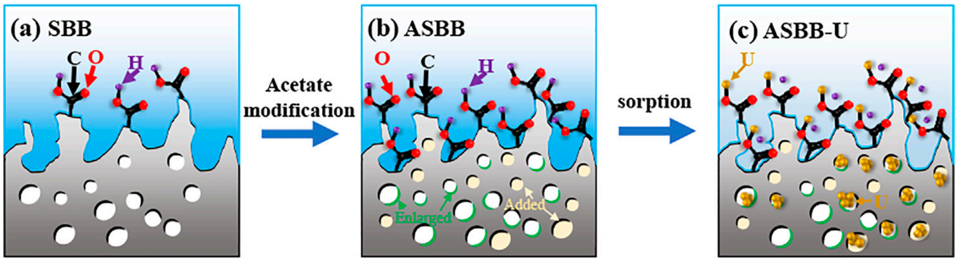

FIGURE 7 | Schematic diagram of SBB modification and uranium adsorbed by ASBB. **(A)** SBB, **(B)** ASBB, **(C)** ASBB-U.

The specific surface area (SSA) of ASBB increased with respect to the untreated biochar. Namely, a pore expansion function of acetic acid was observed. Then SSA for ASBB-U decreased. It indicates that uranyl ion was adsorbed in the pores of the ASBB surface. When the pores were blocked by the absorbed uranyl ion, the SSA of the adsorbent obviously decreased.

Group analysis of Sludge-Based Biochar, Acetic Acid-Modified Sludge-Based biochar, and Acetic Acid-Modified Sludge-Based Biochar-Uranium

FTIR analysis allowed to investigate the functional group modification when SBB was treated by acetic acid to give ASBB and the interaction of these groups with uranium during the sorption of U(VI) on ASBB. Results are illustrated in **Figure 6B**. According to literature (Gulnaz et al., 2005; Weng, 2010; Meng et al., 2019), –OH (3,427 and 1,070 cm^{-1}), –COO (1,406 and 1,617 cm^{-1}), –Si–O–Si (781 cm^{-1}), and -CCl_4 (476 cm^{-1}) were the main groups retrieved on the surface of SBB, ASBB, and ASBB-U. When the FTIR spectra of SBB, ASBB, and ASBB-U are compared, it is seen that –COO (1,406.32 cm^{-1}) was found on the ASBB surface as a new group with respect to SBB, indicating the modification of SBB by acetic acid. Moreover, when uranium was adsorbed on ASBB, some of the peak's position and intensity changed. The peak of –OH stretching vibration at 1,331.37 cm^{-1} disappeared, indicating that –OH might react with U(VI) by deprotonation. In addition, the symmetric stretching vibration peak of –COO at 1,406.32 cm^{-1} moved to 1,384.53 cm^{-1}. Although the peak shape was stable, its intensity was enhanced. The difference of the stretching vibration frequency between –COO antisymmetric stretching vibration peak (1,617.82 cm^{-1}) and –COO symmetric stretching vibration peak (1,384.53 cm^{-1}) was more than 200 cm^{-1} (233.29 cm^{-1}). This indicates that –COO and U(VI) were combined in monodentate coordination mode (Weng, 2010).

Figure 6C shows the acid group content of SBB, ASBB, and ASBB-U. Compared with SBB, the contents of –COOH and –COO in ASBB had been increased by 0.07 and 0.04 mmol/g, respectively, indicating that SBB had been well loaded with acetic acid, and its loading was about 0.11 mmol/g. After the ASBB reaction in UCW was completed, the content of –COOH was significantly reduced, while the content of –COO was increased, indicating the sorption of –COOH on U(VI). Combined with FT-IR analysis, U(VI) could be combined with –COO to purify UCW.

Valence state on Acetic Acid-Modified Sludge-Based Biochar—Uranium's Surface

Figure 6D–F present the XPS analysis results for ASBB-U's surface. From **Figure 6D**, it is seen that the main peak around 532 eV belongs to O1s, the peak around 285 eV to C1s, and the peak around 382 and 375 eV to U4f. It could be concluded that the surface of ASBB-U was mainly composed of C and O elements, and a certain amount of U(VI) adsorbed on the surface. In C1s spectrum (**Figure 6E**), the C1s component near 284.75 eV might be associated with C–H (Ding et al., 2018). Besides, the C1s spectrum could show C = O near 285.75 and 288.86 eV (Zhao et al., 2019). Moreover, the blending energy of $U4f_{2/5}$ (382.4 eV, 385.2 eV) corresponded to U(VI) on the surface of ASBB-U (**Figure 6F**) (Husnain et al., 2017; Tan et al., 2018), indicating that no redox reaction happened in uranium sorption process by ASSB.

Mechanism of Modification and Sorption

Following the experimental results, various characterization methods (BET, SEM, EDS, FTIR, XPS), and relevant references (Li et al., 2021; Liu et al., 2021), the mechanism of SBB modification and uranium sorption by ASBB was inferred. A schematic diagram is displayed in **Figure 7**: 1) The reaction probability of ASBB to uranium was greatly improved, due to the increased pore diameter, specific surface area, and functional group (–COOH) number by acetic acid modification of SBB. 2) The most suitable interaction between uranium ion and adsorbent under suitable reaction conditions might be of van der Waals type (Hussein et al., 2016), as witnessed by the decrease in SSA and pore size after the reaction of ASBB with USW. 3) –COOH had a good uranium sorption behavior (Park et al., 2019). At pH = 5, –H on –COOH could be easily replaced by uranium, which mainly existed in the form of $(UO_2)_3(OH)_5^+$ and $(UO_2)_4(OH)_7^+$. They were combined with –COO in monodentate coordination. The specific equation reads (**Eq.** 7):

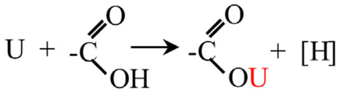

CONCLUSION

Excess sludge (ES) and acetic acid were utilized to obtain a robust adsorbent starting from sludge-based biochar (SBB), for U(VI) abatement in uranium-containing wastewater (UCW). Compared with SBB, the removal efficiency and sorption capacity of the acetic acid-modified biochar (ASBB) could be effectively improved. An optimal U(VI) removal rate of 97.8% could be achieved, while initial conditions were pH = 6.0, U(VI) = 10.0 mg/L (initial concentration), adsorbent dosage = 0.30 g/L, and sorption time = 5.0 min. The beneficial effect was attributed to the double action of expanding pores and increasing –COOH functional groups following the acetic acid modification treatment. The process of U(VI) sorption by modified biochar relies on both physical and chemical sorption. The U(VI) removal mechanism by ASBB was of monodentate coordination binding between –COO– and uranium. In addition, ASBB had good reusable performance. Hence, the quick sorption and outstanding efficiency of ASBB offer a meaningful support for the use of biochar in uranium recovery from UCW and for reutilization of ES.

DATA AVAILABILITY STATEMENT

The original contributions presented in the study are included in the article/Supplementary Material, further inquiries can be directed to the corresponding author.

AUTHOR CONTRIBUTIONS

SY: Resources, Investigation, Writing—Original Draft. XW: Validation, Writing—Review and Editing. JY: Validation. ML: Validation, Visualization. QZ: Investigation. XZ: Validation. CL: Investigation. WX: Investigation. KS: Investigation. YL: Supervision.

FUNDING

This study was financially supported by the National Natural Science Fund of China (Nos. 51704169, 51874180, 11875164), National Defense Science and Technology Bureau of China on the “13th Five-Year Plan” Technology Basic Scientific Research Project (No. JSZL2018****001, JSZL2018****008), Hunan Provincial Innovation Foundation for Postgraduate (No. CX20190711), and Research and Development Projects in Key Areas of Hunan Province (No. 2019SK 2011).

REFERENCES

Abadi, S. R. H., Sebzari, M. R., Hemati, M., Rekabdar, F., and Mohammadi, T. (2011). Ceramic Membrane Performance in Microfiltration of Oily Wastewater [J]. *Desalination* 265 (1-3), 222–228. doi:10.1016/j.desal.2010.07.055

Abdi, S., Nasiri, M., Mesbahi, A., and Khani, M. H. (2017). Investigation of Uranium (VI) Adsorption by Polypyrrole. *J. Hazard. Mater.* 332, 132–139. doi:10.1016/j.jhazmat.2017.01.013

Alatalo, S. M., Repo, E., Mäkilä, E., Salonen, J., Vakkilainen, E., and Sillanpää, M. (2013). Adsorption Behavior of Hydrothermally Treated Municipal Sludge & Pulp and Paper Industry Sludge. *Bioresour. Technol.* 147, 71–76. doi:10.1016/j.biortech.2013.08.034

Ali, Z., Chen, Z., Wang, X., and Zhang, Q. (2019). Microwave-assisted Pyrolysis of Sewage Sludge: A Review[J]. *Fuel Process. Technol.* 187, 84–104.

Anirudhan, T. S., and Deepa, J. R.Binusreejayan (2015). Synthesis and Characterization of Multi-Carboxyl-Functionalized Nanocellulose/nanobentonite Composite for the Adsorption of Uranium(VI) from Aqueous Solutions: Kinetic and Equilibrium Profiles. *Chem. Eng. J.* 273, 390–400. doi:10.1016/j.cej.2015.03.007

Anirudhan, T. S., Lekshmi, G. S., and Shainy, F. (2019). Synthesis and Characterization of Amidoxime Modified Chitosan/bentonite Composite for the Adsorptive Removal and Recovery of Uranium from Seawater. *J. Colloid Interf. Sci.* 534, 248–261. doi:10.1016/j.jcis.2018.09.009

Anna, C.-P., Justyna, S.-B., and Wojciech, L. (2018). Optimization of Copper, lead and Cadmium Biosorption onto Newly Isolated Bacterium Using a Box-Behnken Design[J]. *Ecotoxicology Environ. Saf.* 149, 275–283.

Baur, X., Rihs, H.-P., Altmeyer, P., Degens, P., Conrad, K., Mehlhorn, J., et al. (1996). Systemic Sclerosis in German Uranium Miners under Special Consideration of Autoantibody Subsets and Hla Class Ii Alleles. *Respiration* 63 (6), 368–375. doi:10.1159/000196579

Bruno, J., De Pablo, J., Duro, L., and Figuerola, E. (1995). Experimental Study and Modeling of the U(VI)-Fe(OH)3 Surface Precipitation/coprecipitation Equilibria. *Geochimica et Cosmochimica Acta* 59 (20), 4113–4123. doi:10.1016/0016-7037(95)00243-s

Cai, H., Lin, X., Qin, Y., and Luo, X. (2017). Hydrothermal Synthesis of Carbon Microsphere from Glucose at Low Temperature and its Adsorption Property of Uranium(VI). *J. Radioanal. Nucl. Chem.* 311 (1), 695–706. doi:10.1007/s10967-016-5106-9

Chen, T., Zhang, J., Ge, H., Li, M., Li, Y., liu, B., et al. (2020). Efficient Extraction of Uranium in Organics-Containing Wastewater over G-C3n4/GO Hybrid Nanosheets with Type-II Band Structure. *J. Hazard. Mater.* 384, 121383. doi:10.1016/j.jhazmat.2019.121383

Christou, C., Philippou, K., Krasia-Christoforou, T., and Pashalidis, I. (2019). Uranium Adsorption by Polyvinylpyrrolidone/chitosan Blended Nanofibers. *Carbohydr. Polym.* 219, 298–305. doi:10.1016/j.carbpol.2019.05.041

Deb, A. K. S., Ilaiyaraja, P., Ponraju, D., and Venkatraman, B. (2012). Diglycolamide Functionalized Multi-Walled Carbon Nanotubes for Removal of Uranium from Aqueous Solution by Adsorption[J]. *J. Radioanal. Nucl. Chem.* 291 (3), 877–883.

Ding, L., Tan, W.-F., Xie, S.-B., Mumford, K., Lv, J.-W., Wang, H.-Q., et al. (2018). Uranium Adsorption and Subsequent Re-oxidation under Aerobic Conditions by Leifsonia Sp. - Coated Biochar as green Trapping Agent. *Environ. Pollut.* 242, 778–787. doi:10.1016/j.envpol.2018.07.050

Ebrahim, Y. S. M., Salem Nafisa, A., and Abdeltawab Ahmed, A. (2017). Equilibrium and Thermodynamics for Adsorption of Uranium onto Potassium Hydroxide Oxidized Carbon[J]. *Desalination Water Treat.* 72, 335–342.

El-MagiedAbd, M. O. A., Mohammaden, T. F., El-Aassy, I. K., Gad, H. M. H., Hassan, A. M., and Mahmoud, M. A. (2017). Decontamination of Uranium-Polluted Groundwater by Chemically-Enhanced, Sawdust-Activated Carbon. *Colloids Inter.* 1 (1), 2. doi:10.3390/colloids1010002

Fang-Zhu, X., Cheng, W., Li-Mei, Y., Yi-Qiu, P., Yu-Li, X., Kang, Z., et al. (2019). Fabrication of Magnetic Functionalised Calix 4 Arene Composite for Highly Efficient and Selective Adsorption towards Uranium(VI)[J]. *Environ. Chem.* 16 (8), 577–586.

Feng, Q., Zhang, Z., Chen, Y., Liu, L., Zhang, Z., and Chen, C. (2013). Adsorption and Desorption Characteristics of Arsenic on Soils: Kinetics, Equilibrium, and Effect of Fe(OH)3 Colloid, H2SiO3 Colloid and Phosphate. *Proced. Environ. Sci.* 18, 26–36. doi:10.1016/j.proenv.2013.04.005

Gerber, U., Zirnstein, I., Krawczyk-Bärsch, E., Lünsdorf, H., Arnold, T., and Merroun, M. L. (2016). Combined Use of Flow Cytometry and Microscopy to Study the Interactions between the Gram-Negative Betaproteobacterium Acidovorax Facilis and Uranium(VI). *J. Hazard. Mater.* 317, 127–134. doi:10.1016/j.jhazmat.2016.05.062

Ghosh, P. (2009). Biological Treatment Processes[J]. *Handbook Environ. Eng.* 80 (2), 69–72.

Guanhai, M., Qing, H., Guohua, W., Shuibo, X., Haidu, N., Xiaoling, Z., et al. (2021). Fe_3O_4-modified Sewage Sludge Biochar for U(VI) Removal from Aqueous Solution: Performance and Mechanism[J]. *J. Radioanal. Nucl. Chem.* 329 (1), 225–237.

Gulnaz, O., Saygideger, S., and Kusvuran, E. (2005). Study of Cu(II) Biosorption by Dried Activated Sludge: Effect of Physico-Chemical Environment and Kinetics Study. *J. Hazard. Mater.* 120 (1-3), 193–200. doi:10.1016/j.jhazmat.2005.01.003

Hossain, M. I., Paparini, A., and Cord-Ruwisch, R. (2018). Direct Oxygen Uptake from Air by Novel Glycogen Accumulating Organism Dominated Biofilm Minimizes Excess Sludge Production. *Sci. Total Environ.* 640-641, 80–88. doi:10.1016/j.scitotenv.2018.05.292

Hu, W., Xie, Y., Lu, S., Li, P., Xie, T., Zhang, Y., et al. (2019). One-step Synthesis of Nitrogen-Doped Sludge Carbon as a Bifunctional Material for the Adsorption and Catalytic Oxidation of Organic Pollutants. *Sci. Total Environ.* 680, 51–60. doi:10.1016/j.scitotenv.2019.05.098

Husnain, S. M., KimJu, H. J., Um, W., Chang, Y.-Y., and Chang, Y.-S. (2017). Superparamagnetic Adsorbent Based on Phosphonate Grafted Mesoporous Carbon for Uranium Removal. *Ind. Eng. Chem. Res.* 56 (35), 9821–9830. doi:10.1021/acs.iecr.7b01737

Hussein, A., Fares Mohammad, M., and Abu Al-Rub Fahmi, A. (2016). Removal of Uranium and Associated Contaminants from Aqueous Solutions Using Functional Carbon Nanotubes-Sodium Alginate Conjugates[J]. *Minerals* 6 (1), 9.

Ioanna, L., Georgia, M., Marilena, D., and Ioannis, P. (2017). Uranium Binding by Biochar Fibres Derived from Luffa Cylindrica after Controlled Surface Oxidation[J]. *J. Radioanal. Nucl. Chem.* 311 (1), 871–875.

Ismail Cem, K., and Jale, Y. (2009). Use of Waste Sludge from the Tannery Industry [J]. *Energy & Fuels* 23 (6), 3126–3133.

Jiang, X., Wang, H., Wang, Q., Hu, E., and Duan, Y. (2020). Immobilizing Amino-Functionalized Mesoporous Silica into Sodium Alginate for Efficiently Removing Low Concentrations of Uranium. *J. Clean. Prod.* 247, 119162. doi:10.1016/j.jclepro.2019.119162

Jin, J., Li, S., Peng, X., Liu, W., Zhang, C., Yang, Y., et al. (2018). HNO3 Modified Biochars for Uranium (VI) Removal from Aqueous Solution. *Bioresour. Technol.* 256, 247–253. doi:10.1016/j.biortech.2018.02.022

Kalijadis, A., Vukcevic, M., Jovanovic, Z., Lausevic, Z., and Lausevic, M. (2011). Characterization of Surface Oxygen Groups on Different Carbon Materials by the Boehm Method and Temperature Programmed Desorption. *J. Serbian Chem. Soc.* 76 (5), 757–768. doi:10.2298/jsc091224056k

Kataria, N., and Garg, V. K. (2018). Green Synthesis of Fe3O4 Nanoparticles Loaded Sawdust Carbon for Cadmium (II) Removal from Water: Regeneration and Mechanism. *Chemosphere* 208, 818–828. doi:10.1016/j.chemosphere.2018.06.022

Kathren, R. L., and Burklin, R. K. (2008). Acute Chemical Toxicity of Uranium. *Health Phys.* 94 (2), 170–179. doi:10.1097/01.hp.0000288043.94908.1f

Khani, M. H., Keshtkar, A. R., Ghannadi, M., and Pahlavanzadeh, H. (2008). Equilibrium, Kinetic and Thermodynamic Study of the Biosorption of Uranium onto Cystoseria Indica Algae. *J. Hazard. Mater.* 150 (3), 612–618. doi:10.1016/j.jhazmat.2007.05.010

Khawassek, Y. M., Masoud, A. M., Taha, M. H., and Hussein, A. E. M. (2018). Kinetics and Thermodynamics of Uranium Ion Adsorption from Waste Solution Using Amberjet 1200 H as Cation Exchanger. *J. Radioanal. Nucl. Chem.* 315 (3), 493–502. doi:10.1007/s10967-017-5692-1

Kong, L., Ruan, Y., Zheng, Q., Su, M., Diao, Z., Chen, D., et al. (2020). Uranium Extraction Using Hydroxyapatite Recovered from Phosphorus Containing Wastewater. *J. Hazard. Mater.* 382, 120784. doi:10.1016/j.jhazmat.2019.120784

Li, F., Meng, F., Wang, H., Ge, B., Zhang, Y., and Yu, C. (2019). Urea-modified Grass Ash Activated Sludge Carbon: Structure and Adsorption Properties towards H2S and CH3SH. *New J. Chem.* 43 (44), 17494–17501. doi:10.1039/c9nj03836a

Li, H., Li, Y., Li, B., Dai, Y., and Chen, X. (2020). Melamine-induced Novel MSONs Heterostructured Framework: Controlled-Switching between MOF and SOF via a Self-Assembling Approach for Rapid Uranium Sequestration. *Chem. Eng. J.* 379, 122279. doi:10.1016/j.cej.2019.122279

Li, M., Liu, H., Chen, T., Dong, C., and Sun, Y. (2019). Synthesis of Magnetic Biochar Composites for Enhanced Uranium(VI) Adsorption. *Sci. Total Environ.* 651, 1020–1028. doi:10.1016/j.scitotenv.2018.09.259

Li, M., Liu, Y., Li, F., Shen, C., Kaneti, Y. C., Yamauchi, Y., et al. (2021). Defect-Rich Hierarchical Porous UiO-66(Zr) for Tunable Phosphate Removal[J]. *Environ. Sci. Technol.* 55 (19), 13209–13218.

Li, P., Wang, J., Wang, X., He, B., Pan, D., Liang, J., et al. (2018). Arsenazo-functionalized Magnetic Carbon Composite for Uranium(VI) Removal from Aqueous Solution. *J. Mol. Liquids* 269, 441–449. doi:10.1016/j.molliq.2018.08.073

Liu, F., You, S., Wang, Z., and Liu, Y. (2021). Redox-Active Nanohybrid Filter for Selective Recovery of Gold from Water. *ACS EST Eng.* 1 (9), 1342–1350. doi:10.1021/acsestengg.1c00158

Liu, H., Xie, S., Liao, J., Yan, T., Liu, Y., and Tang, X. (2018). Novel Graphene Oxide/bentonite Composite for Uranium(VI) Adsorption from Aqueous Solution. *J. Radioanal. Nucl. Chem.* 317 (3), 1349–1360. doi:10.1007/s10967-018-5992-0

Lu, B.-q., Li, M., Zhang, X.-w., Huang, C.-m., Wu, X.-y., and Fang, Q. (2018). Immobilization of Uranium into Magnetite from Aqueous Solution by Electrodepositing Approach. *J. Hazard. Mater.* 343, 255–265. doi:10.1016/j.jhazmat.2017.09.037

Lu, S., Liu, Y., Feng, L., Sun, Z., and Zhang, L. (2018). Characterization of Ferromagnetic Sludge-Based Activated Carbon and its Application in Catalytic Ozonation of P-Chlorobenzoic Acid. *Environ. Sci. Pollut. Res.* 25 (6), 5086–5094. doi:10.1007/s11356-017-8680-7

Malenchenko, A. F., Barkun, N. A., and Guseva, G. F. (1978). Effect of Uranium on the Induction and Course of Experimental Autoimmune Orchitis and Thyroiditis. *J. Hyg. Epidemiol. Microbiol. Immunol.* 22 (3), 268–277.

Meng, F., Gong, Z., Wang, Z., Fang, P., and Li, X. (2019). Study on a Nitrogen-Doped Porous Carbon from Oil Sludge for CO2 Adsorption. *Fuel* 251, 562–571. doi:10.1016/j.fuel.2019.04.046

Mishra, V., Sureshkumar, M. K., Gupta, N., and Kaushik, C. P. (2017). Study on Sorption Characteristics of Uranium onto Biochar Derived from Eucalyptus Wood. *Water Air Soil Pollut.* 228 (8), 309. doi:10.1007/s11270-017-3480-8

Morsy, A. M. A., and Hussein, A. E. M. (2011). Adsorption of Uranium from Crude Phosphoric Acid Using Activated Carbon. *J. Radioanal. Nucl. Chem.* 288 (2), 341–346. doi:10.1007/s10967-011-0980-7

NaserHumood, H. A. (2013). Assessment and Management of Heavy Metal Pollution in the marine Environment of the Arabian Gulf: A Review. *Mar. Pollut. Bull.* 72 (1), 6–13. doi:10.1016/j.marpolbul.2013.04.030

Park, J., Bae, J., Jin, K., and Park, J. (2019). Carboxylate-functionalized Organic Nanocrystals for High-Capacity Uranium Sorbents. *J. Hazard. Mater.* 371, 243–252. doi:10.1016/j.jhazmat.2019.03.007

Pu, D., Kou, Y., Zhang, L., Liu, B., Zhu, W., Zhu, L., et al. (2019). Waste Cigarette Filters: Activated Carbon as a Novel Sorbent for Uranium Removal. *J. Radioanal. Nucl. Chem.* 320 (3), 725–731. doi:10.1007/s10967-019-06502-z

Saleh, T. A., Naeemullah, T. M., Tuzen, M., and Sarı, A. (2017). Polyethylenimine Modified Activated Carbon as Novel Magnetic Adsorbent for the Removal of Uranium from Aqueous Solution. *Chem. Eng. Res. Des.* 117, 218–227. doi:10.1016/j.cherd.2016.10.030

Schierz, A., and Zänker, H. (2009). Aqueous Suspensions of Carbon Nanotubes: Surface Oxidation, Colloidal Stability and Uranium Sorption. *Environ. Pollut.* 157 (4), 1088–1094. doi:10.1016/j.envpol.2008.09.045

Sun, S., Zhang, S., Zhang, W., Meng, J., and Wang, L. (2018). Reduction and Heavy Metals Removal of Excess Sludge by Radio Frequency Discharge Plasma. *IOP Conf. Ser. Earth Environ. Sci.* 146, 012069. doi:10.1088/1755-1315/146/1/012069

Sun, Y., Shao, D., Chen, C., Yang, S., and Wang, X. (2013). Highly Efficient Enrichment of Radionuclides on Graphene Oxide-Supported Polyaniline. *Environ. Sci. Technol.* 47 (17), 9904–9910. doi:10.1021/es401174n

Sun, Y., Wang, X., Ai, Y., Yu, Z., Huang, W., Chen, C., et al. (2017). Interaction of Sulfonated Graphene Oxide with U(VI) Studied by Spectroscopic Analysis and Theoretical Calculations. *Chem. Eng. J.* 310, 292–299. doi:10.1016/j.cej.2016.10.122

Tan, Y., Li, L., Zhang, H., Ding, D., Dai, Z., Xue, J., et al. (2018). Adsorption and Recovery of U(VI) from Actual Acid Radioactive Wastewater with Low Uranium Concentration Using Thioacetamide Modified Activated Carbon from Liquorice Residue. *J. Radioanal. Nucl. Chem.* 317 (2), 811–824. doi:10.1007/s10967-018-5952-8

Tu, H., Lan, T., Yuan, G., Zhao, C., Liu, J., Li, F., et al. (2019). The Influence of Humic Substances on Uranium Biomineralization Induced by Bacillus Sp. Dwc-2. *J. Environ. Radioactivity* 197, 23–29. doi:10.1016/j.jenvrad.2018.11.010

Wang, G., Liu, J., Wang, X., Xie, Z., and Deng, N. (2009). Adsorption of Uranium (VI) from Aqueous Solution onto Cross-Linked Chitosan. *J. Hazard. Mater.* 168 (2-3), 1053–1058. doi:10.1016/j.jhazmat.2009.02.157

Wen, T., Wang, X., Wang, J., Chen, Z., Li, J., Hu, J., et al. (2016). A Strategically Designed Porous Magnetic N-Doped Fe/Fe3C@C Matrix and its Highly Efficient Uranium(vi) Remediation. *Inorg. Chem. Front.* 3 (10), 1227–1235. doi:10.1039/c6qi00091f

Weng, Pushi. (2010). *Fourier Transform Infrared Spectrum analysis[M]*. Beijing, China: Chemical Industrial Press.

Wu, F., Pu, N., Ye, G., Sun, T., Wang, Z., Song, Y., et al. (2017). Performance and Mechanism of Uranium Adsorption from Seawater to Poly(dopamine)-Inspired Sorbents. *Environ. Sci. Technol.* 51 (8), 4606–4614. doi:10.1021/acs.est.7b00470

Wu, J., Tian, K., and Wang, J. (2018). Adsorption of Uranium (VI) by Amidoxime Modified Multiwalled Carbon Nanotubes. *Prog. Nucl. Energ.* 106, 79–86. doi:10.1016/j.pnucene.2018.02.020

Wu, Y., Chen, D., Kong, L., Tsang, D. C. W., and Su, M. (2019). Rapid and Effective Removal of Uranium (VI) from Aqueous Solution by Facile Synthesized Hierarchical Hollow Hydroxyapatite Microspheres. *J. Hazard. Mater.* 371, 397–405. doi:10.1016/j.jhazmat.2019.02.110

Xiong, J., Hu, S., Liu, Y., Yu, J., Yu, H., Xie, L., et al. (2017). Polypropylene Modified with Amidoxime/Carboxyl Groups in Separating Uranium(VI) from Thorium(IV) in Aqueous Solutions. *ACS Sustain. Chem. Eng.* 5 (2), 1924–1930. doi:10.1021/acssuschemeng.6b02663

Zeng, T., Mo, G., Zhang, X., Liu, J., Liu, H., and Xie, S. (2020). U(VI) Removal Efficiency and Mechanism of Biochars Derived from Sewage Sludge at Two Pyrolysis Temperatures. *J. Radioanal. Nucl. Chem.* 326 (2), 1413–1425. doi:10.1007/s10967-020-07423-y

Zhao, C., Liu, J., Deng, Y., Tian, Y., Zhang, G., Liao, J., et al. (2019). Uranium(Ⅵ) Adsorption from Aqueous Solutions by Microorganism-Graphene Oxide Composites via an Immobilization Approach. *J. Clean. Prod.* 236, 117624. doi:10.1016/j.jclepro.2019.117624

Zhao, W., Lin, X., Qin, Y., Cai, H., Chen, Y., and Luo, X. (2017). Preparation of Chemically Oxidized Porous Carbon and its Adsorption of Uranium(VI) from Aqueous Solution. *J. Radioanal. Nucl. Chem.* 314 (3), 1853–1864. doi:10.1007/s10967-017-5559-5

Zhao, Z., Li, J., Wen, T., Shen, C., Wang, X., and Xu, A. (2015). Surface Functionalization Graphene Oxide by Polydopamine for High Affinity of Radionuclides. *Colloids Surf. A: Physicochemical Eng. Aspects* 482, 258–266. doi:10.1016/j.colsurfa.2015.05.020

Zhu, J., Liu, Q., Li, Z., Liu, J., Zhang, H., Li, R., et al. (2018). Efficient Extraction of Uranium from Aqueous Solution Using an Amino-Functionalized Magnetic Titanate Nanotubes. *J. Hazard. Mater.* 353, 9–17. doi:10.1016/j.jhazmat.2018.03.042

Zhuang, S., Cheng, R., Kang, M., and Wang, J. (2018). Kinetic and Equilibrium of U(Ⅵ) Adsorption onto Magnetic Amidoxime-Functionalized Chitosan Beads. *J. Clean. Prod.* 188, 655–661. doi:10.1016/j.jclepro.2018.04.047

Zong, P., Cao, D., Cheng, Y., Zhang, H., Shao, D., Wang, S., et al. (2017). Functionally Reduced Graphene Oxide Supported Iron Oxides Composites as an Adsorbent for the Immobilization of Uranium Ions from Aqueous Solutions. *J. Mol. Liquids* 240, 578–588. doi:10.1016/j.molliq.2017.05.101

Zong, P., Wu, X., Gou, J., Lei, X., Liu, D., and Deng, H. (2015). Immobilization and Recovery of Uranium(VI) Using Na-Bentonite from Aqueous Medium: Equilibrium, Kinetics and Thermodynamics Studies. *J. Mol. Liquids* 209, 358–366. doi:10.1016/j.molliq.2015.05.052

Conflict of Interest: The authors declare that the research was conducted in the absence of any commercial or financial relationships that could be construed as a potential conflict of interest.

ORIGINAL RESEARCH
published: 08 March 2022
doi: 10.3389/fchem.2022.850171

Optimize the Preparation of Novel Pyrite Tailings Based Non-sintered Ceramsite by Plackett-Burman Design Combined With Response Surface Method for Phosphorus Removal

Ruihuan Chen[1,2], Zhenlin Pan[1], Shuyi Chu[3], Jibo Xiao[1], Rengui Weng[4], Da Ouyang[5], Yunlong Yang[1], Xiangting Wu[1] and Zhida Huang[6]**

[1]College of Life and Environmental Science, Wenzhou University, Wenzhou, China, [2]Zhejiang Provincial Key Laboratory for Water Environment and Marine Biological Resources Protection, Wenzhou University, Wenzhou, China, [3]Wenzhou Academy of Agricultural Sciences, Wenzhou, China, [4]Indoor Environment Engineering Research Center of Fujian Province, Fujian University of Technology, Fuzhou, China, [5]Key Laboratory of Soil Contamination Bioremediation of Zhejiang Province, School of Environmental and Resource Sciences, Zhejiang Agriculture and Forestry University, Hangzhou, China, [6]Wenzhou Institute of Industry and Science, Wenzhou, China

Edited by:
Qingyi Zeng,
University of South China, China

Reviewed by:
Linsen Li,
Hebei University, China
Min Wang,
Jinan University, China

***Correspondence:**
Jibo Xiao
jbxiao@wzu.edu.cn
Zhida Huang
40098008@qq.com

Specialty section:
This article was submitted to
Inorganic Chemistry,
a section of the journal
Frontiers in Chemistry

Received: 07 January 2022
Accepted: 21 January 2022
Published: 08 March 2022

Citation:
Chen R, Pan Z, Chu S, Xiao J, Weng R, Ouyang D, Yang Y, Wu X and Huang Z (2022) Optimize the Preparation of Novel Pyrite Tailings Based Non-sintered Ceramsite by Plackett-Burman Design Combined With Response Surface Method for Phosphorus Removal.
Front. Chem. 10:850171.
doi: 10.3389/fchem.2022.850171

The large amount of untreated pyrite tailings has caused serious environmental problems, and the recycling of pyrite tailings is considered as an attractive strategy. Here, we reported a novel non-sintered ceramsite prepared with pyrite tailings (PTNC) as the main active raw material for phosphorus control, and the dosage effect of ingredients on total phosphorus (TP) removal ability was investigated. The results from Plackett-Burman Design (PBD) suggested the dosages of dehydrated sludge, sodium bicarbonate, and cement were the factors which significantly affect the TP removal ability. The Box-Behnken Design (BBD) based response surface methodology was further employed, and it indicated the interactions between different factors, and the optimized recipe for PTNC was 84.5 g (pyrite tailings), 10 g (cement), 1 g (calcined lime), 1 g (anhydrous gypsum), 3 g (dehydrated sludge), and 0.5 g (sodium bicarbonate). The optimized PTNC was characterized and which presented much higher specific area (7.21 m^2/g) than the standard limitation (0.5 m^2/g), as well as a lower wear rate (2.08%) rather than 6%. Additionally, the leaching metal concentrations of PTNC were far below the limitation of Chinese National Standard. The adsorption behavior of TP on PTNC was subsequently investigated with batch and dynamic experiments. It was found that the calculated max adsorption amount (q_{max}) was about 7 mg/g, and PTNC was able to offer a stable TP removal ability under different hydraulic retention time (HRT). The adsorption mechanism was discussed by model fitting analysis combined with XRD and SEM characterization, and cobalt phosphide sulfide was observed as the newly formed substance through the adsorption process, which suggested the existing of both physical and chemical adsorption effect. Our research not only offered an economic preparation method of ceramsite, but also broadened the recycling pathway of pyrite tailings.

Keywords: pyrite, solid waste recycling, unburned ceramsite, phosphorus removal, filter material, harmless treatment

1 INTRODUCTION

Pyrite is the most abundant and widespread sulfide mineral which is mainly composed of iron and sulfur, and has been used as the raw material for sulfuric acid production for decades (Chandra and Gerson 2010). However, with the large-scale mining of pyrite, the pyrite tailings have caused serious environmental problems. As sulfide-rich waste materials, pyrite tailings can be oxidized in the presence of air and water (Garcia et al., 2005) spontaneously, which causes acid mine drainage (AMD) consequently (Malmström et al., 2006). AMD is considered as a serious and persistent environmental problem, which leads to the environment acidification and also releasing of significant amounts of various toxic metals into surface and groundwater (Heikkinen and Räisänen, 2009; Wang and Mulligan, 2009; Sahoo et al., 2013; Carvalho et al., 2014). Thus, the control of the pyrite tailings sourced pollution has become an important issue in the past decades, and various methods have been reported (Ouyang et al., 2015; Park et al., 2019; Dong et al., 2020a).

Remediation strategies are effective but unsustainable; thus, recycling of mine tailings is considered as a more economical way for reducing of tailings amount and limiting acid mine drainage formation. Currently, the most popular strategy for tailings recycling is replacing some portion of traditional but expensive construction materials, such as concrete admixture (Guo et al., 2016) and road construction admixture (Oluwasola et al., 2015). However, drawbacks still hindered the application of these strategies, such as higher energy consumption, dust generation increasing, and CO_2 emission (Khale and Chaudhary, 2007), and novel effective and environment friendly method towards pyrite tailings recycling should be proposed. One important property of pyrite tailings should not be ignored, that is, large amounts of active reaction sites due to the existing of Fe and S in pyrite tailings, which can be used for removal of various pollutants (Yang et al., 2017). Thus, it is promising to use pyrite tailings as the active material to enhance the wastewater treatment process.

It is well known that the effluents of municipal wastewater treatment plants (WWTPs) contributed highly to these elements' concentrations in surface water, and the abundant nutrition elements (especially phosphorus) in water have caused a serious eutrophication problem in the past decades (Schindler et al., 2016). Thus the resource utilization and advanced treatment of waste water is a very meaningful way for the sustainable development of human beings, and strategies have been proposed (Bashar et al., 2018; Zeng et al., 2021). The biological aerated filter system (BAFS) has gained increasing attention due to smaller footprint and favorable ability for contaminants removal, which presented effective removal effect on COD, NH_3-N, and TN (Dong et al., 2020b). BAFS generally takes advantages of a granular media for the formation of microbial biofilms and provides the depth filtration action as well. Certainly, the biomass, bioactivity, and filtration action in BAFS is highly depending on the media character, and it also significantly determines the investment of construction and operating cost. Thus, research has reported focusing on the investigation of media performance of different materials in BAFS (Qiu et al., 2010; Bao et al., 2016; Bao et al., 2019), and ceramic particle was found as a favorable candidate due to its large specific surface area, high mechanical strength, and biological affinity (Yue et al., 2009; Han et al., 2013; Yang et al., 2015). However, the phosphorus removal by commercial ceramsites was unfavorable as yet (Jiang et al., 2014), and it is significant to propose strategies to improve its phosphorus removal.

Ceramsite was generally prepared with various active materials such as clay (Zhang et al., 2019), activated sludge (Nie et al., 2021) and fly ash (Mi et al., 2021) by high temperature calcination, which not only aim to improve the material properties and safety, but also promote the recovery and utilization of waste resource. However, the calcination is a high energy consumption process, and the crystal structure of raw material would be destroyed leading to the decrease of active adsorption sites. Consequently, non-sintered is considered as a more economic and effective way for preparation of ceramsites. Shao et al. (2019) prepared a non-sintered fly ash ceramsite for ammonia nitrogen adsorption, and which showed favorable adsorption capacity (4.25 mg/g) and standard-compliant leaching toxicity. Li et al. (2015) investigated the performance of non-sintered fly-ash ceramsite in the dual membrane processes for treatment of ethylene chemical plant wastewater, which indicated the biological aerated filter loaded with non-sintered ceramsite was a reasonable and effective method for pretreatment of reverse osmosis process. Besides fly-ash, the raw materials for non-sintered ceramsite preparation can be various, which provides more opportunities for recycling of solid wastes (He and Wang, 2019; Wang et al., 2021). Previous reports have already proved pyrite as a favorable absorbent candidate for wastewater treatment (Xu et al., 2006; Bulut et al., 2014; Ge et al., 2019; Chero-Osorio et al., 2021), and it is attractive to use pyrite tailings as the raw material for preparation of novel effective ceramsite towards phosphorus removal.

To our knowledge, there is no available report about the investigation of pyrite tailings based ceramsite as yet; thus, in this research, we employed pyrite tailings as the major active material aiming to prepare a novel non-sintered ceramsite (PTNC) for phosphorus control in wastewater treatment process. The main objectives are 1) investigate and optimize the recipe of raw materials mass ratio; 2) characterize the optimized PTNC with XRD, BET, SEM, and confirm its security by leaching toxicity metal concentration determination; and 3) investigate the application potential and clarify the removal mechanism of total phosphorus (TP) with batch adsorption experiment and dynamic column experiment.

2 MATERIALS AND METHODS

2.1 Materials and Chemicals

Pyrite tailings were collected from Anyang, Henan Province, and the chemical composition and XRD data of pyrite tailings are shown in **Supplementary Table S1** and **Supplementary Figure S1** respectively. The commercial $425^{\#}$ cement was used as adhesive and stabilizer, and calcium lime (≥60% effective calcium oxide) and anhydrous gypsum (industrial grade) were used as activator. Dehydrated sludge (**Supplementary Table S2**) is obtained from a sewage treatment plant in Wenzhou and used to reduce the product weight. Sodium bicarbonate (analytical grade) was selected as the pore-forming agent.

2.2 Preparation of PTNC

Firstly, 25 ml deionized water was added into a mixture (totally 100 g) containing pyrite tailings, cement, calcium lime, anhydrous gypsum, sodium bicarbonate, and dehydrated sludge with required mass ratio. After pelleting to spherical ceramsite (6–10 mm), it was air-dried for 12 h at room temperature, then the ceramsites were steam cured with an autoclave at 1.2 MPa and 100°C for 10 h. The final PTUC product was obtained by regularly curing with spraying water for 2 days.

2.3 Optimization of the Components Dosage

2.3.1 Single Factor Experiment

Single factor experiments were performed to preliminary define the dosage of raw materials, and the phosphate removal rate as well as porosity were selected as the indicators. For each single experiment, the total mixture weight was fixed as 100 g, and the amount of pyrite tailings varied with the changing of corresponding ingredient amount. The test amounts of each material were shown as follows: cement (10, 20, 30, 40, and 50 g), calcium lime (1, 2, 3, 4, and 5 g), anhydrous gypsum (1, 2, 3, 4, and 5 g), dehydrated sludge (2, 4, 6, 8, and 10 g), and sodium bicarbonate (05, 1, 2, 3, 4, and 5 g).

2.3.2 Plackett-Burman Experiments

In order to obtain the significant influence factors on the phosphate removal capacity and porosity of PTNC, PBD method was used and the design scheme can be found in **Supplementary Table S3**, where five ingredients were coded respectively from code A to E, phosphate removal capacity was set as Y.

2.3.3 Box-Behnken Design Based Response Surface Methodology

Based on the significantly influence factors obtained from PBD experiments, the dosage of dehydrated sludge, sodium bicarbonate, and cement were selected and coded as X_1, X_2, and X_3 respectively for Box-Behnken design to optimize the PTNC preparation process. Phosphate removal capacity (Y) was used as the indicators, and the design scheme is shown in **Supplementary Table S4**.

2.4 Batch Adsorption Experiment for TP Removal

A total of 4.5 g PTUC was weighted and added into the conical flask (150 ml) and 50.0 ml solution containing required concentration of potassium dihydrogen phosphate was added, and the vials were shaken at 100 rpm for 5 h at 25°C. The TP concentration in the filtered liquid was determined by Mo-Sb anti-spectrophotometry method (λ = 700 nm). The effect of pH, PTNC dosage, co-existing anions, and temperature on adsorption were investigated respectively as well as the adsorption kinetic, and all the experiments were performed in triplicate vials. The removal rate of TP was calculated as follow equation:

$$\text{TP removal rate} = \frac{c_1 - c_0}{c_0} \times 100\% \qquad (1)$$

where c_0 and $c_1$were the initial TP and filtered TP concentration in aqueous respectively.

2.5 Dynamic Adsorption of Total Phosphorus by PTNC in Column Experiment

In order to evaluate to the application potential of PTNC in TP control, an organic glass column (50 × 500 mm) was used to perform the dynamic adsorption experiment. PTNC was prepared according to the optimized results and filled into the column to 400 mm height. Simulated wastewater containing 26 mg/L TP was pumped into the column from the column bottom by a peristaltic pump, and the effect of hydraulic retention time (HRT) on TP removal was investigated in the range of 1–3 h. The diagram of experimental device can be found in **Supplementary Figure S2**.

2.6 Characterization of PTNC

The physicochemical properties such as bulk density, apparent density, crush/wear rate, solubility in hydrochloric acid, voidage, and silt content were tested according to the Chinese standard (CJ/T 299-2008). Water absorption and cylinder compressive strength were tested as Chinese national standard (GB/T 17,431.2-2010). X-ray diffraction (XRD), BET method, and scanning electron microscopy (SEM) were employed to analyze the changes of crystal structure, specific surface area, and morphology after adsorption.

The leaching analysis of heavy metal was performed to evaluate the potential risk of PTNC. Briefly, sulfuric acid and nitric acid were mixed (mass ratio 2:1), and the added to deionized water and the pH was adjusted at 3.2. Then, 100 g PTNC was mixed with 1 L liquid above and shaken at 25°C, 30 rpm, for 20 h. After filtered with 0.45 μm membrane, the concentration of heavy metals was determined by ICP-OES, and the results were compared with the limitation of the standard of Leaching Toxicity Identification of Hazardous Waste (GB5085.3-2007).

3 RESULTS AND DISCUSSION

3.1 Single Factor Experiments

Figure 1 showed the effect of five ingredients on the TP removal capacity of PTNC. In terms of cement, the TP removal rate decreased from 98.23 to 95.04% with the increasing of cement content from 10 to 50 g (**Figure 1A**). It can be found that the removal rate was stable in the dosage range of 10–30 g, which can

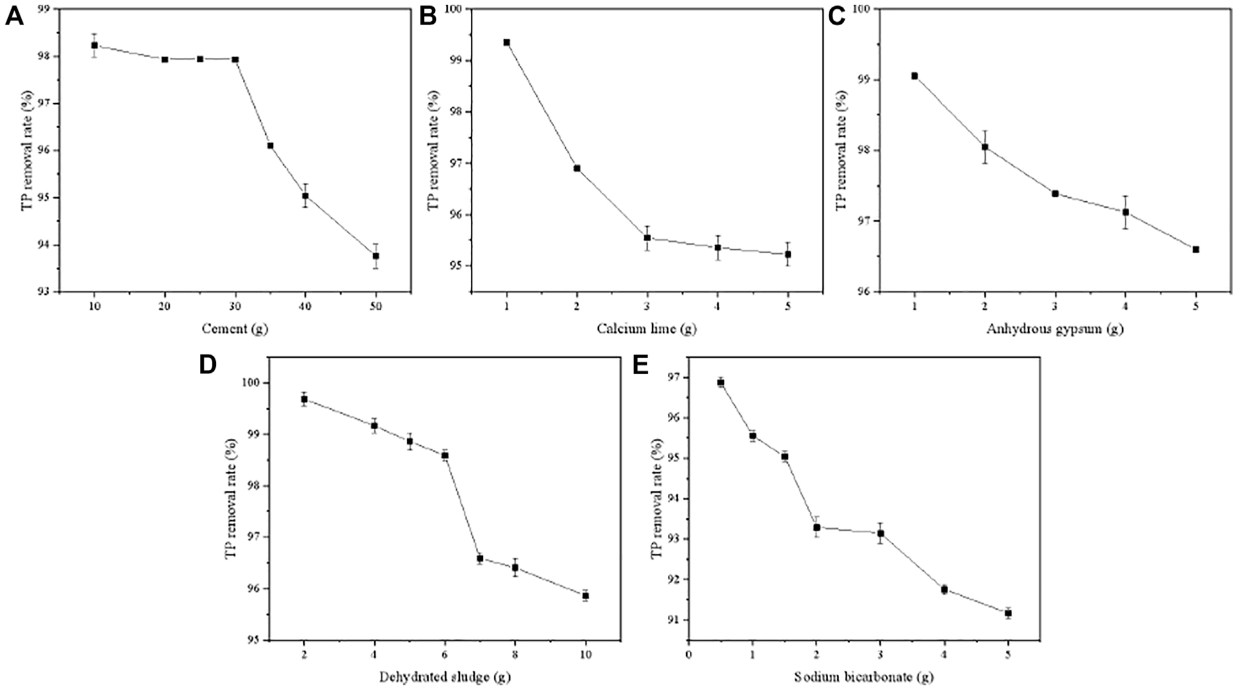

FIGURE 1 | Effect of ingredients on TP removal rate of PTNC.

attributed to the relative high amount of Ca (over 60%) that react with PO_4^{3-} to form a complex compound. As the dosage of cement was over 30 g, the decreasing of removal rate can be ascribed to the lower porosity of PTNC, which was almost 0 as 50 g cement was added. The TP removal rate decreased from 99.35 to 95.23% with the increasing of calcium lime (**Figure 1B**). Adding of quicklime can increase the content of Ca in ceramsite to some extent, which is beneficial to the removal of TP. However, the excess using of quicklime will destroy the Si-O bond in the product due to the alkaline environment, which leads to the reduction of the specific surface area. Therefore, the dosage of quicklime was selected as 1 g. With the increasing of gypsum dosage from 1 to 5 g, the TP removal rate decreased from 99.05 to 96.60% (**Figure 1C**). The main component of gypsum is $CaSO_4$ which could increase the content of Ca in ceramsite, and was conducive to the removal of TP, but the excessive amount of gypsum leads to a longer digestion time of quicklime due to its high hygroscopicity, which reduces its activity and leads to a decrease in specific surface area and porosity. Therefore, the amount limitation of PTUC gypsum is set as 1 g. In the terms of dehydrated sludge (**Figure 1D**), the TP removal rate showed decreasing tendency as the dosage increased. It can be ascribed to the high amount of organic matter that inhibited the hydration reaction and hindered the production of gelled substances, which resulted in a decrease in porosity (**Figure 1E**). A similar tendency can be found in the effect of sodium bicarbonate. Adding sodium bicarbonate can promote the forming of pores structures during steam curing, but too much sodium bicarbonate will release a large amount of CO_2 at high temperature, which makes the skeleton structure become loose and difficult to form into pellets. Thus, the sodium bicarbonate dosage is set as 0.5 g here.

TABLE 1 | Experimental design and response of Plackett-Burman experiment.

Runs	A	B	C	D	E	Removal rate (%)
1	+1	+1	−1	+1	+1	56.77
2	−1	+1	+1	−1	+1	51.37
3	+1	−1	+1	+1	−1	92.84
4	−1	+1	−1	+1	+1	85.68
5	−1	−1	+1	−1	+1	52.83
6	−1	−1	−1	+1	−1	92.14
7	+1	−1	−1	−1	+1	49.71
8	+1	+1	−1	−1	−1	58.05
9	+1	+1	+1	−1	−1	56.86
10	−1	+1	+1	+1	−1	92.30
11	+1	−1	+1	+1	+1	68.05
12	−1	−1	−1	−1	−1	70.23

3.2 Significant Factors Affecting the TP Removal Rate

Based on the results of a signal factor experiment, a two-level PBD factorial design of 12 runs was employed to unbiasedly screen the variables that significantly affect the TP removal rate by PTNC (**Table 1**), and **Figure 2** showed the analysis results. Five ingredients affected the TP removal rate as the following order: D (Dehydrated sludge) >E (Sodium bicarbonate) >A (Cement) >B (Calcium lime) >C (Anhydrous gypsum), and the dosage of dehydrated sludge affected TP removal rate

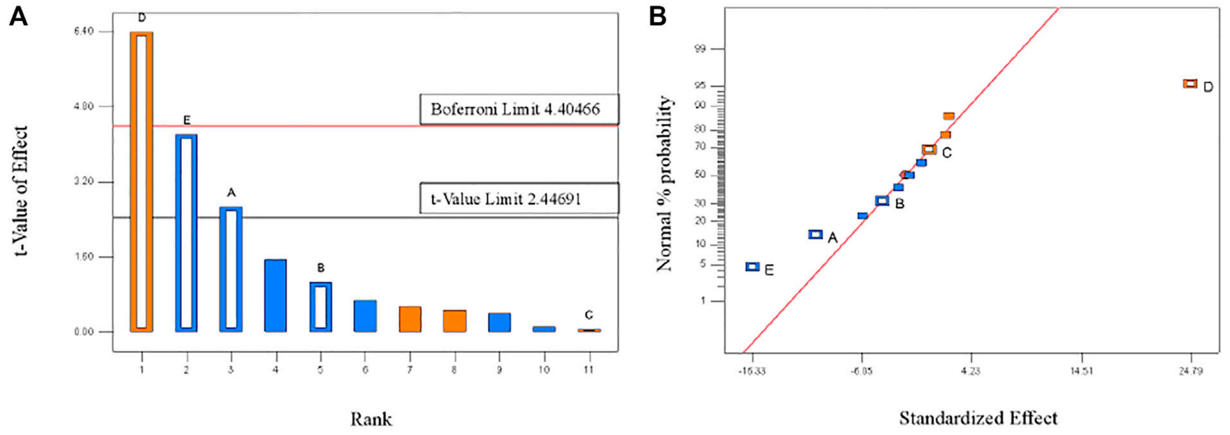

FIGURE 2 | Pareto plot **(A)** and normal distribution plot **(B)** of TP removal rates. The hollow square column represents the experimental data, and the solid square column represents the dummy error. The red line in Pareto plot indicates the 99% confidence interval limitation and black line stands for 95% confidence interval limitation.

TABLE 2 | Significant test for Plackett-Burman design regression model.

	Factors	Adj SS	DF	Adj MS	F	p
TP removal rate	Model	3,018.45	5	603.69	13.41	0.0033
	A	323.00	1	323.00	7.18	0.0366
	B	51.07	1	51.07	1.13	0.3278
	C	0.23	1	0.23	0.00518	0.9451
	D	1843.70	1	1843.70	40.96	0.0007
	E	800	1	800.44	17.78	0.0056
	Error	270.05	6	45.01	—	—
	Total	3,288.50	11	—	—	—

Adj SS, Adjusted Sum of Square; Adj MS, Adjusted Mean Square; DF, Degrees of Freedom, (Wang et al., 2014).

TABLE 3 | Experimental design and results of BBD.

Run order	X_1	X_2	X_3	TP removal rate (%)
1	−1	−1	0	60.45
2	1	−1)	0	89.69
3	−1	+1	0	59.74
4	+1	+1	0	81.03
5	−1	0	−1	64.90
6	+1	0	−1	92.00
7	−1	0	+1	38.85
8	+1	0	+1	78.92
9	0	−1	−1	93.34
10	0	+1	−1	80.88
11	0	−1	+1	87.50
12	0	+1	+1	81.47
13	0	0	0	57.32
14	0	0	0	60.15
15	0	0	0	70.93
16	0	0	0	69.66
17	0	0	0	66.45

most significantly which arrived at the 99% confidence interval. Sodium bicarbonate and cement also showed significant influence effect on TP removal rate, which were observed at 95% confidence interval (**Figure 2A**). It can be also proved by the normal distribution plot (**Figure 2B**), where the points standing for dehydrated sludge, sodium bicarbonate, and cement showed significant dispersion from the fitted line. **Table 2** shows the results of significant inspection of regression, which further proved the factors with significant effect on the TP removal rate were dehydrated sludge, sodium bicarbonate, and cement, and a model **Equation 1** for TP removal rate (%) (Y) was proposed; the p value and R^2 for the model were 0.0366 and 0.9179 which indicated the validity of the model.

$$Y = 68.91 - 5.19A - 2.06B + 0.14C + 12.40D - 8.17E \qquad (2)$$

3.3 Box-Behnken Design for Preparation Optimization

Based on the PBD results, the significant factors dehydrated sludge (X_1), sodium bicarbonate (X_2), and cement (X_3) were considered for further optimization using BBD, and the matrix for BBD along with the experimental results is shown in **Table 3**. By applying multiple regression analysis on the experimental data, the following second order polynomial model was obtained to describe the TP removal rate **(2)**:

$$Y = +64.90 + 14.71X_1 - 3.48X_2 - 5.55X_3 - 1.99X_1X_2 + 3.24X_1X_3 + 1.61X_3X_2 - 4.65X_1^2 + 12.48X_2^2 + 8.42X_3^2 \qquad (3)$$

The adequacy of the model was checked using ANOVA and the results were shown in **Table 4**. The F value of model was 7.54 and the p value (Prob > F) was 0.018, indicating that the model was highly significant, which was also confirmed by the non-significant p value of “Lack of fit.” It can be also found that the variable X_1 as well as the quadratic terms $X_2{}^2$ and $X_3{}^2$ showed significant relationship with the TP removal rates. R^2 of the model was 0.9065, suggesting the model has a good agreement for data

TABLE 4 | ANNOVA for BBD.

Source	Adj SS	DF	Adj MS	F-value	*p*-value
Model	3,197.96	9	355.32	7.54	0.0072
X_1	1731.58	1	1731.58	36.75	0.0005
X_2	97.01	1	97.01	2.06	0.1945
X_3	246.29	1	246.29	5.23	0.0561
X_1X_2	15.80	1	15.80	0.34	0.5806
X_1X_3	42.03	1	42.03	0.89	0.3764
X_2X_3	10.31	1	10.31	0.22	0.6541
X_1^2	91.11	1	91.11	1.93	0.2070
X_2^2	655.62	1	655.62	13.91	0.0074
X_3^2	298.33	1	298.33	6.33	0.0400
Error	329.85	7	47.12	—	—
Lack of fit	188.36	3	62.78	1.78	0.2908
Pure error	141.48	4	35.37	—	—
Total	3,527.81	16	—	—	—

Adj SS, Adjusted Sum of Square; Adj MS, Adjusted Mean Square; DF, Degrees of Freedom, (Wang et al., 2014).
Coefficient of variation - 9.46%; Signal to noise ratio - 9.738; R^2 *- 0.9065;* R^2_{Adj} *- 0.7863.*

fitting. The ratio of signal to noise (Adeq Precision) was 9.738 which was over 4, and the coefficient of variation (C.V.) was lower than 10%, indicating the reproducibility of the model. These statistical analysis results showed that the model was reliable and accurate, and can be used for the analysis and prediction of TP removal by PTNC. The statistical model was further validated by experiments with PTNC prepared under different conditions (**Supplementary Figure S3**). It can be said that the predicted model response for experimental value was close to the predicted value, thus validating the model.

The optimum level of each variable and the effect of their interaction on TP removal rate were investigated by constructing response surface plots and their corresponding contour plots (**Figure 3**). With the increasing of dehydrated sludge dosage, the TP removal rate of PTUC showed an increasing trend. The response surface showed a steep slope (**Figure 3A**), which indicated the interaction between factors. The increasing of dehydrated sludge content increased the active adsorption sites for phosphate combination, which improved the TP removal rate reasonably. When the dehydrated sludge content was fixed as 4 g, the TP removal rate of PTUC showed non-significant change with the increment of cement dosage, which was about 80% (**Figure 3B**). It was reported that the phosphate anion will react with Ca^{2+} and OH^- which formed complex precipitates (Qiu et al., 2015). The addition of cement increased the Ca amount in PTNC; however, the increasing of cement dosage would decrease the porosity which hindered mass diffusion, which can be further proved by the high interaction caused by the pore forming substance sodium bicarbonate (**Figures 3A,C**).

In order to deter the optimum preparation conditions, the primary target value was obtained by calculating the model, and the raw materials dosage was rounded and fitted again with the model for optimal target value. PTNC was prepared consequently, and TP removal rate was tested to calculate the error and determine the fitting result (**Table 5**). The errors between the measured values of TP removal rate and the predicted values of the model fitting were 1.80%, indicating that the fitting effect was favorable and the model was reliable. Thus the optimal raw material ratio (per 100 g) was 84.5 g (pyrite tailings), 10 g (cement), 1 g (calcined lime), 1 g (Anhydrous gypsum), 3 g (dehydrated sludge), and 0.5 g (sodium bicarbonate).

3.4 Characterization of PTNC Prepared Under Optimized Condition

The surface of PTUC is rough, with low smoothness, dark gray color, and pore structure on the outer surface (**Figure 4A**), and the apparent morphology observed by SEM showed many grooves on its surface, with uneven interior and abundant pores, indicating its large specific surface area. The determined specific surface area and pore size was consistent with the above conclusion (**Supplementary Table S5**). It can be said that PTNC was suitable for the attachment and growth of microorganisms. The physical parameters of PTNC meet the requirements of relevant standards favorably (**Supplementary Table S6**). The high apparent density and water absorption rate ensures the adsorption characteristics of PTNC. And the favorable mechanic strength such as low wear rate and higher cylinder compressive strength ensured the application possibility of PTNC, and the porous nature is a benefit for the attachment of functional microbial community. XRD analysis confirmed the PTNC is mainly composed of FeS_2, $CaSO_4$, and SiO_2 (**Supplementary Figure S4**). The peak strength of $CaSO_4$ crystal is the most obvious, followed by SiO_2, indicating the formation of SiO_2 during the steam curing process of PTNC, acting as the framework structure of PTNC, which was also consistent with the low wear rate observed. Moreover, the heavy metal ion concentration in the PTNC leachate is much lower than the limitation of Hazardous Waste Identification Standard Leaching Toxicity Identification (GB5085.3–2007) (**Supplementary Table S7**), which indicate its security to the environment.

3.5 The Adsorption Behavior and Mechanism of TP on PTNC

Simulated wastewater containing 25 mg/L TP was employed to investigate the adsorption kinetic. The adsorption amount showed increased tendency with the increasing of reaction time (**Figure 5A**). The adsorption equilibrium was observed at 16 h, where the TP concentration decreased to 0.43 mg/L, meeting the V level of “Surface water Environmental Quality Standard” (GB 3838-2002), and the equilibrium adsorption capacity was 0.2864 mg/g. As the mostly using models for description of adsorption kinetic, pseudo first-order and pseudo second-order models (Text S1) were used to fit the experimental data (**Supplementary Table S8**) (Chen et al., 2019). Although the correlation coefficients of both two kinetic models were similar (>0.9), the predicted adsorption capacity with pseudo first order model is 0.2995 mg/g which is close to the experimental value (0.2864 mg/g). Therefore, the pseudo first-order kinetic model can describe the TP adsorption process on PTNC better. The both two well fitted models indicated that both of chemisorption and physisorptions

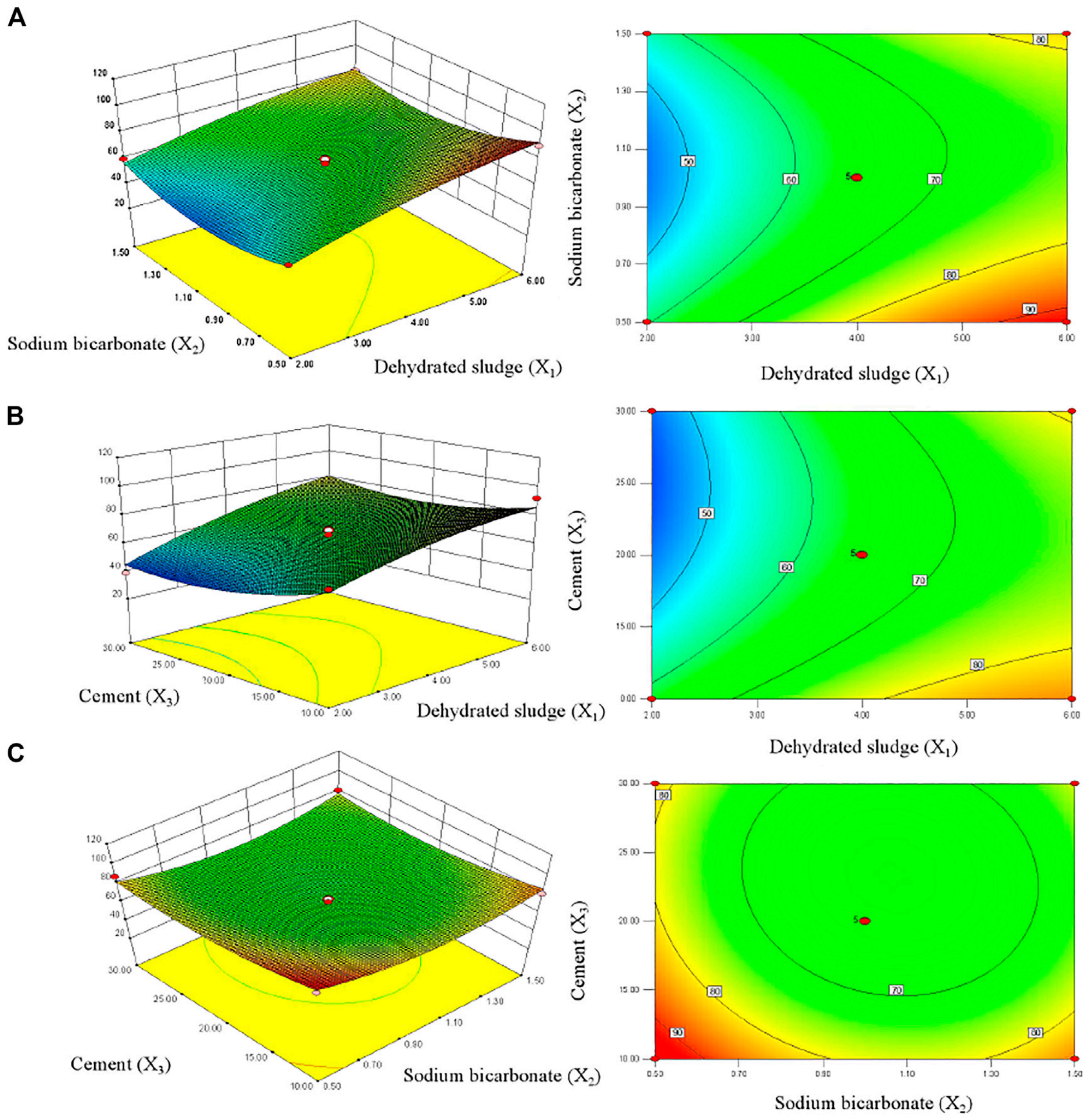

FIGURE 3 | Surface and contour plot showing interactions between variables on TP removal rates by PTNC. **(A)** stands for interaction between dehydrated sludge and sodium bicarbonate; **(B)** shows interaction between dehydrated sludge and cement; **(C)** stands for interaction between sodium bicarbonate and cement.

TABLE 5 | The optimization results of regression.

	X_1	X_2	X_1	TP removal rate (%)	Degree of fitting
Primary	3.1	0.5	10	89.41	96.3
Optimal	3	0.5	10	88.55	95.5
Actual	3	0.5	10	86.96	—
Error	—	—	—	1.80%	—

existed in the process of TP removal by PTNC, which were mainly ion exchange effect and precipitation probably (Yang et al., 2017). Generally, adsorption process can be divided into several steps, firstly the adsorbate in aqueous diffuses from aqueous to the adsorbent surface, then the surface loaded adsorbate diffuses to internal pores (diffusion within particles), and finally the internal adsorption sites are saturated. It can be found that the adsorption rate decreased apparently from 4 to 10 h, which can be attributed to the chemisorption of TP by PTNC leading to the formation of cobalt phosphide sulfide (**Supplementary Figure S4**) and decreased of the pore size of PTNC (**Supplementary Table S5**), thus the diffusion of phosphorus to the internal pores can be hindered.

The adsorption thermodynamics was investigated through three isotherms at different temperatures (**Figure 5B**), through the data fitting with Langmuir and Freundlich isotherm models (Text S2) (Chen et al., 2019). It can be found that Langmuir model fitted better with the isotherms, and indicated the mono-

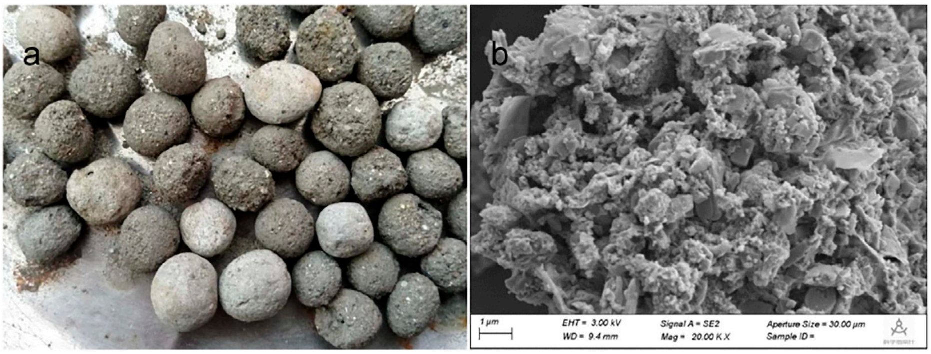

FIGURE 4 | The appearance of PTNC (6–8 mm diameter) **(A)** and SEM images of PTNC **(B)**.

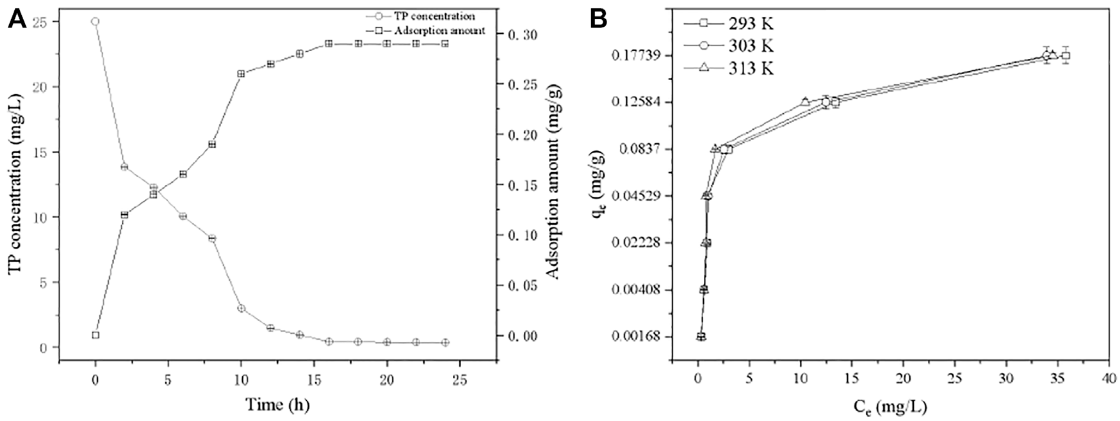

FIGURE 5 | Kinetic curve **(A)** and isotherms **(B)** of TP adsorption by PTNC.

layer adsorption process (**Supplementary Table S9**). The thermodynamic parameters were calculated (Text S3), and the negative ΔG suggested the TP removal is a spontaneous process (**Supplementary Table S10**). Additionally, the obtained negative value of ΔH (-11.69 kJ/mol) and positive value of ΔS (153.09 J/mol/K) together indicate that the adsorption is an exothermic reaction and is both enthalpy and entropy driven. Generally, the adsorption process is an entropy reduction process; however, there are existing adsorption cases that presented entropy-positive with a negative enthalpy change (Wen et al., 2010). For TP removal process by PTNC, it can be ascribed to the releasing of Fe^{3+}, Ca^{2+}, and OH^- from PTNC surface which increased the entropy. And these ions would react with phosphate and formed of precipitation on the surface of PTNC which additionally make contribution to the entropy increasing. It can be found that the specific surface of PTNC increased obviously after adsorption (**Supplementary Table S5**). Moreover, the XRD analysis of the PTNC after adsorption (**Supplementary Figure S4**), which suggested the newly formation of cobalt phosphide sulfide, and the SEM

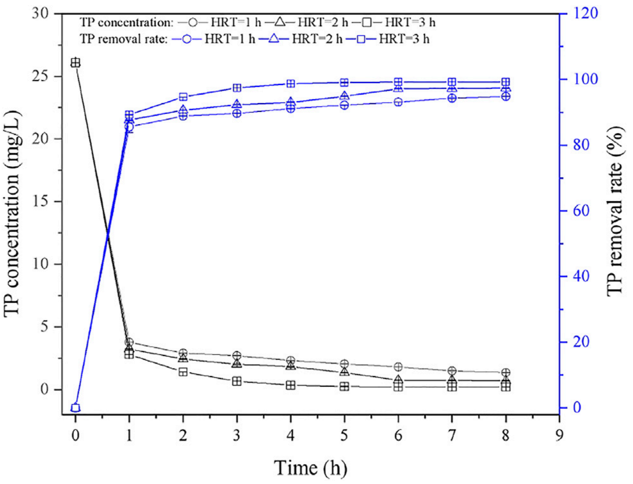

FIGURE 6 | Dynamic adsorption curves of TP removal by PTNC under different HRT.

TABLE 6 | Comparison of the TP removal ability of different ceramsites.

Ceramsite	Calcining temperature (°C)	Initial TP concentration (mg/L	Adsorption capacity (mg/g)	Reference
CFA/WS/OS-op	1,050	100	4.51 (calculated)	Cheng et al. (2018)
Slag ceramsite	1,000	10	10.5	Liu et al. (2021)
N&P-adsorbed ceramsite	800	100	0.93	Shao et al. (2022)
DWTS ceramsite	1,050	20	1.43	Chen et al. (2019b)
PTNC	Non	25	6.9978	This work

morphology observation (**Supplementary Figure S5**) of the PTNC after adsorption further confirmed the precipitation formation during the adsorption process. It is consistent with the previous report (Ge et al., 2019).

Figure 6 showed the dynamic TP removal curves under different HRT (1, 2, 3 h). In the initial stage, the TP concentration in effluent decreased rapidly, which is ascribed to the large amount of active adsorption sites in the initial stage (Chu et al., 2014). The TP concentration tended to be stable after running for 8 h, and it was due to the concentration gradient of phosphorus solution decreased gradually. In terms of HRT = 1 h, the TP concentration in the effluent was about 1.35 mg/L, and the TP removal rate was 94.82% after 8 h. As the HRT increased to 2 h, the final TP concentration in the effluent decreased to 0.69 mg/L, and the removal rate further increased to 97.34%. Similar phenomena can be observed when HRT was set as 3 h, where the stable TP concentration in the effluent is about 0.20 mg/L, which is meeting the standard of Ⅲ class surface water. As expected, the low HRT will lead to the insufficient time for phosphate contact and react with adsorption sites, as well as the released active ions; thus, suitable HRT should be considered in the application. Additionally, it can be found that the performance of PTNC was better than the phosphorus removal effect of the mixture of iron scrap and sand as previous report (88%) (Erickson et al., 2012). **Table 6** showed the comparison of the TP removal ability of PTNC with other ceramsite. It can be found that PTNC presented highest TP adsorption capacity besides the Slag ceramsite reported by Liu et al. (2021). But the non-sintered preparation of PTNC is a more economical way. Thus, the prepared PTNC is promising for TP control and waste recycling.

4 CONCLUSION

In this research, a novel non-sintered ceramsite (PTNC) was prepared with pyrite tailings, and the preparation process was optimized by combination of PBD and BBD based response surface methodology, which confirmed the optimized mass ratios of the ingredients was 84.5 g (pyrite tailings), 10 g (cement), 1 g (calcined lime), 1 g (Anhydrous gypsum), 3 g (dehydrated sludge), and 0.5 g (sodium bicarbonate). PTNC presented favorable properties such as high specific surface, low leaching toxicity, and excellent mechanical strength. And the investigation on the adsorption behavior through batch and dynamic experiments showed the favorable adsorption capacity of PTNC, whose calculated q_{max} was about 7 mg/g, and can offer stable removal ability continuously under different HRT. The analysis of the adsorption mechanism suggested the existing of both physical and chemical adsorption effect. The total results make contribution to the resource of pyrite tailings, which are also benefit to the development of novel effective and economic medium for BAFS in the advanced treatment of wastewater.

DATA AVAILABILITY STATEMENT

The original contributions presented in the study are included in the article/**Supplementary Material**, further inquiries can be directed to the corresponding authors.

AUTHOR CONTRIBUTIONS

All authors contributed to the study conception and design. Material preparation, data collection and analysis were performed by RC, JX and ZP. The first draft of the manuscript was written by RC and all authors commented on previous versions of the manuscript. All authors read and approved the final manuscript.

FUNDING

This work was financially supported by the Public Research Project of Zhejiang Province (LGF20E090001 and LGF19E090002), the Science and Technology Projects of Wenzhou City (ZG2020024), and the Service Project for Science & Technology Innovation of Wenzhou Association for Science and Technology (kjfw36).

ACKNOWLEDGMENTS

The authors appreciate all the participants.

SUPPLEMENTARY MATERIAL

The Supplementary Material for this article can be found online at: https://www.frontiersin.org/articles/10.3389/fchem.2022.850171/full#supplementary-material

REFERENCES

Bao, T., Chen, T., Tan, J., Wille, M.-L., Zhu, D., Chen, D., et al. (2016). Synthesis and Performance of Iron Oxide-Based Porous Ceramsite in a Biological Aerated Filter for the Simultaneous Removal of Nitrogen and Phosphorus from Domestic Wastewater. *Sep. Purif. Technol.* 167, 154–162. doi:10.1016/j.seppur.2016.05.011

Bao, T., Damtie, M. M., Yu, Z. M., Liu, Y., Jin, J., Wu, K., et al. (2019). Green Synthesis of Fe_3O_4@Carbon Filter Media for Simultaneous Phosphate Recovery and Nitrogen Removal from Domestic Wastewater in Biological Aerated Filters. *ACS Sustain. Chem. Eng.* 7 (19), 16698–16709. doi:10.1021/acssuschemeng.9b04119

Bashar, R., Gungor, K., Karthikeyan, K. G., and Barak, P. (2018). Cost Effectiveness of Phosphorus Removal Processes in Municipal Wastewater Treatment. *Chemosphere* 197, 280–290. doi:10.1016/j.chemosphere.2017.12.169

Bulut, G., Yenial, Ü., Emiroğlu, E., and Sirkeci, A. A. (2014). Arsenic Removal from Aqueous Solution Using Pyrite. *J. Clean. Prod.* 84, 526–532. doi:10.1016/j.jclepro.2013.08.018

Carvalho, P. C. S., Neiva, A. M. R., Silva, M. M. V. G., and Antunes, I. M. H. R. (2014). Metal and Metalloid Leaching from Tailings into Streamwater and Sediments in the Old Ag-Pb-Zn Terramonte Mine, Northern Portugal. *Environ. Earth Sci.* 71 (5), 2029–2041. doi:10.1007/s12665-013-2605-7

Chandra, A. P., and Gerson, A. R. (2010). The Mechanisms of Pyrite Oxidation and Leaching: a Fundamental Perspective. *Surf. Sci. Rep.* 65 (9), 293–315. doi:10.1016/j.surfrep.2010.08.003

Chen, R., Liu, C., Johnson, N. W., Zhang, L., Mahendra, S., Liu, Y., et al. (2019a). Removal of 1,4-dioxane by Titanium Silicalite-1: Separation Mechanisms and Bioregeneration of Sorption Sites. *Chem. Eng. J.* 371, 193–202. doi:10.1016/j.cej.2019.03.285

Chen, S., Chen, Y., Pei, H., and Hou, Q. (2019b). Biofilm Development Dynamics and Pollutant Removal Performance of Ceramsite Made from Drinking-water Treatment Sludge. *Water Environ. Res.* 91 (7), 616–627. doi:10.1002/wer.1089

Cheng, G., Li, Q., Su, Z., Sheng, S., and Fu, J. (2018). Preparation, Optimization, and Application of Sustainable Ceramsite Substrate from Coal Fly Ash/Waterworks Sludge/oyster Shell for Phosphorus Immobilization in Constructed Wetlands. *J. Clean. Prod.* 175, 572–581. doi:10.1016/j.jclepro.2017.12.102

Chero-Osorio, S., Chavez, D. M., Vega, A., Morales, A., Gamarra, C., and Rodriguez-Reyes, J. C. F. (2021). Reutilization of Pyrite-Rich Alkaline Leaching Tailings as Sorbent Must Consider the Interplay of Sorption and Desorption. *Minerals Eng.* 170, 107019. doi:10.1016/j.mineng.2021.107019

Chu, S. Y., Xiao, J. B., Tian, G. M., and Wong, M. H. (2014). Preparation and Characterization of Activated Carbon from Aquatic Macrophyte Debris and its Ability to Adsorb Anthraquinone Dyes. *J. Ind. Eng. Chem.* 20 (5), 3461–3466. doi:10.1016/j.jiec.2013.12.035

Dong, Y., Lin, H., and Zhang, X. (2020b). Simultaneous Ammonia Nitrogen and Phosphorus Removal from Micro-polluted Water by Biological Aerated Filters with Different media. *Water Air Soil Poll.* 231 (5), 1–15. doi:10.1007/s11270-020-04616-9

Dong, Y., Zeng, W., Lin, H., and He, Y. (2020a). Preparation of a Novel Water-Soluble Organosilane Coating and its Performance for Inhibition of Pyrite Oxidation to Control Acid Mine Drainage at the Source. *Appl. Surf. Sci.* 531, 147328. doi:10.1016/j.apsusc.2020.147328

Erickson, A. J., Gulliver, J. S., and Weiss, P. T. (2012). Capturing Phosphates with Iron Enhanced Sand Filtration. *Water Res.* 46 (9), 3032–3042. doi:10.1016/j.watres.2012.03.009

Garcia, C., Ballester, A., Gonzalez, F., and Blázquez, M. L. (2005). Pyrite Behaviour in a Tailings Pond. *Hydrometallurgy* 76 (1-2), 25–36. doi:10.1016/j.hydromet.2004.07.010

Ge, Z., Wei, D., Zhang, J., Hu, J., Liu, Z., and Li, R. (2019). Natural Pyrite to Enhance Simultaneous Long-Term Nitrogen and Phosphorus Removal in Constructed Wetland: Three Years of Pilot Study. *Water Res.* 148, 153–161. doi:10.1016/j.watres.2018.10.037

Guo, Z., Feng, Q., Wang, W., Huang, Y., Deng, J., and Xu, Z. (2016). Study on Flotation Tailings of Kaolinite-type Pyrite when Used as Cement Admixture and concrete Admixture. *Proced. Environ. Sci.* 31, 644–652. doi:10.1016/j.proenv.2016.02.118

Han, W., Yue, Q., Wu, S., Zhao, Y., Gao, B., Li, Q., et al. (2013). Application and Advantages of Novel clay Ceramic Particles (CCPs) in an Up-Flow Anaerobic Bio-Filter (UAF) for Wastewater Treatment. *Bioresour. Technol.* 137, 171–178. doi:10.1016/j.biortech.2013.03.124

He, B., and Wang, G. (2019). Is Ceramsite the Last Straw for Sewage Sludge Disposal: a Review of Sewage Sludge Disposal by Producing Ceramsite in China. *Water Sci. Technol.* 80 (1), 1–10. doi:10.2166/wst.2019.223

Heikkinen, P. M., and Räisänen, M. L. (2009). Trace Metal and as Solid-phase Speciation in Sulphide Mine Tailings - Indicators of Spatial Distribution of Sulphide Oxidation in Active Tailings Impoundments. *Appl. Geochem.* 24 (7), 1224–1237. doi:10.1016/j.apgeochem.2009.03.007

Jiang, C., Jia, L., Zhang, B., He, Y., and Kirumba, G. (2014). Comparison of Quartz Sand, Anthracite, Shale and Biological Ceramsite for Adsorptive Removal of Phosphorus from Aqueous Solution. *J. Environ. Sci.* 26 (2), 466–477. doi:10.1016/s1001-0742(13)60410-6

Khale, D., and Chaudhary, R. (2007). Mechanism of Geopolymerization and Factors Influencing its Development: a Review. *J. Mater. Sci.* 42 (3), 729–746. doi:10.1007/s10853-006-0401-4

Li, L., Hu, C., Dai, X., Jin, W., Hu, C., and Ma, F. (2015). The Performance of a Biological Aerated Filter Loaded With a Novel Non-Sintered Fly-Ash Ceramsite as Pretreatment for Dual Membrane Processes. *Environ Technol.* 36 (16), 2024–2034. doi:10.1080/09593330.2015.1019930

Liu, X., Yang, S., Liu, S., and Yang, Y. (2021). Performance and Mechanism of Phosphorus Removal by Slag Ceramsite Filler. *Process Saf. Environ. Prot.* 148, 858–866. doi:10.1016/j.psep.2021.02.016

Malmström, M. E., Gleisner, M., and Herbert, R. B. (2006). Element Discharge from Pyritic Mine Tailings at Limited Oxygen Availability in Column Experiments. *Appl. Geochem.* 21 (1), 184–202.

Mi, H., Yi, L., Wu, Q., Xia, J., and Zhang, B. (2021). Preparation of High-Strength Ceramsite from Red Mud, Fly Ash, and Bentonite. *Ceramics Int.* 47 (13), 18218–18229. doi:10.1016/j.ceramint.2021.03.141

Nie, J., Wang, Q., Gao, S., Poon, C. S., Zhou, Y., and Li, J.-s. (2021). Novel Recycling of Incinerated Sewage Sludge Ash (ISSA) and Waste Bentonite as Ceramsite for Pb-Containing Wastewater Treatment: Performance and Mechanism. *J. Environ. Manage.* 288, 112382. doi:10.1016/j.jenvman.2021.112382

Oluwasola, E. A., Hainin, M. R., and Aziz, M. M. A. (2015). Evaluation of Asphalt Mixtures Incorporating Electric Arc Furnace Steel Slag and Copper Mine Tailings for Road Construction. *Transp. Geotech.* 2, 47–55. doi:10.1016/j.trgeo.2014.09.004

Ouyang, Y., Liu, Y., Zhu, R., Ge, F., Xu, T., Luo, Z., et al. (2015). Pyrite Oxidation Inhibition by Organosilane Coatings for Acid Mine Drainage Control. *Minerals Eng.* 72, 57–64. doi:10.1016/j.mineng.2014.12.020

Park, I., Tabelin, C. B., Jeon, S., Li, X., Seno, K., Ito, M., et al. (2019). A Review of Recent Strategies for Acid Mine Drainage Prevention and Mine Tailings Recycling. *Chemosphere* 219, 588–606. doi:10.1016/j.chemosphere.2018.11.053

Qiu, L., Zhang, S., Wang, G., and Du, M. a. (2010). Performances and Nitrification Properties of Biological Aerated Filters with Zeolite, Ceramic Particle and Carbonate media. *Bioresour. Technol.* 101 (19), 7245–7251. doi:10.1016/j.biortech.2010.04.034

Qiu, L., Zheng, P., Zhang, M., Yu, X., and Abbas, G. (2015). Phosphorus Removal Using Ferric-Calcium Complex as Precipitant: Parameters Optimization and Phosphorus-Recycling Potential. *Chem. Eng. J.* 268, 230–235. doi:10.1016/j.cej.2014.12.107

Sahoo, P. K., Tripathy, S., Panigrahi, M. K., and Equeenuddin, M. K. (2013). Inhibition of Acid Mine Drainage from a Pyrite-Rich Mining Waste Using Industrial By-Products: Role of Neo-Formed Phases. *Water Air Soil Poll* 224 (11), 1–11. doi:10.1007/s11270-013-1757-0

Schindler, D. W., Carpenter, S. R., Chapra, S. C., Hecky, R. E., and Orihel, D. M. (2016). Reducing Phosphorus to Curb lake Eutrophication Is a success. *Environ. Sci. Technol.* 50 (17), 8923–8929. doi:10.1021/acs.est.6b02204

Shao, Q., Lu, M., Zhou, J., Zhu, Z., and Song, Y. (2019). Preparation of Non-sintered Fly Ash Filter (NSFF) for Ammonia Nitrogen Adsorption. *Environ. Technol.* 40 (15), 1988–1999. doi:10.1080/09593330.2018.1435733

Shao, Q., Zhang, Y., Liu, Z., Long, L., Liu, Z., Chen, Y., et al. (2022). Phosphorus and Nitrogen Recovery from Wastewater by Ceramsite: Adsorption Mechanism, Plant Cultivation and Sustainability Analysis. *Sci. Total Environ.* 805, 150288. doi:10.1016/j.scitotenv.2021.150288

Wang, H., Xu, J., Liu, Y., and Sheng, L. (2021). Preparation of Ceramsite from Municipal Sludge and its Application in Water Treatment: A Review. *J. Environ. Manage.* 287, 112374. doi:10.1016/j.jenvman.2021.112374

Wang, S., and Mulligan, C. N. (2009). Enhanced Mobilization of Arsenic and Heavy Metals from Mine Tailings by Humic Acid. *Chemosphere* 74 (2), 274–279. doi:10.1016/j.chemosphere.2008.09.040

Wang, Y., Kim, J., and Song, J. (2014). Optimization for Manufacturing a Brake Booster Valve Body. *Mater Design (1980-2015)* 56, 313–317. doi:10.1016/j.matdes.2013.11.038

Wen, J., Han, X., Lin, H., Zheng, Y., and Chu, W. (2010). A Critical Study on the Adsorption of Heterocyclic Sulfur and Nitrogen Compounds by Activated Carbon: Equilibrium, Kinetics and Thermodynamics. *Chem. Eng. J.* 164 (1), 29–36. doi:10.1016/j.cej.2010.07.068

Xu, N., Christodoulatos, C., and Braida, W. (2006). Adsorption of Molybdate and Tetrathiomolybdate onto Pyrite and Goethite: Effect of pH and Competitive Anions. *Chemosphere* 62 (10), 1726–1735. doi:10.1016/j.chemosphere.2005.06.025

Yang, K., Yue, Q., Han, W., Kong, J., Gao, B., Zhao, P., et al. (2015). Effect of Novel Sludge and Coal Cinder Ceramic media in Combined Anaerobic-Aerobic Bio-Filter for Tetracycline Wastewater Treatment at Low Temperature. *Chem. Eng. J.* 277, 130–139. doi:10.1016/j.cej.2015.04.114

Yang, Y., Chen, T., Sumona, M., Gupta, B. S., Sun, Y., Hu, Z., et al. (2017). Utilization of Iron Sulfides for Wastewater Treatment: a Critical Review. *Rev. Environ. Sci. Biotechnol.* 16 (2), 289–308. doi:10.1007/s11157-017-9432-3

Yue, Q., Han, S., Yue, M., Gao, B., Li, Q., Yu, H., et al. (2009). The Performance of Biological Anaerobic Filters Packed with Sludge-Fly Ash Ceramic Particles (SFCP) and Commercial Ceramic Particles (CCP) during the Restart Period: Effect of the C/N Ratios and Filter media. *Bioresour. Technol.* 100 (21), 5016–5020. doi:10.1016/j.biortech.2009.05.033

Zeng, Q., Chang, S., Wang, M., Li, M., Deng, Q., Xiong, Z., et al. (2021). Highly-active, Metal-free, Carbon-Based ORR Cathode for Efficient Organics Removal and Electricity Generation in a PFC System. *Chin. Chem. Lett.* 32 (7), 2212–2216. doi:10.1016/j.cclet.2020.12.062

Zhang, Q., Chen, X., Wu, H., Luo, W., Liu, X., Feng, L., et al. (2019). Comparison of clay Ceramsite and Biodegradable Polymers as Carriers in Pack-Bed Biofilm Reactor for Nitrate Removal. *Ijerph* 16 (21), 4184–4198. doi:10.3390/ijerph16214184

Conflict of Interest: The authors declare that the research was conducted in the absence of any commercial or financial relationships that could be construed as a potential conflict of interest.

frontiers in Chemistry

ORIGINAL RESEARCH
published: 15 March 2022
doi: 10.3389/fchem.2022.865375

Effect of Gallium as an Additive Over Corresponding Ni–Mo/γ-Al_2O_3 Catalysts on the Hydrodesulfurization Performance of 4,6-DMDBT

*Meng Huang[1], Wenbin Huang[1], Anqi Li[1,2], Han Yang[1], Yijing Jia[1], Zhiqing Yu[1], Zhusong Xu[1], Xiaohan Wang[1], Yasong Zhou[1] and Qiang Wei[1]**

[1]State Key Laboratory of Heavy Oil Processing, College of Chemical Engineering and Environment, China University of Petroleum, Beijing, China, [2]Fushun Research Institute of Petroleum and Petrochemicals, SINOPEC, Fushun, China

Experiments were carried out to research the different contents of Ga_2O_3 modification effects on the hydrodesulfurization (HDS) performance of 4,6-dimethyldibenzothiophene (4,6-DMDBT) catalyzed by the stepwise impregnation method. Characterization techniques such as XRD, BET, HRTEM, NH_3-TPD, and Py-FTIR were performed to determine the effects of each modification of the catalyst by Ga on the properties of the prepared supports and catalysts. The catalytic effect of gallium is reflected in the fact that the empty d-orbitals of Ga elements participate in the formation of molecular orbitals in the active center and change their orbital properties, thus generating a direct desulfurization active phase suitable for complex sulfides for endpoint adsorption. The characterization results indicated that the introduction of Ga_2O_3 with appropriate content (2 wt.%) promoted Ni and Mo species to disperse uniformly and doping of more Ni atoms into the MoS_2 crystals, which also increased the average stacking number and the length of MoS_2. As a result, more NiMoS active phases were favored to form in the system. The specific surface area and the amounts of acid sites were increased, facilitating the adsorption of reactant molecules and the HDS reactions. The HDS results also suggested the effects of Ga modification play a very important role in the catalytic performance of the corresponding catalysts. The catalyst Ga–Ni–Mo/Al_2O_3 exhibited the highest conversion rate towards 4,6-DMDBT HDS when the amount of Ga_2O_3 loading was 2 wt.% with an LHSV of 2.5 h^{-1} at 290°C and Ga modification also can effectively improve the direct desulfurization (DDS) route selectivity in varying degrees.

Keywords: Ga modification, HDS catalyst, 4,6-DMDBT conversion rate, DDS route selectivity, active phase

OPEN ACCESS

Edited by:
Qingyi Zeng,
University of South China, China

Reviewed by:
Min Wang,
Jinan University, China
Yanbiao Liu,
Donghua University, China

****Correspondence:***
Qiang Wei
qwei@cup.edu.cn

Specialty section:
This article was submitted to
Inorganic Chemistry,
a section of the journal
Frontiers in Chemistry

Received: *29 January 2022*
Accepted: *17 February 2022*
Published: *15 March 2022*

Citation:
Huang M, Huang W, Li A, Yang H, Jia Y, Yu Z, Xu Z, Wang X, Zhou Y and Wei Q (2022) Effect of Gallium as an Additive Over Corresponding Ni–Mo/γ-Al_2O_3 Catalysts on the Hydrodesulfurization Performance of 4,6-DMDBT.
Front. Chem. 10:865375.
doi: 10.3389/fchem.2022.865375

INTRODUCTION

With the increase in global environmental pollution and environmental laws and regulations in various countries becoming stricter, exhaust from the combustion of sulfide in automotive diesel has become one of the important sources of pollution (Wang et al., 2017; Liu et al., 2018; Weng et al., 2020; Zeng et al., 2021). The Environmental Protection Agency (EPA) and E.U. stipulate that the sulfur content should not exceed 10 and 15 ppm (Kulkarni and Afonso, 2010; Liu et al., 2020; Guo et al., 2021). Therefore, low sulfurization of diesel fuel and achieving deep desulfurization of diesel fuel have become a key issue in hydrodesulfurization (Humadi et al., 2021). At present, diesel desulfurization technologies being investigated at home and abroad include adsorptive desulfurization (ADS), oxidative desulfurization (ODS), biodesulfurization (BDS), and hydrodesulfurization (HDS). ODS is a technology for oxidizing heavy sulfides by adding one or two oxygen atoms to sulfur using a suitable oxidant at low temperature and pressure; however, the chosen oxidant is not always selective, and the selective solvent for the extraction of sulfur compounds is not necessarily suitable either (Ali et al., 2006). The basic principle of ADS is to use adsorbents to adsorb sulfur compounds in diesel oil so as to remove sulfides from diesel (Selvavathi et al., 2009). However, adsorption desulfurization is difficult to regenerate, and most adsorbents are not highly selective for sulfides such as 4,6-DMDBT, which are difficult to hydrotreat (Jayaraman et al., 2004). BDS is a new technology for the removal of bound sulfur from sulfur-containing heterocyclic compounds in petroleum using aerobic and anaerobic bacteria at atmospheric pressure and temperature, with promising applications (Mohebali and Ball, 2016). Nevertheless, the desulfurization rates of biocatalysts and the ability of organic sulfides limit their large-scale commercialization (Monticello, 2001). Based on the challenges of the abovementioned three technologies, HDS remains the most widely used technology in the world, which is a heterogeneous and conventional hydrogenation reaction (Chandra Srivastava, 2012). Compared with the former three, it has longer catalyst lifetime and stronger catalyst adaptability to the feed and has the advantage of a higher desulfurization rate for HDS (Huang et al., 2018; Weng et al., 2020). However, HDS cannot effectively remove low-reactive sulfur compounds, such as dibenzothiophene (DBT) and its derivatives, especially 4,6-DMDBT. In order to effectively remove 4,6-DMDBT, two pathways, direct desulfurization (DDS) and hydrodesulfurization (HYD), have been studied by many scholars (Gates and Topsøe, 1997; Li et al., 2019). Studies have shown that unsubstituted 4,6-DMDBT HDS reaction is more dependent on the DDS path, where it not only reacts faster but also results in desulfurization under the premise of ensuring that the aromatic rings do not increase. However, it is limited by its steric hindrance of the substituents (Yin et al., 2013; Wang et al., 2020). In order to design and prepare a highly active hydrodesulfurization catalyst, Okamoto and Kubota (2003) synthesized SiO_2-, TiO_2-, ZrO_2-, and Al_2O_3-supported catalysts using the CVD technique and found that the activity of hydrodesulfurization is positively correlated with the amount of CoMoS phases. Wagenhofer et al. (2020) thought that unsupported Ni–Mo sulfides react more rapidly than Al_2O_3-supported catalysts on the rate of hydrodesulfurization. Naboulsi et al. (2017) considered that the DDS route is a mainly hydrodesulfurization route than HYD when dual mesoporous titania is used as a support. Due to the high OH concentration on the surface of the support, an inherent Brönsted acid center is formed that is conducive to direct desulfurization through isomerization and disproportionation reactions. In addition, the exploration of support modification has not stopped, and composite supports such as $SiO_2–TiO_2$ (Gallegos–Hernández et al., 2020), $SiO_2–Al_2O_3$ (Xu et al., 2017), $ZrO_2–Al_2O_3$ (Baston et al., 2015; Díaz–García et al., 2017), and $MgO_2–Al_2O_3$ (Rana et al., 2007; Guevara-Lara et al., 2010; Vázquez–Garrido et al., 2019) are still a hot topic for the majority of scholars. However, due to its low cost, easy industrialization, and high surface area, as well as excellent thermal, mechanical, and chemical stability, γ-Al_2O_3 is still the most widely used carrier for hydrodesulfurization catalysts (Egorova, 2004; Wang et al., 2016).

It has been proposed that most hydrotreating reactions take place at the MoS_2 edge and HDS has been found to occur at the corner sites (Abrams et al., 1996; Eijsbouts, 1997; Kasztelan et al., 1984; Kasztelan, 1990). Schuit and Gates (1973) believed that the S-atom in the upper layer is chemically bonded to the Mo-atom in the immediate lower layer. When the Mo atoms are reduced from Mo^{5+} to Mo^{3+}, the S atoms move out of the surface, thus forming active sites. The cofactor Ni enters into the surface structure of the alumina carrier and induces the formation of a tetrahedral structure of the secondary Al atoms. Each S atom is bonded to two Mo atoms, and when the S atoms are removed, the S hole formed releases the two Mo atoms and causes one of them to form an adsorption site. The performance of the catalyst is directly related to the number of active sites with high catalytic performance. For the NiMoS active phase, Ni mainly contributes to the associated generation of sulfhydryl (SH) groups and their selective incorporation at the MoS_2 slab edge (Copéret, 2013; Schüth, 2009). When metal elements with suitable electronic structures are introduced into Ni–Mo/Al_2O_3 bimetallic catalysts, the active phase of Ni–Mo–S is affected and the concentration of active centers is increased; thus, the activity of the catalyst for hydrodesulfurization reaction is enhanced (Manoli et al., 2004; Varga et al., 2017). Ferdous et al. (2005) suggested the increased activity is related to the decrease of average slab length and the increase of MoS_2 edge along with angular atom dispersion. More importantly, it can promote the formation of more type II NiMoS active phases (Zhou et al., 2017; Zhou et al., 2018; Tanimu and Alhooshani, 2019). It is generally believed that there is a great correlation between the numbers of type II NiMoS active phases and the catalytic activity of the catalyst (Chen et al., 2013). Research shows that the metal–support interaction (MSI) is crucial for electron transfer between the metal and support when the catalysts support multiple metals (Ning et al., 2017). To explore the effect of metal additives on the activity of HDS, a large number of polymetallic catalysts supported on Γ-Al_2O_3 have been investigated, such as Fe (Liu et al., 2021), Zn, Ru, and Ir (Niquillerothlisberger and Prins, 2006), and even noble metal Pt (Liu et al., 2021) and its alloys Pt–Pd (Niquillerothlisberger and Prins, 2006). Pt is favored by scholars over other metals because it has more advantages in providing active hydrogen species, giving the catalyst superior hydrogenation performance. However, the sulfur resistance of Pt-based catalysts is still a major problem that plagues practical applications and needs to be enhanced. In recent years, the addition of Ga as a metal additive for the synthesis of HDS catalysts has started to attract attention due to the advantage of circumventing the high cost of precious metals (Altamirano et al., 2005). Gallium ions not only have a high affinity for tetrahedral sites of alumina but also change the ratio of tetrahedral to octahedral species of Ni (Co) that can participate in the MoS_2 decoration (Cimino et al., 1975; Jacono et al., 1977). Moreover, people have found that the modification of gallium on the surface will not only change the morphology of the MoS_2 slab promoted by active metal Ni but also enhance the vulcanization of Mo species (Zhou et al., 2017). Altamirano et al. (2005) observed the addition of Ga increased the activity of the NiMo catalyst and affected the reaction rate of the HYD route and DDS route in different degrees. Ga has the outer electron arrangement of $4s^2 4p^1$ and has an outer orbit similar to that of Ni ($3d^8 4s^2$) and Mo ($4d^5 5s^1$). As a result, the empty orbitals participate in the formation of active center molecular orbitals and modify the morphology of Ni–Mo–S active phases (Altamirano-Sanchez et al., 2008; Zepeda and Pawelec, 2012; Zhou et al., 2018). Nevertheless, for HDS activity, there is no clear and reasonable explanation about the additional amount of metal content and reaction conditions.

Considering that in this context, a series of catalysts with the Ga content ranging from 2 to 6 wt.% were prepared by the stepwise impregnation method. A succession of characterizations (XRD, BET, TEM, NH3-TPD, and Py-FTIR) were carried out to investigate the effect of Ga loading on the physical and chemical properties of the Ni–Mo/γ-Al_2O_3 catalyst. The hydrodesulfurization reaction was evaluated using 4,6-DMDBT as the probe molecule, and the effects of Ga loading and reaction conditions (temperature and liquid hourly space velocities) on the hydrodesulfurization conversion and DDS selectivity of 4,6-DMDBT were examined.

EXPERIMENTAL

Preparation of the Supports

First, γ-Al_2O_3 was prepared by the strip extrusion method with the following process conditions: pseudo-boehmite (Shandong Aluminum Corporation) and deionized water were mixed thoroughly at a mass ratio of 1:1, and then, 2 wt.% sesbania powder (Shandong Xunda Chemical Group Co., Ltd.) and 5 wt.% nitric acid (HNO_3, Aladdin, 65%) were added. The mixture was extruded by using an extruding machine at 30 MPa pressure, and the extruded strips were shaped into a clover type with a diameter of 1.5 mm. The supports was naturally dried in a place of protection from light and ventilation for 24 h and then dried in a drying oven at 120°C for 12 h, and finally, the required γ-Al_2O_3 supports were obtained in a muffle furnace at a heating rate of 2°C min^{-1}, kept at 500°C for 4.0 h, and naturally cooled to room temperature. The obtained supports were sieved into particles with the size of 20–40 meshes.

Preparation of the Ni–Mo/γ-Al_2O_3 Catalysts

The incipient wetness co-impregnation method was used to synthesize Ni–Mo/γ-Al_2O_3 catalysts, and the active metal loading was MoO_3:16 wt.% and NiO:4 wt.%, respectively. The specific preparation process is as follows: a certain mass of ammonium heptamolybdate tetrahydrate [$(NH_4)_6Mo_7O_{24}\cdot 4H_2O$, Aladdin, ≥99.8%] was added to an appropriate amount of deionized water and ammonia to dissolve it completely, and then, nickel nitrate hexahydrate [$Ni(NO_3)_2\cdot 6H_2O$, Aladdin, ≥99.8%] solution was added and stirred uniformly to obtain the nickel–molybdenum co-impregnated solution. The prepared Ni–Mo co-impregnation solution was evenly added dropwise to the alumina surface, and the samples were naturally dried at room temperature for 24 h, then dried in an oven for 6 h, and finally, heated to 500°C at a rate of 2°C min^{-1} in a muffle furnace kept at a constant temperature for 4.0 h.

Preparation of the Ga-Modified Ni–Mo/γ-Al_2O_3 Series Catalysts

A series of Ga-modified Ni–Mo/γ-Al_2O_3 catalysts were prepared using the stepwise impregnation method, in which the Ga_2O_3 loading amount was 2 wt.%, 4 wt.%, and 6 wt.%, respectively, and the specific steps were as follows: gallium nitrate ($Ga(NO_3)_3\cdot H_2O$, Aladdin, ≥99.5%) was dissolved in the deionized water, and then, the solution was loaded using incipient wetness impregnation on the Ni–Mo/Al_2O_3. The sample was dried in air for 24 h and then dried in an oven at 120°C for 4 h. Finally, it was heated to 500°C at 2°C min^{-1} in a muffle furnace, with a constant temperature for 4.0 h. The obtained catalysts were denoted as SCal (2 wt.% Ga_2O_3), Scam (4 wt.% Ga_2O_3), and SCah (6 wt.% Ga_2O_3) depending on Ga_2O_3 content from low to high.

Material Characterization

All catalyst samples synthesized were characterized on a PANalytical advanced powder diffractometer using Cu Kα radiation with an accelerating voltage of 40 kV and current of 40 mA in the 2θ interval of 5–80 °*via* a scanning rate of 0.2 °s^{-1}, by which the patterns of X-ray diffraction (XRD) were recorded. The surface areas of the tested samples were carefully calculated by using the Brunauer–Emmett–Teller (BET) equation in the relative pressure (P/P0) range of 0.05–0.30. The pore diameter distributions and pore volumes of all the investigated samples were calculated using the Barrett–Joyner–Halenda (BJH) method from the N_2 adsorption isotherms. The catalysts were sulfided in a JQ-III fixed-bed microreactor with 2 wt.% CS_2 cyclohexane solution at 320°C for 4 h. Afterward, the investigated catalysts were taken on a Philips Tecnai G2 F20 instrument with an acceleration voltage of 200 keV to obtain the images of active phases *via* a high-resolution transition electron microscope (HRTEM). To analyze the results of the average slab length and average stacking number of MoS_2, no less than 300 MoS_2 slabs were counted using the equations reported elsewhere (Ortega–Domínguez et al., 2015; W. Zhou et al., 2017).

$$\text{Average slab length } \bar{L} = \sum_{i=1}^{n} n_i l_i \Big/ \sum_{i=1}^{n} n_i, \qquad (1)$$

$$\text{Average stacking number } \bar{N} = \sum_{i=1}^{n} n_i N_i \Big/ \sum_{i=1}^{n} n_i, \qquad (2)$$

where l_i is the length of the slab, n_i is the number of slabs with length l_i, and N_i is the number of layers in slab i.

The acidity of the catalysts was assessed by NH_3 temperature programmed desorption (NH_3-TPD), which was performed on

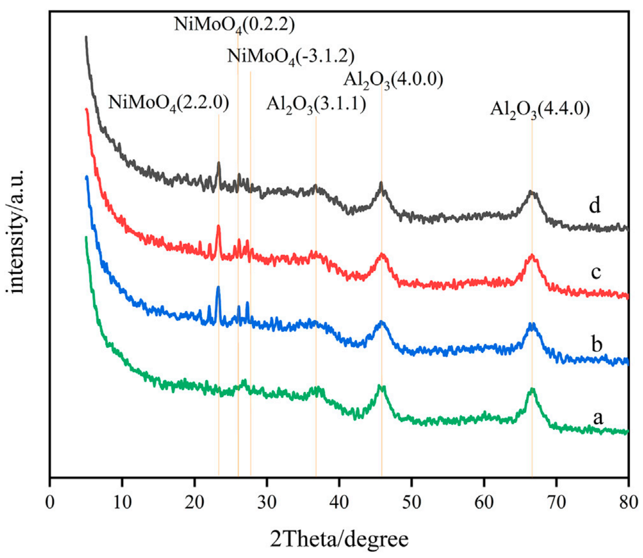

FIGURE 1 | XRD patterns of impregnated Ga-modified Ni–Mo/Al_2O_3: (a) Ni–Mo/Al_2O_3, (b) SGal, (c) SGam, and (d) SGah.

an Auto Chem II 2920 automatic chemical adsorption instrument. All catalysts were pretreated in an Ar and air mixture (v:v = 3:1) at 773k for 60 min and then cooled to 373 k in Ar flow and adsorbed NH_3 for 40 min. Then, the physically adsorbed NH_3 was removed in a continuous Ar flow for 90 min. The reactor temperature was then programmed to increase with a heating rate of 10°Cmin^{-1} for 65 min, and the amount of desorbed NH_3 was detected by using a continuous effluent gas monitor with a thermal conductivity detector (TCD). After the IR spectra were recorded on a Magna 560 FT-IR analyzer, pyridine-adsorbed Fourier transform infrared measurements (Py-FTIR) was used to assess the acidity properties of all the samples by using pyridine as a probe molecule. Firstly, the sample was dehydrated for 3 h at 623 K under 10^{-2} Pa vacuum. Second, to obtain the saturated adsorption of the Py-FTIR spectrum, pure pyridine vapor was added to the measured samples at room temperature for 30 min. Finally, the adsorbed pyridine was evacuated, respectively, at 523k and 623k for an hour so as to obtain the desorbed Py-FTIR spectra.

TABLE 1 | Pore structural properties of impregnated Ga-modified Ni–Mo/Al_2O_3.

Sample	S_{BET}, $m^2 \cdot g^{-1}$	V_{total}, $cm^3 \cdot g^{-1}$	D, nm
NiMo–Al_2O_3	214	0.51	9.5
SGal	218	0.46	6.8
SGam	227	0.45	7.9
SGah	221	0.41	7.5

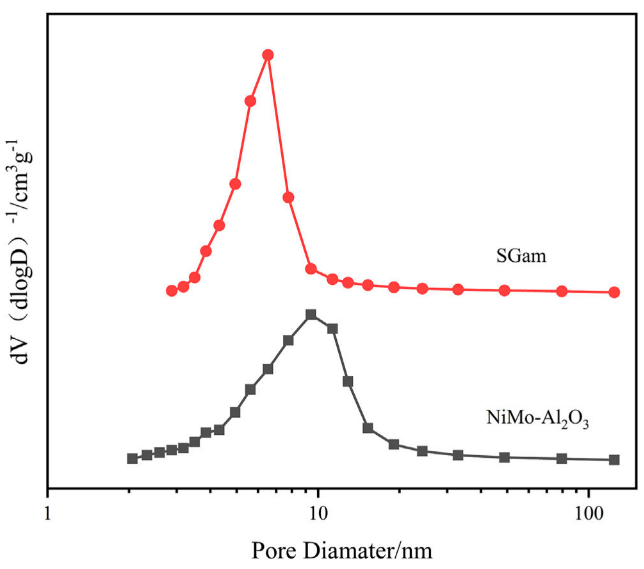

FIGURE 2 | Pore diameter distribution of impregnated Ga-modified Ni–Mo/Al_2O_3.

Catalyst Assessment

4,6-DMDBT was used as a probe to assess the HDS performances of SCal, Scam, and SCah catalysts. On the fixed-bed reactor whose length was 200 mm and inner diameter was 8 mm, 2.0 g of catalyst was loaded with a particle size of 20–40 meshes. In the first place, the pre-sulfidation of tested catalysts was carried out with 2.2 wt.% CS_2 cyclohexane solution at 330°C and 4 MPa with H_2/oil (v/v) of 60 for 4 h. Then, the reactor temperature was allowed to drop to the temperature required for the reaction at the previous condition. Stabilization of the 4,6-DMDBT cyclohexane solution at a mass concentration of 1.0% was carried out for 4 h at 4.0 MPa and 270°C, 280, and 290°C, respectively. The H_2/oil (v/v) was maintained at 120 when all catalysts were evaluated. The collected products of 4,6-DMDBT was determined by the GC–MS technique on an Agilent 4890D gas chromatograph equipped with a 60 m capillary Rtx-1 column (0.25 mm, RESREK). The column temperature was increased from 50 to 300°C at a rate of 15°C min^{-1}, while the N_2 pressure was maintained at 0.3 MPa and the flow rate was 30 ml min^{-1}. The 4,6-DMDBT conversions and DDS route selectivity (3,3′-DMBP selectivity) were counted using the following equations, respectively:

$$4,6-\text{DMDBT conversions } Con = \left(1 - m_{4,6-DMDBT}\right) \times 100\%, \tag{3}$$

$$\text{DDS Route selectivity } S_{DDS} = m_{3,3'-DMBP} / \left(1 - m_{4,6-DMDBT}\right) \times 100\%, \tag{4}$$

where $m_{4,6\text{-}DMDBT}$ is the molar fraction of remaining 4,6-DMDBT and $m_{3,3'\text{-}DMBP}$ is the molar fraction of 3,3′-DMBP tested in the liquid products.

RESULTS AND DISCUSSION

Effect of Ga Modification on Crystalline Structure

The spectra of Ni–Mo/Al_2O_3 modified by the stepwise impregnation method with different Ga loadings determined by powder X-ray diffraction are shown in **Figure 1**. It can be

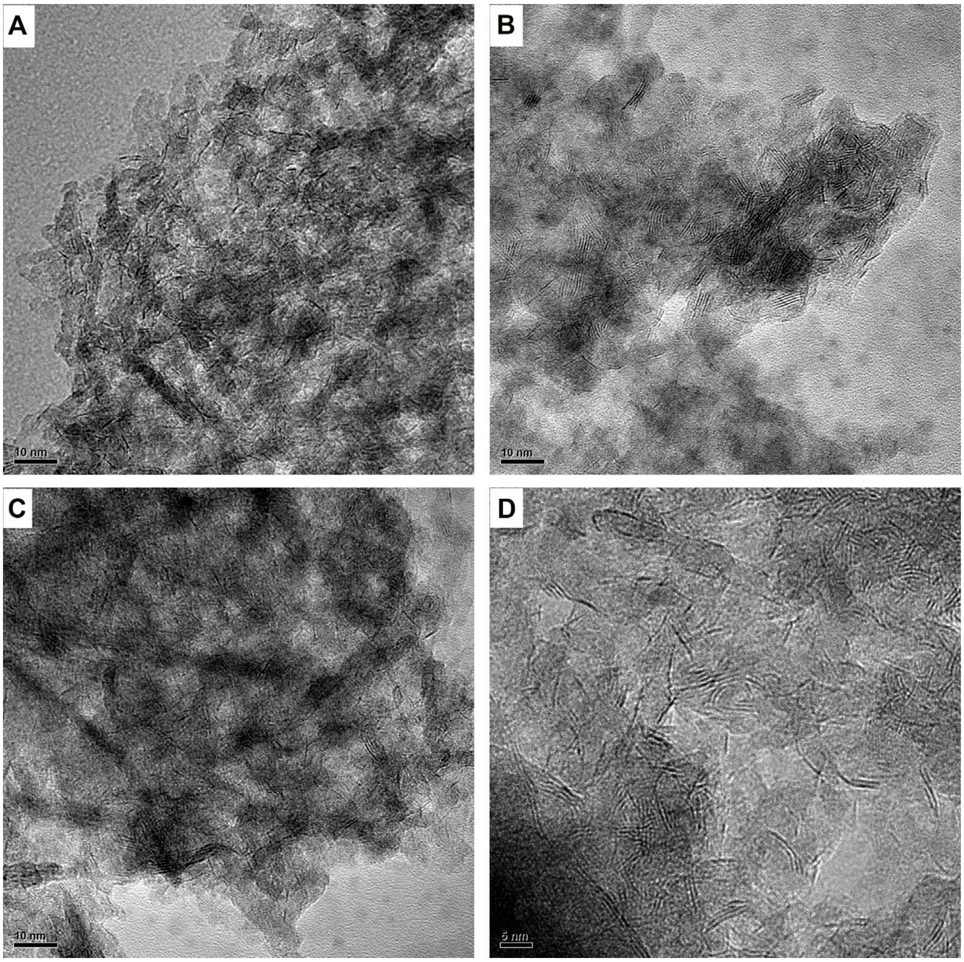

FIGURE 3 | HRTEM of sulfide-impregnated Ga-modified Ni–Mo/Al_2O_3: **(A)** Ni–Mo/Al_2O_3, **(B)** SGal, **(C)** SGam, and **(D)** SGah.

TABLE 2 | Average length and layer stacks of impregnated Ga-modified Ni–Mo/Al_2O_3.

Sample	$\bar{L}$/nm	$\bar{N}$
NiMo–Al_2O_3	2.7	1.1
SGal	2.4	3.6
SGam	3.1	3.4
SGah	3.3	3.3

seen from the diagrams the characteristic diffraction peaks (4.4.0), (4.0.0), and (3.1.1) of γ-Al_2O_3 are almost unchanged, which shows that the crystal structure of γ-Al_2O_3 is not affected. No characteristic peaks of Ga_2O_3 and other Ga compounds are found in **Figure 1**, which indicates that Ga_2O_3 was highly dispersed on Ni–Mo/Al_2O_3 and loaded well. However, diffraction peaks (0.2.2), (-3.1.2), and (2.2.0) of $NiMoO_4$ were observed, illustrating that the introduction of Ga_2O_3 brought about the agglomeration of Ni and Mo elements. In addition, the characteristic peak intensity of $NiMoO_4$ increased with the increase in the content of Ga_2O_3, which manifests that the introduction of excessive Ga_2O_3 is not conducive to the dispersion of Ni and Mo elements.

Effect of Ga Modification on Pore Structure

The method of N_2 physical adsorption–desorption was carried out to confirm the size of the specific surface area, average pore diameter, and pore volume of Ni–Mo/Al_2O_3, SGal, SGam, and SGah. The abovementioned textural properties are calculated and displayed about the four synthesized samples in **Table 1**, and the results of pore size distribution for two samples are recorded in **Figure 2**. From the data in **Table 1**, it is clearly found, especially for SGam, that the specific surface area increased from 214 $m^2 g^{-1}$ to 227 $m^2 g^{-1}$with the addition of Ga_2O_3 in comparison with Ni–Mo/Al_2O_3, indicating that the introduced Ga_2O_3 had a wide distribution in the inner and outer surface of the catalyst; however, the pore volume and pore size decreased to some extent because parts of Ga_2O_3 blocked the pore channel of alumina. It can be seen from **Figure 2** that the pore size distribution curve moved to the direction of small pores, and

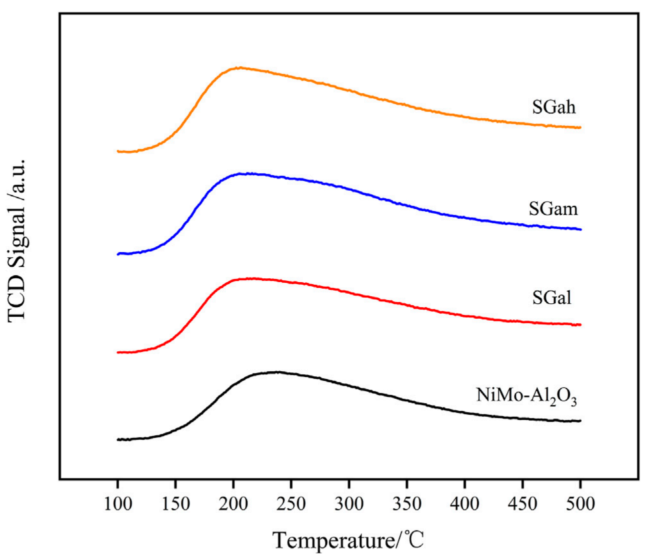

FIGURE 4 | NH_3-TPD patterns of impregnated Ga-modified Ni–Mo/Al_2O_3: (a) Ni–Mo/Al_2O_3, (b) SGal, (c) SGam, (d) SGah.

TABLE 3 | NH_3-TPD results of impregnated Ga-modified Ni–Mo/Al_2O_3.

Sample	Peak temperature/°C	Peak area
Ni–Mo/Al_2O_3	237	1.085
SGal	210	1.423
SGam	207	1.386
SGah	205	1.275

TABLE 4 | Acidity properties of impregnated Ga-modified Ni–Mo/Al_2O_3.

Sample	Weak acid sites/μmol·g^{-1}				Strong acid sites/μmol·g^{-1}			
	B	L	B/L	B + L	B	L	B/L	B + L
Ni–Mo/Al_2O_3	54	106	50.94	160	10	85	11.76	95
SGal	116	217	53.46	333	0	159	0	159
SGam	35	181	19.34	216	0	137	0	137
SGah	35	224	15.63	259	0	165	0	165

the peak area decreases slightly, which also proved that a large number of pores were blocked or even disappeared with the introduction of gallium.

Effect of Ga Modification on Morphological Characteristics

In order to observe the morphologies, characteristics, and dispersion about the sulfide active phase of Ni–Mo/Al_2O_3 and SGax (x stands for l, m, and h) catalysts, the images obtained by HRTEM characterization are shown in **Figure 3.** At least, 300 MoS_2 slabs of each catalyst were counted to statistically analyze the results of the average slab length and average stacking number of the active-phase slabs in **Table 2**. It can be clearly seen from **Table 2** that the introduction of Ga contributed to an increase in the average stacking number of MoS_2 and its change rule kept pace with the increase in Ga loading. Especially, the largest increase of average stacking number for SGal is from 1.1 to 3.6 layers for Ni–Mo/Al_2O_3, which displays that the introduction of Ga weakened the Mo–O–Al bond energy and caused a weaker interaction between MoS_2 and the support, resulting in the formation of more type II Ni–Mo–S reactive phases with high stacking layers. In accordance with the abovementioned regulation, the variation of the average length also has a positive correlation with the Ga_2O_3 content. Also, the degrees of average length increase in the following order: SGal (2.4 nm) < Ni–Mo/Al_2O_3 (2.7 nm) <SGam (3.1 nm) <SGal (3.3 nm). The average length slightly increased from 2.7 nm for sample Ni–Mo/Al_2O_3 to 3.3 nm for sample SGah. This can also be explained by the abovementioned data.

Effect of Ga Modification on Acidity Properties

Acidity plays a crucial role in the formation of the active phase and the HDS reaction, so NH_3-TPD characterization of the series samples was carried out and is displayed in **Figure 4**. The peak temperature and peak area of the NH_3 desorption were calculated for each of the investigated samples and are summarized in **Table 3.** The NH_3-TPD profiles in **Figure 4** reveal the peak temperature of the Ga–Ni–Mo/Al_2O_3 catalyst existed mainly between 150 and 300°C, indicating that the catalyst was mainly the prince of weak acid sites and medium–strong acid sites, which was weaker than that of the Ni–Mo/Al_2O_3 catalyst. It can be seen from **Table 3** that the introduction of Ga made the NH_3 desorption peak shift to a lower temperature, manifesting that the weak acid sites of the catalyst mainly increased. According to the comparison of peak area, the number of acid sites of the Ni–Mo/Al_2O_3 catalyst was increased by introducing Ga_2O_3, but it was negatively correlated with introduced Ga_2O_3 content. Thus, the acid sites varied significantly for SGal. That phenomenon explained that the acid sites were covered by Ga_2O_3, leading to reduction in the degree of increase on the number of acid sites.

Effect of Ga Modification on Acid Types and Strength

It is well known that acid types and strength are the key points to decide the performance of the corresponding catalysts. As a consequence, pyridine desorption FTIR analyses were performed at different temperatures, and the results are listed in **Table 4**, where the specific data of weak and strong Brönsted acid sites (BAS) or Lewis acid sites (LAS) were derived from the information of pyridine desorption at 200 and 350°C, respectively. It can be clearly observed from **Table 4** that the introduction of 2 wt.% Ga_2O_3 enhanced the weak B-acid, and the B-acid enhancement facilitates the desulfurization of 4,6-DMDBT through the isomeric desulfurization pathway (ISOM). Moreover, after the isomerization of the methyl group on 4,6-DMDBT, the steric hindrance to sulfur atoms

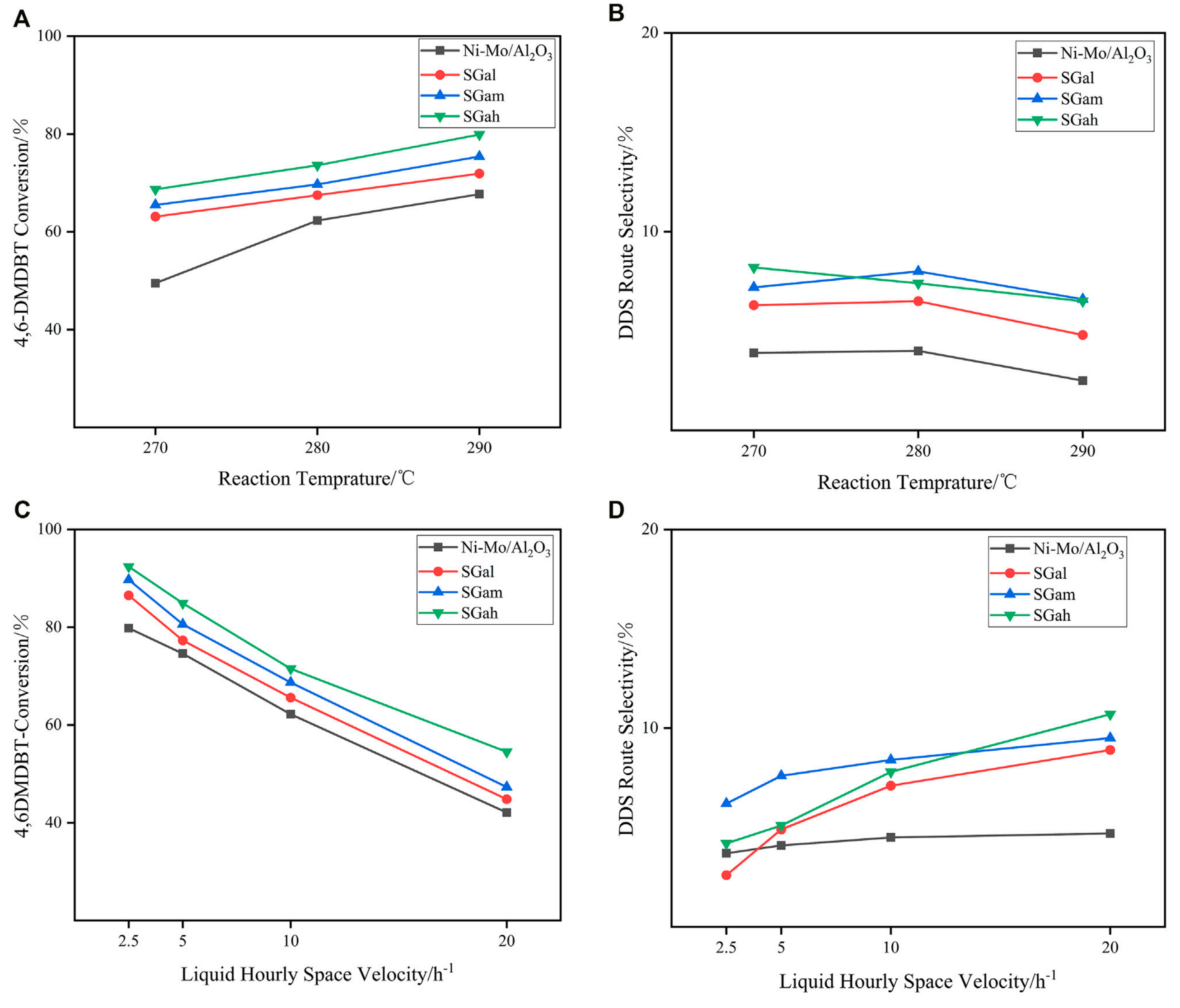

FIGURE 5 | Catalytic performance of impregnated Ga-modified Ni–Mo/Al_2O_3: **(A)** 4,6-DMDBT conversion on different reaction temperatures, **(B)** DDS selectivity of 4,6-DMDBT on different reaction temperatures, **(C)** 4,6-DMDBT conversion on different LHSVs at 280°C, and **(D)** DDS selectivity of 4,6-DMDBT conversion on different LHSVs at 280°C.

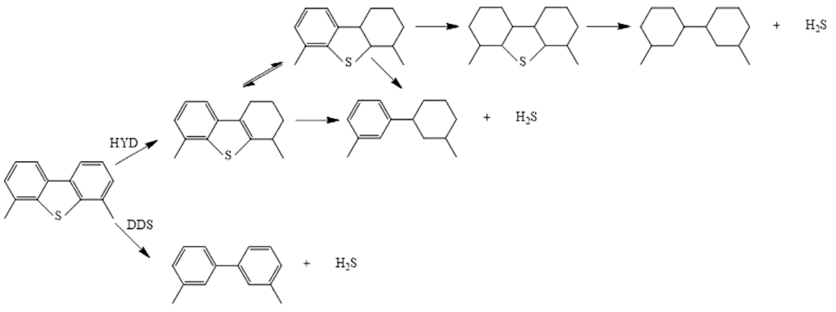

SCHEME 1 | Reaction scheme of HDS for 4,6-DMDBT over Ga–Ni–Mo/Al_2O_3 catalysts. HYD, hydrogenation. DDS, direct desulfurization.

decreased significantly, which provided access to direct desulphurization just by hydrogenolysis of sulfur atoms, and the path to remove sulfur was considered to be very ideal. In addition, the introduction of different contents of Ga increased the Lewis acid, among which the weak Lewis acid increased more and the strong Brönsted acid decreased slightly. This is consistent with the characterization of NH_3-TPD. Except for the enhancement of weak Brönsted acid by SGam, the amount of Ga_2O_3 introduced had little effect on the acid type and amount of Brönsted acid and Lewis acid of Ni–Mo/Al_2O_3, but the amount of Ga_2O_3 introduced increased the total acid amount.

Assessment of Catalytic Activities

As is concretely confirmed, though the appropriate content of Ga_2O_3 modification can effectively improve the physicochemical properties of the catalysts from the characterization results mentioned above, the favorable conditions for conversion and selectivity at different temperatures need to be explored. Thus, 4,6-DMDBT served as the probe molecules in the assessment of the HDS performance of Ni–Mo/Al_2O_3 and SGax series catalysts on a fixed-bed reactor under a total pressure of 4 MPa and the liquid hourly space velocities (LHSVs) of 2.5 h^{-1} at different reaction temperatures (in the range of 270–290°C). The variation of conversions on 4,6-DMDBT at different temperatures is clearly displayed in **Figure 5A**, suggesting that the activities of all the investigated catalysts increased with the increase in the reaction temperature. These results also pointed out that there was no significant disparity in the conversion of SGax series catalysts with different Ga_2O_3 loadings, and the highest conversion rate was obtained when the Ga_2O_3 loading was 2 wt.%. In addition, with the increase in reaction temperature, the difference of conversion rate between SGax series catalysts and the Ni–Mo/Al_2O_3 catalyst became smaller, which resulted from the increase in the conversion rate of 4,6-DMDBT at high temperature close to the reaction end point.

Scheme 1 shows the HDY and DDS reaction route over Ga–Ni–Mo/Al_2O_3 catalysts separately. HYD pathway desulfurization is a tedious step to form the products 3,3′-dimethylcyclohexanebenzene (3,3′-DMCHB) or 3,3′-dimethylbicyclohexyl (3,3′-DMBCH), while DDS pathway desulfurization is achieved with fewer steps and without excess aromatic rings and produces 3,3′-dimethylbiphenyl (3,3′-DMBP). The DDS route selectivity over different catalysts at the same conditions mentioned above was obtained, and the results are shown in **Figure 5B**. It can be observed from **Figure 5B** that, with the increase in reaction temperature, the DDS selectivity of the tested catalysts on the DMDBT decreased, owing to that Ni gradually began to be reduced as the reaction temperature exceeded 290°C. Especially, the metal Ni has a strong hydrogenation performance. The reason mentioned above led to the enhancement of the HYD path. In addition, it was also found that if the reaction temperature is higher than 290°C, the high hydrogenation performance of Ni can even convert a small amount of DDS products into HYD products, but it was generally considered that this reaction will not occur, which was the unique characteristic of Ni-containing hydrotreating catalysts. Further increase in temperature would lead to a profound increase in the proportion of hydrogenation conversion of DDS products to HYD products. In order to properly deal with this situation, the metal promoter can be replaced with the load of Co with low hydrogenation performance, and the amount of the Ni loading or the Ni/Mo atomic ratio ought to be reduced.

The influence of different LHSVs in the investigated series catalysts on the 4,6-DMDBT HDS reaction is shown in **Figure 5C**. As can be clearly noticed from the figure, with the decrease in LHSVs which meant increasing the residence time of raw materials, the conversion rate of 4,6-DMDBT increased gradually and over the tested catalysts was in the order of Ni–Mo/Al_2O_3<SGah < SGam < SGah. When the LHSV decreased gradually, the increasing rate of conversion rates slowed down gradually as the reaction is close to complete conversion. Thus, the conversion rate gap between different Ga_2O_3 loading catalysts was bridged.

Figure 5D reveals the transformation about selectivity of DDS route by stepwise impregnation of the Ga–Ni–Mo/Al_2O_3 catalyst with different LHSVs on 4,6-DMDBT at a reaction temperature of 280°C. As it is vividly shown in **Figure 5D**, the gallium-modified catalysts exhibited higher DDS route selectivity than the Ni–Mo/Al_2O_3 catalyst at high LHSV. However, the DDS route selectivity of SGax series catalysts for 4,6-DMDBT exhibited a negative correlation with the variation of LHSV. With the decrease in LHSV, the DDS selectivity of SGax series catalysts for 4,6-DMDBT even decreased to about the corresponding selectivity of the Ni–Mo/Al_2O_3 catalyst. On the one hand, the incorporation of Ga improved the average stacking number of the active-phase slabs and generated more type II NiMoS active phases which weekly interact with the support or do not interact with the support at all, and it is considered to be very active (Nikulshin et al., 2014; van Haandel et al., 2015), so that the HYD route got strengthened. On the other hand, the residence time of raw materials became longer while the LHSV decreased, which is beneficial to the HYD route with longer reaction path and slower reaction rate. In addition, because of the strong hydrogenation ability of the reduced metal Ni, a small part of DDS products was also transformed into HYD products. All mentioned above were identified as the reason for which the variation of LHSV had impact on the DDS route selectivity.

CONCLUSION

The experiments showed that the introduction of Ga_2O_3 with appropriate content (2 wt.%) promoted not only Ni and Mo species to disperse uniformly but also doping of more Ni atoms into the MoS_2 crystals. In addition, the average stacking number and the length of Mo_2S were increased. Those mentioned above resulted in the formation of more NiMoS active phases. The specific surface area and the amount of acid sites were increased, facilitating the adsorption of reactant molecules and the hydrodesulfurization reactions. Last but not the least, the catalyst Ga–Ni–Mo/Al_2O_3 exhibited the highest conversion rate towards 4,6-DMDBT HDS when the amount of Ga_2O_3 loading was 2 wt.% with an LHSV of 2.5 h^{-1} at 290°C, and Ga modification also can effectively improve the DDS route selectivity in varying degrees.

DATA AVAILABILITY STATEMENT

The original contributions presented in the study are included in the article/**Supplementary Material**, further inquiries can be directed to the corresponding author.

AUTHOR CONTRIBUTIONS

MH designed experimental plans, performed the main experimental work, analyzed and discussed the results and wrote the manuscript. WH assisted in the design of the scheme and performed the main experimental work. AL participated in manuscript writing. QW proposed the themes, ideas, and content of the research work. YJ, HY, ZY, XW and ZX assisted in literature review and manuscript sorting. YZ guided experimental work and manuscript revision.

FUNDING

This work was supported by the National Natural Science Foundation of China under grant No. 22078360.

SUPPLEMENTARY MATERIAL

The Supplementary Material for this article can be found online at: https://www.frontiersin.org/articles/10.3389/fchem.2022.865375/full#supplementary-material

REFERENCES

Ali, M., Almalki, A., Elali, B., Martinie, G., and Siddiqui, M. (2006). Deep Desulphurization of Gasoline and Diesel Fuels Using Non-hydrogen Consuming Techniques. *Fuel* 85 (10-11), 1354–1363. doi:10.1016/j.fuel.2005.12.006

Altamirano, E., De los Reyes, J. A., Murrieta, F., and Vrinat, M. (2008). Hydrodesulfurization of 4,6-dimethyldibenzothiophene over Co(Ni)MoS2 Catalysts Supported on Alumina: Effect of Gallium as an Additive. *Catal. Today* 133-135, 292–298. doi:10.1016/j.cattod.2007.12.085

Altamirano, E., Delosreyes, J., Murrieta, F., and Vrinat, M. (2005). Hydrodesulfurization of Dibenzothiophene and 4,6-Dimethyl-Dibenzothiophene: Gallium Effect over NiMo/AlO Sulfided Catalysts. *J. Catal.* 235 (2), 403–412. doi:10.1016/j.jcat.2005.09.011

Baston, E. P., França, A. B., Neto, A. V. d. S., and Urquieta-González, E. A. (2015). Incorporation of the Precursors of Mo and Ni Oxides Directly into the Reaction Mixture of Sol–Gel Prepared γ-Al_2O_3-ZrO_2 Supports – Evaluation of the Sulfided Catalysts in the Thiophene Hydrodesulfurization. *Catal. Today* 246, 184–190. doi:10.1016/j.cattod.2014.10.035

Chandra Srivastava, V. (2012). An Evaluation of Desulfurization Technologies for Sulfur Removal from Liquid Fuels. *RSC Adv.* 2 (3), 759–783. doi:10.1039/C1RA00309G

Chen, W., Maugé, F., van Gestel, J., Nie, H., Li, D., and Long, X. (2013). Effect of Modification of the Alumina Acidity on the Properties of Supported Mo and CoMo Sulfide Catalysts. *J. Catal.* 304, 47–62. doi:10.1016/j.jcat.2013.03.004

Cimino, A., Jacono, M., and Schiavello, M. (1975). Effect of Zinc, Gallium, and Germanium Ions on the Structural and Magnetic Properties of Nickel Ions Supported on Alumina. *J. Phys. Chem.* 79. doi:10.1021/j100570a010

Copéret, C. (2013). Catalysis by transition metal sulphides. From molecular theory to industrial applications. H. Toulhoat and P. Raybaud, Editors, Technip Edition, Paris, 2013. *Journal of Catalysis* 307, 121. doi:10.1016/j.jcat.2013.06.011

Díaz-García, L., Santes, V., Viveros-García, T., Sánchez-Trujillo, A., Ramírez-Salgado, J., Ornelas, C., et al. (2017). Electronic Binding of Sulfur Sites into Al2O3-ZrO2 Supports for NiMoS Configuration and Their Application for Hydrodesulfurization. *Catal. Today* 282, 230–239. doi:10.1016/j.cattod.2016.08.001

Egorova, M. (2004). Hydrodesulfurization of Dibenzothiophene and 4,6-dimethyldibenzothiophene over Sulfided NiMo/?-Al2O3, CoMo/?-Al2O3, and Mo/?-Al2O3 Catalysts. *J. Catal.* 225 (2), 417–427. doi:10.1016/j.jcat.2004.05.002

Eijsbouts, S. (1997). On the Flexibility of the Active Phase in Hydrotreating Catalysts. *Appl. Catal. A: Gen.* 158, 53–92. doi:10.1016/S0926-860X(97)00035-5

Ferdous, D., Dalai, A. K., Adjaye, J., and Kotlyar, L. (2005). Surface Morphology of NiMo/Al2O3 Catalysts Incorporated with boron and Phosphorus: Experimental and Simulation. *Appl. Catal. A: Gen.* 294 (1), 80–91. doi:10.1016/j.apcata.2005.07.025

Gallegos-Hernández, A. Y., Martínez-Rosales, M., Rico, J. L., and Avalos-Borja, M. (2020). Improvement in the Hydrodesulfurization of Dibenzothiophene over Supported NiMoW Catalysts. *Reac Kinet Mech. Cat* 132 (1), 317–330. doi:10.1007/s11144-020-01909-2

Gates, B. C., and Topsøe, H. (1997). Reactivities in Deep Catalytic Hydrodesulfurization: Challenges, Opportunities, and the Importance of 4-Methyldibenzothiophene and 4,6-Dimethyldibenzothiophene. *Polyhedron* 16, 3213–3217. doi:10.1016/S0277-5387(97)00074-0

Guevara-Lara, A., Cruz-Pérez, A. E., Contreras-Valdez, Z., Mogica-Betancourt, J., Alvarez-Hernández, A., and Vrinat, M. (2010). Effect of Ni Promoter in the Oxide Precursors of MoS2/MgO–Al2O3 Catalysts Tested in Dibenzothiophene Hydrodesulphurization. *Catal. Today* 149 (3-4), 288–294. doi:10.1016/j.cattod.2009.09.014

Guo, D., Liu, Y., Ji, H., Chen, B., Shen, C., Li, F., et al. (2021). Silicate-Enhanced Heterogeneous Flow-Through Electro-Fenton System Using Iron Oxides under Nanoconfinement. *Environ. Sci. Tech.* 55, 4045-4053. doi:10.1021/acs.est.1c00349

Huang, T., Xu, J., and Fan, Y. (2018). Effects of Concentration and Microstructure of Active Phases on the Selective Hydrodesulfurization Performance of Sulfided CoMo/Al2O3 Catalysts. *Appl. Catal. B: Environ.* 220, 42–56. doi:10.1016/j.apcatb.2017.08.029

Humadi, J. I., Gheni, S. A., Ahmed, S. M. R., Abdullah, G. H., Phan, A. N., and Harvey, A. P. (2021). Fast, Non-extractive, and Ultradeep Desulfurization of Diesel in an Oscillatory Baffled Reactor. *Process Saf. Environ. Prot.* 152, 178–187. doi:10.1016/j.psep.2021.05.028

Jacono, M., Schiavello, M., Beer, V., and Minelli, G. (1977). Effect of Gallium Ions and of Preparation Methods on the Structural Properties of Cobalt-Molybdenum-Alumina Catalysts. *J. Phys. Chem.* 81. doi:10.1002/chin.19774702910.1021/j100531a014

Jayaraman, A., Hernandez-Maldonado, A. J., Yang, R. T., Chinn, D., Munson, C. L., and Mohr, D. H. (2004). Clinoptilolites for Nitrogen/methane Separation. *Chem. Eng. Sci.* 59 (12), 2407–2417. doi:10.1016/j.ces.2003.10.030

Kasztelan, S. (1990). A Descriptive Model of Surface Sites on Molybdenum(tungsten) Disulfide Particles. *Langmuir* 6. doi:10.1021/la00093a013

Kasztelan, S., Toulhoat, H., Grimblot, J., and Bonnelle, J. P. (1984). A Geometrical Model of the Active Phase of Hydrotreating Catalysts. *Appl. Catal.* 13, 127–159. doi:10.1016/S0166-9834(00)83333-3

Kulkarni, P. S., and Afonso, C. A. M. (2010). Deep Desulfurization of Diesel Fuel Using Ionic Liquids: Current Status and Future Challenges. *Green Chemistry*, 12 (7). doi:10.1039/c002113j

Li, S., Liu, Y., Feng, X., Chen, X., and Yang, C. (2019). Insights into the Reaction Pathway of Thiophene Hydrodesulfurization over Corner Site of MoS2 Catalyst: A Density Functional Theory Study. *Mol. Catal.* 463, 45–53. doi:10.1016/j.mcat.2018.11.018

Liu, J., Li, W.-Y., Feng, J., and Gao, X. (2021). Effects of Fe Species on Promoting the Dibenzothiophene Hydrodesulfurization over the Pt/γ-Al_2O_3 Catalysts. *Catal. Today* 371, 247–257. doi:10.1016/j.cattod.2020.07.035

Liu, Y., Li, F., Xia, Q., Wu, J., Liu, J., Huang, M., et al. (2018). Conductive 3D Sponges for Affordable and Highly-Efficient Water Purification. *Nanoscale* 10, 4771–4778. doi:10.1039/C7NR09435C

Liu, Y., Liu, F., Ding, N., Hu, X., Shen, C., Li, F., et al. (2020). Recent Advances on Electroactive CNT-Based Membranes for Environmental Applications: The Perfect Match of Electrochemistry and Membrane Separation. *Chin. Chem. Lett.* 31. doi:10.1016/j.cclet.2020.03.011

Manoli, J.-M., Da Costa, P., Brun, M., Vrinat, M., Maugé, F., and Potvin, C. (2004). Hydrodesulfurization of 4,6-dimethyldibenzothiophene over Promoted (Ni,P) Alumina-Supported Molybdenum Carbide Catalysts: Activity and Characterization of Active Sites. *J. Catal.* 221 (2), 365–377. doi:10.1016/j.jcat.2003.08.011

Mohebali, G., and Ball, A. S. (2016). Biodesulfurization of Diesel Fuels - Past, Present and Future Perspectives. *Int. Biodeterioration Biodegradation* 110, 163–180. doi:10.1016/j.ibiod.2016.03.011

Monticello, D. J. (2001). Biodesulfurization and the Upgrading of Petroleum Distillates. *Curr. Opin. Biotechnol.* 11, 540–546. doi:10.1016/s0958-1669(00)00154-3

Naboulsi, I., Felipe Linares Aponte, C., Lebeau, B., Brunet, S., Michelin, L., Bonne, M., et al. (2017). An Unexpected Pathway for Hydrodesulfurization of Gazole over a CoMoS Active Phase Supported on a Mesoporous TiO2 Catalyst. *Chem. Commun.* 53 (18), 2717–2720. doi:10.1039/C7CC00848A

Nikulshin, P. A., Salnikov, V. A., Mozhaev, A. V., Minaev, P. P., Kogan, V. M., and Pimerzin, A. A. (2014). Relationship between Active Phase Morphology and Catalytic Properties of the Carbon-Alumina-Supported Co(Ni)Mo Catalysts in HDS and HYD Reactions. *J. Catal.* 309, 386–396. doi:10.1016/j.jcat.2013.10.020

Ning, X., Li, Y., Dong, B., Wang, H., Yu, H., Peng, F., et al. (2017). Electron Transfer Dependent Catalysis of Pt on N-Doped Carbon Nanotubes: Effects of Synthesis Method on Metal-Support Interaction. *J. Catal.* 348, 100–109. doi:10.1016/j.jcat.2017.02.011

Niquillerothlisberger, A., and Prins, R. (2006). Hydrodesulfurization of 4,6-dimethyldibenzothiophene and Dibenzothiophene over Alumina-Supported Pt, Pd, and Pt-Pd Catalysts. *J. Catal.* 242 (1), 207–216. doi:10.1016/j.jcat.2006.06.009

Okamoto, Y., and Kubota, T. (2003). A Model Catalyst Approach to the Effects of the Support on Co–mo Hydrodesulfurization Catalysts. *Catal. Today* 86 (1-4), 31–43. doi:10.1016/S0920-5861(03)00402-4

Ortega-Domínguez, R. A., Mendoza-Nieto, J. A., Hernández-Hipólito, P., Garrido-Sánchez, F., Escobar-Aguilar, J., Barri, S. A. I., et al. (2015). Influence of Na Content on Behavior of NiMo Catalysts Supported on Titania Nanotubes in Hydrodesulfurization. *J. Catal.* 329, 457–470. doi:10.1016/j.jcat.2015.05.005

Rana, M., Ramirez, J., Gutierrezalejandre, A., Ancheyta, J., Cedeno, L., and Maity, S. (2007). Support Effects in CoMo Hydrodesulfurization Catalysts Prepared with EDTA as a Chelating Agent. *J. Catal.* 246 (1), 100–108. doi:10.1016/j.jcat.2006.11.025

Schuit, G. C. A., and Gates, B. C. (1973). Chemistry and Engineering of Catalytic Hydrodesulfurization. *Aiche J.* 19, 417–438. doi:10.1002/aic.690190303

Schüth, F. (2009). Challenges in Hydrogen Storage. *Eur. Phys. J. Spec. Top.* 176, 155–166. doi:10.1140/epjst/e2009-01155-x

Selvavathi, V., Chidambaram, V., Meenakshisundaram, A., Sairam, B., and Sivasankar, B. (2009). Adsorptive Desulfurization of Diesel on Activated Carbon and Nickel Supported Systems. *Catal. Today* 141 (1-2), 99–102. doi:10.1016/j.cattod.2008.05.009

Tanimu, A., and Alhooshani, K. (2019). Advanced Hydrodesulfurization Catalysts: A Review of Design and Synthesis. *Energy Fuels* 33 (4), 2810–2838. doi:10.1021/acs.energyfuels.9b00354

Van Haandel, L., Bremmer, M., Kooyman, P. J., van Veen, J. A. R., Weber, T., and Hensen, E. J. M. (2015). Structure-Activity Correlations in Hydrodesulfurization Reactions over Ni-Promoted MoxW(1-x)S2/Al2O3 Catalysts. *ACS Catal.* 5 (12), 7276–7287. doi:10.1021/acscatal.5b01806

Varga, Z., Szarvas, T., Tétényi, P., Hancsók, J., and Ollár, T. (2017). The Particular Characteristics of the Active Sites of MoS2, WS2 Catalysts in Thiophene Hydrodesulfurization. *Reac Kinet Mech. Cat* 124 (1), 61–74. doi:10.1007/s11144-017-1283-y

Vázquez-Garrido, I., López-Benítez, A., Berhault, G., and Guevara-Lara, A. (2019). Effect of Support on the Acidity of NiMo/Al2O3-MgO and NiMo/TiO2-Al2O3 Catalysts and on the Resulting Competitive Hydrodesulfurization/hydrodenitrogenation Reactions. *Fuel* 236, 55–64. doi:10.1016/j.fuel.2018.08.053

Wagenhofer, M. F., Shi, H., Gutiérrez, O. Y., Jentys, A., and Lercher, J. A. (2020). Enhancing Hydrogenation Activity of Ni-Mo Sulfide Hydrodesulfurization Catalysts. *Sci. Adv.* 6, eaax5331. doi:10.1126/sciadv.aax5331

Wang, X., Du, P., Chi, K., Duan, A., Xu, C., Zhao, Z., et al. (2017). Synthesis of NiMo Catalysts Supported on Mesoporous Silica FDU-12 with Different Morphologies and Their Catalytic Performance of DBT HDS. *Catal. Today* 291, 146–152. doi:10.1016/j.cattod.2016.10.035

Wang, X., Xiao, C., Zheng, P., Zhao, Z., Alabsi, M. H., Shi, Y., et al. (2020). Dendritic Micro-mesoporous Composites with center-radial Pores Assembled by TS-1 Nanocrystals to Enhance Hydrodesulfurization Activity of Dibenzothiophene and 4,6-dimethyldibenzothiophene. *J. Catal.* 384, 136–146. doi:10.1016/j.jcat.2020.02.013

Wang, X., Zhao, Z., Zheng, P., Chen, Z., Duan, A., Xu, C., et al. (2016). Synthesis of NiMo Catalysts Supported on Mesoporous Al2O3 with Different crystal Forms and superior Catalytic Performance for the Hydrodesulfurization of Dibenzothiophene and 4,6-dimethyldibenzothiophene. *J. Catal.* 344, 680–691. doi:10.1016/j.jcat.2016.10.016

Weng, X., Cao, L., Zhang, G., Chen, F., Zhao, L., Zhang, Y., et al. (2020). Ultradeep Hydrodesulfurization of Diesel: Mechanisms, Catalyst Design Strategies, and Challenges. *Ind. Eng. Chem. Res.* 59 (49), 21261–21274. doi:10.1021/acs.iecr.0c04049

Xu, J., Huang, T., and Fan, Y. (2017). Highly Efficient NiMo/SiO2-Al2O3 Hydrodesulfurization Catalyst Prepared from Gemini Surfactant-Dispersed Mo Precursor. *Appl. Catal. B: Environ.* 203, 839–850. doi:10.1016/j.apcatb.2016.10.078

Yin, C.-l., Zhai, X.-p., Zhao, L.-y., Liu, C.-g., Zhai, X.-p., Zhao, L.-y., et al. (2013). Mechanism of Hydrodesulfurization of Dibenzothiophenes on Unsupported NiMoW Catalyst. *J. Fuel Chem. Tech.* 41 (8), 991–997. doi:10.1016/S1872-5813(13)60043-2

Zeng, Q., Chang, S., Wang, M., Li, M., Deng, Q., Xiong, Z., et al. (2021). Highly-active, Metal-free, Carbon-Based ORR Cathode for Efficient Organics Removal and Electricity Generation in a PFC System. *Chin. Chem. Lett.* 32 (7), 2212–2216. doi:10.1016/j.cclet.2020.12.062

Zepeda, T. A., Pawelec, B., Díaz de León, J. N., de los Reyes, J. A., and Olivas, A. (2012). Effect of Gallium Loading on the Hydrodesulfurization Activity of Unsupported Ga2S3/WS2 catalystsEffect of Gallium Loading on the Hydrodesulfurization Activity of Unsupported Ga_2S_3/WS_2 Catalysts. *Appl. Catal. B: Environ.* 111-112, 10–19. doi:10.1016/j.apcatb.20n.09.00810.1016/j.apcatb.2011.09.008

Zhou, W., Liu, M., Zhang, Q., Wei, Q., Ding, S., and Zhou, Y. (2017a). Synthesis of NiMo Catalysts Supported on Gallium-Containing Mesoporous Y Zeolites with Different Gallium Contents and Their High Activities in the Hydrodesulfurization of 4,6-Dimethyldibenzothiophene. *ACS Catal.* 7 (11), 7665–7679. doi:10.1021/acscatal.7b02705

Zhou, W., Zhang, Q., Zhou, Y., Wei, Q., Du, L., Ding, S., et al. (2018a). Effects of Ga- and P-Modified USY-Based NiMoS Catalysts on Ultra-deep Hydrodesulfurization for FCC Diesels. *Catal. Today* 305, 171–181. doi:10.1016/j.cattod.2017.07.006

Zhou, W., Zhang, Y., Tao, X., Zhou, Y., Wei, Q., and Ding, S. (2018b). Effects of Gallium Addition to Mesoporous Alumina by Impregnation on Dibenzothiophene Hydrodesulfurization Performances of the Corresponding NiMo Supported Catalysts. *Fuel* 228, 152–163. doi:10.1016/j.fuel.2018.04.084

Zhou, W., Zhou, Y., Wei, Q., Du, L., Ding, S., Jiang, S., et al. (2017b). Gallium Modified HUSY Zeolite as an Effective Co-support for NiMo Hydrodesulfurization Catalyst and the Catalyst's High Isomerization Selectivity. *Chem. Eur. J.* 23 (39), 9369–9382. doi:10.1002/chem.201701307

Conflict of Interest: Author AL was employed by SINOPEC.

The remaining authors declare that the research was conducted in the absence of any commercial or financial relationships that could be construed as a potential conflict of interest.

frontiers in Chemistry

ORIGINAL RESEARCH
published: 17 March 2022
doi: 10.3389/fchem.2022.839680

Effect of Borax On Sintering Kinetics, Microstructure and Mechanical Properties of Porous Glass-Ceramics From Coal Fly Ash by Direct Overfiring

Li Zeng[1,2]*, *Hongjuan Sun*[2] *and Tongjiang Peng*[2]

[1]*School of Architecture and Civil Engineering, Chengdu University, Chengdu, China,* [2]*Key Laboratory of Solid Waste Treatment and Resource Recycle, Ministry of Education, Southwest University of Science and Technology, Mianyang, China*

The direct sintering process of coal fly ash for the preparation of glass-ceramics is the liquid-phase sintering process, from non-densification to densification. When the temperature exceeds the densification temperature point, the porosity of glass-ceramics on the contrary increases and the pore diameter increases. This provides a basis to prepare porous glass-ceramics by direct overfiring. Adding borax to coal fly ash can reduce the temperature of liquid phase formation, reduce the preparing temperature of porous glass-ceramics, achieve the purpose of energy saving. The effects of borax on the structure, properties and sintering kinetics of porous glass-ceramics prepared from coal fly ash by overfiring were investigated. It is found that the introduction of B-O bond can change the network structure of non-crystalline vitreous in coal fly ash, reduce the melting temperature, promote the formation of liquid phase, and thus increase the porosity of porous glass-ceramics. This paper provides a certain experimental basis for the preparation of porous glass-ceramics by direct overfiring of coal fly ash at low temperature without adding pore-forming agent, and provides a new possibility for the high-value resource utilization of coal fly ash.

Keywords: coal fly ash, borax, overfiring, porous glass-ceramics, viscous flow

Edited by:
Suqing Wu,
Wenzhou University, China

Reviewed by:
Chunzhen Fan,
Wenzhou University, China
Min Wang,
Jinan University, China

Correspondence:
Li Zeng
zengli512@126.com

Specialty section:
This article was submitted to
Inorganic Chemistry,
a section of the journal
Frontiers in Chemistry

Received: *20 December 2021*
Accepted: *07 February 2022*
Published: *17 March 2022*

Citation:
Zeng L, Sun H and Peng T (2022)
Effect of Borax On Sintering Kinetics,
Microstructure and Mechanical
Properties of Porous Glass-Ceramics
From Coal Fly Ash by Direct Overfiring.
Front. Chem. 10:839680.
doi: 10.3389/fchem.2022.839680

INTRODUCTION

Porous glass-ceramics is a new kind of material which distributes a large number of microcrystalline phases and pores evenly in glass phase based on glass-ceramics. Porous glass-ceramics has been widely used as insulation materials for energy-saving building walls and thermal pipelines due to its large specific surface area, better thermal stability, lower thermal conductivity and higher mechanical strength (Flesoura et al., 2021; Yio et al., 2021). At present, the preparation methods of porous glass-ceramics mainly include crystallization-acid leaching (Wang et al., 2003a; Wang et al., 2003b; Chen et al., 2020), melting sintering with pore-making agent (Ding, et al., 2015; Jiang et al., 2017), direct sintering with pore-making agent (Bernardo and Albertini, 2006; Chen et al., 2016; Hisham et al., 2020; Yio et al., 2021). Among them, the preparation methods of porous glass-ceramic with coal fly ash as raw material are mainly the melting sintering method with adding pore-making agent and the direct sintering method with adding pore-making agent.

The melting sintering method with adding pore-making agent is to add pore-making agent to the basic glass. In the sintering process, pore-making agent through oxidation or release gas to form pores to prepare porous glass-ceramics. The preparation process is similar to that of preparing glass-ceramics by melting and sintering, which includes batching, melting, water quenching, drying, crushing, sieving, forming, nucleation, crystallization and pore forming (Zhu et al., 2012). As environmental protection is deeply rooted in people's mind, people put forward new requirements for resource utilization (Zeng et al., 2021). In order to save energy consumption and simplify the preparation process, the porous glass-ceramics was prepared by adding pore-making agent in the direct sintering process (Bai et al., 2014; Li et al., 2018; Zhu et al., 2016). No matter which method is used to prepare porous glass ceramics, the type and quantity of pore-forming agent are important indicators affecting the porous glass ceramics (Fernandes et al., 2009; Hou et al., 2017; Wang et al., 2018; Fernandes et al., 2020). The key of pore-making agent selection is that the pore-making temperature should be consistent with the softening temperature of the raw material (Wu et al., 2006). However, the composition and properties of coal fly ash from different producing areas vary greatly. Therefore, it is difficult to select the appropriate type and amount of foaming agent according to its softening temperature point.

Dong et al. found that coal fly ash would self-expansion in the high-temperature sintering process, that is, crystals would be precipitated from the molten liquid to form pores in the high-temperature process (Dong et al., 2008; Dong et al., 2009). Moreover, in the previous experiments, it was found that, the process of sintering is actually the transformation of open pore porosity between particles and particles in the sample into closed pore porosity. In this process, there is an optimal temperature point for densification. Once the temperature point is exceeded, the samples will be overfiring and more molten liquid will be formed. With sufficient viscous flow, small pores will be merged to form large pores, and more crystals will be precipitated from the molten liquid, and the total porosity will gradually increase (Zeng et al., 2020; Zheng et al., 2020). This provides a basis for direct overfiring of porous glass-ceramics. However, preliminary experimental results show that the overfiring temperature of coal fly ash reaches about 1,190°C (Zeng et al., 2019). In order to reduce the temperature of porous glass ceramics prepared by overfiring, a fluxing agent must be added. Borax is widely used as a flux in the preparation of porous glass ceramics, it can reduce the temperature of liquid phase formation (Chen et al., 2013; Guo et al., 2014; Yio et al., 2021). In this experiment, borax was added to reduce the temperature of preparing porous glass-ceramics prepared by overfiring method, so as to achieve the purpose of energy saving and consumption reduction.

The purpose of this paper is to discuss the effect of borax on the morphology, performance and sintering kinetics of the coal fly ash porous glass-ceramics prepared by overfiring, so as to achieve the purpose of preparing porous glass-ceramics without adding pore-making agent at low temperature, and to provide a new way for the high-value utilization of coal fly ash.

EXPERIMENTAL PROCEDURE

Raw Materials and Experimental Equipment

Raw materials, the coal fly ash used in the experiment came from a coal-fired power plant in Jiangyou, Sichuan, the pure polyvinyl alcohol (PVA) and borax were purchased from Chengdu Kelon Chemical Co., LTD. The chemical composition analysis and phase composition of coal fly ash are shown in **Table 1** and **Figure 1** respectively. The main constituents of coal fly ash are alumina and silicon oxide, accompanied by a small amount of calcium oxide and iron oxide. The phase composition is mainly the amorphous silicate vitreous represented by the uplift steamed bread peak, crystalline mullite (PDF#00-002-0430,$3Al_2O_3.2SiO_2$), quartz (PDF#00-033-1161, SiO_2) and hematite (PDF#00-024-0072,Fe_2O_3) (Lin et al., 2015).

Experimental equipment, 769YP-24B infrared powder tablet press (Xi 'an minsks testing equipment Co. Ltd., China), KSY-25-16-8X2-20-13 box type resistance furnace (Shanghai shiyan electric furnace, Co. Ltd., China), 305F-2 microcomputer control electronic pressure testing machine (Shenzhen wance testing machine Co. Ltd., China), WT5003GHS hydrostatic balance (Changzhou Wantai Balance Instrument Co. LTD.), XPM-Φ100 × 4 planetary four-cylinder grinding machine (Wuhan prospecting machinery Factory).

Preparation of Porous Glass-Ceramics

The specific process of preparing porous glass-ceramics by direct overfiring with borax is shown below. Borax ($Na_2B_4O_7$ $10H_2O$) and coal fly ash were mixed evenly according to mass ratios of 10:90, 15:85, 20:80, 25:75 and 30:70 (denoted as 10B-90F, 15B-85F, 20B-80F, 25B-75F, 30B-70F) for 5 min by ball grinding. PVA was used as the binder for granulation. The samples were sintered in a box type resistance furnace at different temperatures (800–1100°C) for 60 min after tablet forming. After cooling down, the samples were taken out for phase, morphology and corresponding performance test and characterization. The sample was labeled as 10B-90F, 15B-85F, 20B-80F, 25B-75F, 30B-70F sintering temperature.

Characterization

The phase composition of the raw material and the samples were analyzed by the X-ray diffractometer (XRD) of PANalytical B.V. (2θ range 3–80°, step 0.03°). The chemical composition of raw materials was analyzed by X-ray fluorescence (XRF) of PANalytical B.V. (Rh target, maximum power 2.4 kW). The morphology of porous glass-ceramics was characterized by DV230E3FL optical microscope and the pore size distribution was measured by "Nano Measurer" size statistics software. The three-point bending strength of $5 \times 10 \times 60\ mm^3$ samples was tested at the speed of $0.05\ mm\ min^{-1}$, and the average value was taken three times for each test. The true density (ρ_t) and bulk density (ρ_b) were measured by the gas (A_r) pycnometer and Archimedes method, respectively. The porosity (P) can be calculated by **Eq. 1** (Bai et al., 2014).

$$P = \left(1 - \frac{\rho_b}{\rho_t}\right) \times 100\% \qquad (1)$$

TABLE 1 | Chemical compositions of coal fly ash powder.

Composition	SiO_2	Al_2O_3	CaO	Fe_2O_3	K_2O	SO_3	TiO_2	Na_2O
wt%	53.31	26.55	5.88	4.41	2.42	1.42	1.06	0.60
Composition	MgO	P_2O_5	BaO	MnO	ZrO_2	ZnO	Other	LOI
wt%	0.52	0.47	0.10	0.03	0.03	0.02	0.16	3.02

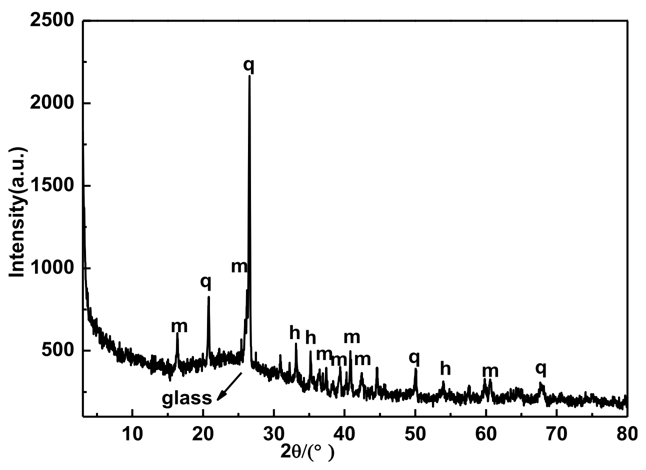

FIGURE 1 | XRD spectra of coal fly ash (q, quartz; m, mullite; h, hematite).

RESULTS AND DISCUSSION

Phase and Microstructural Evolution

Figure 2 shows the XRD patterns of samples sintered at different temperatures with different borax additions. It can be seen from the figure that the addition amount of borax has a great influence on the phase of porous glass-ceramics. When the amount of borax is small (10B-90F, 15B-85F), the phase of the porous glass-ceramics are the same as the glass-ceramics prepared without borax, they all composed of anorthite, quartz and mullite (Zeng et al., 2019). Without borax, anorthite is precipitated from molten quartz and amorphous vitreous at a temperature of 1,000°C (Zeng et al., 2019). When the amount of borax is 10% and 15%, the temperature of anorthite precipitated reduced to 900°C. Indicating that borax will react with the oxides in coal fly ash to reduce the melting temperature of quartz and amorphous vitreous in coal fly ash, so that the molten liquid phase is formed at a lower temperature, and anorthite precipitated (Chen et al., 2013). By comparing the peak strength ratio of anorthite (I_{204}) and quartz (I_{101}) between 10B-90F1000 and 15B-85F1000 at 1,000°C, it is found that the ratio increases from 0.87 of 10B-90F1000 to 0.91 of 15B-85F1000. Meaning that borax can reduce the melting temperature of quartz and amorphous vitreous, and increase the amount of anorthite precipitated from the molten liquid. By comparing the critical temperature point of collapse of porous structure of porous glass-ceramics (10B-90F is 1,100°C, 15B-85F is 1,100°C, 20B-80F is 1,000°C, 25B-75F is 900°C), it is found that with the increase of borax addition, the critical temperature point of collapse of porous structure decreases gradually. In addition, by comparing the peak strength ratio of anorthite (I_{204}) and quartz (I_{101}) at the critical temperature point, it was found that the ratio increased from 1.12 in 10B-90F1100 to 1.32 in 15B-85F1100, and then decreased to 0.68 in 20B-80F1000 and 0.47 in 25B-75F900. The reason may be that, at the low amount of borax (10B-90F, 15B-85F), due to the higher critical temperature point of porous structure collapse (1,100, 1,100°C), the addition of borax can simultaneously reduce the melting temperature point of quartz and amorphous vitreous in coal fly ash to form liquid phase, precipitation of more anorthite. With the addition of borax (20B-80F, 25B-75F), the collapse temperature of porous structure reduced (1,000, 900°C). At this temperature, the addition of borax can only reduce the melting temperature of non-crystalline vitreous body in coal fly ash, cannot promote the melting of quartz in coal fly ash. Therefore, the content of precipitated anorthite is lower than that of 10B-90F and 15B-85F. Continue to increase the amount of borax (30B-70F), no anorthite was observed before the pore structure of porous glass-ceramics collapsed (850°C), meaning the glass liquid phase is formed by the melting of borax. This is also the reason why borax is not detected in XRD (Chen et al., 2012). Under the proper temperature, the B-O bond with low binding energy in borax can changes the network structure of quartz and amorphous vitreous in coal fly ash to form liquid phase (Chen et al., 2012). Therefore, the sintering temperature also plays an important role in the liquid phase formation of porous glass-ceramics.

Figure 3 shows the influence of sintering temperature on the morphology and pore size distribution of porous glass-ceramics under different borax additions. **Figures 3A–E** shows the change of the morphology of the sample with temperature when borax is added at 10%. The average pore size increased from 46 μm in 10B-90F900 to 130 μm in 10B-90F1100, and the distribution of pore size increased from 20–160 μm in 10B-90F900 to 20–430 μm in 10B-90F1100. **Figures 3F–J** is the morphology and pore diameter distribution of the samples at 900–1,100°C when the addition amount of borax is 15%. By comparing **Figures 3A–J**, the average pore diameter and pore diameter range of the samples increase with the addition of borax at the same temperature. For example, the average aperture of 10B-90F1000 is 78 μm, the aperture range is 20–220 μm, the average aperture of 15B-85F1000 increases to 103 μm, and the aperture range is 20–400 μm. On one hand, the increase of borax provides more molten liquid, which reduces the viscosity, promotes the formation of pores and the merging of small pores. On the other hand, the introduction of borax destroyed the quartz and amorphous glass structure of coal fly ash (Zeng et al., 2019), reduced its melting temperature, and formed more liquid phase to promote the formation of pores. The anorthite

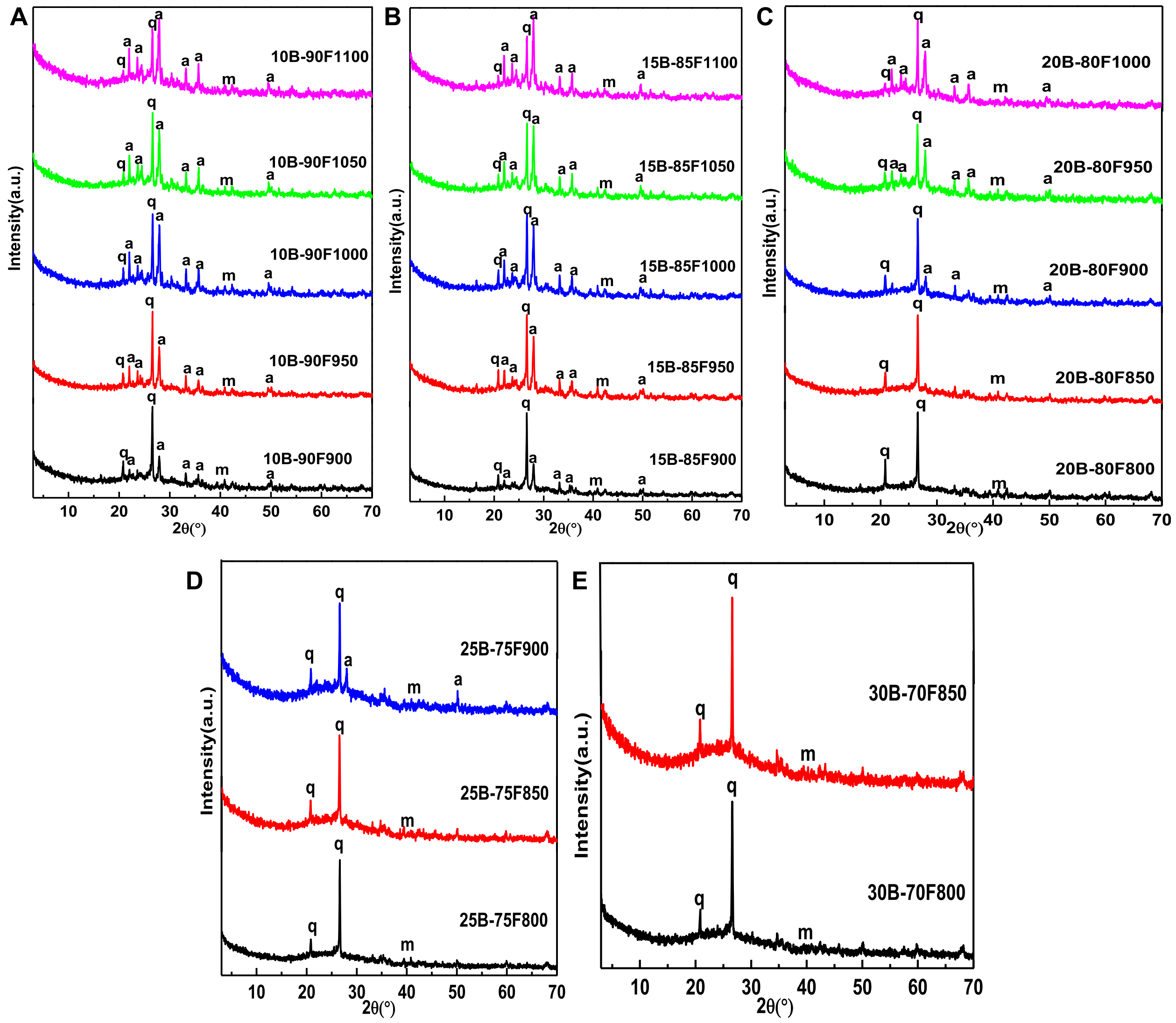

FIGURE 2 | XRD patterns of sintered samples with different borax additions at different temperature (q-quartz, m-mullite, a-anorthite).

precipitated from the molten liquid phase. Therefore, the results are consistent with **Figures 2A,B**, at the same temperature, the amount of anorthite in the sample with the borax additive amount of 15% was higher than that of 10%.

The micromorphology and pore size distribution of the porous samples were shown in **Figures 3K–R**, when the addition amount of borax was 20% and 25%, respectively. It can be seen from the figure that no matter how much borax is added, the average diameter and diameter distribution of the samples increase with the increase of temperature. For example, the average particle size of 20B-80F800 is 71 μm, and the particle size distribution range is 20–280 μm. When the temperature increases to 900°C, the average particle size of 20B-80F900 is 137 μm, and the particle size distribution range is 20–600 μm. As another example, the average particle size of 25B-80F800 is 168 μm, the particle size distribution range is 20-700 μm. The average particle size of 25B-80F850 is 224 μm and the particle size distribution range is 20–800 μm when the temperature increases to 850°C. Interestingly, the average aperture of the 20B-80F1000 is 238 μm and the aperture range is 50–1,000 μm, while the average aperture of the 25B-75F900 is 240 μm and the aperture range is 50–1000 μm. It means that the two have the same liquid phase and the same viscosity at different temperatures and different borax addition. By comparing **Figures 2C,D**, the content of anorthite in 20B-80F1000 is higher than in 25B-75F900, indicating that more liquid phase is provided by coal fly ash in 20B-80F1000, so more anorthite is precipitated out. More liquid phase is provided by borax in 25B-75F900, means increase the amount of borax can decrease the sintering temperature of porous glass-ceramics. So, to obtain porous samples with the same pore size and pore size distribution, borax can be added or sintering temperature can be increased. **Figures 3S,T** show the micromorphology and pore diameter distribution of 30B-70F800 and 30B-70F850. In combination

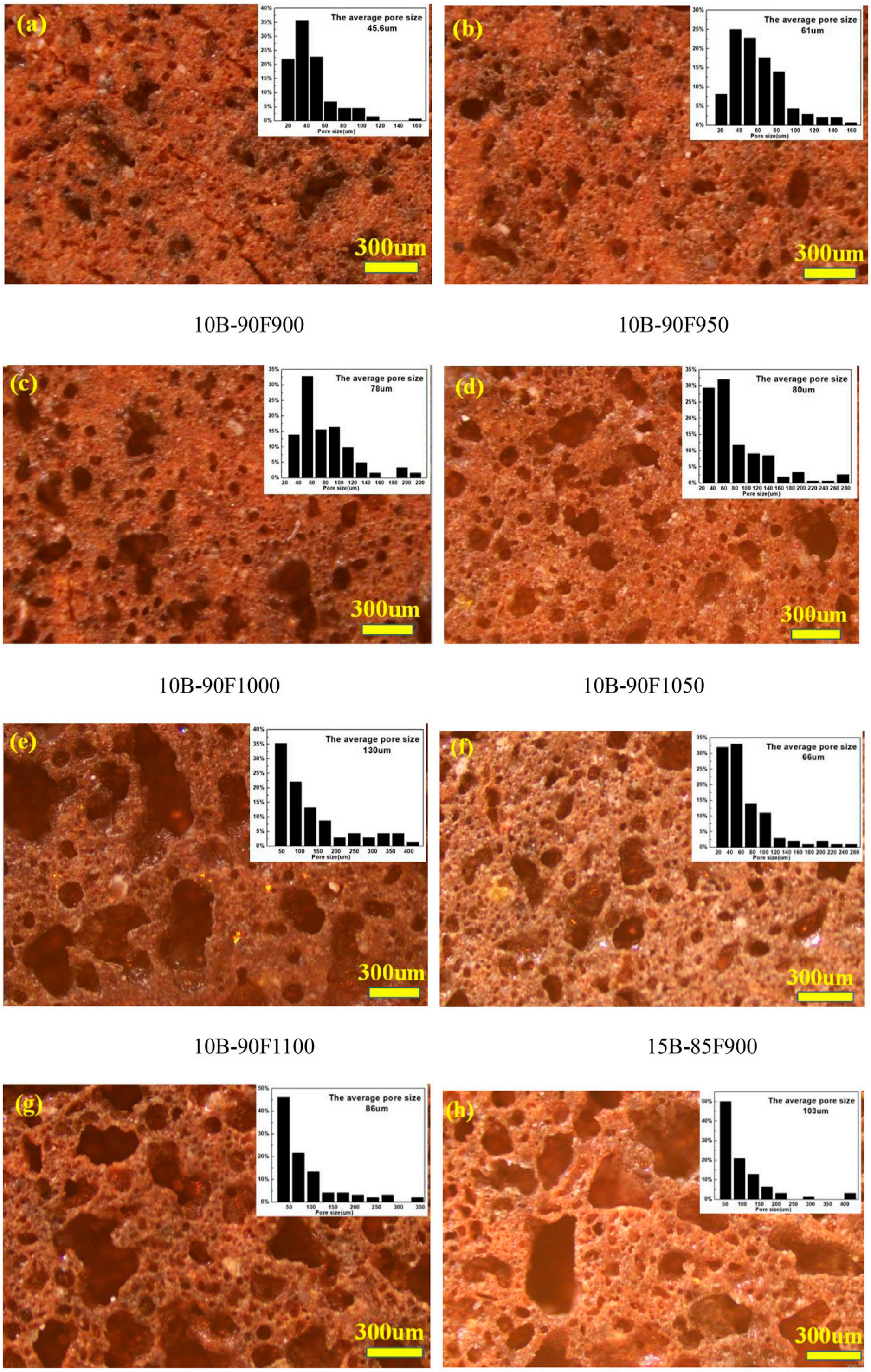

10B-90F900 10B-90F950

10B-90F1000 10B-90F1050

10B-90F1100 15B-85F900

15B-85F950 15B-85F1000

FIGURE 3 | Optical microscopy of sintered samples with different borax additives at different temperatures.

with **Figure 2E**, no anorthite was observed in the sample when the borax addition amount was 30%. Due to the addition amount of borax is large, borax has been completely melted and form a liquid phase to promote the formation of pores before destroy the quartz and amorphous glass structure in coal fly ash. The average pore size of the sample at 850°C has reached 447 μm. In

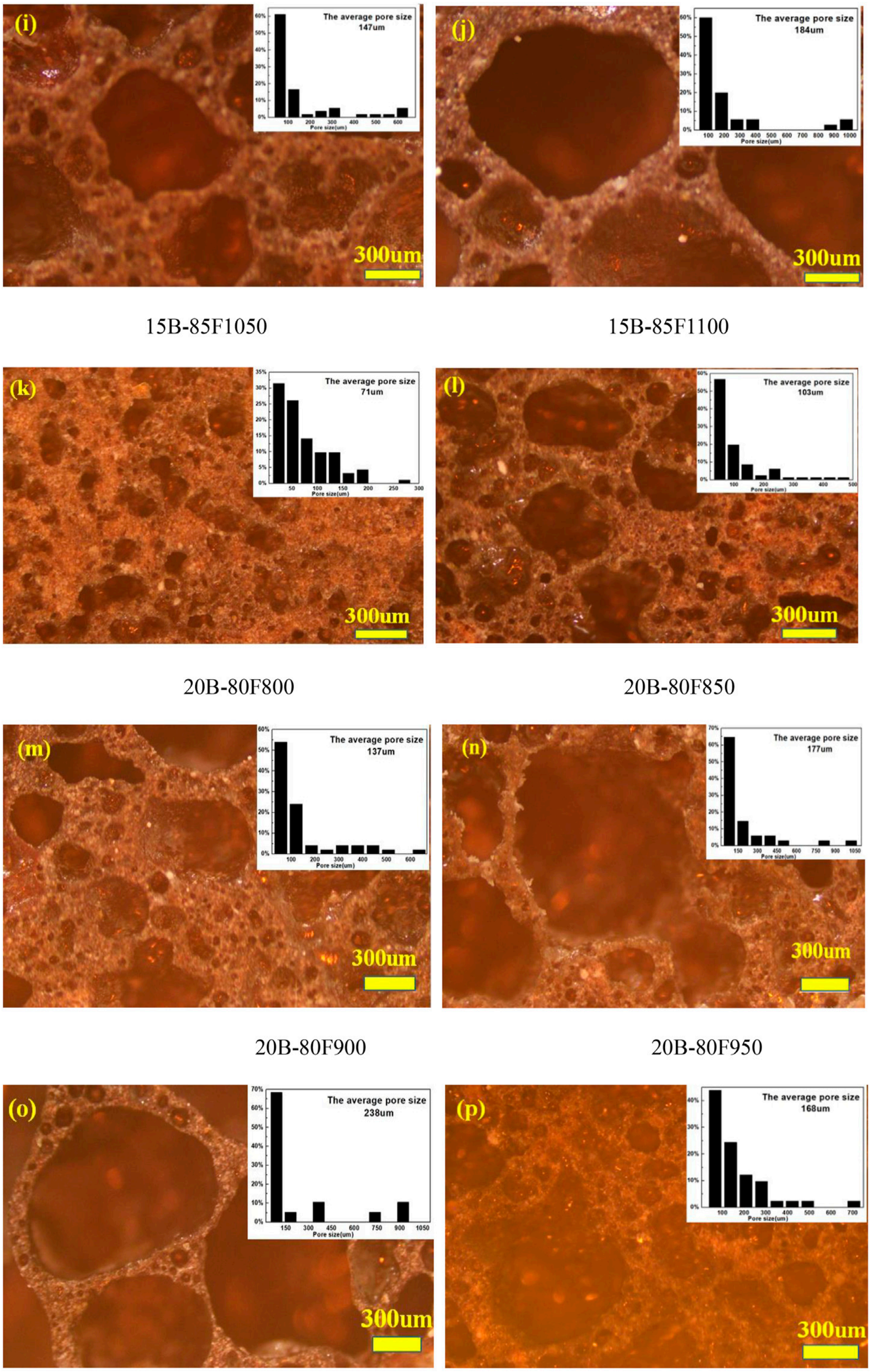

15B-85F1050

15B-85F1100

20B-80F800

20B-80F850

20B-80F900

20B-80F950

20B-80F1000

25B-75F800

FIGURE 3 | (Continued).

conclusion, the addition of borax can increase the high temperature liquid phase, reduce the viscosity and promote the formation of pores. At the same time, it can increase the average pore size and pore size distribution range of porous glass-ceramics, reduce the sintering temperature of porous glass-ceramics, reduce energy consumption.

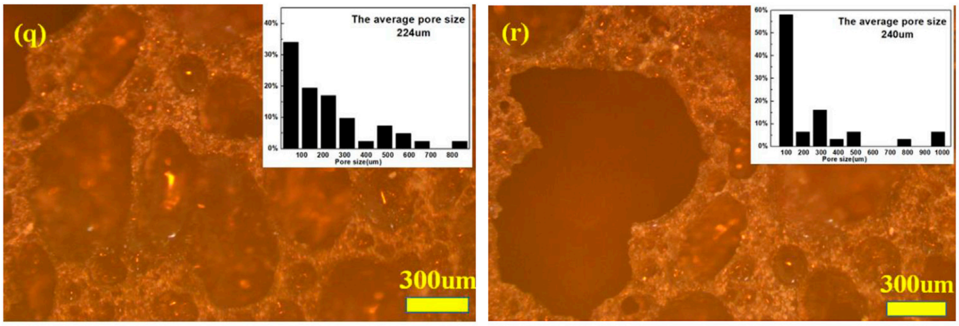

25B-75F850

25B-75F900

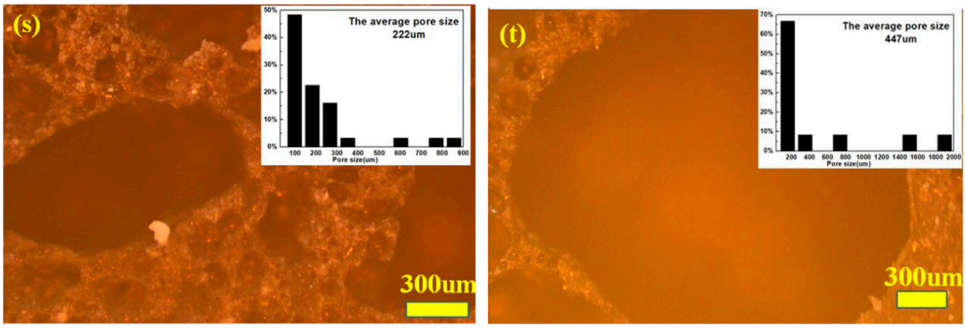

30B-70F800

30B-70F850

FIGURE 3 | (Continued).

Properties

Figure 4 shows the effect of borax addition amount on the performance of porous glass-ceramics, in which 4(1) is bulk density, 2) is true density, 3) is porosity, and 4) is flexural strength. Obviously, the amount of borax has great influence on the bulk density, porosity and flexural strength of porous glass-ceramics, but has little effect on its true density. The main reason is that the true density is not affected by the porosity, but related to the phase. As can be seen from **Figure 2**, although the phases contained in porous glass-ceramics are different, the difference in true density between phases is small, so the addition of borax amount has little impact on the true density of porous glass-ceramics (**Figure 4B**). The bulk density and porosity of porous glass-ceramics are closely related to the viscosity of vitreous. With the increase of borax addition and temperature, the viscosity of vitreous decreases gradually, porosity increases gradually, and bulk density decreases gradually (**Figures 4A,C**). The similar average particle size and the same particle size distribution of 20B-80F1000 and 25B-75F900 in **Figures 3O–R**, meaning that the viscosity of the two high-temperature liquid phases is basically the same. It can be seen that the addition amount of borax and sintering temperature have a great influence on the viscosity of high temperature liquid phase in the preparation process of porous glass-ceramics. Similarly, using the bulk density of 1.0 g/cm^3 as the ordinate plot in **Figure 4A**, showing that in order to get the bulk density of 1.0 g/cm^3 porous glass-ceramics, relatively low sintering temperature of 815°C but high borax content 25% can be used, or a moderate sintering temperature of 925°C and moderate borax content 20% can be selected, or a relatively high temperature of 1,000°C and relative lower borax content 15% can be used. The same trend can be seen in **Figure 4C**. The porosity of porous glass-ceramics sintered at 1,000°C and with borax addition of 15% is the same as that sintered at 925°C and with borax addition of 20%, sintered at 815°C and with borax addition of 25%. It means that the sintering temperature and the amount of borax can adjust the viscosity of the high temperature liquid phase, which has a great influence on the bulk density and porosity of porous glass-ceramics.

The flexural strength of porous glass-ceramics depends on its bulk density and porosity. The larger the bulk density is, the greater the flexural strength is, and the greater the porosity is, the smaller the flexural strength is (Bernardo et al., 2010). It can be seen from **Figure 4D** that, on the whole, with the increase of temperature and borax addition, the flexural strength decreases. As can be seen from the dotted line in **Figure 4D**, when the sintering temperature is 822, 925 and 1,000°C, the amount of borax added is 25%, 20% and 15%, the porous glass-ceramics has the same flexural strength. It means that the flexural strength of porous glass-ceramics is actually affected by the viscosity of high-temperature liquid. Therefore, in the practical application process, the viscosity of high temperature liquid can be adjusted by adjusting the

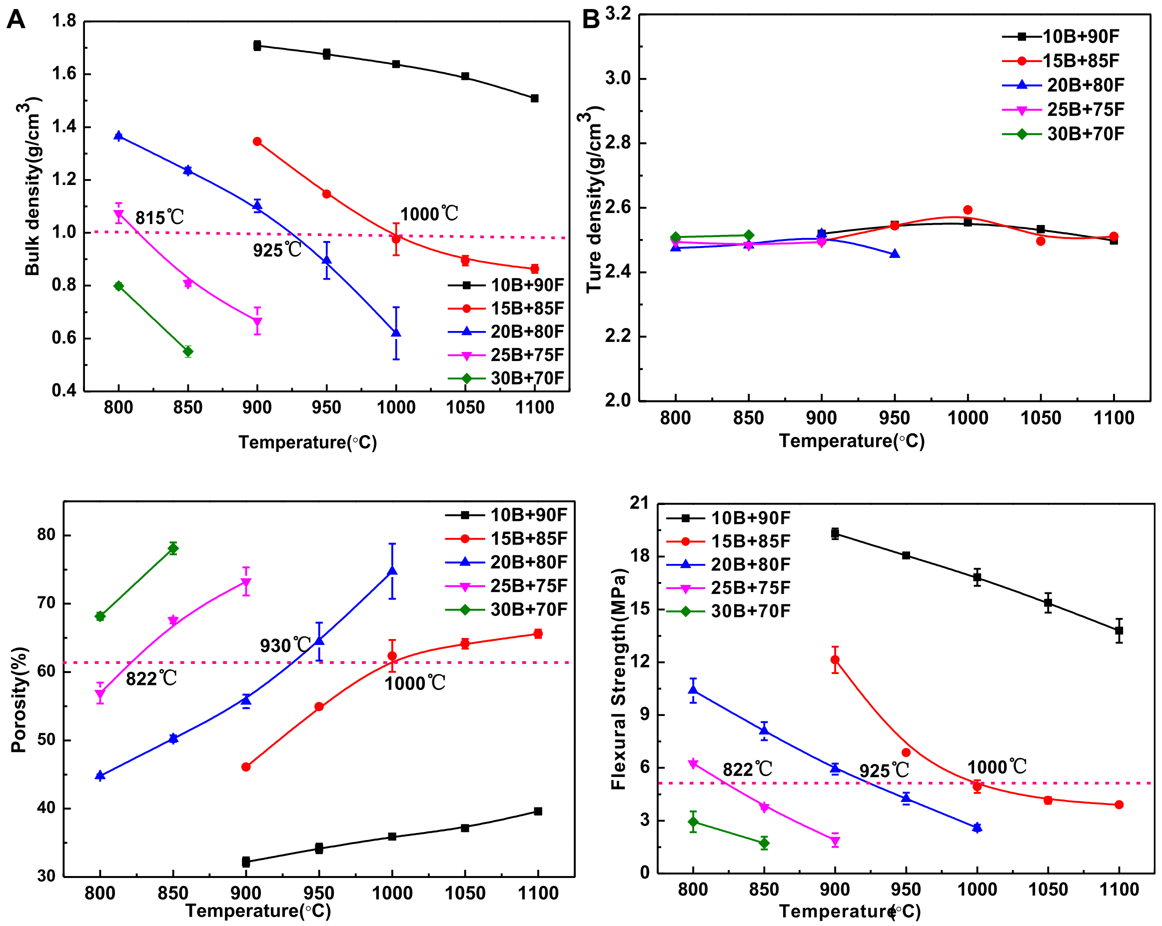

FIGURE 4 | The bulk density **(A)** true density **(B)**, porosity **(C)** and flexural strength **(D)** of porous glass-ceramics with different borax additions vary with temperature.

TABLE 2 | Comparison of properties of porous materials prepared from coal fly ash.

Samples	Raw material	Porosity (%)	Flexural strength (MPa)	Bulk density (g/cm^3)	Compressive strength (MPa)	References
Foam glass ceramic	30% HAFA, 50% Waste glass, 15% clay and 5% Feldspar (2% $CaSO_4$)	—	—	0.98	9.84	Wang et al., 2018
Porous glass-ceramics	55% solid (fly ash:glass-1:1), 27% water glass, 18% dolapix CE 64 (Using polyurethane foam as pore creators)	70	4.5	—	—	Bossert et al., 2004
Foam glass	14.75% fly ash and 84.75% waste glass (0.5% SiC)	81.55	-	0.2672	0.9829	Bai et al. (2014)
Foam glass	50-70% fly ash, 5% Na_2HPO_4, 22.5-37.5% $Na_2B_4O_7$ and 7.5-12.5% $CaCO_3$	52-66.1	1.95-2.59	0.591-0.876	2.09-3.95	Chen et al
Foam glass	20% fly ash and 80% glass (1-5% carbonates)	—	—	0.36-0.41	2.40-2.80	Femandes et al., 2009
Foam ceramics	26.25–40% fly ash, 40–50% red mud, 15–20% sodium borate and 5% sodium silicate	64.14-74.15	2.31-8.52	0.51-0.64	4.04-10.63	Chen et al., 2013
Porous glass-ceramics	70-90% coal fly ash and 10-30% borax	32.2-78.1	1.72-19.29	0.55-1.71	—	This paper

sintering temperature or borax addition, so as to adjust the bulk density, porosity and flexural strength of porous glass-ceramics.

Table 2 compares the properties of porous materials prepared from coal fly ash. After comparison, the amount of coal fly ash used in this experiment is relatively high, ranging from 70% to

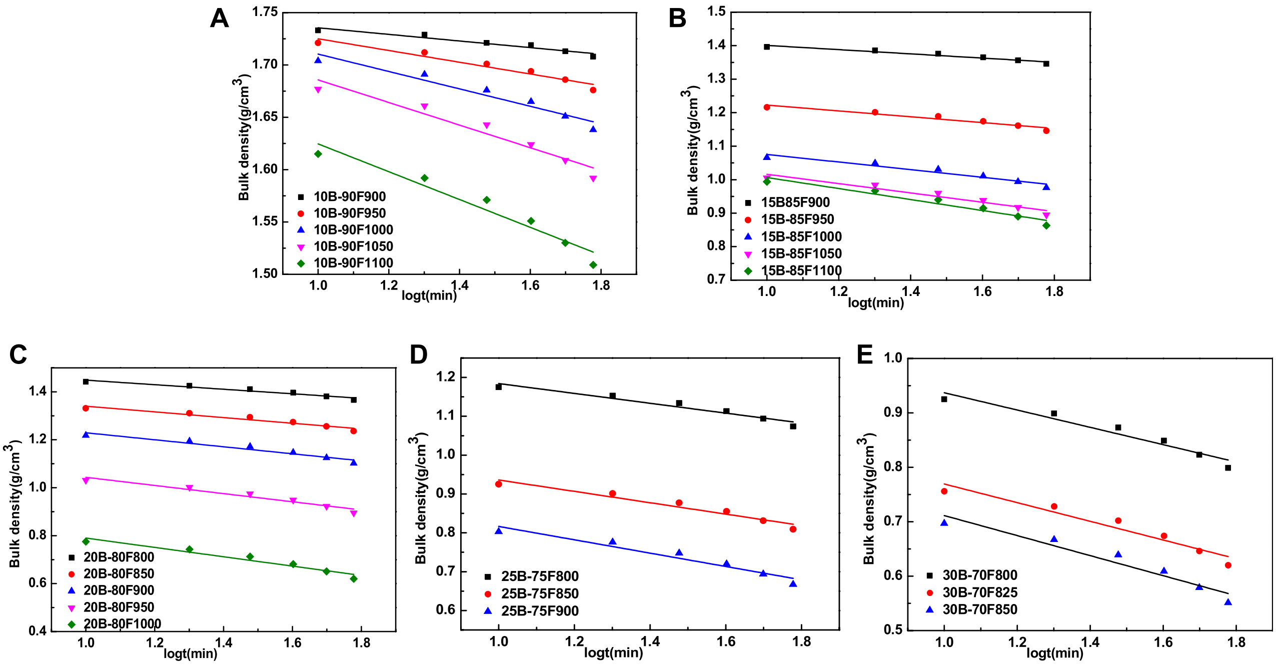

FIGURE 5 | Bulk density (D) vs. log t graph for samples with different borax additions.

90%, with a wide range of porosity, bulk density and flexural strength. The porous materials prepared in this experiment can be adjusted according to their properties of porosity, bulk density and flexural strength. More importantly, the porous materials prepared in this experiment without the pore forming agent, and there was no problem in choosing the amount of the type of pore forming agent.

Sintering Kinetics

According to Kingery's liquid-phase sintering theory, liquid-phase sintering can be divided into three stages: with the increase of sintering temperature, a large number of liquid phase appeared, and the solid particles precipitated from the liquid phase moved and rearranged under the action of capillary force; further rearrangement of grain creep; through liquid phase mass transfer, the grain size and grain shape change constantly, and the rearrangement achieves densification (Luo et al., 2019). In previous experiment, it was found that rise temperature after the sample was densified, the small pores originally existing in the sintered sample would be merged into large pores to form porous structure due to the effect of mass transfer in liquid phase (Zeng et al., 2020). The formation temperature of porous glass-ceramics is between overfiring and softening of the sample, so the sintering activation energy cannot be calculated by the shrinkage rate of the sample with temperature. With the progress of sintering, the porosity of the sample increases and the bulk density decreases. The dynamic empirical formula of ceramic sintering can be used to calculate the activation energy of porous glass-ceramics (**Eq 2**, **3**).

$$D = K\log t + C \tag{2}$$

$$K = A\exp\left(-\frac{Q}{RT}\right) \tag{3}$$

Where, D is the bulk density, C is the characteristic constant of powder, K is the reaction rate constant, T is the sintering time, Q is the sintering activation energy, R is the gas constant, T is the absolute temperature, and A is the constant (Demirkiran et al., 2008; Yürüyen and Toplan, 2009).

Figure 5 is the curve of the logarithm of the bulk density and sintering time of porous glass-ceramics prepared with different borax additions. The bulk density of porous glass-ceramics is linearly correlated with the logarithm of sintering time, which conforms to the dynamic empirical formula of ceramic sintering (2). The relationship between ln (−k) and 1/T was plotted using the reaction rate constant K and sintering temperature T, as shown in **Figure 6**. According to Arrhenius formula, the sintering activation energy of porous glass-ceramics prepared by different borax additives was calculated, as shown in **Table 3**. As can be seen from the correlation factor in **Table 3**, the correlation factor is close to 1, indicating that ln (−k) has a good correlation with 1/T, and Arrhenius formula can be used to calculate the sintering activation energy. The sintering activation energy of porous glass-ceramics decreases with the increase of borax content, from 95.30 kJ/mol to 29.49 kJ/mol. Obviously, more borax is added, lower sintering activation energy is. On the one hand, the addition of borax provides more liquid phase to facilitate liquid phase sintering. On the other hand, the addition of borax provides B-O bond to change the network structure of non-crystalline vitreous of coal fly ash, to reduce its melting temperature, and promote liquid phase sintering.

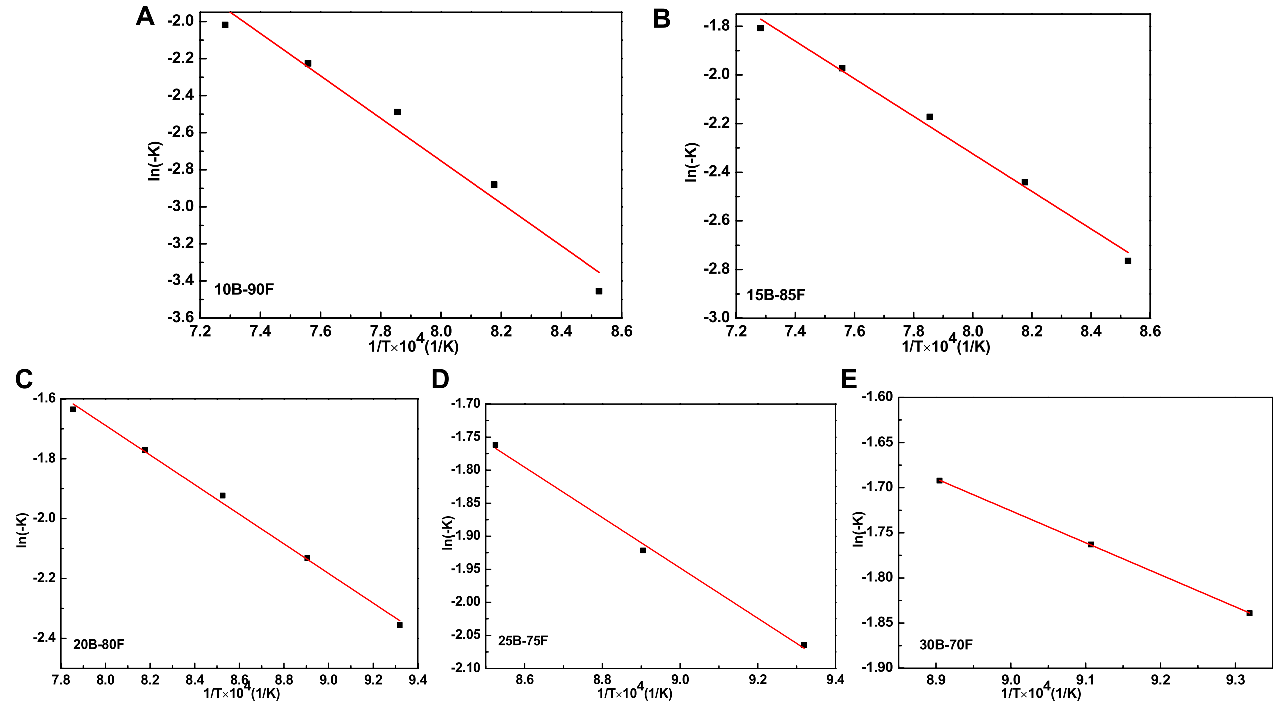

FIGURE 6 | Ln (−k) vs. 1/T graph for samples with different borax additions.

TABLE 3 | Activation energy of sintering samples with different borax additions.

Samples	Borax content (%)	Correlation factor (r)	−Q/R	Activation energy Q (kJ/mol)
10B-10F	10	0.98	11,462.50	95.30
15B-85F	15	0.99	7,715.40	64.15
20B-80F	20	0.99	4,944.10	41.11
25B-75F	25	0.99	3,809.70	31.67
30B-70F	30	0.99	3,547.00	29.49

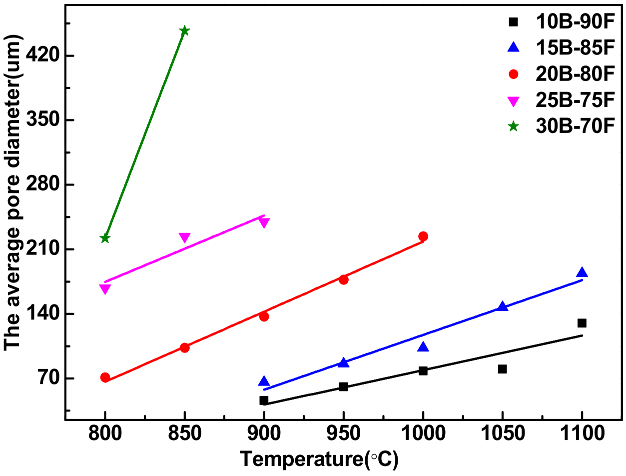

FIGURE 7 | Relationship between average pore diameter of porous galss-ceramics with different borax additions and temperature.

Figure 7 shows the relationship between the average pore diameter and temperature of porous glass-ceramics prepared with different borax additions. With the increase of temperature and borax, the average pore size of porous glass-ceramics increased gradually. It can be seen from the figure that the average aperture has a good linear correlation with the temperature. With the increase of borax addition, the slope of the related line gradually increases. The more borax is added, the more B-O bonds are provided, the more liquid phase is provided, the easier sintering is, and the greater change of average pore diameter is. In other words, with the increase of borax addition, the mass transfer in liquid phase is more obvious, and the process of forming large pores is more affected by temperature. The sintering process of porous glass-ceramics by overfiring can be regarded as the fourth stage after the third stage of glass-ceramics, which is caused by mass transfer in liquid phase and the formation of large pores.

CONCLUSION

In this experiment, the porous glass-ceramics was directly overfired from coal fly ash and borax at low temperature without pore-forming agent. It provides a new possibility for preparing porous glass-ceramics with low energy consumption and high utilization of coal fly ash. The addition of borax has great influence on the phase, morphology and properties of porous glass-ceramics. B-O bond in borax can destroy the structure of quartz and amorphous vitreous body in coal fly ash, reduce its melting temperature and increase the high-temperature liquid phase, thus increasing the content of anorthite. With the increase of borax content from 10% to 15%, the anorthite content in porous glass-ceramics also increases gradually. When the amount of borax increases to 15% and the sintering temperature is 1,100°C (15B-85F1100), the content of anorthite reaches the maximum. Then, with the increase of borax addition, the content of anorthite further decreased. When borax addition was 30% and sintering temperature was 850°C (30B-70F850), the content of anorthite decreased to zero. It shows that although borax can destroy the structure of quartz and amorphous vitreous in coal fly ash to precipitate anorthite, the role of sintering temperature in the preparation of porous glass-ceramics cannot be ignored. The larger the borax addition is, the larger average pore size and porosity of porous glass-ceramics are, the smaller the bulk density and the flexural strength are. The properties of porous glass ceramic can be adjusted by adjusting the sintering temperature or the amount of borax.

The dynamic process of direct overfiring for the preparation of porous glass-ceramics extends to the fourth stage after the three-stage theory of liquid phase sintering. That is, with the increase of temperature, the small pores remaining in the compact stage are merged into large pores due to the mass transfer effect of liquid phase. With the increase of borax, the sintering activation energy of porous glass ceramics decreased obviously. On the one hand, the addition of borax provides more liquid phase to facilitate liquid phase sintering. On the other hand, the addition of borax provides B-O bond to change the network structure of non-crystalline vitreous of fly ash, to reduce its melting temperature and promote liquid phase sintering.

DATA AVAILABILITY STATEMENT

The original contributions presented in the study are included in the article/Supplementary Material, further inquiries can be directed to the corresponding author.

AUTHOR CONTRIBUTIONS

HS designed the research. LZ conceived the experiments and analysed the results with the help of HS and TP. LZ drafted the manuscript.

FUNDING

This work was financially supported by the Youth fund project of Chengdu University (2018XZB16).

REFERENCES

Bai, J., Yang, X., Xu, S., Jing, W., and Yang, J. (2014). Preparation of Foam Glass from Waste Glass and Fly Ash. *Mater. Lett.* 136, 52–54. doi:10.1016/j.matlet.2014.07.028

Bernardo, E., and Albertini, F. (2006). Glass Foams from Dismantled Cathode ray Tubes. *Ceramics Int.* 32 (6), 603–608. doi:10.1016/j.ceramint.2005.04.019

Bernardo, E., De Lazzari, M., Colombo, P., Llaudis, A. S., and Garcìa-Ten, F. J. (2010). Lightweight Porcelain Stoneware by Engineered CeO2Addition. *Adv. Eng. Mater.* 12, 65–70. doi:10.1002/adem.200900280

Chen, B., Wang, K., Chen, X., and Lu, A. (2012). Study of Foam Glass with High Content of Fly Ash Using Calcium Carbonate as Foaming Agent. *Mater. Lett.* 79, 263–265. doi:10.1016/j.matlet.2012.04.052

Chen, C., Feng, K., Shi, H., Xiao, Y., and Zhou, H. (2016). Effect of Heat Treatment Holding Time on Preparation of Foam Glass-Ceramics from High Titanium Blast Furnace Slag. *Trans. Mater. Heat Treat.* 37 (4), 32–36. doi:10.13289/j.issn.1009-6264.2016.04.007

Chen, F., Zhang, W., and Liu, S. (2020). Porous Glass-Ceramics Derived from MgO-CuO-TiO2-P2o5 Glasses with Different Additions of Fe2O3. *Ceramics Int.* 46, 6560–6566. doi:10.1016/j.ceramint.2019.11.140

Chen, X., Lu, A., and Qu, G. (2013). Preparation and Characterization of Foam Ceramics from Red Mud and Fly Ash Using Sodium Silicate as Foaming Agent. *Ceramics Int.* 39 (2), 1923–1929. doi:10.1016/j.ceramint.2012.08.042

Demirkiran, A. Ş., Artir, R., and Avci, E. (2008). Effect of Natural Zeolite Addition on Sintering Kinetics of Porcelain Bodies. *J. Mater. Process. Tech.* 203, 465–470. doi:10.1016/j.jmatprotec.2007.10.053

Ding, L., Ning, W., Wang, Q., Shi, D., and Luo, L. (2015). Preparation and Characterization of Glass-Ceramic Foams from Blast Furnace Slag and Waste Glass. *Mater. Lett.* 141 (15), 327–329. doi:10.1016/j.matlet.2014.11.122

Dong, Y., Feng, X., Feng, X., Ding, Y., Liu, X., and Meng, G. (2008). Preparation of Low-Cost Mullite Ceramics from Natural bauxite and Industrial Waste Fly Ash. *J. Alloys Compd.* 460 (1), 599–606. doi:10.1016/j.jallcom.2007.06.023

Dong, Y., Zhou, J.-e., Lin, B., Wang, Y., Wang, S., Miao, L., et al. (2009). Reaction-sintered Porous mineral-based Mullite Ceramic Membrane Supports Made from Recycled Materials. *J. Hazard. Mater.* 172172 (11), 180180–186186. doi:10.1016/j.jhazmat.2009.06.148

Fernandes, H. R., Gaddam, A., Tulyaganov, D. U., and Ferreira, J. M. F. (2020). Design and Synthesis of Foam Glasses from Recycled Materials. *Int. J. Appl. Ceram. Technol.* 17 (1), 64–74. doi:10.1111/ijac.13393

Fernandes, H. R., Tulyaganov, D. U., and Ferreira, J. M. F. (2009). Preparation and Characterization of Foams from Sheet Glass and Fly Ash Using Carbonates as Foaming Agents. *Ceramics Int.* 35 (1), 229–235. doi:10.1016/j.ceramint.2007.10.019

Flesoura, G., Monich, P. R., Murillo Alarcón, R., Desideri, D., Bernardo, E., Vleugels, J., et al. (2021). Porous Glass-Ceramics Made from Microwave Vitrified Municipal Solid Waste Incinerator Bottom Ash. *Construction Building Mater.* 270, 121452. doi:10.1016/j.conbuildmat.2020.121452

Guo, Y. X., Zhang, Y. H., Huang, H. W., and Hu, P. (2014). Effect of Heat Treatment Process on the Preparation of Foamed Glass Ceramic from Red Mud and Fly Ash. *Amm* 670-671, 201–204. doi:10.4028/www.scientific.net/amm.670-671.201

Hisham, N. A. N., Zaid, M. H. M., Saparuddin, D. I., Aziz, S. H. A., Muhammad, F. D., Honda, S., et al. (2020). Crystal Growth and Mechanical Properties of Porous Glass-Ceramics Derived from Waste Soda-Lime-Silica Glass and Clam Shells. *J. Mater. Res. Tech.* 9 (4), 9295–9298. doi:10.1016/j.jmrt.2020.06.009

Hou, L.-j., Liu, T.-y., and Lu, A.-x. (2017). Red Mud and Fly Ash-Based Ceramic Foams Using Starch and Manganese Dioxide as Foaming Agent. *Trans. Nonferrous Met. Soc. China* 27 (3), 591–598. doi:10.1016/S1003-6326(17)60066-9

Jiang, L., Lu, J., Cao, J., and Wang, Z. (2017). Structure and Properties of Porous Glass-Ceramics Sintered from Metallurgical Silicon Slag. *Trans. Mater. Heat Treat.* 38 (10), 6–11. doi:10.13289/j.issn.1009-6264.2017-0210

Li, J., Zhuang, X., Monfort, E., Querol, X., Llaudis, A. S., Font, O., et al. (2018). Utilization of Coal Fly Ash from a Chinese Power Plant for Manufacturing Highly Insulating Foam Glass: Implications of Physical, Mechanical Properties and Environmental Features. *Construction Building Mater.* 175 (30), 64–76. doi:10.1016/j.conbuildmat.2018.04.158

Lin, B., Li, S., Hou, X., and Li, H. (2015). Preparation of High Performance Mullite Ceramics from High-Aluminum Fly Ash by an Effective Method. *J. Alloys Compd.* 623, 359–361. doi:10.1016/j.jallcom.2014.11.023

Luo, Y., Wu, Y., Xiao, D., Tang, K., Huang, C., Fu, R. K. Y., et al. (2019). Al2O3 Coating for Densification of SiC Ceramics and Sintering Kinetics. *Surf. Coat. Tech.* 374, 603–609. doi:10.1016/j.surfcoat.2019.06.040

Wang, D., Huang, W., and Zhou, N. (2003a). Thermodynamic Analysis on the Post-crystallization for Calcium Titanium Phosphate Glass Ceramics. *J. Inorg. Mater.* 18 (6), 1169–1176. doi:10.3321/j.issn:1000-324X.2003.06.004

Wang, D., Huang, W., Zhou, N., Zhou, L., and Xue, Z. (2003b). Preparation of Porous Na_2O-TiO_2-P_2o_5-CaO Glass-Ceramics for Carrier. *J. building Mater.* 6 (1), 45–49. doi:10.3969/j.issn.1007-9629.2003.01.009

Wang, H., Chen, Z., Ji, R., Liu, L., and Wang, X. (2018). Integrated Utilization of High Alumina Fly Ash for Synthesis of Foam Glass Ceramic. *Ceramics Int.* 44 (12), 13681–13688. doi:10.1016/j.ceramint.2018.04.207

Wu, J. P., Boccaccini, A. R., Lee, P. D., Kershaw, M. J., and Rawlings, R. D. (2006). Glass Ceramic Foams from Coal Ash and Waste Glass: Production and Characterisation. *Adv. Appl. Ceramics* 105 (1), 32–39. doi:10.1179/174367606X81632

Yio, M. H. N., Xiao, Y., Ji, R., Russell, M., and Cheeseman, C. (2021). Production of Foamed Glass-Ceramics Using Furnace Bottom Ash and Glass. *Ceramics Int.* 47, 8697–8706. doi:10.1016/j.ceramint.2020.11.103

Yürüyen, S., and Toplan, H. Ö. (2009). The Sintering Kinetics of Porcelain Bodies Made from Waste Glass and Fly Ash. *Ceramics Int.* 35, 2427–2433. doi:10.1016/j.ceramint.2009.02.005

Zeng, L., Sun, H.-j., Peng, T.-j., and Zheng, W.-m. (2019). The Sintering Kinetics and Properties of Sintered Glass-Ceramics from Coal Fly Ash of Different Particle Size. *Results Phys.* 15, 102774. doi:10.1016/j.rinp.2019.102774

Zeng, L., Sun, H., Peng, T., and Zheng, W. (2020). Preparation of Porous Glass-Ceramics from Coal Fly Ash and Asbestos Tailings by High-Temperature Pore-Forming. *Waste Manage.* 106, 184–192. doi:10.1016/j.wasman.2020.03.008

Zeng, Q., Chang, S., Wang, M., Li, M., Deng, Q., Xiong, Z., et al. (2021). Highly-active, Metal-free, Carbon-Based ORR Cathode for Efficient Organics Removal and Electricity Generation in a PFC System. *Chin. Chem. Lett.* 32, 2212–2216. doi:10.1016/j.cclet.2020.12.062

Zheng, W. M., Sun, H. J., Peng, T. J., and Zeng, L. (2020). Novel Preparation of Foamed Glass-Ceramics from Asbestos Tailings and Waste Glass by Self-Expansion in High Temperature. *J. Non-Crystalline Sol.* 529, 119767. doi:10.1016/j.jnoncrysol.2019.119767

Zhu, K., Lu, L., Ying, C., and Zhang, Y. (2012). Effect of Heat Treatment of the Performance of Porous Micro-crystalline Glass. *China Ceramics* 48 (4), 47–49. doi:10.16521/j.cnki.issn.1001-9642.2012.04.026

Zhu, M., Ji, R., Li, Z., Wang, H., Liu, L., and Zhang, Z. (2016). Preparation of Glass Ceramic Foams for thermal Insulation Applications from Coal Fly Ash and Waste Glass. *Construction Building Mater.* 112, 398–405. doi:10.1016/j.conbuildmat.2016.02.183

Conflict of Interest: The authors declare that the research was conducted in the absence of any commercial or financial relationships that could be construed as a potential conflict of interest.

frontiers in Chemistry

REVIEW
published: 23 March 2022
doi: 10.3389/fchem.2022.884398

Roles of Surfactants in Oriented Immobilization of Cellulase on Nanocarriers and Multiphase Hydrolysis System

Zhiquan Wang [1,2,3], *Chunzhen Fan* [1,2,3], *Xiangyong Zheng* [1,2,3]*, *Zhan Jin* [1,2,3], *Ke Bei* [1,2,3], *Min Zhao* [1,2,3] *and Hainan Kong* [4]

[1]School of Life and Environmental Science, Wenzhou University, Wenzhou, China, [2]State and Local Joint Engineering Research Center for Ecological Treatment Technology of Urban Water Pollution, Wenzhou, China, [3]Zhejiang Provincial Key Lab for Water Environment and Marine Biological Resources Protection, Wenzhou, China, [4]School of Environmental Science and Engineering, Shanghai Jiao Tong University, Shanghai, China

Surfactants, especially non-ionic surfactants, play an important role in the preparation of nanocarriers and can also promote the enzymatic hydrolysis of lignocellulose. A broad overview of the current status of surfactants on the immobilization of cellulase is provided in this review. In addition, the restricting factors in cellulase immobilization in the complex multiphase hydrolysis system are discussed, including the carrier structure characteristics, solid-solid contact obstacles, external diffusion resistance, limited recycling frequency, and nonproductive combination of enzyme active centers. Furthermore, promising prospects of cellulase-oriented immobilization are proposed, including the hydrophilic-hydrophobic interaction of surfactants and cellulase in the oil-water reaction system, the reversed micelle system of surfactants, and the possible oriented immobilization mechanism.

Keywords: cellulase, surfactants, nanocarriers, reversed micelle system, oriented immobilization

Edited by:
Qingyi Zeng,
University of South China, China

Reviewed by:
Ye Du,
Sichuan University, China
Linsen Li,
Hebei University, China

Correspondence:
Xiangyong Zheng
x.zheng@wzu.edu.cn

Specialty section:
This article was submitted to
Inorganic Chemistry,
a section of the journal
Frontiers in Chemistry

Received: *26 February 2022*
Accepted: *09 March 2022*
Published: *23 March 2022*

Citation:
Wang Z, Fan C, Zheng X, Jin Z, Bei K, Zhao M and Kong H (2022) Roles of Surfactants in Oriented Immobilization of Cellulase on Nanocarriers and Multiphase Hydrolysis System. Front. Chem. 10:884398. doi: 10.3389/fchem.2022.884398

INTRODUCTION

Bioethanol, as a renewable, economically affordable, and environmentally safe energy material, will gradually become a substitute for fossil fuels. It has far-reaching research significance and application value for the development of a sustainable energy strategy (Karimi et al., 2021; Zeng et al., 2021; Ziaei-Rad et al., 2021; Suhartini et al., 2022). Due to competition with food supply in the first generation of bioethanol production, lignocellulose, a non-starch material, has become an important raw material for bioethanol production (Alonso et al., 2019; Maia et al., 2020; Winarni et al., 2020). Adsorption of cellulases onto lignin has been considered as the major factor in retarding enzymatic cellulose degradation of lignocellulosic biomass (Djajadi et al., 2018). Hydrophobic interaction, electrostatic interaction and hydrogen bonding have been regarded as the cause of the nonproductive binding of cellulases to lignin (Djajadi et al., 2018; Li et al., 2020; Song et al., 2020). A natural "biodegradable barrier" of lignin cell walls which are connected in a strong, yet resilient network under the action of covalent and non-covalent bonds render the cellulose inaccessible (Mnich et al., 2020; Chu et al., 2021). Therefore, to reduce the recalcitrance of lignocellulosic biomass to biochemical degradation, pretreatment methods have been developed to break down the lignin-hemicellulose-cellulose matrix and increase the enzyme accessibility of the cellulose scaffold (Jiang et al., 2017a; Jia et al., 2018; Rocha-Martin et al., 2018).

TABLE 1 | The characteristics of various immobilization method of enzymes.

Methods		Mechanisms	Characteristics	References
Adsorption	Physical	Adsorbed on the carriers	Active center of the enzyme is not easy to be destroyed, and not obvious structure change occurs	Gao et al. (2009)
	Ionic	Combined with water-insoluble carrier containing ion-exchange group by electrostatic force	Structure and amino acids of the active center rarely change, and the higher activity immobilized enzyme can be obtained	Sui et al. (2015)
Encapsulation		Mixed with polymer monomer and further embedded in the polymer	It is not necessary to combine with amino acid residues of enzyme protein, and rarely change the spatial conformation of enzyme	Singh et al. (2020)
Covalent binding		Covalently bonded to the water-insoluble carrier	Enzyme molecules are firmly connected with the carrier, the structure of the enzyme protein is often changed, resulting in the damage of the active center of the enzyme	Ghasemi et al. (2021)
Cross-linking		Bifunctional reagent or multifunctional reagent is used to form covalent bond between enzyme molecules	Combined with adsorption or encapsulation method, the activity of immobilized enzyme can be increased and the reinforcement effect can be achieved	Ouyang et al. (2020)
Cross-linked enzyme aggregates (CLEAs)		Covalently bound by cross-linking agent to keep the supramolecular structure and activity	Carrier free immobilization, good stability, low cost, large activity per unit volume, and high space efficiency	Xu et al. (2020)
Co-immobilization		Different enzymes are immobilized in the same carrier at the same time	Several kinds of enzymes and cells with different functions work together in the same system	Qiu et al. (2021)
Oriented immobilization		Specific site of enzyme connects with carrier and the active site faces outsid	It is beneficial for the substrates to enter into the active site of the enzyme and can significantly improve the activity of the immobilized enzyme	Zhou et al. (2021)

In general, lignin-derived inhibition is the major physical obstacle restricting the enzymatic hydrolysis of cell wall polysaccharides (Leonidas et al., 2019; Zheng et al., 2021). More importantly, the non-specific binding of free cellulase on lignocellulosic substrates may account for the low rate of hydrolysis at the action mechanism level during enzymatic hydrolysis. Some enzymes remain free after the enzymatic hydrolysis of lignocellulosic substrates, while non-specific binding to the residual substrates also prevents the efficient recycling of cellulase (Rahikainen et al., 2011; Kellock et al., 2017; Bhawna et al., 2020). Moreover, the utility of cellulases has been limited due to their low operational stability, high costs, and poor reutilization when used in the native form (Yang et al., 2017).

To overcome these barriers, immobilization is usually used to improve enzyme stability and even activity or selectivity when properly designed, which can also facilitate the reuse of enzymes and effective cost of catalytic processes (Mita and Eldin, 2014; Li et al., 2016; Mehta et al., 2016; Xu et al., 2016; Zhang et al., 2016). The characteristics of various immobilization methods of enzymes is summarized in **Table 1**. Cellulases represent a large group of enzymes from various organism and with different substrate specificity, biophysical properties, etc. The immobilization behavior is different depending on the enzyme or enzyme mixture investigated. During the immobilization process of cellulase, the structure and properties of carrier materials have significant effects on the performance of the immobilized enzyme (Kalantari et al., 2013; Li et al., 2018). The size of the carriers plays an important role in determining the activity of the immobilized enzyme owing to the inverse relationship between the carrier size and enzyme loading. Thus, large carrier size decreases enzyme activity in general (Valencia et al., 2010), and a reduction in the size of the carriers results in a higher surface area for enzyme binding (Malar et al., 2018; Malar et al., 2020). For the immobilization of cellulase, the smaller size of the surface pore should be kept lower than that of the cellulase macromolecule (6–20 nm), which can further reduce the internal and external diffusion resistance in the heterogeneous system (DiCosimo et al., 2013; Santos et al., 2015). Therefore, nanocarriers are widely used in the immobilization of enzymes because of their unique properties, such as large specific surface area to volume ratio (Cao et al., 2016; Roth et al., 2016; Malar et al., 2020).

Moreover, the immobilization of cellulase has been achieved based on physical adsorption, covalent binding, or affinity interactions (Zang et al., 2014; Hosseini et al., 2018; Zhang and Hay, 2019), including carrier-binding, microemulsion-based organo-gels (MBGs), ultrasonic encapsulation, crosslinking, entrapment, glutathione-labeling, and chelation (Mroczkiewicz et al., 2012; Nicoletti et al., 2015). However, enzymes often display drastically lower activity in organic solvents than in water, and the water layer on the molecular surface of enzymes determines their activity in organic media (Zhang et al., 2012). Therefore, among several approaches to resolve the challenges, one of the most effective methods is immobilization of the enzymes within an aqueous microenvironment in the organic solvents. Microemulsions formed by amphiphilic surfactants have been widely reviewed as effective media for the immobilization of enzymes in hydrophobic solvents (Itabaiana et al., 2014; Rajnish et al., 2021; Savic et al., 2021). The MBGs method based on microemulsions has been used to form matrices for enzyme immobilization to achieve enzymatic catalysis in nonconventional medium as they appear to be rigid and stable for a long time, even within the reaction solution (Zhang et al., 2012). Therefore, the MBGs method has unique advantages of improving the chemical stability of immobilized enzymes and maintaining high catalytic activity (Pavlidis et al., 2010; Itabaiana

TABLE 2 | Applications of surfactants in preparing nanomaterials.

Applications	Types	Characteristics	References
Nanomaterials	Metallic nanoparticles	It is usually prepared in the reversed micelles and microemulsions system	Kawasaki, (2013)
	Semiconductor nanoparticles	It is prepared in the reversed microemulsions system, including the oxides, sulfides, and selenides etc.	Anjum et al. (2019)
	Organic nanoparticles	It includes organic drug nanoparticles and polymer nanoparticles, which can be prepared in microemulsions system	(Li, Kawakami, and Hiramatsu, 2003)
	Nanowires	It can be prepared by the templates from micelles, liquid crystals, vesicles formed by the surfactants	Xu et al. (2010)
	Porous nano-materials	Surfactants can be the structure directing agent of mesoporous materials	Carrillo et al. (2011)
	Nano-films	It mainly includes Langrnuir-Blodgett (LB) film and Molecular-Deposition (MD) film	Shil et al. (2017); Lai et al. (2020)
	Nanocomposites	Organic polymer was encapsulated on inorganic nanoparticles in inverse microemulsion system	Al-Shemmari et al. (2014)
Methods	Template-directed synthesis	The electrostatic attraction, hydrogen bond and Van der Waals force between surfactant molecules and nano materials are used for the formation of special micelle structures, which can further used as the synthesis templates of nano materials	Xu et al. (2010); Kayhomayun et al. (2020)
	Microemlusion method	When the amount of surfactant and polar organic matter is large, the microemulsion can be obtained, which can be used as a microreactor for synthesizing nanomaterials	Anjum et al. (2019); Cui et al. (2019)
	Hydrothermal synthesis	Surfactants are mainly used as auxiliary materials	Cui et al. (2019)
	Sol-gel method	The transparent sol is formed by hydrolysis and condensation reaction, and gradually gelatinization. After drying and heat treatment, nanomaterials can be obtained	Hassanzadeh-Tabrizi et al. (2016)
Surface modification	Physical and chemical properties	Surface adsorption and chemical reactivity of surfactants can modify the surface of nanoparticles	Chaudhary et al. (2014)
	Interfacial modification of nanofilms	Hydrophilicity or lipophilicity of surfactants can be used to modify the interface of nanofilms	Kovalchuk, (2015)
Effects	Dispersion of nanoparticles in media	Prevent particle agglomeration	Fiorati et al. (2021)
	Functional effects on nanoparticles	Improve the compatibility and affinity between polymer materials and inorganic materials	You et al. (2019)

et al., 2014). It is clearly that the surfactants play an important role in the preparation of nanomaterials (Lou et al., 2017; Bao et al., 2019; Ortiz-Martínez et al., 2019; Alexander et al., 2020).

The surfactants have been widely used for the preparation of nanocarriers as shown in **Table 2**, forming the nano-template by micelles and emulsions of surfactants is a common method that can greatly reduce the surface tension of the solvent and change the interface composition and structure (Carter and Puig-Sellart, 2016; Bao et al., 2019). Desirable nanostructured materials can be produced because of the special nanoreactors formed by surfactant micelles and the oriented alignment characteristics of surfactants in solution, such as the Langmuir-Blodgett (LB) membranes and liposomes (Lok Kumar et al., 2014; Gutierrez et al., 2016). Furthermore, the non-ionic surfactants can significantly enhance cellulose hydrolysis, thus reducing enzyme loading (Lou et al., 2017; Bao et al., 2019). However, inhibitory effects have been observed with the addition of amphoteric, anionic, and cationic surfactants (Lou et al., 2017; Bao et al., 2019). Moreover, the loss of enzyme activity during immobilization is a notable problem; the structural distortion caused by the strong enzyme-support interactions may produce steric hindrances and catalytic cleft blockage (Carlsson et al., 2014; Suárez et al., 2018). Although a large dose of original cellulase is added for a higher load of immobilized enzyme to improve the activities of the immobilized enzyme, no significant improvement in enzymatic activity has been observed due to the random and inhomogeneous combination of the nanocarriers and cellulase molecules (Nakayama et al., 2009). Oriented immobilization, as a specific binding method, can effectively prevent the nonproductive combination of enzymes and nanocarriers, which further improves the immobilization and hydrolysis efficiency. The reversed micelles formed by surfactants have been successfully used in the preparation of oriented-immobilized lipase when their concentration exceeds the critical micelle concentration (CMC) (Fan et al., 2016). To date, few studies have reported the oriented immobilization of cellulase. Therefore, this review mainly focuses on the important roles of surfactants in the immobilization of cellulase, mainly including the preparation of nanocarriers and cellulase hydrolysis. Moreover, a novel insight into the oriented immobilization of cellulase in a surfactant reversed micelle (SRM) system was discussed and found to have promising prospects.

EFFECTS OF SURFACTANTS ON NANOCARRIERS

Preparation of Nanocarriers Based on Surfactants

The basic physical and chemical properties of surfactants, such as micelle formation, dispersing, emulsifying, and solubilizing, have made them widely useful in the field of nanotechnology (Yang et al., 2017). Several ordered aggregations formed by the surfactants are used as nano-templates for the preparation of nanocarriers, such as micelles and reversed micelles. The process can greatly reduce the surface tension of the solvent and change the interface composition and structure (Bao et al., 2019). For the preparation of nanocarriers, surfactant micelles are the microreactors of nanocarriers during the preparation process, and the morphology of microreactors is controllable because of the amphiphilic characteristics of surfactants, which have been used for the preparation of desirable nanostructured carriers (Yiamsawas et al., 2017). For instance, hydrophilic surfactants are often used for the preparation of spherical nanocarriers because of their dispersibility in water (Luan and Ramos, 2010). Similarly, the reversed micelles of surfactants can effectively define the particle size and reaction microenvironment in the water, providing a nanoscale reaction space. It has been widely used because the aggregates self-assembled by surfactant molecules can be used to synthesize ordered mesoporous materials with a simpler operation and more uniform channel distribution (Bao et al., 2017; Bao et al., 2019).

Surface Modification of Nanocarriers in the Surfactant System

Surfactants can also change the surface properties of nanocarriers, such as their morphology, magnetic properties, dispersion, and catalytic performances (Asghar et al., 2016; Wei et al., 2018; Lopes et al., 2019; Alexander et al., 2020). This modification may result in a new structure with new surface activity due to the combination of hydrophilic groups of surfactants and surface groups of nanocarriers. For example, the use of surfactants of decylamine and cetyltrimethylammonium bromide can provide an easy and effective way to change the functionality of cellulose nanocrystals with a hydrophobic polylactic acid matrix and to evaluate the effects of surface chemistry on the reinforcement mechanisms (Orellana et al., 2018). Meanwhile, the presence of surfactants can make nanocarriers more difficult to re-agglomerate by reducing the surface energy and form a steric hindrance effect (Wang M. et al., 2013; Tan et al., 2019), the surfactants are coated on the surface of the nanocarriers to form a space barrier layer, the hydrophilic group faces outward and the hydrophobic group faces inward, so that the agglomeration of the particles is avoided.

EFFECTS OF NANOCARRIERS ON IMMOBILIZATION OF CELLULASE

The structure and properties of carrier materials have great influence on the properties of immobilized cellulase, such as internal geometry (e.g., flat surfaces or thin fibers), specific surface area, superficial activation degree, mechanical resistance, and pore diameter (Santos et al., 2015; Begum et al., 2019; Malar et al., 2020). Meanwhile, partitioning and mass transport limitations may yield spatial variations in local reaction rates in porous materials (Neira and Herr, 2017). Therefore, to improve the stability and catalytic activity of immobilized cellulase, various materials, such as chitin, chitosan, nylon, and polyvinyl alcohol, have been widely used as carriers (Cherian et al., 2015; Priydarshani et al., 2018).

The physical effects of nanocarriers on immobilized cellulase are as follows: 1) The pore size and effective surface area of the nanocarriers. Not all porous carriers can be used for immobilization of cellulase due to the limitation of pore size, which should be larger than or equal to that of the cellulase to reduce steric hindrance. The effective surface area occupied by the enzyme determines the maximum load of the immobilized cellulase (Santos et al., 2015). When a stable surface area is maintained, the amount of immobilized or absorbed cellulases is related to the pore size because the pore diameter determines the size of the protein that can be immobilized on that carrier (Teresa et al., 2009; Webster et al., 2015); 2) the number of carrier-bound active groups (CAGs) is another key factor controlling the enzyme-carrier multi-interaction (Cristina et al., 2011; Santos et al., 2015); 3) the size of carriers plays a very important role in the preparation of immobilized cellulase, in that a smaller carrier size with larger specific surface area will be better for the cellulase immobilization load, and the higher surface porosity of the carriers providing numerous binding sites for cellulase is one of the most important factors influencing the activity of immobilized cellulase (Chen et al., 2010; Santos et al., 2015; Malar et al., 2020); 4) the mechanical properties of the carriers need to be controlled considering the final configuration of the reactor. If the reactor is a fixed-bed reactor, such as inorganic supports like porous glass, silicates, it should possess very high rigidity to withstand high pressures without pressure problems, but the situation is different if a stirred-tank reactor is used (Cristina et al., 2011; Santos et al., 2015); 5) after the cellulase penetrates the carriers, the internal morphology of carriers will determine the possibility of obtaining a very intense or very limited enzyme-carrier interaction (Santos et al., 2015). When the diameter of the carriers is smaller than that of the enzyme, it is difficult to obtain an intense enzyme-carrier interaction (Cristina et al., 2011), but if the carriers have sufficiently large internal surfaces, it is possible to get an intense interaction with a similar flat surface (e.g., agarose beads, porous glass, or silicates) (Malar et al., 2018).

In particular, the special superparamagnetism of magnetic nanocarriers has attracted increasing interest as they allow easy recycling and separation of catalysts and biomolecules from high-viscosity liqueurs and high-solid-content broths. This unique characteristic has been well-applied to immobilization of cellulase, and a better hydrolysis efficiency and recycling feasibility have been observed (Alftrén et al., 2014; Cao et al., 2016; Cipolatti et al., 2014; Xing et al., 2015). During immobilization of cellulase, magnetic chitosan microspheres (C-MNPs) are frequently used as carriers because of their significant biological (i.e., biodegradable, biocompatible, bioactive) and chemical properties (polycationic, hydrogel, contains reactive groups, such as -OH and -NH_2). Moreover, the hydrophilic properties of the C-MNPs play an important role in the preparation of oriented-immobilized cellulase based on the

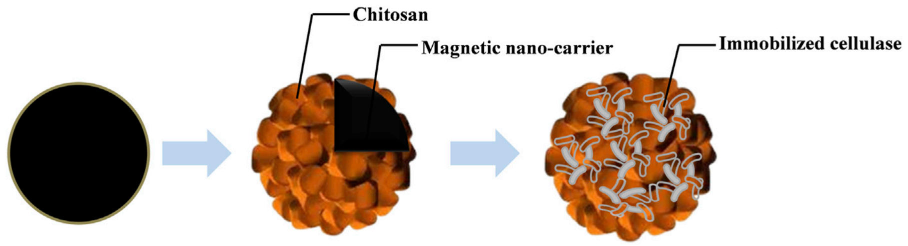

FIGURE 1 | Schematic diagram of immobilized cellulase on a magnetic nanocarrier.

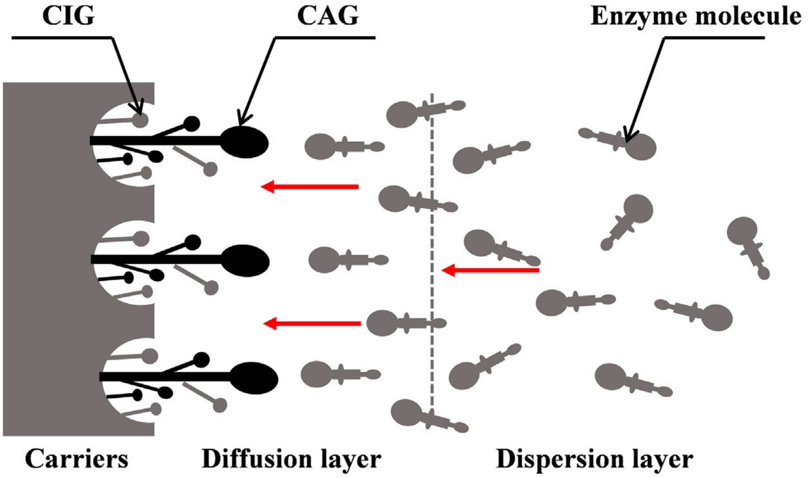

FIGURE 2 | Binding schematic diagram of enzyme and carrier caused by the chemistry properties during the immobilization process. CIGs means the carrier-bound inert groups and CAGs means the carrier-bound active groups; The larger end of enzyme molecule stands for the catalytic domain and the other end stands for the adsorption domain.

SRM system. The conventional immobilization of cellulase molecules on a single magnetic nanocarrier is simple, the chitosan was usually first coated on the magnetic nanocarriers for further combination with cellulase (**Figure 1**). Subsequently, the combined material based on Fe_3O_4 nanocarriers have received extensive attention in cellulase immobilization to improve enzyme activity, loading, and stability because of their low toxicity, biocompatibility, and easy synthesis (Jordan et al., 2011). Magnetite nanocarriers coated with silica and modified by organic-silanes, biocompatible, and with hydrophilic properties, are promising for cellulase immobilization.

The binding sites of enzymes on the surfaces of carriers depend on the chemical properties of the carriers. For non-covalent immobilization, the chemical structure of the skeleton and surface determines the applicability of carriers. The functional groups play a key role in the activity, stability, and selectivity of the enzyme, and the size, charge, polarity, and hydrophilicity/hydrophobicity of groups can affect their binding functions (Watanabe et al., 2010). Different properties of the ionic groups on the surfaces of carriers may result in different enzyme activities and further determine the structure of immobilized cellulase (Santos et al., 2015; Berlin et al., 2016; Frančič et al., 2016; Hui et al., 2016; Zhou et al., 2018). The chemistry properties of enzyme and carrier cause the oriented distribution of catalytic domain of enzyme from dispersion layer to diffusion layer during the immobilization process is shown in **Figure 2**. In this process, the CAGs directly participate in binding with enzyme molecules, but the carrier-bound inert groups (CIGs) are not directly involved. This interaction inevitably disturbs the maintenance of the natural conformation of the enzyme, leading to structural and functional changes in the enzyme molecules. No obvious stability change has been observed when the newly formed conformation is similar to that of the natural enzyme.

The covalent binding between carriers and catalytic cleft of the enzyme not only causes pore plugging of the surface, but also leads to the drag increment of in-diffusion. Although an initial high dosage of cellulase is added, the inhomogeneous distribution of the carrier surface structure results in the uncontrollable immobilization sites, and ineffective immobilization may lead to a significant loss of enzymatic activity and reduce the accessibility of the substrate to the functional sites. Moreover, the partition and mass transport limitations of nanocarriers may cause spatial variation in local reaction rates and further affect enzymatic hydrolysis (Du et al., 2017; Zeng et al., 2019). The chitosan molecules are mostly used because of the large number of -OH and amino groups (-NH_3), which are easier to co-precipitate with cellulase (Bindhu and Abraham, 2010; Urrutia et al., 2018; Saha et al., 2019; Mo et al., 2020). Moreover, surface modification is an important strategy for tuning the properties of nanocarriers. Surface modification can either alter the existing property or introduce new properties onto nanoparticles using various agents, such as organ siloxane, N-(3-dimethylaminopropyl)-N′-ethylcarbodiimide hydrochloride (EDC), and carbodiimide, as well as amino silanes, such as 3-aminopropyltriethoxysilane, aminoethyl aminopropyl polydimethylsiloxane, and silica (Chang et al., 2011; Gokhale et al., 2013; Riedel et al., 2017; Malar et al., 2018; Malar et al., 2020).

ROLES OF SURFACTANTS ON CELLULASE HYDROLYSIS

In most reports about hydrophobic ionic liquids, the enzymes are not dissolved but merely in a dispersed state and therefore regarded as a heterogeneous catalyst. Some hydrophilic ionic liquids can accelerate the dissolution of enzyme molecules, but cause the destruction of the protein secondary structure, leading to the inactivation of the enzyme (Fujita and Ohno, 2010; Moniruzzaman et al., 2010). In pure hydrophilic ionic liquids the enzymes can be dispersed at the monomolecular level. The hydrophilic proteins in almost anhydrous nonpolar solvents form suspensions, whereas proteins with extended hydrophobic surface segments form microemulsions in the same media, greatly reducing the catalytic efficiency of the enzyme (Zuev et al., 2003; Predvoditelev et al., 2010). Nonpolar hydrophobic solvents, such as heptane, octane, and benzene, do not cause the dehydration of biocatalysts. Therefore, the enzyme can maintain its catalytic activity (Muginova et al., 2010). Similarly, the catalytic activity of enzymes can be retained in the surfactant micelle system due to the water-oil amphiphilicity of surfactants (Muginova et al., 2010). Non-ionic surfactants can significantly accelerate the enzymatic hydrolysis of lignocellulose (Qing et al., 2010; Seo et al., 2011b; Eckard et al., 2012; Yiamsawas et al., 2017). For instance, Tween-20 can enhance the specific adsorption of cellulase, and the conversion efficiency of cellulose increased from 9 to 21% within 72 h when a high lignocellulosic substrate was added (Seo et al., 2011a). The prevention of non-productive enzyme adsorption onto lignin is the most widely investigated mechanism for this enhancement (Sipos et al., 2010; Lou et al., 2017). Recently, Djajadi et al. (2018) has proved that the adsorption of cellulases onto lignin substrates is reversible by nature, the reversible adsorption-desorption is existing in the process. But the non-productive adsorption caused by the ineffective combination will occupy large number of catalytic clefts of enzyme molecule which greatly hinder the enzymatic hydrolysis. Non-ionic surfactants can render lignin surfaces more hydrophilic by increasing their polar surface energy component, which can reduce the non-productive adsorption of cellulases onto lignocellulosic substrates caused by the ineffective combination between catalytic clefts of enzymes and lignin substrates (Jiang et al., 2017b), thereby promoting the enzymatic hydrolysis of lignocellulose. However, for the anionic surfactant-cellulase system, the adsorbed surfactants on the surface of cellulase cause a lower negative charge area, which further leads to negative catalytic activity due to the presence of sulfonic acid groups with a higher ionization degree (Yu and Zhang, 2016).

Furthermore, the effect of surfactants on cellulase hydrolysis is related to the concentration of surfactants (Zhou et al., 2015). In the enzymatic hydrolysis process, cellulose molecules are specifically adsorbed by the cellulose-binding domain (carbohydrate-binding module, CBM) and exert a driving force on the enzyme during the hydrolysis of cellulose (Liu et al., 2011; Tomme et al., 2015; Arslan et al., 2016). The adsorption of CBM can increase the cellulase concentration of the substrate surface by promoting the association of enzymes and substrates, but the non-covalent interactions (e.g., hydrogen bonds, electrostatic, and hydrophobic interactions) may lead to a nonproductive combination, because the random combination will occupy the active center of enzyme, resulting in the loss of catalytic activity. Ineffective adsorption can be reduced in the presence of surfactants due to the hydrophobic structure of surfactants, which can interact with the hydrophobic lignocellulosic substrates and form a coating (Kumar and Wyman, 2010; Li et al., 2012). However, contrasting results were obtained when different concentrations of surfactants were added to the enzymatic hydrolysis system. Some studies have suggested that a high concentration of surfactants can inhibit cellulase activity because strong hydrophobic interaction between the surfactant and cellulase can further reduce the effective adsorption of enzymes on cellulose (Wang Z. et al., 2013; Bao et al., 2019). However, the promotion effect of surfactant in enzymatic saccharification was observed in low concentration of lignosulfonate with low molecular weight and good sulfonation, which can be explained that the lignosulfonate can prevent the nonproductive binding of cellulase to lignin substrate, and the formed lignosulfonate-cellulase aggregate can also stabilize and enhance the binding of cellulase to lignin substrate (Lou et al., 2014).

THE ORIENTED IMMOBILIZATION OF CELLULASE IN THE SRM SYSTEM

The oriented immobilization of proteins on a solid support can effectively avoid its denaturation and keep its catalytic clefts fully exposed to solution, thus maximally preserving the bioaffinity or bioactivity. Liu and Yu (2016) has summarized the recent advances in oriented immobilization of proteins with a particular focus on antibodies and enzymes. However, the orientated immobilization of enzymes at the solvent interface is never involved. Thereby, the follow-up content will propose a novel method to achieve the oriented immobilization of cellulase in the SRM system.

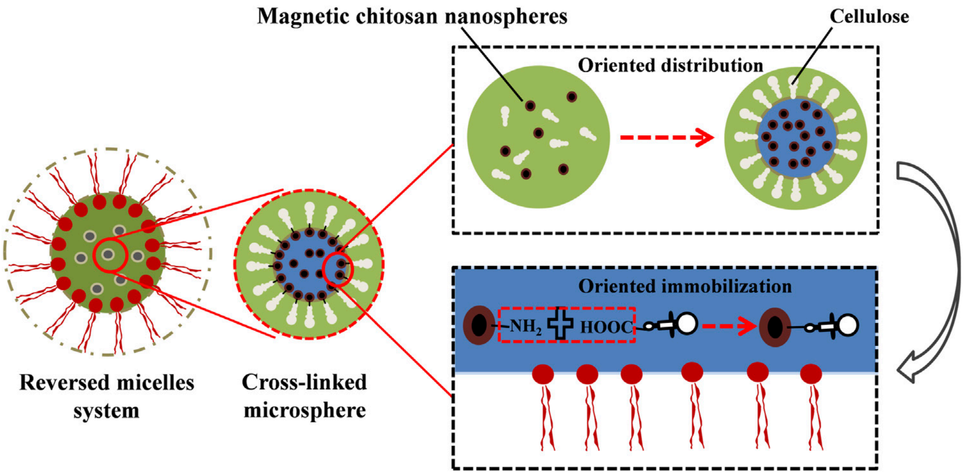

FIGURE 3 | The oriented immobilization diagrammatic sketch of single-layer cellulase in the surfactant reversed micelles system, the "green" represents the internal "pool" of SRM system, "black" represents the magnetic chitosan microspheres (C-MNPs), "brown" represents the cross-linked microsphere.

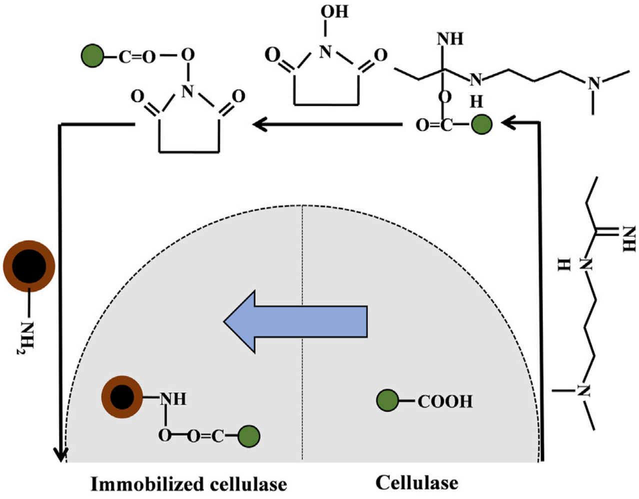

FIGURE 4 | The oriented immobilization process of cellulase on magnetic nanoparticles.

Construction of the SRM System

The SRM system has been widely used in the preparation of immobilized enzymes (Dong et al., 2010; Marhuendaegea et al., 2015). The special structure of surfactant molecules caused a water-oil amphipathy with a hydrophobic nonpolar hydrocarbon chain (alkyl) and a hydrophilic polar group (such as -OH, -COOH, -NH_2, and -SO_3H) distributed at different ends. In the water-oil (W/O) system, the surfactants are dissolved in the nonpolar organic solvent when a trace of water is provided, and the reversed micelles are formed when the concentration exceeds the CMC (Takagi et al., 2019; Chi et al., 2018). In reversed micelles, the nonpolar groups of the surfactants are exposed to the nonpolar organic solvents, while the polar groups are arranged inside. Therefore, a polar core with the ability to dissolve polar substances in the microreactors is formed. The SRMs are nanoscale aggregates that are formed spontaneously, and the W/O microemulsion with low water content provides a stable thermodynamic system (Tao et al., 2013). According to the hydrophilic-hydrophobic interaction of surfactants and cellulase in the oil-water reaction system, the large number of oil-water interfaces in the system provides a good environment for the catalytic reaction of enzyme molecules (Brady and Jordaan, 2009).

Mechanism of Oriented-Immobilized Cellulase in the SRM System

Multipoint covalent attachment is likely the most effective strategy for immobilization, but it is difficult to allow the immobilization of enzymes at a well-defined position since the proteins are usually attached to the solid surface by uncontrolled chemical bonds (Barbosa et al., 2015; Hernandez and Fernandez-Lafuente, 2011; Li et al., 2016). The uncontrolled conformational changes were caused by random immobilization, which may lead to a significant loss of enzyme activity, and the disordered enzyme orientation may also reduce the accessibility of the substrate to functional sites (Orellana et al., 2018; Steen Redeker et al., 2013; Yu et al., 2012). However, the hydrophilic cellulase will be dissolved in the SRM system due to the existence of surfactants, which can maintain the activity of the enzyme and prevent the toxic effects of organic solvents (Tao et al., 2013). The active centers of cellulase molecules are usually clefts, which provide a different microenvironment (Zhang et al., 2015) because the structures of cellulase active centers are mainly composed of eight kinds of amino acids (tryptophan, tyrosine, histidine, phenylalanine, aspartic acid, glutamic acid, and arginine). Aromatic amino acids and some polar amino acids appeared more frequently, such as tryptophan, tyrosine, histidine, aspartate, asparagine and arginine, most of which are hydrophobic tryptophan and phenylalanine residues, especially the tryptophan which has the highest content and plays an important role in the recognition and binding of enzyme molecules and substrate (Zhang et al., 2015). Hydrophobic active centers are conducive to the combination of catalyzed groups of cellulase and substrates. When the specific substrate is close to the active centers, a change in the conformation of the cellulase molecule can be induced so that the reaction groups of the enzyme active centers and substrate are aligned correctly. Meanwhile, the molecular orbitals between the reaction groups of the active centers are strictly located in the right direction for easier enzymatic reactions. Therefore, cellulase is distributed in the W/O interface, and the catalytic active center is toward the organic solvent and the other side toward the "pool". Moreover, the addition of surfactants can enhance the aggregation effect of cellulase on the W/O interface, and the existence of a crosslinking agent promotes the covalent crosslinking of enzyme molecules. The catalytic activity centers of the cross-linked microspheres are distributed uniformly and toward the outside, which solves the challenge of the uncontrollable attachment sites of the cellulase molecules in the immobilization process (Li et al., 2016; Steen Redeker et al., 2013; Yu et al., 2012). In the SRM system, the hydrophobic active molecules are exposed to the outside, which is beneficial for the further combination of immobilized cellulase and lignocellulosic substrates. However, the immobilized sites of cellulase molecules remain stochastic and heterogeneous, which may lead to covalent binding between the carriers and the active center of the enzyme and further cause ineffective immobilization and enzymatic reactions (Li et al., 2016). Therefore, to achieve oriented immobilization and improve the recycling times of cellulase, C-MNPs can be used as carriers as shown in **Figure 3**. This method can effectively prevent the ineffectiveness of cellulase immobilization. In this process, glutaraldehyde is used as the crosslinking agent, and EDC and N-hydroxysuccinimide are the coupling agents (**Figure 4**). In the W/O system, the free carboxyl group (-COOH) in the adsorption zone of the cellulase molecules can realize covalent binding with a large number of amino terminal catalytic residues of chitosan molecules (Fan et al., 2016). The process cannot destroy the catalytic center of cellulase, and the exposed catalytic clefts increase the effective attachment of immobilized cellulase to solid substrates, which further promotes enzymatic hydrolysis. Therefore, the oriented immobilization of enzymes is obtained in the SRM system, which can prevent nonproductive combinations effectively and further promote enzymatic hydrolysis.

CONCLUSION

Cellulase plays an important role in the production of fuel ethanol by the enzymatic hydrolysis of lignocellulose, and the immobilization of cellulase on the nanocarriers is an effective way to improve hydrolysis efficiency. However, the nanocarrier structure characteristics, solid-solid contact obstacles, external diffusion resistance, limited recycling frequency of nanocarriers, and nonproductive combination of enzyme active centers restricted the further improvement of hydrolysis efficiency in the complex multiphase system. Surfactants can promote the enzymatic hydrolysis of lignocellulose and play an important role in the preparation of nanocarriers. The special SRM system caused by the amphiphilicity in the oil-water reaction system can provide effective protection to obtain the immobilization of single-layer cellulase, which can effectively prevent the immobilization of cellulase and increase the effective attachment of immobilized cellulase and solid substrates.

AUTHOR CONTRIBUTIONS

ZW: conceptualization, investigation, methodology, and writing (original draft preparation). CF: methodology and article revision. XZ: data collection and writing (review and editing). ZJ: methodology and investigation. KB: formal analysis and investigation. MZ: data collection, article revision and funding acquisition. HK: methodology, writing (review and editing) and supervision.

FUNDING

This work was supported by the major projects of study on National Social Science Foundation of China and the spirit explanation of the Fifth Plenary Session of the 19th CPC Central Committee (21ZDA028)"Construction of ecological friendly water environment management system in new rural areas of socialist modernization pilot area". And this work was also supported by the Major Project of Science and Technology in Zhejiang Province (No. 2020C02010-002).

REFERENCES

Al-Shemmari, F. H. J., Al-Mulla, E. A. J., and Rabah, A. A. (2014). A Comparative Study of Different Surfactants for Natural Rubber clay Nanocomposite Preparation. *Rend. Fis. Acc. Lincei* 25 (3), 409–413. doi:10.1007/s12210-014-0307-z

Alexander, K., Gajghate, S., Katarkar, A. S., Majumder, A., and Bhaumik, S. (2020). Role of Nanomaterials and Surfactants for the Preparation of Graphene Nanofluid: A Review. *Mater. Today* 44, 1136–1143. doi:10.1016/j.matpr.2020.11.231

Alftrén, J., Hobley, T. J., Prins, W., and Overend, R. (2014). Immobilization of Cellulase Mixtures on Magnetic Particles for Hydrolysis of Lignocellulose and Ease of Recycling. *Biomass Bioenerg.* 65 (3), 72–78. doi:10.1016/j.biombioe.2014.03.009

Alonso-Gómez, L. A., Heredia-Olea, E., Serna-Saldivar, S. O., and Bello-Pérez, L. A. (2019). Whole Unripe Plantain (Musa Paradisiaca L.) as Raw Material for Bioethanol Production. *J. Sci. Food Agric.* 99 (13), 5784–5791. doi:10.1002/jsfa.9847

Anjum, S., Shaheen, S., Awan, M. S., and Zia, R. (2019). Effect of Various Surfactants on Optical and Electrical Properties of Cu+2-Doped ZnS Semiconductor Nanoparticles. *Appl. Phys. A.* 125 (4), 273. doi:10.1007/s00339-019-2558-0

Arslan, B., Colpan, M., Ju, X., Zhang, X., Kostyukova, A., and Abu-Lail, N. I. (2016). The Effects of Noncellulosic Compounds on the Nanoscale Interaction Forces Measured between Carbohydrate-Binding Module and Lignocellulosic

Biomass. *Biomacromolecules* 17 (5), 1705–1715. doi:10.1021/acs.biomac.6b00129

Asghar, K., Qasim, M., Nelabhotla, D. M., and Das, D. (2016). Effect of Surfactant and Electrolyte on Surface Modification of C-Plane GaN Substrate Using Chemical Mechanical Planarization (CMP) Process. *Colloids Surf. A: Physicochemical Eng. Aspects* 497, 133–145. doi:10.1016/j.colsurfa.2016.02.035

Bao, Y., Guo, J., Ma, J., Liu, P., Kang, Q., and Zhang, J. (2017). Cationic Silicon-Based Gemini Surfactants: Effect of Hydrophobic Chains on Surface Activity, Physic-Chemical Properties and Aggregation Behaviors. *J. Ind. Eng. Chem.* 53 (25), 51–61. doi:10.1016/j.jiec.2017.03.045

Bao, Y., Liu, P., and Guo, J. (2019). Research Progress on the Preparation of Nanomaterials and Mesoporous Materials Using Gemini Surfactants. *Mater. Rep.* 33 (21), 3678–3685. doi:10.11896/cldb.18050316

Barbosa, O., Ortiz, C., Berenguer-Murcia, Á., Torres, R., Rodrigues, R. C., and Fernandez-Lafuente, R. (2015). Strategies for the One-step Immobilization-Purification of Enzymes as Industrial Biocatalysts. *Biotechnol. Adv.* 33 (5), 435–456. doi:10.1016/j.biotechadv.2015.03.006

Begum, G., Oschatz, C., Oschatz, M., Kaskel, S., Brunner, E., and Kröger, N. (2019). Influence of Silica Architecture on the Catalytic Activity of Immobilized Glucose Oxidase. *Bioinspired, Biomimetic and Nanobiomaterials* 8 (1), 72–80. doi:10.1680/jbibn.18.00002

Berlin, Z., Jun, R., Li, X., and Lingyun, J. (2016). Direct Site-specific Immobilization of Protein A via Aldehyde-Hydrazide Conjugation. *J. Chromatogr. B.* 1008, 132–138. doi:10.1016/j.jchromb.2015.11.019

Bhawna, S., Christian, L., and Claude-Gilles, D. (2020). Comprehensive Assessment of 2G Bioethanol Production. *Bioresour. Technol.* 313, 123630. doi:10.1016/j.biortech.2020.123630

Bindhu, L. V., and Abraham, E. T. (2010). Immobilization of Horseradish Peroxidase on Chitosan for Use in Nonaqueous media. *J. Appl. Polym. Sci.* 88 (6), 1456–1464. doi:10.1002/app.11815

Brady, D., and Jordaan, J. (2009). Advances in Enzyme Immobilisation. *Biotechnol. Lett.* 31 (11), 1639–1650. doi:10.1007/s10529-009-0076-4

Cao, S., Xu, P., Ma, Y., Yao, X., Yao, Y., Zong, M., et al. (2016). Recent Advances in Immobilized Enzymes on Nanocarriers. *Chin. J. Catal.* 37 (11), 1814–1823. doi:10.1016/s1872-2067(16)62528-7

Carlsson, N., Gustafsson, H., Thörn, C., Olsson, L., Holmberg, K., and Åkerman, B. (2014). Enzymes Immobilized in Mesoporous Silica: A Physical-Chemical Perspective. *Adv. Colloid Interf. Sci.* 205, 339–360. doi:10.1016/j.cis.2013.08.010

Carrillo, A. I., Linares, N., Serrano, E., and García-Martínez, J. (2011). Well-ordered Mesoporous Interconnected Silica Spheres Prepared Using Extremely Low Surfactant Concentrations. *Mater. Chem. Phys.* 129 (1), 261–269. doi:10.1016/j.matchemphys.2011.04.015

C. Carter, K., and Puig-Sellart, M. (2016). Nanocarriers Made from Non-ionic Surfactants or Natural Polymers for Pulmonary Drug Delivery. *Cpd* 22 (22), 3324–3331. doi:10.2174/1381612822666160418121700

Chang, R. H.-Y., Jang, J., and Wu, K. C.-W. (2011). Cellulase Immobilized Mesoporous Silica Nanocatalysts for Efficient Cellulose-To-Glucose Conversion. *Green. Chem.* 13 (10), 2844–2850. doi:10.1039/c1gc15563f

Chaudhary, S., Rohilla, D., and Mehta, S. K. (2014). Surfactant Adsorption and Aggregate Structure of Silica Nanoparticles: a Versatile Stratagem for the Regulation of Particle Size and Surface Modification. *Mater. Res. Express* 1 (1), 015011. doi:10.1088/2053-1591/1/1/015011

Chen, L. F., Gong, C. S., and Tsao, G. T. (2010). Immobilized Glucose Isomerase on DEAE Cellulose Beads. *Starch - Stärke* 33 (2), 58–63. doi:10.1002/star.19810330207

Cherian, E., Dharmendirakumar, M., and Baskar, G. (2015). Immobilization of Cellulase onto MnO2 Nanoparticles for Bioethanol Production by Enhanced Hydrolysis of Agricultural Waste. *Chin. J. Catal.* 36 (8), 1223–1229. doi:10.1016/s1872-2067(15)60906-8

Chi, X., Peters, G. M., Brockman, C., Lynch, V. M., and Sessler, J. L. (2018). Controlling Structure beyond the Initial Coordination Sphere: Complexation-Induced Reversed Micelle Formation in Calix[4]pyrrole-Containing Diblock Copolymers. *J. Am. Chem. Soc.* 140 (41), 13219–13222. doi:10.1021/jacs.8b09620

Chu, Q., Tong, W., Wu, S., Jin, Y., Hu, J., and Song, K. (2021). Modification of Lignin by Various Additives to Mitigate Lignin Inhibition for Improved Enzymatic Digestibility of Dilute Acid Pretreated Hardwood. *Renew. Energ.* 177, 992–1000. doi:10.1016/j.renene.2021.06.048

Cipolatti, E. P., Silva, M. J. A., Klein, M., Feddern, V., Feltes, M. M. C., Oliveira, J. V., et al. (2014). Current Status and Trends in Enzymatic Nanoimmobilization. *J. Mol. Catal. B: Enzymatic* 99 (1), 56–67. doi:10.1016/j.molcatb.2013.10.019

Cristina, G-G., Ángel, B-M., Roberto, F-L., and Rodrigues, R. C. (2011). Potential of Different Enzyme Immobilization Strategies to Improve Enzyme Performance. *Adv. Synth. Catal.* 353, 2885–2904. doi:10.1002/adsc.201100534

Cui, X., Wang, J., Zhang, X., Wang, Q., Song, M., and Chai, J. (2019). Preparation of Nano-TiO2 by a Surfactant-free Microemulsion-Hydrothermal Method and its Photocatalytic Activity. *Langmuir* 35 (28), 9255–9263. doi:10.1021/acs.langmuir.9b01392

DiCosimo, R., McAuliffe, J., Poulose, A. J., and Bohlmann, G. (2013). Industrial Use of Immobilized Enzymes. *Chem. Soc. Rev.* 42 (15), 6437–6475. doi:10.1039/c3cs35506c

Djajadi, D. T., Pihlajaniemi, V., Rahikainen, J., Kruus, K., and Meyer, A. S. (2018). Cellulases Adsorb Reversibly on Biomass Lignin. *Biotechnol. Bioeng.* 115 (12), 2869–2880. doi:10.1002/bit.26820

Dong, X. Y., Feng, X. D., and Sun, Y. (2010). His-tagged Protein Purification by Metal-Chelate Affinity Extraction with Nickel-Chelate Reverse Micelles. *Biotechnol. Prog.* 26 (4), 1088–1094. doi:10.1002/btpr.428

Du, J., Cao, Y., Liu, G., Zhao, J., Li, X., and Qu, Y. (2017). Identifying and Overcoming the Effect of Mass Transfer Limitation on Decreased Yield in Enzymatic Hydrolysis of Lignocellulose at High Solid Concentrations. *Bioresour. Tech.* 229, 88–95. doi:10.1016/j.biortech.2017.01.011

Eckard, A. D., Muthukumarappan, K., and Gibbons, W. (2012). Pretreatment of Extruded Corn stover with Polyethylene Glycol to Enhance Enzymatic Hydrolysis: Optimization, Kinetics, and Mechanism of Action. *Bioenerg. Res.* 5 (2), 424–438. doi:10.1007/s12155-011-9162-2

Fan, Y., Wu, G., Su, F., Li, K., Xu, L., Han, X., et al. (2016). Lipase Oriented-Immobilized on Dendrimer-Coated Magnetic Multi-Walled Carbon Nanotubes toward Catalyzing Biodiesel Production from Waste Vegetable Oil. *Fuel* 178, 172–178. doi:10.1016/j.fuel.2016.03.071

Fiorati, A., Florit, F., Mazzei, A., Buzzaccaro, S., Rossi, B., Piazza, R., et al. (2021). Dispersions of Zirconia Nanoparticles Close to the Phase Boundary of Surfactant-free Ternary Mixtures. *Langmuir* 37 (14), 4072–4081. doi:10.1021/acs.langmuir.0c03401

Frančič, N., Bellino, M. G., Solerillia, G. J., and Lobnik, A. (2016). Mesoporous Titania Thin Films as Efficient Enzyme Carriers for Paraoxon Determination/detoxification: Effects of Enzyme Binding and Pore Hierarchy on the Biocatalyst Activity and Reusability. *Analyst* 141 (13), 4235. doi:10.1039/c4an00152d

Fujita, K., and Ohno, H. (2010). Enzymatic Activity and thermal Stability of Metallo Proteins in Hydrated Ionic Liquids. *Biopolymers* 93 (12), 1093–1099. doi:10.1002/bip.21526

Gao, S., Wang, Y., Wang, T., Luo, G., and Dai, Y. (2009). Immobilization of Lipase on Methyl-Modified Silica Aerogels by Physical Adsorption. *Bioresour. Tech.* 100 (2), 996–999. doi:10.1016/j.biortech.2008.06.060

geor malar, C., Seenuvasan, M., Kumar, K. S., Kumar, A., and Parthiban, R. (2020). Review on Surface Modification of Nanocarriers to Overcome Diffusion Limitations: An Enzyme Immobilization Aspect. *Biochem. Eng. J.* 158, 107574. doi:10.1016/j.bej.2020.107574

Ghasemi, S., Yousefi, M., Nikseresht, A., and Omidi, H. (2021). Covalent Binding and *In-Situ* Immobilization of Lipases on a Flexible Nanoporous Material. *Process Biochem.* 102, 92–101. doi:10.1016/j.procbio.2020.12.013

Gokhale, A. A., Lu, J., and Lee, I. (2013). Immobilization of Cellulase on Magnetoresponsive Graphene Nano-Supports. *J. Mol. Catal. B: Enzymatic* 90 (3), 76–86. doi:10.1016/j.molcatb.2013.01.025

Gonçalves Lopes, R. C. F., Silvestre, O. F., Faria, A. R., C do Vale, M. L., Marques, E. F., and Nieder, J. B. (2019). Surface Charge Tunable Catanionic Vesicles Based on Serine-Derived Surfactants as Efficient Nanocarriers for the Delivery of the Anticancer Drug Doxorubicin. *Nanoscale* 11 (25), 5932–5941. doi:10.1039/c8nr06346j

Gutierrez, J. A., Cruz, J., Rondón, P., Jones, N., and Ortiz, C. (2016). Small Gold Nanocomposites Obtained in Reverse Micelles as Nanoreactors. Effect of Surfactant, Optical Properties and Activity against *Pseudomonas aeruginosa*. *New J. Chem.* 40 (12), 10432–10439. doi:10.1039/c6nj02259f

Hassanzadeh-Tabrizi, S. A., Bigham, A., and Rafienia, M. (2016). Surfactant-assisted Sol-Gel Synthesis of Forsterite Nanoparticles as a Novel Drug

Delivery System. *Mater. Sci. Eng. C* 58 (Jan.), 737–741. doi:10.1016/j.msec.2015.09.020

Hernandez, K., and Fernandez-Lafuente, R. (2011). Control of Protein Immobilization: Coupling Immobilization and Site-Directed Mutagenesis to Improve Biocatalyst or Biosensor Performance. *Enzyme Microb. Tech.* 48 (2), 107–122. doi:10.1016/j.enzmictec.2010.10.003

Hosseini, S. H., Hosseini, S. A., Zohreh, N., Yaghoubi, M., and Pourjavadi, A. (2018). Covalent Immobilization of Cellulase Using Magnetic Poly(ionic Liquid) Support: Improvement of the Enzyme Activity and Stability. *J. Agric. Food Chem.* 66 (4), 789–798. doi:10.1021/acs.jafc.7b03922

Hui, J., Yingwu, W., Yan, B., Rong, L., and Renjun, G. (2016). Site-specific, Covalent Immobilization of Dehalogenase ST2570 Catalyzed by Formylglycine-Generating Enzymes and its Application in Batch and Semi-continuous Flow Reactors. *Molecules* 21 (7), 895. doi:10.3390/molecules21070895

Itabaiana, I., Gonçalves, K. M., Zoumpanioti, M., Leal, I. C. R., Miranda, L. S. M. e., Xenakis, A., et al. (2014). Microemulsion-based Organogels as an Efficient Support for Lipase-Catalyzed Reactions under Continuous-Flow Conditions. *Org. Process. Res. Dev.* 18 (11), 1372–1376. doi:10.1021/op500136c

Jia, W., Collins, S. R. A., Adam, E., Nikolaus, W., Jo, D., Roberts, I. N., et al. (2018). Release of Cell wall Phenolic Esters during Hydrothermal Pretreatment of rice Husk and rice Straw. *Biotechnol. Biofuels* 11 (1), 162. doi:10.1186/s13068-018-1157-1

Jiang, F., Qian, C., Esker, A. R., and Roman, M. (2017). Effect of Nonionic Surfactants on Dispersion and Polar Interactions in the Adsorption of Cellulases onto Lignin. *J. Phys. Chem. B* 121 (41), 9607–9620. doi:10.1021/acs.jpcb.7b07716

Jiang, J., Carrillo-Enríquez, N. C., Oguzlu, H., Han, X., Bi, R., Song, M., et al. (2020). High Production Yield and More Thermally Stable Lignin-Containing Cellulose Nanocrystals Isolated Using a Ternary Acidic Deep Eutectic Solvent. *ACS Sust. Chem. Eng.* 8, 7182–7191. doi:10.1021/acssuschemeng.0c01724

Jordan, J., Kumar, C. S. S. R., and Theegala, C. (2011). Preparation and Characterization of Cellulase-Bound Magnetite Nanoparticles. *J. Mol. Catal. B: Enzymatic* 68 (2), 139–146. doi:10.1016/j.molcatb.2010.09.010

Kalantari, M., Kazemeini, M., and Arpanaei, A. (2013). Evaluation of Biodiesel Production Using Lipase Immobilized on Magnetic Silica Nanocomposite Particles of Various Structures. *Biochem. Eng. J.* 79, 267–273. doi:10.1016/j.bej.2013.09.001

Karimi, S., Karri, R. R., Yaraki, M. T., and Koduru, J. R. (2021). Processes and Separation Technologies for the Production of Fuel-Grade Bioethanol: a Review. *Environ. Chem. Lett.* 19 (4), 1–18. doi:10.1007/s10311-021-01208-9

Kawasaki, H. (2013). Surfactant-free Solution-Based Synthesis of Metallic Nanoparticles toward Efficient Use of the Nanoparticles' Surfaces and Their Application in Catalysis and Chemo-/biosensing. *Nanotechnol. Rev.* 2 (1), 5–25. doi:10.1515/ntrev-2012-0079

Kayhomayun, Z., Ghani, K., and Zargoosh, K. (2020). T Template-Directed Synthesis of $Sm_2Ti_2O_7$ Nanoparticles: a Novel FRET-Based Fluorescent Chemosensor for the Fast and Selective Determination of Picric Acid. *New J. Chem.* 44 (38), 1–12. doi:10.1039/d0nj04219f

Kellock, M., Rahikainen, J., Marjamaa, K., and Kruus, K. (2017). Lignin-derived Inhibition of Monocomponent Cellulases and a Xylanase in the Hydrolysis of Lignocellulosics. *Bioresour. Tech.* 232, 183–191. doi:10.1016/j.biortech.2017.01.072

Kovalchuk, N. M. (2015). Spontaneous Non-linear Oscillations of Interfacial Tension at Oil/water Interface. *Open Chem.* 13 (1), 1–16. doi:10.1515/chem-2015-0009

Kumar, R., and Wyman, C. E. (2010). Effect of Additives on the Digestibility of Corn stover Solids Following Pretreatment by Leading Technologies. *Biotechnol. Bioeng.* 102 (6), 1544–1557. doi:10.1002/bit.22203

Lai, N., Nie, X., Zheng, X., Zhao, W., Zhao, X., and Wang, Y. (2020). Experimental Investigation on a Novel Polyelectrolyte Molecular Deposition Film for Improved Injectivity in Low-Permeability Reservoirs. *ACS Omega* 5 (45), 29300–29311. doi:10.1021/acsomega.0c04084

Leonidas, M., Vijayendran, R., Olga, Y., Gustav, P., Eva, O., Ulrika, R., et al. (2019). Lignin-first Biomass Fractionation Using a Hybrid Organosolv-Steam Explosion Pretreatment Technology Improves the Saccharification and Fermentability of spruce Biomass. *Bioresour. Technol.* 273, 521–528. doi:10.1016/j.biortech.2018.11.055

Li, F. H., Tang, N., Wang, Y. Q., Zhang, L., Du, W., Xiang, J., et al. (2018). Synthesis and Characterization of Magnetic Carriers Based on Immobilized Enzyme. *IOP Conf. Ser. Mater. Sci. Eng.* 359, 012044. doi:10.1088/1757-899x/359/1/012044

Li, J., Li, S., Fan, C., and Yan, Z. (2012). The Mechanism of Poly(ethylene Glycol) 4000 Effect on Enzymatic Hydrolysis of Lignocellulose. *Colloids Surf. B: Biointerfaces* 89 (1), 203–210. doi:10.1016/j.colsurfb.2011.09.019

Li, M., Yue, Y., Zhang, Z.-J., Wang, Z.-Y., Tan, T.-W., and Fan, L.-H. (2016). Site-specific and High-Loading Immobilization of Proteins by Using Cohesin-Dockerin and CBM-Cellulose Interactions. *Bioconjug. Chem.* 27 (7), 1579–1583. doi:10.1021/acs.bioconjchem.6b00282

Li, Y., Guan, X., Chaffey, P. K., Ruan, Y., Ma, B., Shang, S., et al. (2020). Carbohydrate-binding Module O-Mannosylation Alters Binding Selectivity to Cellulose and Lignin. *Chem. Sci.* 11, 9262–9271. doi:10.1039/d0sc01812k

Liu, J., Shi, J., Li, J., and Yuan, X. (2011). Characterization of the Interaction between Surfactants and Enzymes by Fluorescence Probe. *Enzyme Microb. Tech.* 49 (4), 360–365. doi:10.1016/j.enzmictec.2011.06.014

Liu, Y., and Yu, J. (2016). Oriented Immobilization of Proteins on Solid Supports for Use in Biosensors and Biochips: a Review. *Microchim. Acta* 183, 1–19. doi:10.1007/s00604-015-1623-4

Lok-Kumar, S., Rekha, G. S., Neus, V., Carlos, R. A., and Katsuhiko, A. (2014). *In-situ* Formation of Silver Nanoparticles Using Nonionic Surfactant Reverse Micelles as Nanoreactors. *J. Nanosci. Nanotechnol.* 14 (3), 2238–2244. doi:10.1166/jnn.2014.9229

Lou, H., Zeng, M., Hu, Q., Cai, C., Lin, X., Qiu, X., et al. (2017). Nonionic Surfactants Enhanced Enzymatic Hydrolysis of Cellulose by Reducing Cellulase Deactivation Caused by Shear Force and Air-Liquid Interface. *Bioresour. Technol.* 249, 1–8. doi:10.1016/j.biortech.2017.07.066

Lou, H., Zhou, H., Li, X., Wang, M., Zhu, J. Y., and Qiu, X. (2014). Understanding the Effects of Lignosulfonate on Enzymatic Saccharification of Pure Cellulose. *Cellulose* 21 (3), 1351–1359. doi:10.1007/s10570-014-0237-z

Luan, Y., and Ramos, L. (2010). Role of the Preparation Procedure in the Formation of Spherical and Monodisperse Surfactant/polyelectrolyte Complexes. *Chemistry* 13 (21), 6108–6114. doi:10.1002/chem.200601422

Maia, J. L. d., Cardoso, J. S., Mastrantonio, D. J. d. S., Bierhals, C. K., Moreira, J. B., Costa, J. A. V., et al. (2020). Microalgae Starch: A Promising Raw Material for the Bioethanol Production. *Int. J. Biol. Macromolecules* 165, 2739–2749. doi:10.1016/j.ijbiomac.2020.10.159

Malar, C. G., Seenuvasan, M., and Kumar, K. S. (2018). Prominent Study on Surface Properties and Diffusion Coefficient of Urease-Conjugated Magnetite Nanoparticles. *Appl. Biochem. Biotechnol.* 186, 174–185. doi:10.1007/s12010-018-2719-1

Marhuendaegea, F. C., Pieravelázquez, S., Cadenas, C., and Cadenas, E. (2015). Reverse Micelles in Organic Solvents: a Medium for the Biotechnological Use of Extreme Halophilic Enzymes at Low Salt Concentration. *Archaea* 1 (2), 105.

Mehta, J., Bhardwaj, N., Bhardwaj, S. K., Kim, K.-H., and Deep, A. (2016). Recent Advances in Enzyme Immobilization Techniques: Metal-Organic Frameworks as Novel Substrates. *Coord. Chem. Rev.* 322, 30–40. doi:10.1016/j.ccr.2016.05.007

Mita, D. G., and Eldin, M. S. M. (2014). Immobilized Enzymes: Strategies for Overcoming the Substrate Diffusion- Limitation Problem. *Curr. Biotechnol.* 3 (3), 207–217. doi:10.2174/221155010303140918114737

Mnich, E., Bjarnholt, N., Eudes, A., Harholt, J., Holland, C., Jørgensen, B., et al. (2020). Phenolic Cross-Links: Building and De-constructing the Plant Cell wall. *Nat. Prod. Rep.* 37 (4), 919–961. doi:10.1039/c9np00028c

Mo, H., Qiu, J., Yang, C., Zang, L., Sakai, E., and Chen, J. (2020). Porous Biochar/chitosan Composites for High Performance Cellulase Immobilization by Glutaraldehyde. *Enzyme Microb. Tech.* 138, 109561. doi:10.1016/j.enzmictec.2020.109561

Moniruzzaman, M., Kamiya, N., and Goto, M. (2010). Activation and Stabilization of Enzymes in Ionic Liquids. *Org. Biomol. Chem.* 8 (13), 2887–2899. doi:10.1039/b926130c

Mroczkiewicz, M., Bronowska, A., Pietrzak, M., and Malinowska, E. (2012). Different Methods of Acid Phosphatase Immobilization for its Application in FIA Systems with Potentiometric Detection. *Proced. Eng.* 47 (5), 265–268. doi:10.1016/j.proeng.2012.09.134

Muginova, S. V., Galimova, A. Z., Polyakov, A. E., and Shekhovtsova, T. N. (2010). Ionic Liquids in Enzymatic Catalysis and Biochemical Methods of Analysis: Capabilities and Prospects. *J. Anal. Chem.* 65 (4), 331–351. doi:10.1134/s1061934810040027

Nakayama, R.-i., Imai, M., and Suzuki, I. (2009). Enzymatic Cellulose Degradation Using Suitable Combination of Cellulase and Enhancement of Reaction Rate with the Aid of Ultrasonic Pretreatment. *J. Biosci. Bioeng.* 108 (Suppl. S1), S89. doi:10.1016/j.jbiosc.2009.08.261

Neira, H. D., and Herr, A. E. (2017). Kinetic Analysis of Enzymes Immobilized in Porous Film Arrays. *Anal. Chem.* 89 (19), 10311–10320. doi:10.1021/acs.analchem.7b02075

Nicoletti, G., Cipolatti, E. P., Valério, A., Carbonera, N. G., Soares, N. S., Theilacker, E., et al. (2015). Evaluation of Different Methods for Immobilization of Candida antarctica Lipase B (CalB Lipase) in Polyurethane Foam and its Application in the Production of Geranyl Propionate. *Bioproc. Biosyst Eng* 38 (9), 1739–1748. doi:10.1007/s00449-015-1415-6

Orellana, J. L., Wichhart, D., and Kitchens, C. L. (20182018). Mechanical and Optical Properties of Polylactic Acid Films Containing Surfactant-Modified Cellulose Nanocrystals. *J. Nanomater.* 2018, 1–12. doi:10.1155/2018/7124260

Ortiz-Martínez, V., Gómez-Coma, L., Ortiz, A., and Ortiz, I. (2019). Overview on the Use of Surfactants for the Preparation of Porous Carbon Materials by the Sol-Gel Method: Applications in Energy Systems. *Rev. Chem. Eng.* 36 (7), 1–17. doi:10.1515/revce-2018-0056

Ouyang, J., Pu, S., Wang, J., Deng, Y., Yang, C., Naseer, S., et al. (2020). Enzymatic Hydrolysate of Geniposide Directly Acts as Cross-Linking Agent for Enzyme Immobilization. *Process Biochem.* 99, 187–195. doi:10.1016/j.procbio.2020.09.006

Pavlidis, I. V., Tzafestas, K., and Stamatis, H. (2010). Water-in-ionic Liquid Microemulsion-Based Organogels as Novel Matrices for Enzyme Immobilization. *Biotechnol. J.* 5 (8), 805–812. doi:10.1002/biot.201000052

Predvoditelev, D. A., Suvorkin, S. V., and Vasyanina, E. (2010). 4-Chloromethyl-1,3,2-dioxaphospholanes in the Synthesis of New Types of Diglycerophospholipids. *Cheminform* 28, 208. doi:10.1002/chin.200128218

Priydarshani, S., Mustafa, M., Yuan, G., Robinson, A. J., and Ilias, K. (2018). Immobilization and Stabilization of Alcohol Dehydrogenase on Polyvinyl Alcohol Fibre. *Biotechnol. Rep.* 19, e00260. doi:10.1016/j.btre.2018.e00260

Qing, Q., Yang, B., and Wyman, C. E. (2010). Impact of Surfactants on Pretreatment of Corn stover. *Bioresour. Tech.* 101 (15), 5941–5951. doi:10.1016/j.biortech.2010.03.003

Qiu, X., Wang, S., Miao, S., Suo, H., Xu, H., and Hu, Y. (2021). Co-immobilization of Laccase and ABTS onto Amino-Functionalized Ionic Liquid-Modified Magnetic Chitosan Nanoparticles for Pollutants Removal. *J. Hazard. Mater.* 401, 123353. doi:10.1016/j.jhazmat.2020.123353

Rahikainen, J., Mikander, S., Marjamaa, K., Tamminen, T., Lappas, A., Viikari, L., et al. (2011). Inhibition of Enzymatic Hydrolysis by Residual Lignins from Softwood-Study of Enzyme Binding and Inactivation on Lignin-Rich Surface. *Biotechnol. Bioeng.* 108 (12), 2823–2834. doi:10.1002/bit.23242

Rajnish, K. N., Samuel, M. S., John J, A., Datta, S., Chandrasekar, N., Balaji, R., et al. (2021). Immobilization of Cellulase Enzymes on Nano and Micro-materials for Breakdown of Cellulose for Biofuel Production-A Narrative Review. *Int. J. Biol. Macromolecules* 182 (6), 1793–1802. doi:10.1016/j.ijbiomac.2021.05.176

Riedel, M., Sabir, N., Scheller, F. W., Parak, W. J., and Lisdat, F. (2017). Connecting Quantum Dots with Enzymes: Mediator-Based Approaches for the Light-Directed Read-Out of Glucose and Fructose Oxidation. *Nanoscale* 9 (8), 2814–2823. doi:10.1039/c7nr00091j

Rocha-Martín, J., Martínez-Bernal, C., Zamorano, L. S., Reyes-Sosa, F. M., and Díez García, B. (2018). Inhibition of Enzymatic Hydrolysis of Pretreated Corn stover and Sugar Cane Straw by Laccases. *Process Biochem.* 67 (APR), 88–91. doi:10.1016/j.procbio.2018.01.021

Roth, H.-C., Schwaminger, S. P., Peng, F., and Berensmeier, S. (2016). Immobilization of Cellulase on Magnetic Nanocarriers. *Chemistryopen* 5 (3), 183–187. doi:10.1002/open.201600028

Saha, K., Verma, P., Sikder, J., Chakraborty, S., and Curcio, S. (2019). Synthesis of Chitosan-Cellulase Nanohybrid and Immobilization on Alginate Beads for Hydrolysis of Ionic Liquid Pretreated Sugarcane Bagasse. *Renew. Energ.* 133, 66–76. doi:10.1016/j.renene.2018.10.014

Santos, J. C. S. d., Barbosa, O., Ortiz, C., Berenguer-Murcia, A., Rodrigues, R. C., and Fernandez-Lafuente, R. (2015). Importance of the Support Properties for Immobilization or Purification of Enzymes. *Chemcatchem* 7 (16), 2413–2432. doi:10.1002/cctc.201500310

Savic, S., Petrovic, S., Savic, S., and Petronijevic, Z. (2021). Immobilization of Horseradish Peroxidase on Modified Cellulose Carriers via Hydrophobic Interactions: Catalytic Properties and Stability. *Iran J. Sci. Technol. Trans. Sci.* 45 (1), 55–63. doi:10.1007/s40995-020-01027-7

Seo, D.-J., Fujita, H., and Sakoda, A. (2011a). Effects of a Non-ionic Surfactant, Tween 20, on Adsorption/desorption of Saccharification Enzymes Onto/from Lignocelluloses and Saccharification Rate. *Adsorption* 17 (5), 813–822. doi:10.1007/s10450-011-9340-8

Seo, D.-J., Fujita, H., and Sakoda, A. (2011b). Structural Changes of Lignocelluloses by a Nonionic Surfactant, Tween 20, and Their Effects on Cellulase Adsorption and Saccharification. *Bioresour. Tech.* 102 (20), 9605–9612. doi:10.1016/j.biortech.2011.07.034

Shil, A., Hussain, S. A., and Bhattacharjee, D. (2017). Surfactant Concentration Dependent Metachromasy of an Anionic Cyanine Dye in Adsorbed and Deposited Langmuir Films. *Chem. Phys. Lett.* 676, 99–107. doi:10.1016/j.cplett.2017.03.052

Singh, T. A., Jajoo, A., and Bhasin, S. (2020). Optimization of Various Encapsulation Systems for Efficient Immobilization of Actinobacterial Glucose Isomerase. *Biocatal. Agric. Biotechnol.* 29, 101766. doi:10.1016/j.bcab.2020.101766

Sipos, B., Dienes, D., Schleicher, Á., Perazzini, R., Crestini, C., Siika-aho, M., et al. (2010). Hydrolysis Efficiency and Enzyme Adsorption on Steam-Pretreated spruce in the Presence of Poly(ethylene Glycol). *Enzyme Microb. Tech.* 47 (3), 84–90. doi:10.1016/j.enzmictec.2010.05.010

Song, Y., Chandra, R. P., Zhang, X., and Saddler, J. N. (2020). Non-productive Celluase Binding onto Deep Eutectic Solvent (DES) Extracted Lignin from Willow and Corn stover with Inhibitory Effects on Enzymatic Hydrolysis of Cellulose. *Carbohydr. Polym.* 250, 116956. doi:10.1016/j.carbpol.2020.116956

Steen Redeker, E., Ta, D. T., Cortens, D., Billen, B., Guedens, W., and Adriaensens, P. (2013). Protein Engineering for Directed Immobilization. *Bioconjug. Chem.* 24 (11), 1761–1777. doi:10.1021/bc4002823

Suárez, S., Guerrero, C., Vera, C., and Illanes, A. (2018). Effect of Particle Size and Enzyme Load on the Simultaneous Reactions of Lactose Hydrolysis and Transgalactosylation with Glyoxyl-Agarose Immobilized β-galactosidase from Aspergillus oryzae. *Process. Biochem.* 73 (OCT), 56–64. doi:10.1016/j.procbio.2018.08.016

Suhartini, S., Rohma, N. A., Mardawati, E., KasbawatiHidayat, N., and Melville, L. (2022). Biorefining of Oil palm Empty Fruit Bunches for Bioethanol and Xylitol Production in Indonesia: A Review. *Renew. Sust. Energ. Rev.* 154, 11187. doi:10.1016/j.rser.2021.111817

Sui, C., Cheng, W., Dong, S., Han, L., and Pharmacy, D. O. (2015). Immobilization of Glucoamylase onto the Electrospinning PEI/PVA Composite Nanofiber Membrane via Ionic Adsorption. *Biotechnol. Bull.* 2, 167–172. doi:10.13560/j.cnki.biotech.bull.1985.2015.02.025

Takagi, S., Arakawa, K., Shimada, T., and Inoue, H. (2019). Reversed Micelles Formed by Polyfluorinated Surfactant Ii; the Properties of Core Water Phase in Reversed Micelle. *Bcsj* 92 (7), 1200–1204. doi:10.1246/bcsj.20190086

Tan, J., Xiong, X., He, Z., Cao, F., and Sun, D. (2019). Aggregation Behavior of Polyether Based Siloxane Surfactants in Aqueous Solutions: Effect of Alkyl Groups and Steric Hindrance. *J. Phys. Chem. B* 123 (6), 1390–1399. doi:10.1021/acs.jpcb.8b10727

Tao, L., Zhao, Y., Wang, X., Xiang, L., and Yan, Y. (2013). A Novel Oriented Immobilized Lipase on Magnetic Nanoparticles in Reverse Micelles System and its Application in the Enrichment of Polyunsaturated Fatty Acids. *Bioresour. Technol.* 132 (7), 99–102. doi:10.1016/j.biortech.2012.12.191

Teresa, V. S., Rebolledo, A. F., Sevilla, M., Valle-Vigon, P., and Tartaj, P. (2009). Preparation, Characterization, and Enzyme Immobilization Capacities of Superparamagnetic Silica/iron Oxide Nanocomposites with Mesostructured Porosity. *Chem. Mater.* 21 (9), 1806–1814. doi:10.1021/cm8005937

Tomme, P., Creagh, A. L., Kilburn, D. G., and Haynes, C. A. (2015). Interaction of Polysaccharides with the N-Terminal Cellulose-Binding Domain of Cellulomonas Fimi CenC. 1. Binding Specificity and Calorimetric Analysis. *Biochemistry* 35 (44), 13885–13894. doi:10.1021/bi961185i

Urrutia, P., Bernal, C., Wilson, L., and Illanes, A. (2018). Use of Chitosan Heterofunctionality for Enzyme Immobilization: β-galactosidase Immobilization for Galacto-Oligosaccharide Synthesis. *Int. J. Biol. Macromolecules* 116, 182–193. doi:10.1016/j.ijbiomac.2018.04.112

Valencia, P., Wilson, L., Aguirre, C., and Illanes, A. (2010). Evaluation of the Incidence of Diffusional Restrictions on the Enzymatic Reactions of Hydrolysis of Penicillin G and Synthesis of Cephalexin. *Enzyme Microb. Tech.* 47 (6), 268–276. doi:10.1016/j.enzmictec.2010.07.010

Wang, M., Wang, Y., Yu, D., Han, Y., and Wang, Y. (2013a). Salt Effects on the Aggregation Behavior of Tripolar Zwitterionic Surfactants with Different Inter-charge Spacers in Aqueous Solution. *Colloid Polym. Sci.* 291 (7), 1613–1621. doi:10.1007/s00396-013-2895-z

Wang, Z., Lan, T., and Zhu, J. (2013b). Lignosulfonate and Elevated pH Can Enhance Enzymatic Saccharification of Lignocelluloses. *Biotechnol. Biofuels* 6 (1), 9. doi:10.1186/1754-6834-6-9

Watanabe, T., Mori, T., Tosa, T., and Chibata, I. (2010). Immobilization of Aminoacylase by Adsorption to Tannin Immobilized on Aminohexyl Cellulose. *Biotechnol. Bioeng.* 21 (3), 477–486. doi:10.1002/bit.260210309

Webster, I. A., Schwier, C. E., and Bates, F. S. (2015). Using the Rotational Masking Concept to Enhance Substrate Inhibited Reaction Rates: Controlled Pore Supports for Enzyme Immobilization. *Enzyme Microb. Technol.* 7 (6), 266–274. doi:10.1016/0141-0229(85)90084-5

Wei, J., Wen, X., and Zhu, F. (2018). Influence of Surfactant on the Morphology and Photocatalytic Activity of Anatase TiO2 by Solvothermal Synthesis. *J. Nanomater.* 2018, 1–7. doi:10.1155/2018/3086269

Winarni, I., Bardant, T., and Hendra, D. (2020). Enhancement the Added Value of Sengon wood Waste Pulp as Bioenergy Raw Material for Bioethanol Production. *IOP Conf. Ser. Earth Environ. Sci.* 415, 012012. doi:10.1088/1755-1315/415/1/012012

Xing, Z., Su, Y., Zhang, Q., Ruan, X., Lin, Y., Wang, X., et al. (2015). Research Progress on Cellulase Immobilized by Magnetic Nanoparticles as Carriers. *Biotechnol. Bull.* 8, 59–65. doi:10.13560/j.cnki.biotech.bull.1985.2015.08.009

Xu, G., Jiang, Y., Tao, R., Wang, S., Zeng, H., and Yang, S. (2016). A Recyclable Biotransformation System for L-2-Aminobutyric Acid Production Based on Immobilized Enzyme Technology. *Biotechnol. Lett.* 38 (1), 123–129. doi:10.1007/s10529-015-1957-3

Xu, M., Ji, D., Deng, Y., and Agyei, D. (2020). Preparation and Assessment of Cross-Linked Enzyme Aggregates (CLEAs) of β-galactosidase from Lactobacillus Leichmannii 313. *Food Bioproducts Process.* 124, 82–96. doi:10.1016/j.fbp.2020.08.004

Xu, S., Sun, X., Ye, H., You, T., Song, X., and Sun, S. (2010). Selective Synthesis of Copper Nanoplates and Nanowires via a Surfactant-Assisted Hydrothermal Process. *Mater. Chem. Phys.* 120 (1), 1–5. doi:10.1016/j.matchemphys.2009.10.049

Yang, Q., Wang, B., Zhang, Z., Lou, D., Tan, J., and Zhu, L. (2017). The Effects of Macromolecular Crowding and Surface Charge on the Properties of an Immobilized Enzyme: Activity, thermal Stability, Catalytic Efficiency and Reusability. *RSC Adv.* 7 (60), 38028–38036. doi:10.1039/c7ra06544b

Yiamsawas, D., Beckers, S., Lu, H., Landfester, K., and Wurm, F. R. (2017). Morphology-controlled Synthesis of Lignin Nanocarriers for Drug Delivery and Carbon Materials. *ACS Biomater. Sci. Eng.* 3 (10), 1–26. doi:10.1021/acsbiomaterials.7b00278

You, J., Choi, H. H., Kim, T. A., Park, M., Ha, J. S., Lee, S. S., et al. (2019). High-performance Polyketone Nanocomposites Achieved via Plasma-Assisted Mechanochemistry. *Compos. Sci. Technol.* 183 (Oct.20), 107801–107808. doi:10.1016/j.compscitech.2019.107800

Yu, C.-C., Kuo, Y.-Y., Liang, C.-F., Chien, W.-T., Wu, H.-T., Chang, T.-C., et al. (2012). Site-specific Immobilization of Enzymes on Magnetic Nanoparticles and Their Use in Organic Synthesis. *Bioconjug. Chem.* 23 (4), 714–724. doi:10.1021/bc200396r

Yu, Y., and Zhang, J. (2016). Interaction of Cellulase with Surfactants and Their Application in Detergent. *CIESC J.* 67 (7), 3023–3031.

Zang, L., Qiu, J., Wu, X., Zhang, W., Sakai, E., and Wei, Y. (2014). Preparation of Magnetic Chitosan Nanoparticles as Support for Cellulase Immobilization. *Ind. Eng. Chem. Res.* 53 (9), 3448–3454. doi:10.1021/ie404072s

Zeng, Q., Chang, S., Beyhaqi, A., Wang, M., and Hu, C. (2019). Efficient Electricity Production Coupled with Water Treatment via a Highly Adaptable, Successive Water-Energy Synergistic System. *Nano Energy* 67, 104237.

Zeng, Q., Chang, S., Wang, M., Li, M., Deng, Q., Xiong, Z., et al. (2021). Highly-active, Metal-free, Carbon-Based Orr Cathode for Efficient Organics Removal and Electricity Generation in a Pfc System. *Chin. Chem. Lett.* 32 (7), 2212–2216. doi:10.1016/j.cclet.2020.12.062

Zhang, B., Li, P., Zhang, H., Wang, H., Li, X., Tian, L., et al. (2016). Preparation of lipase/Zn3(PO4)2 Hybrid Nanoflower and its Catalytic Performance as an Immobilized Enzyme. *Chem. Eng. J.* 291, 287–297. doi:10.1016/j.cej.2016.01.104

Zhang, H., and Hay, A. G. (2019). Magnetic Biochar Derived from Biosolids via Hydrothermal Carbonization: Enzyme Immobilization, Immobilized-Enzyme Kinetics, Environmental Toxicity. *J. Hazard. Mater.* 384, 121272. doi:10.1016/j.jhazmat.2019.121272

Zhang, W.-W., Wang, N., Zhou, Y.-J., He, T., and Yu, X.-Q. (2012). Enhancement of Activity and Stability of Lipase by Microemulsion-Based Organogels (MBGs) Immobilization and Application for Synthesis of Arylethyl Acetate. *J. Mol. Catal. B: Enzymatic* 78, 65–71. doi:10.1016/j.molcatb.2012.02.005

Zhang, X., Wang, S., Wu, X., Liu, S., Li, D., Xu, H., et al. (2015). Subsite-specific Contributions of Different Aromatic Residues in the Active Site Architecture of Glycoside Hydrolase Family 12. *Sci. Rep.* 5, 18357. doi:10.1038/srep18357

Zheng, Y., Yu, Y., Lin, W., Jin, Y., Yong, Q., and Huang, C. (2021). Enhancing the Enzymatic Digestibility of Bamboo Residues by Biphasic Phenoxyethanol-Acid Pretreatment. *Bioresour. Tech.* 325 (3), 124691. doi:10.1016/j.biortech.2021.124691

Zhou, W., Rao, Y., Zhuang, W., Ge, L., Lin, R., Tang, T., et al. (2021). Improved Enzymatic Activity by Oriented Immobilization on Graphene Oxide with Tunable Surface Heterogeneity. *Composites B: Eng.* 216, 108788. doi:10.1016/j.compositesb.2021.108788

Zhou, Y., Chen, H., Qi, F., Zhao, X., and Liu, D. (2015). Non-ionic Surfactants Do Not Consistently Improve the Enzymatic Hydrolysis of Pure Cellulose. *Bioresour. Tech.* 182, 136–143. doi:10.1016/j.biortech.2015.01.137

Zhou, Y., Zhang, L., and Tao, S. (2018). Porous TiO2with Large Surface Area Is an Efficient Catalyst Carrier for the Recovery of Wastewater Containing an Ultrahigh Concentration of Dye. *RSC Adv.* 8 (7), 3433–3442. doi:10.1039/c7ra11985b

Ziaei-Rad, Z., Fooladi, J., Pazouki, M., and Gummadi, S. N. (2021). Lignocellulosic Biomass Pre-treatment Using Low-Cost Ionic Liquid for Bioethanol Production: An Economically Viable Method for Wheat Straw Fractionation. *Biomass and Bioenergy* 151, 106140. doi:10.1016/j.biombioe.2021.106140

Zuev, Y. F., Vylegzhanina, N. N., and Zakhartchenko, N. L. (2003). Effects of Protein Solubilization on the Structure of the Surfactant Shell of Reverse Micelles. *Appl. Magn. Reson.* 25 (1), 29–42. doi:10.1007/bf03166964

Conflicts of Interest: The authors declare that the research was conducted in the absence of any commercial or financial relationships that could be construed as a potential conflict of interest.

frontiers | Frontiers in Chemistry

REVIEW
published: 05 April 2022
doi: 10.3389/fchem.2022.882876

Preparation of Templated Materials and Their Application to Typical Pollutants in Wastewater: A Review

Hanbing Li, Li Wang, Yifei Wei, Wei Yan and Jiangtao Feng*

Xi'an Key Laboratory of Solid Waste Recycling and Resource Recovery, Department of Environmental Science and Engineering, School of Energy and Power Engineering, Xi'an Jiaotong University, Xi'an, China

As the pollution and destruction of global water resources become more and more severe, the treatment of wastewater has attracted significant attention. The template method is a synthetic method in which the template is the main configuration to control, influence, and modify the morphology as well as control the dimensions of the material, thus achieving the properties that determine the material. It is simple, highly reproducible, and predictable, and more importantly, it can effectively control the pore structure, size, and morphology of the material, providing a novel platform for the preparation of adsorbent materials with excellent adsorption properties. This review focuses on the classification of the templates according to their properties and spatial domain-limiting capabilities, reviews the types of hard and soft template materials and their synthetic routes, and further discusses the modulation of the morphological structure of the materials by the introduction of templates. In addition, the application and adsorption mechanisms of heavy metal ions and dyes are reviewed based on the regulatory behavior of the template method.

Keywords: template method, moderating behavior, heavy metals, dyes, adsorption mechanism

Edited by:
Suqing Wu,
Wenzhou University, China

Reviewed by:
Long Kong,
Shanghai Jiao Tong University, China
Hai Liu,
Jinan University, China
Muhe Diao,
University of Calgary, Canada

***Correspondence:**
Li Wang
wangli-2015@xjtu.edu.cn

Specialty section:
This article was submitted to
Inorganic Chemistry,
a section of the journal
Frontiers in Chemistry

Received: *24 February 2022*
Accepted: *08 March 2022*
Published: *05 April 2022*

Citation:
Li H, Wang L, Wei Y, Yan W and Feng J (2022) Preparation of Templated Materials and Their Application to Typical Pollutants in Wastewater: A Review. Front. Chem. 10:882876. doi: 10.3389/fchem.2022.882876

1 INTRODUCTION

Pollution (Yang et al., 2019; Zhang et al., 2019; Zhao et al., 2019), especially water pollution, has been a global problem that needs to be addressed immediately , with the rapid development of industrial economy. Human production and living activities result in a considerable discharge of pollutant into the water resources, particularly organic dyes and heavy metals, which can pose a serious threat to people's living environment if not properly treated. Dyes are extremely harmful to ecosystems due to their toxicity and the reduction of dissolved oxygen in water, while heavy metals can cause pernicious health effects on humans and other organisms (Zare et al., 2018). Therefore, there is an urgent need to develop remediation strategies that effectively mitigate organic dyes and heavy metal pollution.

Nowadays, several techniques have been successfully used for the purification of heavy metal ions and organic dyes in wastewater, such as chemical precipitation, ion exchange, and adsorption. Among them, adsorption has become one of the most influential and promising methods (Zhou et al., 2018) due to its simplicity, low cost, mature process, and low energy consumption (Liu J. et al., 2016; Yu et al., 2018). At present, various adsorbents such as activated carbon (Ekinci et al., 2002; Zhou et al., 2015; Kuroki et al., 2019), zeolites (Briao et al., 2017; Zanin et al., 2017), nanomaterials (Sarma et al., 2019; Madima et al., 2020; Yu et al., 2021), biochar (Wang et al., 2019a; Wang et al., 2019b; Wang L. et al., 2020; Wang et al., 2021; Wei et al., 2022), and metal organic framework polymers (Huang et al., 2018; Pi et al., 2018), have been developed and widely used for the adsorption of wastewater. However, most adsorbents still have some problems, such as uneven pore size

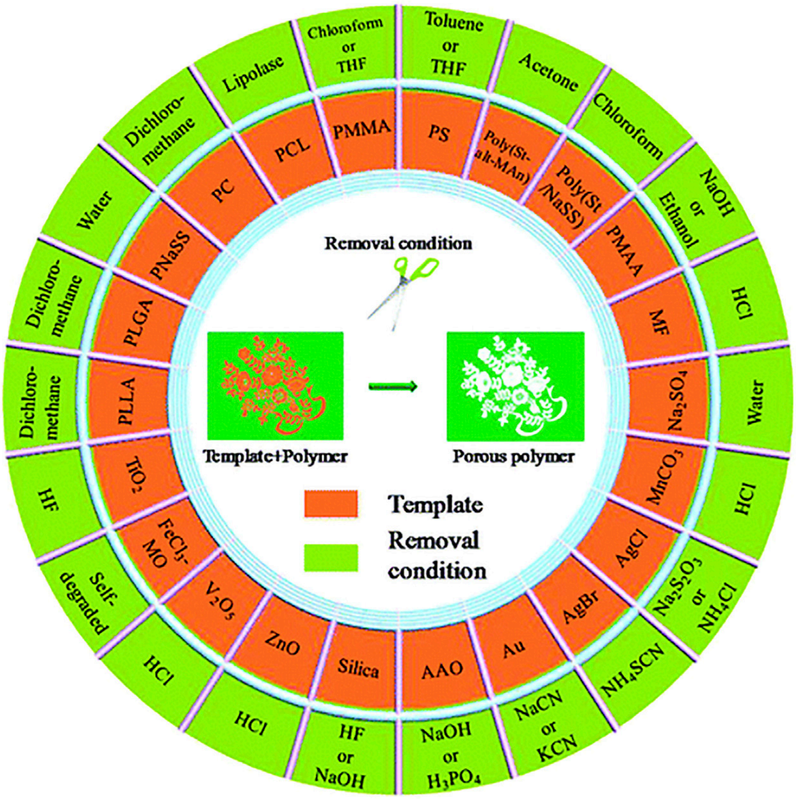

FIGURE 1 | Commonly used polymer templates and their removal conditions (Wu et al., 2012).

distribution and difficulty in achieving effective control of pore size, which directly affect the adsorption capacity of the adsorbent. The template method, which has been developed in recent years, is simple, highly reproducible, and predictable (Liu et al., 2019; Ma et al., 2019). More importantly, the template method enables effective control of the pore structure, dimensions, and morphology of the composite material (Marrakchi et al., 2017), which is expected to be a solution to these problems and achieve efficient adsorption of adsorbents.

The template method, essentially a forming or casting technique, which is different from the conventional methods, in that it needs to introduce a template agent in advance. Whether the reaction takes place in the liquid or solid phase, the template method can effectively modulate the size, morphology, structure, and even the arrangement of the sample. The morphology of the product varies depending on the template chosen, so it is important to select the right template (Liu et al., 2013). The template method is now widely used in water treatment [such as photocatalysis (Ahmad et al., 2017; Yang et al., 2021), adsorption (Libbrecht et al., 2017; Zhao et al., 2020a), and electrochemistry, as well as biology and medicine (Miao et al., 2010; Wu and Xu, 2010; Li et al., 2013)]. This study outlines the classification of the template method, focuses on the hard and soft template methods, discusses the modulating behavior of the template method on the morphological structure of materials, and further discusses the current status of the application of the template method for heavy metal ions and organic dyes in water treatment.

2 PREPARATION AND CLASSIFICATION OF THE TEMPLATE METHOD

The template method is based on the morphological characteristics of the synthetic material, introducing its self-assembly or organic molecular system as a template, and effectively regulating and modifying the morphology, structure, and dimensions of the material through forces like hydrogen bonding and Van der Waals forces. It is essentially a forming or casting technique (Thomas et al., 2008), generally speaking, synthesis of the template method includes three main steps (Knezevic et al., 2018): 1) preparation of templates; 2) synthesis of target materials using the templates; and 3) removal of templates.

In general, there are four requirements for the preparation of template method : 1) in order to achieve successful replication of the template, the surface properties of the template used should be consistent with the raw material; 2) the template should have a well-defined structure, such as an easily adjustable morphology; 3) the template should be easy to remove. **Figure 1** summarizes the commonly used polymer templates and their removal

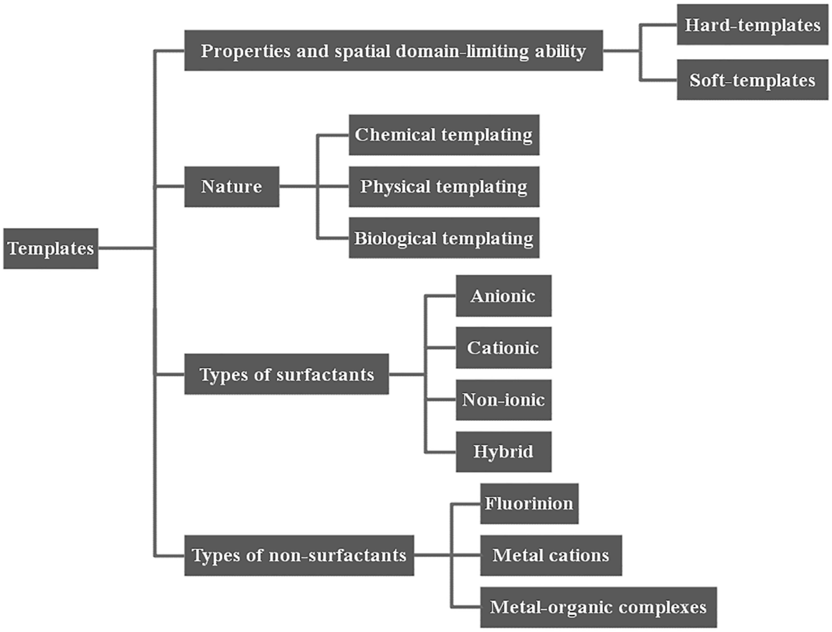

FIGURE 2 | Classifications of templates.

conditions (Wu et al., 2012), such as silica templates, as one of the most commonly used templates, are usually removed using hydrofluoric acid or sodium hydroxide; 4) the polymer template should be robust enough to prevent deformation of the pores after template removal.

At present, there are various classifications of template agents; the specific classification is shown in **Figure 2**. One kind of classification can be divided into hard templates (porous silica, silica) and soft templates (biomolecules, surfactants) according to the templates' own properties and spatial domain-limiting ability (Bao et al., 2016). Depending on the nature of template, it can be subdivided into physical templates, chemical templates, and biological templates (Liu et al., 2013; Zhao et al., 2020b). In addition, some scholars classify it according to surfactants and non-surfactants. The former includes anionic template agents, cationic template agents, non-ionic template agents, and hybrid template agents; while the latter includes metal cations, organic molecules, metal–organic complexes, etc. (**Figure 2**).

Currently, based on different compositions and characteristics of templates, the most common way to classify them is to divide into hard and soft templates, both of which provide a tunable reaction space for the adsorbent. Among them, hard template is mainly selected from material that is prepared already, such as mesoporous carbon (Libbrecht et al., 2015), mesoporous silica (Marciniak et al., 2019), metal oxides (MO) (El-Hankari et al., 2016), etc. During the preparation process, the raw material is adsorbed or permeated on the surface or internal lattice of the template, and the template is removed after the reaction (Petkovich and Stein, 2013). Materials prepared by the hard template method can be precisely regulated in terms of size and structure, but the removal of the template can easily cause structural damage to the raw material (Liu D. et al., 2016). In contrast, soft template is formed during the reaction, that is, a phase interface is formed between the soft template [such as polymers (Liu D. et al., 2016), biological macromolecules (Zhao et al., 2017), and surfactants (Cao et al., 2014)]; the target product by micelles and a certain spatial structure is established by the internal polymerization of the molecules. In comparison, soft template is easier to remove and the production condition is mild and simple, which is a current trend in the preparation of materials by the template method (Xie et al., 2016). The detailed characteristics and preparation of each of the two template methods are described below.

2.1 Hard Template

Hard templates are usually connected by covalent bonds, and the reaction cavity is in dynamic equilibrium, with substances diffusing in and out through the cavity walls, such as molecular sieves, metals (Wang H. et al., 2016), and carbons (Xie et al., 2018). Generally, the preparation process for materials prepared using hard templates is to wrap or infiltrate the selected template with a precursor, transforming the precursors into solid material by chemical or thermal treatment, and then removing the template by chemical etching or high temperature calcination (Petkovich and Stein, 2013).

Depending on the inclusion relationship between the hard template and the precursor, the hard template method can be divided into exotemplating and endotemplating methods (Schuth, 2003). As shown in **Figure 3A** (Wang Y. et al., 2016), endotemplate is the precursor wrapping template. Template molecules enter the precursor and create pore channels, and after the removal of the template, a pore system is formed in the precursor. Exotemplating is the opposite, as shown in **Figure 3B**, where the precursor penetrates the template.

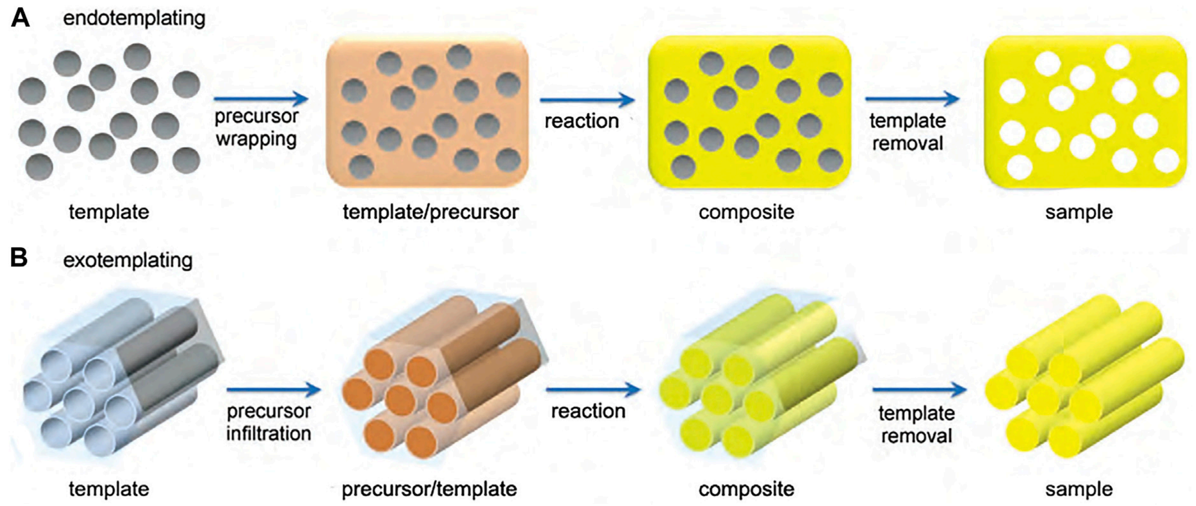

FIGURE 3 | Synthetic mechanism of the hard template method (Wang Y. et al., 2016).

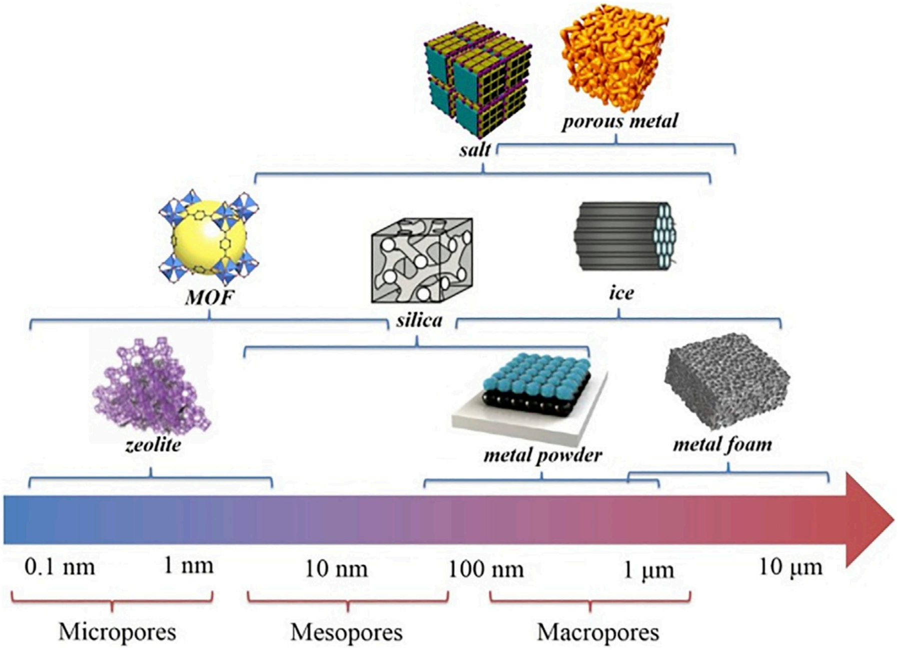

FIGURE 4 | Different types of hard templates and their corresponding length scales (Zhu et al., 2019).

Exotemplate can be materials with structural pores, and the precursor infiltrates into the pore channel. Depending on the connectivity of the template, a porous or finely split material remains after the template removal.

Compared to soft templates, hard templates have better domain limitation and higher stability, so they can achieve a strict regulation of material size and morphology. And different template agents can be selected according to the requirements of the target product to achieve precise regulation of different specific surface areas, pore sizes, morphology, and other characteristics. As shown in **Figure 4**, Zhu et al. (Zhu et al., 2019) classified various hard templates according to the pore sizes of different templates and corresponding composites. It can be seen that different pore sizes correspond to different template materials, therefore, based on the performance requirements of the target product, selecting the most suitable template material, which is one of the key factors for the successful synthesis of template materials. However, hard templates are difficult to be removed; the majority of these templates act as supports, which limits the application of hard template method to a certain extent (Liu D. et al., 2016).

In practice, hard template method has excellent results in the treatment of industrial wastewater, such as the adsorption of heavy metal ions. Currently, numerous types of hard templates have been investigated, such as silica (Fuertes et al., 2005), metal–organic frameworks (MOF) (Amali et al., 2014), mesoporous carbon (Libbrecht et al., 2015), poly (methyl methacrylate) (PMMA) (Liu et al., 2018), etc., and the specific materials are described below.

2.1.1 Mesoporous Silica Templates

Mesoporous silica has a high specific surface area and good hydrophobicity. When used as a hard template for wastewater adsorption treatment, it can improve the morphology and pore structure of the material very well, and is commonly used as a hard template for the synthesis of mesoporous carbon materials in practical applications. Mesoporous silica has a three-dimensional interconnected pore structure, which offers the possibility of introducing carbon precursors. On the other hand, the three-dimensional interconnected pore structure of mesoporous silica also ensures the successful synthesis of mesoporous carbon, rather than obtaining carbon materials with nanowire or rod-like structures.

The preparation process usually starts by immersing the carbon precursor into the pore channel of the template agent to cause polymerization, and then removing the mesoporous silica template with hydrofluoric acid or sodium hydroxide solution after carbonization. The ordered mesoporous carbon CMK-1 was successfully prepared using mesoporous silicas MCM-48 as templates and sucrose as carbon precursors, heated to 1173 K and carbonized, and removed the silicon template using dissolution in sodium hydroxide solution. Moreover, they obtained samples Cn-CMK-1 by controlling the pore size of the template, and the specific surface area and pore size of the samples were 1700 m^2/g, 1.24 cm^3/g (C16-CMK-1), 1800 m^2/g, 1.21 cm^3/g (C18-CMK-1), and 1710 m^2/g, 1.23 cm^3/g (C20-CMK-1), respectively (Kruk et al., 2000). Similarly, Jun et al. (Jun et al., 2000) used ordered mesoporous silica SBA-15 as a template agent and sucrose as the carbon source, carbonized the mixture at 1173 K, and finally the ordered mesoporous carbon CMK-3 was obtained by removing the mesoporous silica template using sodium hydroxide or by washing with hydrofluoric acid. The specific surface area of CMK-3 was 1520 m^2/g, and the total pore volume was 1.3 cm^3/g.

Kim et al. (2005) used mesoporous silica SBA-16 as a template agent; and sucrose, furfuryl alcohol, and acenaphthene as carbon precursors to synthesize cubic mesoporous carbon, respectively. The reactions were all carbonized at 1173 K, and the mesoporous silica templates were removed with hydrofluoric acid. The experimental results showed that the furfuryl alcohol-based mesoporous carbon has a high specific surface area and total pore volume (2050 m^2/g, 2.33 cm^3/g), which is higher than that of sucrose-based mesoporous carbon (1370 m^2/g, 1.20 cm^3/g) and acenaphthene-based mesoporous carbon (1260 m^2/g, 1.68 cm^3/g). It further shows that the selection of suitable silicon templates and carbon precursors can effectively control the mesoporous structure of the materials.

2.1.2 Carbon Templates

Carbon materials, such as mesoporous carbon and carbon nanotubes, are also used as template agents. Among them, mesoporous carbon is stable and has an ordered pore structure, so it is often used as a template agent to synthesize ordered mesoporous materials such as nanoscale zeolite molecular sieves and mesoporous metal oxides. The process of synthesizing mesoporous carbon into a mesoporous material usually involves replicating the pore channels of the mesoporous carbon into the new mesoporous material and removing the mesoporous carbon template under certain conditions. Roggenbuck et al. (2006) chose mesoporous carbon CMK-3 as a hard template, infiltrated the carbon matrix with $Mg(NO_3)_2$, removed the template by heating, and later obtained mesoporous MgO. The specific surface area and total pore volume of mesoporous MgO were 280 m^2/g and 0.52 cm^3/g.

Carbon nanotubes can greatly improve the reactivity of the material due to their characteristic pentagonal defect structure. Liu et al. (2015) prepared MWCNTs@carbon nanocables by a hydrothermal synthetic method using multi-walled carbon nanotubes (MWCNTs) as a template agent and glucose as a carbon source, and used anhydrous ethanol for washing to remove the template during the preparation.

2.1.3 Metal–Organic Framework Polymer Templates

Metal–organic frameworks (MOFs) are a new class of materials with a three-dimensional pore structure, in which specific surface areas are significantly high (in the range of 1000–10000 m^2/g), even higher than that of zeolites (3500 m^2/g). Also, based on the inherent instability of the MOFs, it is easy to remove when they were used as template agents (Zhao et al., 2021).

ZIF-8, as one of the typical MOF materials, has excellent chemical and thermal stability and is an ideal template for the preparation of the material. The ZnS nanocages were prepared using ZIF-8 as template agents and thioacetamide as the sulfur precursor, and the ethanol solution was chosen to remove the template during the preparation process (Jiang et al., 2012). Zhang et al. (2018) prepared PDA/PEG@ZIF-8 composite nanoparticles by grafting polyethylene glycol (PEG) polymers by the template method using ZIF-8 as a hard template. The ZIF-8 template was further removed by etching with dilute hydrochloric acid adjusting the pH to 7 to obtain PDA/PEG composite nanocapsules.

2.1.4 Other Hard Templates

Nanoporous anodic alumina, palygorskite (Pal) and spherical particles (PMMA microspheres, $CaMg(CO_3)_2$ microspheres) are also widely used as hard templates for wastewater adsorption. Mohajeri et al. (2017) used nanoporous anodic alumina as a template agent, ethylene as a carbon precursor, and argon as a carrier gas to synthesize ordered carbon nanotube arrays by chemical vapor deposition (CVD), and the template was

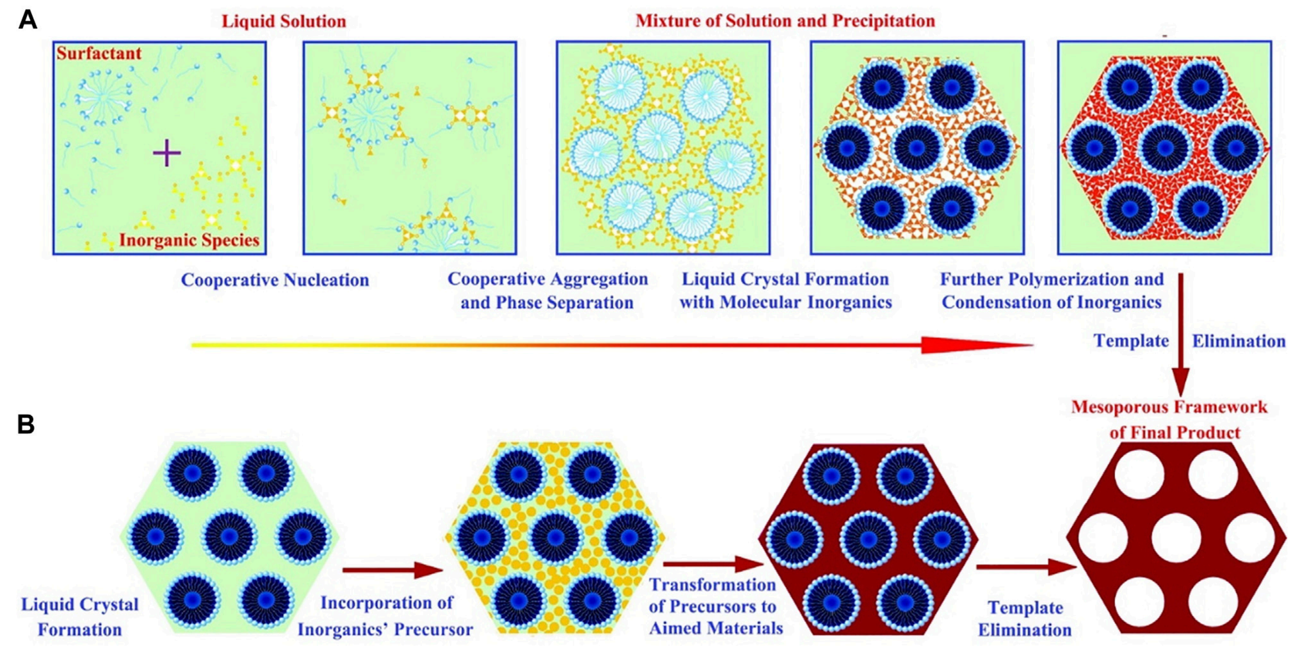

FIGURE 5 | Mechanism of the soft template method (Wan and Zhao, 2007).

removed by pyrolysis during the preparation. Zhong et al. (2019) used modified palygorskite (Pal) as a hard template and glucose as a carbon source to synthesize carbon-coated palygorskite (Pal@ C) by impregnation and carbonization, with further final acid-base treatment to remove the Pal template to obtain amorphous carbon nanotubes (ACNT).

Spherical particles were also successfully applied as hard templates for the synthesis of adsorbents, such as poly (methyl methacrylate) (PMMA) microspheres. Using PMMA colloidal microspheres as template agents can synthesize three-dimensional hierarchical porous graphene-Fe_3O_4 (3D-HPGF) nanocomposites, and the PMMA templates were removed by calcination at 873 K under nitrogen atmosphere (Liu et al., 2018). Similarly, by using $CaMg(CO_3)_2$ microspheres as a template agent and $Al(NO_3)\cdot 9H_2O$ as an aluminium source, Al_2O_3 hollow microspheres can be successfully synthesized with further calcinations, and the $CaMg(CO_3)_2$ microsphere template was also removed by calcination during the preparation process (Tian et al., 2016).

2.2 Soft Template

Soft templates mainly rely on intermolecular interaction forces to maintain the stability of the structure, and the material diffuses through the cavity walls into the interior of the static pore. Wan and Zhao (2007)schematically summarized the two mechanisms for the synthesis of soft templates (**Figure 5**), including the cooperative self-assembly and liquid-crystal templating processes. As shown in **Figure 5A**, cooperative self-assembly is based on inorganic–organic interactions between inorganic and surfactants. In this pathway, inorganic species and surfactants cooperate to nucleate as well as form liquid crystals with molecular inorganics, removing the template after further polymerization and condensation of inorganics. As shown in **Figure 5B**, the "true" liquid crystal templating process is that the liquid crystal mesophases are involved in the templating assembly to synthesize aimed materials, which means the liquid crystals are incorporated directly with precursors, and the template is removed after the transformation of the precursor to target product by reaction.

The advantages of the soft template method typically include simple construction, relatively mild experimental conditions, and its capacity to synthesize different materials with various morphologies. However, it has low structural stability compared to the hard template method, which results in it being a less efficient template. Typically, organic molecules are used as soft templates, such as micelles (Zhao et al., 2006; Gao et al., 2015), emulsified droplets (Bourret and Lennox, 2010; Wang B. et al., 2011; Pang M. et al., 2013), biological molecular assemblies (Yan et al., 2017; Zhao et al., 2017; Wang Y. et al., 2020), gas bubbles (Fan et al., 2004; Yan and Xue, 2007), etc., and the specific materials are described below.

2.2.1 Micelle Templates

Micelles, refer to the aggregates by the mutual attraction of hydrophobic parts of surfactants after they are dissolved in water, which have excellent solubilization effects, are extremely common and highly versatile soft template materials. However, during the preparation process, a single aggregated micellar template tends to be very sensitive to the solvent, resulting in it being unstable in the reaction. In the recent years, it has been found that the introduction of surfactants in the preparation process can effectively improve this phenomenon. For example, Zhao et al. (2006) prepared SnO_2 hollow spheres using micelles composed of terephthalic acid and sodium dodecylbenzene sulfonate (SDBS) as templates, and successfully constructed hollow structures for the materials. Gao et al. (2015) used worm-like micelles as soft templates to prepare Au and Au-based alloy nanowire networks with adjustable composition ratios. The worm-like micelles were obtained by mixing $HAuCl_4$ and 3-(N,N-dimethylpalmitylammonio) propanesulfonate (PAPS) in an aqueous solution, and the AuAg and AuPt alloy nanowire networks were synthesized by a stepwise reduction method using $NaBH_4$-PAPS and ascorbic acid (AA)-PAPS mixtures as reductants.

2.2.2 Emulsion-Based Templates

Emulsified droplets, a non-homogeneous system formed within a mixture of two and more incompatible liquids, are an important class of soft templates. During the preparation process, emulsion droplets usually obtain materials with hollow structures through sol-gel coating, interfacial precipitation, and hydrothermal reactions. Pang M. et al. (2013) chose polyoxyethylene and sorbitan trioleate to form emulsified droplets, and used them as templates to synthesize Fe-soc-MOF cubes *via* solvothermal method. After removing the droplets, Fe-soc-MOF cubic hollow colloids with different sizes and arrangements with a specific surface area of 1100 m^2/g, and a total pore volume of 0.49 cm^3/g were obtained.

Oil-in-water (O/W) microemulsions and water-in-oil (W/O) microemulsions are two important types of emulsified droplets. Wang B. et al. (2011) used glycerol/water as emulsion templates and Fe_2O_3 nanoparticles as raw materials to synthesize α-Fe_2O_3 hollow spheres with lamellar substituents under hydrothermal conditions. The prepared templated material has a large cavity space and well-defined shell layer, and has a specific surface area of 103.3 m^2/g and a wide pore size distribution. Similarly, the W/O microemulsion templates have been widely applied at present. For example, Bourret et al. (Bourret and Lennox, 2010) used CH_2Cl_2 solution as the aqueous phase of the microemulsion and obtained copper hydroxide nanofibers (NF) by interfacial reaction in a two-phase system (H_2O/CH_2Cl_2). As the reaction proceeds, porous microspheres with shell-like structures were finally synthesized, and the prepared CuS nanohollow spheres have a diameter of about 200 nm and a wall thickness of about 30 nm.

2.2.3 Biological Templates

Biological templates, such as biopolymers, cellular tissues, bacteria, and DNA, are some of the most common soft templates, because of their wide source, non-toxicity, non-contamination, and low cost, they have a great potential in the development of template agents. Zhao et al. (2017) treated rape pollen grains with anhydrous ethanol and 8 M hydrochloric acid, respectively, and dried at room temperature to obtain two types of pollen templates. These two pollen templates were used to synthesize ZrO_2 hollow microspheres with scale-like outer walls (S-1) and porous hollow ZrO_2 microspheres (S-2) via the same experimental method, that is, treated by microwave solvothermal method at 110˚C, washed with distilled water and absolute ethanol, dried, and calcined at 580˚C. The specific surface areas of S-1 and S-2 are 27.99˚m^2/g and 40.92˚m^2/g, respectively, while the average pore diameters are 14.57 and 10.19˚nm, respectively.

In addition, cotton is one of the most common biological templates. The dried cotton templates were dipped into the solution for hydrolysis treatment, followed by the reaction in the reactor under nitrogen atmosphere and washed with anhydrous ethanol and deionized water, and dried to obtain the corresponding cotton templated materials. For example, Yan et al. (2017) prepared fibrous magnesium oxide by template-directed synthesis using cotton as a template agent and hydrolyzed in cetyltrimethylammonium bromide solution. Wang Y. et al. (2020) used cotton as a template agent and hydrolyzed it in sulfuric acid solution to synthesize mesoporous carbon lanthanum-doped films (MC-La).

2.2.4 Other Soft Templates

In addition to the template materials mentioned above, bubbles, vesicles, and amphiphilic polymers are also excellent materials for soft templates. The preparation process of bubble templates in the liquid phase usually consists of the following two steps: preparation of the template (generation of bubble emulsion), deposition/adsorption of particles on the template surface, and further growth/aggregation of particles (Fan et al., 2004). In addition, Yan and Xue (2007) used the CO_2 bubbles generated during the reaction as a template agent to obtain ZnO hollow microspheres by pyrolysis.

Vesicles, as one of the most important microreactors for controlled growth, are important materials for soft templates. Zheng et al. (2002) obtained anionic sodium dodecyl sulfate (SDS) vesicles by ultrasonic irradiation and used them as soft templates. The cadmium ions were adsorbed on the surface of the templates by electrostatic interaction, and after washing with distilled water and anhydrous ethanol to remove the templates, CdSe hollow nanoparticles with the size of 100–200 nm were obtained.

Amphiphilic polymers can also be used as soft templates to synthesize hollow structural materials, and different morphologies of materials can be obtained by adjusting the size and composition of the template. For example, Lin et al. (Pang X. et al., 2013) used a star-shaped PS-b-PAA-b-PS triblock copolymer as soft templates to synthesize hollow gold nanoparticles.

3 MODERATING THE BEHAVIOR OF MATERIALS BY THE TEMPLATE METHOD

3.1 Pore Structure Tuning

The size and nature of different template agents vary, and their introduction into the same material or different materials will result in different specific surface areas, pore sizes, and pore volumes; the pore sizes and volumes will show a certain variation with the concentration of the template agent. In general, smaller sized and more concentrated template

TABLE 1 | Structural parameters of the samples synthesized with different templates.

Sample	Template agent	Specific surface area (m^2/g)	Pore volume (cm^3/g)	Average pore size (nm)	References
Al_2O_3 (CTAB)	Cetyltrimethylammonium bromide (CATB)	335.7	0.66	6.1	Bo and Jing (2007)
Al_2O_3 (CA)	Sodium laurate (CA)	312.0	0.44	4.1	
Al_2O_3 (P123)	PPO-PEO-PPO (P123)	318.8	1.00	9.8	
Aluminosilicate materials (CTAB)	Cetyltrimethylammonium bromide (CTAB)	211.5	0.31	4.4	Ma et al. (2020)
Aluminosilicate materials (DETA)	Diethylenetriamine (DETA)	75.2	0.12	4.8	
Aluminosilicate materials (CMC)	Sodium carboxymethylcellulose (CMC)	161.5	0.37	6.2	
Aluminosilicate materials (SDS)	Sodium dodecyl sulfate (SDS)	144.3	0.27	5.4	
Aluminosilicate materials (F68)	PEO_{80}-PPO_{30}-PEO_{80} (F68)	277.6	0.24	6.0	
Aluminosilicate materials (F108)	PEO_{133}-PPO_{50}-PEO_{133} (F108)	289.7	0.24	6.5	
S7	F127 ($EO_{106}PO_{70}EO_{106}$)	1022	1.35	5.3	Yang et al. (2006)
S14	F127 + PEG	1145	0.82	2.9	
Mesoporous Titania (TS-0.1)	Cetyltrimethylammonium chloride (CTAC)	83.8	0.17	9.0	Yusuf et al. (2003)
Mesoporous Titania (TP-0.1)	Polyethylene glycol (PEG)	57.1	0.094	8.4	
Mesoporous Titania (TPS-0.01)	CTAC + PEG	39.6	0.076	6.2	
Nano ferric oxides (C-Fe_2O_3)	Cetyltrimethylammonium bromide (CTAB)	24.8	0.11	11.9	Lei et al. (2018)
Nano ferric oxides (G-Fe_2O_3)	Glycerine (GI)	23.6	0.091	10.2	
Nano ferric oxides (T-Fe_2O_3)	Tartaric acid (TA)	40.8	0.092	4.8	
ZSM-5 Zeolite (NZ)	Tetrapropylammonium hydroxide (TPAOH)	364.0	0.39	—	Zhang et al. (2015)
ZSM-5 Zeolite (MZ)	Cetyltrimethylammonium bromide (CTAB)	374.0	0.45	—	
ZSM-5 Zeolite (NSZ)	N-octadecyl-N′-hexyl-tetramethyl-1,6-hexanediaminium ($C_{18\text{-}6\text{-}6}Br_2$)	505.0	0.63	—	

agents are more favorable for the preparation of templated materials.

3.1.1 Effect of Template Agent Type on Pore Structure

The specific surface area, pore volume, and pore size of the synthesized materials varied considerably depending on the template agent (**Table 1**). The pore size of the materials depends on the size of the template agent used. When the radius of the template agent is smaller than the pore size of the precursor, it can be easily incorporated into the precursor, thus limiting the pore shrinkage of the material during the reaction process. After the reaction, when the radius of the template agent is still smaller than the pore size of the synthetic material, the pore structure will remain after the template agent is removed, resulting in larger pore size of the material and further increasing its specific surface area and pore volume. Therefore, the template with a smaller pore diameter than the material should be selected.

Using different sizes of template agents will produce materials with different structures. Some synthetic materials have many mesopores, as well as slit pores formed by the accumulation of particles, which all can lead to an uneven distribution of pore sizes in the synthesized material and thus affect the structural parameters of the material. Therefore, the specific surface area, pore diameter, and pore volume of the same material synthesized with different templates are different. For instance, mesoporous alumina was prepared using cetyltrimethylammonium bromide (CATB), sodium laurate (CA), and poly (propylene oxide)-Poly (ethylene oxide)-Poly (propylene oxide) (PPO-PEO-PPO, P123) as template agents, respectively (Bo and Jing, 2007); aluminosilicate mesoporous materials were synthesized using cetyltrimethylammonium bromide (CTAB), diethylenetriamine (DETA), sodium carboxymethylcellulose (CMC), sodium dodecyl sulfate (SDS), and polyethylene glycol-polypropylene glycol-polyethylene glycol (PEO_{80}-PPO_{30}-PEO_{80}, F68 and PEO_{133}-PPO_{50}-PEO_{133}, F108) as template agents correspondingly (Ma et al., 2020); and silica spheres were prepared using pluronic triblock copolymer ($EO_{106}PO_{70}EO_{106}$, F127), F127, and PEG respectively as template agents (Yang et al., 2006).

3.1.2 Effect of Template Agent Concentration on Pore Structure

The concentration of the template agent also has a large effect on the specific surface area, pore volume, and pore size of the synthetic material. As the concentration of the template agent increases, the average pore size of the material gradually increases, and the pore capacity also increases accordingly. Nevertheless, the change in specific surface area is related to the porosity of the synthetic material, so for different synthetic materials, the specific surface area has a different change pattern of the change in mass concentration.

For example, the use of polyethylene glycol (PEG) and/or cetyltrimethylammonium chloride (CTAC) as templates enables the preparation of mesoporous titanium dioxide (**Table 2**). It was shown that with the increase of CTAC and PEG concentration, the specific surface area, average pore size,

TABLE 2 | Structural parameters of the samples synthesized with different concentrations of templates.

Template agent	Concentrations (g/ml)	Specific surface area (m^2/g)	Pore volume (cm^3/g)	Average pore size (nm)	References
PEO_{133}-PPO_{50}-PEO_{133} (F108)	0.01	297.6	0.23	6.0	Ma et al. (2020)
	0.02	269.8	0.25	6.4	
	0.03	237.6	0.26	7.2	
	0.04	204.6	0.27	11.7	
Cetyltrimethylammonium chloride (CATC)	0	38.6	0.063	5.2	Yusuf et al. (2003)
	0.001	54.2	0.078	4.6	
	0.01	56.6	0.088	5.0	
	0.05	72.8	0.13	7.6	
	0.1	83.8	0.17	9.0	
Polyethylene glycol (PEG)	0.01	27.8	0.041	4.8	
	0.05	47.3	0.067	4.6	
	0.1	57.1	0.094	8.4	

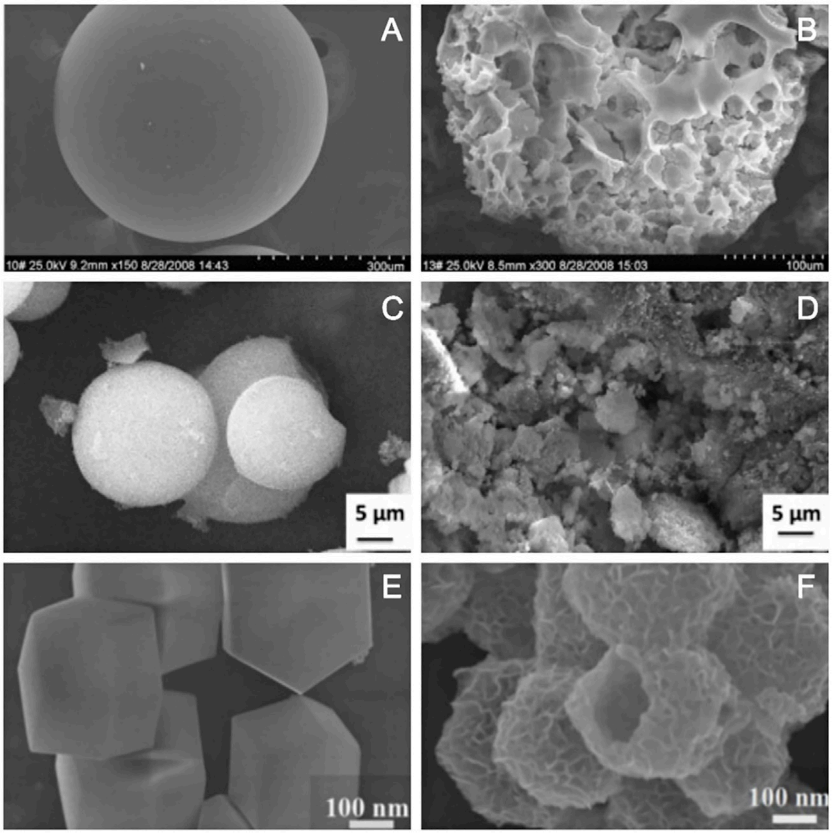

FIGURE 6 | SEM images of D311 resin **(A)** and PCTOM **(B)** (Zhang et al., 2011); SiO_2 **(C)** and Fe_2O_3/SiO_2 composite monoliths **(D)** (Singh et al., 2018); ZIF-67 **(E)** and NiCo-LDH **(F)** (Hu et al., 2019).

and pore volume of the gel increased. These structural parameters of gels prepared from CTAC solution (TS-0.1), gels prepared from PEG solution (TP-0.1), and dry gels prepared from CTAC and PEG were higher than those without additives (TiO_2-0), and the specific surface area and pore size of TS-0.1 were even about twice as large than those of TiO_2-0 (Yusuf et al., 2003). The average pore size and pore volume of the silica-aluminate mesoporous material synthesized using F108 as a template agent gradually increased with increasing mass concentration of F108, but the specific surface area gradually decreased (Ma et al., 2020).

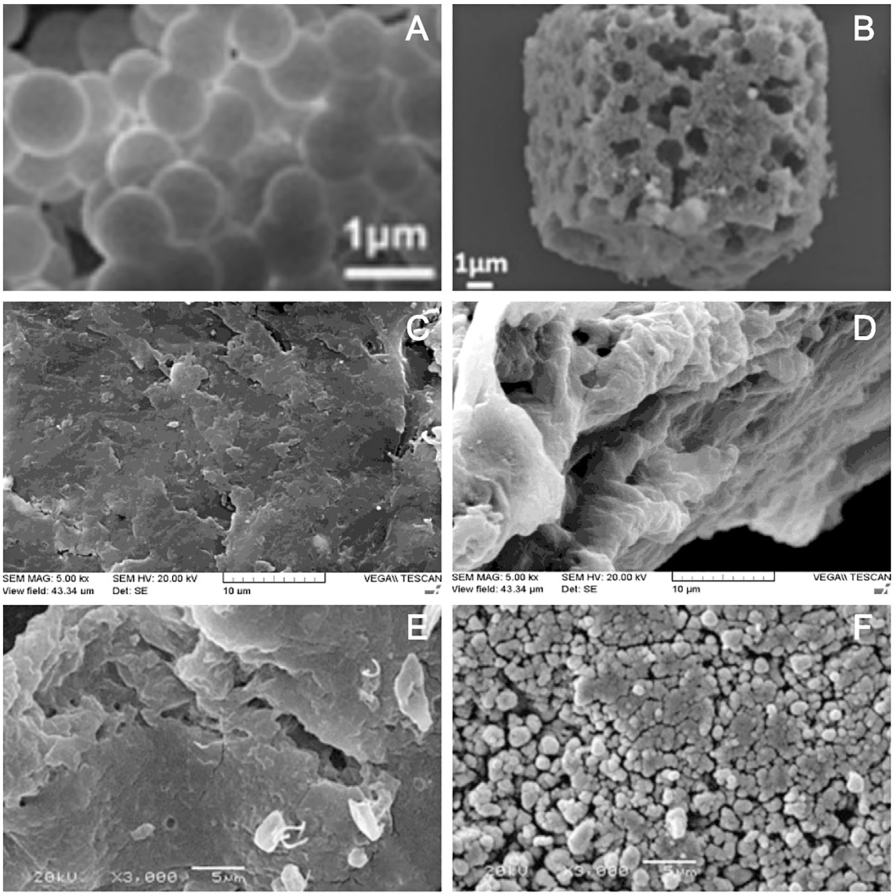

FIGURE 7 | SEM images of carbon sphere **(A)** and DP Mn_2O_3-carbon-PVP cubes **(B)** (Shao et al., 2017); CTS **(C)** and TCCTS **(D)** (Dai et al., 2012); NSC **(E)** and crosslinked NSC resin **(F)** (Sun et al., 2007).

3.2 Morphology Tuning

The introduction of template will change the microstructure of materials. Different template agents will get different structures, such as porous structure, worm-like structure, core-shell structure, etc. As the mass transfer of contaminants within an adsorbent is largely dependent on the pore structure of the material, this section will focus on porous materials, which are subdivided into disordered and ordered pore structures.

3.2.1 Disordered Porous Structure

The template method is mainly used to make the porous structure on the surface of materials or to make the surface rough. In some cases, the porous structure is disordered. Considering the template to be the skeleton, the material with pore structure can be obtained by solution etching, for example, using D311 resin as the template skeleton to synthesize porous nano-calcium titanate microspheres (PCTOM). The D311 resin is a sphere with a smooth surface (**Figure 6A**); the surface of the synthesized material became rough and disordered porous structure was obtained (**Figure 6B**; Zhang et al., 2011). SiO_2 is a spherical particle with smooth surface (**Figure 6C**). Considering it to be the template skeleton and introducing the precursor Fe_2O_3, the Fe_2O_3/SiO_2 composite monoliths with rough surface and pore structure can be obtained (**Figure 6D**; Singh et al., 2018). Zeolitic imidazolate framework-67 (ZIF-67) is a dodecahedral structure with a smooth surface (**Figure 6E**), which is used as a template skeleton to synthesize hierarchical porous Ni/Co-layered double hydroxide (NiCo-LDH), and the NiCo-LDH is a hollow dodecahedron with porous structure (**Figure 6F**; Hu et al., 2019).

The disordered porous material with rough surface can also be obtained by using porous material as the precursor, meanwhile, taking it as skeleton and introducing template into its pores. The carbon spheres are smooth spheres (**Figure 7A**) and when used as templates for the synthesis of double porous Mn_2O_3 (DP Mn_2O_3-carbon-PVP) cube, the carbon spheres embedded the precursor well and the final material with rough surface and porous structure was obtained (**Figure 7B**; Shao et al., 2017). The surface of the chitosan (CTS) is relatively smooth and the structure is compact (**Figure 7C**). After introducing the template Fe(III), the surface of the thiourea cross-linked chitosan (TCCTS) obtained is rough and the structure is incompact and reticular with disordered pore structure (**Figure 7D**; Dai et al., 2012). Crosslinked NSC resin was

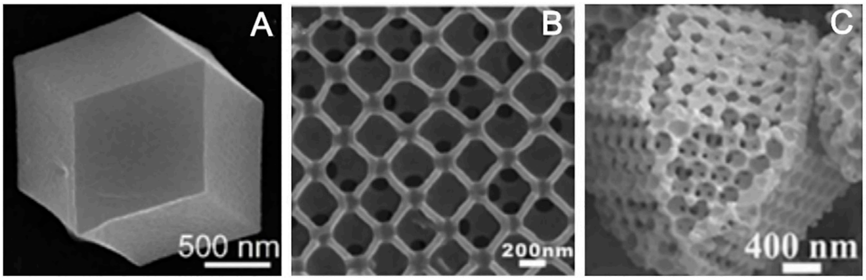

FIGURE 8 | SEM images of ZIF-8 **(A)** (Salunkhe et al., 2016); HKUST-1 **(B)** (Wu et al., 2011); and SOM-ZIF-8**(C)** (Shen et al., 2018).

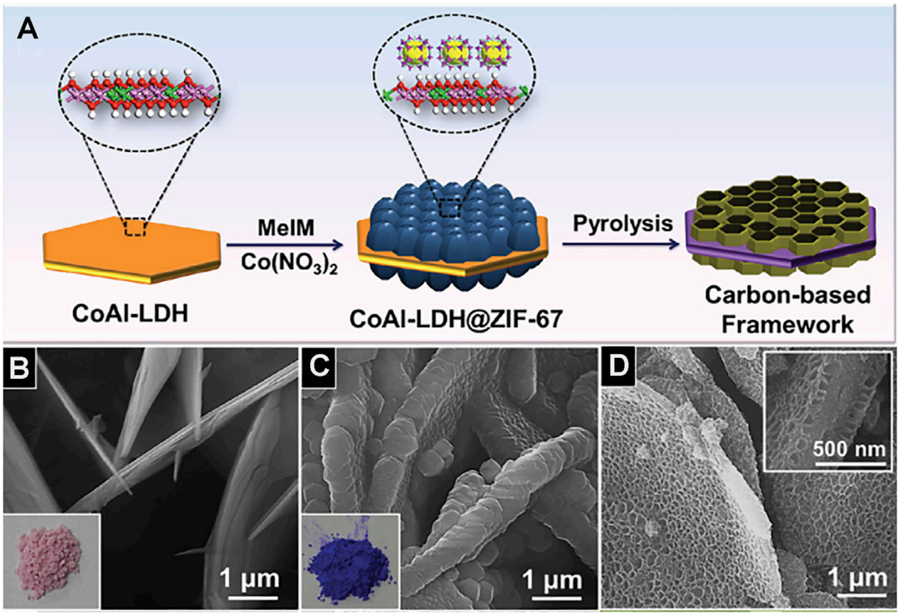

FIGURE 9 | (A) Schematic illustration for the synthesis of porous carbon-based framework. SEM images of CoAl-LDH **(B)**, CoAl-LDH@ZIF-67 **(C),** and LDH@ZIF-67-800 **(D)** (Li et al., 2016).

synthesized with N-succinyl-chitosan (NSC) as the precursor skeleton and Cu (II) as a template agent. After the introduction of template, the surface structure of crosslinked NSC resin was denser than that of NSC and has a porous structure (**Figures 7E,F**; Sun et al., 2007).

3.2.2 Ordered Porous Structure

Template method can also construct the ordered porous structure. Metal–organic framework polymer is one of the most typical examples, although different templates will get different structural materials, they almost have ordered pore structure. For instance, metal–organic frameworks (MOFs) ZIF-8 synthesized by the template-free method has a dodecahedral shape, but without porous structure (**Figure 8A**; Salunkhe et al., 2016). Using polystyrene (PS) as a template agent, MOFs precursor solution was introduced to infiltrate the template. After removing the template, HKUST-1 crystal was obtained. HKUST-1 has three-dimensionally ordered and interconnected macropores (**Figure 8B**; Wu et al., 2011). PS has adjustable and stable morphology in methanol solution (MeOH). After the precursor infiltrates the template PS, it exposed the precursor@PS to NH_3/MeOH solution and SOM-ZIF-8 with three-dimensionally ordered macropores can be obtained (**Figure 8C**; Shen et al., 2018). Using CoAl-layered double hydroxide (CoAl-LDH) as a template skeleton, and introducing ZIF-67 to synthesize CoAl-LDH@ZIF-67, the final material LDH@ZIF-67-800 was obtained after the removal of the template by pyrolysis and the synthetic path is shown in **Figure 9A**. LDH@ZIF-67-800 is a surface ordered porous structure (**Figure 9C**; Li et al., 2016).

In addition to MOF materials, ordered porous structures can also be obtained for some other templated materials. For example, using nanoporous anodic alumina (NPAA) as the template skeleton, the synthesized carbon nanotube arrays have a highly

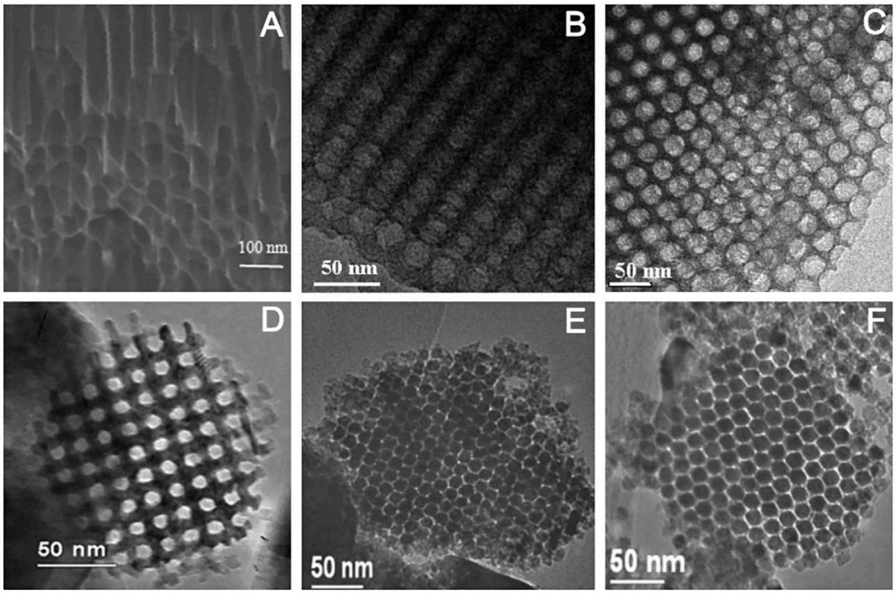

FIGURE 10 | SEM images of s of CNTs arrays/NPAA composite membrane **(A)** (Mohajeri et al., 2017); TEM images of C-FDU-18-800 **(B)** and Si-FDU-18-HC **(C)** (Deng et al., 2007); Cr_2O_3 **(D),** (Jiao et al., 2005), In_2O_3 **(E),** and Co_3O_4 **(F)** (Yue and Zhou, 2007).

ordered pore structure (Mohajeri et al., 2017; **Figure 10A**). The mesoporous carbon (C-FDU-18-800) and mesoporous silica (Si-FDU-18-HC), synthesized using poly (ethylene oxide)-b-polystyrene (PEO-b-PS) diblock copolymers as templates, have highly ordered mesoporous structures (**Figures 10B,C**; Deng et al., 2007). Similarly, metal oxides such as Cr_2O_3 (**Figure 10D**; Jiao et al., 2005), In_2O_3 (**Figure 10E**), and Co_3O_4 (**Figure 10F**; Yue and Zhou, 2007), synthesized with mesoporous silica as the template skeleton, all have regular mesoporous structures.

4 APPLICATION TO TYPICAL POLLUTANTS IN WASTEWATER

Current research on templated materials as adsorbents is focused on two types of pollutants, namely dyes and heavy metals. As mentioned above, the template method can effectively modulate the morphological and structural parameters such as pore size, pore volume, and specific surface area of materials, which are the direct factors affecting the adsorption performance. In addition to enormous specific surface area and rich pore structure, the introduction of templates to modulate the surface functional groups and charges can achieve significant improvements in the adsorption performance of the target pollutants.

4.1 Heavy Metals

Heavy metals in water, even at very low concentrations, are extremely harmful to humans and the ecology. Currently, templated materials have been widely used for the adsorption of heavy metal ions in water like Ni(II), Co(II), Cu(II), Cr(III), Pb(II), etc., and have exhibited relatively outstanding adsorption capacities (**Table 3**). For example, using attapulgite (ATP) as a template agent, a novel polyaniline/attapulgite (PANI/ATP) composite material can be obtained by oxidative polymerization. The PANI/ATP exhibited an excellent adsorption capacity for Hg(II) (824 mg/g) (Cui et al., 2012), which was much higher than those of PANI (600 mg/g) (Wang et al., 2009)– amine resins (156–556 mg/g) (Zhu and Alexandratos, 2005; Alexandratos, 2007), aniline-m-sulfophenylenediamine copolymer (PANSP) (498 mg/g) (Lü et al., 2007), chitosan beads (323 mg/g) (Li et al., 2005), and mercaptopropyl mesoporous adsorbent (461 mg/g) (Brown et al., 2000). Using SiO_2 monoliths as a template agent to synthesize metal oxide monoliths (Fe_2O_3/SiO_2), the Fe_2O_3/SiO_2 demonstrated high adsorption capacities for Pb(II) (850 mg/g) and Cr(III) (770 mg/g) (Singh et al., 2018), which were much higher than those of Fe_2O_3 monoliths (166 mg/g) (Singh et al., 2018), carbon coated monoliths (72 mg/g) (Teoh et al., 2013), and mesoporous silica (184 mg/g) (Awual and Hasan, 2014) for Pb(II), and those of Fe_2O_3 monoliths (125 mg/g) (Singh et al., 2018), modified lignin (68 mg/g) (Demirbaş, 2005), and borax sludge (16 mg/g) (Senberber et al., 2017) for Cr(III).

4.1.1 Factors Affecting the Adsorption of Heavy Metals by Templated Materials

Like conventional adsorbents, adsorbents prepared by the template method are also mainly influenced by factors such as pH and temperature.

Solution pH is one of the most critical factors affecting the adsorption of heavy metal ions by templated materials. Normally, as the pH increases, the proton concentration decreases and the adsorption of heavy metal ions increases accordingly. Nevertheless, when the solution is in an alkaline environment,

TABLE 3 | Properties of various template materials and their ability to adsorb heavy metals.

Samples	Template agent	Surface area (m^2/g)	Adsorbate	Adsorption capacity (mg/g)	Equilibrium time (min)	pH	Kinetics	Thermodynamics	Isotherms	Cycle numbers	References
C_{KIT-6}	KIT-6	821	Ni(II) Co(II)	145 148	— —	5	Pseudo second order	Spontaneous and endothermic	Langmuir	—	Marciniak et al. (2019)
Fe_2O_3/ SiO_2	SiO_2	562	Cd(II) Cr(III) Pb(II)	690 770 850	120	6	Pseudo second order	Spontaneous and exothermic	Freundlich and Langmuir	—	Singh et al. (2018)
CF-S-N	SiO_2	—	Cu(II) Mn(II) Cd(II) Pb(II)	197 195 187 183	200	7	Pseudo second order	Spontaneous and endothermic	Langmuir	—	Ren et al. (2017)
PANI/ATP	ATP	95	Hg(II)	824	200	6	Pseudo second order	Spontaneous and endothermic	Langmuir	5	Cui et al. (2012)
MCMs	SiO_2	682	U(VI)	294	120	4	Pseudo second order	Spontaneous and endothermic	Langmuir	5	Zhang et al. (2017)
NSHS	$CaCO_3$	—	Pb(II)	267	—	—	Pseudo second order	Spontaneous and endothermic	Langmuir	—	Manyangadze et al. (2020)
MP-Silica	Citric acid	504	Ag(I)	115	30	1–7	Pseudo second order	—	Langmuir	—	Pongkitdachoti and Unob (2018)
C_{ST}	F127	426	Ni(II) Co(II)	126 135	— —	5	Pseudo second order	Spontaneous and endothermic	Langmuir	—	Marciniak et al. (2019)
PCTOM	D311 resin	—	Pb(II) Cd(II) Zn(II)	30 30 15	142 18 24	6	Pseudo second order	Spontaneous and endothermic	Langmuir	—	Zhang et al. (2011)
TP-CMCBs	$CaCO_3$	53	Cu(II) Mn(II) Ni(II)	342 262 243	30 30 30	6	Pseudo second order	—	Langmuir	5	Liu et al. (2021)
MSC	CTMAB-MA	239	Ni(II) Cu(II) Zn(II) Pb(II) Mn(II) Cd(II)	278 390 402 452 201 438	80 30 80 40 110 60	5–7.5	Pseudo second order	Spontaneous and endothermic	Langmuir	2	Liu et al. (2020)
TCCTS	Fe(III)	—	Fe(II) Fe(III)	48 72	60	5	Pseudo second order	—	Langmuir	—	Dai et al. (2012)
NiCo-LDH	$Ni(NO_3)_2$	267	Cr(VI)	100	50	—	Pseudo second order	—	Langmuir	5	Hu et al. (2019)
MSNs	CTAB	675	Fe(III)	21	50	—	Pseudo second order	—	Langmuir	4	Meng et al. (2018)

hydroxyl ions form precipitates of hydroxides with metal ions, resulting in a decrease in the adsorption capacity of the adsorbent. For example, as the pH value of the solution is increased from 1 to 5, the adsorption capacity of both Fe(II) and Fe(III) by the thiourea crosslinked-chitosan (TCCTS) synthesized with iron (III) as a template agent gradually increased, and thereby reaching a maximum at pH = 5. In the higher pH range, the adsorption capacity of TCCTS decreases sharply (Dai et al., 2012).

Temperature is also one of the important factors affecting the adsorption of heavy metal ions in solution, as it mainly affects mobility and chain flexibility of metal ions, resulting in an increase in the adsorption capacity of the adsorbent with increasing temperature. For example, as temperature was increased from 25 to 55°C, the adsorption capacity of Cu(II) by the templated material CF-S-N increased from 196 mg/g to 199 mg/g. The adsorption of Cu(II) by polyacrylamide/ functionalized multi-walled carbon nanotube PAAm/ FMWCNTs) composites (Abo-Zahra et al., 2021) and the adsorption of Ni(II) and Co(II) by ordered mesoporous carbon (Marciniak et al., 2019) show this trend.

Furthermore, the adsorption kinetics of the adsorbent synthesized by template method fit the pseudo-second-order kinetic model, indicating that chemisorption primarily promotes the adsorption of heavy metal ions. The relevant thermodynamic parameters were calculated to confirm that the adsorption process is spontaneous and endothermic for most of the adsorbents. And the adsorbents all fit more closely to the Langmuir adsorption model, therefore the adsorption of heavy metal ions onto the synthesized adsorbents can be considered as a monolayer adsorption process.

4.1.2 Mechanisms of Heavy Metal Adsorption

As mentioned in the previous section, the introduction of a template agent can effectively regulate the specific surface area, pore diameter, and pore volume of materials and change the microscopic morphology of materials, all of which provide the possibility to improve the adsorption performance of the material. On the one hand, the pore structure constructed by the template method can provide wider diffusion channels and lower mass transfer resistance, which facilitates the rapid diffusion of heavy metal ions in the internal structure of the adsorbent. On the other hand, the large specific surface area and pore size distribution formed by the template method provide more active sites for the adsorbent. For instance, mesoporous carbon (MCMs), synthesized using ordered mesoporous silica as a template agent, has a specific surface area of 682 m^2/g (Zhang et al., 2017), which is higher than other carbon-based nanomaterials such as graphene oxide supported polyaniline (141 m^2/g) (Sun et al., 2013) and carbonaceous nanofibers (264 m^2/g) (Sun et al., 2016). Correspondingly, MCMs have a good adsorption property for U(VI) of 294 mg/g, which is also higher than that of graphene oxide-supported polyaniline (245 mg/g) and carbonaceous nanofibers (125 mg/g) (**Table 3**).

For templated materials, in addition to the pore adsorption mechanism, ion exchange, electrostatic interaction, and surface complexation are also the predominant adsorption mechanisms of heavy metals. The introduction of templates can alter the surface chemistry of the materials, providing favorable ions and functional groups for adsorption, as well as altering the surface charge properties of the material, all of which contribute to the adsorption performance of the material. For instance, templated material mesoporous carbons (MCMs) containing a large number of oxygenated functional groups such as -OH and -COOH have good adsorption properties for cationic heavy metals such as U(VI) (Zhang et al., 2017). For materials with an intrinsic surface charge that is less conducive for the adsorption of ions, for example, natural attapulgite (ATP), which has negatively charged functional groups on its surface and does not have electrophoretic mobility equal to zero, was used as a template agent to polymerize aniline, the obtained polyaniline/attapulgite (PANI/ATP) exhibits a point of zero charge and achieved a maximum adsorption capacity of Hg(II) over 800 mg/g (Cui et al., 2012). After the introduction of the template, the positively charged hierarchical porous Ni/Co-layered double hydroxide (NiCo-LDH) hollow dodecahedra exhibiting excellent adsorption properties for the negatively charged Cr(VI) ions in aqueous solution, and the NO- 3 ions which initially on the surface of the NiCo-LDH were replaced by Cr(VI) ions after adsorption (Hu et al., 2019; **Table 3**).

4.2 Dyes

Wastewater discharged from the printing, electroplating, textile, and leather industries contains large amounts of toxic and non-biodegradable dyes that have an irreversible effect on humans and the environment. The use of templated materials for the adsorption of dyes such as bisphenol A, rhodamine B, and methylene blue in wastewater exhibit better adsorption properties than the most conventional adsorbents. For example, Al_2O_3 hollow microspheres (AHS) adsorbed as much as 690 mg/g of Congo Red (Tian et al., 2016). Its adsorption performance outperformed many other metal oxide adsorbents such as Co_3O_4-Fe_3O_4 hollow spheres (123 mg/g) (Wang X. et al., 2011), NiO nanospheres (440 mg/g) (Zhu et al., 2012), and MgO-$MgFe_2O_4$ composite (498 mg/g) (Han et al., 2014). The new hollow polydopamine microcapsules (H-PDA-MCs) showed a capacity of 179 mg/g for methylene blue (Feng et al., 2021), exceeding that of PDA microspheres (91 mg/g) (Fu et al., 2015), palm kernel fibres (95 mg/g) (El-Sayed, 2011), and magnetic γ- Fe_2O_3/SiO_2 (116 mg/g) (Chen et al., 2016).

4.2.1 Factors Affecting the Adsorption of Dyes by Templated Materials

The solution pH value is regarded as one of the most important factors affecting the adsorption of organic dyes. In general, the adsorption of anionic dyes increases with decreasing pH, while the opposite is true for cationic dyes. For anionic dyes, competition between OH^- and anionic dyes for adsorption is intense in the high pH range, while at low pH, the hydroxyl and carboxyl groups will be protonated to form -OH+ 2 groups, strengthening the electrostatic gravitational force between the adsorption site and the anionic dyes. For example, poly (acrylamide-acrylic acid-dimethylaminoethyl methacrylate) P(AAm-AA-DMAEMA) resin is effective for the adsorption of indigo carmine and eriochrome black-T anionic dyes, and the

TABLE 4 | Properties of various template materials and their ability to adsorb organic pollutant.

Sample	Template agent	Surface area (m^2/g)	Adsorbate	Adsorption capacity (mg/g)	Equilibrium time (min)	pH	Kinetics	Isotherms	Cycle numbers	References
DP Mn_2O_3-carbon-PVP	Carbon spheres	37	Congo Red	126	20	—	Pseudo second order	Langmuir	4	Shao et al. (2017)
AHS	$CaMg(CO_3)_2$	318	Congo Red	690	120	5–6	Pseudo second order	Langmuir	—	Tian et al. (2016)
MWCNTs@ carbon	MWCNTs	—	Methylene Blue Crystal Violet	298 228	120	8–9	Pseudo second order	Langmuir	—	Liu et al. (2015)
CNTs	Pal	887	Congo Red Methyl Orange	468 253	30	1–13	Pseudo second order	Langmuir	—	Zhong et al. (2019)
CMK-3	CMK	1420	Bisphenol-A	474	20	6	Pseudo second order	Freundlich	—	Libbrecht et al. (2015)
TNC	MCM-22	660	Amoxicillin Ethinylestradiol	69 61	—	—	—	Langmuir	—	Barrera et al. (2014)
NMCS	SiO_2	789	Methyl Orange	352	200	2	Pseudo second order	Langmuir	5	Jiao et al. (2017)
3D-HPGF	PMMA	486	Methylene Blue	70	25	—	Pseudo second order	Langmuir	5	Liu et al. (2018)
P (AAm-AA-DMAEMA)	PAAm	—	Indigo Carmine Eriochrome Black-T	— —	120	2.5	Pseudo second order	Freundlich	—	Abdel-Aziz and Siyam, (2011)
SMC	SMC	476	Bisphenol-A	154	60	1–7	Pseudo second order	Freundlich	—	Libbrecht et al. (2015)
S-2	Rape pollen	41	Congo Red	97	120	—	Pseudo second order	Langmuir	—	Zhao et al. (2017)
OMCs	F127	424	Rhodamine B	—	240	5	Pseudo second order	—	—	Cao et al. (2014)
C-V-50-T-50-600	PEO-PBO-PEO	810	Lysozyme	446	—	—	—	Langmuir	—	Wickramaratne and Jaroniec (2013)
NiCo-LDH	$Ni(NO_3)_2$	267	Congo red	909	80	—	Pseudo second order	Langmuir	5	Hu et al. (2019)

property of adsorption decreases with increasing pH (Abdel-Aziz and Siyam, 2011). The adsorption of methylene blue and crystalline violet by the MWCNTs@carbon with negative surface charge was low in acidic solutions and increased significantly with increasing pH (Liu et al., 2015).

However, unlike the templated materials for the adsorption of heavy metal ions, the templated materials for the adsorption of dyes are either endothermic or exothermic processes, resulting in different trends in their temperature dependence. For example, as the temperature increases, the adsorption of amorphous carbon nanotubes (ACNTs) increases (Zhong et al., 2019) while the adsorption of P(AAm-AA-DMAEMA) resin decreases (Abdel-Aziz and Siyam, 2011).

As can be seen from **Table 4**, the organic dye molecules almost always conform to the quasi-secondary kinetic model on the template materials. Unlike the adsorption of heavy metal ions, while the adsorption isotherms of most of the template materials conform to the Langmuir model, a few conform to the Freundlich model, indicating that for the adsorption of dyes, in addition to monolayer adsorption, multilayer adsorption can occur within the pore channels of a small number of template materials.

4.2.2 Mechanisms of Dye Adsorption

The excellent performance of the templated materials for dyes is partly attributed to the porous structure and high specific surface area. The porous structure and high specific surface area facilitate the exposure of more active sites, thus promoting the diffusion of dye molecules, that is, the efficient adsorption of dyes through adsorption and the filling of pore channels. Dual-porous Mn_2O_3 (DP Mn_2O_3-carbon-PVP) cubes have a specific surface area of 37 m^2/g and the mesopore size of 24 nm, higher than that of the Mn_2O_3-Ncarbon prepared without polyvinylpyrrolidone (PVP) (22 m^2/g, 23 nm) and without carbon sphere templates (15 m^2/g, 4 nm). Comparing their sorption rates to Congo Red, DP Mn_2O_3-carbon-PVP had a sorption capacity of 126 mg/g, but 64 mg/g and 112 mg/g for Mn_2O_3-Ncarbon and Mn_2O_3-carbon (Shao et al., 2017). ACNTs have a high specific surface area of 877.09 m^2/g, which is much higher than that of raw Pal (181.14 m^2/g), H-Pal (157.50 m^2/g), Pal@C (103.41 m^2/g). The maximum adsorption of Congo Red by ACNTs (358 mg/g) was more than 20-fold times that of raw Pal, and nearly 14-fold higher than that of H-Pal and Pal@C (Zhong et al., 2019; **Table 4**).

In addition to the structure of the material, electrostatic interactions and π-π electron coupling interactions are also important mechanisms for the adsorption of dyes. For instance, the adsorption processes of nitrogen-doped mesoporous carbon spheres (NMCS) on methyl orange (Jiao et al., 2017) and ACTNs on Congo red (Zhong et al., 2019) are electrostatic attraction and π-π electron coupling, respectively, while the adsorption processes of hollow polydopamine microcapsules (H-PDAMCs) on methyl blue involve both electrostatic interaction and π-π stacking mechanisms (Feng et al., 2021). However, for materials with an intrinsic charge, the adsorption performance can be unsatisfactory due to electrostatic repulsion between the functional group of the dye and the functional group of the material. The introduction of template to adjust its surface charge can effectively improve this problem. For example, the large number of oxygen-containing functional groups such as -OH and -COOH generated on the surface of MWCNTs@carbon nanocables provides an abundance of active sites for positively charged dyes compared to the original MWCNTs (Zhang et al., 2017). The zero charge of Al_2O_3 is close to 9, using it as a template agent, the obtained alumina hollow microspheres (AHS) still have a high adsorption capacity for Congo Red when the initial solution pH is beyond 10 (Tian et al., 2016; **Table 4**).

5 CONCLUSIONS AND PERSPECTIVES

Based on the properties and spatial domain-limiting capability of templates, this study introduces the types of templates and their synthetic routes, and the regulation behavior of materials by template method and its application in the adsorption of typical pollutants in wastewater has been reviewed. In comparison, hard templates are more stable and allow for precise regulation of material size and structure, but hard templates are often difficult to remove and can easily cause structural damage to the raw material after removal, while soft templates are easy to construct and have relatively mild experimental conditions and allow for the synthesis of different materials with different morphologies, but soft templates are less stable and less efficient. The behavior of the template method in modulating the morphological structure of the materials was further discussed and it was found that the adsorbents prepared by the template method had a high specific surface area and abundant pores and were able to successfully construct pore channel structures. The type and concentration of the template agent are found to be the most crucial factors affecting the morphology of the final product. Therefore, in practice, the most suitable template should be selected according to the performance requirements of the target product and the reaction conditions.

The large specific surface area and porous structure of the templated materials offer the possibility of efficient adsorption of heavy metal ions and dyes. The adsorption mechanism for heavy metal ions includes ion exchange, electrostatic interaction, and complexation, while electrostatic interaction, π-π electron stacking, and hydrogen bonding are possible for dyes. The application of templated materials as effective adsorbents in wastewater and their adsorption mechanisms are still at the research stage. Moreover, during the preparation process of templated materials, the removal of the template may lead to the collapse of the pore structure. Optimization of the textural properties and attention to the removal conditions are desired to ensure the effective diffusion of pollutants within the adsorbent.

Templated materials have good application prospects in removing pollution in wastewater. However, templated materials have been less studied for contaminants such as nutrients, biomolecules, and complex pollutants, and further research into the regeneration and desorption properties of adsorbents is required to achieve large-scale commercial use of templated materials.

AUTHOR CONTRIBUTIONS

HL summarized and wrote the article under the guidance of LW. All authors contributed to the conceptualization and editing of the article and commenting on and reviewing the manuscript.

FUNDING

This work was supported by the National Natural Science Foundation of China (51908457).

ACKNOWLEDGMENTS

The authors thank Zijun Ren from Xi'an Jiaotong University for assistance with SEM analysis.

REFERENCES

Abdel-Aziz, H. M., and Siyam, T. (2011). Radiation Synthesis of Poly(Acrylamide-Acrylic Acid-Dimethylaminoethyl Methacrylate) Resin and its Use for Binding of Some Anionic Dyes. *Water Air Soil Pollut.* 218 (1), 165–174. doi:10.1007/s11270-010-0632-5

Abo-Zahra, S. F., Abdelmonem, I. M., Siyam, T. E., El-Masry, A. M., and Abdel-Aziz, H. M. (2021). Radiation Synthesis of Polyacrylamide/functionalized Multiwalled Carbon Nanotubes Composites for the Adsorption of Cu(II) Metal Ions from Aqueous Solution. *Polym. Bull.* doi:10.1007/s00289-021-03726-6

Ahmad, R., Kim, J., Kim, J., and Kim, J. (2017). Nanostructured Ceramic Photocatalytic Membrane Modified with a Polymer Template for Textile Wastewater Treatment. *Appl. Sci.* 7 (12), 1284. doi:10.3390/app7121284

Alexandratos, S. D. (2007). New Polymer-Supported Ion-Complexing Agents: Design, Preparation and Metal Ion Affinities of Immobilized Ligands. *J. Hazard. Mater.* 139 (3), 467–470. doi:10.1016/j.jhazmat.2006.02.042

Amali, A. J., Sun, J.-K., and Xu, Q. (2014). From Assembled Metal-Organic Framework Nanoparticles to Hierarchically Porous Carbon for Electrochemical Energy Storage. *Chem. Commun.* 50 (13), 1519–1522. doi:10.1039/c3cc48112c

Awual, M. R., and Hasan, M. M. (2014). A Novel fine-tuning Mesoporous Adsorbent for Simultaneous Lead(II) Detection and Removal from Wastewater. *Sensors Actuators B: Chem.* 202, 395–403. doi:10.1016/j.snb.2014.05.103

Bao, Y., Shi, C., Wang, T., Li, X., and Ma, J. (2016). Recent Progress in Hollow Silica: Template Synthesis, Morphologies and Applications. *Microporous Mesoporous Mater.* 227. doi:10.1016/j.micromeso.2016.02.040

Barrera, D., Villarroel-Rocha, J., Tara, J. C., Basaldella, E. I., and Sapag, K. (2014). Synthesis and Textural Characterization of a Templated Nanoporous Carbon from MCM-22 Zeolite and its Use as Adsorbent of Amoxicillin and Ethinylestradiol. *Adsorption* 20 (8), 967–976. doi:10.1007/s10450-014-9640-x

Bo, Z., and Jing, W. (2007). Pore Diameter Adjustment of Mesoporous Alumina with Different Templates. *JOURNAL FUNCTIONAL MATERIALS DEVICES* 13 (2), 150–154. doi:10.3969/j.issn.1007-4252.2007.02.010

Bourret, G. R., and Lennox, R. B. (2010). 1D Cu(OH)2 Nanomaterial Synthesis Templated in Water Microdroplets. *J. Am. Chem. Soc.* 132 (19), 6657–6659. doi:10.1021/ja101579v

Brião, G. V., Jahn, S. L., Foletto, E. L., and Dotto, G. L. (2017). Adsorption of crystal Violet Dye onto a Mesoporous ZSM-5 Zeolite Synthetized Using Chitin as Template. *J. Colloid Interf. Sci.* 508, 313–322. doi:10.1016/j.jcis.2017.08.070

Brown, J., Richer, R., and Mercier, L. (2000). One-step Synthesis of High Capacity Mesoporous Hg2+ Adsorbents by Non-ionic Surfactant Assembly. *Microporous mesoporous Mater.* 37 (1-2), 41–48. doi:10.1016/s1387-1811(99)00191-2

Cao, Y., Zhu, J. Z., Ding, Y., Han, G., Fan, R. L., and Fu, H. Q. (2014). Pore Size Control of Ordered Mesoporous Carbons and Adsorption Performance of Dye Molecules. *Amm* 548-549, 38–42. doi:10.4028/www.scientific.net/AMM.548-549.38

Chen, D., Zeng, Z., Zeng, Y., Zhang, F., and Wang, M. (2016). Removal of Methylene Blue and Mechanism on Magnetic γ-Fe2O3/SiO2 Nanocomposite from Aqueous Solution. *Water Resour. Industry* 15, 1–13. doi:10.1016/j.wri.2016.05.003

Cui, H., Qian, Y., Li, Q., Zhang, Q., and Zhai, J. (2012). Adsorption of Aqueous Hg(II) by a Polyaniline/attapulgite Composite. *Chem. Eng. J.* 211-212, 216–223. doi:10.1016/j.cej.2012.09.057

Dai, J., Ren, F., and Tao, C. (2012). Adsorption Behavior of Fe(II) and Fe(III) Ions on Thiourea Cross-Linked Chitosan with Fe(III) as Template. *Molecules* 17 (4), 4388–4399. doi:10.3390/molecules17044388

Demirbaş, A. (2005). Adsorption of Cr (III) and Cr (VI) Ions from Aqueous Solutions on to Modified Lignin. *Energ. Sourc.* 27 (15), 1449–1455.

Deng, Y., Yu, T., Wan, Y., Shi, Y., Meng, Y., Gu, D., et al. (2007). Ordered Mesoporous Silicas and Carbons with Large Accessible Pores Templated from Amphiphilic Diblock Copolymer Poly(ethylene Oxide)-B-Polystyrene. *J. Am. Chem. Soc.* 129 (6), 1690–1697. doi:10.1021/ja067379v

Ekinci, E., Budinova, T., Yardim, F., Petrov, N., Razvigorova, M., and Minkova, V. (2002). Removal of Mercury Ion from Aqueous Solution by Activated Carbons Obtained from Biomass and Coals. *Fuel Process. Techn.* 77-78, 437–443. doi:10.1016/S0378-3820(02)00065-6

El-Hankari, S., Aguilera-Sigalat, J., and Bradshaw, D. (2016). Surfactant-assisted ZnO Processing as a Versatile Route to ZIF Composites and Hollow Architectures with Enhanced Dye Adsorption. *J. Mater. Chem. A.* 4 (35), 13509–13518. doi:10.1039/c6ta05893k

El-Sayed, G. O. (2011). Removal of Methylene Blue and crystal Violet from Aqueous Solutions by palm Kernel Fiber. *Desalination* 272 (1-3), 225–232. doi:10.1016/j.desal.2011.01.025

Fan, X., Zhang, Z., Li, G., and Rowson, N. A. (2004). Attachment of Solid Particles to Air Bubbles in Surfactant-free Aqueous Solutions. *Chem. Eng. Sci.* 59 (13), 2639–2645. doi:10.1016/j.ces.2004.04.001

Feng, M., Yu, S., Wu, P., Wang, Z., Liu, S., and Fu, J. (2021). Rapid, High-Efficient and Selective Removal of Cationic Dyes from Wastewater Using Hollow Polydopamine Microcapsules: Isotherm, Kinetics, Thermodynamics and Mechanism. *Appl. Surf. Sci.* 542, 148633. doi:10.1016/j.apsusc.2020.148633

Fu, J., Chen, Z., Wang, M., Liu, S., Zhang, J., Zhang, J., et al. (2015). Adsorption of Methylene Blue by a High-Efficiency Adsorbent (Polydopamine Microspheres): Kinetics, Isotherm, Thermodynamics and Mechanism Analysis. *Chem. Eng. J.* 259, 53–61. doi:10.1016/j.cej.2014.07.101

Fuertes, A. B., Lota, G., Centeno, T. A., and Frackowiak, E. (2005). Templated Mesoporous Carbons for Supercapacitor Application. *Electrochimica Acta* 50 (14), 2799–2805. doi:10.1016/j.electacta.2004.11.027

Gao, X., Lu, F., Dong, B., Liu, Y., Gao, Y., and Zheng, L. (2015). Facile Synthesis of Gold and Gold-Based alloy Nanowire Networks Using Wormlike Micelles as Soft Templates. *Chem. Commun.* 51 (5), 843–846. doi:10.1039/c4cc08549c

Han, X., Tian, P., Pang, H., Song, Q., Ning, G., Yu, Y., et al. (2014). Facile Synthesis of Magnetic Hierarchical MgO-MgFe2O4 Composites and Their Adsorption Performance towards Congo Red. *RSC Adv.* 4 (53), 28119–28125. doi:10.1039/c4ra02313g

Hu, H., Liu, J., Xu, Z., Zhang, L., Cheng, B., and Ho, W. (2019). Hierarchical Porous Ni/Co-LDH Hollow Dodecahedron with Excellent Adsorption Property for Congo Red and Cr(VI) Ions. *Appl. Surf. Sci.* 478, 981–990. doi:10.1016/j.apsusc.2019.02.008

Huang, Y., Zeng, X., Guo, L., Lan, J., Zhang, L., and Cao, D. (2018). Heavy Metal Ion Removal of Wastewater by Zeolite-Imidazolate Frameworks. *Separat. Purif. Techn.* 194, 462–469. doi:10.1016/j.seppur.2017.11.068

Jiang, Z., Sun, H., Qin, Z., Jiao, X., and Chen, D. (2012). Synthesis of Novel ZnS Nanocages Utilizing ZIF-8 Polyhedral Template. *Chem. Commun.* 48 (30), 3620–3622. doi:10.1039/c2cc00004k

Jiao, K., Zhang, B., Yue, B., Ren, Y., Liu, S., Yan, S., et al. (2005). Growth of Porous Single-crystal Cr2O3 in a 3-D Mesopore System. *Chem. Commun.* 45, 5618–5620. doi:10.1039/b512080b

Jiao, Y., Xu, L., Sun, H., Deng, Y., Zhang, T., and Liu, G. (2017). Synthesis of Benzxazine-Based Nitrogen-Doped Mesoporous Carbon Spheres for Methyl orange Dye Adsorption. *J. Porous Mater.* 24 (6), 1565–1574. doi:10.1007/s10934-017-0396-z

Jun, S., Joo, S. H., Ryoo, R., Kruk, M., Jaroniec, M., Liu, Z., et al. (2000). Synthesis of New, Nanoporous Carbon with Hexagonally Ordered Mesostructure. *J. Am. Chem. Soc.* 122 (43), 10712–10713. doi:10.1021/ja002261e

Kim, T.-W., Ryoo, R., Gierszal, K. P., Jaroniec, M., Solovyov, L. A., Sakamoto, Y., et al. (2005). Characterization of Mesoporous Carbons Synthesized with SBA-16 Silica Template. *J. Mater. Chem.* 15 (15), 1560. doi:10.1039/b417804a

Kruk, M., Jaroniec, M., Ryoo, R., and Joo, S. H. (2000). Characterization of Ordered Mesoporous Carbons Synthesized Using MCM-48 Silicas as Templates. *J. Phys. Chem. B* 104 (33), 7960–7968. doi:10.1021/jp000861u

Kuroki, A., Hiroto, M., Urushihara, Y., Horikawa, T., Sotowa, K.-I., and Alcántara Avila, J. R. (2019). Adsorption Mechanism of Metal Ions on Activated Carbon. *Adsorption* 25 (6), 1251–1258. doi:10.1007/s10450-019-00069-7

Lei, S., Yu, F., Yang, L., Shuaiguo, Z., Mengmeng, W., and Jie, M. (2018). Impacts of Different Templates on the Morphologies and Sulfuration Performances of Nano Ferric Oxides. *CHEMICAL INDUSTRY ENGINEERING PROGRESS* 37 (5), 1831–1836. doi:10.16085/j.issn.1000-6613.2017-1340

Li, N., Bai, R., and Liu, C. (2005). Enhanced and Selective Adsorption of Mercury Ions on Chitosan Beads Grafted with Polyacrylamide via Surface-Initiated Atom Transfer Radical Polymerization. *Langmuir* 21 (25), 11780–11787. doi:10.1021/la051551b

Li, Y., Liu, C., Xie, Y., Li, X., Fan, X., Yuan, L., et al. (2013). Single-molecule Observation of the K+-induced Switching of Valinomycin within a Template Network. *Chem. Commun.* 49 (79), 9021–9023. doi:10.1039/c3cc44978e

Li, Z., Shao, M., Zhou, L., Zhang, R., Zhang, C., Wei, M., et al. (2016). Directed Growth of Metal-Organic Frameworks and Their Derived Carbon-Based Network for Efficient Electrocatalytic Oxygen Reduction. *Adv. Mater.* 28 (12), 2337–2344. doi:10.1002/adma.201505086

Libbrecht, W., Vandaele, K., De Buysser, K., Verberckmoes, A., Thybaut, J., Poelman, H., et al. (2015). Tuning the Pore Geometry of Ordered Mesoporous Carbons for Enhanced Adsorption of Bisphenol-A. *Materials* 8 (4), 1652–1665. doi:10.3390/ma8041652

Libbrecht, W., Verberckmoes, A., Thybaut, J. W., Van Der Voort, P., and De Clercq, J. (2017). Soft Templated Mesoporous Carbons: Tuning the Porosity for the Adsorption of Large Organic Pollutants. *Carbon* 116, 528–546. doi:10.1016/j.carbon.2017.02.016

Liu, D., Hu, Y.-Y., Hu, Y.-Y., Zeng, C., and Qu, D.-Y. (2016a). Soft-Templated Ordered Mesoporous Carbon Materials: Synthesis, Structural Modification and Functionalization. *Acta Physico-Chimica Sinica* 32 (12), 2826–2840. doi:10.3866/pku.Whxb201609141

Liu, J., Ge, X., Ye, X., Wang, G., Zhang, H., Zhou, H., et al. (2016b). 3D Graphene/δ-MnO2 Aerogels for Highly Efficient and Reversible Removal of Heavy Metal Ions. *J. Mater. Chem. A.* 4 (5), 1970–1979. doi:10.1039/c5ta08106h

Liu, L., Liu, S., Peng, H., Yang, Z., Zhao, L., and Tang, A. (2020). Surface Charge of Mesoporous Calcium Silicate and its Adsorption Characteristics for Heavy Metal Ions. *Solid State. Sci.* 99, 106072. doi:10.1016/j.solidstatesciences.2019.106072

Liu, W., Jiang, X., and Chen, X. (2015). Synthesis and Utilization of a Novel Carbon Nanotubes Supported Nanocables for the Adsorption of Dyes from Aqueous Solutions. *J. Solid State. Chem.* 229, 342–349. doi:10.1016/j.jssc.2015.06.026

Liu, X., Wang, R., He, Y., Ni, Z., Su, N., Guo, R., et al. (2019). Construction of Alternating Layered Quasi-Three-Dimensional Electrode Ag NWs/CoO for Water Splitting: A Discussion of Catalytic Mechanism. *Electrochimica Acta* 317, 468–477. doi:10.1016/j.electacta.2019.06.029

Liu, Y., Goebl, J., and Yin, Y. (2013). Templated Synthesis of Nanostructured Materials. *Chem. Soc. Rev.* 42 (7), 2610–2653. doi:10.1039/C2CS35369E

Liu, Y., Hu, R., and Zhang, Z. (2018). A Facile Colloidal crystal Templating Method to Produce Three-Dimensional Hierarchical Porous Graphene-Fe3O4 Nanocomposite for the Removal of Dyes from Aqueous Solution. *J. Porous Mater.* 26 (1), 271–280. doi:10.1007/s10934-018-0653-9

Liu, Y., Qiao, L., Wang, A., Li, Y., Zhao, L., and Du, K. (2021). Tentacle-type Poly(hydroxamic Acid)-Modified Macroporous Cellulose Beads: Synthesis, Characterization, and Application for Heavy Metal Ions Adsorption. *J. Chromatogr. A* 1645, 462098. doi:10.1016/j.chroma.2021.462098

Lü, Q. F., Huang, M. R., and Li, X. G. (2007). Synthesis and Heavy-metal-ion Sorption of Pure Sulfophenylenediamine Copolymer Nanoparticles with Intrinsic Conductivity and Stability. *Chemistry–A Eur. J.* 13 (21), 6009–6018. doi:10.1002/chem.200700233

Ma, Y., Zhuang, Z., Ma, M., Yang, Y., Li, W., lin, J., et al. (2019). Solid Polyaniline Dendrites Consisting of High Aspect Ratio Branches Self-Assembled Using Sodium Lauryl Sulfonate as Soft Templates: Synthesis and Electrochemical Performance. *Polymer* 182, 121808. doi:10.1016/j.polymer.2019.121808

Ma, Z., Gao, J., Su, W., Zhang, Q., and Wang, X. (2020). Effect of Template Agent on Synthetic Aluminosilicate Mesoporous Material. *MATEIALS SCIENCE TECHNOLOGY* 28 (06), 49–55. doi:10.11951/j.issn.1005-0299.20190015

Madima, N., Mishra, S. B., Inamuddin, I., and Mishra, A. K. (2020). Carbon-based Nanomaterials for Remediation of Organic and Inorganic Pollutants from Wastewater. A Review. *Environ. Chem. Lett.* 18 (4), 1169–1191. doi:10.1007/s10311-020-01001-0

Manyangadze, M., Chikuruwo, N. M. H., Narsaiah, T. B., Chakra, C. S., Charis, G., Danha, G., et al. (2020). Adsorption of lead Ions from Wastewater Using Nano Silica Spheres Synthesized on Calcium Carbonate Templates. *Heliyon* 6 (11), e05309. doi:10.1016/j.heliyon.2020.e05309

Marciniak, M., Goscianska, J., Frankowski, M., and Pietrzak, R. (2019). Optimal Synthesis of Oxidized Mesoporous Carbons for the Adsorption of Heavy Metal Ions. *J. Mol. Liquids* 276, 630–637. doi:10.1016/j.molliq.2018.12.042

Marrakchi, F., Ahmed, M. J., Khanday, W. A., Asif, M., and Hameed, B. H. (2017). Mesoporous-activated Carbon Prepared from Chitosan Flakes via Single-step Sodium Hydroxide Activation for the Adsorption of Methylene Blue. *Int. J. Biol. Macromolecules* 98, 233–239. doi:10.1016/j.ijbiomac.2017.01.119

Meng, C., Zhikun, W., Qiang, L., Chunling, L., Shuangqing, S., and Songqing, H. (2018). Preparation of Amino-Functionalized Fe3O4@mSiO2 Core-Shell Magnetic Nanoparticles and Their Application for Aqueous Fe3+ Removal. *J. Hazard. Mater.* 341, 198–206. doi:10.1016/j.jhazmat.2017.07.062

Miao, Y., Zhai, Z., He, J., Li, B., Li, J., and Wang, J. (2010). Synthesis, Characterizations and Photocatalytic Studies of Mesoporous Titania Prepared by Using Four Plant Skins as Templates. *Mater. Sci. Eng. C* 30 (6), 839–846. doi:10.1016/j.msec.2010.03.020

Mohajeri, M., Akbarpour, H., and Karimkhani, V. (2017). Synthesis of Highly Ordered Carbon Nanotubes/nanoporous Anodic Alumina Composite Membrane and Potential Application in Heavy Metal Ions Removal from Industrial Wastewater. *Mater. Today Proc.* 4 (3), 4906–4911. doi:10.1016/j.matpr.2017.04.094

Pang, M., Cairns, A. J., Liu, Y., Belmabkhout, Y., Zeng, H. C., and Eddaoudi, M. (2013a). Synthesis and Integration of Fe-Soc-MOF Cubes into Colloidosomes via a Single-step Emulsion-Based Approach. *J. Am. Chem. Soc.* 135 (28), 10234–10237. doi:10.1021/ja403994u

Pang, X., Zhao, L., Han, W., Xin, X., and Lin, Z. (2013b). A General and Robust Strategy for the Synthesis of Nearly Monodisperse Colloidal Nanocrystals. *Nat. Nanotech* 8 (6), 426–431. doi:10.1038/nnano.2013.85

Petkovich, N. D., and Stein, A. (2013). Controlling Macro- and Mesostructures with Hierarchical Porosity through Combined Hard and Soft Templating. *Chem. Soc. Rev.* 42 (9), 3721–3739. doi:10.1039/c2cs35308c

Pi, Y., Li, X., Xia, Q., Wu, J., Li, Y., Xiao, J., et al. (2018). Adsorptive and Photocatalytic Removal of Persistent Organic Pollutants (POPs) in Water by Metal-Organic Frameworks (MOFs). *Chem. Eng. J.* 337, 351–371. doi:10.1016/j.cej.2017.12.092

Pongkitdachoti, U., and Unob, F. (2018). Simultaneous Adsorption of Silver Nanoparticles and Silver Ions on Large Pore Mesoporous Silica. *J. Environ. Chem. Eng.* 6 (1), 596–603. doi:10.1016/j.jece.2017.12.046

Ren, C., Ding, X., Li, W., Wu, H., and Yang, H. (2017). Highly Efficient Adsorption of Heavy Metals onto Novel Magnetic Porous Composites Modified with Amino Groups. *J. Chem. Eng. Data* 62 (6), 1865–1875. doi:10.1021/acs.jced.7b00198

Roggenbuck, J., Koch, G., and Tiemann, M. (2006). Synthesis of Mesoporous Magnesium Oxide by CMK-3 Carbon Structure Replication. *Chem. Mater.* 18 (17), 4151–4156. doi:10.1021/cm060740s

Salunkhe, R. R., Young, C., Tang, J., Takei, T., Ide, Y., Kobayashi, N., et al. (2016). A High-Performance Supercapacitor Cell Based on ZIF-8-Derived Nanoporous Carbon Using an Organic Electrolyte. *Chem. Commun.* 52 (26), 4764–4767. doi:10.1039/c6cc00413j

Sarma, G. K., Sen Gupta, S., and Bhattacharyya, K. G. (2019). Nanomaterials as Versatile Adsorbents for Heavy Metal Ions in Water: a Review. *Environ. Sci. Pollut. Res.* 26 (7), 6245–6278. doi:10.1007/s11356-018-04093-y

Savic, S., Vojisavljevic, K., Počuča-Nešić, M., Zivojevic, K., Mladenovic, M., and Knezevic, N. (2018). Hard Template Synthesis of Nanomaterials Based on Mesoporous Silica. *Metall. Mater. Eng.* 24 (4). doi:10.30544/400

Schüth, F. (2003). Endo- and Exotemplating to Create High-Surface-Area Inorganic Materials. *Angew. Chem. Int. Ed.* 42 (31), 3604–3622. doi:10.1002/anie.200300593

Senberber, F. T., Yildirim, M., Mermer, N. K., and Derun, E. M. (2017). Adsorption of Cr(III) from Aqueous Solution Using Borax Sludge. *ACSi* 64 (3), 654–660. doi:10.17344/acsi.2017.3534

Shao, Y., Ren, B., Jiang, H., Zhou, B., Lv, L., Ren, J., et al. (2017). Dual-porosity Mn2O3 Cubes for Highly Efficient Dye Adsorption. *J. Hazard. Mater.* 333, 222–231. doi:10.1016/j.jhazmat.2017.03.014

Shen, K., Zhang, L., Chen, X., Liu, L., Zhang, D., Han, Y., et al. (2018). Ordered Macro-Microporous Metal-Organic Framework Single Crystals. *Science* 359 (6372), 206–210. doi:10.1126/science.aao3403

Singh, J., Sharma, M., and Basu, S. (2018). Heavy Metal Ions Adsorption and Photodegradation of Remazol Black XP by Iron Oxide/silica Monoliths: Kinetic and Equilibrium Modelling. *Adv. Powder Techn.* 29 (9), 2268–2279. doi:10.1016/j.apt.2018.06.011

Sun, S., Wang, Q., and Wang, A. (2007). Adsorption Properties of Cu(II) Ions onto N-Succinyl-Chitosan and Crosslinked N-Succinyl-Chitosan Template Resin. *Biochem. Eng. J.* 36 (2), 131–138. doi:10.1016/j.bej.2007.02.010

Sun, Y., Shao, D., Chen, C., Yang, S., and Wang, X. (2013). Highly Efficient Enrichment of Radionuclides on Graphene Oxide-Supported Polyaniline. *Environ. Sci. Technol.* 47 (17), 9904–9910. doi:10.1021/es401174n

Sun, Y., Wu, Z.-Y., Wang, X., Ding, C., Cheng, W., Yu, S.-H., et al. (2016). Macroscopic and Microscopic Investigation of U(VI) and Eu(III) Adsorption on Carbonaceous Nanofibers. *Environ. Sci. Technol.* 50 (8), 4459–4467. doi:10.1021/acs.est.6b00058

Teoh, Y. P., Khan, M. A., and Choong, T. S. Y. (2013). Kinetic and Isotherm Studies for lead Adsorption from Aqueous Phase on Carbon Coated Monolith. *Chem. Eng. J.* 217, 248–255. doi:10.1016/j.cej.2012.12.013

Thomas, A., and Goettmann, F. (2008). Hard Templates for Soft Materials: Creating Nanostructured Organic Materials. *Chem. Mater.* 20 (3), 738–755. doi:10.1021/cm702126j

Tian, J., Tian, P., Pang, H., Ning, G., Bogale, R. F., Cheng, H., et al. (2016). Fabrication Synthesis of Porous Al 2 O 3 Hollow Microspheres and its superior Adsorption Performance for Organic Dye. *Microporous Mesoporous Mater.* 223, 27–34. doi:10.1016/j.micromeso.2015.09.055

Wan, Y., and Zhao, D. Y. (2007). On the Controllable Soft-Templating Approach to Mesoporous Silicates. *Chem. Rev.* 107 (7), 2821–2860. doi:10.1021/cr068020s

Wang, B., Chen, J. S., Wu, H. B., Wang, Z., and Lou, X. W. (2011a). Quasiemulsion-Templated Formation of α-Fe2O3 Hollow Spheres with Enhanced Lithium Storage Properties. *J. Am. Chem. Soc.* 133 (43), 17146–17148. doi:10.1021/ja208346s

Wang, H., Qu, Z. G., Zhang, W., and Zhang, L. Q. (2016a). A Multi-Scale Porous Composite Adsorbent with Copper Benzene-1,3,5-Tricarboxylate Coating on Copper Foam. *RSC Adv.* 6 (58), 52888–52897. doi:10.1039/c6ra08622e

Wang, J., Deng, B., Chen, H., Wang, X., and Zheng, J. (2009). Removal of Aqueous Hg(II) by Polyaniline: Sorption Characteristics and Mechanisms. *Environ. Sci. Technol.* 43 (14), 5223–5228. doi:10.1021/es803710k

Wang, L., Wang, J., He, C., Lyu, W., Zhang, W., Yan, W., et al. (2019a). Development of Rare Earth Element Doped Magnetic Biochars with Enhanced Phosphate Adsorption Performance. *Colloids Surf. A: Physicochemical Eng. Aspects* 561, 236–243. doi:10.1016/j.colsurfa.2018.10.082

Wang, L., Wang, J., Wang, Z., Feng, J., Li, S., and Yan, W. (2019b). Synthesis of Ce-Doped Magnetic Biochar for Effective Sb(V) Removal: Performance and Mechanism. *Powder Techn.* 345, 501–508. doi:10.1016/j.powtec.2019.01.022

Wang, L., Wang, J., and Wei, Y. (2021). Facile Synthesis of Eggshell Biochar Beads for superior Aqueous Phosphate Adsorption with Potential Urine P-Recovery. *Colloids Surf. A: Physicochemical Eng. Aspects* 622, 126589. doi:10.1016/j.colsurfa.2021.126589

Wang, L., Wang, J., Yan, W., He, C., and Shi, Y. (2020a). MgFe2O4-biochar Based Lanthanum Alginate Beads for Advanced Phosphate Removal. *Chem. Eng. J.* 387, 123305. doi:10.1016/j.cej.2019.123305

Wang, X., Zhong, Y., Zhai, T., Guo, Y., Chen, S., Ma, Y., et al. (2011b). Multishelled Co3O4-Fe3O4 Hollow Spheres with Even Magnetic Phase Distribution: Synthesis, Magnetic Properties and Their Application in Water Treatment. *J. Mater. Chem.* 21 (44), 17680–17687. doi:10.1039/c1jm13180j

Wang, Y., Jiang, Q., Jiang, Q., Shang, J.-K., Xu, J., and Li, Y.-X. (2016b). Advances in the Synthesis of Mesoporous Carbon Nitride Materials. *Acta Physico-Chimica Sinica* 32 (8), 1913–1928. doi:10.3866/pku.Whxb201605052

Wang, Y., Yang, X., Jing, X., Dai, J., Dong, M., and Yan, Y. (2020b). Adsorption of Phosphorus on Lanthanum Doped Carbon Films Guided by Self-Assembly of Cellulose Nanocrystalline. *J. Mol. Liquids* 319, 114148. doi:10.1016/j.molliq.2020.114148

Wei, Y., Wang, L., and Wang, J. (2022). Cerium Alginate Cross-Linking with Biochar Beads for Fast Fluoride Removal over a Wide pH Range. *Colloids Surf. A: Physicochemical Eng. Aspects* 636, 128161. doi:10.1016/j.colsurfa.2021.128161

Wickramaratne, N. P., and Jaroniec, M. (2013). Phenolic Resin-Based Carbons with Ultra-large Mesopores Prepared in the Presence of Poly(ethylene Oxide)-Poly(butylene Oxide)-Poly(ethylene Oxide) Triblock Copolymer and Trimethyl Benzene. *Carbon* 51, 45–51. doi:10.1016/j.carbon.2012.08.007

Wu, D., Xu, F., Sun, B., Fu, R., He, H., and Matyjaszewski, K. (2012). Design and Preparation of Porous Polymers. *Chem. Rev.* 112 (7), 3959–4015. doi:10.1021/cr200440z

Wu, X.-J., and Xu, D. (2010). Soft Template Synthesis of Yolk/silica Shell Particles. *Adv. Mater.* 22 (13), 1516–1520. doi:10.1002/adma.200903879

Wu, Y.-n., Li, F., Zhu, W., Cui, J., Tao, C.-a., Lin, C., et al. (2011). Metal-organic Frameworks with a Three-Dimensional Ordered Macroporous Structure: Dynamic Photonic Materials. *Angew. Chem. Int. Ed.* 50 (52), 12518–12522. doi:10.1002/anie.201104597

Xie, Y., Kocaefe, D., Chen, C., Kocaefe, Y., and Seki, S. (2016). Review of Research on Template Methods in Preparation of Nanomaterials. *J. Nanomater.* 2302595. doi:10.1155/2016/2302595

Xie, Y., Song, Y., Zhang, Y., Xu, L., Miao, L., Peng, C., et al. (2018). Cu Metal-Organic Framework-Derived Cu Nanospheres@Porous Carbon/macroporous Carbon for Electrochemical Sensing Glucose. *J. Alloys Comp.* 757, 105–111. doi:10.1016/j.jallcom.2018.05.064

Yan, C., and Xue, D. (2007). Polyhedral Construction of Hollow ZnO Microspheres by CO2 Bubble Templates. *J. Alloys Comp.* 431 (1-2), 241–245. doi:10.1016/j.jallcom.2006.05.064

Yan, L., Li, Q., Wang, X., Song, H., Chi, H., Qiao, Y., et al. (2017). Synthesis and Absorption Performance of Acrylic Ester and Hollow Fiber MgO Nanoparticle Resin Composite. *Polymer-Plastics Techn. Eng.* 56 (17), 1857–1865. doi:10.1080/03602559.2017.1295310

Yang, L., Li, R., Zhang, L., Jiang, X., Wang, R., and Tian, B. (2021). Preparation of Flower-like G-C_3N_4/Bi_2MoO_6 Microspheres and Their Photocatalytic Degradation of Simulated Dye Wastewater. *Fine Chemicals* 38 (5), 1030–1037.

Yang, L. M., Wang, Y. J., Sun, Y. W., Luo, G. S., and Dai, Y. Y. (2006). Synthesis of Micrometer-Sized Hard Silica Spheres with Uniform Mesopore Size and Textural Pores. *J. Colloid Interf. Sci.* 299 (2), 823–830. doi:10.1016/j.jcis.2006.02.043

Yang, X., Yan, L., Ma, J., Bai, Y., and Shao, L. (2019). Bioadhesion-inspired Surface Engineering Constructing Robust, Hydrophilic Membranes for Highly-Efficient Wastewater Remediation. *J. Membr. Sci.* 591, 117353. doi:10.1016/j.memsci.2019.117353

Yu, G., Wang, X., Liu, J., Jiang, P., You, S., Ding, N., et al. (2021). Applications of Nanomaterials for Heavy Metal Removal from Water and Soil: A Review. *Sustainability* 13 (2), 713. doi:10.3390/su13020713

Yu, L., Wang, L., Xu, W., Chen, L., Fu, M., Wu, J., et al. (2018). Adsorption of VOCs on Reduced Graphene Oxide. *J. Environ. Sci.* 67, 171–178. doi:10.1016/j.jes.2017.08.022

Yue, W., and Zhou, W. (2007). Porous Crystals of Cubic Metal Oxides Templated by Cage-Containing Mesoporous Silica. *J. Mater. Chem.* 17 (47), 4947. doi:10.1039/b709076e

Yusuf, M. M., Imai, H., and Hirashima, H. (2003). Preparation of Mesoporous Titania by Templating with Polymer and Surfactant and its Characterization. *J. sol-gel Sci. Technol.* 28 (1), 97–104. doi:10.1023/a:1025645305557

Zanin, E., Scapinello, J., de Oliveira, M., Rambo, C. L., Franscescon, F., Freitas, L., et al. (2017). Adsorption of Heavy Metals from Wastewater Graphic Industry Using Clinoptilolite Zeolite as Adsorbent. *Process Saf. Environ. Prot.* 105, 194–200. doi:10.1016/j.psep.2016.11.008

Zare, E. N., Motahari, A., and Sillanpää, M. (2018). Nanoadsorbents Based on Conducting Polymer Nanocomposites with Main Focus on Polyaniline and its Derivatives for Removal of Heavy Metal Ions/dyes: A Review. *Environ. Res.* 162, 173–195. doi:10.1016/j.envres.2017.12.025

Zhang, C., Li, X., Chen, Z., Wen, T., Huang, S., Hayat, T., et al. (2017). Synthesis of Ordered Mesoporous Carbonaceous Materials and Their Highly Efficient Capture of Uranium from Solutions. *Sci. China Chem.* 61 (3), 281–293. doi:10.1007/s11426-017-9132-7

Zhang, D., Zhang, C.-l., and Zhou, P. (2011). Preparation of Porous Nano-Calcium Titanate Microspheres and its Adsorption Behavior for Heavy Metal Ion in Water. *J. Hazard. Mater.* 186 (2-3), 971–977. doi:10.1016/j.jhazmat.2010.11.096

Zhang, L.-L., Song, Y., Song, Y., Li, G.-D., Zhang, S.-L., Shang, Y.-S., et al. (2015). ZSM-5 Zeolite with Micro-mesoporous Structures Synthesized Using Different Templates for Methanol to Propylene Reaction. *Acta Physico-Chimica Sinica* 31 (11), 2139–2150. doi:10.3866/pku.Whxb201509281

Zhang, L., Tang, A., Wang, Z., Zhang, M., Xu, L., and Zhu, L. (2018). Preparation of Polydopamine/poly (Ethylene Glycol) Composite Nanocapsules with ZIF-8 Nanoparticles as Templates. *J. Funct. Polym.* 31 (6), 546–552. doi:10.14133/j.cnki.1008-9357.20180714001

Zhang, Y., Sun, H., Sadam, H., Liu, Y., and Shao, L. (2019). Supramolecular Chemistry Assisted Construction of Ultra-stable Solvent-Resistant Membranes for Angstrom-Sized Molecular Separation. *Chem. Eng. J.* 371, 535–543. doi:10.1016/j.cej.2019.04.096

Zhao, J., Shao, Q., Ge, S., Zhang, J., Lin, J., Cao, D., et al. (2020b). Advances in Template Prepared Nano-Oxides and Their Applications: Polluted Water Treatment, Energy, Sensing and Biomedical Drug Delivery. *Chem. Rec.* 20 (7), 710–729. doi:10.1002/tcr.201900093

Zhao, J., Ge, S., Liu, L., Shao, Q., Mai, X., Zhao, C. X., et al. (2017). Microwave Solvothermal Fabrication of Zirconia Hollow Microspheres with Different Morphologies Using Pollen Templates and Their Dye Adsorption Removal. *Ind. Eng. Chem. Res.* 57 (1), 231–241. doi:10.1021/acs.iecr.7b04000

Zhao, J., Shao, Q., Ge, S., Zhang, J., Lin, J., Cao, D., et al. (2020a). Advances in Template Prepared Nano-Oxides and Their Applications: Polluted Water Treatment, Energy, Sensing and Biomedical Drug Delivery. *Chem. Rec.* 20 (7), 710–729. doi:10.1002/tcr.201900093

Zhao, Q., Gao, Y., Bai, X., Wu, C., and Xie, Y. (2006). Facile Synthesis of SnO 2 Hollow Nanospheres and Applications in Gas Sensors and Electrocatalysts. *Eur. J. Inorg. Chem.* 2006 (8), 1643–1648. doi:10.1002/ejic.200500975

Zhao, X., Yu, X., Wang, X., Lai, S., Sun, Y., and Yang, D. (2021). Recent Advances in Metal-Organic Frameworks for the Removal of Heavy Metal Oxoanions from Water. *Chem. Eng. J.* 407, 127221. doi:10.1016/j.cej.2020.127221

Zhao, X., Yuan, Y., Li, P., Song, Z., Ma, C., Pan, D., et al. (2019). A Polyether Amine Modified Metal Organic Framework Enhanced the CO2 Adsorption Capacity of Room Temperature Porous Liquids. *Chem. Commun.* 55 (87), 13179–13182. doi:10.1039/c9cc07243h

Zheng, X., Xie, Y., Zhu, L., Jiang, X., and Yan, A. (2002). Formation of Vesicle-Templated CdSe Hollow Spheres in an Ultrasound-Induced Anionic Surfactant Solution. *Ultrason. Sonochem.* 9 (6), 311–316. doi:10.1016/s1350-4177(02)00086-x

Zhong, L., Tang, A., Yan, P., Wang, J., Wang, Q., Wen, X., et al. (2019). Palygorskite-template Amorphous Carbon Nanotubes as a superior Adsorbent for Removal of Dyes from Aqueous Solutions. *J. Colloid Interf. Sci.* 537, 450–457. doi:10.1016/j.jcis.2018.11.016

Zhou, X., Lai, C., Huang, D., Zeng, G., Chen, L., Qin, L., et al. (2018). Preparation of Water-Compatible Molecularly Imprinted Thiol-Functionalized Activated Titanium Dioxide: Selective Adsorption and Efficient Photodegradation of 2, 4-dinitrophenol in Aqueous Solution. *J. Hazard. Mater.* 346, 113–123. doi:10.1016/j.jhazmat.2017.12.032

Zhou, Y., Zhang, L., and Cheng, Z. (2015). Removal of Organic Pollutants from Aqueous Solution Using Agricultural Wastes: A Review. *J. Mol. Liquids* 212, 739–762. doi:10.1016/j.molliq.2015.10.023

Zhu, S., Zhao, N., Li, J., Deng, X., Sha, J., and He, C. (2019). Hard-template Synthesis of Three-Dimensional Interconnected Carbon Networks: Rational Design, Hybridization and Energy-Related Applications. *Nano Today* 29, 100796. doi:10.1016/j.nantod.2019.100796

Zhu, T., Chen, J. S., and Lou, X. W. (2012). Highly Efficient Removal of Organic Dyes from Waste Water Using Hierarchical NiO Spheres with High Surface Area. *J. Phys. Chem. C* 116 (12), 6873–6878. doi:10.1021/jp300224s

Zhu, X., and Alexandratos, S. D. (2005). Polystyrene-Supported Amines: Affinity for Mercury(II) as a Function of the Pendant Groups and the Hg(II) Counterion. *Ind. Eng. Chem. Res.* 44 (23), 8605–8610. doi:10.1021/ie048736i

Conflict of Interest: The authors declare that the research was conducted in the absence of any commercial or financial relationships that could be construed as a potential conflict of interest.

frontiers | Frontiers in Chemistry

ORIGINAL RESEARCH
published: 06 April 2022
doi: 10.3389/fchem.2022.892680

Ultrasonic-Assisted Synthesis of CdS/Microcrystalline Cellulose Nanocomposites With Enhanced Visible-Light-Driven Photocatalytic Degradation of MB and the Corresponding Mechanism Study

Chaosheng Zhu[1], Xiangli Zhang[2], Yongcai Zhang[3]*, Yunlin Li[1], Ping Wang[1], Yanchi Jia[1] and Jin Liu[4]**

[1]Zhoukou Key Laboratory of Environmental Pollution Prevention and Remediation, School of Chemistry and Chemical Engineering, Zhoukou Normal University, Zhoukou, China, [2]College of Chinese Language and Literature, Zhoukou Normal University, Zhoukou, China, [3]School of Chemistry and Chemical Engineering, Yangzhou University, Yangzhou, China, [4]Henan Key Laboratory of Rare Earth Functional Materials, International Joint Research Laboratory for Biomedical Nanomaterials of Henan, Zhoukou Normal University, Zhoukou, China

Edited by:
Qingyi Zeng,
University of South China, China

Reviewed by:
Li Yuhan,
Chongqing Technology and Business University, China
Yanbiao Liu,
Donghua University, China

***Correspondence:**
Chaosheng Zhu
zhuchsh@foxmail.com
Yongcai Zhang
zhangyc@yzu.edu.cn
Jin Liu
liuzejin1026@126.com

Specialty section:
This article was submitted to Inorganic Chemistry, a section of the journal Frontiers in Chemistry

Received: *09 March 2022*
Accepted: *21 March 2022*
Published: *06 April 2022*

Citation:
Zhu C, Zhang X, Zhang Y, Li Y, Wang P, Jia Y and Liu J (2022) Ultrasonic-Assisted Synthesis of CdS/Microcrystalline Cellulose Nanocomposites With Enhanced Visible-Light-Driven Photocatalytic Degradation of MB and the Corresponding Mechanism Study. Front. Chem. 10:892680. doi: 10.3389/fchem.2022.892680

A simple and efficient ultrasonic-assisted approach was designed to synthesize CdS/microcrystalline cellulose (MCC) nanocomposite photocatalyst. The obtained products have been characterized by XRD, FE-SEM, TEM, UV-Vis DRS, and nitrogen adsorption isotherms. The results showed that the intimate contact of MCC and CdS is beneficial for enhancing the photocatalytic performance because heterojunction formation can efficiently promote the separation of photogenerated electrons and holes of the nanocomposite photocatalyst. By using 10% MCC coupled CdS, the decoloration rate of methylene blue (MB) in the solution under visible-light was increased nearly 50%. In addition, the reuse experiments confirmed that the CdS/MCC nanocomposite photocatalyst had outstanding cycle performance and durability. Mechanism study demonstrated that hydroxyl radicals, photogenerated holes and superoxide radicals were the active species in the photocatalytic oxidization degradation of MB.

Keywords: cds, microcrystalline cellulose, visible-light photocatalysis, MB decolorization, charge separation

INTRODUCTION

Since TiO_2 as a photocatalytic material for water decomposition in 1972, photocatalysis has attracted great interest and is recognized as a promising strategy for treating pollutants because it is highly effective, low cost and environmentally friendly (Liu et al., 2021; Mohua Li et al., 2020b; Ren et al., 2022; Fang Li et al., 2020). In view of the drawbacks of TiO_2 (especially it can only utilize ultraviolet-light from the Sun) (Sheng et al., 2020; Ni et al., 2021; Jiang et al., 2020), narrow bandgap visible-light-active semiconductors such as BiOBr, BiOI, SnS_2, CdS, g-C_3N_4, etc. have been increasingly studied as photocatalysts and their photocatalytic mechanisms have been explored in numerous published works (Yang et al., 2018; Wei et al., 2017; Silva-Gaspar et al., 2022; Liu et al., 2020; Beyhaqi et al., 2021). For developing efficient visible-light-active photocatalyst, CdS is one of the extensively studied semiconductor materials because its bandgap matches well with the spectrum of visible light

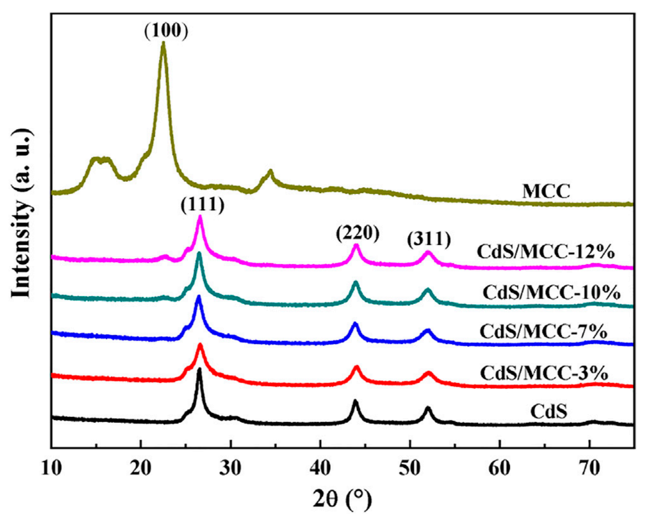

FIGURE 1 | XRD patterns of CdS, MCC, and CdS/MCC composites with different contents of MCC.

(Cheng et al., 2018; Liu et al., 2021). However, the photocatalytic efficiency of CdS is fairly poor by reason of the fast recombination of photo-generated holes and electrons (Gurugubelli et al., 2022). Additionally, CdS nanoparticles are prone to encounter photocorrosion, namely, the surface sulfide ions can be oxidized to sulfur by photogenerated holes under the irradiation (Ning and Lu, 2020). In consideration of that photocatalytic reactions occur on the surface of CdS, necessary modifications are needed to stabilize the surface sulfide ions and to transfer the photogenerated holes out from the surface in order to suppress photocorrosion (Jiang et al., 2021). Many measures have been devoted to improving the photocatalytic efficiency and inhibiting the photocorrosion of CdS, like changing the surface structure of CdS nanoparticles by controlling morphology (Liu et al., 2021), doping with noble metal (Nawrot et al., 2020), combining with other semiconductors or organic polymers (Kiani et al., 2020). Among all the modification measures, combining with organic substances (especially conjugated polymers) shows great advantages owing to their excellent characteristics (Zhang et al., 2020). Polymers can provide a suitable cyberspace so as to limit the continuous growth of crystalline grain and prevent the particle aggregation. Moreover, the high stability, simple synthesis and good environmental compatibility of polymers are helpful for practical application (Chen et al., 2020; Zeng et al., 2021). Besides, the CdS/conjugated polymer nanocomposites possess better machinability and optical performance (Lee and Chang, 2019; Melinte et al., 2019).

Cellulose, as one of renewable resources on the Earth and the most abundant natural polymers (Tian Li et al., 2021), has been widely investigated as a modifier for semiconductors because of its distinctive properties, including biocompatibility, biodegradation, mechanical strength, and chemical stability (Jiang et al., 2019). Microcrystalline cellulose (MCC) is a kind of common organic conjugated polymers, which was obtained by purifying and depolymerizing cellulose. It possesses a lot of properties that eligible for modifying semiconductors, such as large surface area for interaction with water, water insolubility, high water absorption and retention capacity, good blinding nature, remarkable ability to prevent phase separation (Zhou et al., 2019; Amaly et al., 2022). Because of the above advantages, MCC has been considered as a promising material to modify semiconductor photocatalysts for enhanced water purification performance.

In this work, a simple and efficient ultrasound approach was designed to synthesize CdS/MCC nanocomposites. The photocatalytic activity of the products was tested based on the decoloration of MB aqueous solution under visible-light. The degradation mechanism of MB over CdS/MCC nanocomposite was also explored.

MATERIALS AND METHODS

Materials

Microcrystalline cellulose (MCC), $Cd(CH_3CH_2O)_2{\cdot}2H_2O$, thioacetamide (TAA), PVP (MW = 40,000 g/mol), methylene blue (MB), 1, 4–benzoquinone (BQ), triethanolamine (TEOA), and isopropanol (IPA), coumarin (COU) nitroblue tetrazolium (NBT), and ethanol were bought from Sinopharm Chemical Reagent Co., Ltd. The reactants and solvents were analytical grade and used with no further purification. Ultrapure water (resistivity 18.2 MΩ cm) was used in this study.

Preparation of CdS/MCC Nanocomposites

The synthesis was conducted in SK3210HP 53 kHz Ultrasonic Cleaner (Shanghai KUDOS Ultrasonic Instrument Co., Ltd.). 0.2 g PVP and 0.1–0.5 g MCC were dissolved into 20 ml ethanol by sonication (18 W/cm^2) for 30 min. Next 100 ml 0.28 mol/L $Cd(CH_3CH_2O)_2{\cdot}2H_2O$ aqueous solution was added and further ultrasonically treated for 30 min, subsequently 100 ml 0.2 mol/L TAA aqueous solution was introduced. Keep ultrasonic treatment for 3 h. The formed solid product was washed with ultrapure water and ethanol, then dried at 60°C for 12 h. Depending on the different MCC contents, the CdS/MCC composites were marked as CdS/MCC-3%, CdS/MCC-7%, CdS/MCC-10% and CdS/MCC-12%.

For comparison, CdS nanoparticles were synthesized according to the aforementioned procedures but in the absence of MCC.

Characterization of the Prepared Photocatalyst

The compositions and microstructures of the CdS/MCC nanoparticles were analyzed by X-ray diffractometer (XRD, D8, Germany Bruker), field emission scanning electron microscopy (FE–SEM, S4800, Japan Hitachiltd, accelerating voltage 15 kV), and transmission electron microscopy (TEM, JEM–2100UHR, Japanese electronics, accelerating voltage 200 kV). Compositional analysis was carried out by energy-dispersive X–ray analysis (EDS). Nitrogen sorption

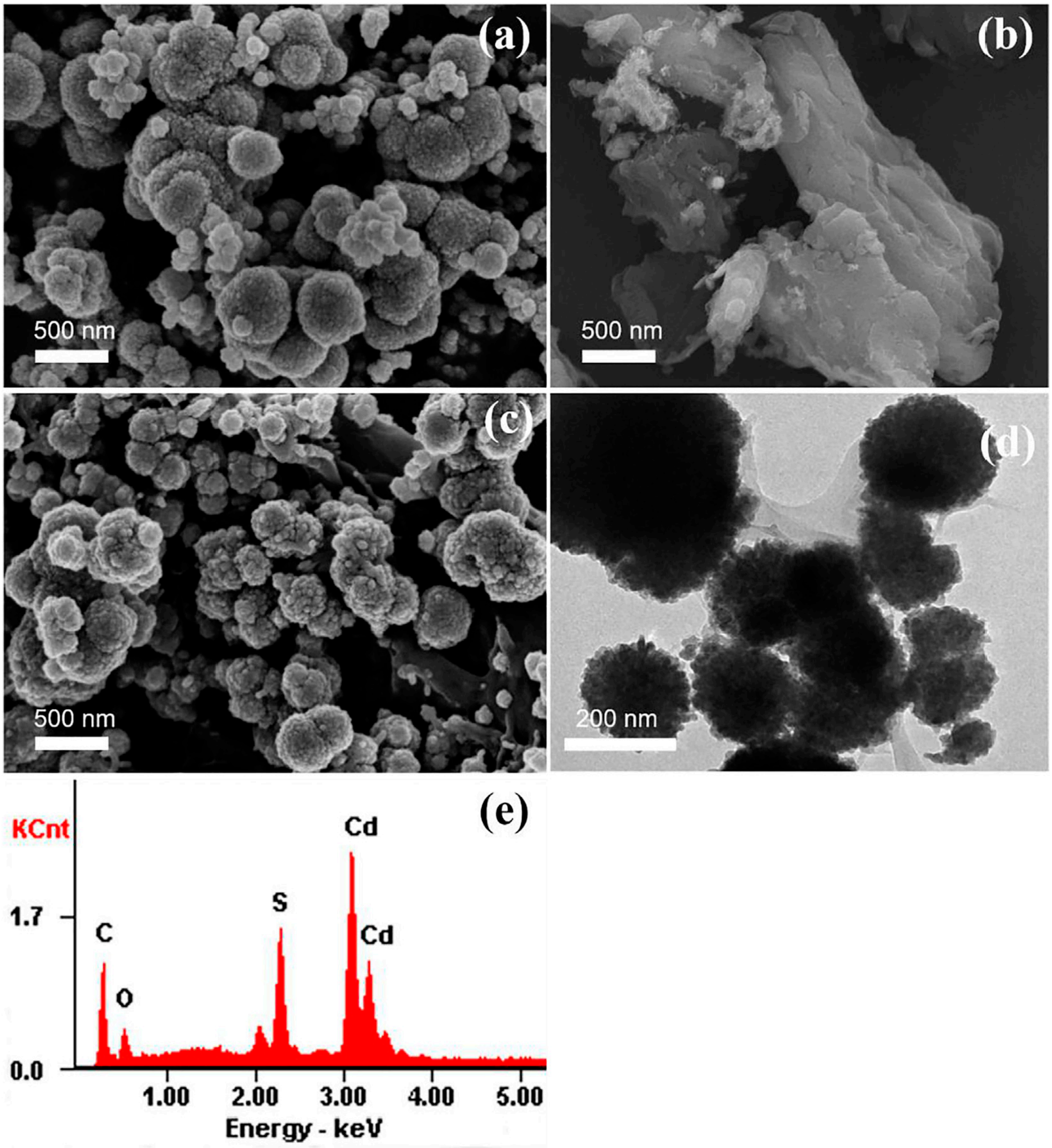

FIGURE 2 | FE-SEM image of **(A)** CdS and **(B)** MCC; **(C)** FE-SEM image, **(D)** TEM image and **(E)** EDS pattern of CdS/MCC-10%.

measurements were performed with N_2 at 77 K after degassing the samples at 300°C under vacuum for 3 h using a Quantachrome Quadra orb SI-MP porosimeter. The specific surface area was obtained by using the Brunauer–Emmett–Teller (BET) model to analyze the N_2 adsorption equilibrium data. UV–Vis diffuse reflectance spectra (UV–Vis DRS) was performed by a UV–Vis spectrophotometer (UV–2600, Shimadzu Corporation).

Photocatalytic Performance Tests

The photocatalytic performance of CdS/MCC nanocomposites synthesized were tested based on the degradation of MB in aqueous solution. 0.05 g CdS/MCC composites and 50 ml 10 mg/L MB solution were mixed by magnetic stirring for 30 min under dark condition to realize an adsorption/desorption equilibrium between the organic dye and photocatalyst. The photoreactor comprises a Xe arc lamp (1000 W) with a 400 nm optical filter, a cold trap to prevent the temperature rise of the reaction solution, and a set of 80 ml capacity cylindrical quartz reactors (Beijing Precise Technology Co., Ltd., PL-02). At the given intervals of irradiation time, 4 ml solution was fetched and filtered through a 0.45 μm filter to get rid of the photocatalyst, then the absorbance of the supernatant was measured at the wavelength of 664 nm using a Shanghai Lengguang Technology Co., Ltd. GS54T UV–Vis spectrophotometer. The degradation efficiency (η) of MB was calculated using the following :

$$\eta = \frac{A_0 - A}{A_0} \times 100\% = \frac{C_0 - C}{C_0} \times 100\% \quad (1)$$

Where η = the decolorization efficiency, C = the MB concentration at a certain irradiation time, and C_0 = the MB

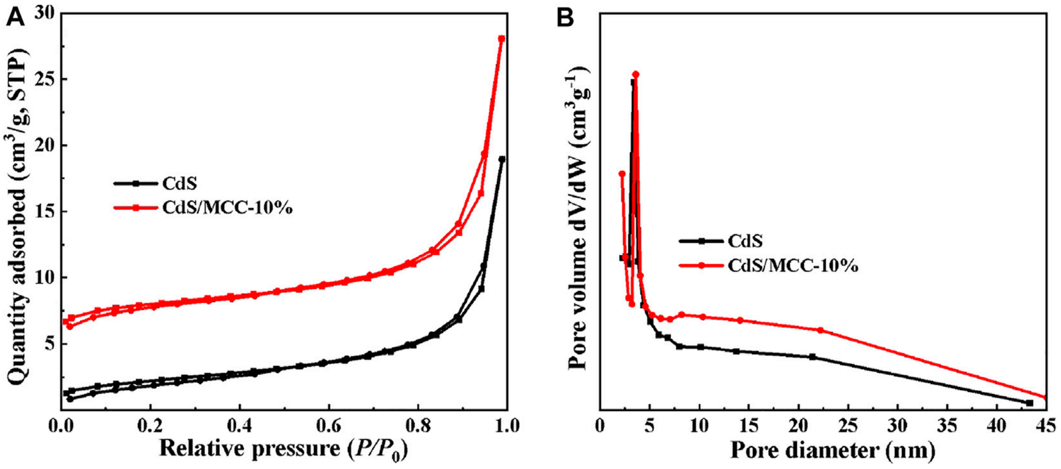

FIGURE 3 | (A) N_2 adsorption-desorption isotherms and **(B)** the corresponding pore-size distribution curves of CdS/MCC-10% and CdS.

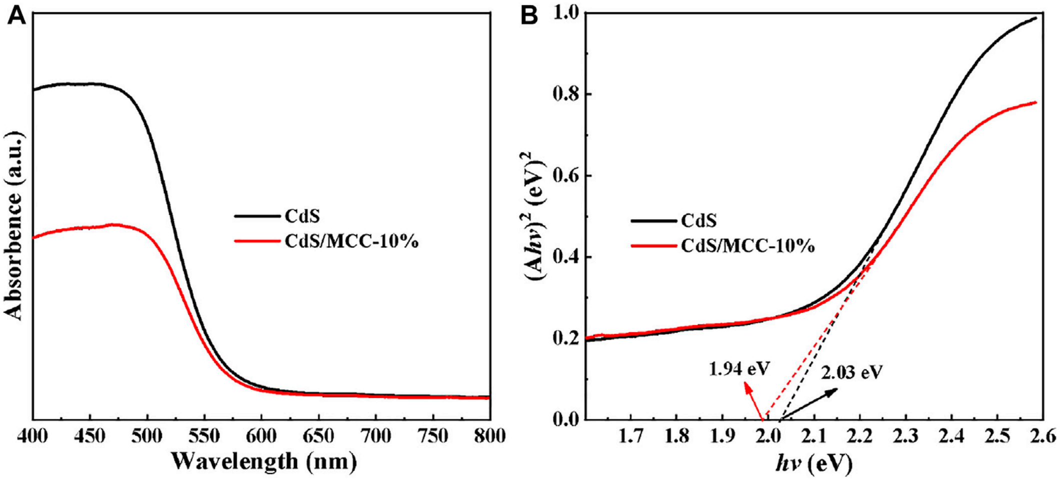

FIGURE 4 | (A) UV–Vis DRS results and **(B)** Plots of $(Ahv)^2$ vs. *hv* to determine the E_g values of pure CdS and CdS/MCC-10%.

concentration at the dark environment adsorption-desorption equilibrium.

RESULTS AND DISCUSSION

Crystal Phase and Morphology Analysis

Figure 1 displays the XRD patterns of the synthesized CdS/MCC composites with different contents of MCC, CdS and MCC. Compared with the standard XRD peaks of cubic phase CdS (JCPDS file No. 80–0019) and hexagonal phase CdS (JCPDS file No. 800–0006), the synthesized CdS comprised a mixture of major cubic phase and minor hexagonal phase. The peaks at 2θ values of 26.5°, 44.0°, and 52.1° were in turn assigned to the (111), (220), and (311) planes of cubic phase CdS. The weaker peaks at 2θ values of 26.7° and 28.3° corresponded to the (111) and (101) planes of hexagonal phase CdS (Kong et al., 2022), respectively. The XRD pattern of MCC showed sharp and high peaks, which revealed that the MCC itself has excellent crystallization. As for the various CdS/MCC composites, they display similar XRD spectra to mere CdS. Apparently, the XRD peaks of MCC did not appear in the XRD spectra of the CdS/MCC-3% and CdS/MCC-7% samples, which may be because that the minor amounts of MCC cannot be detected by the XRD equipment. When the MCC content is more than 10%, the significant (100) peak of MCC at a 2θ value of 22.5° begins to appear in the CdS/MCC composites. This confirmed that the MCC was successfully introduced to CdS and had formed CdS/MCC composites. Nevertheless, the introduction of MCC caused not shift of the XRD peak positions of CdS in the CdS/MCC composites, which suggested that MCC is not doped into the lattice of CdS nanocrystals.

The morphology, size and elemental compositions of the products were investigated using FE-SEM, TEM, and EDS. The

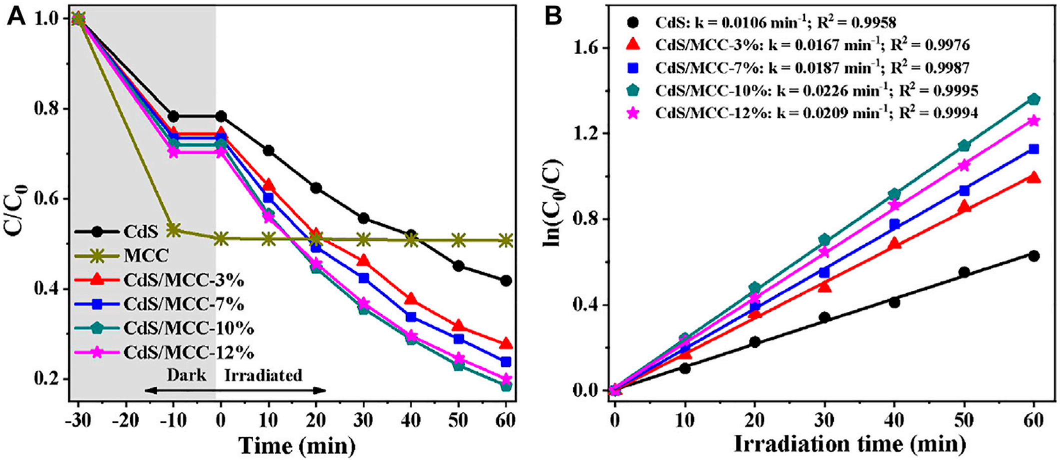

FIGURE 5 | **(A)** Adsorption and photocatalytic decolorization of MB over prepared photocatalysts; **(B)** Corresponding kinetics plots for the photocatalytic MB decolorization reactions in **(A)**.

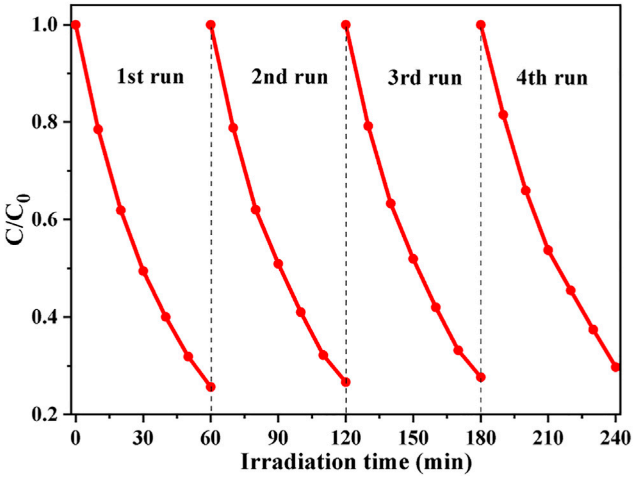

FIGURE 6 | Repeated uses of CdS/MCC-10% in the photocatalytic degradation of MB.

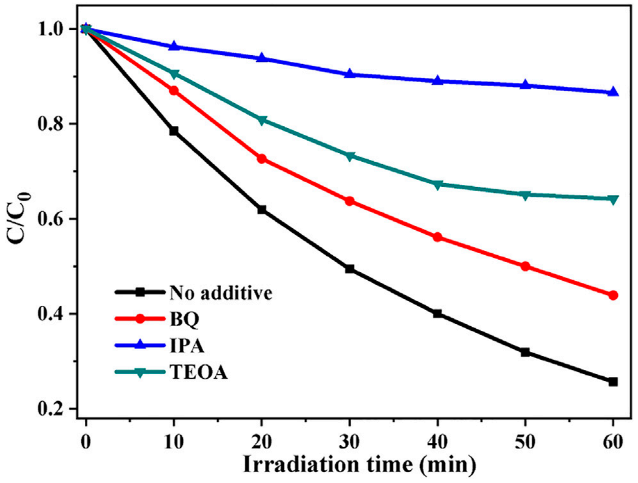

FIGURE 7 | Photocatalytic MB degradation by CdS/MCC-10% with the addition of different scavengers.

SEM images of CdS, MCC and CdS/MCC-10% are shown in **Figures 2A–C**, respectively. The CdS and CdS/MCC-10% samples were both microsphere shape with the sizes around 100–500 nm. On the other hand, the MCC had a rod-like structure, and a large number of pleats were observed on its surface. When combined with MCC, the surface of CdS nanoparticles becomes more rough to a certain degree. The TEM image of CdS/MCC-10% can be seen in **Figure 2D**. MCC in the form of platelike spread around the CdS nanoparticles, forming a tight bonding interface. The corresponding EDS pattern (**Figure 2E**) of the as-prepared CdS/MCC-10% sample revealed that the nanocomposite contained the Cd, S, C, and O elements, and the atomic percentages of Cd, S, C, and O were 39.08, 37.82, 12.91, and 10.19%, respectively. The characteristic signals of C and O come from MCC, whereas S and Cd originate from CdS.

Nitrogen Adsorption Analysis

Nitrogen adsorption tests at 77 K were performed to examine the porosity of the samples of pure CdS and CdS/MCC-10%. The BET specific surface areas of pure CdS and CdS/MCC-10% were 7.89 and 10.26 m^2/g. **Figures 3A,B** show respectively the nitrogen adsorption-desorption isotherms and the corresponding pore-size distribution curves of the prepared products. The isotherms of the CdS/MCC-10% and CdS show similar hysteresis loops ranging at $P/P_0 = 0.8–1.0$ and 0.9–1.0, respectively, which match the type IV on the basis of the IUPAC classification (You et al., 2021). The pore-size distribution curves of both products show some disorder with the pore-size distribution from 3 to 30 nm.

UV-Vis DRS Spectra Analysis

The UV–Vis DRS results of our prepared pure CdS and CdS/MCC samples were used to analyze their optical absorption

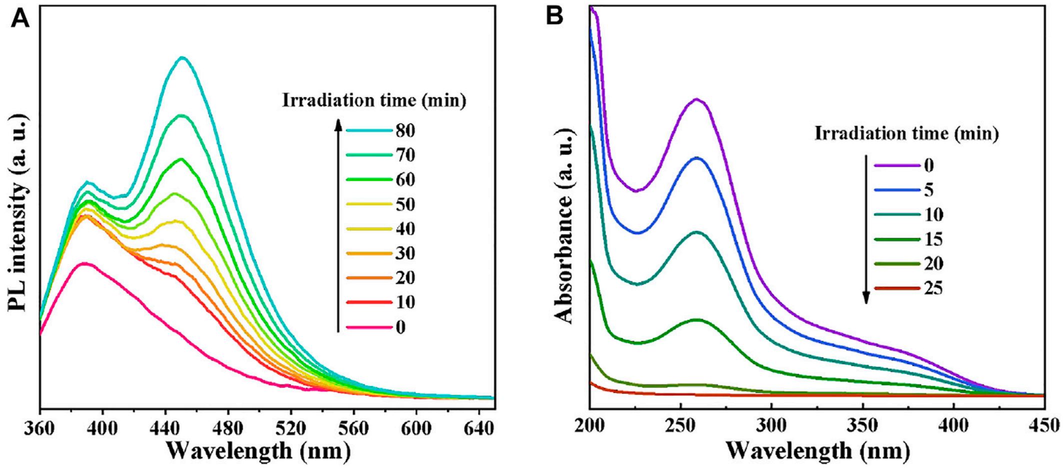

FIGURE 8 | (A) PL intensities emitted by the mixture of CdS/MCC-10% and COU solution at different visible-light irradiation times; **(B)** The time-varying absorption spectra of NBT in the presence of CdS/MCC-10% and visible-light.

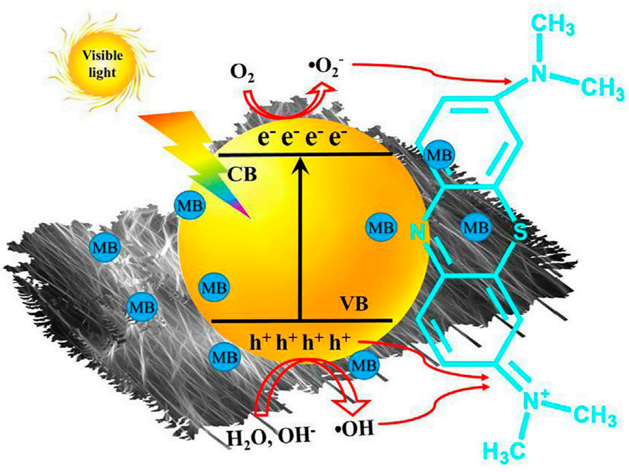

FIGURE 9 | MB degradation mechanism over CdS/MCC composite photocatalyst.

properties and bandgap energies. **Figure 4A** illuminates that both samples exhibit obvious absorption of 400–550 nm visible-light. The bandgaps of the two samples are procured according to the Tauc's plots in **Figure 4B** (Shkir et al., 2021). The determined E_g values of CdS and CdS/MCC are 1.94 and 2.03 eV, respectively. Compared with pure CdS, the narrower bandgap value of CdS/MCC-10% indicates that it can absorb a wider range of visible-light, which can be favorable for photocatalytic reactions (Zhao et al., 2021).

Assessment of Photocatalytic Activity of CdS/MCC Composites

The photocatalytic activities of all the products were assessed for MB degradation under visible-light (λ > 400 nm) irradiation for 60 min. **Figure 5A** and **Figure 5B** displays the degradation of MB photocatalyzed by pure CdS, MCC and CdS/MCC composites under visible-light. From tte figures, MCC has strong adsorption capacity for MB, but almost no photocatalytic effect. The photocatalytic performance of CdS/MCC composites (especially the CdS/MCC-10% sample) improved significantly compared with CdS. When irradiated for 60 min, the CdS/MCC-10% sample has degraded 81.5% of the initial MB aqueous solution while the pure CdS degraded about 58.8%. When the MCC contents in the CdS/MCC composites were 3, 7, and 12%, the photodegradation rates of MB were lower than that over the CdS/MCC-10% sample. This suggests that MCC/CdS-10% had the highest visible-light photocatalytic activity compared with other CdS/MCC composites. Hence, there is an optimum MCC content for CdS/MCC composite to reach the most efficient visible-light photocatalysis. When the combined MCC was excess, the MCC sites may also function as photogenerated charge recombination centers. Accordingly, the excessive MCC sites can significantly reduce the amount of photogenerated charges and decrease the visible-light photocatalytic efficiency of CdS/MCC composites. Nevertheless, too less MCC content in the CdS/MCC composites resulted in less active sites, which also decreased the photocatalytic efficiency. Besides, the MB adsorption by CdS/MCC nanocomposites improved compared with pure CdS, which is consistent with the result of Nitrogen adsorption analysis.

Photocatalytic Stability of Samples

For practical application, it is also important for the photocatalyst to have high photocatalytic stability (Ping Li et al., 2021). The photocatalytic stability of CdS/MCC-10% was further assessed in the MB decoloration reactions. The same photocatalytic process as above-mentioned was repeated for several times, but used 200 ml of MB and 200 mg of photocatalyst. After every cycle of reactions, the photocatalyst was collected, washed and used again, meanwhile the initial concentration of MB was maintained by injecting the stock solution of MB. As **Figure 6** shows, the photocatalytic activity of CdS/MCC-10% had little decrease after the fourth run tests, which indicate that the CdS/MCC-10% photocatalyst is reusable for the environmental purification application.

MB Degradation Mechanism Over CdS/MCC Composite Photocatalyst

To investigate the photocatalytic MB degradation mechanism by the CdS/MCC composite, the major reactive oxygen species involved in the degradation of MB were determined by free radical trapping experiments. The experimental procedure was the same as the photocatalytic activity test, but 50 ml of mixture of MB solution and scavenger, instead of 50 ml of MB solution was used. BQ (0.001 mol/L), TEOA (0.01 mol/L), and IPA (0.02 mol/L), were introduced into the reaction system as the scavengers for $\bullet O_2^-$, h^+, and •OH (Zhu et al., 2016; Gao et al., 2021), respectively. As can be clearly seen from **Figure 7**, the presence of TEOA, IPA and BQ all remarkably reduces the photocatalytic decolorization efficiency of MB under the same condition, which suggests that all $\bullet O_2^-$, h^+, and •OH participated in the decolorization reactions of MB. However, the photocatalytic degradation rate of MB after the addition of IPA is the slowest, indicating that •OH played a major role in the photocatalytic degradation of MB by CdS/MCC composite.

To verify the above experiment results, the generated •OH and $\bullet O_2^-$ species in the photocatalytic process were inspected by COU photoluminescence probing and NBT transformation techniques, respectively. As •OH can react with COU to generate strongly fluorescent substance (7-hydroxycoumarin), the generation of •OH in the light-irradiated CdS/MCC-10% aqueous suspension was detected using fluorescent probe technique. In this experiment, a 50 ml COU solution (0.1 g/L) replaced the 50 ml MB solution. The supernatant was monitored directly using a fluorescence spectrophotometer (the excitation wavelength is 340 nm). The PL intensities emitted by the mixture of CdS/MCC-10% and COU solution at different visible-light irradiation times are shown in **Figure 8A**. Clearly, the PL intensity of the generated 7-hydroxycoumarin at about 453 nm became stronger as the irradiation time increased. These results indicated that the •OH radicals were produced and they might act as the predominant active oxygen species during the photocatalytic process (Wang et al., 2020). The $\bullet O_2^-$ radicals in the mixture of 50 mg CdS/MCC-10% and 50 ml 0.01 mmol/L NBT solution under light irradiation were determined employing NBT (Shi et al., 2020; Du et al., 2021; Feng et al., 2021). The time-varying absorption spectra of NBT in the presence of CdS/MCC-10% and visible-light are shown in **Figure 8B**. The maximum absorbance of NBT at 260 nm decreased fastly as the irradiation time increased, indicating the formation of $\bullet O_2^-$ in the CdS/MCC-10% system under visible-light.

Based on the above analysis, the photodegradation processes of MB over the CdS/MCC composite photocatalyst are interpreted in **Figure 9**. The photogenerated electrons and the photogenerated holes are produced respectively in the conduction band (CB) and valence band (VB) of CdS/MCC by excitation with visible-light (**Eq. 2**). Meanwhile a portion of the photogenerated charges would recombine. When MB molecules were adsorbed on the surface of CdS/MCC composite and excited, they would deliver electrons to the CB of CdS/MCC composites. The VB holes of CdS/MCC can oxidize MB (**Eq. 3**), or react with the surface bound OH^- (or by H_2O) to generate •OH (**Eqs 4**, **5**) (Liu et al., 2022). The •OH can attack the chromophoric structure and the diethylamino groups effectively, causing the cycloreversion of MB molecules (**Eq. 6**) (Sun et al., 2021) as well as final mineralization into CO_2, H_2O, and other inorganic substances. Besides, the highly reducing electrons in the CB of CdS/MCC can reduce O_2 to $\bullet O_2^-$ (Yao et al., 2020), which are also able to oxidize MB (**Eqs 7**, **8**). The MCC can transfer electrons from its excited energy level to the CB of CdS, increasing the reactive oxygen species ($\bullet O_2^-$) and reducing electron-hole recombination (Hasanpour et al., 2021). Moreover, the heterojunction formed between the two components of the synthesized CdS/MCC nanocomposite (**Figure 2C**) also favors the charge separation.

$$\mathrm{CdS} + h\nu \rightarrow h^+ + e^- \tag{2}$$

$$\mathrm{MB} + h^+ \rightarrow \text{oxide product} \tag{3}$$

$$h^+ + OH^- \rightarrow \bullet OH \tag{4}$$

$$h^+ + H_2O \rightarrow \bullet OH + H^+ \tag{5}$$

$$\bullet OH + \mathrm{MB} \rightarrow \text{oxide product} \tag{6}$$

$$e^- + O_2 \rightarrow \bullet O_2^- \tag{7}$$

$$\bullet O_2^- + \mathrm{MB} \rightarrow \text{oxide product} \tag{8}$$

CONCLUSION

CdS/MCC nanocomposite photocatalyst has been successfully prepared by a mild and simple sonochemical method. In addition, the photocatalytic performance of the prepared products was also assessed. The results indicated that the synthesized CdS/MCC nanocomposite exhibited excellent photocatalytic activity, and the optimum content of MCC in the CdS/MCC nanocomposite was found to be 10%. When irradiated by visible-light for 60 min, CdS/MCC-10% can catalyze the degradation of 81.5% of MB, much higher than pure CdS. The boosted photocatalytic efficiency of CdS/MCC-10% was likely resulted from the tight junction between CdS and MCC and the larger surface area. Furthermore, the radicals capture experiments, NBT transformation and coumarin photoluminescence probing suggested that •OH was the dominant active oxygen species in the photocatalytic degradation of MB by CdS/MCC-10%. Our research provides evidence that the modification with MCC can efficiently improve the photocatalytic activity of semiconductors (such as CdS).

DATA AVAILABILITY STATEMENT

The original contributions presented in the study are included in the article/Supplementary Material, further inquiries can be directed to the corresponding authors.

AUTHOR CONTRIBUTIONS

Conceptualization, CZ and YZ; methodology, CZ; investigation, CZ, XZ and YJ; resources, CZ and JL; data curation, CZ and YL; writing—original draft preparation, CZ; writing—review and editing, YZ and JL; visualization, CZ and JL; supervision, YZ and JL; funding acquisition, CZ, YL, PW and JL. All authors have read and agreed to the published version of the manuscript.

FUNDING

This work is financially supported by Natural Science Foundation of Henan Province (No. 202300410521), the National Natural Science Foundation of China (No. 21806194), the Science and Technology Research Plan Program of Henan Province (Nos. 212102310531, 222102320328).

REFERENCES

Amaly, N., El-Moghazy, A. Y., Nitin, N., Sun, G., and Pandey, P. K. (2022). Synergistic Adsorption-photocatalytic Degradation of Tetracycline by Microcrystalline Cellulose Composite Aerogel Dopped with Montmorillonite Hosted Methylene Blue. *Chem. Eng. J.* 430, 133077. doi:10.1016/J.CEJ.2021.133077

Beyhaqi, A., Azimi, S. M. T., Chen, Z., Hu, C., and Zeng, Q. (2021). Exfoliated and Plicated g-C_3n_4 Nanosheets for Efficient Photocatalytic Organic Degradation and Hydrogen Evolution. *Int. J. Hydrogen Energ.* 46, 20547–20559. doi:10.1016/J.IJHYDENE.2021.03.174

Chen, S., Olson, E., Jiang, S., and Yong, X. (2020). Nanoparticle Assembly Modulated by Polymer Chain Conformation in Composite Materials. *Nanoscale* 12, 14560–14572. doi:10.1039/D0NR01740J

Cheng, L., Xiang, Q., Liao, Y., and Zhang, H. (2018). CdS-based Photocatalysts. *Energy Environ. Sci.* 11, 1362–1391. doi:10.1039/C7EE03640J

Du, C., Feng, W., Nie, S., Zhang, J., Liang, Y., Han, X., et al. (2021). Harnessing Efficient *In-Situ* H_2O_2 Production via a KPF6/BiOBr Photocatalyst for the Degradation of Polyethylene. *Separat. Purif. Tech.* 279, 119734. doi:10.1016/J.SEPPUR.2021.119734

Fang Li, F., Sun, L., Liu, Y., Fang, X., Shen, C., Huang, M., et al. (2020). A ClO -mediated Photoelectrochemical Filtration System for Highly-Efficient and Complete Ammonia Conversion. *J. Hazard. Mater.* 400, 123246. doi:10.1016/J.JHAZMAT.2020.123246

Feng, Z., Tian, Q., Yang, Q., Zhou, Y., Zhao, H., and Zhao, G. (2021). Selectively Photoelectrocatalytic Reduction of Oxygen to Hydroxyl Radical and Singlet Oxygen: Mechanism and Validation in Coal Wastewater. *Appl. Catal. B: Environ.* 286, 119908. doi:10.1016/J.APCATB.2021.119908

Gao, J., Shi, N., Guo, X., Li, Y., Bi, X., Qi, Y., et al. (2021). Electrochemically Selective Ammonia Extraction from Nitrate by Coupling Electron- and Phase-Transfer Reactions at a Three-phase Interface. *Environ. Sci. Technol.* 55, 10684–10694. doi:10.1021/ACS.EST.0C08552/SUPPL_FILE/ES0C08552_SI_002.PDF

Gurugubelli, T. R., Ravikumar, R. V. S. S. N., and Koutavarapu, R. (2022). Enhanced Photocatalytic Activity of ZnO–CdS Composite Nanostructures towards the Degradation of Rhodamine B under Solar Light. *Catal.* 12, 84. doi:10.3390/CATAL12010084

Hasanpour, M., Motahari, S., Jing, D., and Hatami, M. (2021). Investigation of Operation Parameters on the Removal Efficiency of Methyl orange Pollutant by Cellulose/Zinc Oxide Hybrid Aerogel. *Chemosphere* 284, 131320. doi:10.1016/J.CHEMOSPHERE.2021.131320

Jiang, Y., Lawan, I., Zhou, W., Zhang, M., Fernando, G. F., Wang, L., et al. (2019). Synthesis, Properties and Photocatalytic Activity of a Semiconductor/Cellulose Composite for Dye Degradation-A Review. *Cellulose* 27, 595–609. doi:10.1007/S10570-019-02851-W

Jiang, W., Liu, Y., Liu, F., Li, F., Shen, C., Yang, B., et al. (2020). Ultra-fast Detoxification of Sb(III) Using a Flow-Through TiO_2-Nanotubes-Array-Mesh Based Photoelectrochemical System. *Chem. Eng. J.* 387, 124155. doi:10.1016/J.CEJ.2020.124155

Jiang, N., Li, X., Guo, H., Li, J., Shang, K., Lu, N., et al. (2021). Plasma-assisted Catalysis Decomposition of BPA over Graphene-CdS Nanocomposites in Pulsed Gas-Liquid Hybrid Discharge: Photocorrosion Inhibition and Synergistic Mechanism Analysis. *Chem. Eng. J.* 412, 128627. doi:10.1016/J.CEJ.2021.128627

Kiani, M., Bagherzadeh, M., Kaveh, R., Rabiee, N., Fatahi, Y., Dinarvand, R., et al. (2020). Novel Pt-Ag_3PO_4/CdS/Chitosan Nanocomposite with Enhanced Photocatalytic and Biological Activities. *Nanomaterials* 10, 2320. doi:10.3390/NANO10112320

Kong, X., Yu, F., Zhang, H., Lv, F., Wang, Y., Yin, L., et al. (2022). Synthesis and Study of Morphology Regulation, Formation Mechanism and Photocatalytic Performance of CdS. *Appl. Surf. Sci.* 576, 151817. doi:10.1016/J.APSUSC.2021.151817

Lee, S., and Chang, C.-J. (2019). Recent Developments about Conductive Polymer Based Composite Photocatalysts. *Polymers* 11, 206. doi:10.3390/POLYM11020206

Liu, X., Ma, R., Zhuang, L., Hu, B., Chen, J., Liu, X., et al. (2020). Recent Developments of Doped g-C_3n_4 Photocatalysts for the Degradation of Organic Pollutants. *Crit. Rev. Environ. Sci. Tech.* 51, 751–790. doi:10.1080/10643389.2020.1734433

Liu, X., Sayed, M., Bie, C., Cheng, B., Hu, B., Yu, J., et al. (2021). Hollow CdS-Based Photocatalysts. *J. Materiomics* 7, 419–439. doi:10.1016/J.JMAT.2020.10.010

Liu, J., Wu, J., Wang, N., Tian, F., and Li, J. (2022). Surface Reconstruction of BiSI Nanorods for Superb Photocatalytic Cr(VI) Reduction under Near-Infrared Light Irradiation. *Chem. Eng. J.* 435, 135152. doi:10.1016/J.CEJ.2022.135152

Melinte, V., Stroea, L., and Chibac-Scutaru, A. L. (2019). Polymer Nanocomposites for Photocatalytic Applications. *Catalysts* 9, 986. doi:10.3390/CATAL9120986

Mohua Li, M., Liu, Y., Shen, C., Li, F., Wang, C.-C., Huang, M., et al. (2020). One-step Sb(III) Decontamination Using a Bifunctional Photoelectrochemical Filter. *J. Hazard. Mater.* 389, 121840. doi:10.1016/J.JHAZMAT.2019.121840

Nawrot, K. C., Wawrzyńczyk, D., Bezkrovnyi, O., Kępiński, L., Cichy, B., Samoć, M., et al. (2020). Functional CdS-Au Nanocomposite for Efficient Photocatalytic, Photosensitizing, and Two-Photon Applications. *Nanomaterials* 10, 715. doi:10.3390/NANO10040715

Ni, C., Li, Y., Meng, X., Liu, S., Luo, S., Guan, J., et al. (2021). Synergistic Role of Electron-Trapped Oxygen Vacancy and Exposed TiO_2 [0 0 1] Facets toward Electrochemical P-Nitrophenol Reduction: Characterization, Performance and Mechanism. *Chem. Eng. J.* 411, 128485. doi:10.1016/J.CEJ.2021.128485

Ning, X., and Lu, G. (2020). Photocorrosion Inhibition of CdS-Based Catalysts for Photocatalytic Overall Water Splitting. *Nanoscale* 12, 1213–1223. doi:10.1039/C9NR09183A

Ping Li, P., Wang, J., Wang, Y., Dong, L., Wang, W., Geng, R., et al. (2021). Ultrafast Recovery of Aqueous Uranium: Photocatalytic U(VI) Reduction over CdS/g-C_3N_4. *Chem. Eng. J.* 425, 131552. doi:10.1016/J.CEJ.2021.131552

Ren, Y., Guo, D., Zhao, Z., Chen, P., Li, F., Yao, J., et al. (2022). Singlet Oxygen Mediated Photocatalytic Antimonite Decontamination in Water Using Nanoconfined TiO_2. *Chem. Eng. J.* 435, 134832. doi:10.1016/J.CEJ.2022.134832

Sheng, W., Shi, J.-L., Hao, H., Li, X., and Lang, X. (2020). Polyimide-TiO_2 Hybrid Photocatalysis: Visible Light-Promoted Selective Aerobic Oxidation of Amines. *Chem. Eng. J.* 379, 122399. doi:10.1016/J.CEJ.2019.122399

Shi, H., Fan, J., Zhao, Y., Hu, X., Zhang, X., and Tang, Z. (2020). Visible Light Driven $CuBi_2O_4/Bi_2MoO_6$ P-N Heterojunction with Enhanced Photocatalytic Inactivation of *E. coli* and Mechanism Insight. *J. Hazard. Mater.* 381, 121006. doi:10.1016/J.JHAZMAT.2019.121006

Shkir, M., Khan, Z. R., Alshammari, A. S., Gandouzi, M., Ashraf, I. M., and AlFaify, S. (2021). A Comprehensive Experimental Investigation of La@CdS Nanostructured Thin Films: Structural, Opto-Nonlinear and Photodetection Properties. *Surf. Inter.* 24, 101063. doi:10.1016/J.SURFIN.2021.101063

Silva-Gaspar, B., Martinez-Franco, R., Pirngruber, G., Fécant, A., Diaz, U., and Corma, A. (2022). Open-Framework Chalcogenide Materials - from Isolated Clusters to Highly Ordered Structures - and Their Photocalytic Applications. *Coord. Chem. Rev.* 453, 214243. doi:10.1016/J.CCR.2021.214243

Sun, G., Xiao, B., Zheng, H., Shi, J.-W., Mao, S., He, C., et al. (2021). Ascorbic Acid Functionalized CdS-ZnO Core-Shell Nanorods with Hydrogen Spillover for Greatly Enhanced Photocatalytic H_2 Evolution and Outstanding Photostability. *J. Mater. Chem. A.* 9, 9735–9744. doi:10.1039/D1TA01089A

Tian Li, T., Chen, C., Brozena, A. H., Zhu, J. Y., Xu, L., Driemeier, C., et al. (2021). Developing Fibrillated Cellulose as a Sustainable Technological Material. *Nature* 590, 47–56. doi:10.1038/s41586-020-03167-7

Wang, H., Zhu, C., Xu, L., Ren, Z., and Zhong, C. (2020). Layer-by-layer Assembled Synthesis of Hollow Yolk-Shell CdS–Graphene Nanocomposites and Their High Photocatalytic Activity and Photostability. *J. Nanoparticle Res.* 22, 1–14. doi:10.1007/S11051-020-04826-6/FIGURES/13

Wei, H., Hou, C., Zhang, Y., and Nan, Z. (2017). Scalable Low Temperature in Air Solid Phase Synthesis of Porous Flower-like Hierarchical Nanostructure SnS_2 with superior Performance in the Adsorption and Photocatalytic Reduction of Aqueous Cr(VI). *Separat. Purif. Tech.* 189, 153–161. doi:10.1016/J.SEPPUR.2017.08.014

Yang, Y., Zhang, C., Lai, C., Zeng, G., Huang, D., Cheng, M., et al. (2018). BiOX (X = Cl, Br, I) Photocatalytic Nanomaterials: Applications for Fuels and Environmental Management. *Adv. Colloid Interf. Sci.* 254, 76–93. doi:10.1016/J.CIS.2018.03.004

Yao, C., Wang, X., Zhao, W., Li, T., He, Y., Ran, X., et al. (2020). Probing the Facet-dependent Intermediate in the Visible-Light Degradation of RhB by Carbon-Coated Anatase TiO_2 Nanoparticles. *J. Alloys Compd.* 846, 156335. doi:10.1016/J.JALLCOM.2020.156335

You, J., Bao, W., Wang, L., Yan, A., and Guo, R. (2021). Preparation, Visible Light-Driven Photocatalytic Activity, and Mechanism of Multiphase CdS/C_3N_4 Inorganic-Organic Hybrid Heterojunction. *J. Alloys Compd.* 866, 158921. doi:10.1016/J.JALLCOM.2021.158921

Zeng, Q., Chang, S., Wang, M., Li, M., Deng, Q., Xiong, Z., et al. (2021). Highly-active, Metal-free, Carbon-Based ORR Cathode for Efficient Organics Removal and Electricity Generation in a PFC System. *Chin. Chem. Lett.* 32, 2212–2216. doi:10.1016/J.CCLET.2020.12.062

Zhang, Y., Zhou, W., Jia, L., Tan, X., Chen, Y., Huang, Q., et al. (2020). Visible Light Driven Hydrogen Evolution Using External and Confined CdS: Effect of Chitosan on Carriers Separation. *Appl. Catal. B: Environ.* 277, 119152. doi:10.1016/J.APCATB.2020.119152

Zhao, H., Xing, Z., Su, S., Song, S., Li, Z., and Zhou, W. (2021). Gear-shaped Mesoporous NH_2-MIL-53(Al)/CdS P-N Heterojunctions as Efficient Visible-Light-Driven Photocatalysts. *Appl. Catal. B: Environ.* 291, 120106. doi:10.1016/J.APCATB.2021.120106

Zhou, W., Sun, S., Jiang, Y., Zhang, M., Lawan, I., Fernando, G. F., et al. (2019). Template *in Situ* Synthesis of Flower-like BiOBr/microcrystalline Cellulose Composites with Highly Visible-Light Photocatalytic Activity. *Cellulose* 26, 9529–9541. doi:10.1007/S10570-019-02722-4/FIGURES/9

Zhu, C., Zhang, L., Jiang, B., Zheng, J., Hu, P., Li, S., et al. (2016). Fabrication of Z-Scheme Ag_3PO_4/MoS_2 Composites with Enhanced Photocatalytic Activity and Stability for Organic Pollutant Degradation. *Appl. Surf. Sci.* 377, 99–108. doi:10.1016/J.APSUSC.2016.03.143

Conflict of Interest: The authors declare that the research was conducted in the absence of any commercial or financial relationships that could be construed as a potential conflict of interest.

frontiers | Frontiers in Chemistry

ORIGINAL RESEARCH
published: 07 April 2022
doi: 10.3389/fchem.2022.857473

Hydroisomerization of n-Hexadecane Over Nickel-Modified SAPO-11 Molecular Sieve-Supported NiWS Catalysts: Effects of Modification Methods

Xiaojun Dai, Yan Cheng, Meng Si, Qiang Wei* and Yasong Zhou

State Key Laboratory of Heavy Oil Processing, China University of Petroleum, Beijing, China

The complexation-excessive impregnation modification method, which was original in this study, and the ion-exchange method and the *in situ* modification method were used to synthesize Ni-modified SAPO-11 molecular sieves. With the Ni-modified SAPO-11 samples as support, the corresponding NiWS-supported catalysts for the hydroisomerization of n-hexadecane were prepared. The effects of Ni-modification on SAPO-11 characteristics and the active phase were studied. The structure, morphology, and acidity of SAPO-11, as well as the interaction between active metals and support, the morphology, dispersibility, and stacking number of the active phase, were all changed by Ni-modification methods. The complexation-excessive impregnation modification method deleted a portion of Al from SAPO-11 molecular sieves while simultaneously integrating Ni into the skeletal structure of the surface layer of SAPO-11 molecular sieves, considerably enhancing the acidity of SAPO-11 molecular sieves. Furthermore, during dealumination, ethylenediaminetetraacetic acid generated more mesoporous structures and increased the mesoporous volume of SAPO-11 molecular sieves. Because the complexation-excessive impregnation modification method increased the amount of Ni in the surface framework of the SAPO-11 molecular sieve, it has weakened the interaction between the active phase and the support, improved the properties of the active phase, and greatly improved the hydroisomerization performance of NiW/NiSAPO-11. The yield of i-hexadecane of NiW/NiSAPO-11 increased by 39.3% when compared to NiW/NiSAPO-11. It presented a realistic approach for increasing the acidity of SAPO-11, reducing the interaction between active metals and support, and improving the active phase stacking problem.

Keywords: Ni-modified, SAPO-11, NiWS-supported catalyst, active phase, hydroisomerization

OPEN ACCESS

Edited by:
Shuaifei Zhao,
Deakin University, Australia

Reviewed by:
Hao Song,
University of Queensland, Australia
Changhai Liang,
Dalian University of Technology, China

****Correspondence:***
Qiang Wei
qwei@cup.edu.cn

Specialty section:
This article was submitted to
Inorganic Chemistry,
a section of the journal
Frontiers in Chemistry

Received: *18 January 2022*
Accepted: *14 March 2022*
Published: *07 April 2022*

Citation:
Dai X, Cheng Y, Si M, Wei Q and Zhou Y (2022) Hydroisomerization of n-Hexadecane Over Nickel-Modified SAPO-11 Molecular Sieve-Supported NiWS Catalysts: Effects of Modification Methods.
Front. Chem. 10:857473.
doi: 10.3389/fchem.2022.857473

INTRODUCTION

The presence of long-chain n-alkanes is thought to be the cause of the high freezing point of diesel and the poor low-temperature fluidity of lubricating base oil (Tao et al., 2017). The formation of branched isomers by hydroisomerization of long-chain n-alkanes can effectively lower the freezing point of diesel and increase the low-temperature fluidity of lubricating base oil (Du et al., 2018). The bifunctional catalyst for the hydroisomerization of n-alkanes contains an acid site for the skeletal isomerization of olefin intermediates and a metal site for de/hydrogenation (Wei et al., 2017). Acidic supports, such as zeolites, usually supply acid sites, whereas noble metals or other transition metals give metal sites (Yang et al., 2017a). Because of their one-dimensional porosity and low acidity, SAPO-11 molecular sieves are commonly employed as a support for n-alkane hydroisomerization catalysts (Guo et al., 2012). Noble metals like platinum and palladium have strong de/hydrogenation activities, whereas nonnoble metals like nickel are also used as metal components in hydroisomerization catalysts (Zhao et al., 2014; Wang et al., 2018).

Although SAPO-11 molecular sieves have been used in industry and have shown to be a solid support for hydroisomerization catalysts, increasing their performance in hydroisomerization is still a concern worth investigating (Blasco et al., 2006). The active sites for catalyzing isomerization of the alkane molecular skeleton are thought to be Brnsted (B) acid sites in the SAPO-11 molecular sieve, particularly the medium strength B acid sites (Guo et al., 2013). As a result, improving the isomerization performance of SAPO-11 requires a better understanding of enhancing the proportion of medium and strong B acid sites. Lyu et al. (2019a) used *in situ* synthesis to introduce varying amounts of Ni into SAPO-11 to investigate the effects of metal-acid balance on n-hexane hydroisomerization and the acidity of SAPO-11. However, up to now, no one has studied the effects of modification methods in the process of Ni modification on the physicochemical properties (such as textural and acidity) of SAPO-11 molecular sieves. Furthermore, despite the remarkable catalytic activity of noble metals as metal components of hydroisomerization catalysts, there are two issues. On the one hand, the high cost of noble metals restricts their use in industry (Tian and Chen., 2014). Noble metals, on the other hand, are poisoned and inactivated due to their sensitivity to sulfur-containing compounds in raw materials (Yang et al., 2017b; Lyu et al., 2020). Although some researchers have reported employing Ni as a metal component instead of noble metals, hydroisomerization results revealed that Ni has a high hydrogenolysis activity, resulting in lower isomer selectivity and yield than noble metal-supported catalysts (Karthikeyan et al., 2016; Yang et al., 2017c). Transition metal sulfides have a good de/hydroisomerization performance and are widely used as the active phase of catalysts for hydrodesulfurization (Díaz de León et al., 2017), hydrodenitrogenation, and hydrocracking (Cui et al., 2019), such as NiMoS (Zhou et al., 2017) and NiWS (Minaev et al., 2019). In the past, there have been many reports on the application of noble metal (Pt, Pd) or Ni-supported catalysts in alkane hydroisomerization (Lyu et al., 2017; Hongloi et al., 2021), but there have been few on the application of transition metal sulfide catalysts in alkane hydroisomerization and the effects of the properties of the transition metal sulfide active phase on alkane hydroisomerization (Shi et al., 2009; Tan et al., 2021).

In this study, the ion-exchange method, the *in situ* modification method, and the complexation-excessive impregnation modification method were used to modify SAPO-11 molecular sieves with Ni in this study. The hydroisomerization of n-hexadecane was carried out using the Ni-modified SAPO-11 molecular sieves, which were supported by NiWS. The impact of various modification methods on the physicochemical properties of SAPO-11, the active phase properties, and the hydroisomerization performance of several catalysts were studied.

EXPERIMENTAL

Materials

Phosphoric acid (H_3PO_4, 85wt%; Aladdin), pseudo-boehmite (Al_2O_3, 70wt%; Macklin), acid silica sol (SiO_2, 30wt%; Dezhou Jinghuo technology Glass Co., Ltd.), di-n-propylamine (DPA, 99wt%; Aladdin), diisopropylamine (DIPA, 99wt%; Aladdin), dodecyltrimethylammonium bromide (DTAB, 99wt%; Aladdin), ammonium chloride (NH_4Cl, 99.5wt%; Macklin), nickel nitrate hexahydrate($Ni(NO_3)_2{\cdot}6H_2O$, 98wt%; Aladdin), ammonium metatungstate hydrate ($(NH_4)_6H_2W_{12}O_{40}{\cdot}xH_2O$, 99.5wt%; Macklin), ethylenediaminetetraacetic acid (EDTA, 98wt%; Aladdin), and deionized water.

Synthesis and Modification of SAPO-11 Molecular Sieves

Deionized water and phosphoric acid were mixed in a normal synthesis procedure, then pseudo-boehmite was added to the solution and agitated for 2 h. DPA and DIPA were added and mixed continuously for 2 h. Drop by drop, acid silica sol was added to the system and aggressively agitated for 2 h. Finally, DTAB was added and agitated for 1 h, resulting in an initial gel with the following molar composition: 1.0 Al_2O_3: 0.75 P_2O_5: 0.45 SiO_2: 0.5 DPA: 0.5 DIPA: 0.05 DTAB: 45 H_2O. The gel was pre-crystallized at 90°C for 12 h before being crystallized at 190°C for 24 h. The SAPO-11 molecular sieves were obtained by washing the solid products collected by filtration to neutrality with deionized water, drying them at 110°C overnight, and calcining them at 600°C for 6 h.

For the ion-exchange procedure, 10.0 g of SAPO-11 was mixed with 100 g of 0.3 mol/L nickel nitrate solution, which was then exchanged at 90°C for 4 h, filtered, dried at 110°C overnight, and calcined at 500°C for 4 h. Ni@SAPO-11 was the name given to the dried and calcined sample. The operation procedures for the *in situ* modification method were similar to the above-mentioned SAPO-11 synthesis steps, with the exception that 3% nickel was added during the initial gel formation process (the molar ratio of Ni/Al_2O_3 was 3%). The products were filtered before being dried at 110°C overnight and calcined for 4 h at 500°C. Ni-SAPO-11 was the name given to the dried and calcined sample. 0.1 mol EDTA was added to 50 ml of 0.3 mol/L nickel nitrate solution for the complexation-excessive impregnation modification procedure, and then 10 g of SAPO-11 molecular sieve particles with 20–40 mesh were impregnated with the resulting solution. SAPO-11 molecular sieve particles after complexation-excessive impregnation were obtained by filtration, dried, and calcined, and designated NiSAPO-11 after soaking for 4 h.

Preparation of NiW-Supported Catalysts

The SAPO-11, Ni@SAPO-11, and Ni-SAPO-11 particles were pressed, crushed, and sieved to a size of 20–40 mesh. The NiW-supported catalysts were made using the incipient-wetness impregnation method with an aqueous solution of nickel nitrate hexahydrate and ammonium metatungstate hydrate, then dried at 110°C for 6 h and calcined at 500°C for 4 h after being evaporated at room temperature overnight. The loading concentration of NiO was 5% and the loading concentration of WO_3 was 15% for each catalyst. NiW/SAPO-11, NiW/Ni@SAPO-11, NiW/Ni-SAPO-11, and NiW/NiSAPO-11 were the names given to the resulting catalysts.

Characterization

The SAPO-11 samples were characterized by X-ray diffraction (XRD) on a Bruker AXS D8 Advance X-ray diffractometer using Cu Kα radiation at 40 kV and 40 mA, and 2θ varied from 5 to 90° at a scanning speed of 5°/min. On a field-emission environmental scanning electron microscope, images of the SAPO-11 samples were taken using scanning electron microscopy (SEM) (FEI Quanta 200F). After degassing the materials at 350°C under vacuum for 15 h, N_2 adsorption-desorption measurements were performed on a Micromeritics ASAP 2020 analyzer at −196°C. The Brunauer-Emmett-Teller (BET) and de Boer *t*-plot methods were used to compute the specific surface area and micropore volume, respectively, while the Barrett-Joyner-Halenda technique was used to calculate the mesopore volume. A Micromeritics auto-chem 2920 device was used to analyze temperature-programmed desorption of ammonia (NH_3-TPD). The sample was heated to 600°C in an Ar flow for 30 min, then switched to an ammonia flow for another 30 min before being cooled to 70°C. The sample was purged with Ar for 2 h to eliminate the physically adsorbed ammonia, and the TPD signal was recorded using a thermal conductivity detector with a heating rate of 10°C/min from 70 to 600°C. A Nicolet 5700 spectrometer was used to record Pyridine adsorbed infrared (Py-IR) spectra. At 200 and 350°C, the pyridine samples were evacuated. On a Quantachrome Autosorb-iQ-C chemical adsorption system, temperature-programmed hydrogen reduction (H_2-TPR) measurements were taken. The samples were heated at a rate of 10°C/min in an H_2-Ar flow containing 5% H_2 from room temperature to 1,050°C. The presulfurized catalysts were analyzed using X-ray photoelectron spectroscopy (XPS) on a Thermo spectrometer using Al Kα radiation as the excitation light source. To calibrate the binding energy scale, all spectra used the Al 2p peak with a binding energy of 74.6 eV. The presulfurized catalysts' XPS spectra were decomposed using XPS PEAK, and the deconvolution was achieved using Gaussian-Lorentzian band shapes. A JEM 2100 LaB_6 transmission electron microscope was used to obtain high-resolution transmission electron microscope (HRTEM) images of the presulfurized catalysts. The average length and average stacking number of WS_2 slabs were determined using methods described in the literature (Yu et al., 2012):

$$\text{Average slab length } \bar{L} = \frac{\sum_{i=1}^{n} n_i l_i}{\sum_{i=1}^{n} n_i} \tag{1}$$

$$\text{Average stacking number } \bar{N} = \frac{\sum_{i=1}^{n} n_i N_i}{\sum_{i=1}^{n} n_i} \tag{2}$$

where l_i denotes the WS_2 slab length, n_i denotes the number of slabs of length l_i, and N_i is the number of layers in a WS_2 slab. The dispersion degree of the WS_2 active phase, f_W, was derived using the following equation, assuming that the WS_2 slabs are presented as perfect hexagons (Tao et al., 2014):

$$f_W = \frac{W_{edge}}{W_{total}} = \frac{\sum_{i=1}^{t} 6(n_i - 1)}{\sum_{i=1}^{t} (3n_i^2 - 3n_i + 1)} \tag{3}$$

where W_{edge} denotes the W atoms on the edges of WS_2 slabs, W_{total} denotes the total number of W atoms, n_i denotes the number of W atoms along one side of a WS_2 slab determined by its length [L = 3.2 (2ni—1) Å], and t denotes the total number of slabs determined by at least 500 WS_2 slabs obtained from HRTEM images of various catalysts.

Catalytic Performance Assessment

In a fixed-bed hydrogenation micro-reactor, the hydroisomerization of n-hexadecane (n-C_{16}) was carried out. In a typical reaction, the tubular furnace held 9.0 ml of catalyst and 22 ml of silica sand. The catalyst was presulfurized using a CS_2 cyclohexane solution containing 2% CS_2 at 320°C and 4 MPa for 5 h with a liquid hourly space velocity (LHSV) of 7 h^{-1} and an H_2/oil ratio of 100 (v/v) before the reaction. After presulfurization, the catalytic performance of the catalyst was examined at 2 MPa, 1.5 h^{-1} LHSV, 600 (v/v) H_2/oil, and 320–400°C reaction temperature. When the temperature was reduced to the reaction temperature, a syringe pump was used to feed the reactant n-hexadecane into the reactor. The products were analyzed using a Shimadzu GC-2014 gas chromatograph with a capillary HP-PONA column and GC-MS for qualitative analysis. The TOF (turnover frequency, which is used to evaluate the catalytic activity of a catalyst) of each active site was calculated using the following equation based on the number of all available active sites and the conversion of n-C_{16} of each catalyst at 340°C (Wen et al., 2020):

$$TOF = \frac{V_{feed} \cdot x}{n_W \cdot f_W} \tag{4}$$

where V_{feed} is the feed rate of the reactant n-C_{16} in mol/h, x is the conversion of n-C_{16} at 340°C, n_w is the amount of W atom in the catalyst in mol, and f_W is the dispersion degree of W species. The following equation was used to compute the hydroisomerization reaction rate constant (Pimerzin et al., 2019):

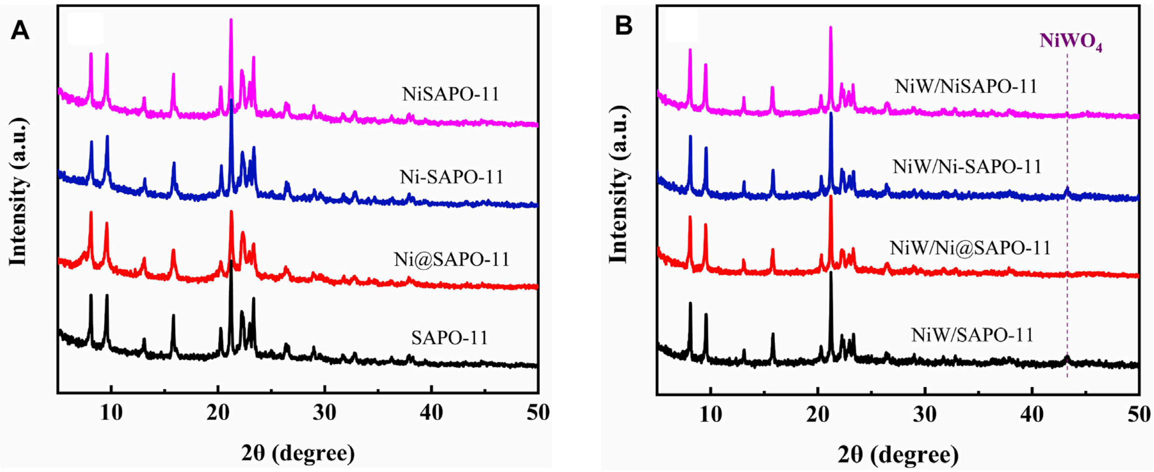

FIGURE 1 | XRD patterns of different SAPO-11 molecular sieves **(A)** and different catalysts **(B)**.

$$k_{iso} = \frac{V_{feed}}{m} \ln (1 - x) \tag{5}$$

where k_{iso}, V_{feed}, m and x are the quasi-first-order reaction rate constant of n-C_{16} hydroisomerization on different catalysts, the feed flow rate of the reactant n-C_{16} in mol/h, the mass of catalyst and the conversion of n-C_{16}, respectively.

RESULTS AND DISCUSSION

Phase Structure

The XRD patterns of Ni-modified SAPO-11 molecular sieves generated by various ways are shown in **Figure 1A**. All samples exhibited diffraction peaks in the 2θ range of 5–50° that were assigned to the normal AEL structure, demonstrating that SAPO-11 samples retained full structural units after Ni alteration by various methods (Lyu et al., 2019b). The prominent characteristic diffraction peaks of Ni-SAPO-11 indicate that it has a high crystallinity (Song et al., 2017). Because Ni species replaced a portion of Al species in the SAPO-11 framework, crystalline Ni species resulted. The strength of the distinctive diffraction peaks of Ni@SAPO-11 reduced slightly when compared to SAPO-11, which could be attributable to a decrease in crystallinity during the ammonium-exchange and nickel ion-exchange processes (rehydration) (Yang et al., 2017c). Furthermore, the intensity of the characteristic diffraction peaks of NiSAPO-11 did not significantly decrease, indicating that EDTA could remove some Al species but not the crystal structure of SAPO-11. A weak characteristic diffraction peak attributed to NiO appeared at 2θ = 37.2° of XRD patterns of all the samples, which indicates that there were a small number of NiO species in all the samples, and the distribution of NiO species in SAPO-11 molecular sieves was relatively uniform. **Figure 1B** shows the XRD spectra of the different catalysts. It can be seen that the different catalysts still retained the characteristic diffraction peaks attributed to AEL structure, indicating that the loading of metal components did not cause the crystal structure of SAPO-11 molecular sieves to be destroyed. In addition, all the catalysts showed a weak characteristic diffraction peak attributed to $NiWO_4$ species around 2θ = 43.2°, which indicates that $NiWO_4$ species existed in all samples and dispersed relatively evenly.

Morphology

SEM images of Ni-modified SAPO-11 molecular sieves generated by various procedures are shown in **Figure 2**. SAPO-11 had pseudospherical particles with a particle size of roughly 5 μm and a fairly uniform particle size distribution. The particle shape of Ni@SAPO-11 was not as regular as that of SAPO-11, and the discrepancy could be due to its particle form being destroyed when it was exchanged in aqueous solution twice. While Ni-SAPO-11 was basically the same as SAPO-11 in particle shape and size. As for NiSAPO-11, a small number of small particles similar to amorphous substances appear in its SEM image, which may be the smaller particles formed by the decomposition of SAPO-11 molecular sieve particles in the process of removing Al species by EDTA.

Textural Properties

Figure 3 shows the N_2 adsorption-desorption isotherms (**Figure 3A**) and pore size distribution (**Figure 3B**) of the Ni-modified SAPO-11 molecular sieves. Isotherms with typical H4-type hysteresis loops were seen in all samples (Chen et al., 2017). At low relative pressure ($10^{-5} \le P/P_0 \le 10^{-2}$), the amount of N_2 adsorption in all samples rose dramatically, which was attributable to N_2 filling the micropores (Du et al., 2019). Within the relative pressure P/P_0 range of 0.4–0.9, all samples showed clear hysteresis loops, showing that these samples have a lot of mesopores (Wen et al., 2019). The hysteresis loop of NiSAPO-11 is clearly larger than that of other samples, indicating that NiSAPO-11 has a more mesoporous structure than other samples. This is because, when eliminating Al species, EDTA dissolved and etched in the crystals of SAPO-11 molecular sieves, forming many new mesoporous structures. **Figure 3B**

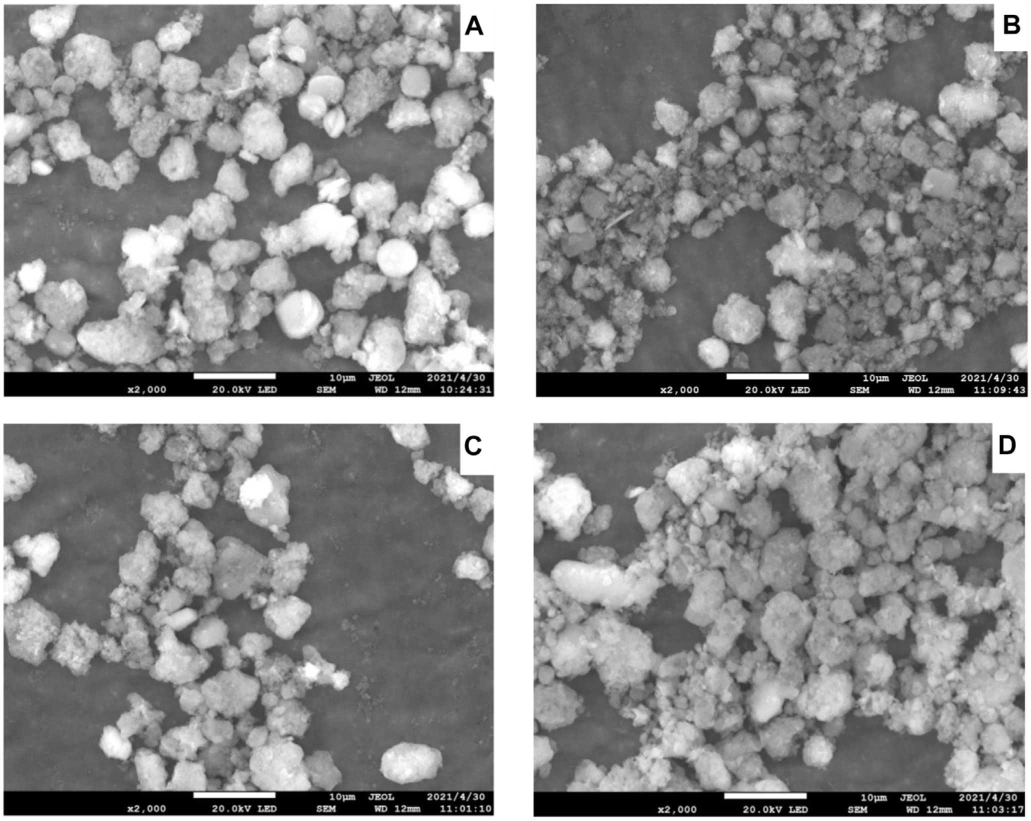

FIGURE 2 | SEM images of Ni-modified SAPO-11: **(A)** SAPO-11, **(B)** Ni@SAPO-11, **(C)** Ni-SAPO-11, and **(D)** NiSAPO-11.

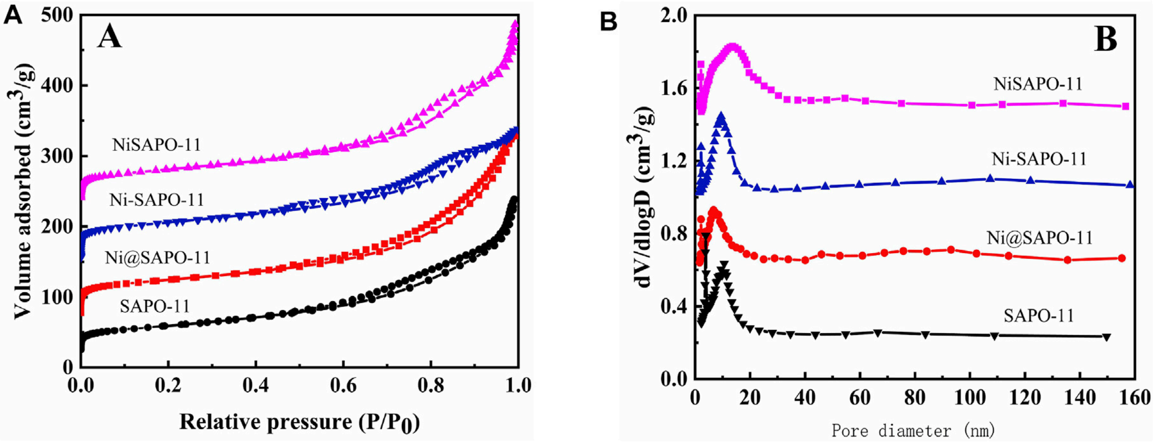

FIGURE 3 | N_2 adsorption-desorption isotherms **(A)** and pore size distribution **(B)** of Ni-modified SAPO-11 molecular sieves.

shows the pore size distribution of all samples, with the pore size of SAPO-11, Ni@SAPO-11, and Ni-SAPO-11 primarily dispersed around 12 nm. The foregoing findings show that these samples include hierarchical micro-mesoporous structures. However, the mesoporous size of NiSAPO-11 is centered at 18 nm, which is larger than that of other samples, implying that EDTA does have a pore-expansion role.

The BET surface area (S_{BET}), exterior surface area (S_{ext}), and pore volume of the Ni-modified SAPO-11 are shown in **Table 1**. The S_{BET} and pore volume of Ni@SAPO-11 were reduced to some

TABLE 1 | Textural properties of Ni-modified SAPO-11.

Sample	S_{BET}, m^2/g	S_{ext}, m^2/g	V_{micro}, cm^3/g	V_{meso}, cm^3/g	V_{total}, cm^3/g
NiSAPO-11	188	96	0.11	0.36	0.47
Ni-SAPO-11	174	94	0.08	0.30	0.38
Ni@SAPO-11	158	88	0.07	0.20	0.27
SAPO-11	166	91	0.09	0.26	0.35

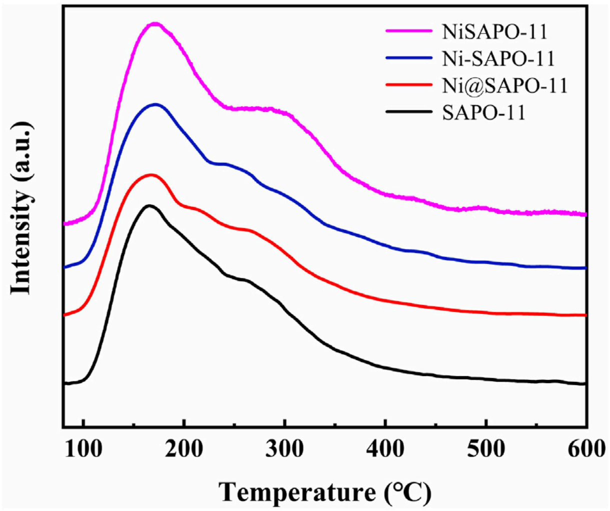

FIGURE 4 | NH_3-TPD profiles of Ni-modified SAPO-11 molecular sieves.

extent when compared to SAPO-11. One probable explanation is that Ni species enter the pores, blocking certain micropores and occupying a portion of the mesopore volume (V_{meso}) in the ion-exchange process. Another possibility is that during the ion-exchange process, a portion of the crystal structure collapses, causing the pore channels to fill. The S_{BET} and V_{meso} of Ni-SAPO-11 have increased, indicating that the addition of Ni *in situ* helps to improve the S_{BET} and V_{meso} of SAPO-11 (Liu et al., 2013). The micropore volume (V_{micro}) of Ni-SAPO-11 decreased, implying that some Ni species remain in the micropores and occupy the micropore volume. The S_{BET}, V_{micro}, and V_{meso} of NiSAPO-11 all increased, with V_{meso} increasing by a substantial margin, confirming the prior conclusion that EDTA has the ability to ream and manufacture new mesopores. The S_{BET} and V_{meso} of the different SAPO-11 samples increased in the order of Ni@SAPO-11 < SAPO-11 < Ni-SAPO-11 < NiSAPO-11, indicating that the textural properties of SAPO-11 molecular sieves can be improved most obviously by the complexation-excessive impregnation modification method.

Acidity Properties

The NH_3-TPD measurements were used to determine the acid amounts and acid strength distribution of the Ni-modified SAPO-11 molecular sieves manufactured using various procedures. **Figure 4** shows the NH_3-TPD profiles of the several Ni-modified SAPO-11 samples. Each NH_3-TPD profile revealed two NH_3 desorption peaks about 180 and 310°C, corresponding to NH_3 adsorbed on weak acid sites, medium and strong acid sites, respectively (Yang et al., 2019). The intensity of the desorption peak represents the acid amount (Li and Wu, 2020). The acid amount of Ni@SAPO-11 was much lower than that of SAPO-11, which was attributable to the fact that part of the acid sites were covered and sheltered by Ni species during Ni ion exchange. The strength of the NH3 desorption peak corresponding to weak acid sites reduced somewhat in Ni-SAPO-11, indicating that the weak acid amount of Ni-SAPO-11 fell slightly (Yang et al., 2017c). This is due to the fact that the acid sites in SAPO-11 are thought to be formed by Si-OH, Al-OH, P-OH, and Si-OH-Al, respectively (Tiuliukova et al., 2018). Some Al precursors were substituted with Ni precursors, resulting in a reduction in acid sites. The intensities of the NH_3 desorption peaks corresponding to medium and strong acid sites increased, indicating that the concentrations of medium and strong acid increased as well. It can be explained by the fact that Ni has a greater average electronegativity (1.91) than Al (1.71), and Ni has a higher covalency than Al. As a result, the Brnsted protons and Lewis caverns generated by Ni substituting part of Al in SAPO-11 have a higher acid density, resulting in more medium and strong acid sites in Ni-SAPO-11. The amount of weak acid, medium and strong acid in NiSAPO-11 were all improved. The increase in weak acid amonut is due to EDTA dredging some blocked channels and establishing new ones, exposing and detecting more acid sites to a large extent. The rise in medium and strong acid amounts in NiSAPO-11 can be attributed to two factors. On the one hand, the exposure of acid sites is caused by an increase in pore volume. In the process of eliminating Al species, EDTA can integrate Ni species into the surface framework of SAPO-11 molecular sieves to generate Ni-OH-Si species, which helps to enhance the density of medium and strong acid in SAPO-11. The results show that the amounts of the weak acid in Ni-modified SAPO-11 decreased in the order of NiSAPO-11 > SAPO-11 > Ni@SAPO-11 > Ni-SAPO-11, while the amounts of medium and strong acid decreased in the order of NiSAPO-11 > Ni-SAPO-11 > SAPO-11 > Ni@SAPO-11.

Py-IR was used to analyze the variations in Brønsted (B) acid sites and Lewis (L) acid sites in the Ni-modified SAPO-11 molecular sieves to determine the acidity of the different SAPO-11 samples (Jin et al., 2018). **Figure 5** shows the Py-IR spectra of the Ni-modified SAPO-11 samples generated using various procedures. Py-IR spectra obtained after pyridine molecules desorbed at 200°C were used to compute the amount of weak acid, whereas Py-IR spectra formed after pyridine molecules desorbed at 350°C were used to calculate the amounts of medium and strong acid. **Table 2** shows the

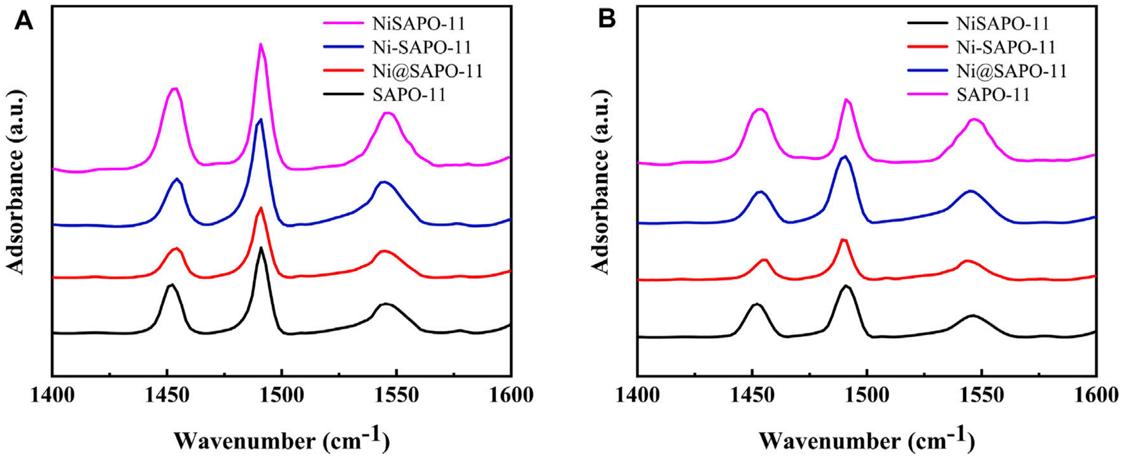

FIGURE 5 | Py-IR spectra of Ni-modified SAPO-11 molecular sieves at 200°C **(A)** and 350°C **(B)**.

TABLE 2 | Acidity properties of Ni-modified SAPO-11 determined by Py-IR.

Sample	Acidity (μmol/g)					
	Weak acid sites (200°C)			Medium and strong acid sites (350°C)		
	B	L	B + L	B	L	B + L
SAPO-11	91.87	29.32	121.19	30.62	20.97	51.59
Ni@SAPO-11	53.09	24.25	77.34	23.51	15.11	38.62
Ni-SAPO-11	69.91	35.84	105.75	48.21	18.16	66.37
NiSAPO-11	82.21	56.88	139.09	58.35	24.66	83.01

results of calculating the number of B acid sites and L acid sites and the accompanying findings. All samples had three peaks in the range of 1,400–1,600 cm^{-1}, as illustrated in **Figure 5**. The peaks at 1,455 cm^{-1} and 1,545 cm^{-1} are assigned to pyridine molecules desorbed on L acid sites and B acid sites, respectively (Wen et al., 2020), whereas the peak at 1,490 cm^{-1} is attributed to a combined line of B acid sites and L acid sites (Zhang et al., 2018). The amounts of weak L acid in Ni-modified SAPO-11 molecular sieves decreased in the following order: NiSAPO-11(56.88 μmol/g) > Ni-SAPO-11 (35.84 μmol/g) > SAPO-11 (29.32 μmol/g) > Ni@SAPO-11 (24.25 μmol/g), while the amounts of medium and strong L acid decreased in the following order: NiSAPO-11 (24.66 μmol/g) > SAPO-11 (20.97 μmol/g) > Ni-SAPO-11 (18.16 μmol/g) > Ni@SAPO-11 (15.11 μmol/g). This can be explained by the fact that during the ion-exchange and *in situ* modifications, certain NiO species covered several strong L acid sites. However, some additional weak L acid sites were generated in Ni species in the surface framework of NiSAPO-11, resulting in an increase in the amount of weak L acid and the amount of medium and strong Lacid in NiSAPO-11. The amounts of weak B acid in Ni-modified SAPO-11 molecular sieves decreased in the order of SAPO-11 (91.87 μmol/g) > NiSAPO-11 (82.21 μmol/g) > Ni-SAPO-11 (69.91 μmol/g) > Ni@SAPO-11 (53.09 μmol/g), while the amounts of medium and strong B acid decreased in the order of NiSAPO-11 (58.35 μmol/g) > Ni-SAPO-11 (48.21 μmol/g) > SAPO-11 (30.62 μmol/g) > Ni@SAPO-11 (23.51 μmol/g). In the process of Ni ion exchange (part of H^+ being swapped by Ni^{2+}), Ni species covered some weak B acid sites and medium and strong B acid sites, resulting in a decrease in both the amount of weak B acid and the amount of medium and strong B acid (MSB) in Ni@SAPO-11. Some Ni species would undoubtedly cover the acid sites during Ni *in situ* alteration, resulting in a reduction in the number of weak B acid sites in Ni-SAPO-11. Meanwhile, Ni species entered the skeleton structure of SAPO-11 and substituted Al species by mechanism (1) and mechanism (2). Whether it is $(NiO_{4/2})^{2-}(PO_{4/2})^{+}$ species produced by mechanism (1) substitution or $(HONiO_{4/2})^{2-}(PO_{4/2})^{+}$ species produced by mechanism (2) substitution, it is beneficial to form more medium and strong B acid sites, which well explains that Ni-SAPO-11 has more medium and strong B acid sites. However, in the process of *in situ* modification, Ni species uniformly enter the bulk and surface framework of SAPO-11 molecular sieves, which is limited to the increase of B acid amount. EDTA only integrates Ni species into the surface framework of SAPO-11 molecular sieves during the complexation-excessive impregnation process, and more Ni species are distributed in the surface framework of SAPO-11 molecular sieves, resulting in a significant improvement of the surface acidity of SAPO-11 molecular sieves, which is the reason why the weak B acid amount, medium and strong B acid amount of NiSAPO-11 reach their maximum. Ni-SAPO-11 modified by Ni by the complexation-excessive impregnation method initiated

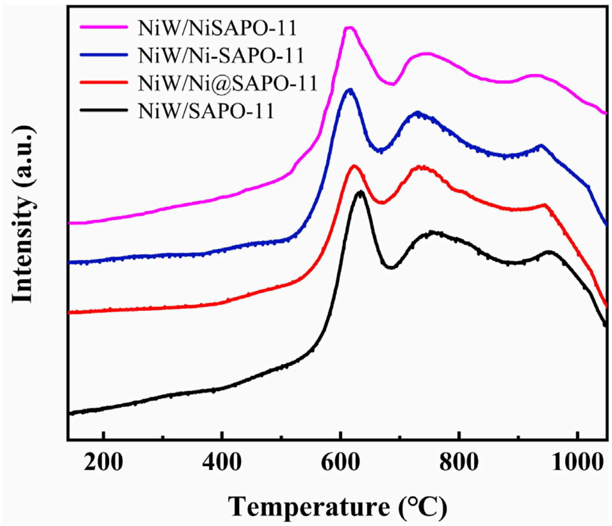

FIGURE 6 | H_2-TPR profiles of the different catalysts.

in this study has the largest amount of medium and strong B acid, which is beneficial to improve the catalytic performance of the catalyst.

Mechanism
(1): $(AlO_{4/2}) - (PO_{4/2}) + \rightarrow (NiO_{4/2})^{2-} (PO_{4/2})^{+} + H^{+}$
Mechanism
(2): $(HOAlO_{3/2}) - (PO_{4/2})^{+} \rightarrow (HONiO_{4/2})^{2-} (PO_{4/2})^{+} + H^{+}$

Active Phase Characterization

On bifunctional catalysts, the reducibility of active metals can effectively reflect the interaction between active metals and supports (Yang Z et al., 2019). As a result, H_2-TPR characterization was used to investigate the reducibility of the active metals on the catalysts. **Figure 6** depicts the H_2-TPR profiles of all catalysts. In the range of 0–1,050°C, all samples revealed three hydrogen consumption peaks. The low-temperature reduction peak at 610–635°C is attributed to the reduction of highly dispersed octahedrally coordinated polymeric tungsten species and mostly NiO species, while the moderate-temperature reduction peak at 710–765°C is attributed to the reduction of $NiWO_4$ species, and the high-temperature reduction peak at 930–955°C is attributed to the reduction of refractory tungsten species in the form of W-O-Al (Cui et al., 2013). The results revealed that the low-temperature reduction peaks, moderate-temperature reduction peaks, and high-temperature reduction peaks of the catalysts all migrated to lower temperatures after Ni alteration. The reduction temperatures of low-temperature reduction peaks decreased in the order of NiW/SAPO-11 (634°C) > NiW/Ni@SAPO-11 (624°C) > NiW/Ni-SAPO-11 (611°C) > NiW/NiSAPO-11 (608°C), and the reduction temperatures of moderate-temperature reduction peaks decreased in the order of NiW/SAPO-11 (760°C) > NiW/Ni@SAPO-11 (737°C) > NiW/Ni-SAPO-11 (726°C) > NiW/NiSAPO-11 (723°C), while the reduction temperatures of high-temperature reduction peaks decreased in the order of NiW/SAPO-11 (957°C) > NiW/Ni@SAPO-11 (944°C) > NiW/Ni-SAPO-11 (936°C) > NiW/NiSAPO-11 (922°C), indicating that the reducibility of active metal NiW on NiW/SAPO-11 catalysts can be improved by introducing Ni into SAPO-11 through the ion-exchange method or the *in situ* modification method.

The sulfided catalysts were studied by HRTEM to visualize the morphologies of the NiWS active phase on the catalysts and compare the dispersibility of sulfided metals on the various Ni-modified SAPO-11 supports. **Figure 7** shows sample HRTEM images of the different supported NiW sulfided catalysts. The WS_2 slab structure is represented by the black line-like layers in the images (Yu et al., 2012). The average length and average stacking number of WS_2 slabs on different catalysts were calculated using statistical analysis (**Eqs 1**, **2**) of at least 500 slabs from different regions of each sulfide catalyst, and the findings are reported in **Table 3**. The results showed that Ni alteration altered the morphologies of the active phase. The average length of WS_2 slabs dropped in the sequence NiW/SAPO-11 (4.62 nm) > NiW/Ni@SAPO-11 (3.95 nm) > NiW/Ni-SAPO-11 (2.98 nm) > NiW/NiSAPO-11 (2.63 nm), whereas the average stacking number rose in the order NiW/SAPO-11 (1.33) < NiW/Ni@SAPO-11 (2.64) < NiW/Ni-SAPO-11 (3.23) < NiW.NiSAPO-11 (3.27). The length of WS_2 slabs on NiW/SAPO-11 ranged from 1 to 7 nm, with the majority falling within the 3–6 nm range. The length of WS_2 slabs on NiW/Ni@SAPO-11 ranged from 1 to 5 nm, with the majority falling between 2 and 5 nm. The length distribution of WS_2 slabs on NiW/Ni-SAPO-11 was 1–4 nm, with the majority in the 2–4 nm region. The length of WS_2 slbs of NiW/NiSAPO-11 ranges between 1–4 nm, but is mainly in the 2–3 nm range. It is often assumed that the dispersibility of the active phase is proportional to its length. The larger the dispersion degree, the shorter the active phase slabs are (Zhou et al., 2018). As a result, the degree of metal dispersion on the catalysts decreased in the following order: NiW/NiSAPO-11 > NiW/Ni-SAPO-11 > NiW/Ni@SAPO-11 > NiW/SAPO-11, which was consistent with the f_W values in **Table 3**. However, in addition to the length of WS_2 slabs, the number of WS_2 slabs stacked can have an impact on the properties of the active phase. The interaction between active metal and support is adequately reflected by the stacking number of WS_2 slabs (Zhou et al., 2017). The average stacking number of WS_2 slabs for NiW/SAPO-11 was only 1.33. There were about half of the monolayer WS_2 slabs, which were classified as the "type I active phase" with low de/hydrogenation activity. This can be explained by the fact that when tungsten species are loaded on SAPO-11, they form strong W-O-Al bonds with the support, and the interaction is too strong. The average stacking number of WS_2 slabs for NiW/Ni@SAPO-11 was 2.64, with around 33% of WS_2 slabs having stacking numbers ranging from 3 to 4. This could be due to a decrease in the L acid sites of Ni@SAPO-11, resulting in a weaker interaction between active phase and support. The average stacking number of WS_2 slabs in NiW/Ni-SAPO-11 was 3.23, with over 70% of WS_2 slabs having stacking numbers ranging from 3 to 4. Because of their moderate dispersibility and stacking number, NiW/NiSAPO-11 slabs had an average stacking number of 3.27, and around 85% of WS_2 slabs had 3-4 stacking layers, which are

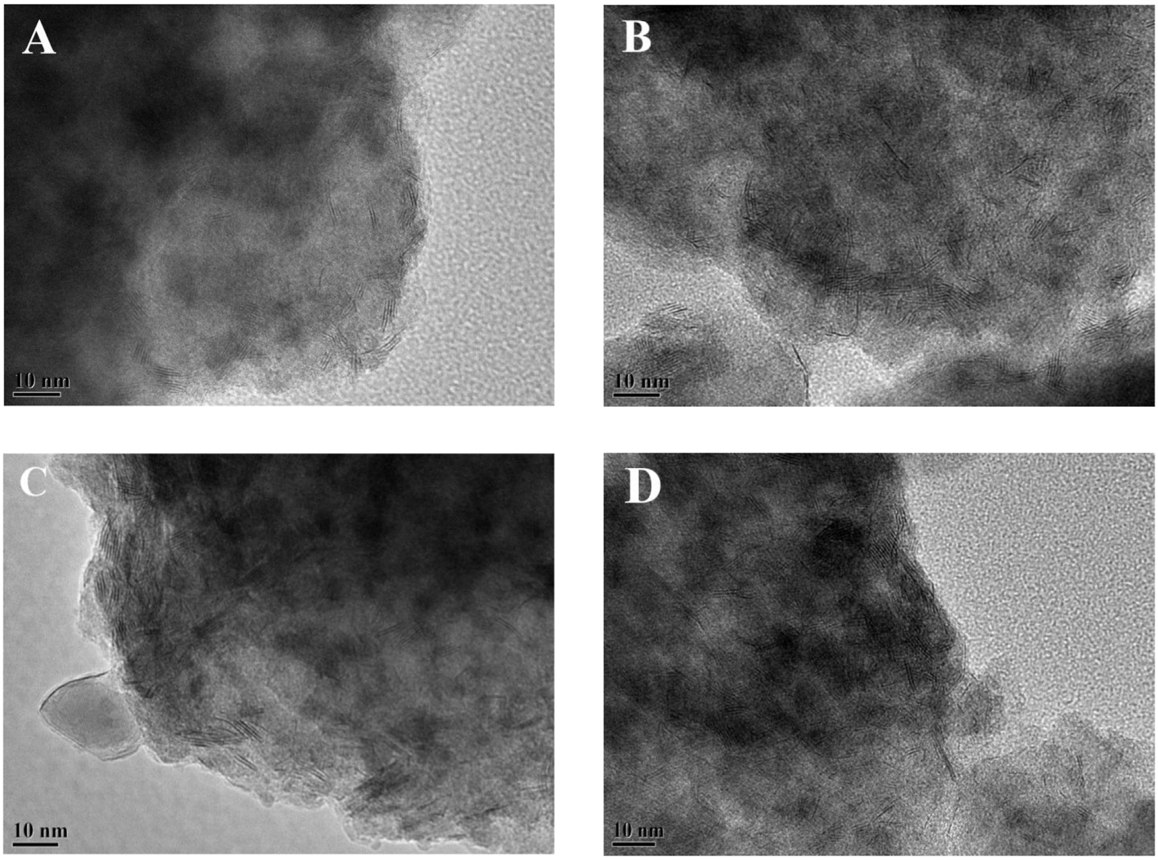

FIGURE 7 | Representative HRTEM images of sulfided catalysts: **(A)** NiW/SAPO-11, **(B)** NiW/Ni@SAPO-11, **(C)** NiW/Ni-SAPO-11, and **(D)** NiW/NiSAPO-11.

TABLE 3 | Average lengths, layer numbers, and f_W values of WS_2 of all catalysts.

Sample	$\bar{L}$ (nm)	$\bar{N}$	f_W
NiW/SAPO-11	4.62	1.33	0.28
NiW/Ni@SAPO-11	3.95	2.64	0.29
NiW/Ni-SAPO-11	2.98	3.23	0.31
NiW/NiSAPO-11	2.63	3.27	0.32

designated the “type II active phase” with good de/hydrogenation activity. This can be explained by the fact that when tungsten species are loaded on Ni-SAPO-11 and NiSAPO-11, they form W-O-Ni bonds with the support, and W-O-Ni bonds are weaker than W-O-Al bonds. Additional Ni species were coupled to the surface framework of SAPO-11 molecular sieves rather than the bulk phase during the complexation-excessive impregnation modification, resulting in the formation of more W-O-Ni species. EDTA can similarly “anchor” Ni species, allowing them to be evenly “anchored” in a specific place and hence uniformly integrated into the surface framework of the SAPO-11 molecular sieve. “Delumination and nickel supplementation” is the term for this phenomenon. Overall, among the Ni-modified SAPO-11-supported NiW catalysts, NiW/NiSAPO-11 had the best metal dispersibility and reducibility, as well as the highest hydrogenation activity.

The catalysts were studied using XPS to determine the covalent states of nickel and tungsten surface species on the sulfided catalysts. The W 4f XPS spectra and Ni 2p XPS spectra of the sulfided catalysts are shown in **Figures 8**, **9**, respectively, and the binding energies (BE) and Sulfidation degree of tungsten and nickel species on the sulfided catalysts are provided in **Tables 4**, **5**, respectively. The W 4f XPS spectra were decomposed into four peaks, each of which consisted of two overlapping W^{4+} and W^{6+} peaks. The W $4f_{7/2}$ and W $4f_{5/2}$ levels of W^{4+} (WS_2) have binding energies of around 32.70 ± 0.50 eV and 35.40 ± 0.50 eV, respectively, while the W $4f_{7/2}$ and W $4f_{5/2}$ levels of W^{6+} (WO_3) have binding energies of about 36.50 ± 0.50 eV and 38.30 ± 0.50 eV, respectively (Cui et al., 2012). The easy metals are to sulfide, the weaker the connection between the metal and the support, and the more metal layers there are. The percentage of W^{4+} species $[W^{4+}/(W^{4+} + W^{6+})]$ has a significant impact on the catalytic performance of hydrotreating catalysts, hence the sulfidation degree of tungsten species on sulfided catalysts was estimated (Cui et al., 2013). The degree of sulfidation of tungsten species on different sulfided catalysts decreased in the order NiW/NiSAPO-11 (62.07%) > NiW/N-SAPO-11 (60.93%) > NiW/Ni@SAPO-11 (56.96%) > NiW/SAPO-11 (56.96%) > NiW/SAPO-11 (56.96%) > NiW/SAPO-11 (56.96%) > NiW/SAPO (54.29%). The decrease in interaction

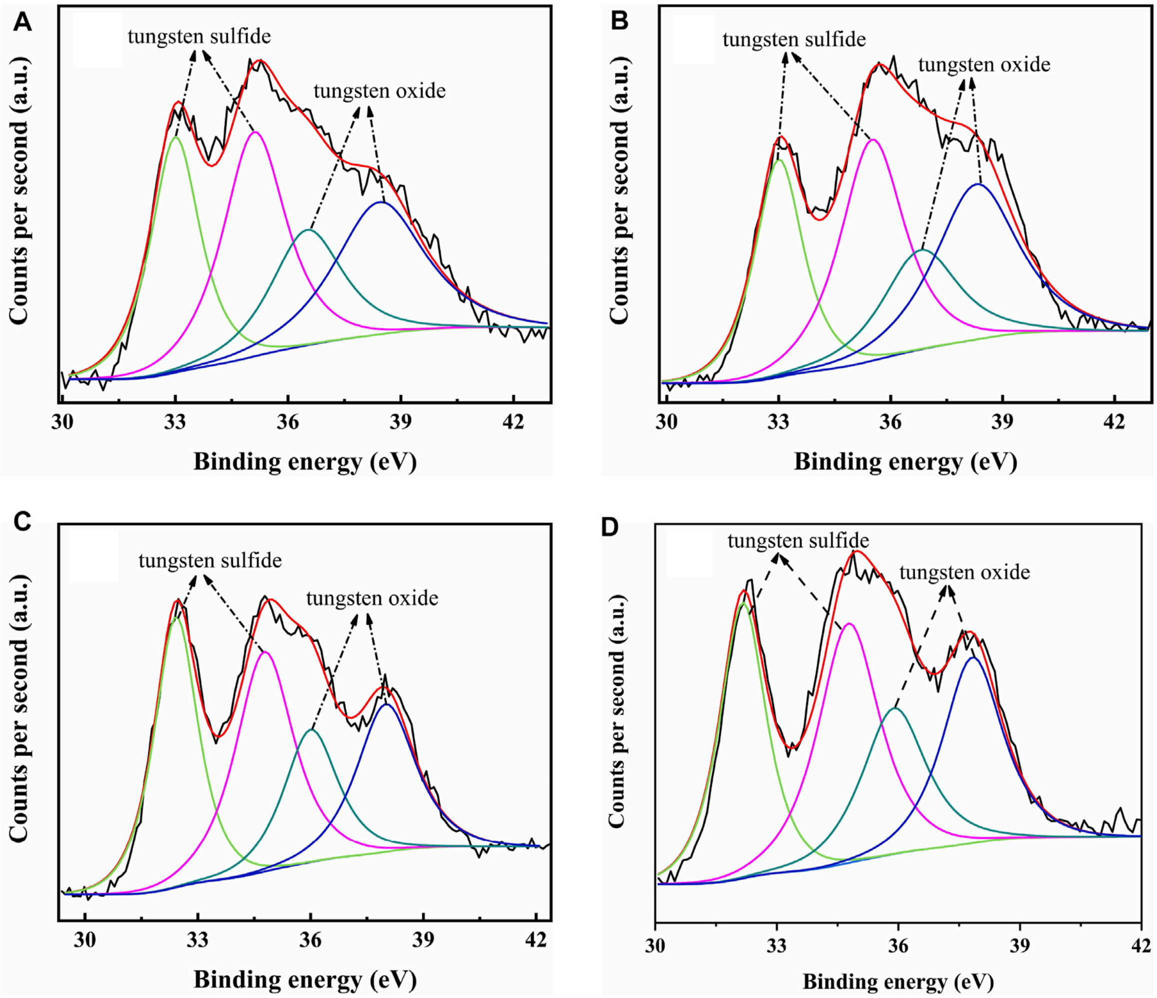

FIGURE 8 | XPS W 4f spectra of sulfided catalysts: **(A)** NiW/SAPO-11, **(B)** NiW/Ni@SAPO-11, **(C)** NiW/Ni-SAPO-11, and **(D)** NiW/NiSAPO-11.

between active metals and support causes the increase in sulfidation degree of tungsten species on NiW/NiSAPO-11, NiW/Ni-SAPO-11, and NiW/Ni@SAPO-11 as compared to NiW/SAPO-11. To some extent, BE value can reflect the interaction between metal species and support. **Table 4** shows that the BE values of tungsten species on the three catalysts, whether oxidic or sulfided, decrease in the order of NiW/SAPO-11 > NiW/Ni@SAPO-11 > NiW/Ni-SAPO-11 > NiW/NiSAPO-11. The results show that the interaction between tungsten species and support decreases in the order of NiW/SAPO-11 > NiW/Ni@SAPO-11 > NiW/Ni-SAPO-11 > NiW/NiSAPO-11, which is completely consistent with the results reflected by H_2-TPR and HRTEM. The Ni 2p XPS spectra were separated into five peaks, including two overlapping nickel oxide and nickel sulfide peaks. The Ni $2p_{3/2}$ and Ni $2p_{1/2}$ levels of nickel oxide (NiO) have binding energies of around 862.50 ± 0.50 eV and 880.50 ± 0.50 eV, respectively, while the Ni $2p_{3/2}$ and Ni $2p_{1/2}$ levels of nickel sulfide (NiS_x) have binding energies of about 856.50 ± 0.50 eV and 874.20 ± 0.50 eV, respectively (Yu et al., 2012). The sulfidation degree of nickel species was defined as the percentage of nickel sulfide species [$NiS_x/(NiO + NiS_x)$] (Cui et al., 2013). The sulfidation degree of nickel species on different sulfided catalysts decreased in the order of NiW/NiSAPO-11 (52.23%) > NiW/Ni-SAPO-11 (49.13%) > NiW/Ni@SAPO-11 (48.35%) > NiW/SAPO-11 (45.41%), and the explanation for this change order is the same as that of tungsten species explained above.

Catalytic Performance

The catalyst was sulfurized ahead of time, and the reaction pressure was set to 2.0 MPa, LHSV was set at 1.5 h^{-1}, and H_2/oil was 600 (v/v) in a typical reaction. In the reaction temperature range of 300–400°C, the catalytic performance of the catalyst was studied. **Figure 10A** depicts n-C_{16} conversion on several catalysts at various reaction temperatures. The conversion on all catalysts increased with the increase in reaction temperature, as shown in **Figure 10A**. The catalytic activity of NiW/NiSAPO-11 was much higher than that of other catalysts. The catalytic activity of all the catalysts increased in the order of NiW/Ni@SAPO-11 < NiW/SAPO-11 < NiW/Ni-SAPO-11 < NiW/NiSAPO-11. The selectivity of all catalysts to i-hexadecane (i-C_{16}) reduced as

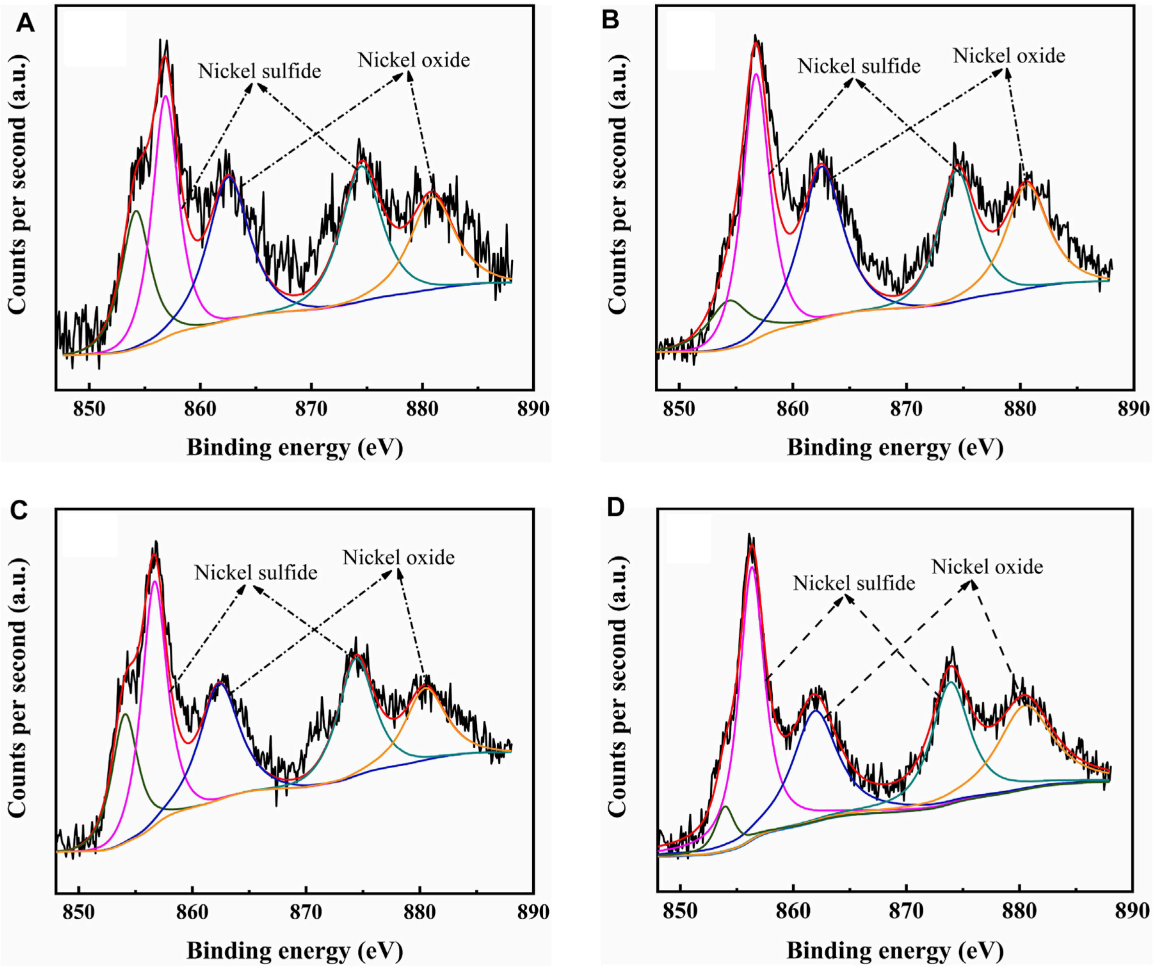

FIGURE 9 | XPS Ni 2p spectra of sulfided catalysts: **(A)** NiW/SAPO-11, **(B)** NiW/Ni@SAPO-11, **(C)** NiW/Ni-SAPO-11, and **(D)** NiW/NiSAPO-11.

TABLE 4 | Binding energy and sulfidation degree of W on different catalysts.

Sample	NiW/SAPO-11	NiW/Ni@SAPO-11	NiW/Ni-SAPO-11	NiW/NiSAPO-11
Oxidic	Binding energy (eV)			
W $4f_7$	36.70	36.50	36.10	35.82
W $4f_5$	38.43	38.30	38.00	37.78
Sulfided	Binding energy (eV)			
W $4f_7$	33.00	32.90	32.42	32.14
W $4f_5$	35.35	35.25	34.77	34.62
Sulfidation degree of W (%)	54.29	56.96	60.93	62.07

reaction temperature climbed, showing that the rate of cracking side reactions increased as reaction temperature increased **Figure 10C**. The selectivity of NiW/NiSAPO-11 to i-C_{16} was clearly higher than that of NiW/SAPO-11, NiW/Ni@SAPO-11, and NiW/Ni-SAPO-11 within the reaction temperature range of catalytic performance evaluation (**Figure 10B**). This can be explained by the fact that NiSAPO-11 has the most medium and strong B acid sites, which are universally recognized as active sites for the isomerization of olefin intermediate skeletons (Yu et al., 2021). Furthermore, on NiW/Ni-SAPO-11, the interaction between active metals and support is weak, and the dispersibility and stacking number of the so-called NiWS active phase are moderate, resulting in good hydrogenation activity for isomeric olefin intermediates that diffuse from the acid to the metal sites. The interaction between the active metals and the support in NiW/SAPO-11 is strong, making it difficult to diminish the active metals and resulting in lower i-C_{16} selectivity than NiW/Ni-SAPO-11. NiW/Ni@SAPO-11

TABLE 5 | Binding energy and sulfidation degree of Ni on different catalysts.

Sample	NiW/SAPO-11	NiW/Ni@SAPO-11	NiW/Ni-SAPO-11	NiW/NiSAPO-11
Oxidic	Binding energy (eV)			
Ni $2p_3$	862.71	862.50	862.15	861.89
Ni $2p_1$	880.90	880.57	880.26	880.11
Sulfided	Binding energy (eV)			
Ni $2p_3$	856.84	856.74	856.65	856.35
Ni $2p_1$	874.51	874.42	874.31	873.88
Sulfidation degree of Ni (%)	45.41	48.35	49.13	52.23

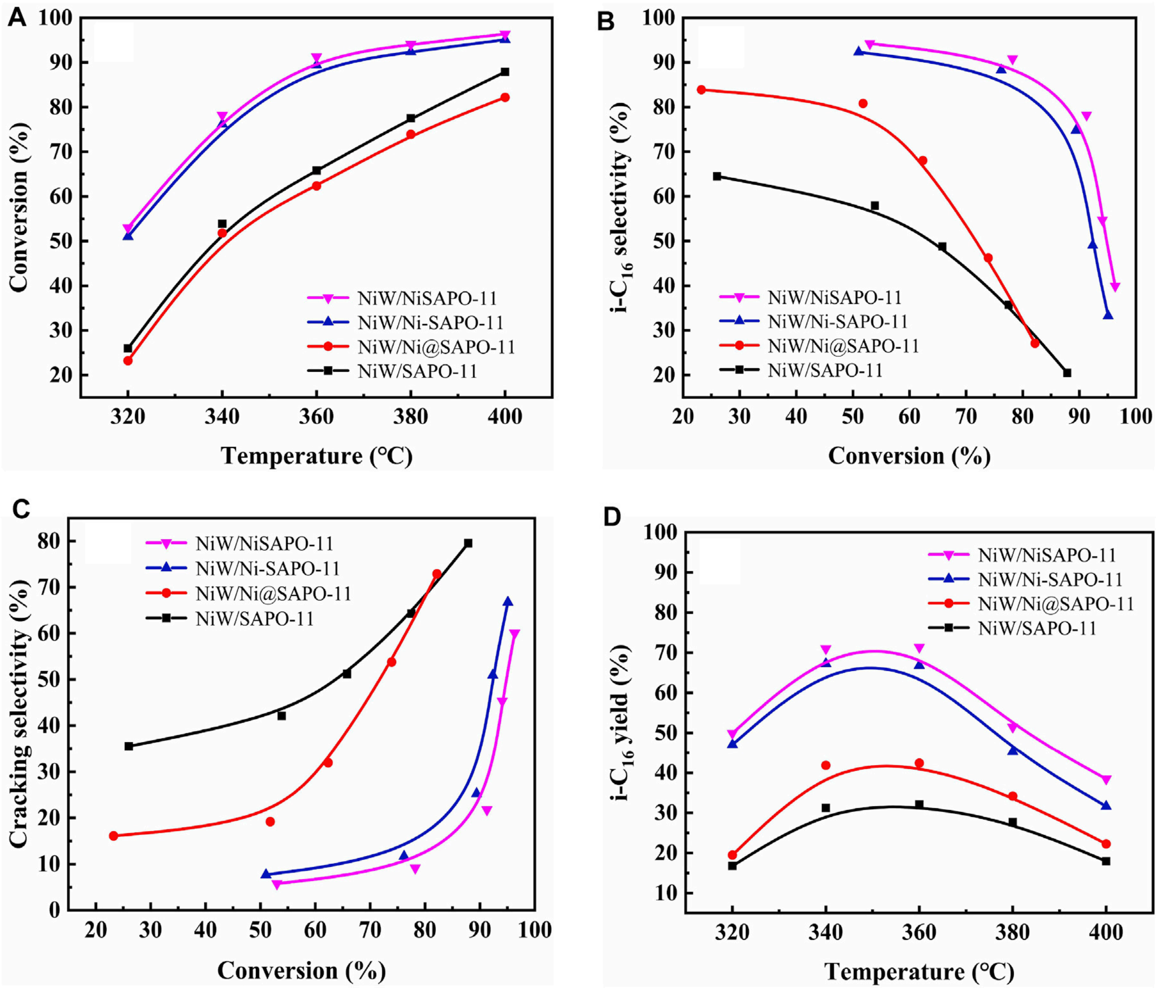

FIGURE 10 | Catalytic performance of the different catalysts: **(A)** n-C_{16} conversion, **(B)** i-C_{16} selectivity, **(C)** cracking selectivity, and **(D)** i-C_{16} yield.

has the fewest medium and strong B acid sites, but its active phase dispersion degree and stacking number are higher than those of NiW/SAPO-11, resulting in lesser n-C_{16} conversion and higher isomer selectivity than NiW/SAPO-11. **Figure 10D** shows the yield of i-C_{16} for various catalysts, and the yield of i-C_{16} for NiW/NiSAPO-11 is clearly higher than the other three catalysts. The maximum yield of i-C_{16} of different catalysts increased in the order of NiW/SAPO-11 (32.10%) > NiW/Ni@SAPO-11 (42.41%) > NiW/Ni-SAPO-11 (66.82%) > NiW/NiSAPO-11 (71.40%). These results indicate that the complexation-excessive impregnation-modified SAPO-11-supported NiWS catalyst has a better catalytic performance than that of ion-exchange modified SAPO-11 support NiWS catalyst, unmodified SAPO-11-supported NiWS catalyst, and *in situ* Ni-modified SAPO-11 support NiWS catalyst for n-hexadecane hydroisomerization.

TABLE 6 | Isomer distributions, TOF values, and k_{iso} values of n-C_{16} hydroisomerization over the different catalysts at 340 °C.

Products	Selectivity (%)			
	NiW/SAPO-11	NiW/Ni@SAPO-11	NiW/Ni-SAPO-11	NiW/NiSAPO-11
Selectivity of C_{16} (%)	57.92	80.81	88.30	90.81
TOF (h^{-1})	26.29	26.72	30.41	31.22
k_{iso} (mol g^{-1} h^{-1})	7.26×10^{-3}	5.80×10^{-3}	1.16×10^{-2}	1.21×10^{-2}
2-MC_{15}	13.57	16.99	17.87	19.77
3-MC_{15}	13.65	19.07	20.43	18.25
4-MC_{15}	7.17	12.74	13.27	16.31
5-MC_{15}	7.18	8.81	10.01	8.78
6-MC_{15}	4.54	5.41	5.95	6.17
2,4-DMC_{14}	3.10	4.18	5.72	5.69
2,5-DMC_{14}	2.92	4.23	4.91	4.42
2,6-DMC_{14}	1.98	3.31	3.35	3.87
3,6-DMC_{14}	1.13	1.88	2.37	3.03
3,7-DMC_{14}	0.77	1.21	1.38	1.77
3-EC_{14}	0.43	0.73	0.76	1.13
5-EC_{14}	0.38	0.78	0.83	0.97
6-EC_{14}	0.32	0.55	0.48	0.55
5,8-DEC_{12}	0.28	0.44	0.25	0.45
Others	0.50	0.48	0.72	0.65

The isomer product distributions, TOF values and k_{iso} values of different catalysts at 340°C are presented in **Table 6**. The reaction rate constants of different catalysts increased in the order of NiW/Ni@SAPO-11 (5.80×10^{-3} mol g^{-1} h^{-1}) < NiW/SAPO-11 (7.26×10^{-3} mol g^{-1} h^{-1}) < NiW/Ni-SAPO-11 (1.16×10^{-2} mol g^{-1} h^{-1}) < NiW/NiSAPO-11 (1.21×10^{-2} mol g^{-1} h^{-1}), which is due to the difference between the amount of medium and strong B acid in the three supports. While the TOF values of the three catalysts decreased in the order of NiW/NiSAPO-11 (31.22 h^{-1}) > NiW/Ni-SAPO-11 (30.41 h^{-1}) > NiW/Ni@SAPO-11 (26.72 h^{-1}) > NiW/SAPO-11 (26.29 h^{-1}), and the calculated TOF values well verified the catalytic activity of the catalysts. This result can be explained by the fact that the weakening of the interaction between the active phase and the support promoted more active phases to form "type II active phase", which increased the desorption rate of carbocation on the active phase. The isomer products of different catalysts were mainly mono-branched isomer products, and monomethyl branched isomer products were the main mono-branched isomer products.

CONCLUSION

The ion-exchange method, *in situ* synthesis method, and complexation-excessive impregnation modification method successfully prepared Ni-modified SAPO-11 molecular sieves, and the corresponding NiW-supported catalysts were successfully prepared by the incipient-wetness impregnation method, and then used for hydroisomerization of n-hexadecane. The effects of several Ni-modification procedures on the properties of SAPO-11, particularly the active phase properties on the related catalysts, were studied. The results showed that the crystal structure of Ni@SAPO-11 prepared by the ion-exchange method collapsed partially, and nickel species occupied a portion of the pore volume and covered a portion of the acid sites, resulting in a drop in specific surface area, pore volume, and acid sites amount. Ni-SAPO-11 produced *in situ* had a larger specific surface area, pore volume, and medium and strong Brønsted acid sites. However, during dealumination, EDTA had the effect of dredging channels and reaming holes, resulting in a larger BET specific surface area and pore volume of NiSAPO-11. Furthermore, EDTA made it simple to incorporate Ni species into the surface framework of the SAPO-11 molecular sieve rather than the bulk phase, resulting in NiSAPO-11 with better acidity. The support of NiW/NiSAPO-11 had the most Brønsted acid sites, the weakest interaction between active metals and support, and the highest dispersibility and stacking number of active phase, all of which were helpful to n-hexadecane hydroisomerization. NiW/NiSAPO-11 had much greater n-C_{16} conversion, i-C_{16} selectivity, and i-C_{16} yield than the other catalysts. It is expected to provide theoretical guidance for the design of high-activity non-noble metal catalysts for the hydroisomerization of alkanes.

DATA AVAILABILITY STATEMENT

The original contributions presented in the study are included in the article/Supplementary Material, further inquiries can be directed to the corresponding author.

AUTHOR CONTRIBUTIONS

XD designed experimental plans, performed main experimental work, analyzed and discussed results, and wrote the manuscript. YC assisted in the design of the scheme, performed the main experimental work and assisted in literature review and manuscript sorting. MS participated in the manuscript writing. QW proposed the themes, ideas, and content of the manuscript research work, assisted in literature review and manuscript sorting. YZ guided experimental work and manuscript revision.

REFERENCES

Blasco, T., Chica, A., Corma, A., Murphy, W., Agundezrodriguez, J., and Perezpariente, J. (2006). Changing the Si Distribution in SAPO-11 by Synthesis with Surfactants Improves the Hydroisomerization/dewaxing Properties. *J. Catal.* 242 (1), 153–161. doi:10.1016/j.jcat.2006.05.027

Chen, Z., Dong, Y., Jiang, S., Song, W., Lai, W., Yi, X., et al. (2017). Low-temperature Synthesis of Hierarchical Architectures of SAPO-11 Zeolite as a Good Hydroisomerization Support. *J. Mater. Sci.* 52 (8), 4460–4471. doi:10.1007/s10853-016-0692-z

Cui, Q., Wang, S., Wei, Q., Mu, L., Yu, G., Zhang, T., et al. (2019). Synthesis and Characterization of Zr Incorporated Small crystal Size Y Zeolite Supported NiW Catalysts for Hydrocracking of Vacuum Gas Oil. *Fuel* 237, 597–605. doi:10.1016/j.fuel.2018.10.040

Cui, Q., Zhou, Y., Wei, Q., Tao, X., Yu, G., Wang, Y., et al. (2012). Role of the Zeolite Crystallite Size on Hydrocracking of Vacuum Gas Oil over NiW/Y-ASA Catalysts. *Energy Fuels* 26 (8), 4664–4670. doi:10.1021/ef300544c

Cui, Q., Zhou, Y., Wei, Q., Yu, G., and Zhu, L. (2013). Performance of Zr- and P-Modified USY-Based Catalyst in Hydrocracking of Vacuum Gas Oil. *Fuel Process. Tech.* 106, 439–446. doi:10.1016/j.fuproc.2012.09.010

Díaz de León, J. N., Zavala-Sánchez, L. A., Suárez-Toriello, V. A., Alonso-Núñez, G., Zepeda, T. A., Yocupicio, R. I., et al. (2017). Support Effects of NiW Catalysts for Highly Selective Sulfur Removal from Light Hydrocarbons. *Appl. Catal. B: Environ.* 213, 167–176.

Du, Y., Feng, B., Jiang, Y., Yuan, L., Huang, K., and Li, J. (20182018). Solvent-Free Synthesis and N -Hexadecane Hydroisomerization Performance of SAPO-11 Catalyst. *Eur. J. Inorg. Chem.* 2018 (22), 2599–2606. doi:10.1002/ejic.201800134

Du, Y., Yao, H., Zhao, L., Yang, H., Wang, M., Yuan, L., et al. (2019). Graphene Oxide Induced High Crystallinity of SAPO-11 Molecular Sieves for Improved Alkane Isomerization Performance. *ChemNanoMat* 5 (9), 1225–1232. doi:10.1002/cnma.201900349

Guo, L., Bao, X., Fan, Y., Shi, G., Liu, H., and Bai, D. (2012). Impact of Cationic Surfactant Chain Length during SAPO-11 Molecular Sieve Synthesis on Structure, Acidity, and N-Octane Isomerization to Di-methyl Hexanes. *J. Catal.* 294, 161–170. doi:10.1016/j.jcat.2012.07.016

Guo, L., Fan, Y., Bao, X., Shi, G., and Liu, H. (2013). Two-stage Surfactant-Assisted Crystallization for Enhancing SAPO-11 Acidity to Improve N-Octane Di-branched Isomerization. *J. Catal.* 301, 162–173. doi:10.1016/j.jcat.2013.02.001

Hongloi, N., Prapainainar, P., and Prapainainar, C. (2021). Review of green Diesel Production from Fatty Acid Deoxygenation over Ni-Based Catalysts. *Mol. Catal.*, 111696. doi:10.1016/j.mcat.2021.111696

Jin, D., Li, L., Ye, G., Ding, H., Zhao, X., Zhu, K., et al. (2018). Manipulating the Mesostructure of Silicoaluminophosphate SAPO-11 via Tumbling-Assisted, Oriented Assembly Crystallization: a Pathway to Enhance Selectivity in Hydroisomerization. *Catal. Sci. Technol.* 8 (19), 5044–5061. doi:10.1039/c8cy01483c

Karthikeyan, D., Atchudan, R., and Sivakumar, R. (2016). Effect of Metal Content on the Activity and Product Selectivity of N-Decane Hydroisomerization over Ni-Pd/HY Zeolite. *Chin. J. Catal.* 37, 1907–1917. doi:10.1016/s1872-2067(16)62507-x

Li, X., and Wu, D. (2020). Synthesis of Co-doped Micro-mesoporous SAPO-11 Zeolite for Glycerol Hydrogenolysis. *Korean J. Chem. Eng.* 37 (2), 216–223. doi:10.1007/s11814-019-0445-1

Liu, Q., Zuo, H., Wang, T., Ma, L., and Zhang, Q. (2013). One-step Hydrodeoxygenation of palm Oil to Isomerized Hydrocarbon Fuels over Ni Supported on Nano-Sized SAPO-11 Catalysts. *Appl. Catal. A: Gen.* 468, 68–74. doi:10.1016/j.apcata.2013.08.009

Lyu, Y., Liu, Y., Xu, L., Zhao, X., Liu, Z., Liu, X., et al. (2017). Effect of Ethanol on the Surface Properties and N-Heptane Isomerization Performance of Ni/SAPO-11. *Appl. Surf. Sci.* 401, 57–64. doi:10.1016/j.apsusc.2016.12.230

FUNDING

This work was supported by the National Natural Science Foundation of China under grant no. 22078360.

Lyu, Y., Yu, Z., Yang, Y., Liu, Y., Zhao, X., Liu, X., et al. (2019). Metal and Acid Sites Instantaneously Prepared over Ni/SAPO-11 Bifunctional Catalyst. *J. Catal.* 374, 208–216. doi:10.1016/j.jcat.2019.04.031

Lyu, Y., Yu, Z., Yang, Y., Wang, X., Zhao, X., Liu, X., et al. (2019). Metal-acid Balance in the In-Situ Solid Synthesized Ni/SAPO-11 Catalyst for N-Hexane Hydroisomerization. *Fuel* 243, 398–405. doi:10.1016/j.fuel.2019.01.013

Lyu, Y., Zhan, W., Wang, X., Yu, Z., Liu, X., and Yan, Z. (2020). Regulation of Synergy between Metal and Acid Sites over the Ni-SAPO-11 Catalyst for N-Hexane Hydroisomerization. *Fuel*, 274, 117855.

Minaev, P. P., Nikul'shina, M. S., Mozhaev, A. V., and Nikul'shin, P. A. (2019). NiWS/Al2O3 Diesel Fraction Deep Hydrotreating Catalyst Synthesized Using Mesostructured Aluminum Hydroxide. *Pet. Chem.* 58 (14), 1186–1191. doi:10.1134/s0965544118140098

Pimerzin, A. A., Roganov, A. A., Verevkin, S. P., Konnova, M. E., Pilshchikov, V. A., and Pimerzin, A. A. (2019). Bifunctional Catalysts with noble Metals on Composite Al2O3-SAPO-11 Carrier and Their Comparison with CoMoS One in N-Hexadecane Hydroisomerization. *Catal. Today* 329, 71–81. doi:10.1016/j.cattod.2018.12.034

Shi, G., Fang, D., and Shen, J. (2009). Hydroisomerization of Model FCC Naphtha over Sulfided Co(Ni)-Mo(W)/MCM-41 Catalysts. *Microporous Mesoporous Mater.* 120 (3), 339–345. doi:10.1016/j.micromeso.2008.11.022

Song, X., Bai, X., Wu, W., Kikhtyanin, O. V., Zhao, A., Xiao, L., et al. (2017). The Effect of Palladium Loading on the Catalytic Performance of Pd/SAPO-11 for N-Decane Hydroisomerization. *Mol. Catal.* 433, 84–90. doi:10.1016/j.mcat.2016.12.017

Tan, Y., Hu, W., Du, Y., and Li, J. (2021). Species and Impacts of Metal Sites over Bifunctional Catalyst on Long Chain N-Alkane Hydroisomerization: A Review. *Appl. Catal. A: Gen.* 611. doi:10.1016/j.apcata.2020.117916

Tao, S., Li, X., Lv, G., Wang, C., Xu, R., Ma, H., et al. (2017). Highly Mesoporous SAPO-11 Molecular Sieves with Tunable Acidity: Facile Synthesis, Formation Mechanism and Catalytic Performance in Hydroisomerization of N-Dodecane. *Catal. Sci. Technol.* 7 (23), 5775–5784. doi:10.1039/c7cy01819c

Tao, X., Zhou, Y., Wei, Q., Yu, G., Cui, Q., Liu, J., et al. (2014). Effect of Morphology Properties of NiW Catalysts on Hydrodesulfurization for Individual Sulfur Compounds in Fluid Catalytic Cracking Diesel. *Fuel Process. Tech.* 118, 200–207. doi:10.1016/j.fuproc.2013.08.023

Tian, S., and Chen, J. (2014). Hydroisomerization of N-Dodecane on a New Kind of Bifunctional Catalyst: Nickel Phosphide Supported on SAPO-11 Molecular Sieve. *Fuel Process. Tech.* 122, 120–128. doi:10.1016/j.fuproc.2014.01.031

Tiuliukova, I. A., Rudina, N. A., Lysikov, A. I., Cherepanova, S. V., and Parkhomchuk, E. V. (2018). Screw-like Morphology of Silicoaluminophosphate-11 (SAPO-11) Crystallized in Ethanol Medium. *Mater. Lett.* 228, 61–64. doi:10.1016/j.matlet.2018.05.118

Wang, J., Zhang, W., Suo, Y., and Wang, Y. (2018). Synthesis of Ni/H-Zr-MCM-48 and Their Isomerization Activity of N-Heptane. *J. Porous Mater.* 25, 1317–1324. doi:10.1007/s10934-017-0542-7

Wei, X., Kikhtyanin, O. V., Parmon, V. N., Wu, W., Bai, X., Zhang, J., et al. (2017). Synergetic Effect between the Metal and Acid Sites of Pd/SAPO-41 Bifunctional Catalysts in N-Hexadecane Hydroisomerization. *J. Porous Mater.* 25 (1), 235–247. doi:10.1007/s10934-017-0437-7

Wen, C., Wang, X., Xu, J., and Fan, Y. (2019). *Hierarchical SAPO-11 Mol. sieve-based catalysts enhancing double-branched hydroisomerization alkanesFuel* 255. doi:10.1016/j.fuel.2019.115821

Wen, C., Xu, J., Wang, X., and Fan, Y. (2020). n-Heptane Hydroisomerization over a SO42-/ZrO2@SAPO-11 Composite-Based Catalyst Derived from the Growth of UiO-66 on SAPO-11. *Energy Fuels* 34 (8), 9498–9508. doi:10.1021/acs.energyfuels.0c01634

Yang, L., Xing, S., Sun, H., Miao, C., Li, M., Lv, P., et al. (2019). Citric-acid-induced Mesoporous SAPO-11 Loaded with Highly Dispersed Nickel for Enhanced Hydroisomerization of Oleic Acid to Iso-Alkanes. *Fuel Process. Tech.* 187, 52–62. doi:10.1016/j.fuproc.2019.01.008

Yang, Z., Li, J., Liu, Y., and Liu, C. (2017). Effect of Silicon Precursor on Silicon Incorporation in SAPO-11 and Their Catalytic Performance for Hydroisomerization of N -octane on Pt-Based Catalysts. *J. Energ. Chem.* 26 (4), 688–694. doi:10.1016/j.jechem.2017.02.002

Yang, Z., Liu, Y., Li, Y., Zeng, L., Liu, Z., Liu, X., et al. (2019). Effect of Preparation Method on the Bimetallic NiCu/SAPO-11 Catalysts for the Hydroisomerization of N-Octane. *J. Energ. Chem.* 28, 23–30. doi:10.1016/j.jechem.2017.10.003

Yang, Z., Liu, Y., Liu, D., Meng, X., and Liu, C. (2017). Hydroisomerization of N -octane over Bimetallic Ni-Cu/SAPO-11 Catalysts. *Appl. Catal. A: Gen.* 543, 274–282. doi:10.1016/j.apcata.2017.06.028

Yang, Z., Liu, Y., Zhao, J., Gou, J., Sun, K., and Liu, C. (2017). Zinc-modified Pt/SAPO-11 for Improving the Isomerization Selectivity to Dibranched Alkanes. *Chin. J. Catal.* 38 (3), 509–517. doi:10.1016/s1872-2067(17)62755-4

Yu, G., Qiu, M., Wang, T., Ge, L., Chen, X., and Wei, W. (2021). Optimization of the Pore Structure and Acidity of SAPO-11 for Highly Efficient Hydroisomerization on the Long-Chain Alkane. *Microporous Mesoporous Mater.* 320. doi:10.1016/j.micromeso.2021.111076

Yu, G., Zhou, Y., Wei, Q., Tao, X., and Cui, Q. (2012). A Novel Method for Preparing Well Dispersed and Highly Sulfided NiW Hydrodenitrogenation Catalyst. *Catal. Commun.* 23, 48–53. doi:10.1016/j.catcom.2012.03.002

Zhang, P., Liu, H., Yue, Y., Zhu, H., and Bao, X. (2018). Direct Synthesis of Hierarchical SAPO-11 Molecular Sieve with Enhanced Hydroisomerization Performance. *Fuel Process. Tech.* 179, 72–85. doi:10.1016/j.fuproc.2018.06.012

Zhao, L., Hu, Y., Wang, Y., and Ma, S. (2014). Preparation and Property of Ni/TiO2-SAPO-11 Catalyst for N-Heptane Isomerization. *Mrc* 03, 63–67. doi:10.4236/mrc.2014.33009

Zhou, W., Zhang, Y., Tao, X., Zhou, Y., Wei, Q., and Ding, S. (2018). Effects of Gallium Addition to Mesoporous Alumina by Impregnation on Dibenzothiophene Hydrodesulfurization Performances of the Corresponding NiMo Supported Catalysts. *Fuel* 228, 152–163. doi:10.1016/j.fuel.2018.04.084

Zhou, W., Zhou, Y., Wei, Q., Zhang, Y., Zhang, Q., Jiang, S., et al. (2017). Gallium Modified HUSY Zeolite as an Effective Co-support for NiMo Hydrodesulfurization Catalyst and the Catalyst's High Isomerization Selectivity. *Chem. Eur. J.* 23 (39), 9369–9382. doi:10.1002/chem.201701307

Conflict of Interest: The authors declare that the research was conducted in the absence of any commercial or financial relationships that could be construed as a potential conflict of interest.

frontiers | Frontiers in Chemistry

ORIGINAL RESEARCH
published: 14 April 2022
doi: 10.3389/fchem.2022.892424

Enhanced Heterogeneous Fenton Degradation of Organic Pollutants by CRC/Fe_3O_4 Catalyst at Neutral pH

Chuan Wang[1], *Rui Jiang*[1,2], *Jingxin Yang*[1]* *and Pingshan Wang*[1]*

[1]*A Key Laboratory for Water Quality and Conservation of the Pearl River Delta, Institute of Environmental Research at Greater Bay, Ministry of Education, Guangzhou University, Guangzhou, China,* [2]*Economic Development Bureau of Yongzhou Economic and Technological Development Zone, Yongzhou, China*

Fe_3O_4-based heterogeneous Fenton catalysts have been widely employed for degrading organic pollutants, however it is challenging to use them in highly efficient and recyclable application in wastewater treatment. In this work, carboxylate-rich carbon (CRC)-modified Fe_3O_4 magnetic particles are prepared by the sol-gel self-combustion method, where CRC is obtained from the carbonization of sodium gluconate. The CRC/Fe_3O_4 catalyst exhibits high heterogeneous Fenton degradation performance. The complete 10 mg L^{-1} methylene blue (MB) removal is achieved in 180 min under conditions of 10 mM H_2O_2 and 1.00 g of L^{-1} CRC/Fe_3O_4 at neutral pH. After five cycles, the structure and morphology of CRC/Fe_3O_4 composites remained unchanged and the catalytic activity also remained unaltered. Moreover, phenol, benzoic acid (BA), sulfamethazine (SMT), and tetracycline (TC) were also degraded in the heterogeneous Fenton reaction using CRC/Fe_3O_4 as a catalyst. The strong coordinating ability of –COOH/ –COO^- functionalities of CRC formed strong bonds with Fe(II/III) ions on the surfaces of Fe_3O_4 particles, which was conducive to adsorption of organic matter on the surface of the catalyst and promoted the occurrence of heterogeneous Fenton reactions. It was found that CRC/Fe_3O_4 had higher removal rates for the adsorptive exclusions of pollutants, such as TC and MB, whereas there were lower removal rates for phenol, BA, and SMT. This work brings potential insights for development of a novel adsorption-enhanced heterogeneous Fenton reaction for wastewater treatment.

Keywords: heterogeneous fenton, CRC@Fe3O4 catalyst, degradation, methylene blue, adsorption

Edited by:
Qingyi Zeng,
University of South China, China

Reviewed by:
Chen Zhao,
Beijing University of Civil Engineering and Architecture, China
Zhengqing Cai,
East China University of Science and Technology, China

***Correspondence:**
Jingxin Yang
yangjx@gzhu.edu.cn
Pingshan Wang
chemwps@csu.edu.cn

Specialty section:
This article was submitted to Inorganic Chemistry, a section of the journal Frontiers in Chemistry

Received: 09 March 2022
Accepted: 18 March 2022
Published: 14 April 2022

Citation:
Wang C, Jiang R, Yang J and Wang P (2022) Enhanced Heterogeneous Fenton Degradation of Organic Pollutants by CRC/Fe_3O_4 Catalyst at Neutral pH.
Front. Chem. 10:892424.
doi: 10.3389/fchem.2022.892424

1 INTRODUCTION

Fenton oxidation technology is the most representative advanced oxidation process (AOP). The Fenton process has gained widespread acceptance for efficient degradation of recalcitrant organic contaminants (Pignatello et al., 2006; Wang and Wang, 2020; Coha et al., 2021; Zeng et al., 2021). However, the requirement of low pH and generation of huge amounts of iron sludge hinder widespread application. In order to avoid the drawbacks of the traditional Fenton reaction, iron oxide heterogeneous Fenton-like technology has been developed recently, in which iron oxide-catalyzed decomposition of H_2O_2 occurs to generate OH (He et al., 2016; Thomas et al., 2021). In fact, heterogeneous Fenton oxidation possesses inherent advantages, such as a wide pH application range, lower peroxide consumption, and recyclability *via* catalyst regeneration, over homogeneous Fenton oxidation (Lai et al., 2021; Xiea et al., 2021). The principal objectives behind developing heterogeneous Fenton oxidation technology are to prepare highly efficient, cheap, and easy to separate solid-phase catalysts.

Fe_3O_4 has been widely studied for its excellent magnetic separation performance (Wu et al., 2015; Xu et al., 2018; Adewunmi et al., 2020). Its magnetic properties allow for easy, fast, and inexpensive separation from the reaction medium. In addition, the potential of Fe_3O_4 derives from the higher ability for degradation of recalcitrant pollutants compared to the conventional iron-supported catalysts due to the presence of both Fe(II) and Fe(III) species (Munoz et al., 2015). However, Fe_3O_4 magnetic nanoparticles agglomerate easily because of their highly specific surface energy, resulting in uneven particle size (Liu et al., 2020). Therefore, the exposed Fe_3O_4 is easily oxidized, resulting in the reduction of magnetic properties (Yan et al., 2009). Again, at low pH, Fe_3O_4 magnetic nanoparticles are easily etched, affecting their morphology and properties, whereas Fe_3O_4 Fenton catalytic performance is inhibited when the pH of solution is weakly alkaline.

In order to overcome the above drawbacks, functionalization of nanoparticles is expected to be an effective alternative method (Zhu et al., 2018). Wrapping of inorganic materials, organic functional groups, such as –COOH, $–NH_2$, and –SH, and biological macromolecules on the particle surface or superficial modification improve stability and functionalities of particles (Wulandari et al., 2018; Khatamian et al., 2019; Wang et al., 2021). The as-obtained multifunctional magnetic nanoparticles possess broader application prospects.

For synthesizing Fenton catalysis, Fe_3O_4 is first modified by humic acid (HA) to impart elevated photosensitivity, followed by modification with organic chelating agents to enhance the iron cycle and superficial compounding of the polymer to improve dispersion and stability. Klamerth et al. (Klamerth et al., 2011) pointed out that HA is a good choice for the improved optical Fenton system with a pH value of 6.5. Hua et al. (Hua et al., 2021) reported that the coating of catechol polymer on Fe_3O_4 enhanced the iron cycle and promoted the Fenton reaction. Again, Xue et al. (Xue et al., 2019) used electrospinning technology to prepare porous polycaprolactone composite nano Fe_3O_4 membrane synergy of the porous surface and embedded Fe_3O_4 nanoparticles to degrade methylene blue in the Fenton reaction. The surface modification of Fe_3O_4 improved its stability and catalytic efficiency, which is a potential research direction of Fenton heterogeneous catalysis.

Hence, in this work, CRC/Fe_3O_4 magnetic composites were synthesized by the sol-gel self-combustion method (Qu et al., 2016). The CRC/Fe_3O_4 samples were characterized and applied in the Fenton process to degrade MB. The effects of H_2O_2 and catalyst dosage, initial MB concentration, and pH value on the catalytic activity were investigated. The stability and recyclability of catalysts were also evaluated. The adsorption and heterogeneous Fenton degradation of phenol, benzoic acid (BA), sulfamethazine (SMT), tetracycline (TC), and MB were discussed to propose a possible adsorption/catalytic mechanism.

2 EXPERIMENTAL

2.1 Chemicals

All chemicals were of analytical grade and used without further purification. Ferric chloride ($FeCl_3·6H_2O$), sodium gluconate ($C_6H_{11}NaO_7$), hydrogen peroxide (H_2O_2, 30 wt.%), methylene blue ($C_{16}H_{18}ClN_3S$), tetracycline ($C_{22}H_{24}N_2O_8$), sulfamethazine ($C_{12}H_{14}N_4O_2S$), phenol (C_6H_6O), and benzoic acid (C_6H_5COOH) were purchased from Sigma-Aldrich (China). All solutions and suspensions were prepared by using deionized water.

2.2 Preparation and Characterization of Catalysts

Preparation of CRC/Fe_3O_4 magnetic composites by sol-gel self-combustion: A certain mass of sodium gluconate and $FeCl_3·6H_2O$ were dissolved in 20 ml of distilled water, followed by the addition of 1.0 mol L^{-1} of NaOH solution to adjust the pH to 7. The as-obtained solution was stirred continuously at room temperature for 30 min, followed by solvent evaporation on a petri dish at 80°C for 1–2 h to obtain the gel. The as-obtained gel was then transferred to the crucible, covered, heated in a muffle furnace at 350°C for 2 h, and neutrally cooled to room temperature. Thereafter, the synthetic composite was ground and crushed, washed several times with distilled water and ethanol, separated by magnet, and dried at 60°C for 2 h.

The morphology and size distribution of CRC/Fe_3O_4 were observed by a scanning electron microscope (SEM, Pheonom ProX, Netherlands). The phase structures were determined by X-ray diffraction (XRD, PANalytical-PW3040/60, Netherlands). To verify the formation of CRC, surface chemistry was analyzed using a Fourier transform infrared (FTIR) spectrometer (Bruker TENSOR II Hyperion 2000, Germany). Thermal stabilities of CRC/Fe_3O_4 were assessed by a thermogravimetric analyzer (TGA, TGA/DSC PerkinElmer- TGA4000, US). The zeta potentials of the catalyst suspensions at different pH values were determined by an analyzer (Zetasizer, Malvern 3000).

2.3 Degradation Procedures

The degradation procedures were carried out in a 100 ml beaker shaken at a speed of 200 rpm. In a typical reaction, 50 ml of MB solution of a certain concentration was prepared by adding the specified amount of CRC/Fe_3O_4. The pH of reaction solution was adjusted to the required value by using 1.0 mol L^{-1} of H_2SO_4 or 1.0 mol L^{-1} of NaOH solutions. Degradation reactions were initiated by adding H_2O_2 to the suspension after attainment of the adsorption equilibrium. At pre-determined time intervals, 0.5 ml of sample suspension was withdrawn and the on-going reaction was quenched immediately by adding 30 μL of pure methanol. The solid particles were separated from the solution using an external magnet. The supernatant liquid was collected for analysis. Each experiment was run in triplicate and the arithmetic mean of the three measured values was used in the reported data.

2.4 Analytical Methods

The concentration of MB was measured by UV-*vis* spectroscopy at the fixed wavelength of 660 nm, which is the maximum absorption wavelength of MB. The concentration of other organic matters (Phenol, BA, SMT, TC) were determined by liquid chromatography-mass spectrometry (H-class/ QDA, waters, United States). The total leached iron was measured using the orthophenantroline complexometric method (λ = 510 nm).

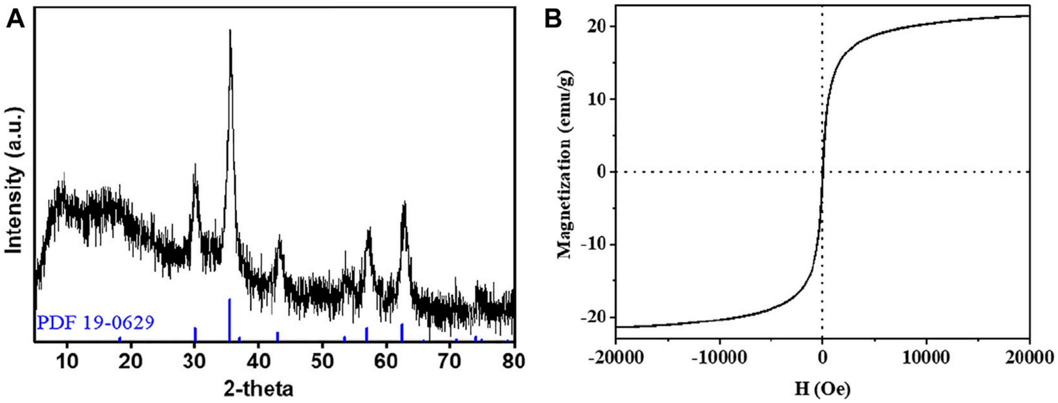

FIGURE 1 | (A) XRD pattern and **(B)** magnetization curves of CRC/Fe_3O_4.

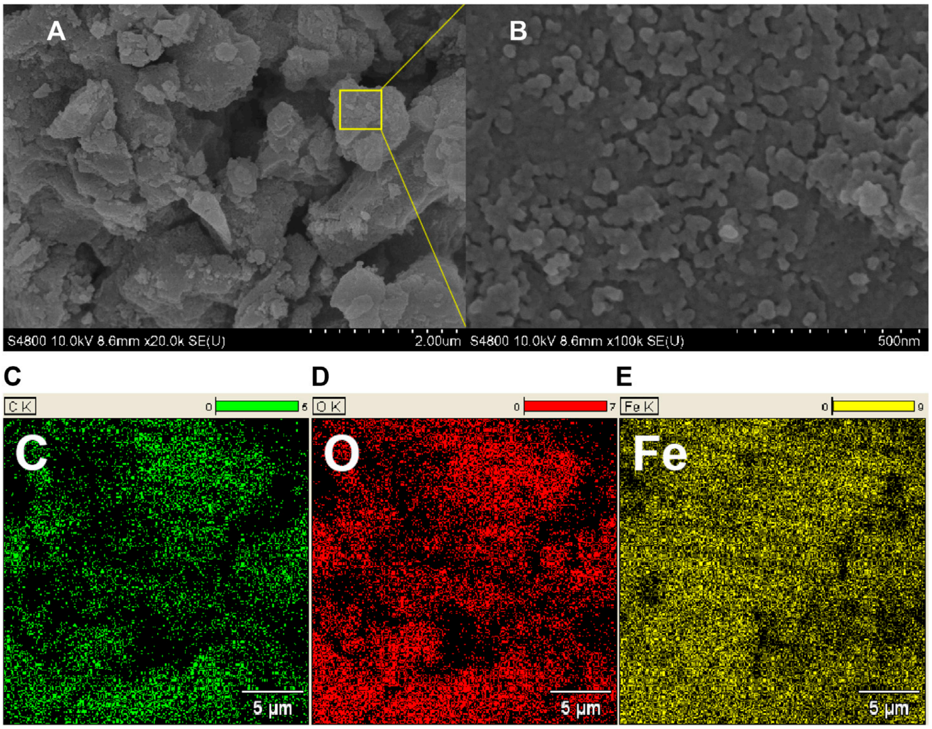

FIGURE 2 | (A,B) SEM photomicrographs and **(C–E)** EDX mapping of C/ O/ Fe in CRC/Fe_3O_4.

3 RESULTS AND DISCUSSION

3.1 Formation of CRC/Fe_3O_4

The XRD patterns of CRC/Fe_3O_4 contained sharp crystalline peaks at $2\theta = 30.3, 35.6, 43.3, 53.7, 57.2$, and 62.7° (**Figure 1A**), attributed to (220), (311), (400), (422), (511), and (440) planes of the cubic spinel structure of Fe_3O_4 (JCPDS 19–0629), respectively. In CRC/ Fe_3O_4, the absence of the characteristic peaks of carbon either individually or overlapped with the strong peaks of Fe_3O_4 inferred the presence of amorphous carbon. The magnetic properties of CRC/Fe_3O_4 were studied using a superconducting quantum interference device (SQUID) magnetometer at room temperature. The hysteresis loop of CRC/Fe_3O_4 (**Figure 1B**) indicated the magnetic saturation (Ms) of CRC/Fe_3O_4 was approximately 21.4 emu g^{-1}.

From the SEM photomicrograph of CRC/ Fe_3O_4 (**Figure 2**), particles of uniform sizes and shapes were observed. The particle size distribution of cubic Fe_3O_4 was within 30–40 nm. Meanwhile, the energy dispersive X-ray (EDX) spectroscopy study verified the existence and even distribution of Fe, O, and C in CRC/ Fe_3O_4.

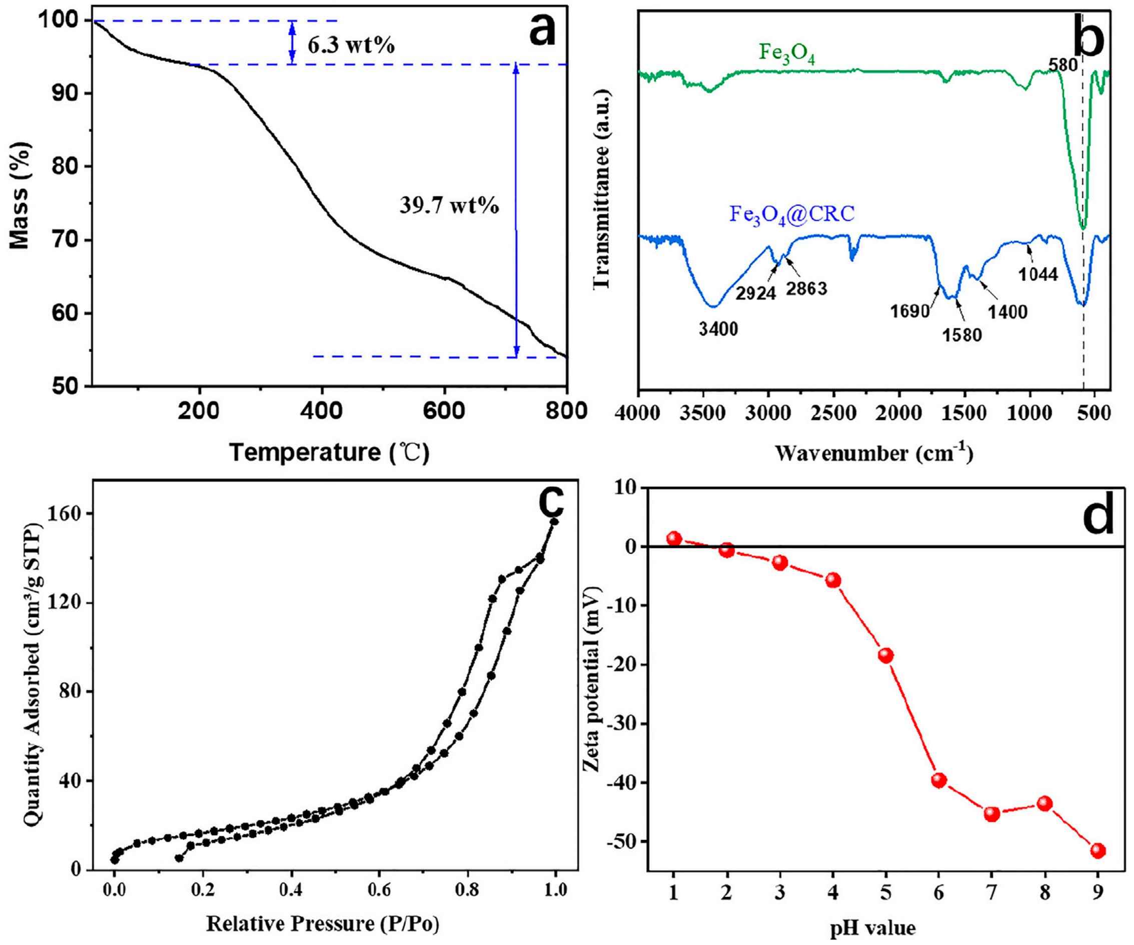

FIGURE 3 | (A) TG curve, **(B)** FTIR spectra, **(C)** nitrogen adsorption/ desorption isotherms, and **(D)** zeta potential of CRC/Fe_3O_4.

The carbon content in CRC/Fe_3O_4 was determined by TG analysis performed under air (**Figure 3A**). The 6.3 wt% mass loss in CRC/Fe_3O_4 up to 190 °C was attributed to the loss of loosely adhered water and structural water molecules. However, major degradation took place within 190–800°C because of the combustion of carbon giving rise to a large weight loss of about 39.7 wt%. While considering that Fe_3O_4 would be converted to Fe_2O_3 when heated in air, the actual carbon content in CRC/ Fe_3O_4 could be estimated to be lower.

Figure 3B displays the FTIR spectra of the as-prepared samples. In Fe_3O_4, the presence of Fe–O was identified by the peaks around 580 cm^{-1} (Leng et al., 2013). In CRC/Fe_3O_4, the incorporation of CRC was envisaged from the prevalent CRC-specific functionalities, such as C–O, C–C, C=O, C–H, and O–H. For instance, the small peaks at 1,044 and 1,580 cm^{-1} indicated C–O *str.* and C–C *str.* of the aromatic ring, respectively (Qu et al., 2013). Again, peaks at 1,690 and 1,400 cm^{-1} were assigned to C=O *str.*, which envisaged the abundance of carboxylate functionalities in the carbon shell. The absorption peaks of H–C–H *str.* were detected at 2,924 and 2,863 cm^{-1} (Le et al., 2021). The peaks at 3400 cm^{-1} indicated the presence of large numbers of hydroxyl groups in CRC/ Fe_3O_4 (Kong et al., 2002).

Surface area, pore volume, and pore size distribution of CRC/ Fe_3O_4 were analyzed by nitrogen adsorption-desorption techniques. According to **Figure 3C**, the type-IV isotherm pattern of CRC/Fe_3O_4 was characteristic of mesoporous materials. However, in CRC/Fe_3O_4, the prevalent narrower hysteresis loop and steep increase in adsorption at P/P_0 close to 0.7 indicated the presence of macropores. The BET surface area and total pore volume were measured to be 42.44 $m^2 g^{-1}$ and 0.0125 $cm^3 g^{-1}$, respectively. Because of the significant population of carboxylate functionalities in CRC, the zero point charge of CRC/Fe_3O_4 was found to be approximately 1.7 (**Figure 3D**). Moreover, zeta potentials of CRC/Fe_3O_4 became more negative with the increasing suspension pH. Abundant numbers of negative charges on the surface of CRC/Fe_3O_4 benefited the sorption of positively charged metal ions, such as Fe(II) ions.

3.2 Heterogeneous Fenton Catalytic Activity of CRC/Fe_3O_4

3.2.1 CRC/ Fe_3O_4 Catalytic Activity

The catalytic activity of CRC/Fe_3O_4 was evaluated by MB degradation experiments through the Fenton reaction. As

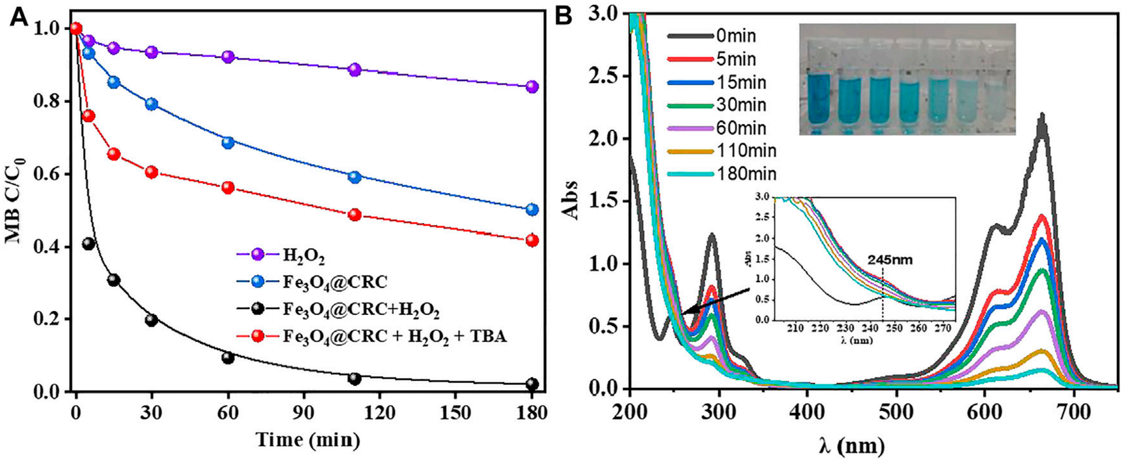

FIGURE 4 | (A) Removal of MB under different conditions, **(B)** time-dependent UV–vis spectra for degradation of MB by CRC/Fe_3O_4 + H_2O_2 [(CRC/Fe_3O_4) = 1.00 g L^{-1}, (MB) = 10 mg L^{-1}, (H_2O_2) = 10 mM, (TBA) = 100 mM, and pH_0 = 7].

indicated in **Figure 4A**, after 180 min of reaction, MB was removed almost completely, whereas in absence of the catalyst, the degradation of MB in the H_2O_2 system was kinetically slower to ensure only 16% removal at 180 min. Again, in the absence of H_2O_2, 50% of MB was adsorbed onto CRC/Fe_3O_4. Interestingly, in **Figure 4B**, absorption peaks at 660/ 290 and 245 nm decreased significantly and disappeared, respectively, after initiation of the reaction. At the same time, the UV absorption within 200–270 nm increased significantly, indicating degradation of MB and the simultaneous formation of some small molecular organics.

TBA was added into the CRC/Fe_3O_4-H_2O_2 system to capture ·OH, as shown in **Figure 4A**. Herein, after TBA was added, the removal rate of MB dropped to 59% at 180 min, confirming that ·OH is the most important active oxygen species in the system. At neutral conditions, there were few iron ions dissolved in the bulk solution, and the reaction mainly occurred on the surface of the catalyst. The CRC/Fe_3O_4 catalytic degradation of MB can be attributed to the synergistic effects of catalyst adsorption and degradation. Since the surface of the sodium gluconate-modified Fe_3O_4 catalyst possessed a highly developed pore structure and plenty of functionalities, the porous CRC/Fe_3O_4 structure provided a larger specific surface area to adsorb a higher amount of MB, thereby increasing the relative concentration of pollutants. At the same time, H_2O_2 also reacted on the surface of the catalyst to form ·OH and reacted with MB. Adsorption is a controlled step of MB degradation.

3.2.2 Effects of Degradation Conditions

In the study of conventional Fenton treatment, the best result can be obtained at pH 3. Under neutral or alkaline conditions, it is not conducive to treat MB wastewater because of the restricted degradation treatment and research of MB. Herein, the catalytic activities of CRC/Fe_3O_4 were studied at different pH values. As can be seen from **Figure 5A**, MB could be completely degraded within 180 min within pH 3-7, indicating that CRC/ Fe_3O_4 has good applicability in a wide pH range. In fact, the fastest degradation rate at pH 3 was mainly caused by the dissolution of iron ions (~0.16 mmol/L), replicating the homogeneous Fenton reaction. However, no significant difference in the reaction rates were observed for pH = 5 and 7 because of the poor iron ion concentration (<0.01 mmol/L). The heterogeneous Fenton catalytic degradation reaction occurred after adsorption of MB on the catalyst.

Figure 5B shows the degradation of MB by CRC/Fe_3O_4 under different catalyst dosages. Results showed that when the dose of CRC/ Fe_3O_4 increased from 0.25 to 1.00 g L^{-1}, the removal efficiency of MB improved gradually, while the removal efficiency exhibited negligible change when the dose of CRC/Fe_3O_4 increased beyond 1.50 g L^{-1}. This was because with the increase in the amount of catalyst, the surface area and active sites, responsible for the acceleration of H_2O_2 decomposition, also increased. However, with the further increment in the amount of catalyst, agglomeration of catalyst particles and excessive iron accumulation removed ·OH, which inhibited the increment of the removal efficiency of MB (Phan et al., 2018; Qin et al., 2018; Xiao et al., 2018). When the amount of catalyst was varied within 1.00–1.50 g L^{-1}, no significant effect on the final removal rate of MB was observed.

The concentration of H_2O_2 plays an important role in the heterogeneous Fenton process because it is directly related to the amount of ·OH produced. Generally, the amount of ·OH produced is directly proportional to the concentration of H_2O_2, that is, the higher the concentration of H_2O_2, the more ·OH produced, and the more degradation of pollutants. However, when the concentration of H_2O_2 exceeds the critical value, the degradation rate may be limited because of the reaction of ·OH with excess H_2O_2 and the conversion into a hydrogen peroxide radical (Liu et al., 2019). As shown in **Figure 5C**, with an increase in the initial H_2O_2 concentration from 5 to 20 mM, the removal rate of MB did not improve significantly. This observation inferred that a lower concentration of H_2O_2 is sufficient for the degradation of MB, and CRC/Fe_3O_4 as a catalyst has a good utilization rate of peroxide.

The initial concentration of MB affects the adsorption and degradation of the catalyst. As seen in **Figure 5C**, with the increase in MB concentration, the degradation efficiency was found to decrease gradually. When the initial MB concentration was 5 mg L^{-1}, 90% MB removal could be achieved after 30 min. The

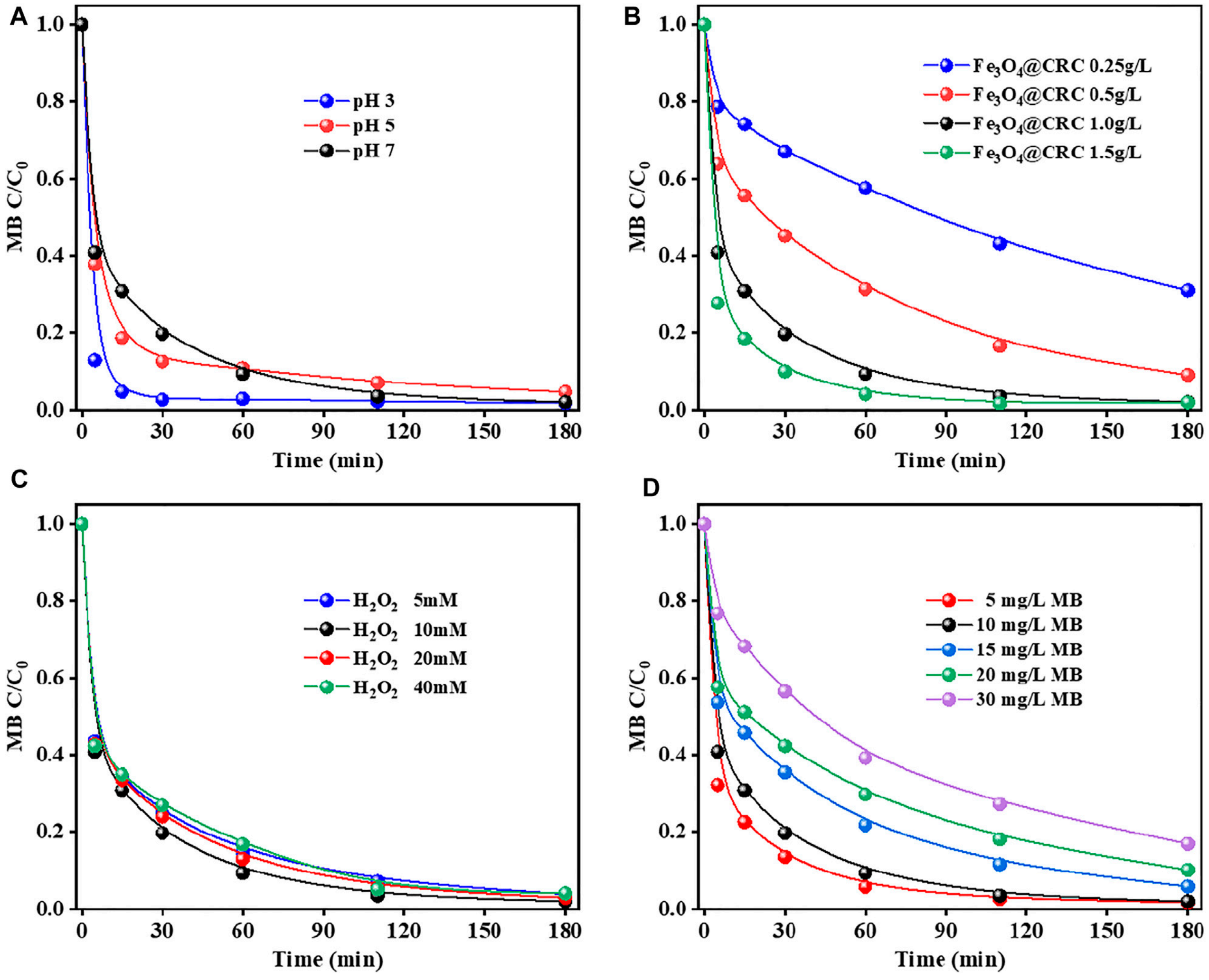

FIGURE 5 | Factors affecting MB degradation by CRC/Fe_3O_4: **(A)** initial solution pH, **(B)** catalyst dosage, **(C)** H_2O_2 concentration, and **(D)** MB concentration [(CRC/Fe_3O_4) = 1.00 g L^{-1}, (MB) = 10 mg L^{-1}, (H_2O_2) = 10 mM, and pH_0 = 7].

degradation of 10 mg L^{-1} MB was similar to that of 5 mg L^{-1}. However, the degradation rates of MB at 15, 20, and 30 mg L^{-1} were 46.41, 42.47, and 23.30%, respectively. However, the degradation rates of MB at 15, 20, and 30 mg L^{-1} were 46.41, 42.47, and 23.30%, respectively (**Figure 5D**). The higher the MB concentration, the longer the duration of the degradation process. This was because the amount of ·OH produced in the reaction system became constant when the dose of the CRC/Fe_3O_4 catalyst and H_2O_2 were constant. For the lower dye concentration, the ·OH in the solution would be relatively excessive. However, with the increase in dye concentration, the ·OH produced in the solution should be relatively insufficient. Therefore, it became necessary to prolong the reaction time to remove the higher concentration of the MB solution.

3.2.3 CRC/Fe_3O_4 Stability and Reusability

Stability and reusability of materials are extremely important for an effective catalyst. In this study, MB was continuously degraded by the heterogeneous Fenton reaction with CRC/Fe_3O_4 under the same conditions, and its stability was evaluated. As shown in **Figure 6A**, the catalytic performance of CRC/Fe_3O_4 declined in six consecutive cycles, because of the possible loss of active sites and adsorption of by-products during MB degradation (Doan et al., 2019). Importantly, after five continuous uses, the CRC/Fe_3O_4 composite still maintained high degradation efficiency. Additionally, at pH = 7, the total dissolved concentration of leached iron was lower than that of the detection limit. As demonstrated in **Figure 6B**, there was no obvious change in XRD pattern after five consecutive cycles.

Figure 7A shows the adsorption and degradation efficiency of CRC/Fe_3O_4 for phenol, BA, SMT, MB, and TC, of which adsorption and degradation of phenol and BA were poor. The adsorption/removal rates of SMT, MB, and TC were 12/20%, 50/98%, and 65/95%, respectively. The degradation trend of organic pollutants was similar to the adsorption trend on the surface of the CRC/Fe_3O_4 catalyst, since adsorption of contaminants promotes their catalytic degradation. The same trend is also reflected in the degradation rate in **Figure 7B**. The synergistic effects of adsorption and catalytic degradation significantly improved the removal effect of organic matter.

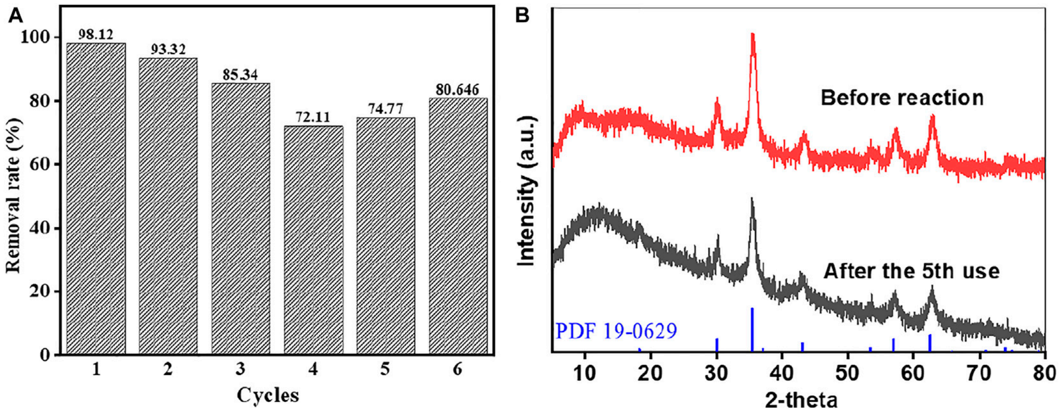

FIGURE 6 | Reusability of CRC/Fe_3O_4 for the degradation of MB: **(A)** removal rates for the six consecutive cycles and **(B)** XRD patterns before reaction/after five consecutive cycles [(CRC/Fe_3O_4) = 1.00 g L^{-1}, (pollutant) = 10 mg L^{-1}, (H_2O_2) = 10 mM, and pH_0 = 7].

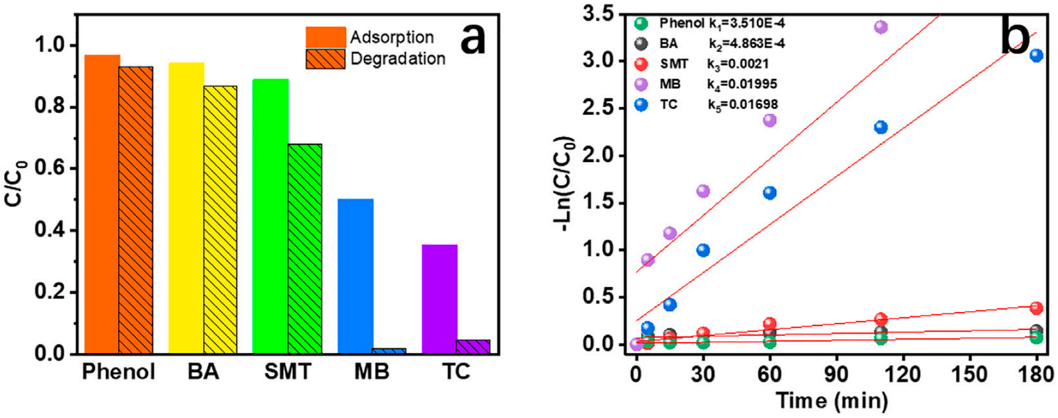

FIGURE 7 | **(A)** Adsorption and degradation efficiency and **(B)** degradation rate of different pollutants by the CRC/Fe_3O_4 heterogeneous Fenton system in 180 min [(CRC/Fe_3O_4) = 1.00 g L^{-1}, (pollutant) = 10 mg L^{-1}, (H_2O_2) = 40 mM, and pH = 7].

4 CONCLUSION

This study reports the spontaneous synthesis of CRC/Fe_3O_4 magnetic particles by the sol-gel combustion method and their catalytic properties and related mechanisms. CRC is conducive towards adsorption of organic matter on the surface of the catalyst and promotes the occurrence of heterogeneous Fenton reactions. Under neutral conditions, the CRC/Fe_3O_4 heterogeneous Fenton reaction predominantly occurs on the surface of the catalyst. Therefore, adsorption of pollutants on the surface of the catalyst is closely related to the CRC/Fe_3O_4 heterogeneous Fenton degradation effect, and the larger the adsorption amount, the higher the degradation removal rate. Experimental results infer that CRC/Fe_3O_4 is negatively charged and therefore possesses better adsorption and degradation of positively charged substances. Further modification of materials is expected to enable selective removal of specific contaminants.

DATA AVAILABILITY STATEMENT

The original contributions presented in the study are included in the article/Supplementary Material, further inquiries can be directed to the corresponding authors.

AUTHOR CONTRIBUTIONS

CW: Conceptualization, methodology, and writing—original draft. RJ: Investigation and formal analysis. JY: Conceptualization, Writing—Reviewing and Editing. PW: Resources and Supervision.

FUNDING

This work was financially supported by the National Natural Science Foundation of China (Nos 51978181 and 42077159).

REFERENCES

Adewunmi, A. A., Kamal, M. S., and Solling, T. I. (2020). Application of Magnetic Nanoparticles in Demulsification: A Review on Synthesis, Performance, Recyclability, and Challenges. *J. Pet. Sci. Eng.* 196, 107680. doi:10.1016/j.petrol.2020.107680

Coha, M., Farinelli, G., Tiraferri, A., Minella, M., and Vione, D. (2021). Advanced Oxidation Processes in the Removal of Organic Substances from Produced Water: Potential, Configurations, and Research Needs. *Chem. Eng. J.* 414, 128668. doi:10.1016/j.cej.2021.128668

Doan, V. D., Le, V. T., Le, T. T. N., and Nguyen, H. T. (2019). Nanosized Zincated Hydroxyapatite as a Promising Heterogeneous Photo-Fenton-Like Catalyst for Methylene Blue Degradation. *Adv. Mater. Sci. Eng.* 2019, 1–9. doi:10.1155/2019/5978149

He, J., Yang, X., Men, B., and Wang, D. (2016). Interfacial Mechanisms of Heterogeneous Fenton Reactions Catalyzed by Iron-Based Materials: A Review. *J. Environ. Sci.* 39, 97–109. doi:10.1016/j.jes.2015.12.003

Hua, Y., Wang, C., Wang, S., and Xiao, J. (2021). Poly(catechol) Modified Fe3O4 Magnetic Nanocomposites with Continuous High Fenton Activity for Organic Degradation at Neutral pH. *Environ. Sci. Pollut. Res.* 28, 62690–62702. doi:10.1007/s11356-021-15088-7

Khatamian, M., Divband, B., and Shahi, R. (2019). Ultrasound Assisted Co-precipitation Synthesis of Fe3O4/ Bentonite Nanocomposite: Performance for Nitrate, BOD and COD Water Treatment. *J. Water Process Eng.* 31, 100870. doi:10.1016/j.jwpe.2019.100870

Klamerth, N., Malato, S., Maldonado, M. I., Agüera, A., and Fernández-Alba, A. (2011). Modified Photo-Fenton for Degradation of Emerging Contaminants in Municipal Wastewater Effluents. *Catal. Today* 161 (1), 241–246. doi:10.1016/j.cattod.2010.10.074

Kong, Y., Mu, S., and Mao, B. (2002). Synthesis of Polycatechol with Electrochemical Activity and its Properties. *Chin. J. Polym Sci.* 20, 517–524. doi:10.3321/j.issn:0256-7679.2002.06.003

Lai, C., Shi, X., Li, L., Cheng, M., Liu, X., Liu, S., et al. (2021). Enhancing Iron Redox Cycling for Promoting Heterogeneous Fenton Performance: A Review. *Sci. Total Environ.* 775, 145850. doi:10.1016/j.scitotenv.2021.145850

Le, V. T., Doan, V. D., Le, T. T. N., Dao, M. U., Vo, T.-T. T., Do, H. H., et al. (2021). Efficient Photocatalytic Degradation of crystal Violet under Natural Sunlight Using Fe3O4/ZnO Nanoparticles Embedded Carboxylate-Rich Carbon. *Mater. Lett.* 283, 128749. doi:10.1016/j.matlet.2020.128749

Leng, Y., Guo, W., Shi, X., Li, Y., and Xing, L. (2013). Polyhydroquinone-Coated Fe3O4 Nanocatalyst for Degradation of Rhodamine B Based on Sulfate Radicals. *Ind. Eng. Chem. Res.* 52, 13607–13612. doi:10.1021/ie4015777

Liu, J., Du, Y., Sun, W., Chang, Q., and Peng, C. (2019). Preparation of New Adsorbent-Supported Fe/Ni Particles for the Removal of crystal Violet and Methylene Blue by a Heterogeneous Fenton-like Reaction. *RSC Adv.* 9 (39), 22513–22522. doi:10.1039/c9ra04710g

Liu, S., Yu, B., Wang, S., Shen, Y., and Cong, H. (2020). Preparation, Surface Functionalization and Application of Fe3O4 Magnetic Nanoparticles. *Adv. Colloid Interf. Sci.* 281, 102165. doi:10.1016/j.cis.2020.102165

Munoz, M., de Pedro, Z. M., Casas, J. A., and Rodriguez, J. J. (2015). Preparation of Magnetite-Based Catalysts and Their Application in Heterogeneous Fenton Oxidation - A Review. *Appl. Catal. B Environ.* 176/177, 249–265. doi:10.1016/j.apcatb.2015.04.003

Phan, T. T. N., Nikoloski, A. N., Bahri, P. A., and Li, D. (2018). Adsorption and Photo-Fenton Catalytic Degradation of Organic Dyes over Crystalline LaFeO3-Doped Porous Silica. *RSC Adv.* 8 (63), 36181–36190. doi:10.1039/c8ra07073c

Pignatello, J. J., Oliveros, E., and Mackay, A. (2006). Advanced Oxidation Processes for Organic Contaminant Destruction Based on the Fenton Reaction and Related Chemistry. *Crit. Rev. Environ. Sci. Technol.* 36 (1), 1–84. doi:10.1080/10643380500326564

Qin, Q., Liu, Y., Li, X., Sun, T., and Xu, Y. (2018). Enhanced Heterogeneous Fenton-like Degradation of Methylene Blue by Reduced CuFe2O4. *RSC Adv.* 8 (2), 1071–1077. doi:10.1039/c7ra12488k

Qu, L., Jia, J., Shi, H., and Luo, Z. (2016). One-step Synthesis of Fe3O4/carboxylate-Rich Carbon Composite and its Application for Cu(ii) Removal. *New J. Chem.* 40, 2895–2903. doi:10.1039/c5nj02545a

Qu, L., Luo, Z., and Tang, C. (2013). One Step Synthesis of Bi@Bi2O3@carboxylate-Rich Carbon Spheres with Enhanced Photocatalytic Performance. *Mater. Res. Bull.* 48 (11), 4601–4605. doi:10.1016/j.materresbull.2013.07.047

Thomas, N., Dionysiou, D. D., and Pillai, S. C. (2021). Heterogeneous Fenton Catalysts: A Review of Recent Advances. *J. Hazard. Mater.* 404, 124082. doi:10.1016/j.jhazmat.2020.124082

Wang, J., and Wang, S. (2020). Reactive Species in Advanced Oxidation Processes: Formation, Identification and Reaction Mechanism. *Chem. Eng. J.* 401, 126158. doi:10.1016/j.cej.2020.126158

Wang, Y., Gao, P., Wei, Y., Jin, Y., Sun, S., Wang, Z., et al. (2021). Silver Nanoparticles Decorated Magnetic Polymer Composites (Fe3O4@PS@Ag) as Highly Efficient Reusable Catalyst for the Degradation of 4-nitrophenol and Organic Dyes. *J. Environ. Manage.* 278, 111473. doi:10.1016/j.jenvman.2020.111473

Wu, W., Wu, Z., Yu, T., Jiang, C., and Kim, W. S. (2015). Recent Progress on Magnetic Iron Oxide Nanoparticles: Synthesis, Surface Functional Strategies and Biomedical Applications. *Sci. Technol. Adv. Mater.* 16 (2), 023501–023543. doi:10.1088/1468-6996/16/2/023501

Wulandari, I. O., Mardila, V. T., Santjojo, D. J. D. H., and Sabarudin, A. (2018). Preparation and Characterization of Chitosan-Coated Fe3O4 Nanoparticles Using *Ex-Situ* Co-precipitation Method and Tripolyphosphate/Sulphate as Dual Crosslinkers. *IOP Conf. Ser. Mater. Sci. Eng.* 299, 012064. doi:10.1088/1757-899x/299/1/012064

Xiao, C., Li, J., and Zhang, G. (2018). Synthesis of Stable Burger-like α-Fe2O3 Catalysts: Formation Mechanism and Excellent Photo-Fenton Catalytic Performance. *J. Clean. Prod.* 180, 550–559. doi:10.1016/j.jclepro.2018.01.127

Xiea, Z.-H., Zhou, H.-Y., Hea, C.-S., Pan, Z.-C., Yao, G., and Lai, B. (2021). Synthesis, Application and Catalytic Performance of Layered Double Hydroxide Based Catalysts in Advanced Oxidation Processes for Wastewater Decontamination: A Review. *Chem. Eng. J.* 414, 128713. doi:10.1016/j.cej.2021.128713

Xu, Y., Zhang, Y., Song, X., and Liu, H. (2018). Facile Hydrothermal Synthesis of Fe$_3$O$_4$ Nanoparticle and Effect of Crystallinity on Performances for Supercapacitor. *Funct. Mater. Lett.* 12, 1950019. doi:10.1142/S179360471950019X

Xue, W., Hu, Y., Wang, F., Yang, X., and Wang, L. (2019). Fe3O4/Poly(caprolactone) (PCL) Electrospun Membranes as Methylene Blue Catalyst with High Recyclability. *Colloids Surf. A: Physicochemical Eng. Aspects* 564, 115–121. doi:10.1016/j.colsurfa.2018.12.037

Yan, H., Zhang, J-C., You, C-X., Song, Z.-W., Yu, B.-W., and Shen, Y. (2009). Surface Modification of Fe$_3$O$_4$ Nanoparticles and Their Magnetic Properties. *Int. J. Minerals, Metall. Mater.* 16 (2), 226–229. doi:10.1016/s1674-4799(09)60038-8

Zeng, Q., Chang, S., Wang, M., Li, M., Deng, Q., Xiong, Z., et al. (2021). Highly-active, Metal-free, Carbon-Based ORR Cathode for Efficient Organics Removal and Electricity Generation in a PFC System. *Chin. Chem. Lett.* 32, 2212–2216. doi:10.1016/j.cclet.2020.12.062

Zhu, N., Ji, H., Yu, P., Niu, J., Farooq, M. U., Akram, M. W., et al. (2018). Surface Modification of Magnetic Iron Oxide Nanoparticles. *Nanomaterials (Basel)* 8 (10), 27. doi:10.3390/nano8100810

Conflict of Interest: The authors declare that the research was conducted in the absence of any commercial or financial relationships that could be construed as a potential conflict of interest.

Frontiers in Chemistry

REVIEW
published: 04 May 2022
doi: 10.3389/fchem.2022.900660

Synergistic Fluoride Adsorption by Composite Adsorbents Synthesized From Different Types of Materials—A Review

Yifei Wei, Li Wang, Hanbing Li, Wei Yan and Jiangtao Feng*

Xi'an Key Laboratory of Solid Waste Recycling and Resource Recovery, Department of Environmental Science and Engineering, School of Energy and Power Engineering, Xi'an Jiaotong University, Xi'an, China

The reduction of fluoride concentrations in water is one of many concerns. Adsorption is the most widely used technology for fluoride removal and the center to development of adsorption technology is the improvement of adsorbents. This review classifies the typical fluoride removal adsorbents into four types: metal oxides/hydroxides, biopolymers, carbon-based, and other adsorbents. The exploitation of new materials and the synthesis of composite materials are two ways of developing new adsorbents. In comparison to the discovery of novel adsorbents for fluoride adsorption, research into the composite synthesis of different types of conventional adsorbents has proliferated in recent years. The traditional adsorbents used the earliest, metal oxides, can act as active centers in a wide range of applications for modifying and compounding with other types of adsorbents. This study emphasizes reviewing the research on fluoride removal by composite adsorbents synthesized from different types of metal-modified materials. Seven factors were compared in terms of material characterization, initial fluoride concentration, adsorbent dose, pH, temperature, reaction time, and maximum adsorption capacity. The modification of composite adsorbents is facile and the synergistic effect of the different types of adsorbents significantly improves fluoride adsorption capacity. Metal composite adsorbents are synthesized by facile coprecipitation, hydrothermal, or impregnation modification methods. The adsorption mechanisms involve electrostatic attraction, ion exchange, complexation, and hydrogen bonding. The fluoride adsorption capacity of composite adsorbents has generally improved, indicating that most modifications are successful and have application prospects. However, to achieve significant breakthroughs in practical applications, numerous issues such as cost, separation/regeneration performance, and safety still need to be considered.

Keywords: fluoride adsorption, metal oxides/hydroxides, carbon-based adsorbents, biopolymer, modification

Edited by:
Suqing Wu,
Wenzhou University, China

Reviewed by:
Weifeng Liu,
Dalian Maritime University, China
Yuanyuan Sun,
Qingdao University, China

***Correspondence:**
Li Wang
wangli-2015@xjtu.edu.cn

Specialty section:
This article was submitted to Inorganic Chemistry, a section of the journal Frontiers in Chemistry

Received: *21 March 2022*
Accepted: *07 April 2022*
Published: *04 May 2022*

Citation:
Wei Y, Wang L, Li H, Yan W and Feng J (2022) Synergistic Fluoride Adsorption by Composite Adsorbents Synthesized From Different Types of Materials—A Review. Front. Chem. 10:900660. doi: 10.3389/fchem.2022.900660

1 INTRODUCTION

Fluoride ions in water have a strong affinity with positively charged elements such as calcium (Bhatnagar et al., 2011), which is a major component of human bone and tooth structure (Rehman et al., 2015). Low concentrations of fluoride in drinking water (0.5–1.5 mg/L) (Chen et al., 2017) can strengthen bones and prevent dental caries, while excessive concentrations of fluoride (4–10 mg/L) can cause diseases such as fluorosis, osteoporosis, brittle bones, brain damage, and several thyroid disorders (Kumar et al., 2020). Excessive fluoride concentrations in water have become a public health concern in developing countries. High concentration (>10 mg/L) fluorinated wastewater is easier to treat and can be removed or reduced by coagulation, precipitation, electrochemistry, and other methods. The treatment of low concentration (2–10 mg/L) fluorinated wastewater is relatively difficult and is also a current research hotspot. The treatment methods include adsorption (Lin et al., 2016), membrane separation, ion exchange (Xu et al., 2017), nanofiltration (Wang A. et al., 2018), reverse osmosis (Ye et al., 2019), and electrodialysis (Fan et al., 2019). Among them, the adsorption method has the advantages of low cost, high flexibility, simple operation, and high efficiency (Sarkar et al., 2019). It is the most widely used and the treatment effect is more satisfactory.

The treatment effectiveness of the adsorption method is influenced by a number of factors, including adsorbent properties, fluoride ion selectivity, compatibility, solution pH, temperature, co-existing ions, and contact time (Pigatto et al., 2020). It mainly depends on the adsorbent properties such as particle size, pore size structure, zero charge point (pH_{PZC}), and specific surface area (S_{BET}) (Biswas et al., 2017). High specific surface area (developed pore structure) and ideal chemical surface (abundant functional groups) are two essentials for effective removal of fluoride by adsorbents. Although not systematically categorized, this review found that the main traditional sorbents frequently used for fluoride removal are metal oxides/hydroxides (Dhillon et al., 2017), low-cost carbon materials (Zhang X. et al., 2021), biomolecular materials (Jia et al., 2018), and others such as clay, hydroxyapatite, and graphite. This review classifies the more researched fluoride removal adsorbents into four categories: metal oxide/hydroxide adsorbents, biopolymer adsorbents, carbon-based adsorbents, and other adsorbents (industrial waste, minerals, etc.).

For the development of new adsorbents, the discovery of novel adsorbents that have never been used before and the composite material synthesis by combining traditional adsorbents are the two main approaches to improve adsorption capacity. In comparison to the discovery of novel adsorbents that have never been used before, research into the composite synthesis of different types of conventional adsorbents for fluoride adsorption has proliferated in recent years. The emphasis of this study is placed on the fluoride adsorption effect of this adsorbent compounded from different types of conventional adsorbents. The study of other types of metal-modified adsorbents accounts for a major part. A total of seven factors were compared in terms of material characterization, initial fluoride concentration, adsorbent dose, pH, temperature, reaction time, and maximum adsorption capacity.

2 CONVENTIONAL TYPES OF ADSORBENTS

2.1 Metal Oxide/Hydroxide Adsorbents

Metal oxide/hydroxide nanoparticles were reported to show an affinity for fluoride and high performance in fluoride removal. The high reactivity (Lanas et al., 2016), specificity, specific surface area (Rathore and Mondal 2017), stability, and self-assembly potential have attracted attention in fluoride removal studies. Nanoscale dimensions with desirable physicochemical properties, such as high density of hydroxyl ions on the high specific surface area, will further enhance the fluoride adsorption capacity.

2.1.1 Aluminum Oxide/Hydroxide

Aluminum oxide/hydroxide was the earliest studied and used adsorbents for fluoride removal (Chinnakoti et al., 2016a). Typically, aluminum hydroxide is first prepared by electrolysis or pyrolysis and then partially converted to aluminum oxide by calcination. One of the advantages of aluminum oxide/hydroxide adsorbents is the large specific surface area (Hafshejani et al., 2017), as shown in **Table 1**, and in general, S_{BET} > 200 m^2/g. Generally, high pH_{PZC} allows its surface to appear positively charged in water (Dhawane et al., 2018). Several studies have reported that the mechanism of fluoride adsorption by alumina mainly consists of electrostatic attraction and ion exchange (Rathore and Mondal 2017), as shown in **Figure 1A**; the monodentate complex Al-F is the major formation after adsorption (Kang et al., 2018; Lin et al., 2020). Kang et al. (2018) synthesized an amorphous alumina microsphere using solvothermal reaction and calcination, with S_{BET} = 400 m^2/g and a maximum adsorption capacity of 129.4 mg/g; they proposed that the adsorption mechanism involves chemical reaction and pore filling in addition to ion exchange and electrostatic attraction. However, aluminum is easily leached out in aqueous solutions, especially under acidic conditions (Lin et al., 2020), leading to high concentration of aluminum residues in drinking water, which is also a major threat to human health.

2.1.2 Rare Earth Metal Compounds

Compared to aluminum, the rare earth metals (cerium, titanium, lanthanum, etc.) have further affinity for fluoride due to the ability to stabilize in the +3 or +4 valence state with a few numbers of outermost electrons; therefore, sufficient empty orbitals are available for fluoride ions (Zhang K. et al., 2016). The solubility of rare earth metals is relatively limited over a wide pH range (Dhillon et al., 2016), so rare earth oxides/hydroxides have been increasingly investigated as substitution for aluminum in recent years. Among these, CeO_2 readily forms oxygen vacancies and, therefore, has particularly high oxygen storage/release capacity with high adsorption capacity (Kullgren et al., 2014; Wu and Gong 2016; Kang et al., 2017). Kang et al. (2017) compared the physicochemical characteristics and adsorption performance of different

TABLE 1 | Summary of the preparation methods, characteristics, and adsorption mechanisms of four traditional adsorbents.

Adsorbents	Preparation method	Dimension	S_{BET} (m^2/G)	Aperture (nm)	pH_{PZC}	Adsorption mechanism	Ref
Cactus-like amorphous alumina oxide microspheres	Solvothermal method without templates	40 μm	419.6	5.3	6.6	Chemical coordination, electrostatic attraction, and ion exchange	Kang et al. (2018)
Nano γ-alumina	Surfactant-assisted combustion	—	221	—	6.5	—	Chinnakoti et al. (2016a)
Mesoporous micro alumina	γ-AlOOH calcined at 873 K	0.9 mm	254.1	12.96	9.0	Electrostatic attraction	Lanas et al. (2016)
Al_2O_3 nanoparticles	Flame spray pyrolysis (FSP)	9.8 nm	213	93	—	Electrostatic attraction	Hafshejani et al. (2017)
Porous-layered Al_2O_3	Roasting of AlFu MOFs	—	329.3	3.8	—	Ion exchange, complexation	Yang et al. (2020)
Activated alumina	Al_2O_3 cauterized at 673 K	1–3 mm	185.6	5.1	8.5	Lewis acid and base	Dhawane et al. (2018)
Aluminum oxide/hydroxide	Electrolysis, calcination at 973 K	1.5 mm	253.2	4.7	7.52	Electrostatic attraction	Rathore and Mondal (2017)
Cubical ceria nano-adsorbent	Coprecipitation, calcination at 473 K	4.5 nm	98	2.62	6	Ligand exchange, complexation	Dhillon et al. (2016)
CeO_2 nanorods	Hydrothermal at 373 K	20*200 nm	111.4	8.65	—	Ce^{3+}-O defect, ion exchange,	—
Pore filling	Kang et al. (2017)	—	—	—	—	—	—
CeO_2 octahedron	Hydrothermal at 453 K	14 nm	160.2	9.66	—	—	—
CeO_2 nanocubes	Hydrothermal at 473 K	25 nm	55.8	15.1	—	—	—
$CeCO_3OH$ nanosphere	Hydrothermal	250 nm	10.6	15.5	—	Electrostatic attraction, ion exchange	Zhang et al. (2016b)
Porous MgO nanoplates	Solvothermal, calcination	—	47.4	3.3	—	Ligand exchange	Jin et al. (2016)
Hollow MgO spheres	Hydrothermal, calcination at 773 K	2 μm	—	—	10	Ligand exchange	Zhang et al. (2021b)
Microsphere-like MgO	Hydrothermal, calcination at 773 K	46 μm	120.7	5.12	-	Ion exchange	Lee et al. (2017)
Pillar-like MgO	Hydrothermal, calcination at 773 K	2*20 μm	99.44	6.26	-	Ion exchange	Lee et al. (2017)
γ-Fe_2O_3 nanoparticles	Precipitation	5–20 nm	—	—	8.13	Complexation	Jayarathna et al. (2015)
Trititanate nanotubes	Hydrothermal at 403 K, 1 h	8–12 nm	282	-	2.5	Ion exchange, electrostatic attraction	Chinnakoti et al. (2016b)
TiO_2	Solvothermal method	1 μm	31.9	—	6.5	Complexation	Zhou et al. (2019b)
Lanthanum alginate bead	$LaCl_3$ cross-linking	1 mm	2.618	1.441	—	Ion exchange	Huo et al. (2011)
Biopolymer pectinandalginate	Glutaraldehyde cross-linking mixture	—	—	—	—	—	Raghav et al. (2019)
Porous zirconium alginate	$CaCl_2$ cross-linking SA, $Zr(NO_3)_4$ immersion	2 mm	3	—	—	Electrostatic attraction, ion exchange	Qiusheng et al. (2015)
Shell biochar	Calcination at 1073 K	0.5 mm	4	413	6	Complexation	Lee et al. (2021)
Nanoscale rice husk biochar	Calcination at 873 K, ball milling	—	—	—	—	Ion exchange	Goswami and Kumar (2018)
Mustard ash biochar	Carbonization at 873 K	—	—	—	—	—	Jadhav and Jadhav (2021)
Peanut shell biochar	Pyrolysis at 673 K, 1 h	—	98	7.05	—	—	Kumar et al. (2020)
Rhodophyta biochar	Calcined in muffle for 2 h	75 μm	320	1.28	5.4	Complexation	Naga Babu et al. (2020)
Rice husk biochar	Pyrolysis at 698 K in tube furnace	—	3	13.29	5.9	Ion exchange	Yadav and Jagadevan (2020)
Activated sugarcane ash	Burning at 773 K in muffle furnace	150 μm	64	—	—	Ion exchange	Mondal et al. (2016)
KOH-treated jamun seed	KOH activation, pyrolysis at 1173 K	—	748	2.19	4.9	Ligand exchange	Araga et al. (2017)
KOH-treated activated carbon	Carbonization with solid KOH at 873 K	—	1,006	1.95	6.11	Protonation, ion exchange	Bhomick et al. (2019)
Activated carbon	Surfactant modification	—	—	—	6.86	Electrostatic attraction	Chen et al. (2019)
Coconut-shell carbon	Carbonization at 1173 K in tube furnace	500 nm	358	—	—	Electrostatic attraction	Araga et al. (2019)
Chicken bone biochar	Burning at 873 K in muffle furnace	159 μm	126	—	—	Ion exchange	Herath et al. (2018)
Bone char	—	0.8 mm	104	11.4	8.4	Electrostatic attraction	Medellin-Castillo et al. (2014)

(Continued on following page)

TABLE 1 | (*Continued*) Summary of the preparation methods, characteristics, and adsorption mechanisms of four traditional adsorbents.

Adsorbents	Preparation method	Dimension	S_{BET} (m^2/G)	Aperture (nm)	pH_{PZC}	Adsorption mechanism	Ref
Bovine bone biochar	Burning at 773 K in muffle furnace	—	115	3.823	2.2	Ion exchange	Zhou et al. (2019a)
Kaolinite	Alkali–hydrothermal	—	18	4	5	Ion exchange	Wang et al. (2017b)
Activated clay	Sulfuric acid activation	—	167	4.9	—	—	Guiza et al. (2019)
Fly ash–paper mill lime mud	Mixing, calcination	60 μm	58.9	—	—	Ligand exchange, complexation	Ye et al. (2019)
Natural clay	—	-	-	—	8	—	Nabbou et al. (2019)
Natural pumice	—	200 μm	9.5	—	3	—	Dehghani et al. (2016)
Natural zeolite	NaOH activation	—	—	—	—	Ion exchange, H-bonding	Cheng et al. (2018)
Clay	Heat treatment at 573 K	—	44.29	—	6	—	Zhang et al. (2016c)
Scoria	HCl immersion for 24 h	—	—	—	—	Ion exchange, complexation	Asadi et al. (2018)
Porous nanohydroxyapatite	Organic template coprecipitation	25 nm	41.3	-	6.8	Lattice substitution, precipitation	Wimalasiri et al. (2021)
Hierarchical hydroxyapatite	Ca and phosphate hydrothermal at 393 K	2 μm	83.17	11.52	7.73	Electrostatic attraction, ion exchange	Gao et al. (2019)
NaP-hydroxyapatite	Hydrothermal with zeolite gel at 373 K	2 μm	45	13.7	—	Ion exchange	Zendehdel et al. (2017)
Hydroxyapatite	Aqueous double decomposition	—	—	—	—	Ion exchange	Mourabet et al. (2015)

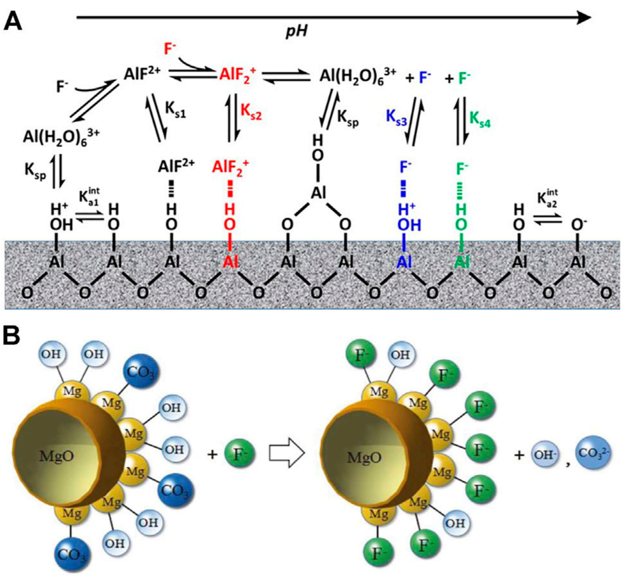

FIGURE 1 | Mechanism of fluoride adsorption by activated alumina **(A)** (Lin et al., 2020) and MgO **(B)** (Zhang Y. et al., 2021).

morphologies of CeO_2 (nanorods, octahedrons, and nanocubes) prepared under different hydrothermal conditions. The different morphologies of CeO_2 were found to expose distinct crystalline surfaces and proportions of oxygen defects, leading to significant differences in fluoride adsorption capacity, with CeO_2 nanorods having the largest Q_{max} (71.5 mg/g). However, rare earth metal oxides are costly, prone to agglomeration, and high leaching concentrations can be toxic to water (Yu et al., 2015).

2.1.3 Magnesium Oxide

MgO is less dissolved, nontoxic, abundant in reserves compared to other metals, and has an affinity for fluoride (Jin et al., 2016), giving it an opportunity to be used. It has been reported that MgO has a high isoelectric point and relies on electrostatic attraction to adsorb fluoride (Suzuki et al., 2013). Y. Zhang et al. tested the zeta potential of hollow MgO spheres of pH_{PZC} = 10, which is the highest value reported. In order to improve the morphology, Z. Jin et al. used a typical solvothermal method followed by calcination to form porous MgO nanoplates with an increased maximum adsorption capacity from 115.5 mg/g to 185.5 mg/g. They suggested that the mechanism of adsorption mainly consists of ligand exchange between fluoride and hydroxyl groups and carbonates on the surface of MgO (**Figure 1B**). Thus, the presence of carbonate in the solution can affect the fluoride adsorption capacity of MgO.

The most significant problem concerning metal oxide/hydroxide nanoparticles is low structural stability and the tendency to leach in water causing secondary contamination (Lin et al., 2020).

2.2 Biopolymer Adsorbents

Biopolymers are the natural macromolecular materials derived from cellular or extracellular substances with properties such as biodegradability, nontoxicity, low waste generation, low leaching, biocompatibility, and hydrophilicity. The most researched fluoride removal biopolymer adsorbents in recent years include sodium alginate (SA), pectin, chitosan (CS), and carboxymethyl cellulose (CMC) (Araga and Sharma 2019). Hydrogels formed by chemical or physical cross-linking of biopolymers have hydrophobic, three-dimensional network structures, which are easier to separate compared to the

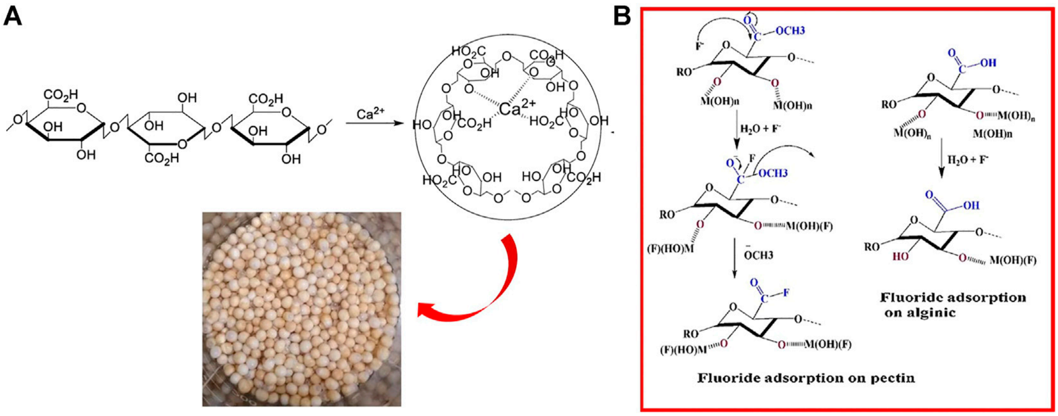

FIGURE 2 | Ionic cross-linking procedure of sodium alginate **(A)** (Sharma et al., 2019) and fluoride adsorption mechanism of pectin **(B)** (Raghav and Kumar 2019).

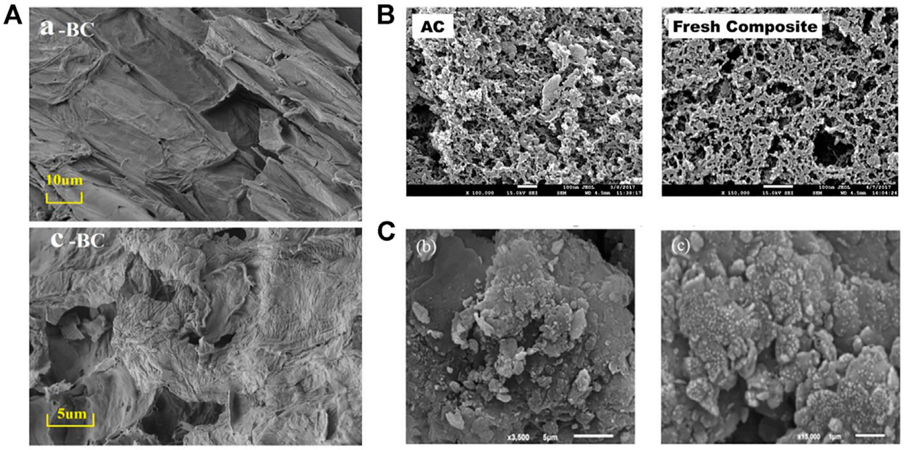

FIGURE 3 | Rough surface of biochar **(A)** (Zhang X. et al., 2021), activated carbon **(B)** (Mullick and Neogi 2018), and clay **(C)** (Mobarak et al., 2018).

powder state, making them an environment-friendly adsorbent.

2.2.1 Sodium Alginate

Sodium alginate (SA) and pectin are both natural polysaccharides in colloidal form. Sodium alginate contains large numbers of -OH and -COOH groups on the main chain. The -COOH in the M unit is more bound by the surrounding electron cloud, while the -COOH in the G unit is arranged in the corner of the peak consisting of two adjacent carbon atoms; thus, G unit is more reactive (Wu T. et al., 2017). In the ionic cross-linking process (**Figure 2A**), when the dissolved colloidal sodium alginate is dropped into the solution of high-valent metal cations (Ca^{2+}, Ce^{3+}, Fe^{3+}, Al^{3+}, La^{3+}, etc.), the high-valent cations in the solution will rapidly replace Na^+ (Wu et al., 2016a). The embedded high-valent cations form ligand chelate crosslinks with the oxygen atoms in the carboxyl and hydroxyl groups of the G-units, which form irreversible hydrogel-like microbeads (Qiusheng et al., 2015). The thermal stability and acid resistance of sodium alginate are further improved after the formation of the gel, while some of the carboxyl functional groups are occupied by high-valent metal cations, so the active sites with an affinity for fluoride ions are increased. Huo et al. (2011) used ionic cross-linking to prepare lanthanum alginate with stable skeletal junctions. SEM showed cracks in the dense surface structure after adsorption, with Q_{max} = 197.2 mg/g.

2.2.2 Pectin

Pectin is also rich in -COOH and -$COOCH_3$ groups. The active sites of sodium alginate and pectin are essentially identical, the only difference being the presence of -$COOCH_3$ in pectin (Sharma et al., 2019), whereas sodium alginate contains only -COOH. The ester group chelates better with metals through its lone pair of electron contribution. The carboxyl group is present in a dimeric form due to the conjugation effect, with the lone pair participating in the conjugation. Therefore, the ester group has a nucleophilic reaction to F^- (**Figure 2B**), providing more active sites, and the pectin should have a higher fluoride removal

TABLE 2 | Adsorption conditions and performance of fluoride by four conventional adsorbents.

Adsorbents	Adsorption condition					Isotherm model	Regeneration performance	Q_{max} (mg/g)	Ref
	Initial C_{F^-} (mg/L)	Adsorbent dose (g/L)	Reaction pH	Temperature (K)	Equilibrium time (min)				
Cactus-like amorphous alumina oxide microspheres	50	1	5–8	298	300	Langmuir	80% at 5th cycle	129.40	Kang et al. (2018)
Nano γ-alumina	8	1	4	303	120	Freundlich	80% at 5th cycle	32.00	Chinnakoti et al. (2016a)
Mesoporous micro alumina	80	0.5	5.5	298	60	Langmuir	—	26.00	Lanas et al. (2016)
Al_2O_3 nanoparticles	10	0.5	4–6	298	60	Langmuir	—	13.70	Hafshejani et al. (2017)
Amorphous porous-layered Al_2O_3	120	5	2–5	313	150	Langmuir	—	12.05	Yang et al. (2020)
Activated alumina	10	2	6–8	318	120	Freundlich	—	4.31	Dhawane et al. (2018)
Aluminum oxide/ hydroxide	10	8	4–7	298	300	Langmuir	—	2.00	Rathore and Mondal (2017)
Cubical ceria nano-adsorbent	20	1	7	298	120	Langmuir	—	80.64	Dhillon et al. (2016)
CeO_2 nanorods	50	0.5	3.5	298	1,500	Langmuir	—	71.50	Kang et al. (2017)
CeO_2 octahedron	10	1	3–10	293	400	Langmuir	—	40.13	Zhang et al. (2016b)
CeO_2 nanocubes	50	0.5	3.5	298	1,500	Langmuir	—	28.30	Kang et al. (2017)
$CeCO_3OH$ nanosphere	50	0.5	3.5	298	1,500	Langmuir	—	7.00	Kang et al. (2017)
Porous MgO nanoplates	20	1	2–11	298	180	Freundlich	—	185.50	Jin et al. (2016)
Hollow MgO spheres	10	1	3–11	298	250	Freundlich	—	182.40	Zhang et al. (2021b)
Microsphere-like MgO	100	1	3–9	298	300	Langmuir	40% at second cycle	166.70	Lee et al. (2017)
Pillar-like MgO	100	1	3–9	298	300	Langmuir	40% at second cycle	151.50	Lee et al. (2017)
γ-Fe_2O_3 nanoparticles	100	10	4.5	298	15	-	—	3.65	Jayarathna et al. (2015)
Trititanate nanotubes	10	0.5	2	298	10	Langmuir	—	58.60	Chinnakoti et al. (2016b)
TiO_2	5	0.5	7	298	30	Langmuir	—	5.00	Zhou et al. (2019b)
Lanthanum alginate bead	10	1	4	298	1,440	Langmuir	—	197.20	Huo et al. (2011)
Biopolymer pectin and alginate	60	0.1	7	298	35	Langmuir	—	50.00	Raghav et al. (2019)
Porous zirconium alginate	20	1	2	303	1,200	Langmuir	—	27.95	Qiusheng et al. (2015)
Shell biochar	300	3.33	7	298	1,440	Langmuir	60% at third cycle	82.93	Lee et al. (2021)
Nanoscale rice husk biochar	5	1	7	303	60	Freundlich	—	21.70	Goswami and Kumar (2018)
Mustard ash biochar	5	2	2	298	150	Langmuir	30% at third cycle	4.42	Jadhav and Jadhav (2021)
Peanut shell biochar	10	8	7	298	120	Langmuir	—	3.66	Kumar et al. (2020)
Rhodophyta biochar	15	0.6	6	303	90	Freundlich	80% at fifth cycle	2.10	Naga Babu et al. (2020)
Rice husk biochar	4	5	6	303	360	Langmuir	-	1.86	Yadav and Jagadevan (2020)
Activated sugarcane ash	5	2	2	303	100	Langmuir	-	10.99	Mondal et al. (2016)
KOH-treated jamun seed	10	0.4	2.5	298	120	D-R	-	3.65	Araga et al. (2017)
KOH-treated activated carbon	5	3	4	303	100	Langmuir	-	2.52	Bhomick et al. (2019)
Activated carbon	380	2	3	298	—	—	50% at fifth cycle	1.15	Chen et al. (2019)
Coconut-shell carbon	4.4	10	2	323	180	Langmuir	—	0.36	Araga et al. (2019)
Chicken bone biochar	10	—	—	298	1,440	Langmuir	—	11.20	Herath et al. (2018)

(Continued on following page)

TABLE 2 | (*Continued*) Adsorption conditions and performance of fluoride by four conventional adsorbents.

Adsorbents	**Adsorption condition**					**Isotherm model**	**Regeneration performance**	**Q_{max} (mg/g)**	**Ref**
	Initial C_{F^-} (mg/L)	**Adsorbent dose (g/L)**	**Reaction pH**	**Temperature (K)**	**Equilibrium time (min)**				
Bone char	10	1	7	298	1,440	Langmuir	—	5.40	Medellin-Castillo et al. (2014)
Bovine bone biochar	20	5	8	298	—	Langmuir	50% at fourth cycle	5.05	Zhou et al. (2019a)
Kaolinite	100	1	7	298	150	Langmuir	—	125.00	Wang et al. (2017b)
Activated clay	30	1	5	298	80	Langmuir	—	75.76	Guiza et al. (2019)
Fly ash–paper mill lime mud	15	1.5	5	298	120	Langmuir	—	7.37	Ye et al. (2019)
Natural clay	5	1	6	301	120	Langmuir	—	3.74	Nabbou et al. (2019)
Natural pumice	3	0.7	3	298	50	Freundlich	—	1.17	Dehghani et al. (2016)
Natural zeolite	80	1	6–7	293	300	Freundlich	—	1.83	Cheng et al. (2018)
Clay	5	20	6	398	600	Langmuir	80% at sixth cycle	1.30	Zhang et al. (2016c)
Scoria	7	4	7	298	60	Freundlich	—	0.32	Asadi et al. (2018)
Porous nanohydroxyapatite	5	2	6.5	303	30	Langmuir	—	54.40	Wimalasiri et al. (2021)
Hierarchical hydroxyapatite	20	0.4	4	298	10	Langmuir	—	29.82	Gao et al. (2019)
NaP-hydroxyapatite	5	3	4.5	298	50	Langmuir	—	11.95	Zendehdel et al. (2017)
Hydroxyapatite	15	0.7	7.5	303	60	Langmuir	—	3.12	Mourabet et al. (2015)

capacity in comparison (Raghav and Kumar 2019). SA and pectin hydrogels accomplish adsorption by exchanging hydroxyl groups in the structure with fluoride.

2.3 Carbon-Based Adsorbents

Carbon-based adsorbents have developed pore structures, large specific surface areas, stable chemical properties, easily adjustable surface properties, good regenerability, and widely available and general waste, which is of low cost with promising applications.

2.3.1 Biochar

Biochar (BC) is made from waste biomass from a wide range of sources such as reed (Singh and Majumder 2018), rice husks (Yadav and Jagadevan 2020), straw (Angelin et al., 2021), teak peel, and algae. BC is a carbon-rich, fine-grained, porous, and highly aromatized material and well suited as an adsorbent for the resource utilization of waste. BC contains lignocellulosic components capable of effectively adsorbing fluoride (Yadav and Jagadevan 2020). The pyrolysis temperature is a key factor in controlling the number of functional groups on the surface of BC (Wang et al., 2021). Generally, biochar prepared by hydrothermal pyrolysis below 573 K is rich in oxygen-containing functional groups (-COOH, -OH, etc.) and has stronger ion exchange capacity (Naga Babu et al., 2020). As the pyrolysis temperature increases, the abundance of hydroxyl, amino, and carboxyl groups decrease and the degree of carbonation increases (Kumar et al., 2020). Biochar prepared at 673–973 K has developed porosity (**Figure 3A**) and thermal stability (Goswami and Kumar 2018). Brunson and Sabatini (2015) recorded a significant increase in specific surface area (from 0.9 m^2/g to 327 m^2/g) and surface zero charge point (from pH_{PZC} = 5.8 to pH_{PZC} = 9.4) when the pyrolysis temperature of charcoal was increased from 573 to 873 K. BC also contains minerals such as potassium, calcium, magnesium, and phosphorus, which can be complex with fluoride ions or precipitate. Lee et al. (2021) found that the shell biochar could contain up to 56.9% $CaCO_3$, and when the pyrolysis temperature was raised to 1073 K, $CaCO_3$ was converted to $Ca(OH)_2$; the structure was more conducive to the adsorption of fluoride. The adsorption mechanism was outer-sphere complexation between Ca and F. Although shell biochar has low carbon content and small specific surface area (S_{BET} = 4.363 m^2/g), the maximum fluoride adsorption capacity of their prepared shell biochar MCS-800 could reach 82.93 mg/g. The biochar obtained by pyrolysis alone has an average low adsorption effect but has the advantage of being easily modified (Wang et al., 2021).

2.3.2 Activated Carbon

Activated carbon (AC) is usually made from coconut shells, hard cores, bamboo, coal, wood, and other raw materials (Collivignarelli et al., 2020), and the pyrolysis temperature is generally higher than 1173 K (Araga et al., 2019). After pyrolysis, further physical or chemical activation is required (Chen et al., 2019). Chemical activation has high activation yield but is highly corrosive to the equipment (Tomar et al., 2014). As shown in **Figure 3B**, AC has the advantage of high porosity and large

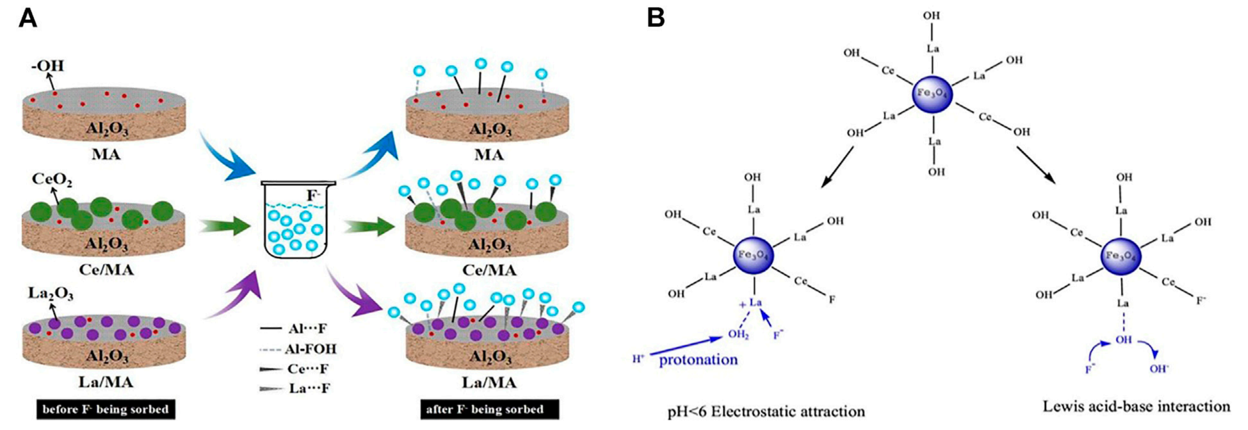

FIGURE 4 | Schematic principle of modification on Al_2O_3 **(A)** (He et al., 2019) and Fe_3O_4 **(B)** (Han et al., 2019) by La, Ce, and fluoride adsorption mechanism.

specific surface area. Araga et al. (2017) and Bhomick et al. (2019) used KOH to activate mustard seed activated carbon and commercially available activated carbon, respectively, and the modified specific surface area reached 747 m^2/g and 1,005 m^2/g, respectively. The -OH group on the AC surface is protonated with fluoride at $pH < pH_{PZC}$ (acidic media). Numerous studies have demonstrated that fluoride adsorption on AC consists of the mechanism for the deprotonation of -OH functional groups on carbon surfaces (He et al., 2020).

2.3.3 Bone Char

Bone char is the charring product of animal bones and generally contains about 20% carbon and 80% hydroxyapatite (HAp) (Medellin-Castillo et al., 2014), with the content of each component varying slightly depending on the charring temperature. When the charring temperature is below 573 K, more organic matter remains in the bones, but the specific surface area and pore structure is not well developed (Zhou J. et al., 2019). The charring temperatures above 873 K may change the structure of the hydroxyapatite and also lead to reduction in fluoride adsorption capacity. The fluoride adsorption by bone char is reported to be mainly carried out by hydroxyapatite. Medellin-Castillo et al. (2014) found that fluoride in aqueous solutions was mainly adsorbed to HAp in bone char but not to other components. HAp in bone char contains most of the OH^- that can be replaced by F^-; the adsorption mechanism includes ion exchange and chemical precipitation. The detailed mechanism of fluoride adsorption by HAp is described in the following section.

2.4 Other Types of Adsorbents

Other materials such as natural mineral clays (clay (Zhang S. et al., 2016), bentonite (Mudzielwana et al., 2017), etc), industrial solid waste (zeolite (Ghosal and Gupta 2018), etc), and hydroxyapatite are also used for fluoride adsorption. Natural clay (**Figure** 3C) contains the main compounds SiO_2 and Al_2O_3 and has the chemical potential to adsorb fluoride (Guiza et al., 2019). Zeolite is an aqueous skeletal structure composed of aluminosilicate minerals with the lattice of many pores and channels that have the structural potential to adsorb fluoride. However, these two types of materials usually show weak fluoride adsorption capacities (**Table 2**) and are generally modified by chemical activation or metal loading.

2.4.1 Hydroxyapatite

Hydroxyapatite [$(Ca_{10}(PO_4)_6(OH)_2$, HAp] is also a promising inorganic material for fluoride adsorption, with excellent biocompatibility, stability, and mechanical properties. Due to its unique crystal structure, HAp has a porous surface, large specific surface area, and high ion exchange capacity. The hydroxyl group in HAp is prone to rapid exchange with anion and has a strong binding capacity with fluoride (Raghav et al., 2018). F^- replaces OH^-, fills in the lattice of HAp forming insoluble fluorapatite (FAp), and OH^- is released into solution. When high concentrations of fluoride ions are present in the solution, Ca^{2+} in HAp reacts with F^- forming CaF_2 precipitate, and phosphate is correspondingly released into the solution. Various forms of HAp have been reported for fluoride adsorption in water, such as nano-hydroxyapatite (Mourabet et al., 2015; Zendehdel et al., 2017), porous hydroxyapatite (Nijhawan et al., 2020), and layered hollow hydroxyapatite (Gao et al., 2019). The mechanism of fluoride adsorption by HAp mainly consists of the following: 1) electrostatic attraction by the surface of HAp to F^-. 2) Anion exchange between OH^- or PO_4^{2-} and F^-. 3) Complexation reaction of Ca^{2+} with F^- ligates and forms surface precipitation. 4) F^- can also form hydrogen bonds with OH^- in the HAp lattice.

3 NEW COMPOSITE ADSORBENTS OBTAINED FROM METAL MODIFICATION

Over long periods of use and development, traditional adsorbents have gradually revealed the unique application value and drawbacks. Compared to the exploitation of novel adsorbents, research tends more to synthesize complexes of two or more adsorbents to produce synergistic fluoride adsorption. The

TABLE 3 | Adsorption conditions and performance of fluoride by muti-metal and metal-biopolymer composite adsorbents.

Adsorbents	Adsorption condition					Isotherm model	Regeneration performance	Q_{max} (mg/g)	Ref
	Initial C_{F^-} (mg/L)	Adsorbent dose (g/L)	Reaction pH	Temperature (K)	Equilibrium time (min)				
Mn–Al binary metals	380	—	7	298	720	Langmuir	-	94.83	Wu et al. (2017a)
Ce–Zn binary metals	10	0.15	3–7	298	45	Langmuir	68% at sixth cycle	64.66	Dhillon et al. (2017)
Ce–Ti oxide	10	1	7	298	—	Langmuir	—	44.37	Abo Markeb et al. (2017)
Mg/Fe-LDHs	30	4	7	298	150	Langmuir	—	28.65	Wu et al. (2015)
Fe-La	10	1	6	298	60	Langmuir	—	27.42	Wang et al. (2018c)
La/MA	10	2	6	298	360	Sips	70% at fifth cycle	26.45	He et al. (2019)
Fe–Ag magnetic oxide	10	0.5	3	298	20	Langmuir	85% at sixth cycle	20.57	Azari et al. (2015)
La-modifying Fe_3O_4	5	10	7.4	303	600	Langmuir	—	1.51	García-Sánchez et al. (2016)
Al-modifying Fe_3O_4	5	10	6.6	303	600	Langmuir	—	1.42	García-Sánchez et al. (2016)
Ca-Mg-Zr oxide	100	0.5	7	298	160	Freundlich	70% at fifth cycle	370.37	Wang et al. (2022)
Ce-Ti@Fe_3O_4	10	1	7	298	15	Langmuir	93% at fifth cycle	91.04	Abo Markeb et al. (2017)
Fe_3O_4@La-Ce	10	0.5	4	303	60	Freundlich	—	56.80	Han et al. (2019)
Fe_3O_4@Fe-Ti	4	1	7	298	2	Langmuir	77% at ninth cycle	41.80	Zhang et al. (2016a)
Fe-Mg-La	10	0.1	7	298	300	Langmuir	90% at third cycle	185.90	Yu et al. (2015)
Al-Zr-La	200	0.5	3	308	500	Langmuir	—	90.48	Zhou et al. (2018)
Mg/Fe/La	5	0.5	7	308	100	Langmuir	57% at fifth cycle	59.34	Wu et al. (2017b)
Fe-Mg-La	20	1	7	298	360	Langmuir	—	40.40	Chen et al. (2018)
Mg-Al-Fe LDH	2	1.5	6	298	600	Sips	—	20.00	Hongtao et al. (2018)
Fe-Al-Ce-Ni	10	0.4	5	303	50	Freundlich	50% at sixth cycle	250.00	Raghav and Kumar (2018)
SA-Ca@Fe/La/Ni	10	30	5	303	30	Freundlich	55% at fifth cycle	333.00	Sapna et al. (2018)
Pectin-Fe/Al/Ni	10	0.4	7	318	90	Freundlich	86% at fifth cycle	285.00	Raghav and Kumar (2019)
Alginate-Fe/Al/Ni	10	0.4	7	298	90	Langmuir	84% at fifth cycle	200.00	Raghav and Kumar (2019)
SA/pectin-Fe/Al/Ce	60	0.1	7	298	35	Halsey	65% at ninth cycle	142.90	Raghav et al. (2019)
SA/CMC-Ca-Al	40	-	2	298	600	Langmuir	—	101.40	Wu et al. (2016b)
SA-Mg/Fe oxide	10	10	7	298	600	Langmuir	80% at third cycle	32.31	Wu et al. (2017c)
SA-Mg/Al/Zr	40	2.5	6	303	1800	Freundlich	—	31.72	Wang et al. (2017a)
SA-Mg/Al/Ce	40	5	6	303	3,600	Freundlich	65% at third cycle	26.12	Wang et al. (2018a)
Pectin Fe bead	10	2	5	298	600	Freundlich	—	20.00	Sharma et al. (2019)
CS-Ce	30	0.3	3	293	400	Langmuir	80% at fourth cycle	153.00	Zhu et al. (2017)
Fe_3O_4/CS/$Al(OH)_3$	10	0.1	5	298	60	Langmuir	—	76.63	Hu et al. (2018)
Fe-Al-Mn@CS	6	0.5	7	298	160	Langmuir	—	40.50	Chaudhary et al. (2021)
Rare earth CS bead	10	2	5	298	480	Freundlich	70% at seventh cycle	22.35	Liang et al. (2018)
La^{3+} magnetic CS	10	2	5	298	480	Langmuir	40% at seventh cycle	20.53	—
Zr-CS bead	20	1	7	303	80	Freundlich	—	17.47	Prabhu and Meenakshi (2015)
La-CS bead	20	1	7	303	80	Freundlich	—	14.49	—
Ce-CS bead	20	1	7	303	60	—	—	11.50	—
Al-CS bead	20	1	7	303	40	—	—	7.45	—
Fe_3O_4@TiO_2-CS	2	0.4	5	298	30	Langmuir	75% at sixth cycle	14.62	Sadeghi et al. (2019)
Fe_3O_4-CS	5	1	7	293	60	Freundlich	88% at fifth cycle	9.26	Mohseni-Bandpi et al. (2015)

(Continued on following page)

TABLE 3 | (*Continued*) Adsorption conditions and performance of fluoride by muti-metal and metal-biopolymer composite adsorbents.

Adsorbents	Adsorption condition					Isotherm model	Regeneration performance	Q_{max} (mg/g)	Ref
	Initial C_{F^-} (mg/L)	Adsorbent dose (g/L)	Reaction pH	Temperature (K)	Equilibrium time (min)				
La-CS/β cyclodextrin	10	2	7	303	30	Freundlich	56% at fifth cycle	8.14	Preethi and Meenakshi (2018)
Ce-cellulose nanobead	2.5	1	3	303	50	Langmuir	82% at fifth cycle	39.88	Sarkar and Santra (2015)
CMKGM-La-Al	40	2	2	40	120	Langmuir	-	20.37	Wu et al. (2016a)

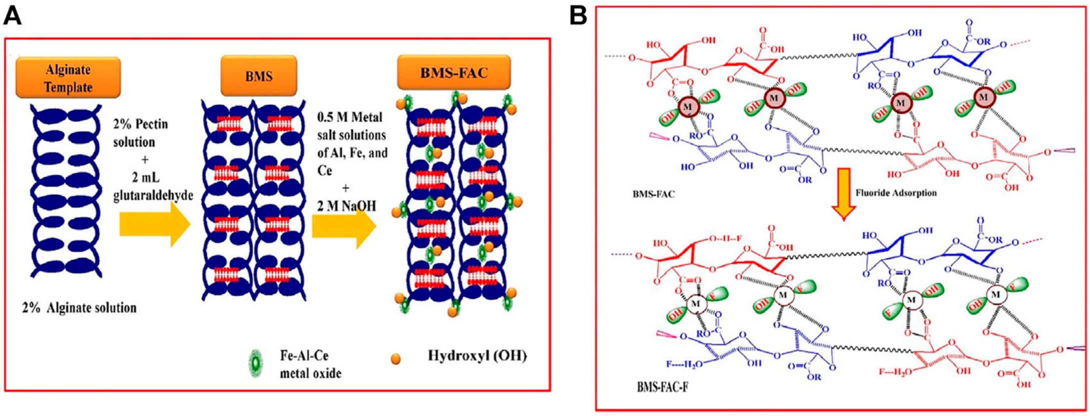

FIGURE 5 | Schematic principle **(A)** and fluoride adsorption mechanism **(B)** of multi-metal–modified sodium alginate and pectin (Raghav et al., 2019).

synthesis of metal modifications to other types of adsorbents accounts for the majority.

3.1 Multi-Metal Oxide/Hydroxide Adsorbents

Different metal oxide adsorbents have their individual strengths and weaknesses for fluoride removal, so recently there have been research studies using multi-metal oxide/ hydroxide adsorbents (Chen et al., 2018). Compared to conventional metal oxides, various valence cations are often present in one multi-metal oxide, providing more chemisorption sites (Raghav and Kumar 2018). The tunability of the chemistry of each element ensures an abundance of active sites, and the components can be adjusted to each other, possessing different outstanding properties and therefore having unique quantum coupling effect and synergistic effects, resulting in more than doubling or tripling of the adsorption capacity. There are two common types of multi-metal oxide adsorbents. One is prepared by compounding each metal element in a certain ratio (Wu K. et al., 2017) such as layered double/triple hydroxides (Wu P. et al., 2017), and the other is to modify one metal oxide with others; the ones mostly reported are modified alumina (He et al., 2019) or magnetic iron oxides.

3.1.1 Layered Double/Triple Hydroxides

A series of layered double/triple hydroxides (LDHs) have a high affinity for anions with high ion exchange capacity and high adsorption volume, which are often used as anion exchangers and trapping agents. LDHs are two-dimensional layered materials whose structural formula can be expressed as $[M^{2+}_{1-x} M^{3+}_{x} (OH)_2]^{x+} (A^{n-})_{x/n} \cdot mH_2O$, where M^{2+} is the positive divalent metal ion (Mg^{2+}, Cu^{2+}, Ni^{2+}, Zn^{2+}, etc.), M^{3+} is the positive trivalent metal ion (Fe^{3+}, Al^{3+}, La^{3+}, Ce^{3+}, etc.), and A is the interlayer anion (Cl^-, CO_3^{2-}, NO_3^-, etc.). LDH consists of positively charged main lamellae and negatively charged interlayer ions. The lamellar structure of LDH is longitudinally stable (Wu et al., 2015). This lamellar structure facilitates adequate contact between the metal sites and the fluoride ions during adsorption and accelerates the charge transfer at the interface. The surface of the main layer is rich in hydroxyl functional groups, which bind to cations in different ways such as electrostatic gravitational forces and hydrogen bonding, providing a large anion exchange capacity with fluoride ions. The synthesis of triple hydroxide by doping of layered double hydroxide with high-valent metal cations has been shown to be effective in enhancing its adsorption activity. When the highly valent cation M^{3+} replaces M^{2+}, the main lamellae are positively charged and therefore require the interlayer anions to be negatively charged to balance the overall charge (Hongtao

TABLE 4 | Summary of modification methods, characteristics, and adsorption mechanisms of muti-metal and metal-biopolymer composite adsorbents.

Adsorbents	Modification method	Dimension	SBET (m2/G)	Aperture (nm)	pHPZC	Adsorption mechanism	Ref
Mn–Al binary metals	Oxidation and coprecipitation	—	43	0.33	8.7	Surface complexation	Wu et al. (2017a)
Ce–Zn binary metals	Coprecipitation, calcination at 873 K	22.4 nm	499	15	6	Ion exchange	Dhillon et al. (2017)
Ce–Ti oxide	Coprecipitation	1–2 nm	—	—	—	Ion exchange	Abo Markeb et al. (2017)
Mg/Fe-LDHs	Coprecipitation, hydrothermal at 543 K	100 nm	—	—	10.42	Ion exchange	Wu et al. (2015)
Fe-La	Coprecipitation, hydrothermal at 423 K	—	113	21.78	8.5	Ion exchange	Wang et al. (2018c)
La/MA	Impregnation, calcination at 673 K	—	237	4.81	10.2	Electrostatic attraction, chemisorption	He et al. (2019)
Fe–Ag magnetic oxide	Coprecipitation	5 nm	254	0.13	6.03	Ion exchange	Azari et al. (2015)
La-modifying Fe3O4	Lanthanum hydroxide soaking	—	6	—	> 10	Electrostatic attraction	García-Sánchez et al. (2016)
Al-modifying Fe3O4	Aluminum hydroxide soaking	—	5	—	> 10	Electrostatic attraction	García-Sánchez et al. (2016)
Ca-Mg-Zr oxide	Hydrothermal, calcination at 923 K	—	119	14.03	11.5	Electrostatic attraction, ion exchange	Wang et al. (2022)
Ce-Ti@Fe3O4	Coprecipitation	15 nm	—	—	—	Ion exchange	Abo Markeb et al. (2017)
Fe3O4@La-Ce	Coprecipitation	—	40	20.3	6	Ligand exchange, electrostatic attraction	Han et al. (2019)
Fe3O4@Fe-Ti	Precipitation of Fe3O4@Fe-Ti, granulation	10 μm	99	15.3	-	Ion exchange	Zhang et al. (2016a)
Fe-Mg-La	Coprecipitation	40 μm	—	—	6.3	Ion exchange	Yu et al. (2015)
Al-Zr-La	Coprecipitation	—	36	—	8.4	Electrostatic attraction, ion exchange	Zhou et al. (2018)
Mg/Fe/La	Hydrothermal, calcination at 873 K	—	59	22.3	—	Surface complexation, ion exchange	Wu et al. (2017b)
Fe-Mg-La	Coprecipitation	65 nm	78	30	8.8	Ligand exchange	Chen et al. (2018)
Mg-Al-Fe LDH	Coprecipitation	—	130	24.47	—	Interlayer ion exchange	Hongtao et al. (2018)
Fe-Al-Ce-Ni	Coprecipitation, calcination at 873 K	—	184	51.43	6.2	Ion exchange, electrostatic attraction	Raghav and Kumar (2018)
SA-Ca@Fe/La/Ni	Fe-La-Ni oxides mixing SA, CaCl2 cross-linking	1–2 mm	257	10.4	7	Ion exchange, H-bonding	Sapna et al. (2018)
Pectin-Fe/Al/Ni	Aerogel formation by coprecipitation, freezing	886 nm	275	0.15	—	Isomorphic substitution	Raghav and Kumar (2019)
Alginate-Fe/Al/Ni	Aerogel formation by coprecipitation, freezing	914 nm	96	0.13	—	Isomorphic substitution	Raghav and Kumar (2019)
SA/pectin-Fe/Al/Ce	Fe-Al-Ce coprecipitation with pectin and alginate	—	275	—	7.17	Ion exchange, H-bonding, complexation	Raghav et al. (2019)
SA/CMC-Ca-Al	SA/CMC mixing, Ca2+ cross-linking, Al3+ soaking	2–2 mm	—	—	—	Coordination reaction	Wu et al. (2016b)
SA-Mg/Fe oxide	Mg/Fe oxide mixing SA, CaCl2 cross-linking	1 mm	—	—	10.52	Ligand exchange, electrostatic attraction	Wu et al. (2017c)
SA-Mg/Al/Zr	Mg-Al-Zr oxide mixing SA, CaCl2 cross-linking	1 mm	—	—	—	Ion exchange, electrostatic attraction	Wang et al. (2017a)
SA-Mg/Al/Ce	Mg-Al-Ce oxide mixing SA, CaCl2 cross-linking	—	—	—	—	Ion exchange	Wang et al. (2018a)
Pectin Fe bead	Grafting, FeCl3 impregnation	43 nm	—	—	—	Ligand exchange	Sharma et al. (2019)
CS-Ce	Coprecipitation, glutaraldehyde cross-linking	200 nm	17	—	5.3	Electrostatic attraction, ligand exchange, and complexation	Zhu et al. (2017)
Fe3O4/CS/Al(OH)3	AlCl3 mixing, Fe3O4 NP adding	200 nm	—	—	—	Electrostatic attraction, complexation	Hu et al. (2018)
Fe-Al-Mn@CS	Coprecipitation	—	42	—	—	—	Chaudhary et al. (2021)
Rare earth CS bead	Rare earth mixing, Fe3O4 adding, cross-linking	—	21	7.92	5	Ligand exchange	Liang et al. (2018)
La3+ magnetic CS	La mixing, Fe3O4 adding, cross-linking	—	17	8.15	5	Ligand exchange	—

(Continued on following page)

TABLE 4 | (*Continued*) Summary of modification methods, characteristics, and adsorption mechanisms of muti-metal and metal-biopolymer composite adsorbents.

Adsorbents	Modification method	Dimension	SBET (m2/G)	Aperture (nm)	pHPZC	Adsorption mechanism	Ref
Hyper-branched CS beads	Glutaraldehyde cross-linking, Zr, La, Ce, Al solution immersion	1.7 mm	3	—	7	Electrostatic attraction, ligand	Prabhu and Meenakshi (2015)
Fe3O4@TiO2-CS	Fe3O4@TiO2 impregnation CS	—	—	—	6	Electrostatic attraction, H-bonding	Sadeghi et al. (2019)
Fe3O4-CS	FeCl3 impregnating CS, coprecipitation	0.15 mm	499	3.4	7	—	Mohseni-Bandpi et al. (2015)
La-CS/β cyclodextrin	Mixing, 5% glutaraldehyde cross-linking	—	—	—	4.56	Electrostatic attraction, H-bonding	Preethi and Meenakshi (2018)
Ce-cellulose nanobead	Impregnation	45 nm	—	—	—	Ion exchange	Sarkar and Santra (2015)
CMKGM-La-Al	La, Al mixed solution cross-linking	-	—	—	—	Ion exchange, electrostatic attraction	Wu et al. (2016a)

et al., 2018). The addition of rare earth metals has been reported to further enhance the affinity with fluoride. Wu P. et al. (2017) introduced La into Mg/Fe LDH to form Mg/Fe/La hydrotalcite-like compounds with layered porous structure, which significantly enhanced the fluoride adsorption capacity of Mg/Fe LDH.

3.1.2 Metal-Modified Magnetic Iron Oxides

Al- and Fe-based oxides are mostly doped or load-modified by another metal. Metal-modified Al_2O_3 generally adsorbs fluoride by complexation and ion exchange (**Figure 4A**). Iron oxides (Fe_3O_4 or γ-Fe_2O_3), in addition to adsorption advantages, provide strong magnetic properties and large magnetic response with easy separability and controllability; thus, there have been more reported recently. Magnetic iron oxide nanoparticles can be used directly for fluoride adsorption or as a nucleus material for core-shell particles. The magnetic core particles are generally combined with metal oxide nano-shells by methods such as surface coating to ensure stronger magnetic response, more functional groups, and better properties (Zhang C. et al., 2016). Recent research has mostly used rare earth metals to modify magnetite. Rare earth ions are greater in radius than other elements in the iron oxides; doping with the appropriate amount of rare earth elements to replace some of the other elements in the iron oxides with a smaller ion radius distorts the lattice and can improve the physical activity. Most importantly, the hard Lewis acid nature of the rare earth metal ions (especially La) has a strong affinity for fluoride (**Figure 4B**) (Han et al., 2019). Ce can promote the dispersion of nanoparticles, giving the adsorbent a larger specific surface area, pore volume, and more active functional sites. Correspondingly, magnetic particles can attenuate the agglomeration effect of rare earth metal oxides, reducing the amount of precious metals used and improving the separation characteristics by magnetic assistance to reduce residues in water and avoid rare earth metal toxicity (Abo Markeb et al., 2017). Han et al. (2019) used VSM tests to show that Fe_3O_4 and Fe_3O_4@La-Ce were both superparamagnetic, and it was easy to separate the particles from the solution using the external magnetic field. The adsorption amount of Fe_3O_4@La-Ce was increased up to 20 times compared to Fe_3O_4.

3.2 Metal-Biopolymer Adsorbents

Large-scale applications for fluoride removal in aqueous systems require the development of composite hydrogel materials with good mechanical properties and stability. For hydrogels with poor adsorption properties, the cross-linking of composites by cementing other high performance adsorbent materials onto biopolymers can effectively reduce the degradation of properties. The preparation of biopolymer-based composites is divided into three types: 1) doping of metals/metal oxides (Sapna et al., 2018), 2) blending with inorganic materials (Wang et al., 2020), and 3) mixing between polymeric organic substances (Preethi and Meenakshi 2018). This section summarizes the doping by metal oxide modification studies.

3.2.1 Metal-Doped Alginate/Pectin

The biocompatibility and biodegradability of natural polymeric materials make sodium alginate and pectin effective substrates for the incorporation of multivalent metal ions. Studies have reported to dope SA with metals; co-mingling and cross-linking to form a stable gel structure can improve both the stability and mechanical properties of SA (Wu T. et al., 2017), while having an anchoring effect on metal oxides, reducing the agglomeration and leaching of metal oxides and maximizing the adsorption properties (He et al., 2020). Furthermore, the doping of metals can increase the metal active sites in the porous structure and combine the properties of organic and inorganic components to improve the adsorption capacity (Zhao et al., 2021). Mono and multi-metal doping options are available. Recent research has focused on the doping of sodium alginate and pectin with multi-metals. Compared to monometals, the multi-metals provide an enhanced abundance of active sites as mentioned earlier. In addition, the multi-metals used in the studies tend to be the composite of +2 valent and higher valent cations. The addition of +3 and +4 valent metal ions, especially rare earth metals, can improve the stability, recyclability, and adsorption capacity. Raghav and Kumar (2019) obtained a high adsorption capacity (**Table 3**) for all the composite hydrogels prepared by SA and pectin embedding Fe-Al-Ni (285 mg/g and 200 mg/g) and SA/pectin co-embedding Fe-Al-Ce (142.9 mg/g) (Raghav et al., 2019). **Figure 5** shows the

TABLE 5 | Summary of modification methods, characteristics, and adsorption mechanisms of metal-modified carbon and other adsorbents.

Adsorbents	Modification method	Dimension	S_{BET} (m^2/G)	Aperture (nm)	pH_{PZC}	Adsorption mechanism	Ref
Wood biochar-La	Impregnation, pyrolysis	0.8 mm	165	3.91	6.6	Ion exchange	Habibi et al. (2019)
Al-modified corn biochar	Pyrolysis at 623 K, coprecipitation	—	1	410	2	Ion exchange	Zhang et al. (2021a)
MgO shell biochar	Impregnation, one-step calcination	0.5 μm	182	2–10	—	Electrostatic attraction, complexation	Wan et al. (2019)
Pomelo peel BC-La	Impregnation, calcination at 1073 K	—	269	—	5.8	Ion exchange	Wang et al. (2018b)
ZrO_2-seed shell biochar	One-step impregnation and calcinationT	—	—	—	4.45	Ion exchange	Mei et al. (2020)
Magnetic biochar	Charring, impregnation-pyrolysis	100 μm	494	0.3	11	Electrostatic attraction, H-bonding	Bombuwala Dewage et al. (2018)
Mg-Mn-Zr AC	Ultrasound impregnation, coprecipitation	—	834	2.43	11.9	Electrostatic attraction, ion exchange	Mullick and Neogi (2019)
Zr-impregnated AC	Ultrasonic impregnation	14 μm	1,104	2.30	5.03	Electrostatic attraction	Mullick and Neogi (2018)
La-functionalized AC	Impregnation, rotary evaporation, heat	0.5 mm	367	0.68	7.3	Ligand exchange, electrostatic attraction	Merodio-Morales et al. (2019)
Activated carbon@ SnO_2	Ultrasound impregnation, precipitation	—	126	3.54	3	Ion exchange, physical adsorption	Mohanta and Ahmaruzzaman (2018)
Ce-containing bone char	Impregnation, heat treatment	0.7 mm	—	—	—	Electrostatic attraction, ion exchange	Zúñiga-Muro et al. (2017)
Magnetic bone biochar	Impregnated biomass, calcination	—	42	17.45	2.4	Ion exchange	Zhou et al. (2019a)
Graphene oxide with Ti	Hydrothermal at 453 K, calcination	—	278	2.55	7	Electrostatic attraction, ion exchange	Nehra et al. (2019)
Al-polyacrylic acid	Impregnation	—	44	84.63	6	Electrostatic attraction, ion exchange	Xu et al. (2017)
CeO_2@SiO_2 microsphere	Coprecipitation	117 μm	86	25–97	3.9	Electrostatic attraction, chemisorption	Wang et al. (2019a)
Magnetic γ-Fe_2O_3-GO-La	Fe coprecipitation, La impregnation, calcination	—	—	—	7.9	Ion exchange, complexation	Wen et al. (2015)
Zn-modifying slag	Impregnation	0.1 mm	58	—	7.9	Ion exchange	Sarkar et al. (2019)
ZrO_2-graphene oxide	One-step ultrasound hydrothermal	—	632	—	7.3	Ligand exchange, electrostatic attraction	Mohan et al. (2016)
Hydrous Fe/Al GO	Coprecipitation, impregnation	200 μm	—	—	6	Electrostatic attraction, ion exchange	Kanrar et al. (2016)
Fe-modifying pumice	Impregnation	200 μm	25	—	3	—	Dehghani et al. (2016)
FeOOH–graphene oxide	In-suit hydrolysis	—	203	7.1	1.8	Ion exchange	Kuang et al. (2017)
Aluminum/olivine	Wet impregnation, calcination	—	—	—	—	Physical adsorption	Ghosal and Gupta (2018)
Polyhydroxy-iron	Impregnation	—	100	—	8	—	Muschin et al. (2021)
3D Y-GO hydrogels	GO-mixing SA, YCl_3 cross-linking	—	147	15.26	6.74	Ion exchange	He et al. (2018)
Al2O3-chitosan biochar	HBO_3 cross-linking, calcination	—	—	—	6	Ion exchange	Jiang et al. (2018)
Graphene oxide/ eggshell	Impregnation	—	—	—	—	—	Nor et al. (2020)
Ce-SA/BC beads	SA/BC mixing, $CeCl_3$ cross-linking, calcination	2 mm	237	3.97	8.26	Ion exchange, electrostatic attraction	Wei et al. (2022)
Ca-pectin-hydroxyapatite	Coprecipitation	—	157	3.1	7	Ion exchange, electrostatic attraction	Raghav et al. (2018)
Polypyrrole onto BC	Mixing, $FeCl_3$ impregnation	—	—	—	8.6	Ion exchange	Wang et al. (2017c)

reaction process of multi-metal–modified SA and pectin and the exchange sites for fluoride adsorption.

3.2.2 Metal-Doped Chitosan

Chitosan (CS) is an N-deacetylated derivative of the natural polysaccharide chitin and is rich in free amino acids. The -NH_2 group in chitosan is more reactive (Zhu et al., 2017), easy to be chemically modified (Chaudhary et al., 2021), and exhibits high adsorption potential. Despite the numerous advantages such as biodegradability, biocompatibility, flexibility, hydrophilicity, and versatility, CS tends to be readily soluble in acidic solutions and has a weak chemical resistance

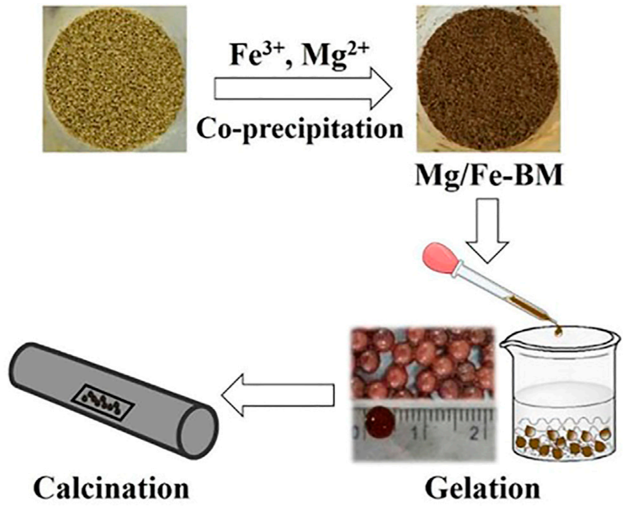

FIGURE 6 | Coprecipitation method for preparation of $MgFe_2O_4$-doped biochar and ionic cross-linking process of composite sols (Wang et al., 2020).

(Dong and Wang 2016), especially in column continuous flow adsorption. Current research into the adsorption of fluoride ions by CS is also mostly metal-doped, but unlike sodium alginate and pectin, the modification of CS is more oriented toward monometallic impregnation followed by cross-linking using glutaraldehyde (**Table 4**). The size of the beads formed is much smaller, typically in the micron range (Prabhu and Meenakshi 2015). One of the top research hotspots is the magnetic modification of Fe_3O_4, mainly because the hydroxyl group on the surface of Fe_3O_4 can interact with the amino and hydroxyl groups of CS through hydrogen bonding (Sadeghi et al., 2019), enabling CS to remain stable under acidic conditions. The CS composite adsorbent is also endowed with magnetic ease of separation properties (Mohseni-Bandpi et al., 2015). Hu et al. (2018) obtained nano-microsphere Fe_3O_4/CS/Al$(OH)_3$ beads by facile impregnation, which can rapidly accomplish high capacity adsorption of fluoride and rapid sedimentation under low magnetic fields.

3.3 Metal-Carbon Adsorbents

Carbon-based adsorbents have the advantage of large specific surface area and rich pore structure (Shang et al., 2022), but they have low adsorption capacity for fluoride removal alone and require some modification. Research on carbon composites has focused on the doping or surface loading of carbon with nano-metal oxides/hydroxides (Dehghani et al., 2018). The affinity between fluoride ions and highly valent cations such as Al^{3+}, Fe^{3+}, Ca^{2+}, and Mg^{2+} can improve the selectivity of carbon to fluoride. When the two are compounded, on the one hand, the metal nanoparticles provide a large number of active sites (Mohanta and Ahmaruzzaman 2018) to compensate for the absence of functional groups that can interact with fluoride ions after high temperature carbonization. On the other hand, the carbon-based adsorbent has large specific surface area and pores, which can act as carriers and dispersants to avoid agglomeration of the metal nanoparticles (Cai et al., 2022). More individual metal loadings are used, and multi-metal modifications are also available. More active sites enhance the adsorption performance, and the modified adsorbent surface is richer in specific types of adsorption sites, which may further increase the adsorption capacity.

3.3.1 Metal-Modified Biochar

The ability of biochar to remove pollutants is greatly influenced by the nature of the raw material, preparation technology, and pyrolysis conditions. Unsuitable pyrolysis conditions tend to under-carbonize or over-carbonize BC, so the adsorption performance of unmodified BC is limited. The raw biochar has a relatively poor adsorption effect on anions as the negative charge occupies the majority of the functional groups (Mei et al., 2020). Highly valent metal cations can provide sufficient positive charge to effectively alter surface physicochemical properties (Wang et al., 2019c). $AlCl_3$ has been reported to generally increase the anion exchange capacity in all BC. Brunson and Sabatini (2015) studied the changes in charcoal surface area and surface chemistry following aluminum nitrate impregnation and found that the aluminum modification reduced the zero charge point of the charcoal in water (from pH_{PZC} = 9.6 to pH_{PZC} = 5.7) but significantly increased the adsorption capacity. Rare earth metal ions such as Ce^{3+}, Zr^{4+}, and La^{3+} are more alkaline, have a relatively low ionic potential, and show strong tendency to dissociate hydroxyl groups into ions. The possibility of ionic exchange with F^- is higher and the affinity is stronger. Habibi et al. (2019) modified woody BC with $LaCl_3$ and showed that the maximum adsorption capacity of 164.23 mg/g and adsorption equilibrium could be reached within 30 min. They concluded that H^+ in functional groups such as carboxyl and sulfate groups on the surface of BC may exchange with La^{3+} ions. The presence of La^{3+} increased the adsorption mechanism with Lewis acid–base interaction and ion exchange. The F^- adsorption rate of the adsorbent was still 80% at fifth recycling, indicating that the rare earth metals loaded on the BC are not easily leached. The modification of iron oxides can confer magnetic properties to BC, improving the separation and recovery performance. BC has good electrical conductivity, which is conducive to electron transfer and reduction of Fe^{3+}. The stronger synergistic effect can further promote the fluoride adsorption performance (Wang et al., 2019c).

3.3.2 Metal-Modified Activated Carbon

Activated carbon has large specific surface area and pores, which can act as carriers and dispersants to avoid agglomeration of the metal nanoparticles (Cai et al., 2022). More individual metal loadings are used, and multi-metal modifications are also available. More active sites enhance the adsorption performance, and the modified adsorbent surface is richer in specific types of adsorption sites, which may further increase the adsorption capacity. Li et al. (2018) precipitated $Ti(OH)_4$ on the surface of AC, which further increased the specific surface area of Ti-AC to 1700 m^2/g, providing more adsorption sites for fluoride ions. They confirmed that the adsorption capacity of Ti-AC was

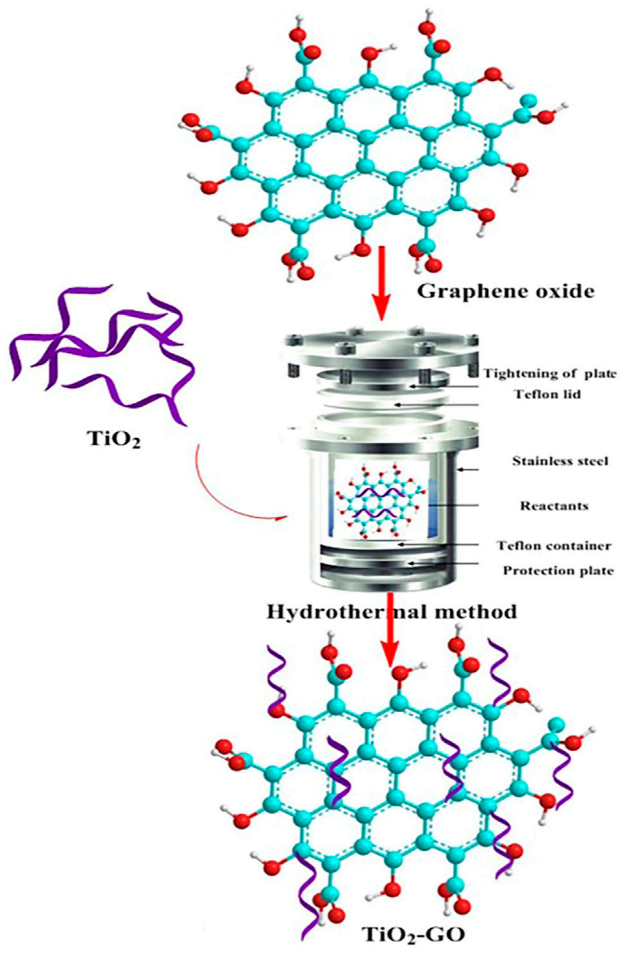

FIGURE 7 | Hydrothermal for the preparation of TiO_2-modified graphite (Nehra et al., 2019).

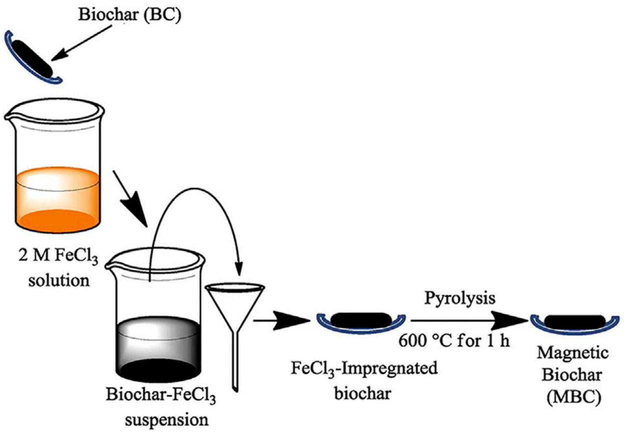

FIGURE 8 | Preparation of magnetic biochar by impregnation and subsequent calcination (Bombuwala Dewage et al., 2018).

produced by $Ti(OH)_4$ loaded on AC. The saturation adsorption capacity of $Ti(OH)_4$ in Ti-AC was 62.1 mg/g, which was much higher than that of $Ti(OH)_4$. It has also been reported that the loading of different metal oxides/hydroxides can form new functional groups on the AC surface with high affinity for fluoride adsorption, significantly improving the adsorption efficiency. A et al. used ultrasonically assisted polymetallic impregnation of AC (Mohanta and Ahmaruzzaman 2018; Mullick and Neogi 2018). The specific surface area decreased after modification, but the pH_{PZC} increased to 11.9 and the adsorption capacity increased by four times compared to monometallic impregnation (Mullick and Neogi 2019).

3.3.3 Metal—Other Types of Adsorbents

Graphene oxide (GO) is a two-dimensional honeycomb carbon nanomaterial formed by the close packing of carbon atoms in a sp-hybridization pattern (Kanrar et al., 2016). GO carries various functional oxygen-containing groups (such as -OH, -COOH, C=O, and -CH(O)CH-) and provides active sites to connect to other substances (Jeyaseelan et al., 2021). GO generally adsorbs fluoride through electrostatic attraction, π-π stacking, and hydrogen bonding. It has been reported to have a huge theoretical specific surface area (up to 2,630 m^2/g) (Mohan et al., 2017) and can be an excellent host for metal nanoparticles. In turn, nanometallic particles provide structural rigidity by inhibiting the restacking of different layers of GO and provide a higher surface area and many active centers (Mohan et al., 2017). Mohan et al. (2017) hydrothermally synthesized ZrO_2/GO with S_{BET} = 632 m^2/g. The fixed-bed continuous flow experiments showed that the desorption elution efficiency of the adsorption column regenerated with 10% NaOH solution was greater than 95% for F^- within three cycles, indicating the role of the ion exchange mechanism in the adsorption of F^-. Nehra et al. (2019) hydrothermally synthesized TiO_2/GO with a maximum fluoride adsorption capacity of 342 mg/g, which is the highest reported capacity available. Ti^{4+} forms strong bonds with the oxygen-containing functional groups of GO by electrostatic attraction and reacts with NaOH on the GO side to form basic titanium hydroxide on the GO layer. The adsorption mechanism for fluoride consists of a complexation reaction with Ti and F and an ion exchange between OH^- and F^-.

3.4 Multiple Types of Metal-Modified Composite Adsorbents

Studies have also reported on composite adsorbents synthesized from three or more types of materials, with combinations of metal-modified biopolymers and inorganic materials making up the bulk of the adsorbents (**Table 5**). The compound of metallic, inorganic, and biomaterials effectively combine the advantages of different types and can yield further synergistic effects. He et al. (2018) achieved a maximum adsorption capacity of 288.96 mg/g for yttrium-based GO/SA hydrogels prepared by sol–gel. Wei et al. (2022) mixed reed biomass powder with SA, cross-linked with $CeCl_3$ solution, and then calcined to obtain cerium alginate biochar beads. The composite adsorbent RBM-Ce has greatly

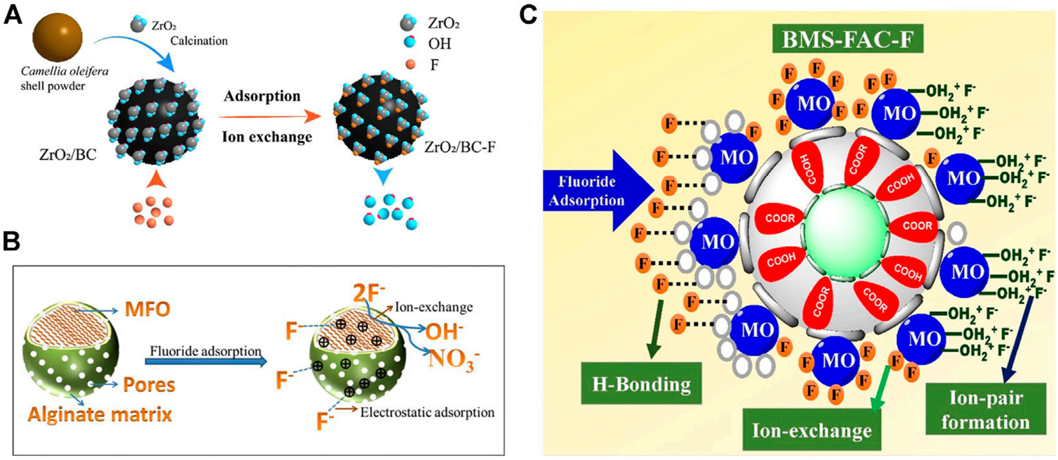

FIGURE 9 | Respective adsorption mechanisms of composite adsorbents from different metal-modified materials. **(A)**: ion exchange (Mei et al., 2020), **(B)**: electrostatic attraction (Wu T. et al., 2017), **(C)**: ion pair (Raghav et al., 2019).

improved the maximum adsorption capacity, S_{BET}, pH_{PZC}, and stability compared to individual components.

3.5 Modified Synthesis Methods

In summary of the aforementioned composite adsorbent synthesis methods (**Tables 4**, **5**), it can be seen that the general principle of metal-modifying adsorbents is to coat the opposing surface with metal salts. The main methods of modification are chemical coprecipitation, impregnation, and hydrothermal methods, which are described here.

3.5.1 Chemical Coprecipitation

Chemical coprecipitation is a common method for the preparation of multi-metals (**Table 4**) and metal-modified inorganic adsorbents (**Table 5**). In the preparation of multi-metal nanoparticles, the chemical coprecipitation method first mixes each metal salt solution in proportion to the atoms of the target product to be prepared to form an aqueous solution of the metal ions. The metal ions are then simultaneously precipitated out of the solution by the addition of appropriate precipitants to form hydroxide precipitate (Wu et al., 2013). The precipitates are separated out and then dried or calcined to obtain powdered multi-metal hydroxide/oxide nanoparticle adsorbents (Zhou et al., 2018). When modifying inorganic adsorbents with metals, the inorganic material is first put into a metal salt solution *via* methods such as adjusting the pH of the solution; the metal ions in the solution are induced to produce nano-metal particles that precipitate and load onto the surface and pore paths of the inorganic material, which are then dried or calcined to form composite adsorbents (**Figure 6**) (Wang et al., 2019b). The coprecipitation method is simple and not time-consuming. However, due to the different precipitation rates of different elements, there is sometimes a stratification of the precipitation, which makes the precipitate not uniformly dispersed and the composition of the product somewhat biased.

3.5.2 Hydrothermal

The hydrothermal method is also commonly used for the preparation of multi-metals (**Table 4**), and some studies have also been used for the modification of other materials by metals. Similarly, the metal ions are first prepared in a mixed solution in a certain proportion and then placed in a hydrothermal reactor at 423–573 K for a specific time. The principle of the hydrothermal method is that in a closed reaction environment, the precursor undergoes high temperature and pressure to fully dissolve in the solvent (Nehra et al., 2019). Then hydrolysis and nucleation according to a certain crystallization mode to grow nano-microcrystalline particles, to obtain a uniform particle size and good dispersion of composite powder (**Figure 7**). The nanomaterials prepared by the hydrothermal method have homogeneous morphology and the products are well dispersed. However, high pressure and temperature-resistant instrumentation are required, with long reaction times and production cycles, which are not conducive to mass production. Thus, it is often used in the laboratory to prepare nanomaterials with special morphologies for research. By controlling the crystallization time, crystallization temperature, and other factors, nanopowders with different morphologies can be prepared.

3.5.3 Impregnation

Impregnation is commonly used for metal-modified inorganic materials (carbon, clay, GO, etc. **Table 5**). The powdered inorganic material is first pre-treated by immersion in a metal salt solution ($AlCl_3$, $CaCl_2$, $FeCl_3$, $LaCl_3$, etc.). The metal ions in the solution can be loaded on an inorganic surface or internally *via* auxiliary heating and ultrasonic dispersion. The composite adsorbent is then dried or calcined (**Figure 8**). The impregnation preparation method is also facile but slightly more time-consuming, relying on the specific surface area of the inorganic material and bonding of the active sites on the surface to the metal.

TABLE 6 | Adsorption conditions and performance of fluoride by metal-modified carbon and other adsorbents.

Adsorbents	Adsorption condition					Isotherm model	Regeneration performance	Q_{max} (mg/g)	Ref
	Initial C_{F}^{-} (mg/L)	Adsorbent dose (g/L)	Reaction pH	Temperature (K)	Equilibrium time (min)				
Wood biochar-La	40	5	6	298	50	Langmuir	53% at sixth cycle	164.20	Habibi et al. (2019)
Al-modified corn biochar	50	1	6.8	298	100	Langmuir	—	74.14	Zhang et al. (2021a)
MgO shell biochar	20	1	6–8	298	360	Langmuir	—	57	Wan et al. (2019)
Pomelo peel BC-La	10	2	6.5	298	1,200	Freundlich	66% at sixth cycle	19.86	Wang et al. (2018b)
ZrO_2-seed shell biochar	10	1.6	3–9	298	180	Langmuir	50% at third cycle	9.63	Mei et al. (2020)
Magnetic biochar	10	2	2–9	308	5	Langmuir	—	9.04	Bombuwala Dewage et al. (2018)
Mg-Mn-Zr AC	10	1	2–10	303	180	Langmuir	—	26.27	Mullick and Neogi (2019)
Zr-impregnated AC	10	2	4	303	180	Langmuir	33% at fifth cycle	5.40	Mullick and Neogi (2018)
La-functionalized AC	200	1	7	303	180	Sips	—	10.51	Merodio-Morales et al. (2019)
Activated carbon@ SnO_2	10	0.3	6	303	180	Langmuir	80% at third cycle	4.60	Mohanta and Ahmaruzzaman (2018)
Ce-containing bone char	50	2	5	303	840	Sips	—	47.16	Zúñiga-Muro et al. (2017)
Magnetic bone biochar	20	5	8	298	1,440	Freundlich	38% at fourth cycle	5.23	Zhou et al. (2019a)
Graphene oxide with Ti	50	3.5	6	308	100	Langmuir	54% at sixth cycle	342	Nehra et al. (2019)
Al-polyacrylic acid	10	1	2	298	200	Freundlich	—	283.48	Xu et al. (2017)
CeO_2@SiO_2 microsphere	50	1.5	3	298	45	Langmuir	57% at fourth cycle	257.70	Wang et al. (2019a)
Magnetic γ-Fe_2O_3-GO-La	10	0.2	7	298	30	Langmuir	78% at sixth cycle	77.12	Wen et al. (2015)
Zn-modifying slag	50	0.5	5	298	30	Freundlich	—	60	Sarkar et al. (2019)
ZrO_2-graphene oxide	25	0.5	7	303	50	Langmuir	59% at fifth cycle	45.7	Mohan et al. (2016)
Hydrous Fe/Al GO	10	3	5	308	60	Langmuir	—	22.9	Kanrar et al. (2016)
Fe-modifying pumice	3	0.7	3	298	50	Freundlich	—	21.74	Dehghani et al. (2016)
FeOOH–graphene oxide	25	2.5	2–10	298	120	Langmuir	—	17.672	Kuang et al. (2017)
Aluminum/olivine	10	2	6	303	60	Langmuir	—	12.94	Ghosal and Gupta (2018)
Polyhydroxy-iron	25	1	7	298	40	Freundlich	—	11.09	Muschin et al. (2021)
3D Y-based GO hydrogels	20	0.2	4	293	1,440	Langmuir	72% at third cycle	288.96	He et al. (2018)
Al2O3-chitosan biochar	20	1	3	298	1,440	Langmuir	—	196.1	Jiang et al. (2018)
Graphene oxide/ eggshell	30	0.25	7	298	120	Langmuir	—	56.6	Nor et al. (2020)
Ce-SA/BC beads	10	1	3–9	293	20	Langmuir	—	34.86	Wei et al. (2022)
Ca-pectin-hydroxyapatite	10	1	7	298	30	Freundlich	—	28.47	Raghav et al. (2018)
Polypyrrole onto BC	10	1	6.5	298	—	Langmuir	53% at 4th cycle	18.52	Wang et al. (2017c)

Some preparations are calcined after coprecipitation, impregnation, or hydrothermal treatment (**Figures 6–8**). For example, metal-modified biochar is calcined to form metal oxide nanoparticles on the surface of BC, which further enhances the adsorption capacity (**Table 5**). LDH is also sometimes calcined (**Table 4**). During heating, LDH can be transformed into mixed metal oxides as the interlayer anions are eliminated by thermal decomposition. After the adsorbent is put into a fluoride solution, it will undergo a rehydration process. During rehydration, these oxides are in turn rebuilt into original layered structures by adsorbing various anions from the aqueous solution, known as the "memory effect" (Wu P. et al., 2017). The specific surface area and anion exchange capacity of LDH increases further after calcination. After coprecipitation or impregnation, the modification of biopolymers is generally achieved by the sol–gel method for the preparation of hydrogels (Wang A. et al., 2017).

3.6 Adsorption Mechanism

The adsorption mechanism can be divided into physical adsorption and chemisorption. Physical adsorption is generally considered to be caused by van der Waals forces, which are nonselective and reversible, and can be desorbed under certain conditions. Current research on the physical adsorption of fluoride ions is mainly based on electrostatic attraction and hydrogen bonding. Chemisorption is mainly the formation of chemical bonds between molecules and is described by the Langmuir model; the adsorption is selective and irreversible and desorption is more difficult. Physical adsorption depends mainly on the active pore volume and specific surface area (Wang H. et al., 2017), while chemisorption depends more on chemical or electro-affinity. The fluoride adsorption mechanism by various metal-modified adsorbents is summarized in **Tables 4**, **5**. A total of four main adsorption mechanisms can be found: electrostatic attraction, ion exchange, hydrogen bonding, and complexation. The actual adsorption process is usually accompanied by several mechanisms (**Figure 9**).

When metal oxide enters the aqueous solution, the hydrogen ions are attracted to lone pair electrons of the oxygen element in metal oxide, forming a hydroxyl ligand (Zhang and Jia 2016). The fluoride removal by metal oxides and metal-modified composite adsorbents exploits the large number of hydroxyl groups on the surface (**Figure 9A**). When the solution pH is less than zero charge point (pH_{PZC}) of the composite adsorbent, hydroxyl functional groups become protonated, forming OH_2^+ and are positively charged. The positive charge surface attracts negatively charged fluoride ions by electrostatic attraction (**Figure 9B**).

Fluoride is attracted to the surface of composite adsorbents for immobilization, but ion pairs (**Figure 9C**) are weakly interacting with each other and easily desorbed. Several studies have confirmed the involvement of hydroxyl groups in the adsorption reaction by FTIR and XPS characterization. F^- has the same charge and similar radius composition as OH^- and can replace OH^- in the structure of composite adsorbents (**Figure 9A**). F^- is bonded to a metal-occupying active site, OH^- is released, and the solution pH rises after adsorption. Most studies have been based on the anion exchange mechanism. As pH rises above the pH_{PZC} of the adsorbent, there is no significant decrease in adsorption. indicating that adsorption is mainly controlled by ion exchange. Generally, when the solution pH > 10, the large amount of free OH^- in the solution competes with F^-, resulting in a significant decrease in adsorption capacity. Complexation between metals and fluoride has also been suggested (Suzuki et al., 2013).

Metal-modified composite adsorbents often have polar functional groups containing hydrogen, such as -OH, -COOH, and $-NH_2$ (Yang et al., 2017). The shared electron pairs of polar functional groups are strongly biased toward oxygen or nitrogen, leaving the hydrogen atom almost naked. The lone pair electrons of electronegative fluoride will interact with the hydrogen atom forming a hydrogen bond with a bond angle of 180° and immobilize (**Figure 9C**).

4 CONCLUSION AND FUTURE DIRECTION

Comparison of **Table 2** with **Tables 3**, **6** reveals an overall increase in fluoride adsorption capacity of metal-modified composites. It indicates that most of the modifications are successful with application prospects. However, there are still many issues that need to be considered to achieve a big breakthrough in practical applications. The multi-metals enrich active sites for fluoride, but agglomeration and easy leaching are still problems, and individual preparation still requires some cost. Metal-modified biopolymers improve the stability of hydrogels, and metals can also be dispersed and immobilized in the macromolecular structure. However, it is reported that the dense surface of hydrogel makes it difficult for fluoride ions to enter the internal pores of beads, and beads sink easily so they have a limited contact area with fluoride. Metal-modified carbon, mineral clay, and other inorganic materials can also improve the dispersion and immobilization of metals to some extent, but there are still problems of dissolution, and loaded metals are easily dislodged and poorly recycled. Low-cost inorganic materials balance the price of rare earth metals and reduce the amount of metals, but at the same time, present the safety risk of waste use. The metal and inorganic materials are both in powder form, and the issue of separation and recycling has not been addressed. Studies combining metals, inorganic materials, and biopolymers appear to address the agglomeration and immobilization of metals, expanding the pore space and fluoride contact area of hydrogel beads, while improving the separation and recovery properties of inorganic materials. However, more than 90% of studies mentioned in this review avoided exploring metal dissolution concentrations and less than 10% of adsorbents were able to achieve more than 80% fluoride adsorption at the fifth cycle. Future studies will need to pay attention to the simplicity, efficiency, and cost of preparation procedure. Overall, the search for future defluoridation adsorbents is not limited to the requirement for increasing adsorption capacity. More important is the attention to cost levels, regeneration performance, separation and recovery, and safety issues for practical applications.

AUTHOR CONTRIBUTIONS

YW summarized and wrote the article under the guidance of LW. All authors contributed to conceptualizing, editing, commenting on, and reviewing the manuscript.

FUNDING

This work is supported by the National Natural Science Foundation of China (51908457).

ACKNOWLEDGMENTS

The authors thank Zijun Ren from Xi'an Jiaotong University for assistance with SEM analysis.

REFERENCES

Abo Markeb, A., Alonso, A., Sánchez, A., and Font, X. (2017). Adsorption Process of Fluoride from Drinking Water with Magnetic Core-Shell Ce-Ti@Fe 3 O 4 and Ce-Ti Oxide Nanoparticles. *Sci. Total Environ.* 598, 949–958. doi:10.1016/j.scitotenv.2017.04.191

Angelin, A., Kalpana, M., Govindan, K., and Kavitha, S. (2021). Characterizations and Fluoride Adsorption Performance of Wattle Humus Biosorbent. *Environ. Sci. Pollut. Res. Int.* doi:10.1007/s11356-021-14864-9

Araga, R., Kali, S., and Sharma, C. S. (2019). Coconut-Shell-Derived Carbon/Carbon Nanotube Composite for Fluoride Adsorption from Aqueous Solution. *CLEAN. – Soil Air Water* 47 (5). doi:10.1002/clen.201800286

Araga, R., and Sharma, C. S. (2019). Amine Functionalized Electrospun Cellulose Nanofibers for Fluoride Adsorption from Drinking Water. *J. Polym. Environ.* 27 (4), 816–826. doi:10.1007/s10924-019-01394-2

Araga, R., Soni, S., and Sharma, C. S. (2017). Fluoride Adsorption from Aqueous Solution Using Activated Carbon Obtained from KOH-Treated Jamun (Syzygium Cumini) Seed. *J. Environ. Chem. Eng.* 5 (6), 5608–5616. doi:10.1016/j.jece.2017.10.023

Asadi, A., Sharafi, K., Mohammadi, H., and Pirsaheb, M. (2018). Fluoride and Nitrate Adsorption from Water by Fe(III)-doped Scoria: Optimizing Using Response Surface Modeling, Kinetic and Equilibrium Study. *Water Supply* 18 (3), 1117–1132.

Azari, A., Kalantary, R. R., Ghanizadeh, G., Kakavandi, B., Farzadkia, M., and Ahmadi, E. (2015). Iron-silver Oxide Nanoadsorbent Synthesized by Co-precipitation Process for Fluoride Removal from Aqueous Solution and its Adsorption Mechanism. *RSC Adv.* 5 (106), 87377–87391. doi:10.1039/c5ra17595j

Bhatnagar, A., Kumar, E., and Sillanpää, M. (2011). Fluoride Removal from Water by Adsorption-A Review. *Chem. Eng. J.* 171 (3), 811–840. doi:10.1016/j.cej.2011.05.028

Bhomick, P. C., Supong, A., Karmaker, R., Baruah, M., Pongener, C., and Sinha, D. (2019). Activated Carbon Synthesized from Biomass Material Using Single-step KOH Activation for Adsorption of Fluoride: Experimental and Theoretical Investigation. *Korean J. Chem. Eng.* 36 (4), 551–562. doi:10.1007/s11814-019-0234-x

Biswas, G., Kumari, M., Adhikari, K., and Dutta, S. (2017). A Critical Review on Occurrence of Fluoride and its Removal through Adsorption with an Emphasis on Natural Minerals. *Curr. Pollut. Rep* 3 (2), 104–119. doi:10.1007/s40726-017-0054-8

Bombuwala Dewage, N., Liyanage, A. S., Pittman, C. U., Jr., Mohan, D., and Mlsna, T. (2018). Fast Nitrate and Fluoride Adsorption and Magnetic Separation from Water on α-Fe2O3 and Fe3O4 Dispersed on Douglas Fir Biochar. *Bioresour. Technology* 263, 258–265. doi:10.1016/j.biortech.2018.05.001

Brunson, L. R., and Sabatini, D. A. (2015). Role of Surface Area and Surface Chemistry during an Investigation of Eucalyptus Wood Char for Fluoride Adsorption from Drinking Water. *J. Environ. Eng.* 141 (2). doi:10.1061/(asce)ee.1943-7870.0000891

Cai, P., Zhao, J., Zhang, X., Zhang, T., Yin, G., Chen, S., et al. (2022). Synergy between Cobalt and Nickel on NiCo2O4 Nanosheets Promotes Peroxymonosulfate Activation for Efficient Norfloxacin Degradation. *Appl. Catal. B: Environ.* 306. doi:10.1016/j.apcatb.2022.121091

Chaudhary, M., Jain, N., and Maiti, A. (2021). A Comparative Adsorption Kinetic Modeling of Fluoride Adsorption by Nanoparticles and its Polymeric Nanocomposite. *J. Environ. Chem. Eng.* 9 (5). doi:10.1016/j.jece.2021.105595

Chen, C.-L., Park, S.-W., Su, J. F., Yu, Y.-H., Heo, J.-e., Kim, K.-d., et al. (2019). The Adsorption Characteristics of Fluoride on Commercial Activated Carbon Treated with Quaternary Ammonium Salts (Quats). *Sci. Total Environ.* 693, 133605. doi:10.1016/j.scitotenv.2019.133605

Chen, J., Shu, C., Wang, N., Feng, J., Ma, H., and Yan, W. (2017). Adsorbent Synthesis of polypyrrole/TiO2 for Effective Fluoride Removal from Aqueous Solution for Drinking Water Purification: Adsorbent Characterization and Adsorption Mechanism. *J. Colloid Interf. Sci.* 495, 44–52. doi:10.1016/j.jcis.2017.01.084

Chen, P., Wang, T., Xiao, Y., Tian, E., Wang, W., Zhao, Y., et al. (2018). Efficient Fluoride Removal from Aqueous Solution by Synthetic Fe Mg La Tri-metal Nanocomposite and the Analysis of its Adsorption Mechanism. *J. Alloys Compounds* 738, 118–129. doi:10.1016/j.jallcom.2017.12.142

Cheng, L., Guan, Z., Si, L., Mang, C., Weng, X., Zhang, Q., et al. (2018). Fluoride Ion Adsorption from Wastewater Using Magnesium(II), Aluminum(III) and Titanium(IV) Modified Natural Zeolite: Kinetics, Thermodynamics, and Mechanistic Aspects of Adsorption. *J. Water Reuse Desalination* 8 (4), 479–489.

Chinnakoti, P., Chunduri, A. L. A., Vankayala, R. K., Patnaik, S., and Kamisetti, V. (2016a). Enhanced Fluoride Adsorption by Nano Crystalline γ-alumina: Adsorption Kinetics, Isotherm Modeling and Thermodynamic Studies. *Appl. Water Sci.* 7 (5), 2413–2423. doi:10.1007/s13201-016-0437-9

Chinnakoti, P., Vankayala, R. K., Chunduri, A. L. A., Nagappagari, L. R., Muthukonda, S. V., and Kamisetti, V. (2016b). Trititanate Nanotubes as Highly Efficient Adsorbent for Fluoride Removal from Water: Adsorption Performance and Uptake Mechanism. *J. Environ. Chem. Eng.* 4 (4), 4754–4768. doi:10.1016/j.jece.2016.11.007

Collivignarelli, M. C., Abbà, A., Carnevale Miino, M., Torretta, V., Rada, E. C., Caccamo, F. M., et al. (2020). Adsorption of Fluorides in Drinking Water by Palm Residues. *Sustainability* 12 (9). doi:10.3390/su12093786

Dehghani, M. H., Faraji, M., Mohammadi, A., and Kamani, H. (2016). Optimization of Fluoride Adsorption onto Natural and Modified Pumice Using Response Surface Methodology: Isotherm, Kinetic and Thermodynamic Studies. *Korean J. Chem. Eng.* 34 (2), 454–462. doi:10.1007/s11814-016-0274-4

Dehghani, M. H., Farhang, M., Alimohammadi, M., Afsharnia, M., and McKay, G. (2018). Adsorptive Removal of Fluoride from Water by Activated Carbon Derived from CaCl2-Modified Crocus Sativus Leaves: Equilibrium Adsorption Isotherms, Optimization, and Influence of Anions. *Chem. Eng. Commun.* 205 (7), 955–965. doi:10.1080/00986445.2018.1423969

Dhawane, S. H., Khan, A. A., Singh, K., Tripathi, A., Hasda, R., and Halder, G. (2018). Insight into Optimization, Isotherm, Kinetics, and Thermodynamics of Fluoride Adsorption onto Activated Alumina. *Environ. Prog. Sustainable Energ.* 37 (2), 766–776. doi:10.1002/ep.12814

Dhillon, A., Kumar Sharma, T., Soni, S. K., and Kumar, D. (2016). Fluoride Adsorption on a Cubical Ceria Nanoadsorbent: Function of Surface Properties. *RSC Adv.* 6 (92), 89198–89209. doi:10.1039/c6ra16962g

Dhillon, A., Soni, S. K., and Kumar, D. (2017). Enhanced Fluoride Removal Performance by Ce-Zn Binary Metal Oxide: Adsorption Characteristics and Mechanism. *J. Fluorine Chem.* 199, 67–76. doi:10.1016/j.jfluchem.2017.05.002

Dong, S., and Wang, Y. (2016). Characterization and Adsorption Properties of a Lanthanum-Loaded Magnetic Cationic Hydrogel Composite for Fluoride Removal. *Water Res.* 88, 852–860. doi:10.1016/j.watres.2015.11.013

Fan, Z., Gao, Y., Ning, X., Pan, F., and Ming, J. (2019). Adsorption of Fluoride Ions from Water by SF/PP Nonwoven Fabrics. *Fibers Polym.* 20 (4), 863–867. doi:10.1007/s12221-019-1085-0

Gao, M., Wang, W., Yang, H., and Ye, B.-C. (2019). Hydrothermal Synthesis of Hierarchical Hollow Hydroxyapatite Microspheres with Excellent Fluoride Adsorption Property. *Microporous Mesoporous Mater.* 289. doi:10.1016/j.micromeso.2019.109620

García-Sánchez, J. J., Solache-Ríos, M., Martínez-Gutiérrez, J. M., Arteaga-Larios, N. V., Ojeda-Escamilla, M. C., and Rodríguez-Torres, I. (2016). Modified Natural Magnetite with Al and La Ions for the Adsorption of Fluoride Ions from Aqueous Solutions. *J. Fluorine Chem.* 186, 115–124.

Ghosal, P. S., and Gupta, A. K. (2018). Thermodynamics of Fluoride Adsorption on Aluminum/Olivine Composite (AOC): Influence of Temperature on Isotherm, Kinetics, and Adsorption Mechanism. *Water Air Soil Pollut.* 229 (11). doi:10.1007/s11270-018-4003-y

Goswami, R., and Kumar, M. (2018). Removal of Fluoride from Aqueous Solution Using Nanoscale rice Husk Biochar. *Groundwater Sustainable Development* 7, 446–451. doi:10.1016/j.gsd.2017.12.010

Guiza, S., Hajji, H., and Bagane, M. (2019). External Mass Transport Process during the Adsorption of Fluoride from Aqueous Solution by Activated clay. *Comptes Rendus Chim.* 22 (2-3), 161–168. doi:10.1016/j.crci.2019.02.001

Habibi, N., Rouhi, P., and Ramavandi, B. (2019). Modification of Tamarix Hispida Biochar by Lanthanum Chloride for Enhanced Fluoride Adsorption from Synthetic and Real Wastewater. *Environ. Prog. Sustainable Energ.* 38 (s1), S298–S305.

Hafshejani, L. D., Tangsir, S., Daneshvar, E., Maljanen, M., Lähde, A., Jokiniemi, J., et al. (2017). Optimization of Fluoride Removal from Aqueous Solution by Al 2 O 3 Nanoparticles. *J. Mol. Liquids* 238, 254–262. doi:10.1016/j.molliq.2017.04.104

Han, M., Zhang, J., Hu, Y., and Han, R. (2019). Preparation of Novel Magnetic Microspheres with the La and Ce-Bimetal Oxide Shell for Excellent Adsorption of Fluoride and Phosphate from Solution. *J. Chem. Eng. Data* 64 (8), 3641–3651. doi:10.1021/acs.jced.9b00434

He, J., Cui, A., Ni, F., Deng, S., Shen, F., and Yang, G. (2018). A Novel 3D Yttrium Based-Graphene Oxide-Sodium Alginate Hydrogel for Remarkable Adsorption of Fluoride from Water. *J. Colloid Interf. Sci.* 531, 37–46. doi:10.1016/j.jcis.2018.07.017

He, J., Yang, Y., Wu, Z., Xie, C., Zhang, K., Kong, L., et al. (2020). Review of Fluoride Removal from Water Environment by Adsorption. *J. Environ. Chem. Eng.* 8 (6). doi:10.1016/j.jece.2020.104516

He, Y., Zhang, L., An, X., Wan, G., Zhu, W., and Luo, Y. (2019). Enhanced Fluoride Removal from Water by Rare Earth (La and Ce) Modified Alumina: Adsorption Isotherms, Kinetics, Thermodynamics and Mechanism. *Sci. Total Environ.* 688, 184–198. doi:10.1016/j.scitotenv.2019.06.175

Herath, H. M. A. S., Kawakami, T., and Tafu, M. (2018). The Extremely High Adsorption Capacity of Fluoride by Chicken Bone Char (CBC) in Defluoridation of Drinking Water in Relation to its Finer Particle Size for Better Human Health. *Healthcare (Basel)* 6 (4). doi:10.3390/healthcare6040123

Hongtao, L., Shuxia, L., Hua, Z., Yanling, Q., Daqiang, Y., Jianfu, Z., et al. (2018). Comparative Study on Synchronous Adsorption of Arsenate and Fluoride in Aqueous Solution onto MgAlFe-LDHs with Different Intercalating Anions. *RSC Adv.* 8 (58), 33301–33313. doi:10.1039/c8ra05968c

Hu, H., Yang, L., Lin, Z., Xiang, X., Jiang, X., and Hou, L. (2018). Preparation and Characterization of Novel Magnetic Fe3O4/chitosan/Al(OH)3 Beads and its Adsorption for Fluoride. *Int. J. Biol. Macromolecules* 114, 256–262. doi:10.1016/j.ijbiomac.2018.03.094

Huo, Y., Ding, W., Huang, X., Xu, J., and Zhao, M. (2011). Fluoride Removal by Lanthanum Alginate Bead: Adsorbent Characterization and Adsorption Mechanism. *Chin. J. Chem. Eng.* 19 (3), 365–370. doi:10.1016/s1004-9541(09)60222-6

Jadhav, A. S., and Jadhav, M. V. (2021). Utilization of Black Mustard Husk Ash for Adsorption of Fluoride from Water. *Korean J. Chem. Eng.* 38 (10), 2082–2090. doi:10.1007/s11814-021-0913-2

Jayarathna, L., Bandara, A., Ng, W. J., and Weerasooriya, R. (2015). Fluoride Adsorption on γ – Fe2O3 Nanoparticles. *J. Environ. Health Sci. Engineer* 13, 54. doi:10.1186/s40201-015-0210-2

Jeyaseelan, A., Katubi, K. M. M., Alsaiari, N. S., Naushad, M., and Viswanathan, N. (2021). Design and Fabrication of Sulfonic Acid Functionalized Graphene Oxide for Enriched Fluoride Adsorption. *Diamond Relat. Mater.* 117. doi:10.1016/j.diamond.2021.108446

Jia, Z., Hao, S., and Lu, X. (2018). Exfoliated Mg-Al-Fe Layered Double Hydroxides/polyether Sulfone Mixed Matrix Membranes for Adsorption of Phosphate and Fluoride from Aqueous Solutions. *J. Environ. Sci.* 70, 63–73. doi:10.1016/j.jes.2017.11.012

Jiang, X., Xiang, X., Hu, H., Meng, X., and Hou, L. (2018). Facile Fabrication of Biochar/Al2O3 Adsorbent and its Application for Fluoride Removal from Aqueous Solution. *J. Chem. Eng. Data* 64 (1), 83–89. doi:10.1021/acs.jced.8b00556

Jin, Z., Jia, Y., Zhang, K.-S., Kong, L.-T., Sun, B., Shen, W., et al. (2016). Effective Removal of Fluoride by Porous MgO Nanoplates and its Adsorption Mechanism. *J. Alloys Compounds* 675, 292–300. doi:10.1016/j.jallcom.2016.03.118

Kang, D., Yu, X., Ge, M., Lin, M., Yang, X., and Jing, Y. (2018). Insights into Adsorption Mechanism for Fluoride on Cactus-like Amorphous Alumina Oxide Microspheres. *Chem. Eng. J.* 345, 252–259. doi:10.1016/j.cej.2018.03.174

Kang, D., Yu, X., and Ge, M. (2017). Morphology-dependent Properties and Adsorption Performance of CeO2 for Fluoride Removal. *Chem. Eng. J.* 330, 36–43. doi:10.1016/j.cej.2017.07.140

Kanrar, S., Debnath, S., De, P., Parashar, K., Pillay, K., Sasikumar, P., et al. (2016). Preparation, Characterization and Evaluation of Fluoride Adsorption Efficiency from Water of Iron-Aluminium Oxide-Graphene Oxide Composite Material. *Chem. Eng. J.* 306, 269–279. doi:10.1016/j.cej.2016.07.037

Kuang, L., Liu, Y., Fu, D., and Zhao, Y. (2017). FeOOH-graphene Oxide Nanocomposites for Fluoride Removal from Water: Acetate Mediated Nano FeOOH Growth and Adsorption Mechanism. *J. Colloid Interf. Sci.* 490, 259–269. doi:10.1016/j.jcis.2016.11.071

Kullgren, J., Wolf, M. J., Castleton, C. W. M., Mitev, P., Briels, W. J., and Hermansson, K. (2014). Oxygen Vacancies versus Fluorine atCeO2(111): A Case of Mistaken Identity? *Phys. Rev. Lett.* 112 (15), 156102. doi:10.1103/physrevlett.112.156102

Kumar, P., Prajapati, A. K., Dixit, S., and Yadav, V. L. (2020). Adsorption of Fluoride from Aqueous Solution Using Biochar Prepared from Waste Peanut hull. *Mater. Res. Express* 6 (12). doi:10.1088/2053-1591/ab6ca0

Lanas, S. G., Valiente, M., Aneggi, E., Trovarelli, A., Tolazzi, M., and Melchior, A. (2016). Efficient Fluoride Adsorption by Mesoporous Hierarchical Alumina Microspheres. *RSC Adv.* 6 (48), 42288–42296. doi:10.1039/c5ra27371d

Lee, J.-I., Kang, J.-K., Hong, S.-H., Lee, C.-G., Jeong, S., and Park, S.-J. (2021). Thermally Treated *Mytilus coruscus* Shells for Fluoride Removal and Their Adsorption Mechanism. *Chemosphere* 263, 128328. doi:10.1016/j.chemosphere.2020.128328

Lee, S. G., Ha, J.-W., Sohn, E.-H., Park, I. J., and Lee, S.-B. (2017). Synthesis of Pillar and Microsphere-like Magnesium Oxide Particles and Their Fluoride Adsorption Performance in Aqueous Solutions. *Korean J. Chem. Eng.* 34 (10), 2738–2747. doi:10.1007/s11814-017-0160-8

Li, Y., Zhang, C., Jiang, Y., and Wang, T.-J. (2018). Electrically Enhanced Adsorption and green Regeneration for Fluoride Removal Using Ti(OH)4-loaded Activated Carbon Electrodes. *Chemosphere* 200, 554–560. doi:10.1016/j.chemosphere.2018.02.112

Liang, P., An, R., Li, R., and Wang, D. (2018). Comparison of La3+ and Mixed Rare Earths-Loaded Magnetic Chitosan Beads for Fluoride Adsorption. *Int. J. Biol. Macromolecules* 111, 255–263. doi:10.1016/j.ijbiomac.2017.12.151

Lin, J.-Y., Chen, Y.-L., Hong, X.-Y., Huang, C., and Huang, C. P. (2020). The Role of Fluoroaluminate Complexes on the Adsorption of Fluoride onto Hydrous Alumina in Aqueous Solutions. *J. Colloid Interf. Sci.* 561, 275–286. doi:10.1016/j.jcis.2019.10.085

Lin, K.-Y. A., Liu, Y.-T., and Chen, S.-Y. (2016). Adsorption of Fluoride to UiO-66-NH 2 in Water: Stability, Kinetic, Isotherm and Thermodynamic Studies. *J. Colloid Interf. Sci.* 461, 79–87. doi:10.1016/j.jcis.2015.08.061

Medellin-Castillo, N. A., Leyva-Ramos, R., Padilla-Ortega, E., Perez, R. O., Flores-Cano, J. V., and Berber-Mendoza, M. S. (2014). Adsorption Capacity of Bone Char for Removing Fluoride from Water Solution. Role of Hydroxyapatite Content, Adsorption Mechanism and Competing anionsRole of Hydroxyapatite Content, Adsorption Mechanism and Competing Anions. *J. Ind. Eng. Chem.* 20 (6), 4014–4021. doi:10.1016/j.jiec.2013.12.105

Mei, L., Qiao, H., Ke, F., Peng, C., Hou, R., Wan, X., et al. (2020). One-step Synthesis of Zirconium Dioxide-Biochar Derived from Camellia Oleifera Seed Shell with Enhanced Removal Capacity for Fluoride from Water. *Appl. Surf. Sci.* 509. doi:10.1016/j.apsusc.2019.144685

Merodio-Morales, E. E., Reynel-Ávila, H. E., Mendoza-Castillo, D. I., Duran-Valle, C. J., and Bonilla-Petriciolet, A. (2019). Lanthanum- and Cerium-Based Functionalization of Chars and Activated Carbons for the Adsorption of Fluoride and Arsenic Ions. *Int. J. Environ. Sci. Technol.* 17 (1), 115–128. doi:10.1007/s13762-019-02437-w

Mobarak, M., Selim, A. Q., Mohamed, E. A., and Seliem, M. K. (2018). Modification of Organic Matter-Rich clay by a Solution of Cationic surfactant/H2O2: A New Product for Fluoride Adsorption from Solutions. *J. Clean. Prod.* 192, 712–721. doi:10.1016/j.jclepro.2018.05.044

Mohan, S., Kumar, V., Singh, D. K., and Hasan, S. H. (2016). Synthesis and Characterization of rGO/ZrO2 Nanocomposite for Enhanced Removal of Fluoride from Water: Kinetics, Isotherm, and Thermodynamic Modeling and its Adsorption Mechanism. *RSC Adv.* 6 (90), 87523–87538. doi:10.1039/c6ra15460c

Mohan, S., Singh, D. K., Kumar, V., and Hasan, S. H. (2017). Effective Removal of Fluoride Ions by rGO/ZrO2 Nanocomposite from Aqueous Solution: Fixed Bed Column Adsorption Modelling and its Adsorption Mechanism. *J. Fluorine Chem.* 194, 40–50. doi:10.1016/j.jfluchem.2016.12.014

Mohanta, D., and Ahmaruzzaman, M. (2018). Bio-inspired Adsorption of Arsenite and Fluoride from Aqueous Solutions Using Activated carbon@SnO2 Nanocomposites: Isotherms, Kinetics, Thermodynamics, Cost Estimation and Regeneration Studies. *J. Environ. Chem. Eng.* 6 (1), 356–366. doi:10.1016/j.jece.2017.11.076

Mohseni-Bandpi, A., Kakavandi, B., Kalantary, R. R., Azari, A., and Keramati, A. (2015). Development of a Novel Magnetite-Chitosan Composite for the Removal of Fluoride from Drinking Water: Adsorption Modeling and Optimization. *RSC Adv.* 5 (89), 73279–73289. doi:10.1039/c5ra11294j

Mondal, N. K., Bhaumik, R., and Datta, J. K. (2016). Fluoride Adsorption by Calcium Carbonate, Activated Alumina and Activated Sugarcane Ash. *Environ. Process.* 3 (1), 195–216. doi:10.1007/s40710-016-0130-x

Mourabet, M., El Rhilassi, A., El Boujaady, H., Bennani-Ziatni, M., El Hamri, R., and Taitai, A. (2015). Removal of Fluoride from Aqueous Solution by Adsorption on Hydroxyapatite (HAp) Using Response Surface Methodology. *J. Saudi Chem. Soc.* 19 (6), 603–615. doi:10.1016/j.jscs.2012.03.003

Mudzielwana, R., Gitari, W. M., Akinyemi, S. A., and Msagati, T. A. M. (2017). Synthesis, Characterization, and Potential Application of Mn2+-Intercalated Bentonite in Fluoride Removal: Adsorption Modeling and Mechanism Evaluation. *Appl. Water Sci.* 7 (8), 4549–4561. doi:10.1007/s13201-017-0608-3

Mullick, A., and Neogi, S. (2018). Acoustic Cavitation Induced Synthesis of Zirconium Impregnated Activated Carbon for Effective Fluoride Scavenging from Water by Adsorption. *Ultrason. Sonochem.* 45, 65–77. doi:10.1016/j.ultsonch.2018.03.002

Mullick, A., and Neogi, S. (2019). Ultrasound Assisted Synthesis of Mg-Mn-Zr Impregnated Activated Carbon for Effective Fluoride Adsorption from Water. *Ultrason. Sonochem.* 50, 126–137. doi:10.1016/j.ultsonch.2018.09.010

Muschin, T., Zulchin, H., and Jia, M. (2021). Adsorption Behavior of Polyhydroxy-Iron-Modified Coal-Bearing Kaolin for Fluoride Removal. *ChemistrySelect* 6 (13), 3075–3083. doi:10.1002/slct.202100226

Nabbou, N., Belhachemi, M., Boumelik, M., Merzougui, T., Lahcene, D., Harek, Y., et al. (2019). Removal of Fluoride from Groundwater Using Natural clay (Kaolinite): Optimization of Adsorption Conditions. *Comptes Rendus Chim.* 22 (2-3), 105–112. doi:10.1016/j.crci.2018.09.010

Naga Babu, A., Srinivasa Reddy, D., Suresh Kumar, G., Ravindhranath, K., and Krishna Mohan, G. V. (2020). Sequential Synergetic Sorption Analysis of Gracilaria Rhodophyta Biochar toward Aluminum and Fluoride: A Statistical Optimization Approach. *Water Environ. Res.* 92 (6), 880–898. doi:10.1002/wer.1283

Nehra, S., Nair, M., and Kumar, D. (2019). Hydrothermally Shape-Controlled Synthesis of TiO2/Graphene for Fluoride Adsorption Studies. *J. Chem. Eng. Data* 64 (12), 5373–5384. doi:10.1021/acs.jced.9b00591

Nijhawan, A., Butler, E. C., and Sabatini, D. A. (2020). Fluoride Adsorption on Porous Hydroxyapatite Ceramic Filters: A Study of Kinetics. *Environ. Eng. Sci.* 37 (6), 409–416. doi:10.1089/ees.2019.0392

Nor, N. M., Kamil, N. H. N., Mansor, A. I., and Maarof, H. I. (2020). Adsorption Analysis of Fluoride Removal Using Graphene Oxide/Eggshell Adsorbent. *Indonesian J. Chem.* 20 (3). doi:10.22146/ijc.43481

Pigatto, R. S., Franco, D. S. P., Netto, M. S., Carissimi, É., Oliveira, L. F. S., Jahn, S. L., et al. (2020). An Eco-Friendly and Low-Cost Strategy for Groundwater Defluorination: Adsorption of Fluoride onto Calcinated Sludge. *J. Environ. Chem. Eng.* 8 (6). doi:10.1016/j.jece.2020.104546

Prabhu, S. M., and Meenakshi, S. (2015). A Dendrimer-like Hyper Branched Chitosan Beads toward Fluoride Adsorption from Water. *Int. J. Biol. Macromolecules* 78, 280–286. doi:10.1016/j.ijbiomac.2015.04.002

Preethi, J., and Meenakshi, S. (2018). Fabrication of La3+ Impregnated Chitosan/β-Cyclodextrin Biopolymeric Materials for Effective Utilization of Chromate and Fluoride Adsorption in Single Systems. *J. Chem. Eng. Data* 63 (3), 723–731. doi:10.1021/acs.jced.7b00889

Qiusheng, Z., Xiaoyan, L., Jin, Q., Jing, W., and Xuegang, L. (2015). Porous Zirconium Alginate Beads Adsorbent for Fluoride Adsorption from Aqueous Solutions. *RSC Adv.* 5 (3), 2100–2112. doi:10.1039/c4ra12036a

Raghav, S., and Kumar, D. (2018). Adsorption Equilibrium, Kinetics, and Thermodynamic Studies of Fluoride Adsorbed by Tetrametallic Oxide Adsorbent. *J. Chem. Eng. Data* 63 (5), 1682–1697. doi:10.1021/acs.jced.8b00024

Raghav, S., and Kumar, D. (2019). Comparative Kinetics and Thermodynamic Studies of Fluoride Adsorption by Two Novel Synthesized Biopolymer Composites. *Carbohydr. Polym.* 203, 430–440. doi:10.1016/j.carbpol.2018.09.054

Raghav, S., Nehra, S., and Kumar, D. (2019). Biopolymer Scaffold of Pectin and Alginate for the Application of Health Hazardous Fluoride Removal Studies by Equilibrium Adsorption, Kinetics and Thermodynamics. *J. Mol. Liquids* 284, 203–214. doi:10.1016/j.molliq.2019.03.155

Raghav, S., Sapnaand Kumar, D. (2018). Cubical-Shaped Rods of Pectin-Hydroxyapatite Composite for Adsorption Studies of Fluoride by Statistical Method and Adsorption Experiments. *ACS Omega* 3 (8), 9675–9688. doi:10.1021/acsomega.8b01330

Rathore, V. K., and Mondal, P. (2017). Competitive Adsorption of Arsenic and Fluoride onto Economically Prepared Aluminum Oxide/Hydroxide Nanoparticles: Multicomponent Isotherms and Spent Adsorbent Management. *Ind. Eng. Chem. Res.* 56 (28), 8081–8094. doi:10.1021/acs.iecr.7b01139

Rehman, M. A., Yusoff, I., and Alias, Y. (2015). Fluoride Adsorption by Doped and Un-doped Magnetic Ferrites CuCexFe2-xO4: Preparation, Characterization, Optimization and Modeling for Effectual Remediation Technologies. *J. Hazard. Mater.* 299, 316–324. doi:10.1016/j.jhazmat.2015.06.030

Sadeghi, A., Tajbakhsh, M., and Abri, A. (2019). Adsorption of Fluoride on a Chitosan-Based Magnetic Nanocomposite: Equilibrium and Kinetics Studies. *Water Supply* 19 (1), 40–51.

Sapna, S., Raghav, S., Nair, M., and Kumar, D. (2018). Trimetallic Oxide Entrapped in Alginate Polymeric Matrix Employed for Adsorption Studies of Fluoride. *Surf. Inter.* 13, 112–132. doi:10.1016/j.surfin.2018.08.005

Sarkar, C., Basu, J. K., and Samanta, A. N. (2019). Experimental and Kinetic Study of Fluoride Adsorption by Ni and Zn Modified LD Slag Based Geopolymer. *Chem. Eng. Res. Des.* 142, 165–175. doi:10.1016/j.cherd.2018.12.006

Sarkar, M., and Santra, D. (2015). Modeling Fluoride Adsorption on Cerium-Loaded Cellulose Bead—Response Surface Methodology, Equilibrium, and Kinetic Studies. *Water Air Soil Pollut.* 226 (3). doi:10.1007/s11270-015-2307-8

Shang, Y., Duan, X., Wang, S., Yue, Q., Gao, B., and Xu, X. (2022). Carbon-based Single Atom Catalyst: Synthesis, Characterization, DFT Calculations. *Chin. Chem. Lett.* 33 (2), 663–673. doi:10.1016/j.cclet.2021.07.050

Sharma, P., Sen, K., Thakur, P., Chauhan, M., and Chauhan, K. (2019). Spherically Shaped Pectin-G-Poly(amidoxime)-Fe Complex: A Promising Innovative Pathway to Tailor a New Material in High Amidoxime Functionalization for Fluoride Adsorption. *Int. J. Biol. Macromolecules* 140, 78–90. doi:10.1016/j.ijbiomac.2019.08.098

Singh, T. P., and Majumder, C. B. (2018). Batch and Column Performance of Fluoride Adsorption by Java Plum Seeds. *J. Hazard. Tox. Radioactive Waste* 22 (3). doi:10.1061/(asce)hz.2153-5515.0000394

Suzuki, T., Nakamura, A., Niinae, M., Nakata, H., Fujii, H., and Tasaka, Y. (2013). Immobilization of Fluoride in Artificially Contaminated Kaolinite by the Addition of Commercial-Grade Magnesium Oxide. *Chem. Eng. J.* 233, 176–184. doi:10.1016/j.cej.2013.08.042

Tomar, V., Prasad, S., and Kumar, D. (2014). Adsorptive Removal of Fluoride from Aqueous media Using Citrus Limonum (Lemon) Leaf. *Microchemical J.* 112, 97–103. doi:10.1016/j.microc.2013.09.010

Wan, S., Lin, J., Tao, W., Yang, Y., Li, Y., and He, F. (2019). Enhanced Fluoride Removal from Water by Nanoporous Biochar-Supported Magnesium Oxide. *Ind. Eng. Chem. Res.* 58 (23), 9988–9996. doi:10.1021/acs.iecr.9b01368

Wang, A., Zhou, K., Chen, W., Zhang, C., Liu, X., Chen, Q., et al. (2018a). Adsorption of Fluoride by the Calcium Alginate Embedded with Mg-Al-Ce Trimetal Oxides. *Korean J. Chem. Eng.* 35 (8), 1636–1641. doi:10.1007/s11814-018-0056-2

Wang, A., Zhou, K., Liu, X., Liu, F., Zhang, C., and Chen, Q. (2017a). Granular Tri-metal Oxide Adsorbent for Fluoride Uptake: Adsorption Kinetic and Equilibrium Studies. *J. Colloid Interf. Sci.* 505, 947–955. doi:10.1016/j.jcis.2017.06.074

Wang, F., Wang, K., Muhammad, Y., Wei, Y., Shao, L., and Wang, X. (2019a). Preparation of CeO2@SiO2 Microspheres by a Non-sintering Strategy for Highly Selective and Continuous Adsorption of Fluoride Ions from Wastewater. *ACS Sustainable Chem. Eng.* 7 (17), 14716–14726. doi:10.1021/acssuschemeng.9b02643

Wang, H., Feng, Q., Liu, K., Li, Z., Tang, X., and Li, G. (2017b). Highly Efficient Fluoride Adsorption from Aqueous Solution by Nepheline Prepared from Kaolinite through Alkali-Hydrothermal Process. *J. Environ. Manage.* 196, 72–79. doi:10.1016/j.jenvman.2017.03.015

Wang, J., Chen, N., Feng, C., and Li, M. (2018b). Performance and Mechanism of Fluoride Adsorption from Groundwater by Lanthanum-Modified Pomelo Peel Biochar. *Environ. Sci. Pollut. Res.* 25 (16), 15326–15335. doi:10.1007/s11356-018-1727-6

Wang, J., Chen, N., Li, M., and Feng, C. (2017c). Efficient Removal of Fluoride Using Polypyrrole-Modified Biochar Derived from Slow Pyrolysis of Pomelo Peel: Sorption Capacity and Mechanism. *J. Polym. Environ.* 26 (4), 1559–1572. doi:10.1007/s10924-017-1061-y

Wang, J., Wu, L., Li, J., Tang, D., and Zhang, G. (2018c). Simultaneous and Efficient Removal of Fluoride and Phosphate by Fe-La Composite: Adsorption Kinetics and Mechanism. *J. Alloys Compounds* 753, 422–432. doi:10.1016/j.jallcom.2018.04.177

Wang, L., Wang, J., He, C., Lyu, W., Zhang, W., Yan, W., et al. (2019b). Development of Rare Earth Element Doped Magnetic Biochars with Enhanced Phosphate Adsorption Performance. *Colloids Surf. A: Physicochemical Eng. Aspects* 561, 236–243. doi:10.1016/j.colsurfa.2018.10.082

Wang, L., Wang, J., Wang, Z., Feng, J., Li, S., and Yan, W. (2019c). Synthesis of Ce-Doped Magnetic Biochar for Effective Sb(V) Removal: Performance and Mechanism. *Powder Technology* 345, 501–508. doi:10.1016/j.powtec.2019.01.022

Wang, L., Wang, J., and Wei, Y. (2021). Facile Synthesis of Eggshell Biochar Beads for superior Aqueous Phosphate Adsorption with Potential Urine P-Recovery. *Colloids Surf. A: Physicochemical Eng. Aspects* 622. doi:10.1016/j.colsurfa.2021.126589

Wang, L., Wang, J., Yan, W., He, C., and Shi, Y. (2020). MgFe2O4-biochar Based Lanthanum Alginate Beads for Advanced Phosphate Removal. *Chem. Eng. J.* 387. doi:10.1016/j.cej.2019.123305

Wang, X., Pfeiffer, H., Wei, J., Dan, J., Wang, J., and Zhang, J. (2022). 3D Porous Ca-Modified Mg-Zr Mixed Metal Oxide for Fluoride Adsorption. *Chem. Eng. J.* 428. doi:10.1016/j.cej.2021.131371

Wei, Y., Wang, L., and Wang, J. (2022). Cerium Alginate Cross-Linking with Biochar Beads for Fast Fluoride Removal over a Wide pH Range. *Colloids Surf. A: Physicochemical Eng. Aspects* 636. doi:10.1016/j.colsurfa.2021.128161

Wen, S., Wang, Y., and Dong, S. (2015). Performance and Characteristics of Fluoride Adsorption Using Nanomagnetite Graphite-La Adsorbent. *RSC Adv.* 5 (109), 89594–89602. doi:10.1039/c5ra15215a

Wimalasiri, A. K. D. V. K., Fernando, M. S., Williams, G. R., Dissanayake, D. P., de Silva, K. M. N., and de Silva, R. M. (2021). Microwave Assisted Accelerated Fluoride Adsorption by Porous Nanohydroxyapatite. *Mater. Chem. Phys.* 257. doi:10.1016/j.matchemphys.2020.123712

Wu, K., Zhang, N., Liu, T., Ma, C., Jin, P., Zhang, F., et al. (2017a). Competitive Adsorption Behaviors of Arsenite and Fluoride onto Manganese-Aluminum Binary Adsorbents. *Colloids Surf. A: Physicochemical Eng. Aspects* 529, 185–194. doi:10.1016/j.colsurfa.2017.05.039

Wu, L., Lin, X., Wu, J., Zhou, X., and Luo, X. (2016a). Adsorption Behavior of Carboxymethyl Konjac Glucomannan Microspheres for Fluoride from Aqueous Solution. *RSC Adv.* 6 (92), 89417–89429. doi:10.1039/c6ra17183d

Wu, L., Lin, X., Zhou, X., and Luo, X. (2016b). Removal of Uranium and Fluorine from Wastewater by Double-Functional Microsphere Adsorbent of SA/CMC Loaded with Calcium and Aluminum. *Appl. Surf. Sci.* 384, 466–479. doi:10.1016/j.apsusc.2016.05.056

Wu, P., Wu, J., Xia, L., Liu, Y., Xu, L., and Song, S. (2017b). Adsorption of Fluoride at the Interface of Water with Calcined Magnesium-Ferri-Lanthanum Hydrotalcite-like Compound. *RSC Adv.* 7 (42), 26104–26112. doi:10.1039/c7ra04382a

Wu, T., Mao, L., and Wang, H. (2017c). Adsorption of Fluoride from Aqueous Solution by Using Hybrid Adsorbent Fabricated with Mg/Fe Composite Oxide and Alginate via a Facile Method. *J. Fluorine Chem.* 200, 8–17. doi:10.1016/j.jfluchem.2017.05.005

Wu, T., Mao, L., and Wang, H. (2015). Adsorption of Fluoride on Mg/Fe Layered Double Hydroxides Material Prepared via Hydrothermal Process. *RSC Adv.* 5 (30), 23246–23254. doi:10.1039/c4ra16839a

Wu, X. P., and Gong, X. Q. (2016). Clustering of Oxygen Vacancies at CeO2(111): Critical Role of Hydroxyls. *Phys. Rev. Lett.* 116 (8), 086102. doi:10.1103/PhysRevLett.116.086102

Wu, X., Zhang, Y., Dou, X., Zhao, B., and Yang, M. (2013). Fluoride Adsorption on an Fe-Al-Ce Trimetal Hydrous Oxide: Characterization of Adsorption Sites and Adsorbed Fluorine Complex Species. *Chem. Eng. J.* 223, 364–370. doi:10.1016/j.cej.2013.03.027

Xu, W., He, Q., Zhang, S., and Zhang, W. (2017). Adsorption of Fluoride from Aqueous Solutions by Polyacrylic Acid Modified with Aluminium. *Polym. Bull.* 75 (3), 1171–1184. doi:10.1007/s00289-017-2082-3

Yadav, K., and Jagadevan, S. (2020). Effect of Pyrolysis of Rice Husk–Derived Biochar on the Fuel Characteristics and Adsorption of Fluoride from Aqueous Solution. *BioEnergy Res.* 14, 964–977. doi:10.1007/s12155-020-10189-6

Yang, K., Li, Y., Zhao, Z., Tian, Z., and Lai, Y. (2020). Amorphous Porous Layered-Al2O3 Derived from AlFu MOFs as an Adsorbent for Removing Fluorine Ions in Industrial ZnSO4 Solution. *Chem. Eng. Res. Des.* 153, 562–571. doi:10.1016/j.cherd.2019.11.019

Yang, W., Tian, S., Tang, Q., Chai, L., and Wang, H. (2017). Fungus Hyphae-Supported Alumina: An Efficient and Reclaimable Adsorbent for Fluoride Removal from Water. *J. Colloid Interf. Sci.* 496, 496–504. doi:10.1016/j.jcis.2017.02.015

Ye, C., Yan, B., Ji, X., Liao, B., Gong, R., Pei, X., et al. (2019). Adsorption of Fluoride from Aqueous Solution by Fly Ash Cenospheres Modified with Paper Mill Lime Mud: Experimental and Modeling. *Ecotoxicology Environ. Saf.* 180, 366–373. doi:10.1016/j.ecoenv.2019.04.086

Yu, Y., Yu, L., and Paul Chen, J. (2015). Adsorption of Fluoride by Fe-Mg-La Triple-Metal Composite: Adsorbent Preparation, Illustration of Performance and Study of Mechanisms. *Chem. Eng. J.* 262, 839–846. doi:10.1016/j.cej.2014.09.006

Zendehdel, M., Shoshtari-Yeganeh, B., Khanmohamadi, H., and Cruciani, G. (2017). Removal of Fluoride from Aqueous Solution by Adsorption on NaP: HAp Nanocomposite Using Response Surface Methodology. *Process Saf. Environ. Prot.* 109, 172–191. doi:10.1016/j.psep.2017.03.028

Zhang, C., Li, Y., Wang, T.-J., Jiang, Y., and Wang, H. (2016a). Adsorption of Drinking Water Fluoride on a Micron-Sized Magnetic Fe3O4@Fe-Ti Composite Adsorbent. *Appl. Surf. Sci.* 363, 507–515. doi:10.1016/j.apsusc.2015.12.071

Zhang, K., Wu, S., He, J., Chen, L., Cai, X., Chen, K., et al. (2016b). Development of a Nanosphere Adsorbent for the Removal of Fluoride from Water. *J. Colloid Interf. Sci.* 475, 17–25. doi:10.1016/j.jcis.2016.04.037

Zhang, S., Lyu, Y., Su, X., Bian, Y., Yu, B., and Zhang, Y. (2016c). Removal of Fluoride Ion from Groundwater by Adsorption on Lanthanum and Aluminum Loaded clay Adsorbent. *Environ. Earth Sci.* 75 (5). doi:10.1007/s12665-015-5205-x

Zhang, X., Qi, Y., Chen, Z., Song, N., Li, X., Ren, D., et al. (2021a). Evaluation of Fluoride and Cadmium Adsorption Modification of Corn Stalk by Aluminum Trichloride. *Appl. Surf. Sci.* 543. doi:10.1016/j.apsusc.2020.148727

Zhang, Y.-X., and Jia, Y. (2016). Fluoride Adsorption onto Amorphous Aluminum Hydroxide: Roles of the Surface Acetate Anions. *J. Colloid Interf. Sci.* 483, 295–306. doi:10.1016/j.jcis.2016.08.054

Zhang, Y., Jin, Z., Min-He, L., Guang-Song, X., Min-Da, X., Cheng, H., et al. (2021b). Facile Synthesis of Hollow MgO Spheres and Their Fluoride Adsorption Properties. *Adv. Condensed Matter Phys.* 2021, 1–10. doi:10.1155/2021/6655593

Zhao, X., Yu, X., Wang, X., Lai, S., Sun, Y., and Yang, D. (2021). Recent Advances in Metal-Organic Frameworks for the Removal of Heavy Metal Oxoanions from Water. *Chem. Eng. J.* 407. doi:10.1016/j.cej.2020.127221

Zhou, J., Liu, Y., Han, Y., Jing, F., and Chen, J. (2019a). Bone-derived Biochar and Magnetic Biochar for Effective Removal of Fluoride in Groundwater:

Effects of Synthesis Method and Coexisting Chromium. *Water Environ. Res.* 91 (7), 588–597. doi:10.1002/wer.1068

Zhou, J., Zhu, W., Yu, J., Zhang, H., Zhang, Y., Lin, X., et al. (2018). Highly Selective and Efficient Removal of Fluoride from Ground Water by Layered Al-Zr-La Tri-metal Hydroxide. *Appl. Surf. Sci.* 435, 920–927. doi:10.1016/j.apsusc.2017.11.108

Zhou, Z., Yu, Y., Ding, Z., Zuo, M., and Jing, C. (2019b). Competitive Adsorption of Arsenic and Fluoride on {2 0 1} TiO2. *Appl. Surf. Sci.* 466, 425–432. doi:10.1016/j.apsusc.2018.10.052

Zhu, T., Zhu, T., Gao, J., Zhang, L., and Zhang, W. (2017). Enhanced Adsorption of Fluoride by Cerium Immobilized Cross-Linked Chitosan Composite. *J. Fluorine Chem.* 194, 80–88. doi:10.1016/j.jfluchem.2017.01.002

Zúñiga-Muro, N. M., Bonilla-Petriciolet, A., Mendoza-Castillo, D. I., Reynel-Ávila, H. E., and Tapia-Picazo, J. C. (2017). Fluoride Adsorption Properties of Cerium-Containing Bone Char. *J. Fluorine Chem.* 197, 63–73.

Conflict of Interest: The authors declare that the research was conducted in the absence of any commercial or financial relationships that could be construed as a potential conflict of interest.

frontiers | Frontiers in Chemistry

ORIGINAL RESEARCH
published: 31 May 2022
doi: 10.3389/fchem.2022.922701

Synthesis and Photocatalytic Activity of Pt-Deposited TiO_2 Nanotubes (TNT) for Rhodamine B Degradation

Xiaojian Qiu[1], Zhenning Wan[2], Mengjie Pu[2], Xiuru Xu[3]*, Yuanyao Ye[4] and Chunhua Hu[1]*

[1]School of Resources and Environment, Nanchang University, Nanchang, China, [2]College of Life and Environmental Science, Wenzhou University, Wenzhou, China, [3]School of Agricultural and Biological Technology, Wenzhou Vocational College of Science and Technology, Zhejiang, China, [4]School of Environmental Science and Engineering, Huazhong University of Science and Technology, Wuhan, China

Dye wastewater has attracted more and more attention because of its high environmental risk. In this study, a novel TiO_2 nanotube (TNT) catalyst was prepared and its morphology and structure were characterized. The synthetic catalyst was used to degrade Rhodamine B (RhB) under UV light and evaluated for the application performance. According to the characterization results and degradation properties, the optimum synthetic conditions were selected as 400°C calcination temperature and 10 wt% Pt deposition. As a result, the degradation efficacies were sequenced as TNT-400-Pt > TNT-500-Pt > TNT-400 > TNT-300-Pt. In addition, the effect of pH and initial concentration of RhB were explored, and their values were both increased with the decreased degradation efficacy. While the moderate volume of 11 mm of H_2O_2 addition owned better performance than that of 0, 6, and 15 mm. Scavengers such as tertbutanol (*t*-BuOH), disodium ethylenediaminetetraacetate (EDTA-Na_2), and nitroblue tetrazolium (NBT) were added during the catalytic process and it proved that superoxide radical anions ($O_2^{-\bullet}$), photogenerated hole (h^+) and hydroxyl radical (OH•) were the main active species contributing for RhB removal. For the application, TNT-Pt could deal with almost 100% RhB, Orange G (OG), Methylene blue (MB), and Congo red (CR) within 70 min and still kept more than 50% RhB removal in the fifth recycling use. Therefore, TNT-Pt synthesized in this study is potential to be applied to the dye wastewater treatment.

Keywords: photocatalysis, TNT-Pt, morphology and structure, Rh B, superoxide radical anions

OPEN ACCESS

Edited by:
Zhu Xiong,
Guangzhou University, China

Reviewed by:
Yanlong Sun,
Zhejiang Normal University, China
Ming Zheng,
Shanghai University, China

****Correspondence:***
Xiuru Xu
wkyxxr@163.com
Chunhua Hu
chhu@ncu.edu.cn

Specialty section:
This article was submitted to
Inorganic Chemistry,
a section of the journal
Frontiers in Chemistry

Received: *18 April 2022*
Accepted: *02 May 2022*
Published: *31 May 2022*

Citation:
Qiu X, Wan Z, Pu M, Xu X, Ye Y and Hu C (2022) Synthesis and Photocatalytic Activity of Pt-Deposited TiO_2 Nanotubes (TNT) for Rhodamine B Degradation.
Front. Chem. 10:922701.
doi: 10.3389/fchem.2022.922701

INTRODUCTION

With increasing technological and industrial development, a diverse set of pollutants have been discharged into water bodies, leading to the increasing concern about water contamination and environmental risks (Xu et al., 2021; Zeng et al., 2021). Colored dyes, represented by Rhodamine B (RhB), Orange G (OG), methylene blue (MB), and Congo red (CR) are widely used in the textile, printing, and plastic industries, which have high concentration levels in wastewater (Skjolding et al., 2021). Seriously, most dye pollutants cannot be easily degraded in water due to their complex composition, deep color, and chemical and physical stability (Sutar et al., 2022). Therefore, several techniques, such as adsorption, coagulation, biodegradation, and photocatalysis have been used in treating dyeing wastewater (Hao et al., 2021; Liu et al., 2021; Pu et al., 2017). Among these technologies, photocatalysis is increasingly regarded as a favorable option in recent years due to the advantages of its simple operation process, low energy consumption, and comparatively high degradation efficacy for pollutant removal (Xu et al., 2017a; Xu et al., 2017b).In addition, compared with photolysis, photocatalysis has the synergistic benefit of a specific catalyst combined with light irradiation (Xu et al., 2018; Xu et al., 2020a). Among many candidates of photocatalysts, TiO_2 is the most widely studied material, currently the most likely photocatalyst for industrial-scale application in terms of high chemical stability, durability, high hydrophilicity, photoactivity efficiency, low toxicity, and low cost (Xu et al., 2020b; Hao et al., 2022).

While during photocatalysis by TiO_2, the high recombination rates of photogenerated electron-hole pairs result in reduced photocatalytic efficiency (Perera et al., 2012). Accordingly, a series of strategies for the preparation of TiO_2-based nanocomposites have been developed (Mi et al., 2021; Wang et al., 2021; Wu et al., 2021). TiO_2-based nanotubes (TNTs) were first synthesized by electrochemical deposition in a porous aluminum oxide mold (Hoyer, 1996). Compared with commonly used TiO_2 nanoparticles (NPs), TNTs exhibit unique photocatalytic properties including larger specific surface area (up to 478 m^2/g) and larger pore volume (up to 1.25 cm^3/g), comparatively strong ion-exchange capability; significant fast and long-distance electron-transport ability; and enhanced light absorption due to the high tube diameter ratio (Liu et al., 2014).

In addition, noble metals (e.g., Pt, Pd, and Ag) with TiO_2 deposited can bend the valence band (VB) and conduction band (CB) as the difference in the Fermi level between metals and semiconductors (SC) to form a Schottky barrier (Christoforidis and Fornasiero, 2017). The work function (φ) increases with the greater Schottky barrier in the metal-SC heterojunction, causing a better charge separation effect, which is a key step in most photocatalytic processes. For example, TiO_2 modified with Pt, Pd, and Ag has higher decomposition activity for the pollutants removal, with the pseudo-first-order kinetic rate constants of were 0.7267, 0.4369, and 0.1257 h^{-1}, which were 12.5, 7.5, and 2.2 times higher than that of pure TiO_2, respectively (Li et al., 2016). While among these noble metals, platinum (Pt) has a comparatively high work function ($\varphi = 5.93$ eV) with good performance as a TiO_2co-catalyst (Fu et al., 2008; Chiarello et al., 2010). The reason has been explained that photogenerated electrons are used more efficiently in Pt atoms (Nguyen and Juang, 2019). In this study, TNT-Pt was prepared by hydrothermal synthesis, calcined at different temperatures (300, 400, 500°C), and different amounts of Pt loading (3, 5, 10, and 20 wt%). All catalysts were characterized for their morphology and structure and tested for the degradation performance of RhB in the photochemical reactor under UV irradiation. Meanwhile, the solution pH, initial concentration of the pollutants, and H_2O_2 addition affecting the degradation efficacy was discussed and the photocatalytic mechanism was explored by quenching experiments.

MATERIALS AND METHODS

Preparation of TNT-Pt

Briefly, 1.2 g commercial TiO_2 (AeroxideP25) and 75 ml NaOH aqueous solution (10 M) were placed in a 100 ml Teflon lined hydrothermal autoclave reactor and kept in an oven at 110°C for 12 h. Then, the sample was washed several times with deionized water and filtered. Afterward, the sample was ultrasonically treated with 0.1 M HCl aqueous solution for 15 min and filtered. After filtering, the sample was washed several times with deionized water. The obtained samples were kept in an oven at 80°C for 12 h. After being completely dried, the samples were collected and ground, which were identified as TiO_2 nanotubes (TNT). All chemicals are of analytical grade. TNT was calcined at different temperatures in a tube furnace (Nabertherm P330) with the following temperature program: from 25°C to the calcination temperatures (T_{calc}, °C) at a heating rate of 5°C/min, and keeping 3 h at T_{calc}. The T_{calc} values were set at 300, 400, and 500°C, respectively. These three samples are labeled as TNT-300, TNT-400, and TNT-500.

Pt was photo-deposited on all the samples (P25, TNT, TNT-300, TNT-400, TNT-500). Firstly, 50 mg photocatalyst was added into 1.05 ml H_2PtCl_6 aqueous solution (10 g/L) to prepare 50 ml solutions and then mixed with 4 ml CH_3OH. After irradiating under the 300 W mercury lamp for 3 h, the suspension was washed with deionized water and filtered to obtain the precipitate. After keeping in an oven at 80°C for 12 h, the sample was collected and determined to be TNT-Pt, TNT-300-Pt, TNT-400-Pt, and TNT-500-Pt, which were subsequently used in this study.

Catalyst Characterization

The crystalline structure of the samples was determined by an XRD PANalytical Empyrean diffractometer, a Cu Kα radiation of 1.54 Å, scan step-size 0.0167°and a 2θ scan range of 10–90°. Absorption spectra of doped and undoped Pt samples were analyzed using a UV spectrometer (Shimadzu) scanning wavelengths from 200 to 800 nm. TEM and STEM-EDS analysis were performed by using Tecnai G2 and Titan FEI transmission electron microscopes, operating at 200 and 300 kV, respectively. The sample was prepared by suspending the powder in 2-propanol, ultrasounds treated, and finally dropping 5 μL of the suspension three consecutive times on a 400-mesh Cu grid provided by Tedpella, letting the solvent evaporate at room temperature. The specific surface area and pore volume of the derived nanotubes were determined by BET (Micromeritics, ASAP 2460/2020). Determination of Pt loading on TNT-Pt by ICP-MS (Agilent 7700s). Zeta potential values were determined using a laser particle size zeta potential analysis (Malvern Zetasizer Nano As). Zeta potential was measured three times at each pH value. The preparation method referred to the previous studies by some modifications (Xiong and Xu, 2016; Scandura et al., 2019).

Photocatalytic Evaluation

The photodegradation of RhB in water was performed in a photochemical reaction instrument, which consisted of a 100 W mercury lamp with a wavelength of 365 nm, a condensation cup, and a magnetic stirrer inside a box. For degradation of RhB, the synthesized catalyst samples were added to the RhB solution with an initial concentration of 20 mg/L. Then, the suspensions were strongly stirred for 0.5 h

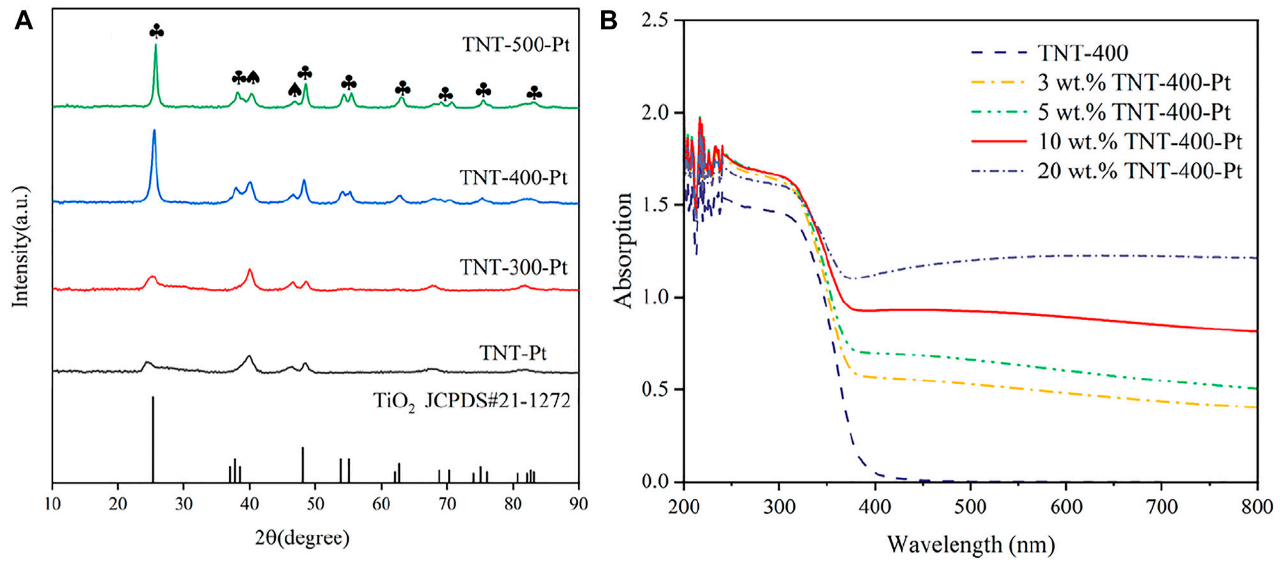

FIGURE 1 | XRD patterns of different samples with most important planes indicated **(A)**, and UV absorption of samples with different Pt loading **(B)**, ♣: the typical diffraction peak of anatase, ♠: the diffraction peak of Pt oxide.

in the dark to reach the adsorption equilibrium state. After that, the solution was exposed to UV irradiation for 70 min. During the photocatalytic process, 2 ml solution was sampled every 10 min (8 times in total) and filtered to remove the catalyst. The supernatant was analyzed to measure the concentration of RhB with a Hitachi UV-3010 UV-vis spectrometer. All experiments were conducted in triplicate.

RESULTS AND DISCUSSION

Morphologies and Structures

The evaluation of the phase and structure of the calcined TNT was observed through XRD patterns (**Figure 1A**). The crystallinity of these samples gets higher with the increase in calcination temperature (T_{calc}). It can be seen that TNT-300 has only a small amount of anatase diffraction peaks (**Supplementary Figure S1**). The spectra of TNT-400 show characteristic diffraction peaks located at 25.281°, 37.8°, and 48.049°, corresponding to the (101), (004), and (200) reflection plane (JCPDS card 21-1,272) (Lazarte et al., 2018). $H_2Ti_3O_7$ (202), brookite (200), and rutile (210) reflection plane appear in TNT-500 at 24.670°, 33.050°, and 44.699°. Thus, TNT-400 owns the highest amount and purest anatase type crystal phase than that TNT-300 and 500. After Pt was deposited on the surface of TNT, new diffraction peaks at 40.186° and 63.024°that derived from PtO_2 (101) and PtO (222), respectively, appeared in the catalyst samples (JCPDS card 38-1355 and 47-1171). Moreover, the addition of Pt only passivates the diffraction peaks of anatase and does not affect the overall crystal form of the sample. In order to determine the photo absorbance properties, the UV absorption of TNT and Pt-TNT under different Pt loadings were analyzed by UV-Vis at wavelengths of 200–800 nm as shown in **Figure 1B**. The main light absorption wavelength of TNT-400 is in the ultraviolet range. However, with increasing Pt loading, the amount of visible light absorbed by the catalyst steadily increased, with only a slight increase in the amount of light absorption in the UV range, where 10 wt% loadings showed the best absorption of UV light in the UV rangeability. This illustrates the increased photosensitivity of Pt-modified TNTs in the visible and near-visible light wavelength range relative to pure TNTs.

Furthermore, TNT-300, 400, and 500 were modified with Pt deposition, respectively. While no obvious change in the morphology of Pt-loaded samples was observed in SEM images (**Supplementary Figure S2**). EDS results verified the presence of Ti, O, and Pt elements (**Figure 2**), indicating the successful photo-deposition of Pt particles. BET results provided in **Table 1**, claim that the surface areas were followed the sequence as TNT-300-Pt = 286.2 m^2/g > TNT-400 = 155.8 m^2/g > TNT-400 = 148.2 m^2/g > TNT-500-Pt = 81.5 m^2/g proving maximum specific surface area of TNT-300 Pt. TEM was used to further analyze the morphology of the TNT-300, 400, and 500-Pt samples as shown in **Figure 3**. From the images, all the TNT tubes present a uniform distribution with an average diameter of 7–10 nm, with an opened tube orifice (**Figures 3A–C**), while the surface-adsorbed Pt nanoparticles exhibit a size of about 2–5 nm (**Figure 3D**), demonstrated again the emergence of new photocatalytic sites. A layered structure with an apparent edge was observed, illustrating the incomplete curling of part of the TNT tube. With the increase of calcination temperature from 300 to 500 °C, TNT tube curling degree increased and the loading content of Pt nanoparticles raised (**Figures 3A–C**).

Photocatalytic Behavior

The irradiation time versus the RhB concentration curves has been given in **Figure 4**. Obviously, TNT prepared under T_{calc}

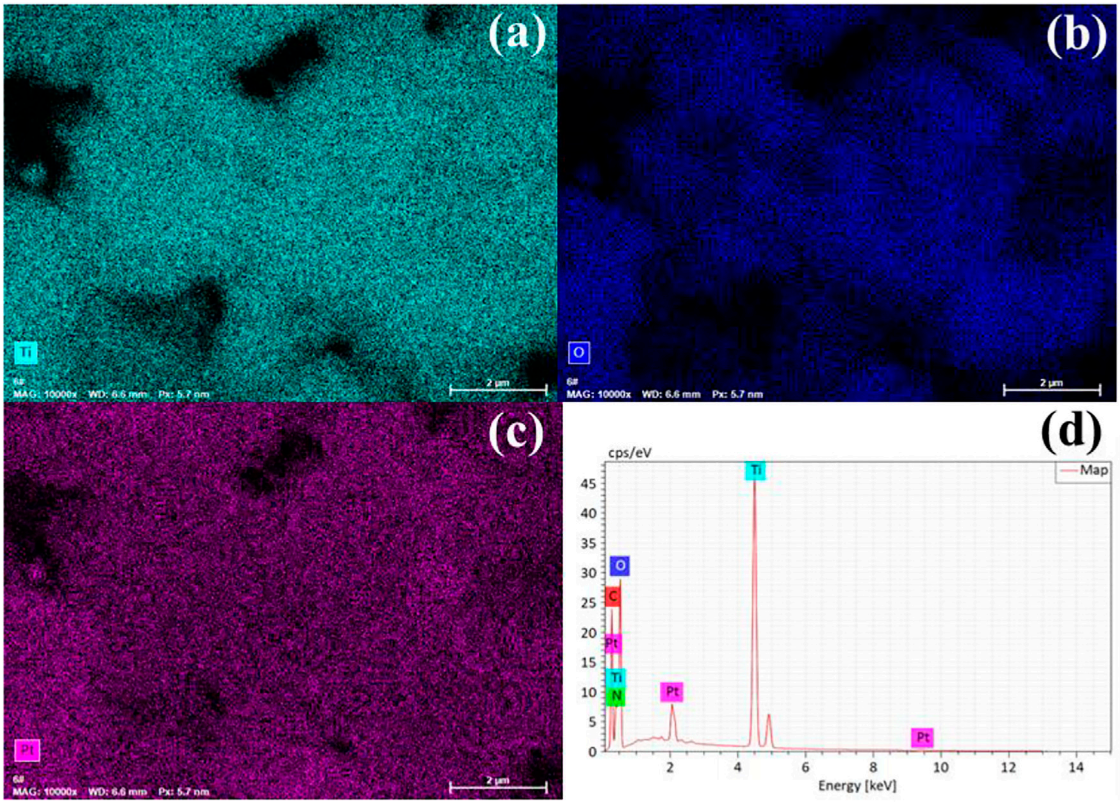

FIGURE 2 | EDS mapping of elements Ti **(A)**, O **(B)**, Pt **(C)**, and elements composition **(D)** of TNT-400-Pt.

TABLE 1 | Surface areas and particle sizes of TNT-400 and TNT-Pt photocatalysts.

Catalyst	Surface areas (m^2/g)	Pore volume (cm^3/g)	Pore sizes (nm)
TNT-400	155.8403	1.0586	23.632
TNT-300-Pt	286.2142	1.005651	12.3963
TNT-400-Pt	148.194	0.646873	13.9094
TNT-500-Pt	81.4997	0.450061	17.1476

400°C (TNT-400) exhibited higher photocatalytic ability for RhB removal than that of TNT-300, 500, and primitive material (TNT) as shown in **Figures 4A,B**. This could be explained that TNT-400 owns the highest amount of anatase type crystal phase according to the characterization results mentioned above. Commonly, the anatase type crystal phase contains more defects and vacancies, resulting in more oxygen vacancies to capture electrons, so it has higher activity (Li et al., 2021). Comparatively, TNT-300 and 500 own fewer amounts of anatase type crystal phase, especially TNT-500 with part of rutile type crystal phase, which has almost no photocatalytic activity (Phuong and Yoo, 2020). Thus, TNT-300 and 500 had poor photocatalytic capacity for RhB Removal. While after the Pt loading, the degradation performance was highly promoted as RhB was completely bleached by TNT-400-Pt within 70 min (**Figure 4C**). The kinetics of the photodegradation of RhB fitted well to the pseudo-first-order model ($R^2 > 0.90$) based on **Eq. 1** (Mansurov et al., 2022):

$$\mathrm{In}\,(C_0/C_t) = kt \qquad (1)$$

where k is the rate constant, C_0 and C_t are the concentration of RhB in solution at irradiation time 0 and t (min^{-1}), respectively. As shown in **Figure 4D**, the rate constant (k) was ranked as $k_{TNT\text{-}400\text{-}Pt} = 0.035\ min^{-1} > k_{TNT\text{-}400} = 0.015\ min^{-1}$. As Pt loading on TNT was favorable for O_2 adsorption and the superoxide radical ($O_2^{-\bullet}$) formation, which plays the key role for RhB degradation. Similarly, TNT-400-Pt owned better catalytic ability than TNT-300, 400 and original TNT-Pt, with the sequence of k value as $k_{TNT\text{-}400\text{-}Pt} = 0.035\ min^{-1} > k_{TNT\text{-}500\text{-}Pt} = 0.015\ min^{-1} > k_{TNT\text{-}300} = 0.002\ min^{-1} \approx k_{TNT\text{-}Pt} = 0.002\ min^{-1}$, which further proved the high activity of TNT-400-Pt. This might be attributed to the various Pt contents deposited in TNT. Under different T_{calc}, the

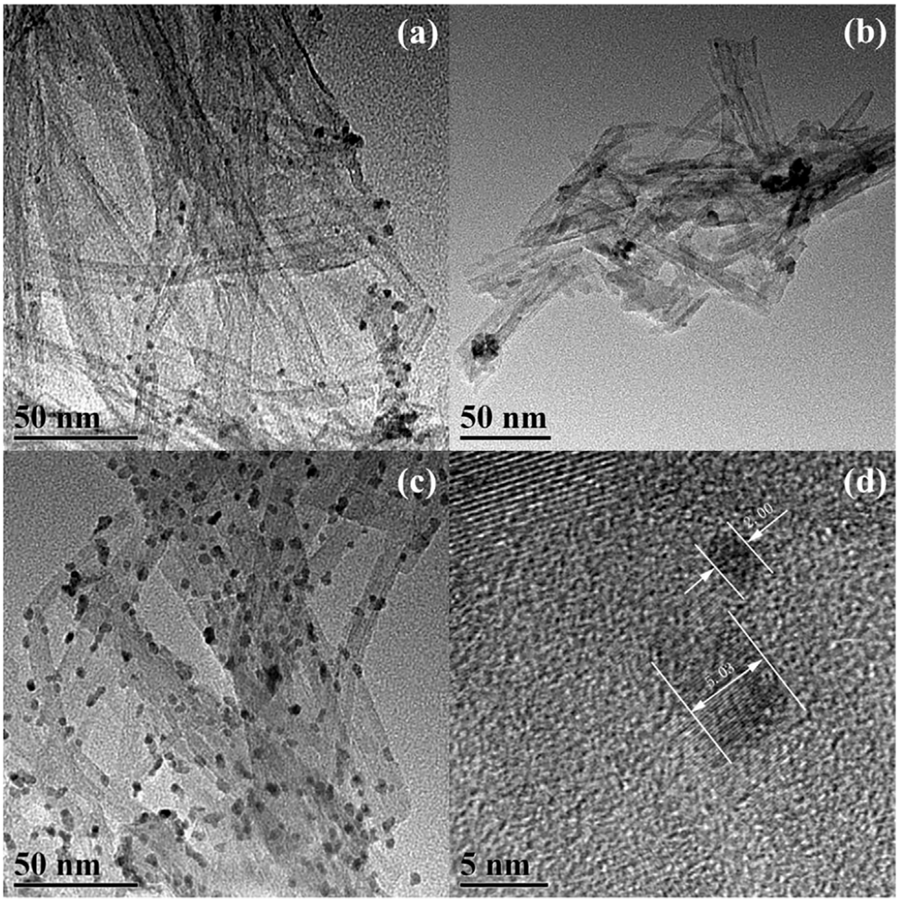

FIGURE 3 | TEM images of TNT-300-Pt **(A)**, TNT-400-Pt **(B),** and TNT-500-Pt **(C)**, scale bar: 50 nm, Pt nanoparticle size **(D)**.

Pt contents deposited in TNT-300, 400, 500 detected by ICP-MS were 7.3 wt%, 7.5 wt%, and 6.8 wt%, thus TNT-400-Pt owned the highest amount of Pt deposited in the catalyst. Furthermore, TNT-400 owns the highest amount of anatase type crystal phase, leading to the stronger photocatalytic ability for pollutant removal.

In this case, the effects of different experimental factors were investigated on photocatalysis by TNT-400-Pt. First, the loading amount of Pt during the synthesis process is essential for the catalytic performance as shown in **Figure 5A**. As a result, only a proper amount of Pt 10 wt% loading has a positive effect on RhB removal. A higher or lower amount of Pt (20 wt% or 5 wt% and 3 wt%) loading had the reduced degradation efficacies, which were all better than that of pure TNT. This could be explained that Pt deposition could provide active species for the pollutant oxidation, while the excess loading may cover active sites on the TiO_2 surface, thereby reducing photodegradation efficiency, which was also discussed by previous literature (Shawky et al., 2020). In addition, the UV-vis results (**Figure 1B**) exhibit that 20 wt% TNT-Pt had higher absorption values than that of others, which also could be the reason for its higher degradation performance.

Moreover, the photodegradation of RhB by TNT-400-Pt (10 wt%) was evaluated at various initial solution pHs of 3, 5, 7, and 9 as shown in **Figure 5B**. The degradation efficacy is higher under acid conditions than that under neutral and alkali conditions, which is probably due to fact that the charge of TNT-400-Pt at the pH of 6.1 is zero as shown in **Supplementary Figure S3** in the appendix. This suggests that the TNT surface was positively charged at pH < 6.1, while negatively charged at pH > 6.1. At low pH, H^+ adsorbed on the catalyst surface has a large proton exchange capacity, which could react with the photogenerated electrons to form hydrogen radical (H•). Meanwhile, a lower pH solution has electronegative centers, leading to the promoted adsorption on the surface of TiO_2, which also increase the degradation rate under acid condition. A similar explanation has also been mentioned in the previous literature (Mohanty et al., 2020).

Figure 5C exhibits the effect of initial concentration in the range of 5–25 mg L^{-1} on the catalytic performance. The results show that the degradation efficacy was highest at the RhB concentration of 5 mg L^{-1}. While it decreased with the concentration increasing as the rate constant (k) was ranked from highest to lowest as $k_{5\ \mathrm{mg/L}} = 0.092\ \mathrm{min}^{-1} > k_{10\ \mathrm{mg/L}} = 0.055\ \mathrm{min}^{-1} > k_{20\ \mathrm{mg/L}} = 0.034\ \mathrm{min}^{-1} > k_{30\ \mathrm{mg/L}} = 0.011\ \mathrm{min}^{-1}$, which could be explained as the active radicals generated on the catalyst surface were reduced due to the occupation of pollutant molecules in the active sites. Furthermore, H_2O_2 reported as an

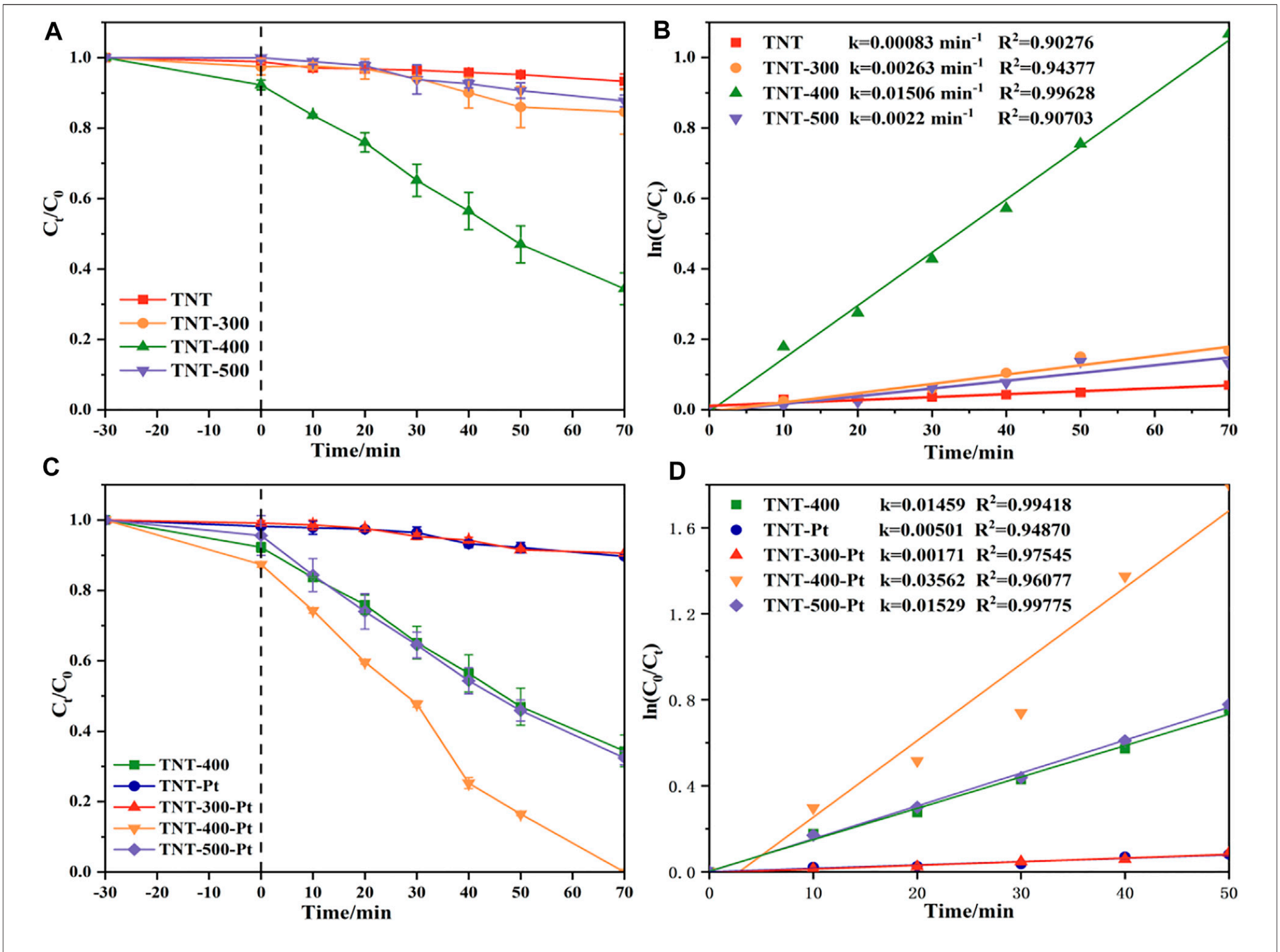

FIGURE 4 | (A) Photocatalytic decomposition of RhB and **(B)** pseudo-first-order kinetic model by TNT, TNT-300, TNT-400, and TNT-500, **(C)** photocatalytic decomposition of RhB, and **(D)** pseudo-first-order kinetic model by TNT-Pt, TNT-300-Pt, TNT-400-Pt and TNT-500-Pt, pH = 6.83, initial RhB concentration = 20 mg/L.

electron acceptor also plays role in the RhB removal. **Figure 5D** reveals that H_2O_2 in the RhB solution enhanced the degradation efficacy, especially 11 mm addition with the promoted rate constant of 0.057 min^{-1}, higher than that of 7 mm and no H_2O_2 addition. The reason could be attributed to the generation of hydroxyl radical (OH•) reacting from the reaction of H_2O_2 with electron (e$^-$) as the **Eq. 2** (Wang J.-F. et al., 2022).

$$e^- + H_2O_2 \rightarrow OH^- + OH\bullet \tag{2}$$

While a limiting value for the degradation rate occurred when the H_2O_2 addition achieved 15 mM due to the scavenging reaction as shown in **Eq. 3**.

$$H_2O_2 + OH\bullet \rightarrow H_2O + HO_2\bullet \tag{3}$$

Photocatalytic Mechanism

During the photocatalytic process, the main active species include photogenerated holes (h$^+$) and electrons (e$^-$), hydroxyl radicals (OH•), and superoxide radical anions ($O_2^{-\bullet}$) that could be produced based on the following **Eq. 4–6**.

$$TNT - Pt + hv \rightarrow TNT - Pt\left(h^+ + e^-\right) \tag{4}$$

$$h^+ + H_2O \rightarrow OH\bullet + H^+ \tag{5}$$

$$e^- + O_2 \rightarrow O_2^{-\bullet} \tag{6}$$

To confirm the significance of these active species, tertbutanol (*t*-BuOH), disodium ethylenediaminetetraacetate (EDTA-Na$_2$), and nitroblue tetrazolium (NBT) as the scavengers of OH•, h$^+$, and $O_2^{-\bullet}$, respectively were added during the photocatalytic process. As shown in **Figure 6A**, it could be easily observed that the degradation efficacy was poorest with NBT addition, followed by EDAT-Na$_2$ and *t*-BuOH addition, compared with the performance by TNT-Pt without scavengers. This proves that $O_2^{-\bullet}$ plays an essential role in the RhB degradation, then was a photogenerated hole (h$^+$) and OH• contributed to the pollutant removal. Accordingly, the possible photocatalytic mechanism could be speculated as shown in **Figure 7**. Under UV irradiation, the RhB molecules were activated as short-lived active transient, adsorbed over Pt metal sites. Meanwhile, Pt

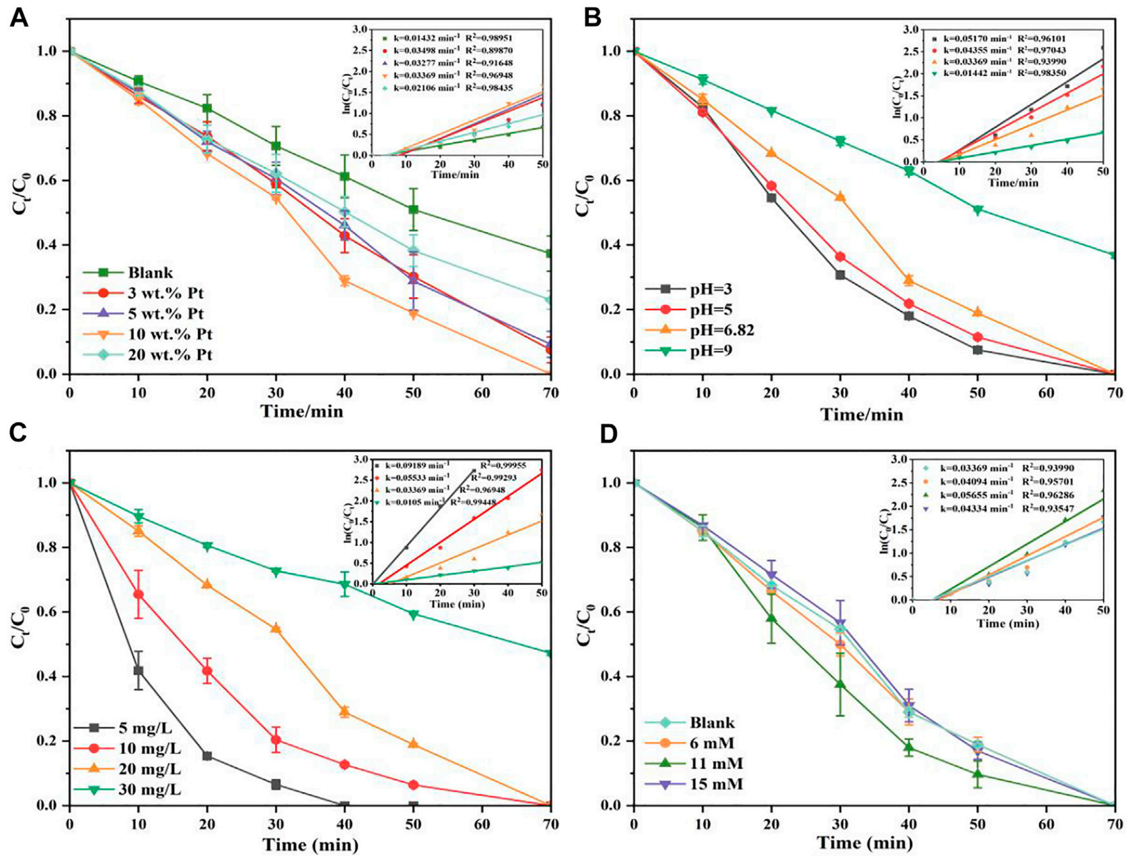

FIGURE 5 | Change Pt load on TNT-400 **(A),** effects of pH_{ini} **(B)** on RhB photodegradation by TNT-400-Pt (10), the effect of initial concentration of RhB on the photocatalytic degradation of TNT-400-Pt (10) **(C)**, effects of H_2O_2 **(D)** on RhB photodegradation by TNT-400-Pt.

loading induced the $O_2^{-\bullet}$ generation of pollutant oxidation, and nano-structure holes of TNT could provide unique space and electronic environments for Pt active sites, which was easier to inhibit the recombination of photogenerated electron and hole pairs, leading to the prior photocatalytic ability dealing with RhB. This was consistent with the literature (Ding et al., 2022; Wang X. et al., 2022). Therefore, the catalytic activity for RhB was significantly improved by TNT with Pt deposition.

Application to Other Dye Pollutants and Recycling

TNT-Pt-400 (10wt%) was also used for other dye pollutants such as CR, MB, and MO as shown in **Figures 6B,C**. As a result, at initial concentrations of 10 mg/L, almost all RhB, CR, MB, and OG could be removed within 70 min by TNT-Pt. While at the concentration of 20 mg/L, 100% RhB and CR, 65% MB and 90% OG could be degraded within 70 min. Thus, the obtained catalysts of TNT-Pt own a comparatively strong capacity for dye pollutants removal. In addition, the reuse capacity of the synthesized materials (TNT-Pt-400, 10 wt%) was evaluated by five cycling usages as shown in **Figure 6D**. Obviously, the performance stained well as almost 100% RhB removal in the first three cycles, 80% removal remained in the third time of cycling, and more than 60% removal was achieved in the fifth time, indicating that the synthesized catalysts were reusable and exhibited high potential on the applications of real wastewater treatment.

CONCLUSION AND FUTURE PERSPECTIVE

In summary, TNT-Pt was synthesized successfully and exhibited well-characterized morphology and structure. During the synthetic process, 400°C calcination temperature and 10 wt% Pt deposition was determined to be the preferable condition to form a better crystal morphology based on the characterization results. In the photodegradation experiments, the rate constant (k) was ranked as $k_{TNT\text{-}400\text{-}Pt} = 0.045\ min^{-1} > k_{TNT\text{-}400} = 0.014\ min^{-1}$. In addition, acid solution (pH 3) and lower initial concentration of RhB (5 mg/L) both increased the degradation process, while a moderate volume of 11 mm H_2O_2 addition had the promoted degradation performance. Furthermore, in the quenching experiment, NBT had the most significant inhibition effect on the photocatalytic efficacy than other scavengers, suggesting the dominant active species $O_2^{-\bullet}$. Besides, the synthesized TNT-Pt could remove almost CR, MB, and OG as well as RhB, and its catalytic capacity stained well in five recycling usages.

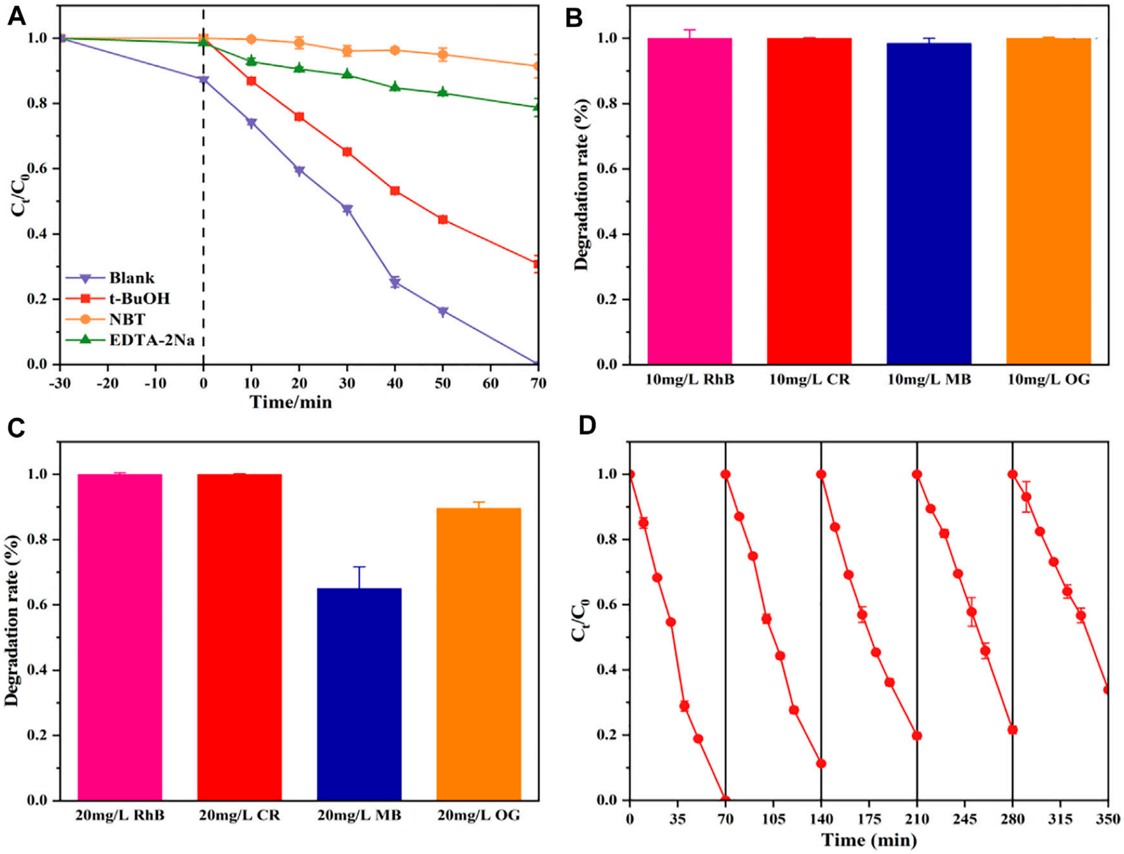

FIGURE 6 | Photocatalytic activities of the TNT-400-Pt sample for RhB degradation with disparate scavengers **(A)**, photocatalytic degradation of different dyes within 70 min by TNT-400-Pt at an initial concentration of 10 mg/L **(B),** and 20 mg/L **(C)**, five cycles of degradation of TNT-400-Pt **(D)**.

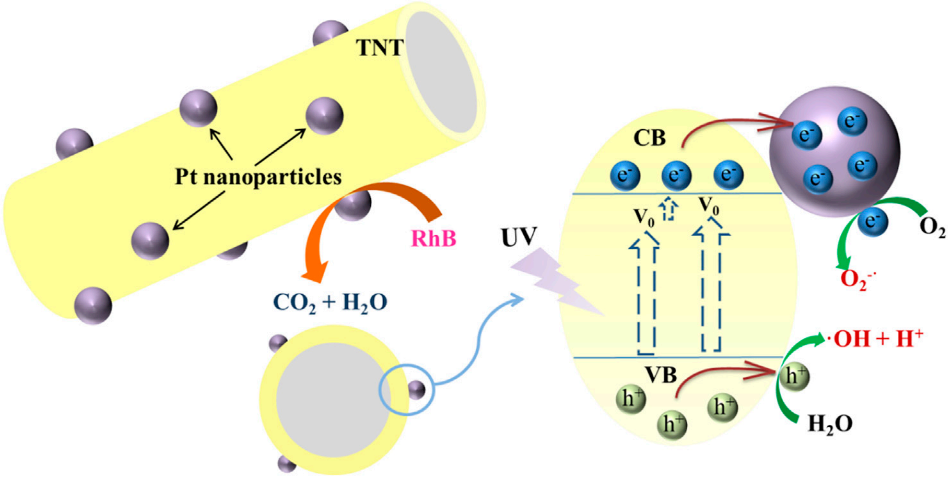

FIGURE 7 | The possible photocatalytic mechanism of TNT-PT for RhB removal.

So far, large datasets have existed on the synthesis of photocatalyst materials and their degradation ability for particular pollutant removal (Xu et al., 2020a). Nevertheless, information on the controlling factors of the photocatalysis process and the immobilization and recycling use of catalysts are limited. Thus, future research should focus on the follows:

◆ Assessing dissolved oxygen (DO) and dissolved organic matters (DOM) effect on the photocatalytic performance of the as-synthesized TNT-Pt;

◆ Exploring the immobilization of the synthesized catalysts when dealing with real dye wastewater;

◆ Utilizing the electron paramagnetic resonance (EPR) to detect the active radicals directly for the further investigation of the reaction mechanism;

◆ Synthesizing more functionalized yet low-cost catalyst polymers decomposing the dye water with high efficacy.

DATA AVAILABILITY STATEMENT

The raw data supporting the conclusions of this article will be made available by the authors, without undue reservation.

AUTHOR CONTRIBUTIONS

XQ, ZW, XX and YY designed the study and wrote the main manuscript. XQ, MP made theoretical calculations and prepared the figures and tables. XQ, ZW and MP performed the experiments and data collection. MP and CH obtained funding for the research. All authors reviewed the manuscript, made amendments, and contributed with their expertise.

FUNDING

This study was financially supported by the Major Projects of Study on National Social Science Foundation of China (No. 21ZDA028), National Natural Science Foundation of China (Grant No. 51908127), and the National Key Research and Development Project (No. 2018YFE0110400).

SUPPLEMENTARY MATERIAL

The Supplementary Material for this article can be found online at: https://www.frontiersin.org/articles/10.3389/fchem.2022.922701/full#supplementary-material

REFERENCES

Chiarello, G. L., Aguirre, M. H., and Selli, E. (2010). Hydrogen Production by Photocatalytic Steam Reforming of Methanol on Noble Metal-Modified TiO2. *J. Catal.* 273 (2), 182–190. doi:10.1016/j.jcat.2010.05.012

Christoforidis, K. C., and Fornasiero, P. (2017). Photocatalytic Hydrogen Production: A Rift into the Future Energy Supply. *ChemCatChem* 9 (9), 1523–1544. doi:10.1002/cctc.201601659

Ding, D., Li, Z., Yu, S., Yang, B., Yin, Y., Zan, L., et al. (2022). Piezo-photocatalytic Flexible PAN/TiO2 Composite Nanofibers for Environmental Remediation. *Sci. Total Environ.* 824, 153790. doi:10.1016/j.scitotenv.2022.153790

Fu, X., Long, J., Wang, X., Leung, D., Ding, Z., Wu, L., et al. (2008). Photocatalytic Reforming of Biomass: A Systematic Study of Hydrogen Evolution from Glucose Solution. *Int. J. Hydrogen Energy* 33 (22), 6484–6491. doi:10.1016/j.ijhydene.2008.07.068

Hao, B., Guo, J., Zhang, L., and Ma, H. (2022). Magnetron Sputtered TiO_2/CuO Heterojunction Thin Films for Efficient Photocatalysis of Rhodamine B. *J. Alloys Compd.* 903, 163851. doi:10.1016/j.jallcom.2022.163851

Hao, D., Wei, Y., Mao, L., Bai, X., Liu, Y., Xu, B., et al. (2021). Boosted Selective Catalytic Nitrate Reduction to Ammonia on Carbon/bismuth/bismuth Oxide Photocatalysts. *J. Clean. Prod.* 331, 129975. doi:10.1016/j.jclepro.2021.129975

Hoyer, P. (1996). Formation of a Titanium Dioxide Nanotube Array. *Langmuir* 12 (6), 1411–1413. doi:10.1021/la9507803

Lazarte, J., Dipasupil, R., Pasco, G., Eusebio, R., Orbecido, A., Doong, R.-a., et al. (2018). Synthesis of Reduced Graphene Oxide/Titanium Dioxide Nanotubes (rGO/TNT) Composites as an Electrical Double Layer Capacitor. *Nanomaterials* 8 (11), 934. doi:10.3390/nano8110934

Li, F., Wang, D., and Gong, X. Q. (2021). Subtle Structure Matters: Boosting Surface-Directed Photoelectron Transfer via the Introduction of Specific Monovalent Oxygen Vacancies in TiO2. *Phys. Chem. Chem. Phys.* 23 (35), 19854–19861. doi:10.1039/d1cp02787e

Li, M., Yu, Z., Liu, Q., Sun, L., and Huang, W. (2016). Photocatalytic Decomposition of Perfluorooctanoic Acid by Noble Metallic Nanoparticles Modified TiO 2. *Chem. Eng. J.* 286, 232–238. doi:10.1016/j.cej.2015.10.037

Liu, N., Chen, X., Zhang, J., and Schwank, J. W. (2014). A Review on TiO2-Based Nanotubes Synthesized via Hydrothermal Method: Formation Mechanism, Structure Modification, and Photocatalytic Applications. *Catal. Today* 225, 34–51. doi:10.1016/j.cattod.2013.10.090

Liu, X., Xu, B., Duan, X., Hao, Q., Wei, W., Wang, S., et al. (2021). Facile Preparation of Hydrophilic In2O3 Nanospheres and Rods with Improved Performances for Photocatalytic Degradation of PFOA. *Environ. Sci. Nano* 8 (4), 1010–1018. doi:10.1039/d0en01216e

Mansurov, R. R., Zverev, V. S., and Safronov, A. P. (2022). Dynamics of Diffusion-Limited Photocatalytic Degradation of Dye by Polymeric Hydrogel with Embedded TiO2 Nanoparticles. *J. Catal.* 406, 9–18. doi:10.1016/j.jcat.2021.12.026

Mi, Y., Wang, N., Fang, X., Cao, J., Tao, M., and Cao, Z. (2021). Interfacial Polymerization Nanofiltration Membrane with Visible Light Photocatalytic Self-Cleaning Performance by Incorporation of CQD/TiO2. *Sep. Purif. Technol.* 277, 119500. doi:10.1016/j.seppur.2021.119500

Mohanty, S., Moulick, S., and Maji, S. K. (2020). Adsorption/photodegradation of Crystal Violet (Basic Dye) from Aqueous Solution by Hydrothermally Synthesized Titanate Nanotube (TNT). *J. Water Process Eng.* 37, 101428. doi:10.1016/j.jwpe.2020.101428

Nguyen, C. H., and Juang, R.-S. (2019). Efficient Removal of Cationic Dyes from Water by a Combined Adsorption-Photocatalysis Process Using Platinum-Doped Titanate Nanomaterials. *J. Taiwan Inst. Chem. Eng.* 99, 166–179. doi:10.1016/j.jtice.2019.03.017

Perera, S. D., Mariano, R. G., Vu, K., Nour, N., Seitz, O., Chabal, Y., et al. (2012). Hydrothermal Synthesis of Graphene-TiO2 Nanotube Composites with Enhanced Photocatalytic Activity. *ACS Catal.* 2 (6), 949–956. doi:10.1021/cs200621c

Phuong, D. V., and Yoo, H. (2020). Physicochemical Characterization and Photocatalytic Activity of Reduced TiO2 Prepared by Birch-type Reduction. *J. Nanosci. Nanotechnol.* 20 (9), 5614–5617. doi:10.1166/jnn.2020.17653

Pu, M., Ma, Y., Wan, J., Wang, Y., Wang, J., and Brusseau, M. L. (2017). Activation Performance and Mechanism of a Novel Heterogeneous Persulfate Catalyst: Metal-Organic Framework MIL-53(Fe) with FeII/FeIII Mixed-Valence Coordinatively Unsaturated Iron Center. *Catal. Sci. Technol.* 7 (5), 1129–1140. doi:10.1039/c6cy02355j

Scandura, G., Rodríguez, J., and Palmisano, G. (2019). Hydrogen and Propane Production from Butyric Acid Photoreforming over Pt-TiO2. *Front. Chem.* 7, 563. doi:10.3389/fchem.2019.00563

Shawky, A., Alhaddad, M., Al-Namshah, K. S., Mohamed, R. M., and Awwad, N. S. (2020). Synthesis of Pt-Decorated CaTiO3 Nanocrystals for Efficient Photoconversion of Nitrobenzene to Aniline under Visible Light. *J. Mol. Liq.* 304, 112704. doi:10.1016/j.molliq.2020.112704

Skjolding, L. M., Jørgensen, L. v., Dyhr, K. S., Köppl, C. J., McKnight, U. S., Bauer-Gottwein, P., et al. (2021). Assessing the Aquatic Toxicity and Environmental Safety of Tracer Compounds Rhodamine B and Rhodamine WT. *Water Res.* 197, 117109. doi:10.1016/j.watres.2021.117109

Sutar, S., Patil, P., and Jadhav, J. (2022). Recent Advances in Biochar Technology for Textile Dyes Wastewater Remediation: A Review. *Environ. Res.* 209, 112841. doi:10.1016/j.envres.2022.112841

Wang, C., Du, P., Duan, X., Luo, L., and Li, W. (2021). Tailoring of Visible Light Driven Photocatalytic Activities of Flower-Like BiOBr Microparticles towards Wastewater Purification Application. *Adv. Mater. Inter* 9, 2101671. doi:10.1002/admi.202101671

Wang, J.-F., Liu, Y., Shao, P., Zhu, Z.-Y., Ji, H.-D., Du, Z.-X., et al. (2022). Efficient Ofloxacin Degradation via Photo-Fenton Process over Eco-Friendly MIL-88A(Fe): Performance, Degradation Pathways, Intermediate Library Establishment and Toxicity Evaluation. *Environ. Res.* 210, 112937. doi:10.1016/j.envres.2022.112937

Wang, X., Lian, M., Yang, X., Lu, P., Zhou, J., Gao, J., et al. (2022). Enhanced Activity for Catalytic Combustion of Ethylene by the Pt Nanoparticles Confined in TiO2 Nanotube with Surface Oxygen Vacancy. *Ceram. Int.* 48 (3), 3933–3940. doi:10.1016/j.ceramint.2021.10.180

Wu, Q., Cao, J., Wang, X., Liu, Y., Zhao, Y., Wang, H., et al. (2021). A Metal-free Photocatalyst for Highly Efficient Hydrogen Peroxide Photoproduction in Real Seawater. *Nat. Commun.* 12 (1), 483. doi:10.1038/s41467-020-20823-8

Xiong, X., and Xu, Y. (2016). Synergetic Effect of Pt and Borate on the TiO2-Photocatalyzed Degradation of Phenol in Water. *J. Phys. Chem. C* 120 (7), 3906–3912. doi:10.1021/acs.jpcc.5b11923

Xu, B., Ahmed, M. B., Zhou, J. L., and Altaee, A. (2020b). Visible and UV Photocatalysis of Aqueous Perfluorooctanoic Acid by TiO2 and Peroxymonosulfate: Process Kinetics and Mechanistic Insights. *Chemosphere* 243, 125366. doi:10.1016/j.chemosphere.2019.125366

Xu, B., Ahmed, M. B., Zhou, J. L., Altaee, A., Wu, M., and Xu, G. (2017b). Photocatalytic Removal of Perfluoroalkyl Substances from Water and Wastewater: Mechanism, Kinetics and Controlling Factors. *Chemosphere* 189, 717–729. doi:10.1016/j.chemosphere.2017.09.110

Xu, B., Ahmed, M. B., Zhou, J. L., Altaee, A., Xu, G., and Wu, M. (2018). Graphitic Carbon Nitride Based Nanocomposites for the Photocatalysis of Organic Contaminants under Visible Irradiation: Progress, Limitations and Future Directions. *Sci. Total Environ.* 633, 546–559. doi:10.1016/j.scitotenv.2018.03.206

Xu, B., Liu, S., Zhou, J. L., Zheng, C., Weifeng, J., Chen, B., et al. (2021). PFAS and Their Substitutes in Groundwater: Occurrence, Transformation and Remediation. *J. Hazard. Mater.* 412, 125159. doi:10.1016/j.jhazmat.2021.125159

Xu, B., Wu, M., Pan, C., Sun, Y., Yuan, D., Tang, L., et al. (2017a). Aquatic Photolysis of Hydroxylated Polybromodiphenyl Ethers under Direct UV Irradiation: a Case Study of 2′-HO-BDE-68. *Environ. Sci. Pollut. Res.* 24 (16), 14409–14416. doi:10.1007/s11356-017-8726-x

Xu, B., Zhou, J. L., Altaee, A., Ahmed, M. B., Johir, M. A. H., Ren, J., et al. (2020a). Improved Photocatalysis of Perfluorooctanoic Acid in Water and Wastewater by Ga2O3/UV System Assisted by Peroxymonosulfate. *Chemosphere* 239, 124722. doi:10.1016/j.chemosphere.2019.124722

Zeng, Q., Chang, S., Wang, M., Li, M., Deng, Q., Xiong, Z., et al. (2021). Highly-active, Metal-free, Carbon-Based ORR Cathode for Efficient Organics Removal and Electricity Generation in a PFC System. *Chin. Chem. Lett.* 32 (7), 2212–2216. doi:10.1016/j.cclet.2020.12.062

Conflict of Interest: The authors declare that the research was conducted in the absence of any commercial or financial relationships that could be construed as a potential conflict of interest.

frontiers | Frontiers in Chemistry

ORIGINAL RESEARCH
published: 02 June 2022
doi: 10.3389/fchem.2022.864143

Fabrication of Cocatalyst NiO-Modified $BiVO_4$ Composites for Enhanced Photoelectrochemical Performances

Zhi-Qiang Wang[1]* *and HongJun Wang*[2]

[1]School of Materials Science and Engineering, North University of China, Taiyuan, China, [2]School of Materials Science and Engineering, Jilin University, Changchun, China

In this work, NiO modified $BiVO_4$ ($BiVO_4$/NiO) nanocomposite was synthesized using hydrothermal and calcination method. The composite of $BiVO_4$/NiO, further employed as a low-overpotential photoanode, was consisted of $BiVO_4$ nanoparticles and NiO nanosheets, in which the $BiVO_4$ nanoelectrode served as the matrix for the attachment of NiO nanosheets. Photoelectrochemical (PEC) tests show that $BiVO_4$/NiO displayed improved PEC performance compared with pure $BiVO_4$. The $BiVO_4$/NiO photoanode delivers a photocurrent density of 1.2 mA/cm^2 at 1.23 V vs. RHE in a Na_2SO_4 electrolyte under an AM 1.5G solar simulator, which is 0.3 mA/cm^2 higher than pure $BiVO_4$ photoanode. Meanwhile, the onset potential also generates a 350 mV cathodic shift. The enhanced performance of the $BiVO_4$/NiO nanocomposite is attributed to NiO unique lamellar structure capable of providing a large number of active sites. Measurements of electrochemical impedance spectra (EIS) and the incident photon-to-current efficiency (IPCE) illustrate that the enhanced PEC activities are ascribed to the improved charge carrier separation/transport and the promoted water oxidation kinetics furnished by the decoration of NiO cocatalyst.

Keywords: bismuth vanadate, nickel oxide, photoelectrochemical, cocatalyst, water oxidation

Edited by:
Qingyi Zeng,
University of South China, China

Reviewed by:
Qizhao Wang,
Chang'an University, China
Min Wang,
Jinan University, China
Ligang Xia,
Shanghai University of Electric Power, China

Correspondence:
Zhi-Qiang Wang
Zhiqiang_Wang2021@126.com

Specialty section:
This article was submitted to Inorganic Chemistry, a section of the journal Frontiers in Chemistry

Received: *28 January 2022*
Accepted: *18 March 2022*
Published: *02 June 2022*

Citation:
Wang Z-Q and Wang H (2022) Fabrication of Cocatalyst NiO-Modified $BiVO_4$ Composites for Enhanced Photoelectrochemical Performances. Front. Chem. 10:864143. doi: 10.3389/fchem.2022.864143

INTRODUCTION

Due to the excessive consumption of fossil energy that results in severe environmental pollution worldwide, the development of clean and sustainable energy technologies has received increasing attention. (Iwase et al., 2011; Guo et al., 2014; Zeng et al., 2021a) Clean hydrogen production is seen as a promising strategy, capable of simutaneously addressing climate change and environmental issues related to fossil fuel combustion. (Wang L. et al., 2018; Fukuzumi et al., 2018; Kim et al., 2018) Photoelectrochemical (PEC) water splitting, capable of directly converting solar energy into chemical energy, is considered a promising technology for converting solar energy into stable chemical energy, thus becoming attractive for reducing pollution associated with energy production. (Zhang J. et al., 2016; Wang and Wang, 2018; Weng et al., 2018; Zeng et al., 2019) In the PEC system, the photoanode acts the role of reaction sites for effective oxygen evolution. (Liu et al., 2014; Roger et al., 2017) In conclusion, the development of efficient photoanode materials is of great significance for constructing a practical PEC water splitting system. Various semiconductors including TiO_2 (Crake et al., 2017; Zeng et al., 2020), ZnO (Han et al., 2015; Hong et al., 2015), α-Fe_2O_3 (Dotan et al., 2011; Huang et al., 2016), WO_3 (Huang et al., 2017; Li et al., 2018), $BiVO_4$ (Wang et al., 2017a; Wang Q. et al., 2018) and BiOBr (Wang Z.-Q. et al., 2020) etc. have been developed as photocatalytic materials. Among them, scheelite-monoclinic bismuth vanadate ($BiVO_4$) has been widely studied for PEC water splitting owing to its relatively narrow band gap of 2.4 eV for visible-light absorption, as well as an appropriate band position for effective water oxidation and high stablility. (Malathi et al., 2018) However, the application of $BiVO_4$ is still restricted by its inherent defects such as low charge transport (Zhou et al., 2018), high charge recombination (Zhang Y. et al., 2016) and slow poor water oxidation kinetics (Zhai et al., 2017). The photocurrent density of the pure $BiVO_4$ is obviously lower than its theoretical value of 7.5 mA/cm^2 (Xu et al., 2014; Chen, 2015) To overcome these issues, transition metal-based catalysts used as cocatalysts are one of the effective ways to improve the PEC water splitting performance.

Transition metal-based materials, especially (Co., Ni, Fe)-based materials, comparable to precious metals because of their low cost and advanced catalytic performance, are considered to be the most promising OER catalysts. (Zhang Q. et al., 2016; Kuang et al., 2016; Wang Z. et al., 2020)The combination of the OER catalyst and the semiconductor light absorber can not only improve the PEC activity by providing an interface reaction active site that reduces overpotential, but also improve the PEC stability by rapidly consuming photo-generated carriers of semiconductor materials against electrolytes (Zhou et al., 2015). (Trotochaud et al., 2014; Zeng et al., 2021b) Recently, Dai (Kenney et al., 2013; Li et al., 2017) and colleagues deposited an ultra-thin nickel film on the n-type silicon substrate as a physical protective layer. It was found that a 2 nm nickel film played a crucial role in the sustainability of n-type silicon photoanodes in the solar-driven water oxidation process. The ultra-thin nickel was used as a protective layer and a passivation layer, and the natural NiO_x formed during the test was employed as an OER promoter. The NiOx/Ni/n-Si photoanode can work under constant photocurrent of 10 mA/cm^2, and still have excellent stability after water oxidation of 80 h. In addition, Lewis (Zhou et al., 2019) and his colleagues introduced an ultra-thin CoO_x film as an intermediate layer between NiO_x layer and n-Si to enhance the interaction between co-catalysts/semiconductors. It was found that further passivation of the CoO_x layer on the n-Si surface can change the initiation. The potential was more negative than NiO_x/SiO_x/n-Si photoanode. NiOx/CoO_x/SiO_x/n-Si showed the most negative flat band position, which was related to the barrier height in the semiconductor, and therefore highly improved the separation and collection of charge carriers. The above results indicate that the combination of NiO and other favorable semiconductors can remarkably reduce the overpotential of the photoelectrode.

In this study, a $BiVO_4$ photoanode, acting the role of photoelectrocatalysis substrate, is synthesised by a electrodeposition-calcination method. On the other hand, a nanosheet structured NiO, playing the performance of the water oxidation cocatalyst to combine with the $BiVO_4$ photoanode and thus improve the PEC performance, is preprared via a hydrothermal-calcination. Under AM 1.5G sunlight, the $BiVO_4$/NiO film produced a relatively high photocurrent density of 1.2 mA/cm^2 at 1.23 V vs. RHE, much higher than that of the pure $BiVO_4$ film. More importantly, the onset potential is negatively shifted by 350 mV relative to pure $BiVO_4$. The special structure of NiO is believed to be beneficial to absorb more incident photons through the light-harvesting effect, thereby enhancing the separation and transport of photo-induced charge carriers. Furthermore, the deposition of NiO cocatalyst on the surface of the $BiVO_4$ photoanode significantly promotes the water oxidation kinetics.

EXPERIMENTAL

Chemicals

$Bi(NO_3)_3{\cdot}5H_2O$ (Sinopharm Chemical Reagent Co., Ltd., 99.0%), potassium iodide, ethylene glycol are purchased from chemical reagent co, Ltd. P-benzoquinone (Tianjin Institute of Fine Chemicals, 99.0%). $Ni(NO_3)_2{\cdot}6H_2O$ (Sinopharm Chemical Reagent Co., Ltd., 99.0%), hexamethylenetetramine (HMTA, Chengdu Cologne Chemicals Co., Ltd., 99.0%), Anhydrous ethanol was purchased from Sinopharm Chemical Reagent Co., Ltd. All aqueous solutions were prepared with deionized water.

Preparation of $BiVO_4$

The preparation of $BiVO_4$ was synthesized with reference to previous reported work. Systematically, 50 ml of 0.4 M KI solution was first adjusted to pH 1.7 with 1 M HNO_3, and then 5 mmol $Bi(NO_3)_3{\cdot}5H_2O$ was added with rapid stirring until dissolved, resulting in an orange-red mixed solution. Then 20 ml of ethanol containing 4.6 mmol of 1,4-benzoquinone was slowly added dropwise to the above solution and stirred for several tens of minutes. Next, BiOI nanosheets were synthesized in a three-electrode system by electrodeposition. Among them, the platinum electrode was used as the counter electrode, the clean FTO glass was used as the working electrode, and the Ag/AgCl (3.5 M KCl) electrode was used as the reference electrode. Cyclic voltammetry (CV) was used for electrodeposition, and the resulting membrane was rinsed with distilled water to obtain a clean BiOI membrane. Immediately after, 150 µl of 0.2 M vanadyl acetylacetonate ($VO(acac)_2$) DMSO solution was dropped onto the above BiOI nanosheets. Calcined at 450°C for 2 h at a ramp rate of 2°C/min. The cooled membrane was washed with 1 M NaOH solution to remove excess V_2O_5 from the $BiVO_4$ electrode.

Preparation of $BiVO_4$/NiO Photoanode

The $BiVO_4$/NiO photoanode was prepared by a hydrothermal method. The configuration takes 60 ml of solution in which the volume ratio of deionized water and ethanol solution is 2:1. After ultrasonically mixed uniformly, 1.5 mmol $Ni(NO_3)_2{\cdot}6H_2O$ and 6 mmol HMTA were added thereto, and stirred until dissolved. Then 20 ml of the above mixture was added to a PTFE-lined stainless steel autoclave (100 ml). And the as-prepared $BiVO_4$ photoanode was placed obliquely with the conductive side facing upwards, heated at 90°C for 4 h. The photoanode was washed three times with water and ethanol and dried at 60°C for 12 h.

Finally, the $BiVO_4/NiO$ photoanode was obtained after calcination in air with a heating rate of 2°C/min at 300°C for 2 h.

Characterizations

The microscopic morphology of the samples was characterized by scanning electron microscopy (SEM, JSM-6701E). The crystal structure of the as-prepared photoanode was measured by X-ray diffraction (XRD) tests on the X-ray diffractometer (D/MAX-2200/PC). UV-Vis diffuse reflectance spectroscopy was used to investigate the response of the prepared photoelectrode to visible light on a UV-3100 spectrometer.

PEC Characterizations

The photoelectrochemical tests of the as-prepared photoanodes were carried out on a CHI 660D electrochemical workstation. A three-electrode system was used, in which a platinum sheet, Ag/AgCl (3.5 M KCl), and the samples were the counter electrode, the reference electrode and the working electrode, respectively. The electrolyte is 0.5 M Na_2SO_4 solution (pH = 6.86). All tests were performed with FTO backside irradiation at room temperature. The scan rate for linear sweep voltammetry (LSV) was $10\ \mathrm{mV\ s^{-1}}$. The light intensity was calibrated to $100\ \mathrm{mW/cm^2}$ with an optical power meter. And the incident photon current efficiency (IPCE) was measured using a 300 W xenon lamp with a monochromator in 0.5 M Na_2SO_4 electrolyte at 1.23 V vs. RHE. The photogenerated photocurrent (J_{abs}) undergo two major losses of charge carriers recombination in bulk and at interface. Hence the measured photocurrent during water oxidation (J_{H_2O}) is expressed as follows:

$$J_{H_2O} = J_{abs} \times \eta_{inj} \times \eta_{sep}$$

where J_{abs} is obtained by integrating the distribution of solar power density $P(\lambda)$ with light absorption $\alpha(\lambda)$ of the photoanode as equation:

$$J_{abs} = e\int_0^{\lambda_{abs}} \alpha(\lambda)\frac{P(\lambda)}{h\upsilon}d\lambda$$

where $\alpha(\lambda) = 1 - 10^{-A}$, A is the absorbance according to the UV-vis spectrum, $P(\lambda)$ = the distribution of solar power density.

The photocurrent during sodium sulfite oxidation was measured ($J_{SO_3^{2-}}$) in order to calculate charge separation efficiencies. Since the interface charge separation efficiency of sodium sulfite oxidation is almost 100% ($\eta_{sep,\ SO_3^{2-}} = 1$), the charge separation efficiencies can be calculated as follows:

$$\eta_{inj} = J_{SO_3^{2-}} \big/ J_{abs}$$

$$\eta_{sep} = J_{H_2O} \big/ J_{SO_3^{2-}}$$

RESULTS AND DISCUSSION

Characterization of the $BiVO_4/NiO$ Composite Photoanode

The morphology and elemental compositions of the synthesized $BiVO_4$, $BiVO_4/NiO$ composite photoanode were studied with SEM and energy dispersive spectroscopy (EDS) in **Figures 1A–H**. **Figure 1A** exhibits the SEM image of nanoporous $BiVO_4$ film. **Figure 1B** shows the SEM image of $BiVO_4/NiO$. NiO nanosheets with size distribution about 5–10 nm are fairly continuous and uniformly loaded on the surface of $BiVO_4$ in large area. The elemental composition and content of $BiVO_4/NiO$ anodes were further investigated by EDS. **Figure 1C** shows the EDS pattern of $BiVO_4/NiO$ photoanode, the weight percentage of elements present in the $BiVO_4/NiO$ photoanode composites are 39.4%, 31.1%, 18.6% and 10.09% for Bi, O, V and Ni, respectively. No other elements or impurities are found. The elemental composition and distribution in the $BiVO_4/NiO$ photoanode were further observed by EDS elemental mapping (**Figures 1D–H**). The results clarify that the elements of Bi, O, V and Ni are present and uniformly distributed in the $BiVO_4/NiO$ photoanode.

The optical absorption properties of pure $BiVO_4$ and $BiVO_4/NiO$ films were investigated by UV-Vis diffuse reflectance spectroscopy. It can be seen that $BiVO_4$ and $BiVO_4/NiO$ show good light absorption properties around 500 nm (**Figure 2A**), corresponding to a band gap of 2.4 eV. Notably, the $BiVO_4/NiO$ sample shows almost the same absorption edge as bare $BiVO_4$ due to the blocking by the thicker $BiVO_4$ layer, indicating that coating of NiO almost rarely affects light absorption of $BiVO_4/NiO$. But the $BiVO_4$ photocathode loaded with NiO co-catalyst shows the relatively low light absorption capacity. The reason is primarily ascribed to the poor optical transparency of the nickel based co-catalyst. (Zhou et al., 2020)

The XRD pattern characterization reveals that the product is composed of three kinds of materials with distinct crystal structures. **Figure 2B** displays the XRD patterns of $BiVO_4$ and $BiVO_4/NiO$ nanocomposites. The XRD diffraction peaks of $BiVO_4$ and $BiVO_4/NiO$ nanocomposites are completely consistent with monoclinic $BiVO_4$ (JCPDS No. 14-0688) and tetragonal SnO_2 (JCPDS No. 46-1088) derived from FTO substrates. No other impurity phases were detected. The appearance of characteristic diffraction peaks at $2\theta = 43.3°$ is corresponding to the (200) crystal plane of the cubic phase NiO, which can be concluded that the composite sample has been successfully prepared.

Performance of the $BiVO_4/NiO$ Composite Photoanode

In order to explore the effect of supported NiO on the PEC performance, the photoelectrochemical water splitting performance of $BiVO_4$ photoanode modified by NiO cocatalyst was studied by electrochemical workstation. Linear sweep voltammetry (LSV) curves reflect the water oxidation properties of $BiVO_4/NiO$ and pure $BiVO_4$. As shown in **Figure 3A**, the photocurrent density of unmodified $BiVO_4$ at 1.23 V vs. RHE is $0.9\ \mathrm{mA/cm^2}$ and the onset potential is about 0.58 V vs. RHE, which is due to its unique structure and specific crystal orientation, leading to rapid transfer and separation of photogenerated carriers. After loading the NiO cocatalyst on $BiVO_4$, the photoelectrode showed significant enhancement at all potentials, obtaining a photocurrent of $1.2\ \mathrm{mA/cm^2}$ at 1.23 V

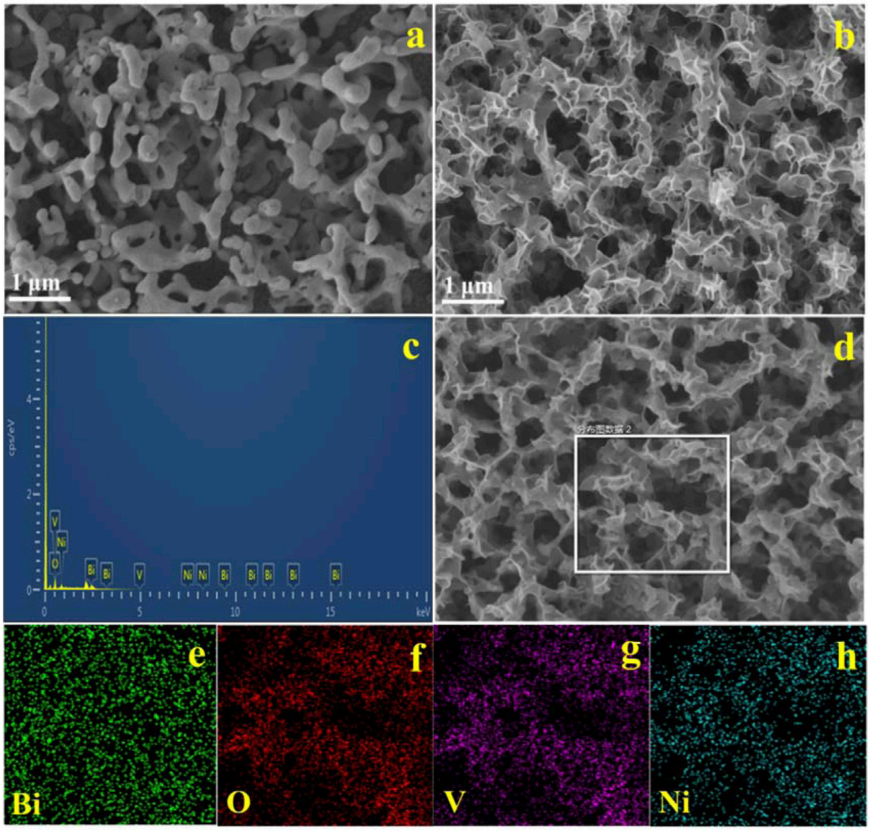

FIGURE 1 | SEM images of the typical samples: **(A)** $BiVO_4$, **(B)** $BiVO_4$/NiO, EDS pattern **(C)** and the EDS elemental mapping **(D–H)** of as prepared $BiVO_4$/NiO photoanode.

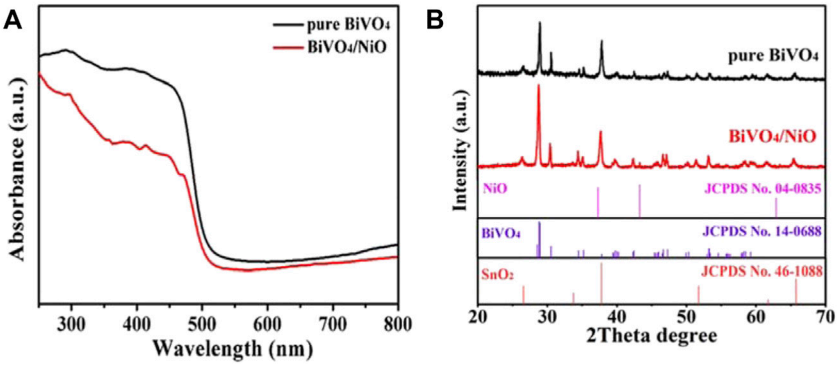

FIGURE 2 | (A) UV–Vis diffuse reflectance spectra of $BiVO_4$ and $BiVO_4$/NiO. **(B)** XRD patterns of the $BiVO_4$ and $BiVO_4$/NiO photoanodes.

vs. RHE, which was higher than that of pristine $BiVO_4$. In particular, $BiVO_4$/NiO obtained a more negative onset potential compared to pure $BiVO_4$, with a negative shift of about 0.35 V (**Figure 3B**). The increased photocurrent density and negatively shifted onset potential clearly indicate that the addition of NiO cocatalyst is a feasible way to enhance the water oxidation capacity of $BiVO_4$ photoanode. **Figure 3C** shows the chopped photocurrent density–voltage (J–V) curves of $BiVO_4$/NiO and pure $BiVO_4$. All the photoanodes show an obvious "photo-switching" effect with fast response. Clearly, the $BiVO_4$/NiO photoanode exhibits a much better PEC performance than $BiVO_4$ film.

The electron-hole pair recombination and charge generation kinetics of photoanode in PEC water oxidation process can be analyzed by EIS. The photoanode was measured at 1.23 V vs. RHE at AM 1.5G (100 mW/cm^2), and the frequency range of the

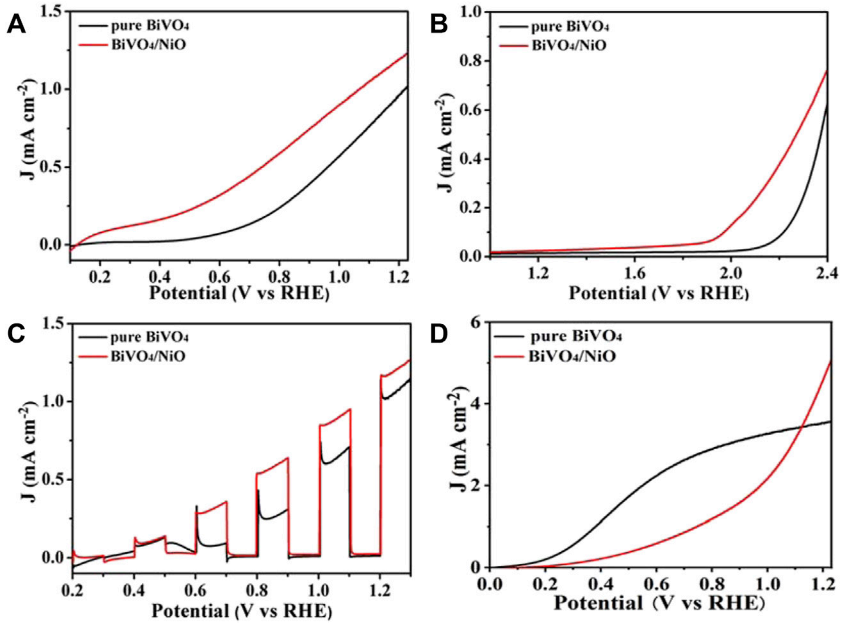

FIGURE 3 | (A) Photocurrent density-voltage curve of $BiVO_4$ and $BiVO_4$/NiO photoanodes. **(B)** Photocurrent density-voltage curve of $BiVO_4$ and $BiVO_4$/NiO photoanodes in the absence of light. **(C)** Chopped linear sweep photocurrent-potential curve of $BiVO_4$ and $BiVO_4$/NiO. **(D)** Sulfite oxidation current curves.

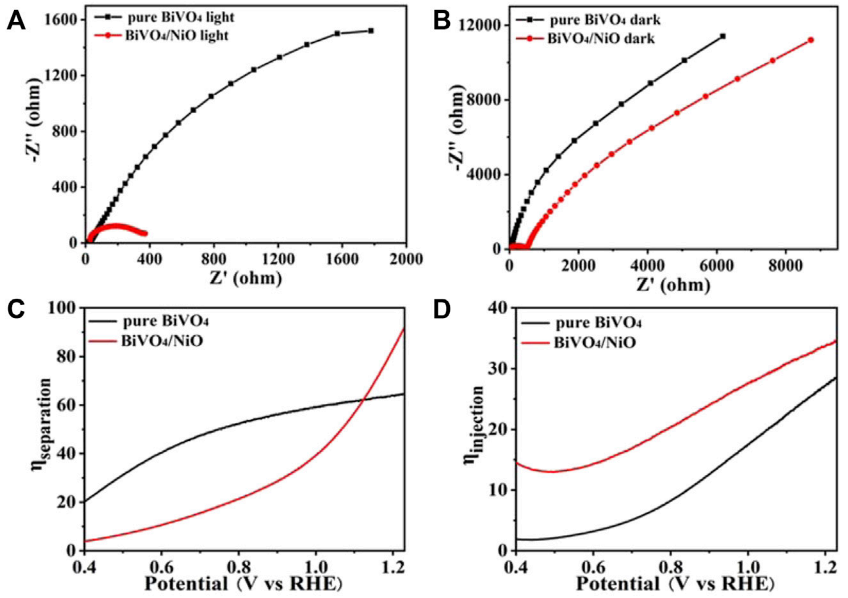

FIGURE 4 | (A) EIS curves of pure $BiVO_4$ and $BiVO_4$/NiO under the light, **(B)** and in the dark. The EIS was measured at 1.23 V vs. RHE under an AM 1.5G solar simulator. **(C)** Charge separation efficiency versus potential curves and **(D)** charge injection efficiency versus potential curves of $BiVO_4$, $BiVO_4$/NiO.

Nyquist plot was from 100 kHz to 0.1 Hz. The results of impedance spectra are useful for analyzing electrochemical surface reactions. The charge transfer resistance of the photoanode surface is estimated from the small semicircle in the Nyquist diagram, and the smaller the radius, the more effective the separation of charges. In addition, the EIS test result of dark reaction condition (**Figure 4B**) is consistent with that under light conditions in **Figure 4A**. The $BiVO_4$/NiO photoanode exhibits the highest charge transportation, suggesting good charge separation ability.

To further explore the charge recombination at the $BiVO_4$ and $BiVO_4$/NiO photoanode interfaces, the charge separation and

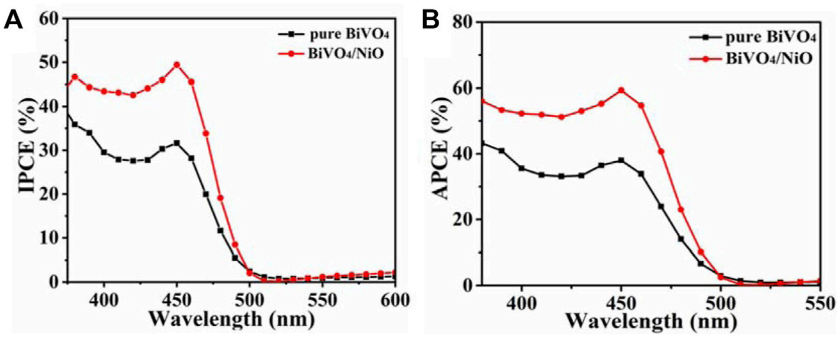

FIGURE 5 | (A) IPCE of $BiVO_4$, $BiVO_4$/NiO measured at 1.23 V vs. RHE in the incident wavelength range from 380 to 600 nm. **(B)** APCE spectra for $BiVO_4$, $BiVO_4$/NiO photocathodes along with the AM 1.5 irradiance spectrum.

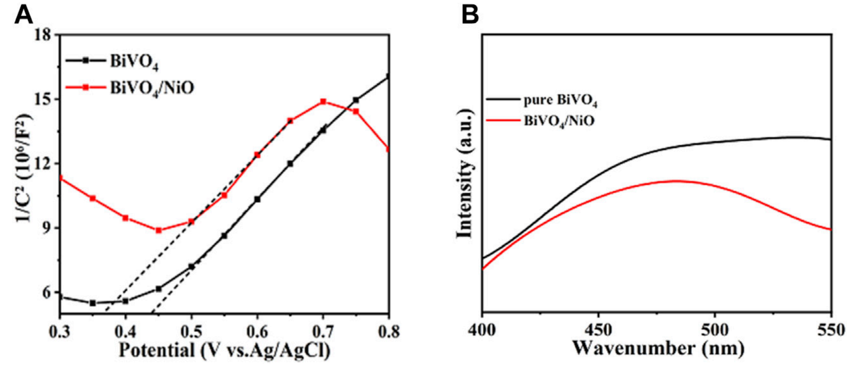

FIGURE 6 | M-S diagram **(A)** and PL spectra of electrodes **(B)**.

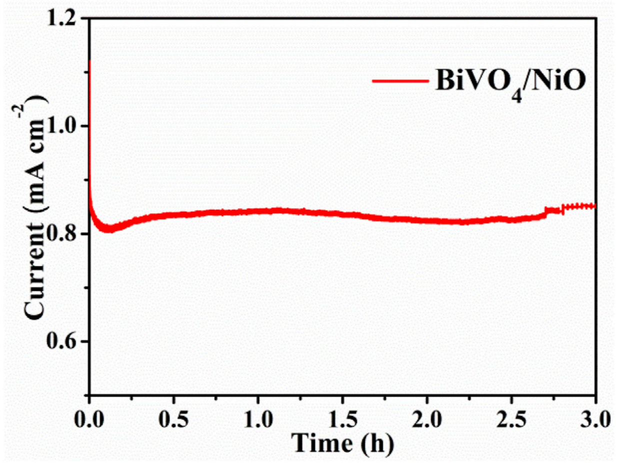

FIGURE 7 | Stability curves of NiO/$BiVO_4$ photoanode under the same conditions.

injection efficiencies were tested in **Figures 4B,C**. Charge separation efficiency is an important parameter to evaluate the proportion of carriers reaching the electrode surface/electrolyte interface to participate in water oxidation (Wang et al., 2017b). Therefore, the constant charge separation efficiency is shown in **Figure 3D**, ascribed to the photocurrent density of the $BiVO_4$/NiO photoanode at an applied potential of 0.6 V vs. RHE when Na_2SO_3 was added to the electrolyte. The separation efficiency of the pure $BiVO_4$ photoanode increases with the applied potential, especially it can reach about 60% at 1.23 V vs. RHE. However, the $BiVO_4$/NiO nanostructured array photoanode exhibits a charge separation efficiency of 90% at 1.23 V vs. RHE. From this point of view, the cocatalyst NiO supported on $BiVO_4$ can significantly improve the charge separation efficiency and facilitate the flow of charge carriers to the electrode surface/electrolyte interface to participate in water oxidation.

The photogenerated holes generated on the surface of the photoanode participate in the water oxidation reaction or recombine with electrons. The charge injection efficiency, defined as the fraction of those holes at the photoanode and electrolyte interface that is used for water oxidation reactions, can be improved by reducing surface recombination or accelerating hole transfer kinetics. (Zhou et al., 2020) As shown in **Figure 4D**, the charge injection efficiency of the pure $BiVO_4$ photoanode reaches 28% 1.23 V vs. RHE. While the charge injection efficiency of the $BiVO_4$/NiO photoanode increases to 35% in the potential range of 1.23 V vs. RHE.

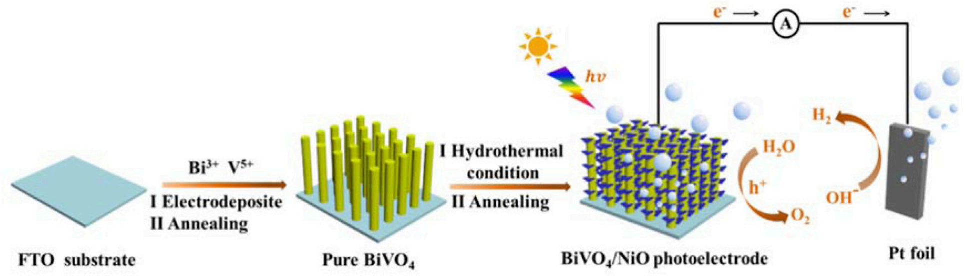

FIGURE 8 | Schematic illustration of the fabrication process of $BiVO_4$/NiO and the light harvesting and carrier separation mechanism in the $BiVO_4$/NiO composite photoanode system.

The quantum efficiencies of $BiVO_4$, $BiVO_4$/NiO photoanodes were determined by measuring incident photon current efficiency (IPCE) and absorbed photon current efficiency (APCE). (Wang et al., 2017b) The calculation of IPCE can refer to the following equation:

$$\text{IPCE} = (J \times 1240)/(P \times \lambda)$$

where J is the current density (mA/cm^2) measured at each specific wavelength, λ is the wavelength of the incident light (nm), and P is the power density of the incident light (mW/cm^2). As shown in **Figure 5A**, $BiVO_4$/NiO nanocomposites exhibit slightly higher IPCE values in the 450–500 nm range compared to bare $BiVO_4$. The PEC performance mainly depends on the light-harvesting efficiency, charge separation efficiency, and collection yield. Since the light-harvesting efficiency is almost unchanged after the modification of the NiO cocatalyst, the enhancement of IPCE may be due to the fast separation of charge carriers and the accelerated water oxidation kinetics of the reaction, resulting in the enhanced photocurrent. The IPCE results are consistent with the above J-V measurements.

To obtain the absorbed photon-current efficiency, the APCE value of the photoanode was measured at 0.6 V vs. RHE, as shown in **Figure 5B**. The APCE value of $BiVO_4$/NiO photoanode is significantly higher than that of $BiVO_4$ from 380 to 500 nm, which is consistent with the overall PEC performance.

Figure 6A shows the Mott Schottky barrier of $BiVO_4$ and $BiVO_4$/NiO. The capacitance-voltage curve is usually used to analyze the reasons for the enhancement of semiconductor performance. In order to better study the reasons for the increase of photocurrent after supporting the cocatalyst. Therefore, the capacitance-voltage curves of $BiVO_4$ and $BiVO_4$/NiO electrodes were measured under dark reaction conditions, and the *x*-axis tangent was made on the curves of $BiVO_4$ and $BiVO_4$/NiO. The tangent was positive, indicating that $BiVO_4$ and $BiVO_4$/NiO are both n-type semiconductors. The smaller slope of the composite electrode, the greater the carrier density. Thus, the $BiVO_4$/NiO electrode has the largest carrier density. The increased carrier density causes the conductivity of $BiVO_4$ to increase and ultimately increases its photocurrent density. Fluorescence spectroscopy (PL) can be used to effectively analyze the separation and recombination effects of photogenerated carriers. As shown in **Figure 6B**, it can be observed that the peak intensity of the $BiVO_4$/NiO electrode is weaker than that of the pure $BiVO_4$ electrode, which indicates that after NiO is loaded on the $BiVO_4$ surface, the recombination rate of photo-generated electrons and holes becomes slower and the charge separation efficiency is improved.

Stability test is an important index parameter to evaluate the effect of photoelectric catalyst and whether it has application value. The stability test of the $BiVO_4$/NiO photoanode was analyzed under continuous irradiation under AM 1.5G. As shown in **Figure 7**, it can be observed that under the continuous irradiation of 3 h, the photocurrent density of the NiO/$BiVO_4$ electrode is not significantly attenuated, indicating that the stability of the $BiVO_4$ photoanode can be improved after loading NiO.

DISCUSSION ON MECHANISM

Based on above results, the possible mechanisms for the enhancement in photoelectrocatalytic activity of $BiVO_4$/NiO composite photoanode and the specific photogenerated charge carriers transfer are shown in **Figure 8**. In $BiVO_4$ with monoclinic scheelite structure, the Bi 6s and O 2p orbits hybridize to form the valence band. When the $BiVO_4$/NiO composite is irradiated with visible light, electron-hole pairs are generated in $BiVO_4$, in which electrons in the valence band are excited to the conduction band and holes stay in the conduction band. With the NiO coated on the surface of $BiVO_4$, NiO as a cocatalyst regulates the built-in electric field of $BiVO_4$ photocatalyst, accelerates the charge separation rate of $BiVO_4$, and thus the PEC performance of $BiVO_4$ is improved.

CONCLUSION

In conclusion, we successfully fabricated an efficient nanostructured $BiVO_4$/NiO photoanode by a two-step method of hydrothermal calcination synthesis. The PEC performance of the NiO-modified $BiVO_4$ photoanode was improved in 0.5 M Na_2SO_4 (pH = 6.86) electrolyte, reaching 1.2 mA/cm^2 at 1.23 V vs. RHE, higher than that of the pure $BiVO_4$ sample. In particular, the onset potential of the composite photoanode has a significant negative shift. The excellent PEC performance could be attributed to NiO abundant nano flake structure, the improved charge separation/transport efficiency and accelerated water oxidation kinetics thanks to the deposited NiO cocatalyst. Our work shed a light for design and fabrication of nanostructured photoelectrode with efficient PEC performances.

DATA AVAILABILITY STATEMENT

The original contributions presented in the study are included in the article/Supplementary Material, further inquiries can be directed to the corresponding author.

REFERENCES

Chen, P. (2015). A Promising Strategy to Fabricate the Cu/BiVO4 Photocatalysts and Their Enhanced Visible-Light-Driven Photocatalytic Activities. *J. Mater. Sci. Mater. Electron.* 27 (3), 2394–2403. doi:10.1007/s10854-015-4037-5

Crake, A., Christoforidis, K. C., Kafizas, A., Zafeiratos, S., and Petit, C. (2017). CO 2 Capture and Photocatalytic Reduction Using Bifunctional TiO 2/MOF Nanocomposites under UV-Vis Irradiation. *Appl. Catal. B: Environ.* 210, 131–140. doi:10.1016/j.apcatb.2017.03.039

Dotan, H., Sivula, K., Grätzel, M., Rothschild, A., and Warren, S. C. (2011). Probing the Photoelectrochemical Properties of Hematite (α-Fe2O3) Electrodes Using Hydrogen Peroxide as a Hole Scavenger. *Energy Environ. Sci.* 4 (3), 958–964. doi:10.1039/c0ee00570c

Fukuzumi, S., Lee, Y.-M., and Nam, W. (2018). Thermal and Photocatalytic Production of Hydrogen with Earth-Abundant Metal Complexes. *Coord. Chem. Rev.* 355, 54–73. doi:10.1016/j.ccr.2017.07.014

Guo, K., Liu, Z., Zhou, C., Han, J., Zhao, Y., Liu, Z., et al. (2014). Fabrication of TiO2 Nano-Branched arrays/Cu2S Composite Structure and its Photoelectric Performance. *Appl. Catal. B: Environ.* 154-155, 27–35. doi:10.1016/j.apcatb.2014.02.004

Han, J., Liu, Z., Guo, K., Wang, B., Zhang, X., and Hong, T. (2015). High-efficiency Photoelectrochemical Electrodes Based on ZnIn2S4 Sensitized ZnO Nanotube Arrays. *Appl. Catal. B: Environ.* 163, 179–188. doi:10.1016/j.apcatb.2014.07.040

Hong, T., Liu, Z., Liu, H., Liu, J., Zhang, X., Han, J., et al. (2015). Preparation and Enhanced Photoelectrochemical Performance of Selenite-Sensitized Zinc Oxide Core/shell Composite Structure. *J. Mater. Chem. A.* 3 (8), 4239–4247. doi:10.1039/c4ta05973e

Huang, J., Hu, G., Ding, Y., Pang, M., and Ma, B. (2016). Mn-doping and NiFe Layered Double Hydroxide Coating: Effective Approaches to Enhancing the Performance of α-Fe2O3 in Photoelectrochemical Water Oxidation. *J. Catal.* 340, 261–269. doi:10.1016/j.jcat.2016.05.007

Huang, J., Zhang, Y., and Ding, Y. (2017). Rationally Designed/Constructed CoOx/WO3 Anode for Efficient Photoelectrochemical Water Oxidation. *ACS Catal.* 7 (3), 1841–1845. doi:10.1021/acscatal.7b00022

Iwase, A., Ng, Y. H., Ishiguro, Y., Kudo, A., and Amal, R. (2011). Reduced Graphene Oxide as a Solid-State Electron Mediator in Z-Scheme Photocatalytic Water Splitting under Visible Light. *J. Am. Chem. Soc.* 133 (29), 11054–11057. doi:10.1021/ja203296z

Kenney, M. J., Gong, M., Li, Y., Wu, J. Z., Feng, J., Lanza, M., et al. (2013). High-performance Silicon Photoanodes Passivated with Ultrathin Nickel Films for Water Oxidation. *Science* 342 (6160), 836–840. doi:10.1126/science.1241327

Kim, C.-H., Han, J.-Y., Lim, H., Lee, K.-Y., and Ryi, S.-K. (2018). Hydrogen Production by Steam Methane Reforming in Membrane Reactor Equipped with Pd Membrane Deposited on NiO/YSZ/NiO Multilayer-Treated Porous Stainless Steel. *J. Membr. Sci.* 563, 75–82. doi:10.1016/j.memsci.2018.05.037

Kuang, Y., Jia, Q., Nishiyama, H., Yamada, T., Kudo, A., and Domen, K. (2016). A Front-Illuminated Nanostructured Transparent BiVO$_4$ Photoanode for >2% Efficient Water Splitting. *Adv. Energ. Mater.* 6, 1501645. doi:10.1002/aenm.201501645

Li, L., Xiao, S., Li, R., Cao, Y., Chen, Y., Li, Z., et al. (2018). Nanotube Array-like WO3 Photoanode with Dual-Layer Oxygen-Evolution Cocatalysts for Photoelectrocatalytic Overall Water Splitting. *ACS Appl. Energ. Mater.* 1 (12), 6871–6880. doi:10.1021/acsaem.8b01215

Li, S., Chen, Z., Kong, W., Jia, X., Cai, J., and Dong, S. (2017). Effect of Polyethylene Glycol on the NiO Photocathode. *Nanoscale Res. Lett.* 12, 501. doi:10.1186/s11671-017-2267-6

AUTHOR CONTRIBUTIONS

Z-QW: Writing—review and editing. HJW: Methodology.

FUNDING

This work was financially supported by the National Natural Science Foundation of China (Nos. 51773184 and U1810114).

Liu, Z., Guo, K., Han, J., Li, Y., Cui, T., Wang, B., et al. (2014). Dendritic TiO2/ln2S3/AgInS2Trilaminar Core-Shell Branched Nanoarrays and the Enhanced Activity for Photoelectrochemical Water Splitting. *Small* 10 (15), 3153–3161. doi:10.1002/smll.201400622

Malathi, A., Madhavan, J., Ashokkumar, M., and Arunachalam, P. (2018). A Review on BiVO$_4$ Photocatalyst: Activity Enhancement Methods for Solar Photocatalytic Applications. *Appl. Catal. A: Gen.* 555, 47–74. doi:10.1016/j.apcata.2018.02.010

Roger, I., Shipman, M. A., and Symes, M. D. (2017). Earth-abundant Catalysts for Electrochemical and Photoelectrochemical Water Splitting. *Nat. Rev. Chem.* 1 (1), 0003. doi:10.1038/s41570-016-0003

Trotochaud, L., Young, S. L., Ranney, J. K., and Boettcher, S. W. (2014). Nickel-Iron Oxyhydroxide Oxygen-Evolution Electrocatalysts: The Role of Intentional and Incidental Iron Incorporation. *J. Am. Chem. Soc.* 136 (18), 6744–6753. doi:10.1021/ja502379c

Wang, L., Duan, S., Jin, P., She, H., Huang, J., Lei, Z., et al. (2018). Anchored Cu(II) Tetra(4-Carboxylphenyl)porphyrin to P25 (TiO2) for Efficient Photocatalytic Ability in CO2 Reduction. *Appl. Catal. B: Environ.* 239, 599–608. doi:10.1016/j.apcatb.2018.08.007

Wang, Q., He, J., Shi, Y., Zhang, S., Niu, T., She, H., et al. (2017b). Designing non-noble/semiconductor Bi/BiVO4 Photoelectrode for the Enhanced Photoelectrochemical Performance. *Chem. Eng. J.* 326, 411–418. doi:10.1016/j.cej.2017.05.171

Wang, Q., He, J., Shi, Y., Zhang, S., Niu, T., She, H., et al. (2017a). Synthesis of MFe 2 O 4 (M = Ni, Co)/BiVO 4 Film for Photolectrochemical Hydrogen Production Activity. *Appl. Catal. B: Environ.* 214, 158–167. doi:10.1016/j.apcatb.2017.05.044

Wang, Q., Niu, T., Wang, L., Yan, C., Huang, J., He, J., et al. (2018). FeF2/BiVO4 Heterojuction Photoelectrodes and Evaluation of its Photoelectrochemical Performance for Water Splitting. *Chem. Eng. J.* 337, 506–514. doi:10.1016/j.cej.2017.12.126

Wang, Z.-Q., Wang, H., Wu, X.-F., and Chang, T.-L. (2020). Oxygen Vacancies and P-N Heterojunction Modified BiOBr for Enhancing Donor Density and Separation Efficiency under Visible-Light Irradiation. *J. Alloys Compd.* 834, 155025. doi:10.1016/j.jallcom.2020.155025

Wang, Z., Lei, Q., Wang, Z., Yuan, H., Cao, L., Qin, N., et al. (2020). *In-situ* Synthesis of Free-Standing Feni-Oxyhydroxide Nanosheets as a Highly Efficient Electrocatalyst for Water Oxidation. *Chem. Eng. J.* 395, 125180. doi:10.1016/j.cej.2020.125180

Wang, Z., and Wang, L. (2018). Photoelectrode for Water Splitting: Materials, Fabrication and Characterization. *Sci. China Mater.* 61 (6), 806–821. doi:10.1007/s40843-018-9240-y

Weng, B., Grice, C. R., Meng, W., Guan, L., Xu, F., Yu, Y., et al. (2018). Metal-Organic Framework-Derived CoWP@C Composite Nanowire Electrocatalyst for Efficient Water Splitting. *ACS Energ. Lett.* 3 (6), 1434–1442. doi:10.1021/acsenergylett.8b00584

Xu, X., Zou, Q., Yuan, Y., Ji, F., Fan, Z., and Zhou, B. (2014). Preparation of BiVO4-Graphene Nanocomposites and Their Photocatalytic Activity. *J. Nanomater.* 2014, 1–6. doi:10.1155/2014/401697

Zeng, Q., Chang, S., Beyhaqi, A., Lian, S., Xu, H., Xie, J., et al. (2020). Efficient Solar Hydrogen Production Coupled with Organics Degradation by a Hybrid Tandem Photocatalytic Fuel Cell Using a Silicon-Doped TiO2 Nanorod Array with Enhanced Electronic Properties. *J. Hazard. Mater.* 394, 121425. doi:10.1016/j.jhazmat.2019.121425

Zeng, Q., Chang, S., Beyhaqi, A., Wang, M., and Hu, C. (2019). Efficient Electricity Production Coupled with Water Treatment via a Highly Adaptable, Successive

Water-Energy Synergistic System. *Nano Energy* 67, 104237. doi:10.1016/j.nanoen.2019.104237

Zeng, Q., Chang, S., Wang, M., Li, M., Deng, Q., Xiong, Z., et al. (2021a). Highly-active, Metal-free, Carbon-Based ORR Cathode for Efficient Organics Removal and Electricity Generation in a PFC System. *Chin. Chem. Lett.* 32 (7), 2212–2216. doi:10.1016/j.cclet.2020.12.062

Zeng, Q., Fu, X., Chang, S., Zhang, Q., Xiong, Z., Liu, Y., et al. (2021b). Ordered Ti-Doped Fevo4 Nanoblock Photoanode with Improved Charge Properties for Efficient Solar Water Splitting. *J. Colloid Interf. Sci.* 604, 562–567. doi:10.1016/j.jcis.2021.07.037

Zhai, Y., Yin, Y., Liu, X., Li, Y., Wang, J., Liu, C., et al. (2017). Novel Magnetically Separable BiVO 4/Fe 3 O 4 Photocatalyst: Synthesis and Photocatalytic Performance under Visible-Light Irradiation. *Mater. Res. Bull.* 89, 297–306. doi:10.1016/j.materresbull.2017.01.011

Zhang, J., Liu, Z., and Liu, Z. (2016). Novel WO3/Sb2S3 Heterojunction Photocatalyst Based on WO3 of Different Morphologies for Enhanced Efficiency in Photoelectrochemical Water Splitting. *ACS Appl. Mater. Inter.* 8 (15), 9684–9691. doi:10.1021/acsami.6b00429

Zhang, Q., Li, Z., Wang, S., Li, R., Zhang, X., Liang, Z., Han, H., et al. (2016). The Effect of Redox Cocatalysts Location on Photocatalytic Overall Water Splitting over Cubic $NaTaO_3$ Semiconductor Crystals Exposed with Equivalent Facets. *ACS Catal.* 4, 2182–2191. doi:10.1021/acscatal.5b02503

Zhang, Y., Wang, D., Zhang, X., Chen, Y., Kong, L., Chen, P., et al. (2016). Enhanced Photoelectrochemical Performance of Nanoporous BiVO 4 Photoanode by Combining Surface Deposited Cobalt-Phosphate with Hydrogenation Treatment. *Electrochimica Acta* 195, 51–58. doi:10.1016/j.electacta.2016.02.137

Zhou, C., Wang, S., Zhao, Z., Shi, Z., Yan, S., and Zou, Z. (2018). A Facet-dependent Schottky-Junction Electron Shuttle in a BiVO4 {010}-Au-Cu2 O Z-Scheme Photocatalyst for Efficient Charge Separation. *Adv. Funct. Mater.* 28 (31), 1801214. doi:10.1002/adfm.201801214

Zhou, S., Chen, K., Huang, J., Wang, L., Zhang, M., Bai, B., et al. (2020). Preparation of Heterometallic CoNi-MOFs-Modified $BiVO_4$: a Steady Photoanode for Improved Performance in Photoelectrochemical Water Splitting. *Appl. Catal. B: Environ.* 266, 118513. doi:10.1016/j.apcatb.2019.118513

Zhou, S., Yue, P., Huang, J., Wang, L., She, H., and Wang, Q. (2019). High-performance Photoelectrochemical Water Splitting of BiVO4@Co-MIm Prepared by a Facile *In-Situ* Deposition Method. *Chem. Eng. J.* 371, 885–892. doi:10.1016/j.cej.2019.04.124

Zhou, X., Liu, R., Sun, K., Friedrich, D., McDowell, M. T., Yang, F., et al. (2015). Interface Engineering of the Photoelectrochemical Performance of Ni-Oxide-Coated N-Si Photoanodes by Atomic-Layer Deposition of Ultrathin Films of Cobalt Oxide. *Energ. Environ. Sci.* 8, 2644–2649. doi:10.1039/c5ee01687h

Conflict of Interest: The authors declare that the research was conducted in the absence of any commercial or financial relationships that could be construed as a potential conflict of interest.

frontiers | Frontiers in Chemistry

ORIGINAL RESEARCH
published: 03 June 2022
doi: 10.3389/fchem.2022.900962

Electrocatalytic Reduction of Nitrate *via* Co_3O_4/Ti Cathode Prepared by Electrodeposition Paired With IrO_2-RuO_2 Anode

Chuan Wang*[1], *Zhifen Cao*[1], *Hongtao Huang*[1], *Hong Liu*[2] *and Sha Wang*[2]***

[1]Key Laboratory for Water Quality and Conservation of the Pearl River Delta, Ministry of Education, Institute of Environmental Research at Greater Bay, Guangzhou University, Guangzhou, China, [2]Chongqing Institute of Green and Intelligent Technology, Chinese Academy of Sciences, Chongqing, China

Nitrate pollution is already a global problem, and the electrocatalytic reduction of nitrate is a promising technology for the remediation of wastewater and polluted water bodies. In this work, Co_3O_4/Ti electrodes were prepared by electrodeposition for the electrocatalytic reduction of nitrate. The morphology, chemical, and crystal structures of Co_3O_4/Ti and its catalytic activity were investigated. Then, the electrocatalytic nitrate reduction performance of Co_3O_4/Ti as the cathode was evaluated by monitoring the removal efficiencies of nitrate (NO_3^--N) and total nitrogen (TN), generation of reduction products, current efficiency (CE), and energy consumption (EC) at different operating conditions. Under the catalysis of Co_3O_4/Ti, NO_3^- was reduced to N_2 and NH_4^+, while no NO_2^- was produced. After the introduction of chloride ions and IrO_2-RuO_2/Ti as the anode, NH_4^+ was selectively oxidized to N_2. The removal efficiencies of NO_3^--N (at 100 mg/L) and TN after 2 h were 91.12% and 60.25%, respectively (pH 7.0; Cl^- concentration, 2000 mg/L; current density, 15 mA/cm^2). After 4 h of operation, NO_3^--N and TN were completely removed. However, considering the EC and CE, a 2-h reaction was the most appropriate. The EC and CE were 0.10 kWh/g NO_3^-N and 40.3%, respectively, and electrocatalytic performance was maintained after 10 consecutive reduction cycles (2 h each). The cathode Co_3O_4/Ti, which is prepared by electrodeposition, can effectively remove NO_3^--N, with low EC and high CE.

Keywords: nitrate removal, electrocatalytic, Co_3O_4/Ti, reduction, IrO_2-RuO_2

Edited by:
Qingyi Zeng,
University of South China, China

Reviewed by:
Huawei Song,
Sun Yat-sen University, China
Qing Lan,
Guangdong Polytechnic of Environmental Protection Engineering, China

****Correspondence:***
Sha Wang
wangsha@cigit.ac.cn

Specialty section:
This article was submitted to Inorganic Chemistry, a section of the journal Frontiers in Chemistry

Received: 21 March 2022
Accepted: 19 April 2022
Published: 03 June 2022

Citation:
Wang C, Cao Z, Huang H, Liu H and Wang S (2022) Electrocatalytic Reduction of Nitrate via Co_3O_4/Ti Cathode Prepared by Electrodeposition Paired With IrO_2-RuO_2 Anode.
Front. Chem. 10:900962.
doi: 10.3389/fchem.2022.900962

1 INTRODUCTION

Nitrate (NO_3^-) contamination of surface water and groundwater is a global environmental problem associated with increasing populations, and its hazards have attracted much attention (Jasper et al., 2014; Khalil et al., 2016; Serio et al., 2018). The accumulation of plant nutrients such as NO_3^- and phosphate in water can accelerate eutrophication, a process that increases the biomass of a water body as its biological diversity decreases, for example, due to increases in invertebrates and fish. In the extreme, a state of hypoxia can exist, resulting in the loss of the aquatic ecosystems (Kubicz et al., 2018; Zhang et al., 2021). Although NO_3^- is chemically stable, it can be microbially reduced to reactive nitrite in the oral cavity and stomach, which has been linked to liver damage, methemoglobinemia, and cancer in animals (Spalding and Exner, 1993; Elmidaoui et al., 2001; Barakat et al., 2020).

Currently, microbial denitrification is widely used for the large-scale remediation of NO_3^- pollution (Clauwaert et al., 2007; Della Rocca and Belgiorno V Meriç, 2007). Many other methods of NO_3^- removal have been explored such as reverse osmosis, ion exchange, ammonia stripping, electrodialysis, catalytic reduction, and electrocatalytic reduction (Kapoor and Viraraghavan, 1997; Yang and Lee, 2005; Della Rocca and Belgiorno V Meriç, 2007). Among these techniques, the electrocatalytic reduction of NO_3^- is a promising and clean technology because the electron reductants neither introduce pollutants nor adversely affect the environment (Garcia-Segura et al., 2018; Gayen et al., 2018).

The mechanism of the electrochemical NO_3^- reduction reaction (NO_3^--RR) involves anodic oxidation and cathodic reduction in which NO_3^- is reduced to NO_2^-, NH_4^+, and N_2 on the active sites of the cathode according to **Eqs 1–3** (Zhang et al., 2021):

$$NO_3^- + 2e^- + H_2O \rightarrow NO_2^- + 2OH^-, \tag{1}$$

$$NO_2^- + 6e^- + 6H_2O \rightarrow NH_4^+ + 8OH^-, \tag{2}$$

$$2NO_3^- + 10e^- + 6H_2O \rightarrow N_2 + 12OH^-. \tag{3}$$

The choice of the cathode material is important in this process. To date, most studies have used high-cost noble metal cathodes, such as Pt, Rh, and Pd, which may limit their commercial application (Taguchi and Feliu, 2007; Yang et al., 2014; Soto-Hernández et al., 2019). Co_3O_4 is a cost-effective catalyst, and the preparation of a CuO-Co_3O_4/Ti electrode by the sol-gel method for electrochemical reduction of NO_3^- was recently reported (Yang et al., 2020). The system demonstrated the complete removal of NO_3^- after 3 h at a current density of 20 mA/cm^2.

NO_2^- and NH_4^+ generated at the cathode (**Eqs. (1)** and **(2)**) diffuse to the anode where they are adsorbed onto the surface and subsequently oxidized to NO_3^- and N_2 (**Eqs. (4)** and **(5)**) (Zhang et al., 2021):

$$NO_2^- + H_2O \rightarrow NO_3^- + 2e^- + 2H^+, \tag{4}$$

$$2NH_4^+ \rightarrow N_2 + 6e^- + 6H^+. \tag{5}$$

When Cl^- is present in the electrolyte, the following reactions also occur at the anode (**Eqs. 6–9**) (Zhang et al., 2021):

$$2Cl^- \rightarrow Cl_2 + 2e^-, \tag{6}$$

$$Cl_2 + H_2O \rightarrow HOCl + Cl^- + H^+, \tag{7}$$

$$HOCl \rightarrow ClO^- + H^+, \tag{8}$$

$$2NH_4^+ + 3ClO^- \rightarrow N_2 + 3H_2O + 2H^+ + 3Cl^-. \tag{9}$$

The electrochemical NO_3^--RR involves NO_3^- reduction at the cathode and ammonium nitrogen (NH_4^+-N) oxidation at the anode. Cl_2 generated at the anode (**Eq. (6)**) immediately forms hypochlorite (**Eq. (7)**), which selectively oxidizes NH_4^+ to N_2 (Su et al., 2017). Hence, the efficient anodic oxidation of chloride ions is a key requirement for this process, and the anode materials used in the chlor-alkali industry, which obtain Cl_2 by electrolysis of sodium chloride, provide a useful reference (Yi et al., 2007). Among these materials, IrO_2-RuO_2 is a good choice due to its low overpotential, high chlorine selectivity, and long-term stability (Chen et al., 2007). In addition, the electrocatalytic reduction of NO_3^--N is also affected by reaction potential, current, solution pH, battery structure, and anode material.

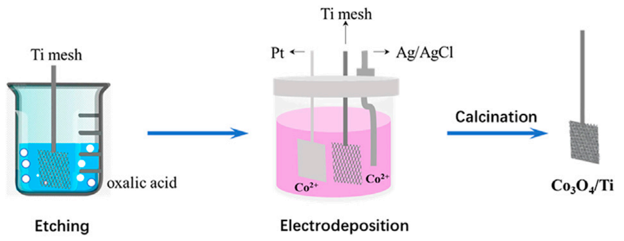

FIGURE 1 | Schematic of the preparation procedure.

Here, a catalytic cathode was prepared by the *in situ* electrodeposition of Co_3O_4 on a titanium substrate (Co_3O_4/Ti) to obtain improved electrocatalytic performance. IrO_2-RuO_2/Ti was employed as the anode for the effective removal of NH_4^+-N and TN. The aim of this study was to obtain simultaneous electrochemical NO_3^- reduction and oxidation of the *in situ*-generated NO_2^- and NH_4^+ into N_2 gas. The morphology and structure of Co_3O_4/Ti were characterized using conventional methods, and its performance in NO_3^- removal was evaluated under different operating conditions. The current efficiency (CE) and energy consumption (EC) of the system were also measured to assess its commercial application.

2 EXPERIMENTAL SECTION

2.1 Chemicals and Materials

The Ti mesh and Ti plate (99.5% purity, 0.6 mm, 10 mesh) were purchased from Lanruiyinde Electrochemical Materials Co., Ltd. (China). The Pt plate was obtained from Aidahengsheng Co., Ltd., (Tianjin, China). All chemicals were of analytical grade. Potassium nitrate and sodium hydroxide were purchased from Aladdin Biochemical Technology Co., Ltd. (Shanghai, China). Cobalt nitrate hexahydrate, sodium eicosyl, hexachloroiridic acid, and ruthenium (III) chloride were obtained from Macklin Biochemical Technology Co., Ltd. (Shanghai, China). Solutions were prepared using deionized water (>15 MΩ cm) obtained from an Elix® 3 purification system (Millipore, United States). Simulated wastewater was prepared by adding potassium nitrate to deionized water.

2.2 Preparation of Co_3O_4/Ti Cathode and IrO_2-RuO_2/Ti Anode

Samples of the Ti mesh and Ti plate (3 × 4 cm, 12 cm^2) were degreased with NaOH solution (40 wt%) at 95°C for 2 h before etching by boiling in oxalic acid solution (10 wt%) for 2 h. The treated samples were then rinsed with deionized water and stored in ethanol until further use.

As shown in **Figure 1**, the Co_3O_4/Ti electrode was prepared using an electrodeposition method. A three-electrode system was employed in a single compartment cell using the pretreated Ti mesh as the cathode, the Pt plate as the anode, and an Ag/AgCl reference electrode. The electrodeposition solution comprised boric acid (0.5 M), cobalt nitrate hexahydrate (0.1 M), and sodium eicosyl sulfonate (2.0 g/L). Following electrodeposition at a current of 0.25 A for 5 min, the electrode was cleaned with deionized water and oven-dried (60°C) before heating at 5°C/min to 500°C (hold 2 h) in a muffle furnace to effect calcination. The treated samples were allowed to cool naturally to room temperature.

The IrO_2-RuO_2/Ti anode was prepared by using a thermal decomposition method. A mixed solution of hexachloroiridic acid and ruthenium (III) chloride in n-butanol (molar ratio, 2:1) was evenly coated onto the surfaces of the pretreated titanium plate, dried at 105°C for 10 min, and then calcined at 500°C for 15 min. The process was repeated until the weight of the titanium plate increased by about 10 g/cm^2. Finally, the electrode was washed with deionized water before use.

2.3 Characterization of the Co_3O_4/Ti Cathode

Surface morphology and elemental composition were studied by field-emission scanning electron microscopy (SEM) and energy-dispersive X-ray spectroscopy (EDS) on a Phenom ProX system (Thermo Fisher Scientific, United States) at an accelerating voltage of 15 kV. The crystal structure of Co_3O_4 was examined by X-ray diffraction (XRD) with an X'pert Powder system (Malvern Panalytical, Malvern, UK) using Cu Kα (λ = 1.5406 Å) irradiation.

2.4 Electrochemical Measurements

NO_3^--RR tests were performed in a single chamber electrolytic cell (200 ml) using a three-electrode system, with Co_3O_4/Ti (or Ti as required), Pt plate, and Ag/AgCl as the working, counter, and reference electrodes, respectively. The electrolyte was prepared using Na_2SO_4 (0.1 M) and different concentrations of NO_3^--N (KNO_3) as required. Linear sweep voltammetry (LSV), and electrolysis tests were performed in an electrochemical workstation (Metrohm Autolab M204, Switzerland). Prior to the electrochemical test, oxygen was removed by bubbling high-purity N_2 through the electrolyte for ≥20 min, and continuously fed during the experiments.

Electrolysis measurements were performed at an optimum current density of 15 mA/cm^2, and aliquots of the reaction solutions (2 ml) were removed at predetermined time intervals to measure the concentrations of NO_3^--N, NO_2^--N, and NH_4^+-N. The effects of chlorine on NO_3^--RR and the stability of the Co_3O_4/Ti cathode electrode were assessed at a current density of 15 mA/cm^2 for 2 h and an initial NO_3^--N concentration of 100 mg/L.

2.5 Analytical Methods

During the NO_3^--RR, the formation of NO, N_2O, and NH_3 are negligible, and hence, the generated gaseous products can be considered as N_2 (Teng et al., 2018). UV-Vis spectroscopy was used to measure the concentrations of NO_3^--N, NO_2^--N, NH_4^+-N, and total nitrogen (TN) (Evolution 201, Thermofisher Scientific Co., Ltd.), and their removal efficiencies were calculated according to **Eqs (10)–(12)**:

$$NO_3^- - N\ removal = \frac{C_0\left(NO_3^- - N\right) - C_t\left(NO_3^- - N\right)}{C_0\left(NO_3^- - N\right)} \times 100\%, \tag{10}$$

$$NH_4^+ - N\ generation = \frac{C_t\left(NH_4^+ - N\right)}{C_0\left(NO_3^- - N\right)} \times 100\%, \tag{11}$$

$$TN\ removal = \frac{C_0\left(TN\right) - C_t\left(TN\right)}{C_0\left(TN\right)} \times 100\%, \tag{12}$$

where $C_0(NO_3^-$-N) (mg/L) is the initial concentration of NO_3^--N, $C_t(NO_3^-$-N) (mg/L) is the concentration of NO_3^--N at time t, $C_t(NH_4^+$-N) (mg/L) is the concentration of NH_4^+-N at time t, C_0(TN) (mg/L) is the initial concentration of TN, and C_t(TN) (mg/L) is the concentration of TN at time t.

EC was calculated using **Eq. 13** (Zhang et al., 2016):

$$\mathrm{EC} = \frac{\mathrm{UIt}}{\mathrm{V}\left(\mathrm{C_0} - \mathrm{C_t}\right)}, \tag{13}$$

where U is the cell potential (V), I is the current (A), t is the reaction time (h), and V is the volume of reaction solution (L).

The CE for TN removal rates was obtained using **Eq. 14**:

$$\mathrm{CE}\,(\%) = \frac{\left(\mathrm{C_0} - \mathrm{C_t}\right) \times \mathrm{V}}{\mathrm{M} \times \mathrm{Q}} \times \mathrm{n} \times 96485 \times 100\%, \tag{14}$$

where M is the molar mass of N (14 g/mol), Q is the amount of electricity passing through the electrode, and n is the number of electrons obtained from the complete reduction of NO_3^--N (calculated according to the conversion of NO_3^- to N, n = 5).

3 RESULTS AND DISCUSSION

3.1 Electrode Characterizations and Chemical Tests

SEM was used to depict the electrode surface morphology of Co_3O_4/Ti. **Figure 2** shows that spherical particles (3–5 μm) of Co_3O_4 were observed on the surface of Co_3O_4/Ti at different magnifications, confirming its deposition on the Ti mesh. SEM-EDS elemental mapping of a surface region of the Co_3O_4/Ti cathode (**Figure 3**) gave a value of 26.26 atom% for Co, indicating that the element was successfully deposited on the titanium mesh.

Figure 4 shows the XRD patterns of the calcined Co_3O_4/Ti electrode and their comparison with the reference powder patterns of cubic phase Co_3O_4 (PDF#42–1467) and Ti (PDF#44–1294). The characteristic peaks observed at 2θ of 35.1°, 38.4°, 40.2°, 53.0°, 62.9°, 70.7°, 76.2°, and 77.4° correspond to (100), (002), (101), (102), (110), (103), (112), and (201) planes of Ti (PDF#44–1294), respectively (**Figure 4A**). Inspection of the enlarged pattern obtained from the Co_3O_4/Ti cathode (**Figure 4B**) showed that the main peaks of Co_3O_4 at 2θ=31.3°, 36.9°, 44.8°, 59.4°, 65.2°, and 74.1°, correspond to the (220), (311), (400), (511), (440), and (620) planes of Co_3O_4, respectively. These results were in good agreement with the standard cubic phase (PDF#42–1467).

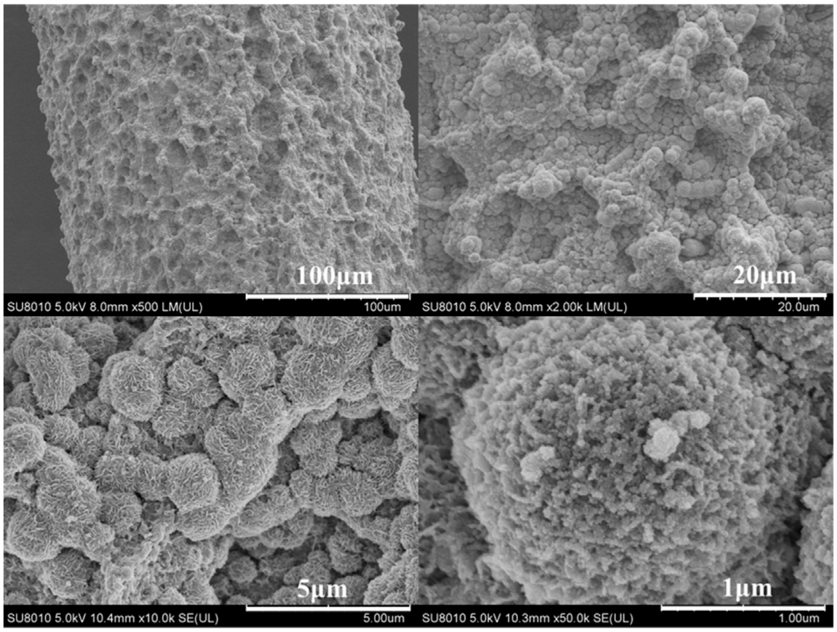

FIGURE 2 | SEM image of Co_3O_4/Ti at different resolutions.

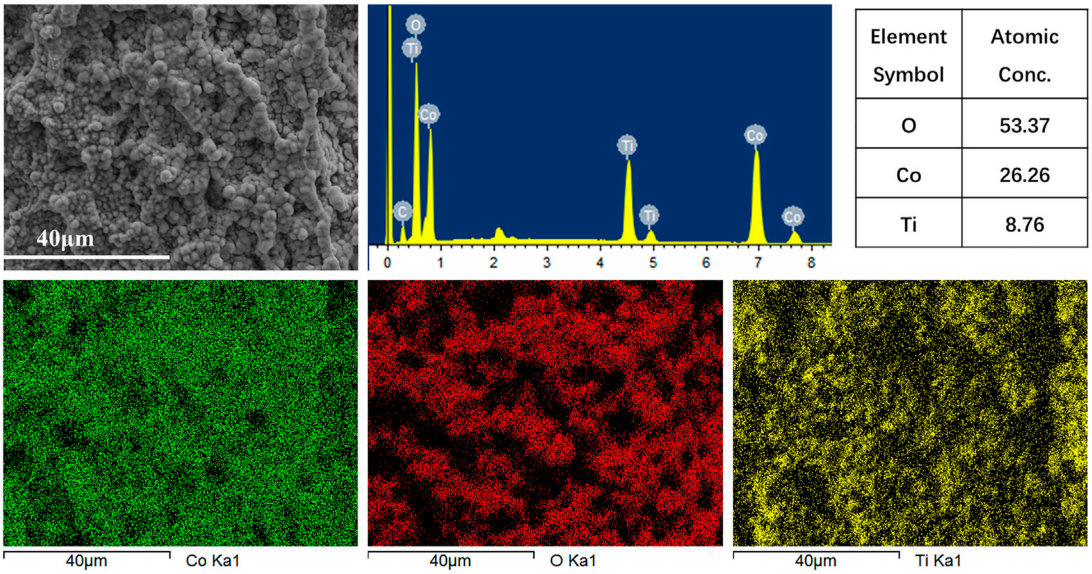

Element Symbol	Atomic Conc.
O	53.37
Co	26.26
Ti	8.76

FIGURE 3 | EDS elemental analysis of the surface of Co_3O_4/Ti cathode.

LSV was used to evaluate the electrocatalytic performance of the catalysts toward NO_3^--RR. **Figure 5A** shows the LSV curves obtained with Co_3O_4/Ti and Ti in the presence of NO_3^--N. The onset potential for NO_3^--RR using the Co_3O_4/Ti cathode (-0.7 V) was more positive than that using the Ti mesh (-1.0 V), indicating the improved performance with the composite catalyst. From −0.7 to −1.6 V, Co_3O_4/Ti gave a larger current response at all potentials due to its higher activity toward the NO_3^--RR compared with the Ti mesh. **Figure 5B** shows the effects of increasing NO_3^--N (0–500 mg/L) using Co_3O_4/Ti as the cathode. In the absence of NO_3^--N, the onset potential (i.e., for the electrolysis of water to produce H_2) was −0.9 V. The addition of NO_3^- produced a positive shift in the onset potential, and the corresponding current increased with increasing initial NO_3^--N due to the enhanced reduction reaction activity.

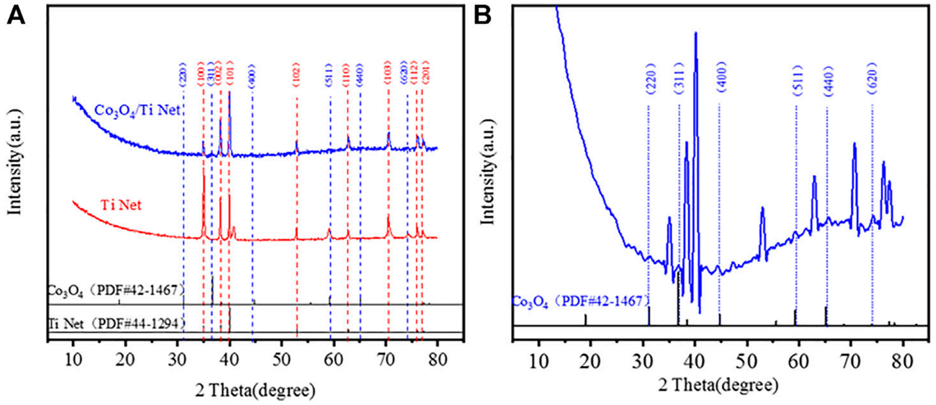

FIGURE 4 | Crystal structure of Co_3O_4/Ti cathode and comparison with the reference XRD powder patterns: **(A)** XRD patterns of Ti and Co_3O_4/Ti cathodes; **(B)** enlarged XRD patterns of Co_3O_4/Ti cathode.

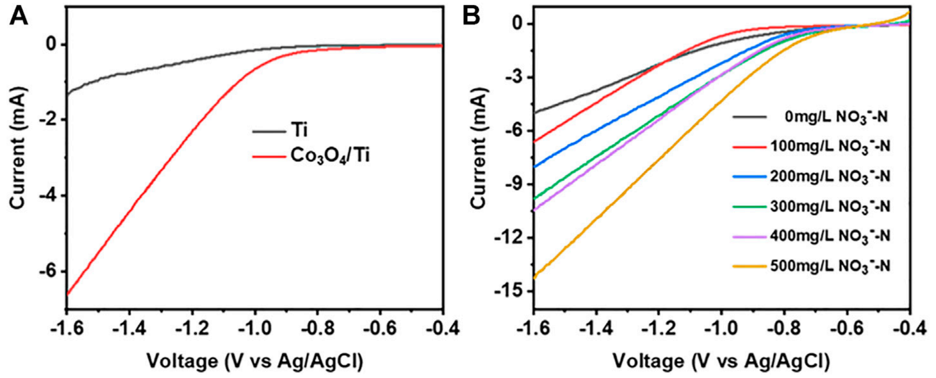

FIGURE 5 | LSV curves illustrating the NO_3^--N removal performance of the catalysts (0.1 M Na_2SO_4, 10 mV/s). **(A)** Effects of different catalysts at constant initial NO_3^--N concentration (100 mg/L). **(B)** Effects of increasing initial NO_3^--N concentrations using the Co_3O_4/Ti cathode.

3.2 Effects of Electrochemical Reaction Parameters on NO_3^--RR Using the Co_3O_4/Ti Cathode

3.2.1 Catalytic Activity of the Co_3O_4/Ti Cathode

To determine the effect of Co_3O_4 on NO_3^-RR activity, the NO_3^--N (100 mg/L) removal efficiencies of the Co_3O_4/Ti and Ti mesh cathodes were compared at a current density of 15 mA/cm^2 with a Pt plate as the anode (**Figure 6**). The results showed that the Co_3O_4/Ti cathode could achieve a NO_3^--N removal efficiency of ~98% in 2 h, compared with 6.4% using the Ti mesh, demonstrating the important role of Co_3O_4 in improving the performance of NO_3^--RR.

3.2.2 Effects of Current Density

Figure 7A,B show the rate of NO_3^--N removal using the Co_3O_4/Ti cathode and the corresponding fit of the experimental data to first-order kinetics. The increased removal efficiency with increasing current density over 5–15 mA/cm^2 could be attributed to enhanced electron transfer on the electrode surface of Co_3O_4/Ti, which increased the rate of NO_3^--RR. However, when the current density was increased from 15 to 20 mA/cm^2, the removal efficiency of NO_3^--N did not improve significantly. At higher current densities, the competing hydrogen evolution reaction consumes the extra charge, and the NO_3^--N removal efficiency decreases. **Figure 7C** shows that there was good correspondence between the reduction of NO_3^--N and the generation of NH_4^+-N. The reduction products were NH_4^+-N and N_2, while NO_2^--N was not detected (**Figure 7D**).

3.2.3 Effect of Initial NO_3^--N Concentration

The effects of initial NO_3^-N concentration on its removal efficiency using the Co_3O_4/Ti cathode and the generation of reduction products are shown in **Figure 8**. At initial NO_3^--N concentrations of <100 mg/L, the removal efficiency of the system was close to 100% at 2 h; and the corresponding reduction products were NH_4^+-N (60%) and N_2. At an initial NO_3^--N concentration of 200 mg/L, the removal efficiency decreased to ~58%, while the NH_4^+-N generation efficiency increased to ~79%. Under this condition, the higher

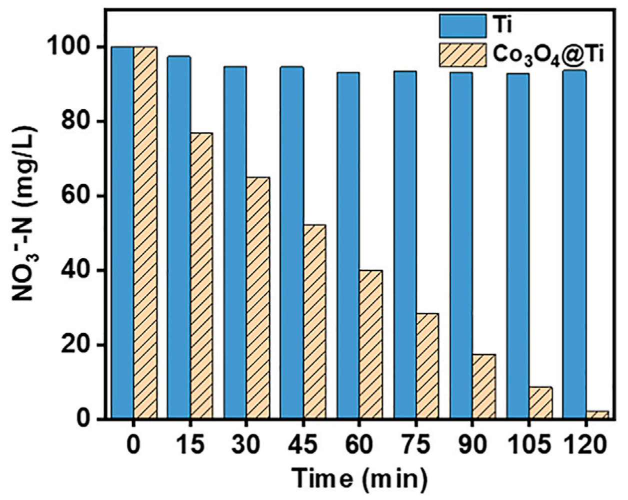

FIGURE 6 | Removal efficiencies of NO$_3^-$-N by the Ti and Co$_3$O$_4$/Ti cathodes (Pt anode; [NO$_3^-$-N], 100 mg/L, 150 ml; current density, 15 mA/cm^2; pH, 7.0; reaction time, 2 h).

initial NO$_3^-$-N concentration suppressed the competing hydrogen evolution reaction, thus reducing its charge consumption at the electrode.

3.3 Effects of Cl$^-$

The main product of electrocatalytic NO$_3^-$ reduction is NH$_4^+$, which is also a contaminant requiring removal. However, in the presence of Cl$^-$, which is widely present in drinking water and industrial water, the active species participating in the oxidative transformation of NH$_4^+$-N to N$_2$ at the anode (**Eqs 6–9**) will increase TN removal. The IrO$_2$-RuO$_2$/Ti electrode is widely employed in the chlor-alkali industry because of its high chlorine evolution performance. To investigate the effects of Cl$^-$ on NH$_4^+$-N generation and NO$_3^-$-N removal, various concentrations of Cl$^-$ were presented to a Co$_3$O$_4$/Ti/IrO$_2$-RuO$_2$/Ti NO$_3^-$-N removal system (**Table 1**). As the concentration of Cl$^-$ increased from 0 to 2000 mg/L, the removal efficiencies of NO$_3^-$-N were all >90%. At 4,000 mg/L Cl$^-$, the removal efficiency decreased to 83.99% due to the oxidation of NH$_4^+$ to NO$_3^-$ by HClO/ClO$^-$. The increase in Cl$^-$ concentration increased the amount of HClO/ClO$^-$ generated by anodic oxidation to reduce NH$_4^+$-N to N$_2$. Hence, NH$_4^+$-N generation decreased and TN removal efficiency increased with increasing Cl$^-$ concentration. The TN removal efficiency reached 78.1% with negligible NH$_4^+$-N generation (0.34%) and without NO$_2^-$-N accumulation.

3.4 Long-Term Stability

In addition to the initial activity, the long-term performance of a catalyst is an essential requirement for its commercial application.

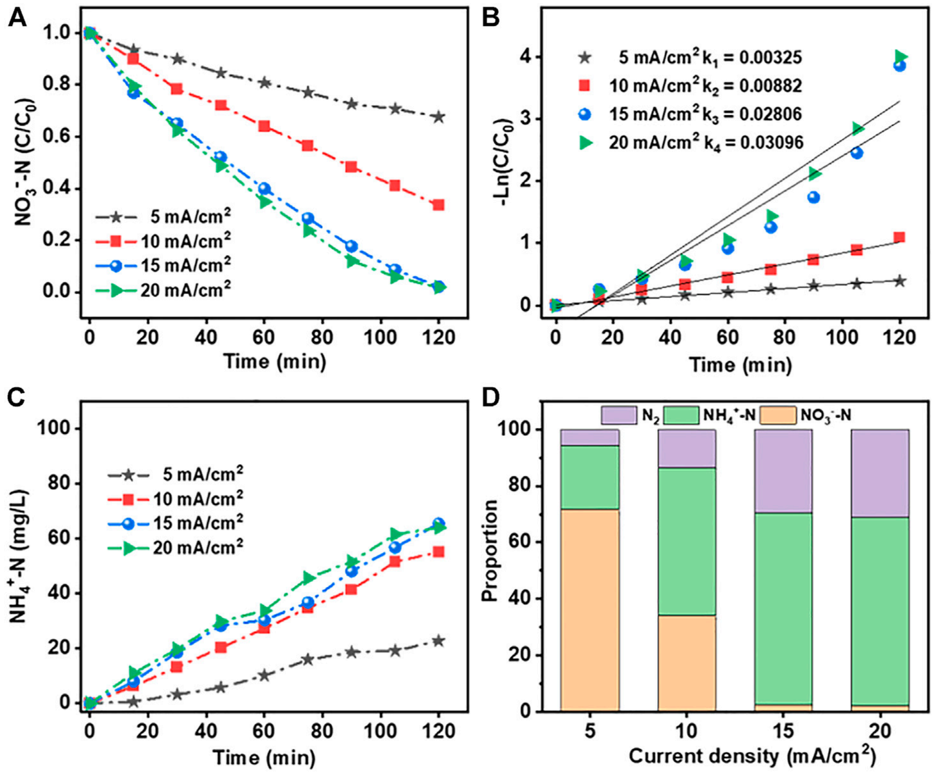

FIGURE 7 | Effects of current density on the NO$_3^-$-RR using the Co$_3$O$_4$/Ti cathode (Pt anode; [NO$_3^-$-N], 100 mg/L, 150 ml; initial pH, 7.0; reaction time, 2 h): **(A)** and **(B)** rate of loss of NO$_3^-$-N and the fit of the data to first-order kinetics; **(C)** rate of generation of NH$_4^+$-N; and **(D)** distribution of the products formed.

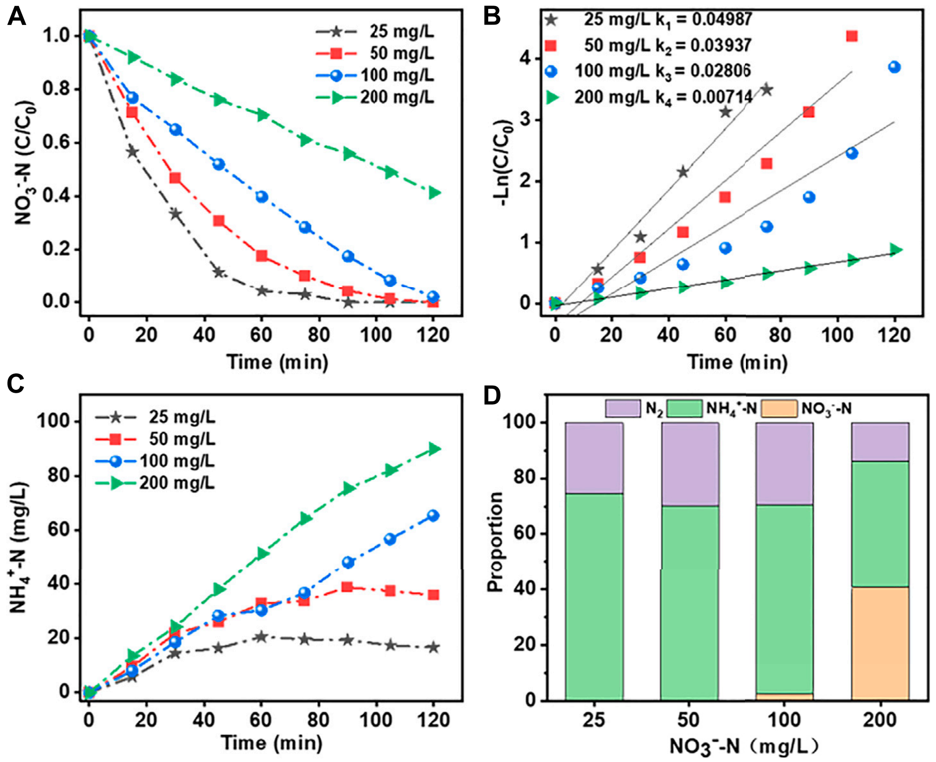

FIGURE 8 | Effects of different initial NO_3^--N concentrations on NO_3^--RR using the Co_3O_4/Ti cathode (Pt anode; reaction solution, 150 ml; current density, 15 mA/cm^2; initial pH, 7.0; reaction time, 2 h): **(A)** and **(B)** Rate of loss of NO_3^--N and the fit of the data to first-order kinetics; **(C)** generation of NH_4^+-N; and **(D)** product distributions.

TABLE 1 | Effects of Cl$^-$ on the Co_3O_4/Ti/IrO_2-RuO_2/Ti NO_3^--N removal system.

Cl$^-$ Concentration (mg/L)	NO_3^--N removal (%)	NO_2^--N generation (%)	NH_4^+-N generation (%)	TN removal (%)
0	92.2	—	54.5	24.8
1000	90.7	—	37.2	38.3
2000	91.1	—	19.9	60.3
4,000	84.0	—	0.340	78.1

Figure 9 shows the changes in NO_3^--N removal and distribution of generated products over 4 h, and 10 consecutive cycles of 2 h each, using the system. At an initial concentration of 100 mg/L, almost all NO_3^--N is converted into N_2 after 4 h (**Figure 9A**). After 10 cycles (**Figure 9B**), the removal efficiencies of NO_3^--N (~90%) and TN remained unchanged.

3.5 EC and CE

EC and CE are key evaluation factors for the commercial electrochemical treatment process (Zeng et al., 2020). The EC and CE under different process conditions using the system were calculated. It can be seen from **Figure 10A,B** that within 1 h after the start of the reaction, EC is lower and CE is higher than those of the follow-up experiments, but the NO_3^--N removal rate is only 58.52%. After 2 h, the NO_3^--N removal efficiency reaches 93.39% with an EC of 0.10 kW h/g NO_3^--N and a CE of 40.3%. There was no significant improvement in the follow-up, but the EC continued to rise, and the CE continued to decline.

The effect of the initial NO_3^--N concentration is demonstrated in **Figures 10C,D**. As the NO_3^--N concentration increased, the EC decreased and CE increased. This can be explained by the increase in the contact area between NO_3^--N and the electrode surface with increasing concentrations, which promotes the reduction reaction. From an economic viewpoint, the results indicate that the Co_3O_4/Ti/IrO_2-RuO_2/Ti electrocatalytic process is more suitable for wastewater with high concentrations of NO_3^-. The small amount of NO_3^- remaining in the electrochemically treated wastewater can be removed by other processes, such as the electrocatalytic removal of NO_3^--N, which can be combined with constructed wetlands for wastewater control/remediation.

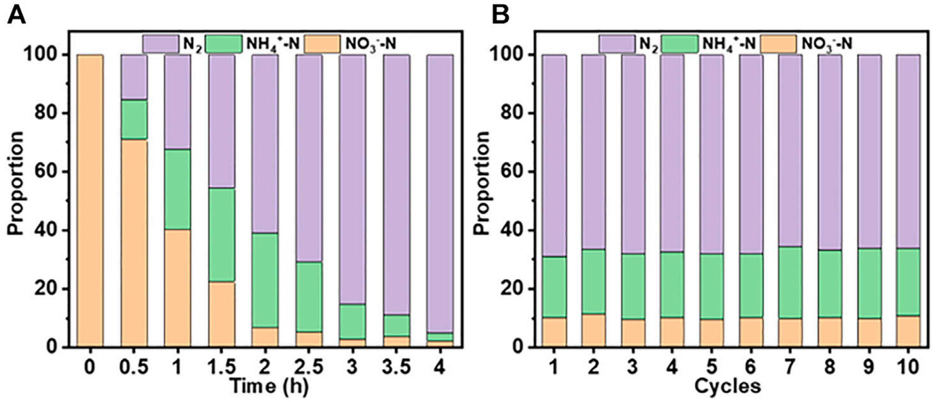

FIGURE 9 | Changes in NO_3^--N removal and the distribution of generated products for the Co_3O_4/Ti/IrO_2-RuO_2/Ti system ([NO_3^--N], 100 mg/L, 150 ml; current density, 15 mA/cm^2; pH, 7.0; cycle time, 2 h). **(A)** Changes over 4 h. **(B)** Changes over 10 cycles.

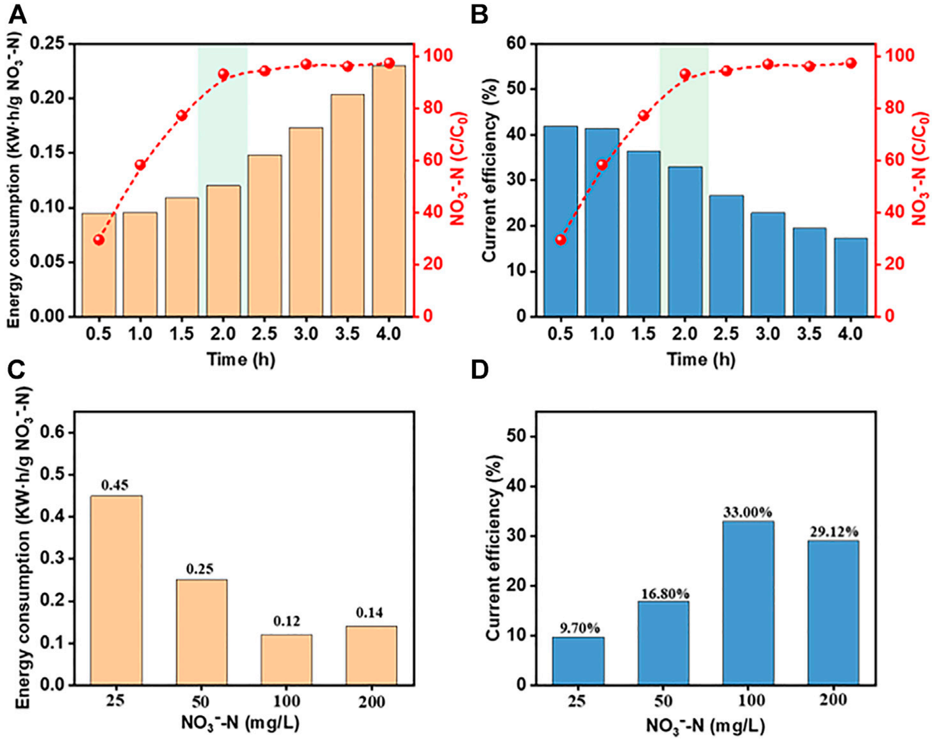

FIGURE 10 | Effects of reaction time and initial NO_3^--N concentrations on the operational efficiency. **(A)** and **(C)** EC; **(B)** and **(D)** CE (pH, 7.0; current density, 15 mA/cm^2; [Cl^-], 2000 mg/L; reaction time, 2 h).

4 CONCLUSION

A Co_3O_4/Ti electrode was successfully prepared by electrodeposition, and the material showed good electrocatalytic performance toward NO_3^--RR. At an initial concentration of 100 mg/L NO_3^--N, the removal rate was ~98% in 2 h (Pt anode; pH, 7.0; current density, 15 mA/cm^2). The corresponding generation of NH_4^+-N was ~60%, while NO_2^--N was not detected. When IrO_2-RuO_2/Ti was employed as the anode in the presence of Cl^- (2000 mg/L), the removal efficiencies for NO_3^--N and TN under the same operating conditions were ~91% and ~60%, respectively, with an EC of 0.10 kW h/g NO_3^--N and a CE of 40.3%. After 4 h of continuous operation, 100% of NO_3^--N was converted into N_2. In addition, the system could maintain the removal efficiencies of ~90% and ~60% for NO_3^--N and TN, respectively, after 10 consecutive cycles (2 h each). This work provides a simple preparation method of electrodeposited Co_3O_4/Ti with good catalytic performance and stability, which provides a new preparation strategy for the Co_3O_4 catalytic electrode.

DATA AVAILABILITY STATEMENT

The original contributions presented in the study are included in the article/Supplementary Material, further inquiries can be directed to the corresponding author.

REFERENCES

Barakat, A., Mouhtarim, G., Saji, R., and Touhami, F. (2020). Health Risk Assessment of Nitrates in the Groundwater of Beni Amir Irrigated Perimeter, Tadla Plain, Morocco. *Hum. Ecol. Risk Assess. Int. J.* 26 (7), 1864–1878. doi:10.1080/10807039.2019.1613631

Chen, J., Shi, H., and Lu, J. (2007). Electrochemical Treatment of Ammonia in Wastewater by RuO2-IrO2-TiO2/Ti Electrodes. *J. Appl. Electrochem* 37 (10), 1137–1144. doi:10.1007/s10800-007-9373-6

Clauwaert, P., Rabaey, K., Aelterman, P., De Schamphelaire, L., Pham, T. H., Boeckx, P., et al. (2007). Biological Denitrification in Microbial Fuel Cells. *Environ. Sci. Technol.* 41 (9), 3354–3360. doi:10.1021/es062580r

Della Rocca, C., Belgiorno Vand Meriç, S. (2007). Overview of *In-Situ* Applicable Nitrate Removal Processes. *Desalination J.* 204 (1), 46–62. doi:10.1016/j.desal.2006.04.023

Elmidaoui, A., Elhannouni, F., Menkouchi Sahli, M. A., Chay, L., Elabbassi, H., Hafsi, M., et al. (2001). Pollution of Nitrate in Moroccan Ground Water: Removal by Electrodialysis. *Desalination J.* 136 (1), 325–332. doi:10.1016/s0011-9164(01)00195-3

Garcia-Segura, S., Lanzarini-Lopes, M., Hristovski, K., and Westerhoff, P. (2018). Electrocatalytic Reduction of Nitrate: Fundamentals to Full-Scale Water Treatment Applications. *Appl. Catal. B Environ.* 236, 546–568. doi:10.1016/j.apcatb.2018.05.041

Gayen, P., Spataro, J., Avasarala, S., Ali, A.-M., Cerrato, J. M., and Chaplin, B. P. (2018). Electrocatalytic Reduction of Nitrate Using Magnéli Phase TiO2 Reactive Electrochemical Membranes Doped with Pd-Based Catalysts. *Environ. Sci. Technol.* 52 (16), 9370–9379. doi:10.1021/acs.est.8b03038

Jasper, J. T., Jones, Z. L., Sharp, J. O., and Sedlak, D. L. (2014). Nitrate Removal in Shallow, Open-Water Treatment Wetlands. *Environ. Sci. Technol.* 48 (19), 11512–11520. doi:10.1021/es502785t

Kapoor, A., and Viraraghavan, T. (1997). Nitrate Removal from Drinking Water-Review. *J. Environ. Eng.* 123 (4), 371–380. doi:10.1061/(asce)0733-9372(1997)123:4(371)

Khalil, A. M. E., Eljamal, O., Jribi, S., and Matsunaga, N. (2016). Promoting Nitrate Reduction Kinetics by Nanoscale Zero Valent Iron in Water via Copper Salt Addition. *Chem. Eng. J.* 287, 367–380. doi:10.1016/j.cej.2015.11.038

Kubicz, J., Pawełczyk, A., and Lochyński, P. (2018). Environmental Health Risk Posed by Contamination of the Individual Water Wells. *Chemosphere* 208, 247–256. doi:10.1016/j.chemosphere.2018.05.182

Serio, F., Miglietta, P. P., Lamastra, L., Ficocelli, S., Intini, F., De Leo, F., et al. (2018). Groundwater Nitrate Contamination and Agricultural Land Use: A Grey Water Footprint Perspective in Southern Apulia Region (Italy). *Sci. Total Environ.* 645, 1425–1431. doi:10.1016/j.scitotenv.2018.07.241

Soto-Hernández, J., Santiago-Ramirez, C. R., Ramirez-Meneses, E., Luna-Trujillo, M., Wang, J-A., Lartundo-Rojas, L., et al. (2019). Electrochemical Reduction of NOx Species at the Interface of Nanostructured Pd and PdCu Catalysts in Alkaline Conditions. *Appl. Catal. B Environ. J.* 259, 118048.

Spalding, R. F., and Exner, M. E. (1993). Occurrence of Nitrate in Groundwater-A Review. *J. Environ. Qual.* 22 (3), 392–402. doi:10.2134/jeq1993.00472425002200030002x

Su, L., Li, K., Zhang, H., Fan, M., Ying, D., Sun, T., et al. (2017). Electrochemical Nitrate Reduction by Using a Novel Co 3 O 4/Ti Cathode. *Water Res.* 120, 1–11. doi:10.1016/j.watres.2017.04.069

Taguchi, S., and Feliu, J. M. (2007). Electrochemical Reduction of Nitrate on Pt(S) [n(111)×(111)] Electrodes in Perchloric Acid Solution. *Electrochimica Acta* 52 (19), 6023–6033. doi:10.1016/j.electacta.2007.03.057

Teng, W., Bai, N., Liu, Y., Liu, Y., Fan, J., and Zhang, W.-x. (2018). Selective Nitrate Reduction to Dinitrogen by Electrocatalysis on Nanoscale Iron Encapsulated in Mesoporous Carbon. *Environ. Sci. Technol.* 52 (1), 230–236. doi:10.1021/acs.est.7b04775

Yang, G. C. C., and Lee, H.-L. (2005). Chemical Reduction of Nitrate by Nanosized Iron: Kinetics and Pathways. *Water Res.* 39 (5), 884–894. doi:10.1016/j.watres.2004.11.030

Yang, J., Sebastian, P., Duca, M., Hoogenboom, T., and Koper, M. T. M. (2014). pH Dependence of the Electroreduction of Nitrate on Rh and Pt Polycrystalline Electrodes. *Chem. Commun.* 50 (17), 2148–2151. doi:10.1039/c3cc49224a

Yang, M., Wang, J., Shuang, C., and Li, A. (2020). The Improvement on Total Nitrogen Removal in Nitrate Reduction by Using a Prepared CuO-Co3O4/Ti Cathode. *Chemosphere* 255, 126970. doi:10.1016/j.chemosphere.2020.126970

Yi, Z., Kangning, C., Wei, W., Wang, J., and Lee, S. (2007). Effect of IrO2 Loading on RuO2-IrO2-TiO2 Anodes: A Study of Microstructure and Working Life for the Chlorine Evolution Reaction. *Ceram. Int.* 33 (6), 1087–1091. doi:10.1016/j.ceramint.2006.03.025

Zeng, Y., Priest, C., Wang, G., and Wu, G. (2020). Restoring the Nitrogen Cycle by Electrochemical Reduction of Nitrate: Progress and Prospects. *Small Methods* 4, 2000672. doi:10.1002/smtd.202000672

Zhang, X., Wang, Y., Liu, C., Yu, Y., Lu, S., and Zhang, B. (2021). Recent Advances in Non-Noble Metal Electrocatalysts for Nitrate Reduction. *Chem. Eng. J.* 403, 126269. doi:10.1016/j.cej.2020.126269

Zhang, Z., Xu, Y., Shi, W., Wang, W., Zhang, R., Bao, X., et al. (2016). Electrochemical-catalytic Reduction of Nitrate over Pd-Cu/γAl 2 O 3 Catalyst in Cathode Chamber: Enhanced Removal Efficiency and N 2 Selectivity. *Chem. Eng. J.* 290, 201–208. doi:10.1016/j.cej.2016.01.063

AUTHOR CONTRIBUTIONS

CW: conceptualization, methodology, data analysis, and writing—original draft. ZC: data curation. HH: validation. HL: resources and funding acquisition. SW: conceptualization, investigation, and writing—review and editing.

FUNDING

This work was supported by the National Natural Science Foundation of China (grant numbers 51978181, 51808527, 51727812, and 52131003).

Conflict of Interest: The authors declare that the research was conducted in the absence of any commercial or financial relationships that could be construed as a potential conflict of interest.

Advantages of publishing in Frontiers

OPEN ACCESS
Articles are free to read
for greatest visibility
and readership

FAST PUBLICATION
Around 90 days
from submission
to decision

HIGH QUALITY PEER-REVIEW
Rigorous, collaborative,
and constructive
peer-review

TRANSPARENT PEER-REVIEW
Editors and reviewers
acknowledged by name
on published articles

Frontiers
Avenue du Tribunal-Fédéral 34
1005 Lausanne | Switzerland

Visit us: www.frontiersin.org
Contact us: frontiersin.org/about/contact

REPRODUCIBILITY OF RESEARCH
Support open data
and methods to enhance
research reproducibility

DIGITAL PUBLISHING
Articles designed
for optimal readership
across devices

FOLLOW US
@frontiersin

IMPACT METRICS
Advanced article metrics
track visibility across
digital media

EXTENSIVE PROMOTION
Marketing
and promotion
of impactful research

LOOP RESEARCH NETWORK
Our network
increases your
article's readership